UNIVERSITY OF LONDON THESIS

Degree PhD Year 2007 Name of Author SRITHAI, Boontanika

Geochemistry and Petrogenesis of Corundum from the Bo Ploi Deposit, Kanchanaburi, Thailand

Boontarika Srithai

Department of Earth Sciences

University College London

A thesis submitted for the degree of

Doctor of Philosophy

July 2007

ProQuest LLC
789 East Eisenhower Parkway
P.O. Box 1346
Ann Arbor, MI 48106-1346

อตฺตา หิ อตฺตโน นาโถ

ตนเป็นที่พึ่งแห่งตน

Acknowledgements

I am so overwhelmed by all sorts of feelings and trying to concentrate on what to write in this context after some (ten) years of twenty starts and stops writing up the thesis then reaching the full stop at this moment. Since it took several years to do, there must be many people, whom directly and indirectly involved in this thesis and I would like to, firstly, express my deeply appreciation to my supervisors Dr Adrian P Jones and Professor G David Price for their timeless supervising, sharp and stimulated discussions that shaping my idea on the research and supporting me on my being. Special thanks to Adrian and his family, Ruth-Nathalie-Marcus, for their cordially company that makes me feel at home.

I would also like to express my gratitude to people who greatly involved in this thesis including Professor Andrew H Rankin for teaching me the study of fluid inclusions and allowing me to work at Kingston University. Professor Anthony Fallick and Dr Adrian Boyce are thanked for the knowledge of oxygen isotope and allowing me on the SURRC facilities. Professor Hilary Downs and Dr Andy Beard are grateful for assistances with microprobe & XRF and their consultation. Dr Michael Wiedenbeck is thanked for his work on SIMS analyses at the GeoForschungZentrum, Potsdam, Germany.

I thank all the staffs at the Department of Earth Sciences, UCL, for their all helps and assistances toward my thesis as well as their friendship and joyful time in London. Thank is also expressed to Steve Ed & Dave U, Tracey, Paula, Hannah, Alison, Andy, Wilson, Ossie, Kamrul, Nickie, Thomai, Giunluigi, Gerd, Rupert, Naser, particularly those who were in OG-11, KLB, I had an amusement time sharing office with you people (Pim-the operator). I owe to my colleagues at the Department of

Geological Sciences, CMU, for helping and giving me all the supports that they can, especially, a valuable time. A special thank is for Associate Professor Dr Y. Panjasawatwong who always has the answers for me and inspiring me in the study of igneous petrology. Without helps from Mr W. Tankaya and Mr J. Taokaew, the field works would not be completed smoothly, thank you very much. My best friend, Tum, is grateful for her affectionate and never tired of giving. Mr Richard Rabe and Ms Tersia Crispim, my god-brother and god-sister, have done so many wonderful things for me. Thank you so much for your hilarious company and your profound and warm advices. You have shown me the art of unconditional giving.

My family, the strongest and dearest alliances; Pol.Lt. Pasawat Srithai, Mrs Uaboonma Srithai, Pam, Krapuk, auntie Jeab & uncle Tong, Jan and Pat, are thanked for their love and understanding, encouragement and always have hope on me. Special thanks to Jo, my (marathon) fiancé, who has been going for a walk with me for more than a decade. Finally, I would like to dedicate the credit of this thesis to my beloved grandparents, Mr Uen and Mrs Boonyuen Kruapanich, who laid a strong foundation of my life with for their loves and beautiful times of my childhood that made me be me.

The darkest hour is the hour before dawn,,,

Abstract

Corundum from the Bo Ploi deposit, Kanchanaburi, Thailand and its associated Tertiary alkali basalt were studied in terms of mineralogy, geochemistry and petrogenesis to ascertain the genetic link between these materials. Gem quality corundum, sapphire variety, is composed of almost pure Al_2O_3 with a small but significant amount of FeO and TiO_2. Optical spectroscopic studies reveal that the blue colour is caused by Fe^{2+} - Ti^{4+} intervalence charge transfer. The syn-genetic inclusions are mineral inclusions, including, feldspar, zircon, spinel, pyrochlore, boehmite, rutile, monazite, and opaque minerals; fluid inclusions and silicate melt inclusions. Microthermometric studies of fluid and silicate-melt inclusions trapped in these sapphires suggest that they grew from silicate-melt under H_2O-, CO_2-rich and hypersaline brine conditions at the temperature approximately 800-1000°C. The silicate-melt inclusions are trachyandesitic compositions indicating that the Bo Ploi corundum is magmatic origin forming from the extreme fractionation of trachyandesitic magma with additional alumina contamination from crustal materials and brought to the surface by later eruption of the Bo Ploi basalt. The sapphires oxygen isotope chemistry, $\delta^{18}O$ 6.5-9.6‰, suggests a mingling of crustal and mantle oxygen isotope thus confirming the role of crustal contamination. The Bo Ploi Tertiary basalt is a within-plate magma of basanite composition, which differentiated through the fractional crystallisation process without a significant crustal contamination, $\delta^{18}O$ 6.0-6.9‰, although numbers of crustal xenoliths including granites, nepheline syenite and quartzite are found in it. The basanites also accommodated mantle xenoliths, mainly spinel lherzolite, which provided P-T scheme based on thermodynamic calculations of coexisting mineral equilibria in the range of 11 to 24 kbar and temperature of 1000 to 1200 °C correspond to the depths of 36 to 79 km in the upper mantle.

Contents

Chapter 3 Fluid Inclusions

Chapter 4 Oxygen Stable Isotope

List of Figures

Chapter 1 Introduction

Chapter 2 Characterisation of Corundum from the Bo Ploi deposit

Chapter 3 Fluid inclusions

Chapter 4 Oxygen isotope

Chapter 5 Mantle xenoliths

Chapter 6 Geochemistry and Petrogenesis of the Bo Ploi Basalt

Chapter 7 Geochemistry and Petrogenesis of the Bo Ploi Basalt

List of Tables

Chapter 1 Introduction

Chapter 2 Characterisation of corundum from the Bo Ploi deposit

Chapter 3 Fluid inclusions

Chapter 4 Oxygen isotope

Chapter 1

Introduction

1.1 Tectonic setting and geology of Thailand

Tectonic setting of Thailand

Thailand is composed of two continental plates i.e. the Shan-Thai, so called Shibumasu, plate to the west and the Indochina, so called Indosina, plate to the east (Bunopas, 1981; Gatinsky *et al.*, 1978; Mitchell, 1981; Piyasin, 1991; Hall, 1996). The Shan-Thai plate is characterised by Precambrian granitoids and high-grade metamorphic rocks and Palaeozoic - Mesozoic sedimentary rocks. The Indochina terrain is including the eastern part of Thailand, Laos, Cambodia and western part of Vietnam, which is characterised by a sequence of the Lower Palaeozoic sedimentary rocks and Permian carbonate and deep-water clastic rocks. The basement rock is, subsequently, overlain by Mesozoic continental sedimentary sequences, known as the Khorat Group. The two plates collided together at the different suggesting timing, including, Devono-Carboniferous (Hahn *et al.*, 1986; Altermann, 1991), middle to late Carboniferous (Wolfart, 1987), middle Permian (Helmcke and Lindenberg, 1983; Helmcke, 1985), late Permian (Burton, 1985), late Permian to early Triassic (Thanasutthipitak, 1978; Cooper *et al.*, 1989; Sattayarak *et al.*, 1989; Hayashi, 1989; Piyasin, 1991), early Triassic (Metcalfe, 1990), middle to late Triassic (Bunopas and Vella, 1978, 1983; Gatinsky *et al.*, 1978; Asnachinda, 1978; Hada, 1990; Panjasawatwong, 1991), late Jurassic (Stokes *et al.*, 1996) and middle to late Cretaceous (Audley-Charles, 1988). The oblique collision of the two plates (Lepvrier, *et al.*, 2004) produced a suture zone, known as the Nan-Chanthaburi Suture zone (Hada *et al.*, 1991) or Nan Suture or Nan-Uttaradit Suture (Barr and Macdonald, 1987, 1989; Hada *et al.*, 1999; Metcalfe, 1999), which is NNW/SSE in orientation. It is recognised by the presence of an ophiolite belt (Hutchison, 1989; Barr and Macdonald, 1991), herein called pre-Permian ophilitic

mafic and ultramafic rocks with blueschists associated distributed in the northeastern of the trend (Barr *et al.*, 1985; Barr and Macdonald, 1987). This suture zone also extended to Lao People Democrat Republic and Vietnam in the north, whereas the evidence of suture on land in the south outcropped in Malaysia peninsular, the Raub-Bentong Suture Zone (Metcalfe, 2000). The plates and plate boundaries of Southeast Asia are illustrated in figure 1.1.

It is believed that the Shan-Thai and the Indochina plates were parts of the margin of the Gondwana (Sengör, 1979, 1984, Bunopas and Vella, 1992; Hall, 1996; Metcalfe, 1999), which are supported by the evidence from fossils, stratigraphic sequences and palaeolatitude. The tectonic events during the formation of Thailand can be divided into two main episodes; palaeotectonic and neotectonic. The palaeotectonic is the events that occurred during mid Palaeozoic to Lower Triassic and it started in Silurian to Lower Carboniferous when the Shan-Thai and the Indochina plates drifted away from the Gondwana (Australia at present) but still in proximity to the parent craton and later on began to build their own sedimentary basins. During Lower Carboniferous to Upper Permian, they drifted further north but still in the lower latitude in the lower Palaeotethys. The Shan-Thai plate moved across the equator to the lower Northern Hemisphere with great speed and distance until it collided with Indochina, which was at that location during the Permian. The collision occurred together with a controversial issue on the degree of underthrusting of the Shan-Thai plate by the Indochina plate (Singharajwarapan and Berry, 2000) or the Shan-Thai plate subducted under the Indochina plate (Barr and McDonald, 1991; Barr *et al.*, 2000; Hisada *et al.*, 2005). The Palaeomagnetic data indicates the northbound movement of the Shan-Thai plate from the low latitude in the southern hemisphere to the low latitude in the northern hemisphere, meanwhile it rotated nearly 180° to the horizontal plane during early Carboniferous to early Triassic. During the mid-Triassic, the Shan-Thai and the

Indochina plates formed suture zone concurrent with the Indochina and the South China suture zone resulted in orogeny episodes where ranges of mountain formed along the suture zones. Granite intruded into the shallow level and perturbed sediments in the basins, simultaneously, rhyolite effused vastly on the land surface. The erosion processes accelerated after the orogeny due to high topographic relief and led to deposits of molasse, including alluvial plain and red beds, however, only the Khorat Basin that formed on the underthrusting west of Indochina plate was completely developed. The palaeotectonics of Thailand is shown in figure 1.2. The Neotectonic is governed by the rifting together with rotating of continental Southeast Asia, where the main influenced force came from the collision of the Indian sub-continent to the Eurasia plate during late Cretaceous to Tertiary enhanced a pre-existing tensional regime and caused the opening of the Gulf of Thailand.

Geology of Thailand

The rocks that are distributed in Thailand have been reported as old as Precambrian to as recent as Quaternary. The complete sequence of rocks is observed only on Shan-Thai plate but not on the Indo-China plate. Here, the distribution of rocks in Thailand are grouped according to their ages as Precambrian rocks, lower Palaeozoic rocks, upper Palaeozoic rocks, Mesozoic rocks and Caenozoic rocks. The geology of Thailand can be simplified and shown in figure 1.3.

Precambrian basement is formed of high grade metamorphic rocks that were regionally metamorphosed and include anatexite or migmatite, orthogneiss, paragneiss, schist, calc-silicate and marble. The rocks distributed along the western margin of the Shan-Thai plate. Pongsapich *et al.*, (1983) suggested that high-grade metamorphic rocks in Thailand showed similar sequence; as orthogneiss, paragneiss, schist, calc-silicate, quartzite and marble, respectively. However, quartzite and marble are present only in relatively minor.

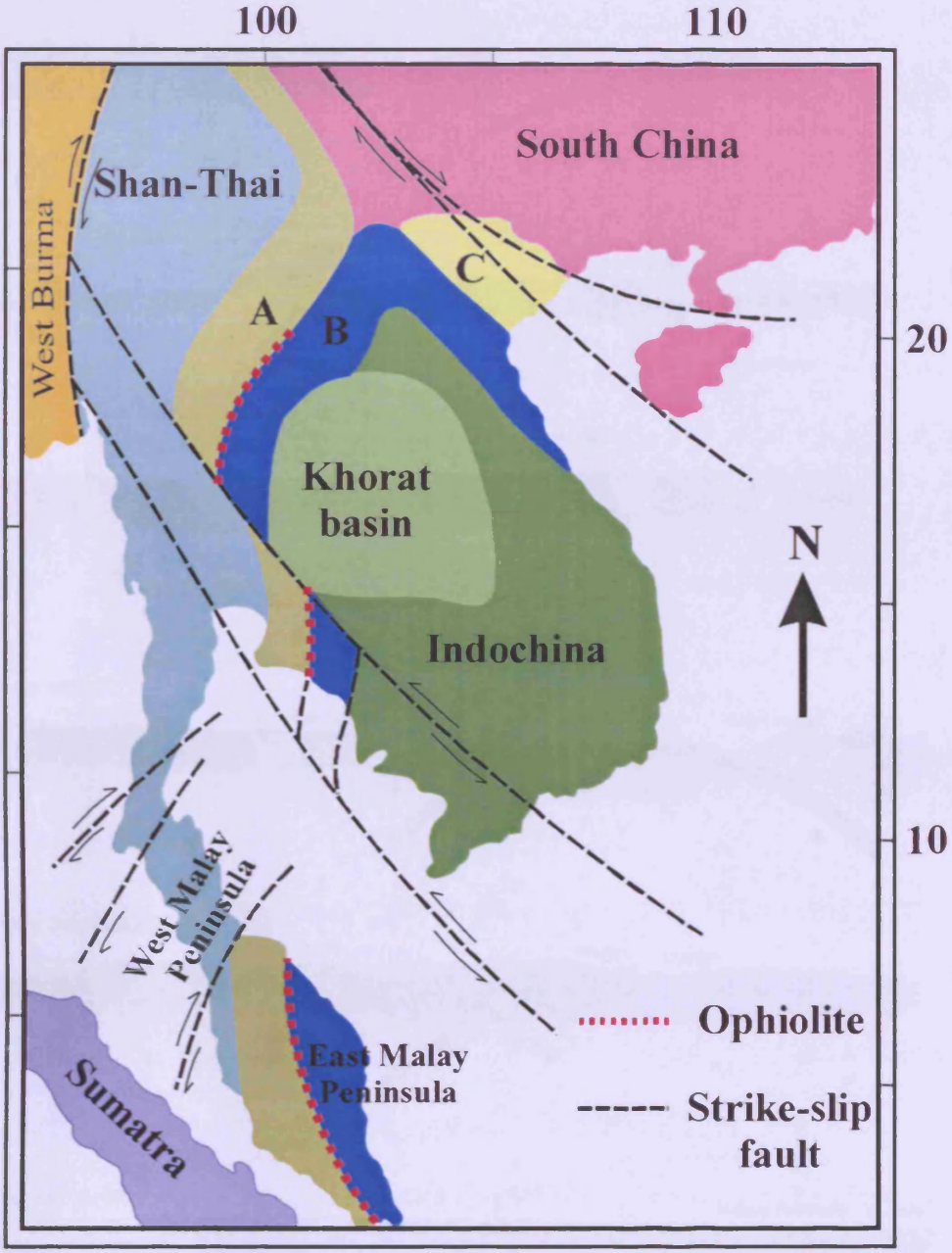

Figure 1.1 Map shows plates and plate boundaries in Southeast Asia; West Burma, Shan-Thai (eastern Burma, western Thailand and northwestern Malaysia), South China and Indochina plates. The fold belts (A=Sukhothai, B=Loei, C=South China) are formed by thick sedimentation along plate margins with trend of ophiolites lie between adjacent fold belts. Modified after Bunopas, 1981)

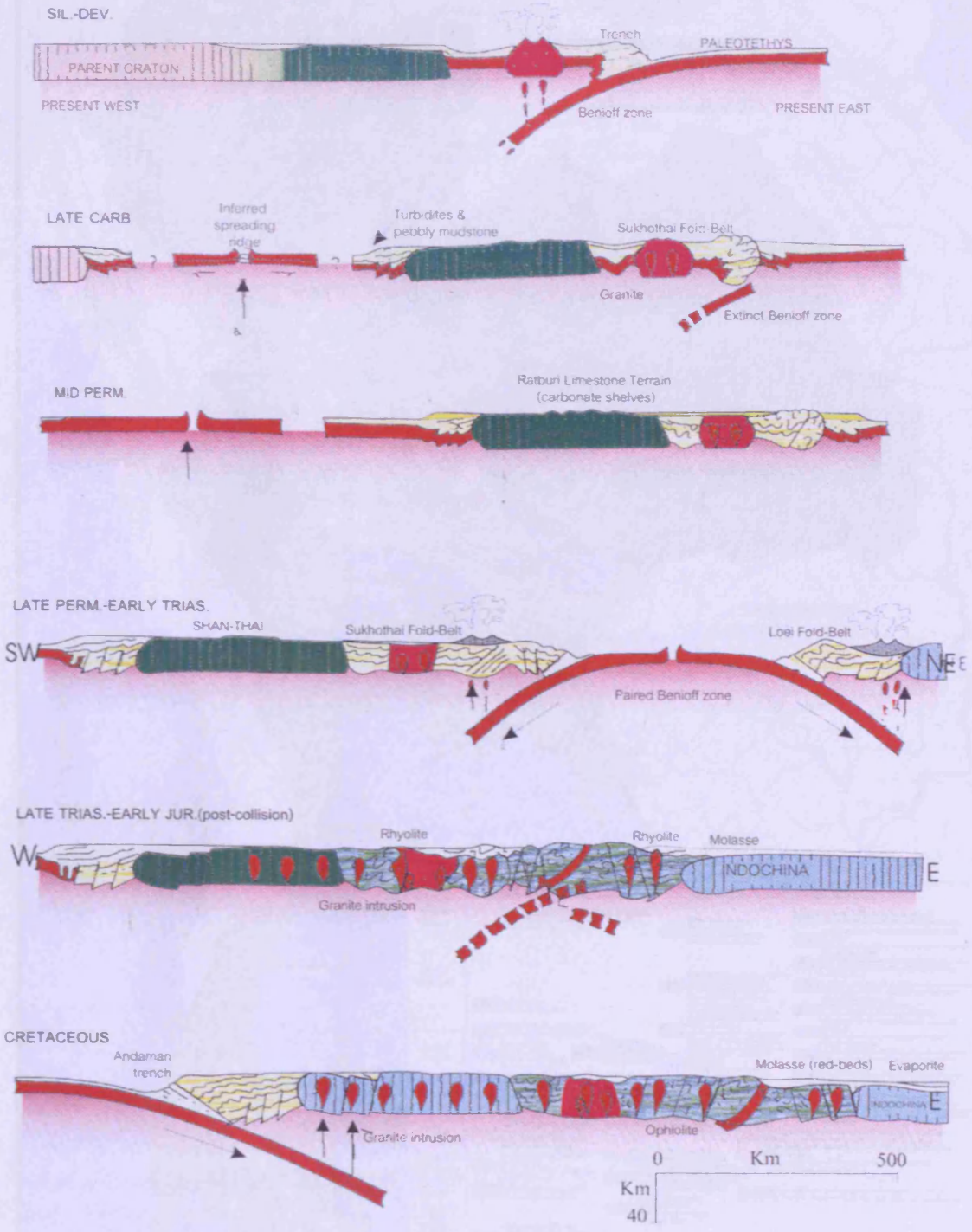

Figure 1.2 Palaeo-tectonic setting of Thailand during Palaeozoic-Mesozoic era (from Bunopas, 1981)

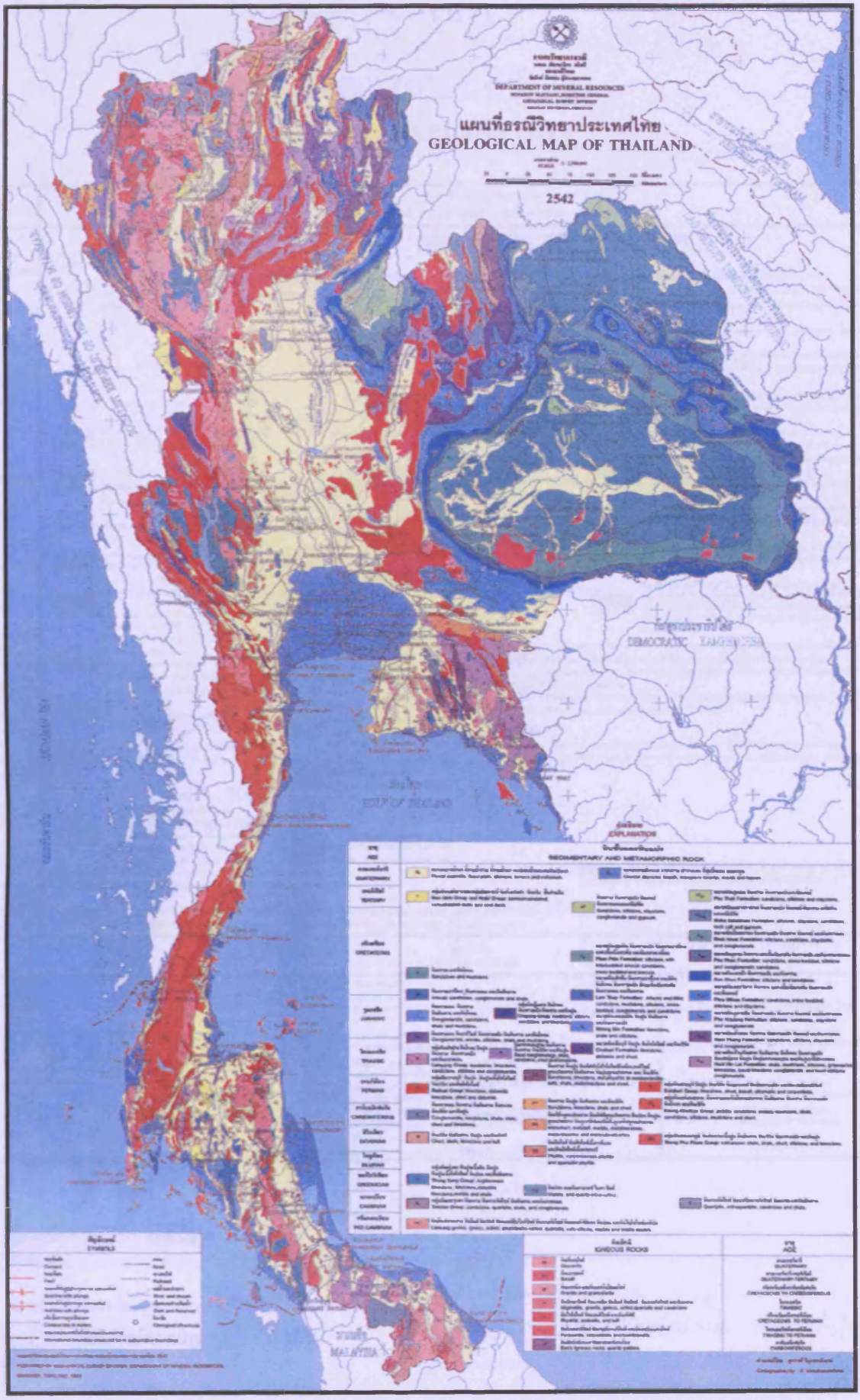

Figure 1.3 Geologic map of Thailand compiled by Geological Survey Division, the Department of Mineral Resources, Bangkok, 1999

EXPLANATION

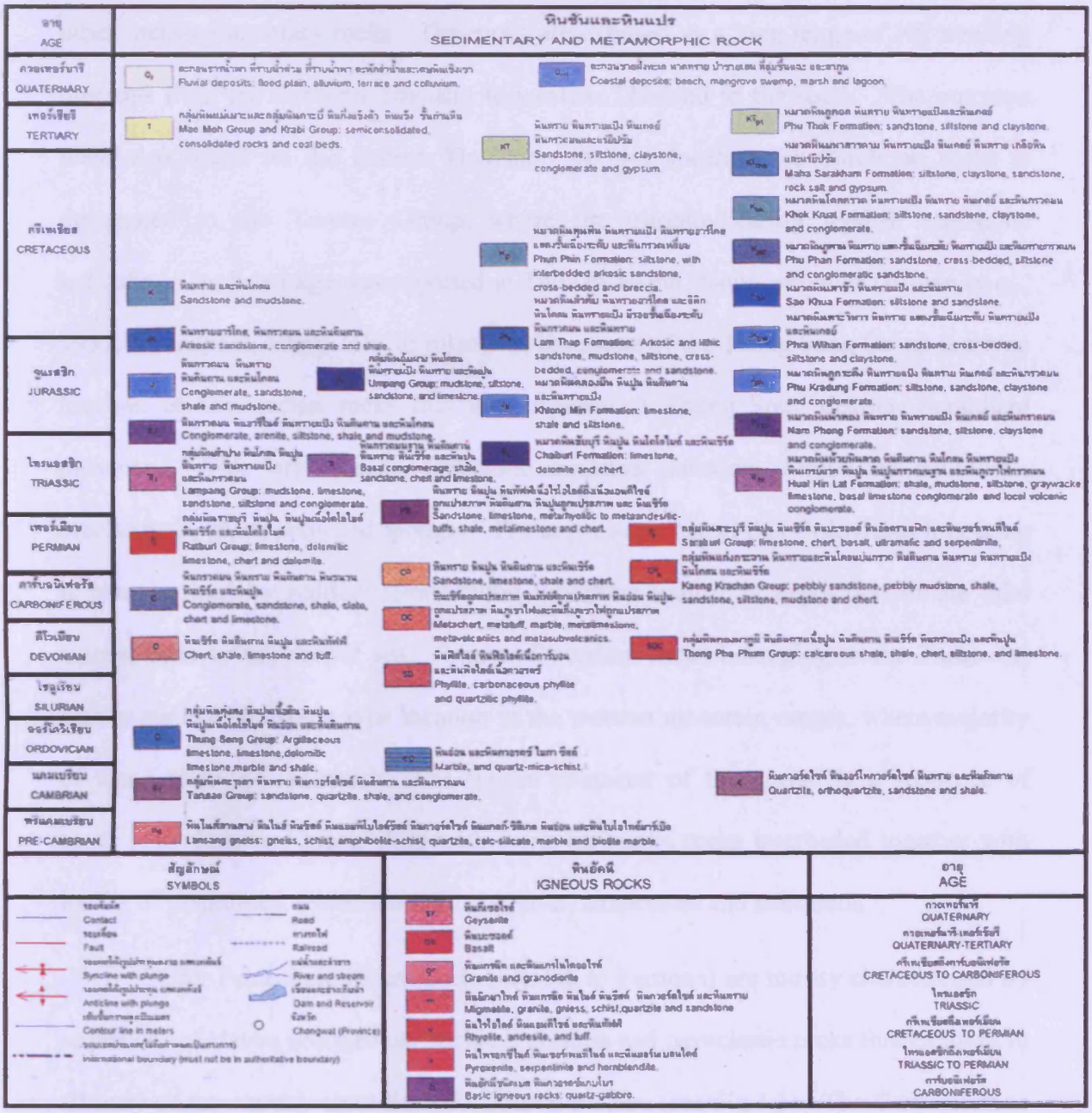

Lower Palaeozoic rocks are composed of the rocks of Cambrian to Devonian age. This group is dominated by sequences of sedimentary rocks and low grade metamorphic rocks including sandstone, shale, carbonated rocks, phyllite, slate and other meta-sedimentary rocks. The rocks are exposed as a long range of NS trending outcrops from the northern Thailand to western Thailand to the south. The outcrops were also found on the eastern Thailand. A type location for Cambrian rocks is designated to the Tarutao Group, where the trilobite-bearing reddish sandstone indicating Cambrian age was reported at Tarutao Island, Satun province (Brown *et al.*, 1951; Javanaphet, 1969). The argillaceous limestone of the Thung Song Group is a type location of Ordovician rocks that was exposed at Thung Song district, Suratthani province. This argillaceous limestone contains abundant fossils of nautiloids, brachiopods, gastropods and sponges. The upper sequence of this Ordovician limestone is characterised by reddish stromatolitic limestone indicating deposition in the tidal marine zone to the deeper sea. Silurian-Devonian rocks belonging to the Tanao Sri Group are named from a type location in the western mountain ranges, where majority of these rocks are exposed. The typical character of this group is a sequence of sandstone, shale and black chert with some carbonate rocks interbeded together with fossils of graptolites, tentaculites, brachiopods, ammonites and nautiloids.

Upper Palaeozoic rocks (Carboniferous to Permian) are mostly characterised by sequences of clastic sedimentary rocks, limestone and pyroclastic rocks that exposed in all parts of the country apart from the Khorat Plateau (see Fig.1.1). The Carboniferous rocks are made up of sandstone, arkosic conglomerate, greywacke, pebbly mudstone and shale with occasionally limestone or chert interbedded. They were partly metamorphosed by Permo-Triassic volcanism and Triassic intrusive bodies, as a result, the rocks in contact boundaries were harden by infiltrating of silica from igneous bodies. The formation of Carboniferous greywacke, pebbly mudstone and diamictite in

the western part of the country has led to a controversy about its genesis, including a process of mass flow deposits (Mitchell *et al.*, 1970; Garson *et al.*, 1975; Sawata *et al.*, 1975; Altermann, 1986) and glaciomarine origin (Ridd, 1971; Bunopas, 1981; Stauffer and Mantajit, 1981), which has gained a wider acceptation. Bunopas and Vella, (1983) reported that paleolatitude of Thailand around Carboniferous – Permian was approximately 30°- 40° in the Southern Hemisphere and the Gondwana was extensively covered by glaciers around that time. The typical Permian rocks are limestone with subordinate amount of sandstone, shale and chert. The Permian limestones are called differently according to their locations. The Ratburi limestone or the Ratburi Group exposed on the western to the southern Thailand. In the eastern Thailand, Permian limestone is so called the Saraburi limestone and the Ngao Group is for Permian limestone in the North. The Permian limestone is a major supplying limestone for construction and cement industries. Numbers of fossils have been reported from these limestones indicating Permian age, for example, rugosa, fusulinids, brachiopods, bivalves and algae (Piyasin, 1972; Ingavat and Douglas, 1981; Sakagami and Hatta, 1982; Tantiwanit *et al.*, 1985; Carey *et al.*, 1995).

Mesozoic rocks in Thailand are dominated by sedimentary sequences exposed on both the Shan-Thai and the Indochina plate. The Mesozoic rocks on the Shan-Thai plate deposited in marine environment, while the rocks on the Indochina plates are rather young and nearly entirely non-marine origin. The Triassic sedimentary sequence includes marine sandstone, shale and limestone. These Triassic rocks distributed mostly on the Shan-Thai plate, particularly in the northern and western Thailand. The Lampang Group is designated for this marine Mesozoic rocks in the North, where the type location is in Lampang province. The Jurassic-Cretaceous rocks are mainly conglomerate, sandstone, siltstone and shale. The reddish sandstone and shale indicate a non-marine depositional environment. The Jurassic-Cretaceous rocks cover nearly the

entire area of the Khorat Plateau, and so they are collectively called the Khorat Group. The Jurassic shale and limestone exposed on lower part of the western and the southern Thailand are marine environment.

The Tertiary sedimentary basins both on-shore and off-shore formed an alignment extending from the north to the south of the country with nearly NS basin axes orientation. These structural controlled half-graben basins are resulted from transtensional tectonic regime after the collision of the Indian plate to the Eurasian plate. The Tertiary basins in Thailand were filled with sandstone, shale and mudstone. Similar to most of Tertiary basins in this region, they are the hosts of hydrocarbon deposits. About one third of Thailand is covered by semi-consolidated and unconsolidated Quaternary sediments, particularly along the major river systems. The Quaternary sediments are gravel, sand, silt, clay, laterite formation and rock fragments that deposited along the alluvial terraces, flood plains, shore lines and lagoons.

The igneous activities occurred at different episodes from Palaeozoic to Caenozoic era and can be divided according to their distribution into three belts; the eastern belt, the central belt and the western belt. The majority of the intrusive igneous rocks are granitic rocks while extrusive igneous are basaltic, andesitic and rhyolitic rocks. Mafic and ultramafic plutonic rocks are restricted to narrow distributed along the suture zone of the Shan-Thai and the Indochina plates.

1.2 Basalts in Thailand

The distribution of basalts in Thailand can be divided into two episodes: pre-Tertiary basalt and Caenozoic basalt. The two groups were separated by an important event, the Shan-Thai and Indochina amalgamation, where the time of collision is still a controversy. However, all the evidence indicates that Caenozoic volcanism was erupted after the formation of the suture. The Pre-Tertiary volcanic rocks can be categorised into four volcanic belts; Chiang Rai - Chiang Mai volcanic belt, Chiang Khong – Tak volcanic belt, Nan – Chanthaburi volcanic belt along the suture zone and Loei – Phetchabun – Phai Sali volcanic belt (Panjasawatwong *et al.,* 1997; Phajuy, 2001). The summary distribution of the pre-Tertiary basalts in Thailand is illustrated in figure 1.4.

The Chiang Rai – Chiang Mai volcanic belt is characterised by mafic volcanic rocks, hyaloclastite and pillow breccia. The time of eruption was proposed by various workers, for instance, during Carboniferous (Hess and Koch, 1979; Macdonald and Barr, 1978; Barr *et al.*, 1990) or during Permian to Permo-Triassic period (Chuaviroj *et al.,* 1980; Bunopas, 1981; Bunopas and Vella, 1983; Panjasawatwong, 1999).

The Chiang Khong – Tak volcanic belt, which is voluminously more than other belts, composed of basalt/andesite, dacite and rhyolite and their pyroclastic equivalents. The eruption period is, therefore, longer and can be divided into two events; the Permo – Triassic and the Early Jarassic – Late Triassic (Jungyusuk and Khositanont, 1992). Additionally, the age determination from zircon U-Pb of 240 ± 1 Ma was obtained (Barr *et al.*, 2000).

The volcanic belt along the Nan – Chanthaburi suture zone is associated with other blocks of rock wrapped by foliated serpentinite in melange zone. The volcanic rocks in the northern part of the suture are ocean island basalts, incipient backarc basin basalt and andesite and oceanic island-arc basalt erupted during Carboniferous to Middle Permian (Panjasawatwong, 1991; Crawford and Panjasawatwong, 1996).

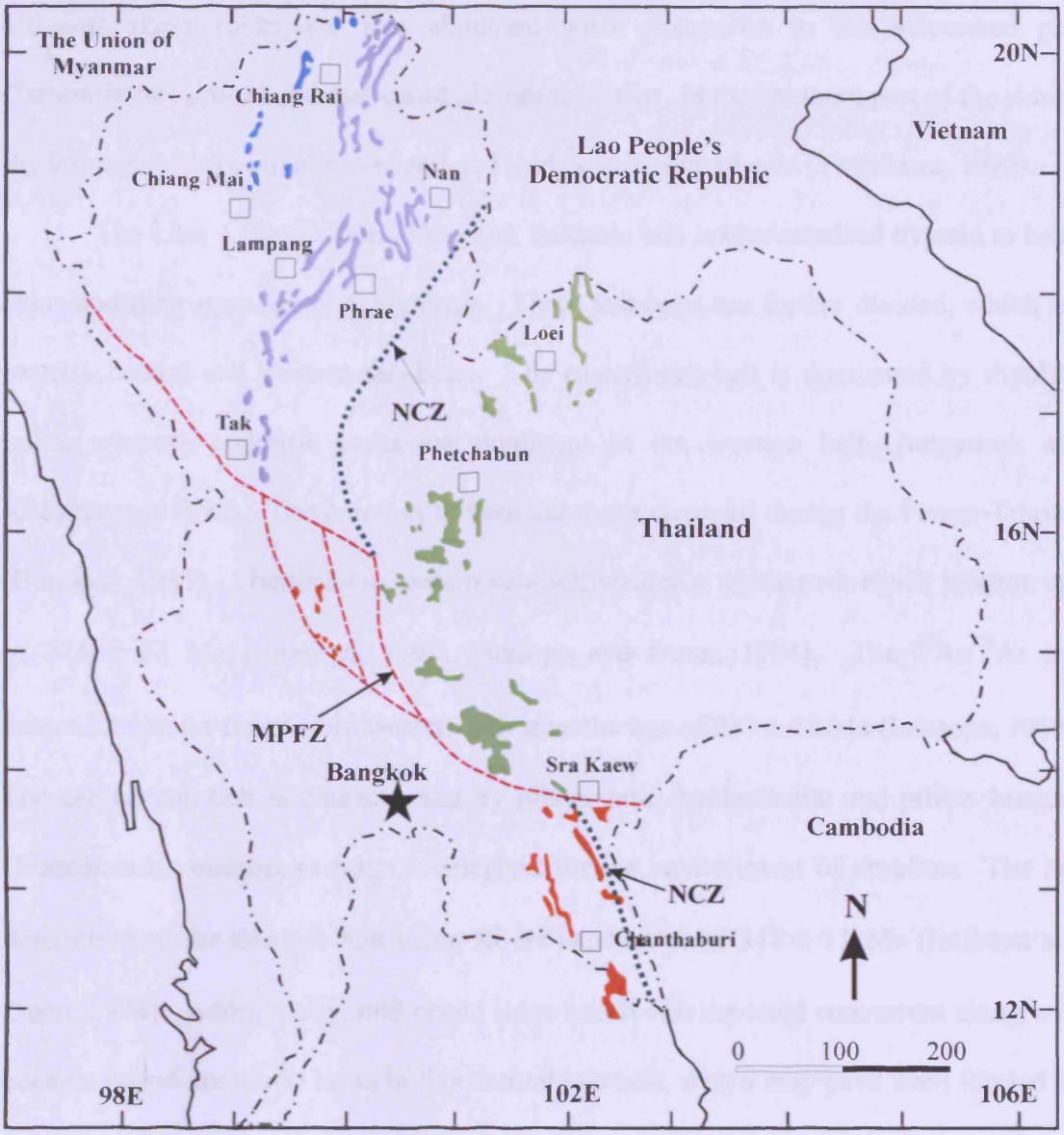

Chiang Rai – Chiang Mai volcanic belt

Chiang Khong – Tak volcanic belt

Volcanic rocks along the Nan – Chanthaburi suture zone (NCZ)

Loei-Phetchabun-Nakhon Nayok volcanic belt

Mae Ping Fault Zone (MPFZ)

Figure 1.4 Distribution of the pre-Tertiary volcanic rocks in Thailand (modified from Panjasawatwong *et al.*, 2003 and Kosowan, 2004). The Mae Ping Fault Zone is from Morley (2002).

although these rocks are less abundant when compared to the associated pre-Carboniferous arc-related mafic and ultramafic rocks. In the southern part of the suture, the volcanic blocks are ocean-island and mid-ocean ridge basalts (Yoshikura, 1990).

The Loei – Phetchabun –Phai Sali volcanic belt is characterised by acid to basic lavas and their pyroclastic equivalents. Three sub-belts are further divided, which are eastern, central and western sub-belts. The eastern sub-belt is dominated by rhyolitic lavas, whereas andesitic lavas are dominant in the western belt (Jungyusuk and Khositanont, 1992). The eruption of both sub-belts occurred during the Permo-Triassic (Bunopas, 1981). The rocks in eastern sub-belt yielded a whole rock Rb-Sr isochon age of 374 ± 33 Ma (Intasopa, 1993; Intasopa and Dunn, 1994). The $^{40}Ar/^{39}Ar$ age determination for rocks from western belt give the age of 237 ± 12 Ma (Intasopa, 1993). The central sub-belt is characterised by pillow lava, hyaloclastite and pillow breccia. Consequently, mid-ocean ridge is assigned for the environment of eruption. The age determination for this sub-belt using Rb-Sr isochon yield 341 ± 11 Ma (Intasopa and Dunn, 1994). Additionally, mid-ocean ridge basalt was reported concurrent along with oceanic island-arc mafic lavas in this central sub-belt, which may have been formed on an oceanic basement of a major ocean basin or a mature backarc basin.

The Caenozoic basalt in Thailand is believed to be part of the Late Caenozoic basalt of mainland Southeast Asia (Barr and Macdonald, 1981). The ages of eruption range from 24 Ma to recent. Smith, (1996) proposed that the Late Caenozoic basalt in mainland Southeast Asia had about equal proportions of alkalic and tholeiitic magmas. It is, however, noteworthy that the Caenozoic basalt in Thailand is nearly entirely alkalic in affinity, while tholeiitic compositions have been reported only in a few areas. The eruption of Caenozoic basalt is in a continental rift environment that possibly relates to the opening of the Gulf of Thailand and the South China Sea as a consequence of the collision of Indian and Eurasia plates (Jungyusuk and Khositanont, 1992; Smith,

1996). On the other hand, a mantle-plume related hypothesis has also been proposed (Barr and James, 1990; Smith, 1996). The Caenozoic alkalic basalt is further categorised into three main groups; nephelinite, basanitoid and alkalic olivine basalt series. The basalt in the basanitoid series is basanite, nepheline-hawaiite and nepheline-mugearite. The alkalic olivine basalt series comprises alkalic olivine basalt, hawaiite and mugearite. Such basanitoid magma may be produced by partial melting of garnet peridotite mantle at the pressure of approximately 20-30 kbar (Barr and Macdonald, 1978; Sirinawin, 1981; Yaemniyom, 1982; Hall, 1996). The degree of alkalinity of basaltic magma i.e. highly alkalic, moderately alkalic and mildly alkalic depends on the degree of partial melting of garnet peridotite, where they exhibit an inverse relation, therefore, the lower degree of the partial melting, the more alkalic the magma (Barr and James, 1990), alternatively, mildly alkalic basalt could have generated by alteration of potassic trachybasalt (Panjasawatwong *et al.*, 1995). The Caenozoic basalt in Thailand is geographically distributed in various parts of the country and can be summarised as northern, central and eastern Thailand.

In northern Thailand, the Caenozoic basalt is found along major pre-Tertiary volcanic belts; Chiang Khong – Tak volcanic belt, which have localities in Phrae province (Denchai basalt), Lampang province (Mae Tha basalt, Sob Prap basalt and Nam Cho basalt) and Chiang Rai province (Chiang Khong basalt and Thoeng basalt). Sob Ngao basalt or Mae Lama basalt is located in Mae Hong Son province (German Geological Mission, 1972). The Ngom Tham basalt occurs along the Nan - Uttaradit suture zone in Uttaradit province (Panjasawatwong and Yaowanoiyothin, 1983). In central Thailand, the basalt outcrops are in Lopburi province in the vicinity of Lamnarai district (Lamnarai basalt) and in Wichianburi district of Petchabun province (Wichianburi basalt), where the outcrops are parallel with the western margin of the Khorat plateau. In the eastern Thailand, the basalts distributed in two main locations;

the Chanthaburi-Trat viscinities and the southern rim of the Khorat plateau. The basalts in Chanthaburi – Trat area are Tha Mai basalt, Pong Nam Ron basalt, Sapan Hin basalt, Nong Bon basalt, Bo Rai basalt, Sae O basalt and Ko Kut basalt. The other area along southern margin of the Khorat plateau consists of Nakorn Ratchasima basalt, Phu Phra Angkhan baslt, Burirum basalt/Khao Kradong basalt, Surin basalt/Khao Phanom Sawai basalt, Khao Phanom Rung basalt, Phra Bat basalt, Phu Ngoen basalt, Phu Kom basalt, Sri Saket basalt/Phu Fai basalt, Nong Nam Khun basalt and Nam Yun basalt. Finally, in the western part of central Thailand found the Bo Ploi basalt in Bo Ploi district, Kanchanaburi province. The distribution of Caenozoic basalts in Thailand is illustrated in figure 1.5.

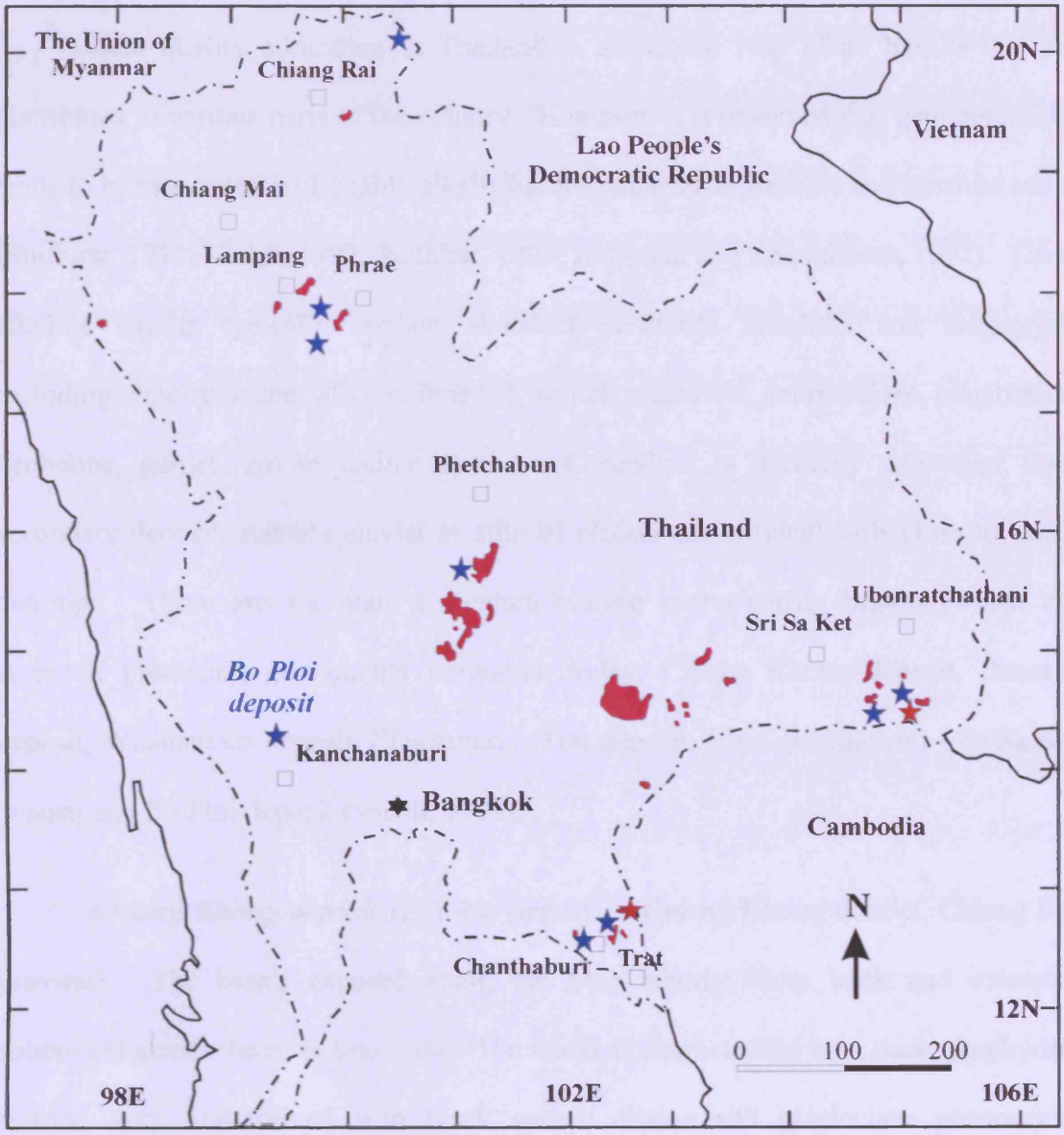

Figure 1.5 Distribution of the Caenozoic corundum-bearing basalts and corundum-barren basalts in Thailand. Blue stars represent sapphire deposits and red stars stand for ruby deposits (modified from Barr and MacDonald, 1978; Vichit, 1992).

1.3 Corundum-bearing basalt in Thailand

Gem quality corundum in Thailand is associated with alkali basalts that are distributed in various parts of the country. However, it is observed that gem corundum tends to be associated with highly alkalic basalts, such as nephelinite and basanite series (Sutthirat, 1992; Vichit, 1992; Sutthirat, 1995; Junyusuk and Khositanont, 1992). These alkaline basalts typically contain abundant peridotite xenoliths and megacrysts including clinopyroxene, olivine, ilmenite, spinel, magnetite, anorthoclase, plagioclase, nepheline, garnet, zircon and/or apatite. Corundum is normally recovered from secondary deposits namely eluvial or alluvial placers and residual soils close to basalt outcrops. There are six main corundum-bearing source/carrier basalts, which are currently producing gem-quality corundum today; Chiang Khong deposit, Denchai deposit, Wichianburi deposit, Chantaburi – Trat deposit, Ubon Ratchathani – Si Sa Ket deposit and Bo Ploi deposit (Vichit, 1992).

Chiang Khong deposit is in the vicinity of Chiang Khong district, Chiang Rai province. The basalt exposed along the Mae Khong River bank and extended southward across the river into Laos. The basalt is characterised by a dark, porphyritic texture, very fine-grained with black spinel, olivine and plagioclase phenocrysts (Saminpanya, 2000). The basalt is assigned to the basanite series (Barr and Macdonald, 1981; Panjasawatwong and Yongsnong, 1996). It was given an age of 1.74 ± 0.12 Ma by K/Ar age determination (Barr and Macdonald, 1981). Gem-quality corundum recovered from basaltic soils alluvial deposits is mostly blue sapphire.

Denchai deposit located in Ban Bo Kaew, Denchai district, Phrae province. The rock is sub-aerial eruption and can be clearly defined at least seven flows part (Barr and Macdonald, 1981; Panjasawatwong, 1983), where each flow is defined by vesicular texture in the upper part. The first to the fourth flows are transitional hawaiite in

composition, while the fifth and the sixth flows are hawaiite. They are fine to medium-grained with olivine phenocrysts. The seventh flow is readily to distinguish from other flows by the well-developed columnar jointing and accommodates abundant lherzolite mantle xenoliths and megacrysts of aluminous clinopyroxene and black spinel. The genesis of gem corundum and zircon is believed to relate to the seventh flow (Vichit *et al.*, 1978; Barr and Macdonald, 1981). An age of 5.64 ± 0.28 Ma was obtained from K/Ar age determination (Barr and Macdonald, 1981).

Wichianburi deposit is located in Phetchabun province, associated with the Wichianburi basalt that formed as volcanic plugs in hilly topography. Columnar jointing is normally observed. The basalts flowed on sedimentary rocks of Permian and Tertiary (Jungyusuk and Sinsakul, 1989). They are black, fine-grained, porphyritic texture and partly accommodated some ultramafic xenoliths and black spinel. The rock was intruded by dolerite dykes and minor intrusions that crosscut the outcrops in many locations. The basalt is alkalic in affinity and composed of alkali olivine basalt, hawaiite, nepheline hawaiite and basanite (Vichit *et al.*, 1988). It was given ages of 9.08 ± 0.29 Ma and 11.03 ± 0.03 Ma by Intasopa (1993) and Sutthirat *et al.*, (1994), respectively.

Chanthaburi – Trat deposits are, perhaps, the largest corundum deposits in Thailand. They are famous for supplying fine rubies and other coloured sapphires like yellow sapphires, green sapphires and star sapphires. The associated basalts are located in Klung and Pong Nam Ron district in Chanthaburi province then extended southward to Bo Rai district, Trat province. There have been some detailed investigations of basalts in various parts of this deposit. Khao Ploi Waen basalt was classified as nephelinite by Barr and Macdonald, (1981), where they described the rocks as black to dark gray, fine-grained with enclosed mantle xenoliths, clinopyroxene and spinel

megacrysts. It was assigned an age of 0.44 ± 0.11 Ma from K/Ar age determination. The younger age of 3.0 ± 0.19 Ma was obtained from basalt in Khao Wua area by Ar/Ar age dating (Sutthirat *et al.*, 1994). In the northern part of this deposit at Ban Saphan Hin occurs fine-grained, porphyritic hawaiite (Sirinawin, 1981) while basanite was reported exposed in the southern rim at Ban We Lu, Ban Ang Et and Ban I Ram (Jungyusuk and Sirinawin, 1983). Fission track age dating on basalt sample from the east of Chanthaburi yield an age of 2.57 ± 0.2 Ma (Carbonnel *et al.*, 1972). Basalt of basanitoid series was reported by Vichit *et al.*, (1978) in the area of Nong Bon, which was dark gray to black, fine-grained, porphyritic texture and contained ultramafic xenoliths and megacrysts of clinopyroxene, garnet, spinel and ilmenite. Nong Bon basalt was given an age of 1.13 ± 0.7 Ma for dating method of K/Ar (Barr and Macdonald, 1981), however, 2.38 ± 0.16 Ma from $^{40}Ar/^{39}Ar$ age determination was proposed by Sutthirat *et al.*, (1994).

Ubon Ratchathani – Si Sa Ket deposits are located in the southeastern corner of the Khorat Plateau. The basaltic lava-related deposits include the Nam Yun district in Ubon Ratchathani province and extend to some parts in Kantharalak district, Si Sa Ket province. However, the basalt outcrops extend to a wider area of both provinces and they formed volcanic cones in many localities such as Phu Ngoen, Phu Kom and Phu Khamint. Phu Ngoen basalt is characterised by vesicular texture with crustal and mantle xenoliths. Phu Khamint basalt is dark grey, fine- to medium-grained, diabasic texture. Phu Fai basalt is classified as subvolcanic basalt (Sutthirat, 1992) and further classified as coarse-grained gabbroid, medium-grained gabbroid and fine-grained gabbroid with transitional boundaries. They are characterised by plagioclase, clinopyroxene, olivine, apatite and ilmenite containing. Barr and Macdonald (1981) suggested the composition of these rocks as nepheline mugearite, whereas, nepheline hawaiite was proposed by Sutthirat (1992). An age of 3.28 ± 0.48 Ma was obtained

from K/Ar age determination (Barr and Macdonald, 1981). Another localities of basaltic outcrop in this area are exposed at southern margin of Ubon Ratchathani, where they can be found in Ban Nong Khun and Khao Noi Keereebunpot in the vicinity of Nam Yun district. These basalts are characterised as dark grey, fine-grained and vesicular textured. The rocks are slightly porphyritic with microphenocrystic phases of olivine and titanoaugite embedded in a groundmass of plagioclase, clinopyroxene, magnetite and sphene. Zeolite was found as amygdale minerals filling the cavities in vesicular basalt. The basalt was assigned hawaiite composition (Junyusuk and Khositanont, 1992). It is noticed that though corundum is normally found associated with basanitoid, but in this deposit it was recovered near outcrops of hawaiite. Accordingly, the absence of basanitoid outcrops was believed as a result of weathering and erosion (Jungyusuk and Khositanont, 1992).

Bo Ploi deposit is renowned for its fine blue sapphire and black spinel. The outcrops form small hills, where the plug outline of an intrusive volcanic remnant can be seen in aerial photographs (Fig.1.6). The basalt is dark, dense, fine-grained and porphyritic texture. There are abundant peridotite xenoliths enclosed in the rock as well as numerous megacrysts including pyroxene, spinel, sanidine and olivine. The basalt has been named nepheline olivine basalt (Charaljavanaphet, 1951; Bunopas and Bunjitradulya, 1975), olivine basalt (Kaewbaidhoon and Potisat, 1974), nepheline hawaiite (Barr and Macdonald, 1978 and 1981; Yaemniyom, 1982) and basanitoid (Vichit *et al.*, 1978). It was given K-Ar age determination of 3.14±0.17 Ma (Barr and Macdonald, 1981). Additionally, an age of 4.17±0.11 Ma from $^{40}Ar/^{39}Ar$ age determination was reported by Sutthirat *et al.*, 1994.

Figure 1.6 Satellite images of the studied area show outcrops boundary of the Bo Ploi basalt that form sub-circular shape recognised by reddish brown basaltic soil (orange dashed line). Number 1 to 6 represent approximate locations of basaltic rock collections. The image is captured and modified from www.PointAsia.com (22/11/2006)

(a) Image was taken at altitude 3 km. (b) Image was taken at altitude 1 km

Table 1.1 Summary of corundum-bearing and non corundum-bearing Caenozoic basalts in Thailand and their age determinations.

Formation and localities	Corundum bearing	Age (Million years)	Determination methods	References
Bo Ploi basalt Bo Ploi district Kanchanaburi	Yes	3.14 ± 0.17 4.17 ± 0.11	K/Ar Ar/Ar	Barr & Macdonald, 1981 Sutthirat *et al.*, 1994
Thamai basalt Khao Ploi Waen, Chanthaburi	Yes	0.44 ± 0.11	K/Ar	Barr & Macdonald, 1981
Khao Kradong basalt Kao Kradong, Buriram	Yes	0.92 ± 0.30	K/Ar	Barr & Macdonald, 1981
Ban Ta Bad Bo Rai district, Trat	Yes	1.13 ± 0.17	K/Ar	Barr & Macdonald, 1981
Chiang Khong Basalt Chiang Khong district, Chiang Rai	Yes	1.74 ± 0.18	K/Ar	Barr & Macdonald, 1981
Den Chai basalt Denchai district, Phrae	Yes	5.64 ±0.28	K/Ar	Barr & Macdonald, 1981
Thamai basalt East of Chanthaburi	Yes	2.57 ± 0.2	Fission track	Carbonnel *et al.*, 1972
Khao Wua basalt Chanthaburi	Yes	3.00 ± 0.19	Ar/Ar	Sutthirat *et al.*, 1994
Phu Fai basalt Phu Fai, Sisaket	Yes	3.28 ± 0.48	K/Ar	Barr & Macdonald, 1981
Lam Narai basalt Lam Narai district, Lopburi	Yes	11.29 ± 0.64 18.1 ± 0.70 24.1 ± 1.00	K/Ar Ar/Ar Ar/Ar	Barr & Macdonald, 1981 Intasopa, 1993 Intasopa, 1993
Wichianburi basalt Wichianburi district, Petchabun	Yes	9.08 ± 0.29 8.82 ± 0.09 11.03 ± 0.03	Ar/Ar Ar/Ar Ar/Ar	Intasopa, 1993 Sutthirat *el al.*, 1994 Sutthirat *el al.*, 1994
Mae Tha basalt Mae Tha district, Lampang	No	0.80 ± 0.30 0.60 ± 0.20 0.50 ± 0.05 0.69 ± 0.95	K/Ar K/Ar Ar/Ar Paleomagnetic	Sasada *et al.*, 1987 Sasada *et al.*, 1987 Sutthirat *et al.*, 1994 Barr *et al.*, 1976
Thoeng basalt Ban Chang Khian, Chiang Rai	No	1.69 ± 1.25	K/Ar	Barr & Macdonald, 1981
Nam Cho basalt Sop Prab district, Lampang	No	2.02 ± 0.10	Ar/Ar	Sutthirat *et al.*, 1994
Sop Prab basalt Sop Prab district, Lampang	No	2.30 ± 0.13 2.36 ± 0.31 2.38 ± 0.17 2.41± 0.17	Ar/Ar Ar/Ar Ar/Ar Ar/Ar	Sutthirat, 1995 Sutthirat, 1995 Sutthirat, 1995 Sutthirat, 1995
Ko Kut basalt Ko Kut, Trat	No	8.5 ± 1.0	K/Ar	Barr & Macdonald, 1981

1.4 Geology of the Bo Ploi Deposit

1.4.1 Location, accessibility and geographic features

The Bo Ploi deposit is in Bo Ploi District, the northeastern part of Kanchanaburi Province. The studied area covers approximately 48 km^2 located between lattitudes 14°15′ N and 14°30′ N and longitude 99°30′ E and 99°35′ E. The area is identified on a topographic map 1:50,000 scale; series L7017, sheets 4937 IV (Amphoe Bo Phloi), however, the basalt outcrop covered only small a area about 1 km^2.

The studied area is generally characterised by hilly landscape alternating with narrow flat plains. The mountain range that is almost north/south in orientation situated in the very central of the area. The major drainage system is a river called the Huay Lam Ta Phoen, where three sapphire mines operate on its palaeo-channel along the river at various depths. Sapphires have been recovered by local people from weathered basaltic soil, which covered the base of basalt hills as well as from alluvial placer and palaeo-channel deposits. The outcrops form small hills in a sub-circular shape resemble a plug remnant, which can be seen clearly from aerial photographs (Fig.1.6).

1.4.2 Geology of Bo Ploi Deposit

The oldest rock in the studied area is of Pre-Cambrian age, the Thabsila formation, which consists of gneiss, quartzite, schist and calc-silicate. The outcrop is clearly observed at Khao Chong Insi. Ordovician rock, Thung Song Group, is characterised by greyish black limestone interbedded by thin laminae of shale and sandstone. Silurian-Devonian rocks are a metamorphic sequence of phyllite, quartzite, tuffaceous sandstones, limestone bands, chert bed and brownish shale with *Tentaculites* graptolite (Bunopas, 1977). The rock forms folded mountains of Khao Khiao, Khao Pu and Khao Kradung Hai. Quaternary semi-consolidated and unconsolidated sediments cover the rest of area. The igneous rock, the Bo Ploi basalt, is exposed as a small hill related to a fracture zone in the quartzite. The outcrop is found in the area of Khao Lan

Thom and Huay Ma Kha, where gravel beds were baked as the basalt flowed on gravel bed of unconsolidated sedimentary bank. The major structure found in the field is folding together with subsequent faulting. Thrust fault was observed at Khao Chong Insi, where pre-Cambrian rocks were thrusted over Silurian – Devonian rocks as shown in figure 1.7(b). The geological map of Bo Ploi area is illustrated in figure 1.7a-1.7b and sample location map is shown in figure 1.8.

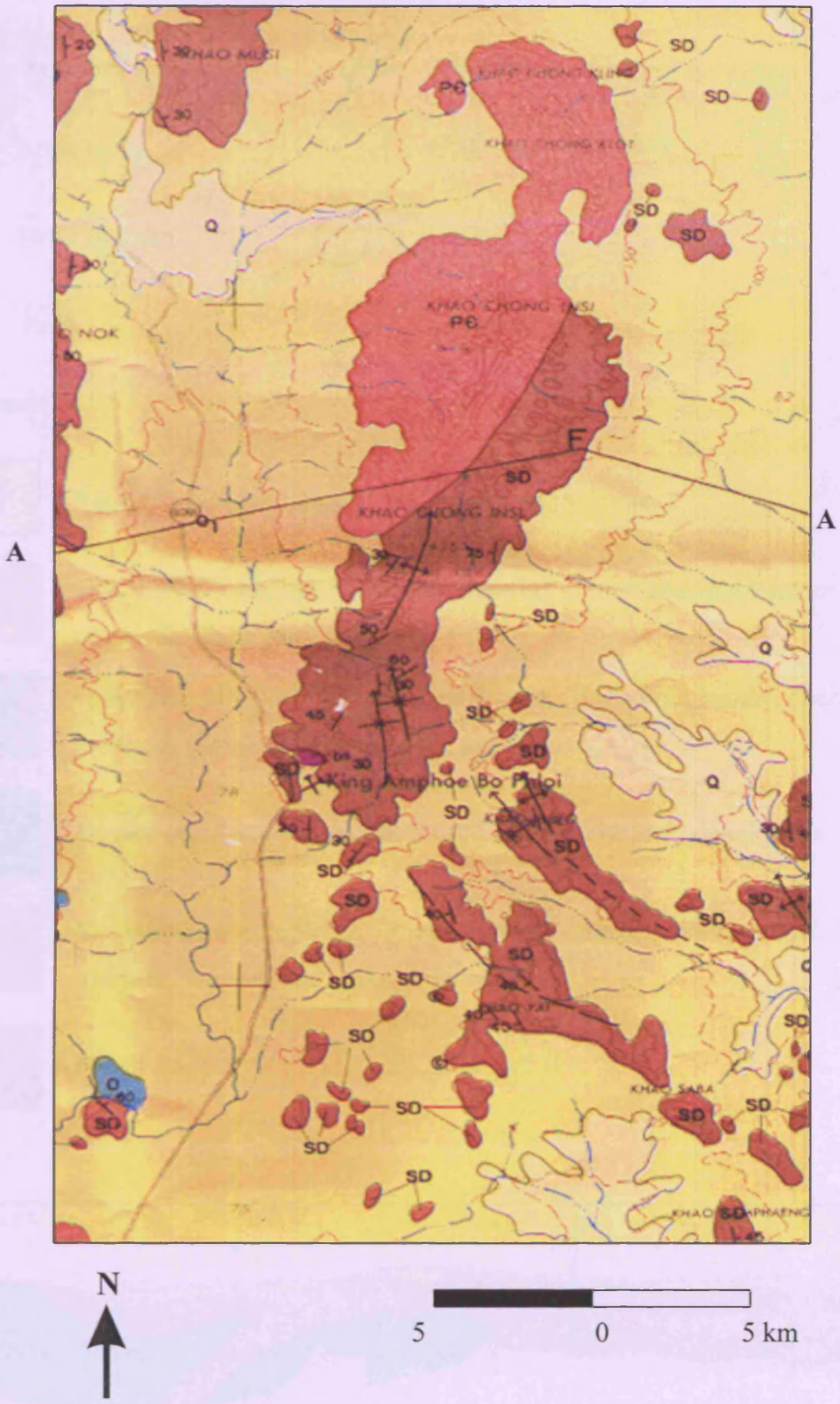

Figure 1.7a The geologic map of the study area, Bo Ploi, Kanchanaburi

Modified after Bunopas, 1977.

Symbols

Syncline

Anticline

Strike and dip

Fault

Stream

Lithologic boundary

10 Road

Inferred fault

Legends

Q	Recent flood plain alluvial, sands, silts and swamps
Q_1	Old alluvial fans, old flood plain deposits at high and low terraces consist of gravel, sands, silts, laterite.
SD	Quartzite, phyllite, tuffacous sandstone, limestone bands, chert beds, brownish shale with Tentaculites, graptolite
O	Banded argillaceous limestone, argillite, quatzite and cephalopods
P-Ɛ	Metamorphic complexes; gneiss, granite gneiss, biotite schist, banded quartzite, calc-silicate rocks and marble
B	Basalt

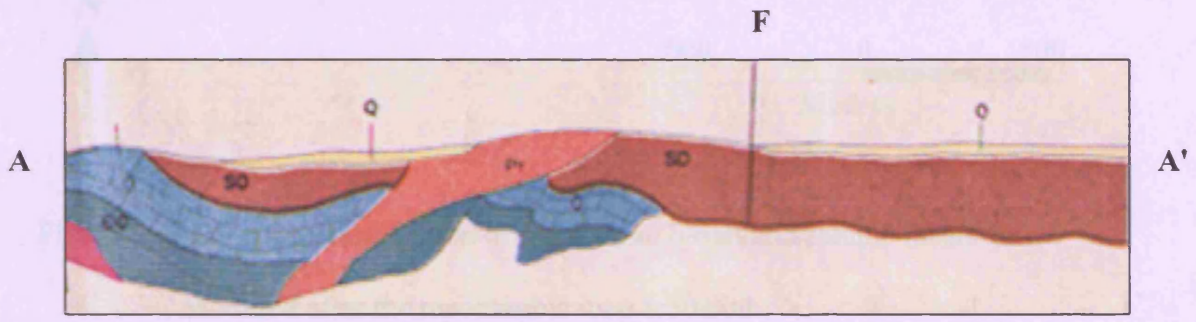

Fig. 1.7b Cross-section along A-F-A' line shows Pre-Cambrian rock (PƐ) is thrusted on Silurian Devonian rock (SD). Modified after Bunopas, 1977.

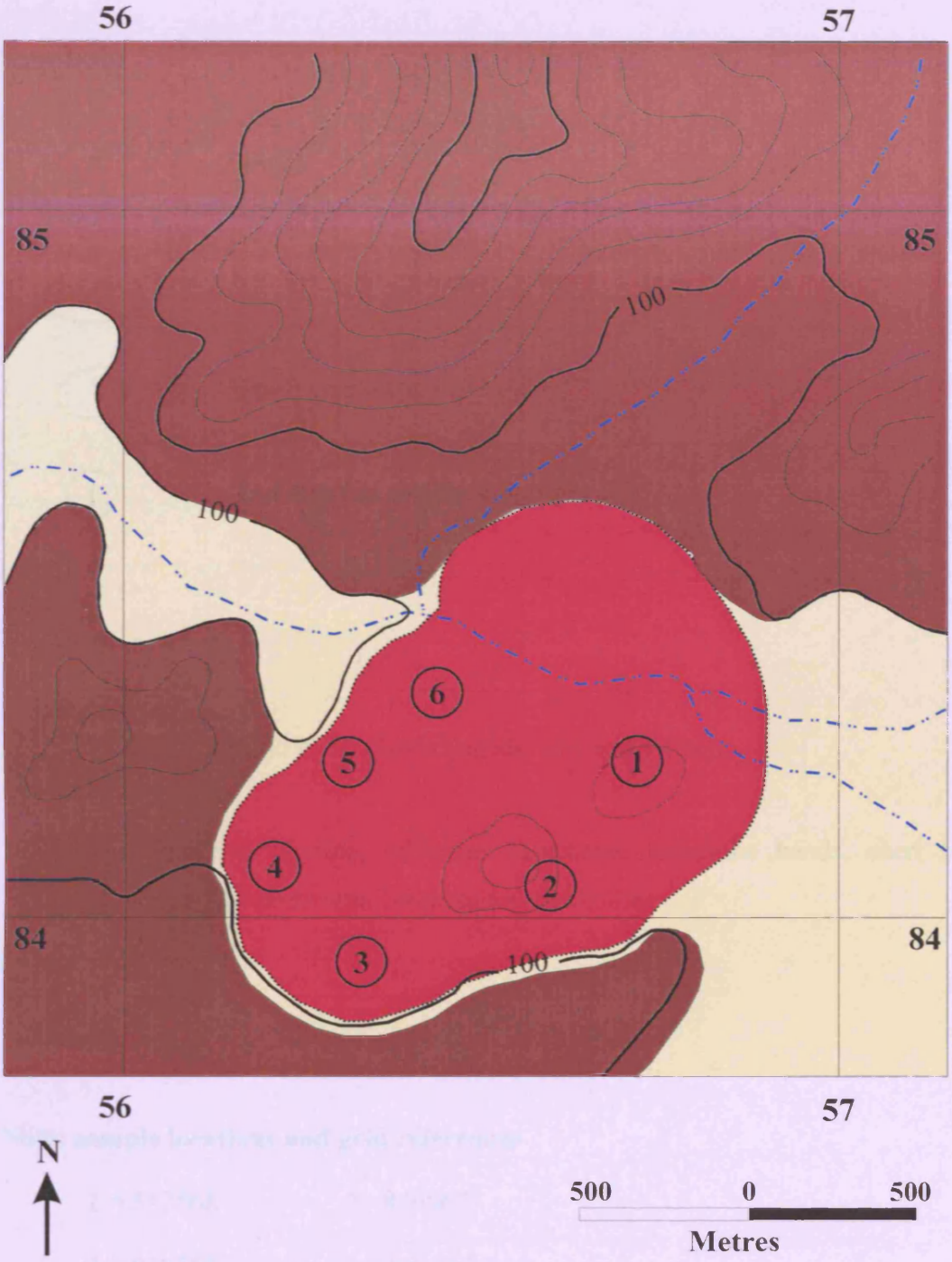

Figure 1.8 Map shows distribution of the Bo Ploi basalt and sample locations

Modified after the topographic map 1:50,000

Series L7017, Sheet 4937IV

Symbols

Stream

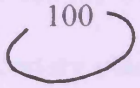

Contour interval (20 metres)

Basalt boundary

Outcrop and sample locations

Legend

Recent flood plain alluvial, sands, silts and swamps

Quartzite, phyllite, tuffacous sandstone, limestone bands, chert beds, brownish shale with Tentaculites, graptolite

Basalt

Note: sample locations and grid references

1 = 842568	2 =840567
3 = 839564	4 = 841562
5 = 842563	6 = 843565

1.5 Previous models for corundum genesis

The corundum associated with basaltic terrains, in particular gem-quality corundum, is established but the genetic relationship remains a highly controversial issue in geology. Because of its economic importance, the majority of worldwide productions of ruby and sapphire supplies are from mines that generally operate on secondary placer deposits associated with alkali basalt rocks. These include economic deposits in Thailand, Laos, Vietnam, Cambodia, eastern China, eastern Australia, Kenya and Nigeria and also additional primary occurrences in Scotland and the United States of America that are not considered to be of economic interest. As a result, several researchers have been trying to answer the enigmatic questions regarding its origin and various petrogenetic models have been proposed. There are some fundamental textural criteria to establish for each occurrence of corundum associated with alkali basalt. First, can it be determined whether the corundum occurs as a phenocrystic phase or a xenocrystic phase in the host igneous alkali basalt; second, whether it is of primary magmatic or metamorphic origin. The two modes of formation are not mutually exclusive and more complicated multi-stage processes involving various stages of crystal growth may be attributed to metamorphism, metasomatism and magmatism. The physical and chemical properties of corundum from both magmatic and metamorphic origin are almost identical. There is so far a lack of an in situ specimen found entrained in host basaltic rocks, therefore, it is rather difficult to have a direct connection to the original genetic processes. Cawthorn *et al.*, 1976 compiled several plausible explanations about the origin of corundum-normative magmas regarding various genetic processes including secondary alteration, vapour phase transfer, assimilation, crustal remelting, melting of hydrous peridotite and fractional crystallisation. For example, the secondary alteration is a result from removing alkalis after eruption, such as from pumice fragments, which could generate corundum-

normative compositions (Heming and Carmichael, 1973). Vapour phase transfer concerns the processes of alkali removal from the interaction of aqueous vapour phase with magma (Luth *et al.,* 1964). Assimilation and magma contamination was described for the production of normative corundum in the Taupo Volcanics, New Zealand (Ewart and Stipp, 1968). Crustal remelting was proposed from experiments on the melting of andesitic crust to demonstrate the chemical variation of Siera Nevada batholith, where the corundum-normative liquids could be generated from amphibole-rich residue (Presnall and Bateman, 1973). Experimental melting of hydrous peridotite can produce corundum-normative melts, however, requires high geothermal gradients to produce corundum as a liquidus phase at the pressure under 10 kbar and the corundum-normative melt were not obtained at 20 kbar pressure (Kushiro, 1972; Kushiro and Yoder, 1972; Green and Ringwood, 1968). Another igneous model proposed amphibole fractionation from melts cause a residue rich in corundum and yield corundum-normative magma (Cawthorn *et al.*, 1976 and references therein). Other authors have suggested that corundum crystallised from residual pegmatitic melts that evolved to become compositionally peraluminous (Upton *et al.*, 1983). Irving (1986) suggested that corundum crystallised from highly fractionated felsic melts such as phonolite at high pressure. Aspen *et al.*, (1990), proposed that volatile fluids from the deep upper mantle triggered the partial melting of lithospheric mantle and enriched the melted fraction, the extreme differentiated residue, syenitic, crystallised corundum. Coenraads *et al.*, (1990), proved that the ages of zircon inclusions in sapphires from New South Wales are in the same range as the host basalt, therefore, they concluded that sapphires formed during the volcanic episode in the area and have a complicated relation to the host basalt. In this case the crystallisation process entailed a strongly evolved magma generated from small degree partial melting of upper mantle peridotites with a volatile enriched source. Corundum and its assemblage minerals were, then,

disintegrated and possibly partly resorbed during the transport to the surface by basalt. Oakes *et al.,* (1996) studied the sapphire suites in Eastern Australia and suggested that volatile-rich volcaniclastic magma was a major conveyor system that transported corundum from its source to the surface. The basaltic magma alone carried corundum suites to the surface as a latter event after the explosive eruption, thus the magma was rich in volatile components, thereby explaining, the lack of corundum found in situ in alkali basalt outcrops (Oakes *et al.*, 1996). It was noticed also that the igneous volcaniclastic host rock is compositionally more evolved than the basalt lavas. Similarly, felsic melt is, once again, considered for the generation of corundum as in the studies of sapphire/zircon assemblages from Australia (Sutherland, 1996). The process may have been triggered by metasomatism of upper mantle by repeated ascending plumes that produced small volumes of felsic partial melts. Levinson and Cook (1994) which involves subduction of aluminous rock leading to metasomatism that allows corundum to crystallise. It is then transported as a xenocryst in subsequent basaltic eruptions. Although no obvious evidence supporting the relationship between the occurrence of sapphire and granite has been presented, it has been suggested that granite may play a role inducing corundum crystallisation because this is an aluminium-rich potential source rock (Sutherland, 1999; Oakes *et al.,* 1996). Hence "granite" (and related coarse grained felsic rock) would be available following tectonic subduction episodes and could also be involved in the fluid present metasomatism of upper mantle wedge. Moreover, there is no such manifest evidence of major felsic extrusion or xenoliths in the deposit areas, so the possibility that granitic rock was responsible for the crystallisation of corundum is not obvious. A 'Hybrid rock hypothesis' of Guo *et al.*, (1996a) proposed that corundum develops at mid-crustal levels through interaction of felsic melts, for example granite/syenite pegmatite, with carbonatite and was brought up to the surface by later basaltic lavas. They identified and analysed numbers of

mineral inclusions in sapphires from different geographic distributions and highlighted the conditions of the co-occurrence of exotic inclusions such as Hf-rich zircon, titaniferous columbite, oxides of REE, Nb, Ta like samarkite, uraninite and sodian plagioclase and alkali feldspar (Guo *et al.*, 1992; Guo *et al.*, 1994, 1996a; 1996b). These minerals are distinctive characteristic of extreme evolved silicic and carbonatitic melts and they, therefore, concluded that the interaction of those two melts, possibly in the mid-crust, was responsible for the crystallisation of corundum. Sutherland *et al.*, (1998a) examined and analysed syngenetic mineral inclusions in corundum, mainly of the blue-green-yellow suite and reported a diversity of inclusions with chemical compositions indicating feldspar, zircon, Nb-Ta oxides and hercynite-magnetite, gahnospinel, rutile-ilmenite solid solution, calcic plagioclase, Ni-rich pyrrhotite, thorite and low-Si and Fe-rich glassy inclusions. They favoured enriched granitic pegmatite silicate melt as the origin of the corundum. The hypothesis was modelled on MELTS programme (Ghiorso and Sack, 1995) and the result confirmed the suggestion that activation of amphibole-rich mantle by the thermal aureole of a magmatic plume enabled corundum to crystallise. After upward movement of the plume, the corundum was brought to the surface during accompanying volcanism. Upton *et al.*, (1999), explained the occurrences of exotic composite megacrysts in Scottish alkaline basalt, which including corundum as a result from metasomatism of lithospheric peridotites which generated syenitic composition melt. The latter process changed the melt composition to peraluminous enabling corundum to be crystallised. They suggested that the process towards peraluminous melt composition involved a loss of alkalis after interaction of the silicate melt with a separate carbonatite melt. However, they preferred the shallow mantle provenance for the occurrence to the mid-crustal origin proposed by Guo *et al.*, (1996a). The discovery of corundum as syngenetic inclusion in the clinopyroxene megacryst and garnet inclusion in corundum associated with alkali

basalt from Eastern Thailand provided a different prospect on the origin of that corundum. In which Sutthirat *et al.*, (2001) explained these coexisting minerals, including clinopyroxene – garnet – corundum, as having originated from corundum-garnet pyroclasite or corundum-garnet clinopyroxenite within the upper mantle. The mineral pairs; clinopyroxene-corundum or garnet-corundum provided the crystallisation temperature between 800 - 1150 (±100°C) and the pressure during crystallisation of clinopyroxene is 10-25 kbar, corresponds to 35 to 88 km depth. Garnet yielded a higher range of crystallisation pressure, more than 18 kbar, although it overlapped the clinopyroxene geobarometry. In Northern Thailand, a similar explanation for a sapphire deposit associated with alkali basalt in the location called Denchai, was proposed by Limtrakun *et al.* (2001). They present information from fluid inclusions and trapped melt inclusion in Denchai sapphires, which include CO_2-rich fluid inclusions, polyphase inclusions of vapour-liquid-solid cubic mineral and silicate–melt inclusions. They suggested trapping temperatures of fluid and melt inclusions, which implies minimum corundum crystallisation temperature, is in the range of 770 to 1200°C. The melt inclusions are quite high in of K_2O (~4wt%), CaO (~0.5wt%), TiO_2 (~1wt%), FeO (~2wt%), MnO (~0.1wt%), V_2O_5 (0.03wt%) with Rb (~70ppm) and Zr (~200ppm). Therefore, they concluded that Denchai sapphire originated from CO_2-rich alkaline magmatism as a phenocrystic phase.

Some ideas for the genesis of sapphires from the Bo Ploi deposit were briefly mentioned by authors who studied the petrology of the Bo Ploi basalt (see section 1.3). The Bo Ploi sapphire and the basalt connection were first reported by Phra Udompitayaphumichan and Khun Phian Lohapitaya in 1934 (Hansawek, 1996 and reference therein). The basalt rocks were later analysed and classified by several workers; nepheline olivine basalt (Charaljavanaphet, 1951 and Bunopas and Bunjitradulya, 1975), olivine basalt (Kaewbaidhoon and Potisat, 1974), nepheline

hawaiite (Barr and Macdonald, 1978; 1981), basanitoid (Vichit *et al.*, 1978) and nepheline hawaiite (Yaemniyom, 1982). It was determined for its age by K-Ar dating of 3.14±0.17 Ma (Barr and Macdonald, 1981). Additionally, an age of 4.17±0.11 Ma was obtained from $^{40}Ar/^{39}Ar$ (Sutthirat *et al.*, 1994). Both estimates indicate that Bo Ploi basalt erupted in the late Tertiary. Previous authors inferred that corundum was brought up to the surface as xenocrysts in the Bo Ploi basalt (Kaewbaidhoon and Potisat, 1974; Vichit *et al.*, 1978; Yaemniyom, 1982; Amour and Linnen, 1999). Mineral inclusions in the Bo Ploi sapphires were identified by Guo *et al.*, (1996a; 1996b) including the discovery of a rare cobalt-rich spinel inclusion trapped in a sapphire crystal. They suggested the occurrence of extraordinary spinel is a result from magma mixing processes in the lower crust, therefore, they inferred to the genesis of Bo Ploi sapphire to be magmatic but complex in origin. Pisutha-Arnond *et al.*, (1998) suggested that high-grade metamorphic rocks in the lower to middle crust were responsible for its origin, and they drew attention to a discovery of corzirsilspite, an unusual xenolith pebble found in the placer deposit. The aggregated xenolith is composed of colourless to greyish brown corundum, fibrolite sillimanite, zircon and hercynite spinel, which is compatible with a metamorphic origin.

1.6 Thesis plan

This thesis is a summary of the works that I have carried out in order to investigate the genesis of corundum from the Bo Ploi deposit, Kanchanaburi, Thailand. Now that the background literature has been presented, it is appropriate to outline the objectives and layout of this thesis. It starts with the characterisation of rough stones both from chemical compositions and their optical properties and spectroscopy. The next chapter reports direct evidence of trapped inclusions, herein, the discovery of important melt inclusions and fluid inclusions, which have genetic implications.

Microthermometric studies of the fluid and melt inclusions are used to constrain the conditions of crystallisation of corundum, whether magmatic or metamorphic origin. Concurrently, in situ microscopic geochemical analyses of the significant melt inclusions provide direct evidence of the composition of melt that was trapped during crystallisation of corundum. Further geochemical confirmations were carried out employing oxygen stable isotope analyses, which it was hoped would distinguish between crustal and mantle sources with possible bearing on metamorphic versus magmatic origins, respectively. The entrained mantle xenoliths were analysed for mineral chemistry to calculate thermodynamics equilibria from which the likely geothermal gradient in this vicinity can be obtained. This also provides constraints for genetic models of the corundum and the host Bo Ploi basalt. Lastly, the mineral chemistry of the host Bo Ploi Basalt and its entrained materials are also characterised in detail in order to understand the relationship among these materials (Bo Ploi basalt, mantle and crustal xenoliths, megacrysts phase including corundum). A pilot experimental petrology programme was carried out to test the dissolution rate of sapphire in the host Bo Ploi basalt. The experiments provide information on transport and entrapment of corundum in the basalt.

Chapter 2

Characterisation of corundum from the Bo Ploi deposit

This chapter presents an overview characterisation of corundum, sapphire variety, from the Bo Ploi Deposit, Kanchanaburi, Thailand in terms of its physical and optical properties. It was studied for its optical spectroscopy, and thus the causes of the colours can be explained. The presence of colouring agent is confirmed by chemical analyses of the samples, additionally; correlations between colouring elements and a variety of blue colours were established. The chemical compositions of Bo Ploi corundum are compared with those corundum compositions from other deposits worldwide, including both igneous (basaltic) and metamorphic terrains.

2.1 Physical and optical properties of the Bo Ploi corundum

The studied samples are rough corundum crystals from placer deposits. The stones were deposited along the paleo-channels at various depths and also found as a residue in the weathered basaltic soil. They show diversity of colours, sizes, and shapes, however, their physical properties are generally constant, which are described as follows;

Crystal form and habit: The samples show rather poor crystal forms as a result of abrasion and/or corrosion processes. The common form is a hexagonal prism, hexagonal dipyramids, and a combination of these two forms. Rhombohedral faces may also be present in some samples. The crystal habits of corundum from this deposit are stubby prismatic that usually taper to ends of the C-axis, a spindle shape or barrel shape. Tabular crystals were frequently observed and possibly resulted from partial disintegration of other forms. The lamellar twinning on $\{10\ \bar{1}1\}$ and simple twinning on $\{0001\}$ cause the crystals to cleave easily and produce a considerably flat and smooth surface. Most of the crystals ("stones") are broken in pieces along their perfect cleavage.

The photographs of sapphire crystal forms are illustrated in Fig.2.1.

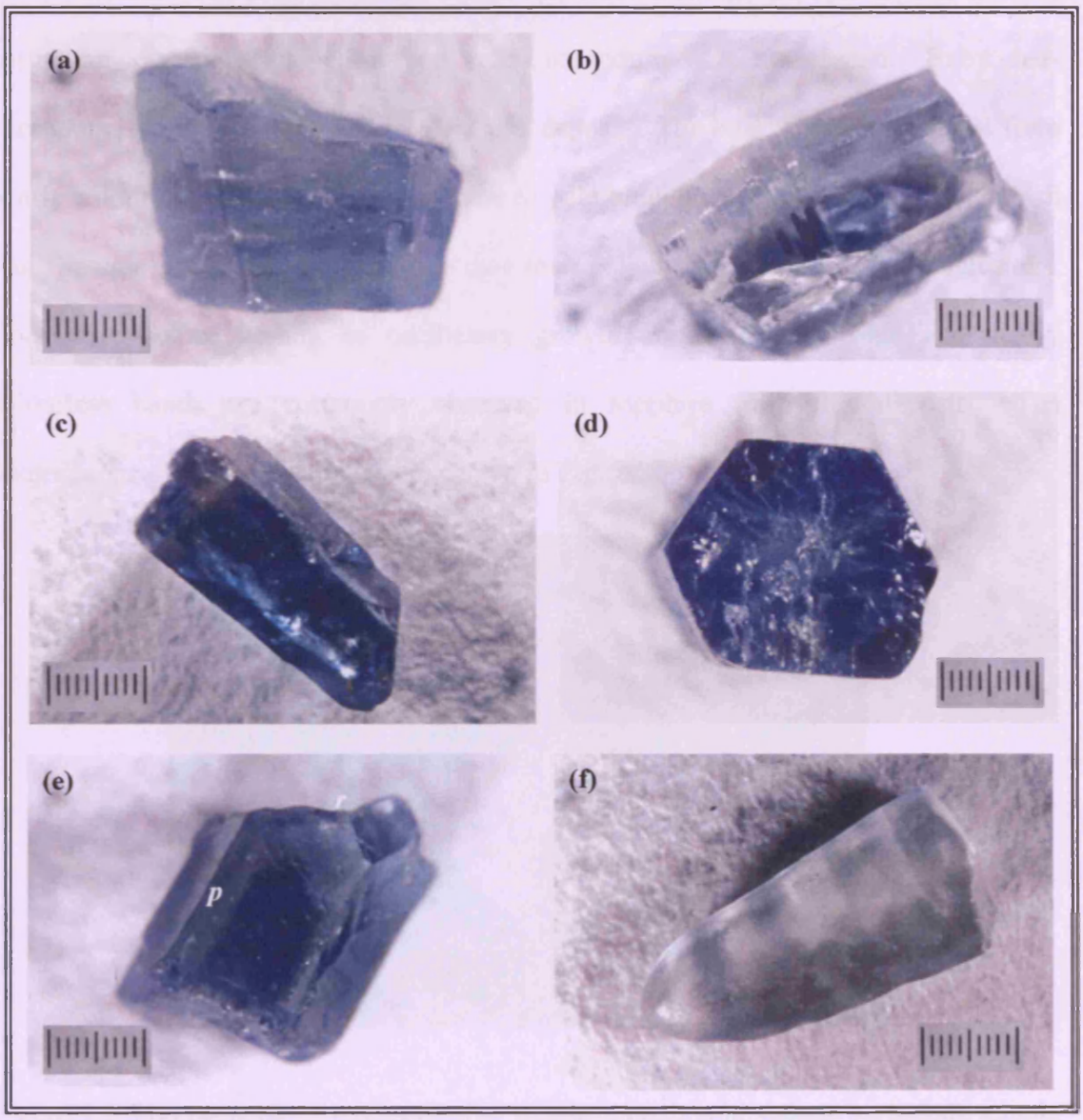

Figure 2.1 Photomicrographs of selected sapphire crystals from the Bo Ploi deposit, scale on the pictures is 1 cm with 1 mm graduations

(a), (b), and (c) Fragments of hexagonal dipyramidal forms and the basal parting. Note also the colour zoning perpendicular to the C-axis in 2.1(b).

(d) Hexagonal prism form cleaved perpendicular to the C-axis

(e) Combination forms of hexagonal prism (*p*) and rhombohedron (*r*)

(f) Fragment of rounded hexagonal dipyramidal forms that resemble a cigar. Note also the colour zoning parallel to the C-axis

Specific gravity: 4.00 ± 0.05

Colour: The majority of the stones recovered from the Bo Ploi deposit are blue corundum, occasionally, yellow and green corundum were also found. Ruby, red-corundum, is rarely found associated in this deposit. The blue colour suite range from nearly colourless with slightly tint of blue to pale blue, intense blue, dark blue, greyish blue, opaque and black, the latter two owe their colour to the dense opaque inclusions. Concentric colour zoning or oscillatory growth zones between blue and nearly colourless bands are commonly observed in sapphire from this deposit. The photographs of sapphire samples are shown in Fig. 2.2.

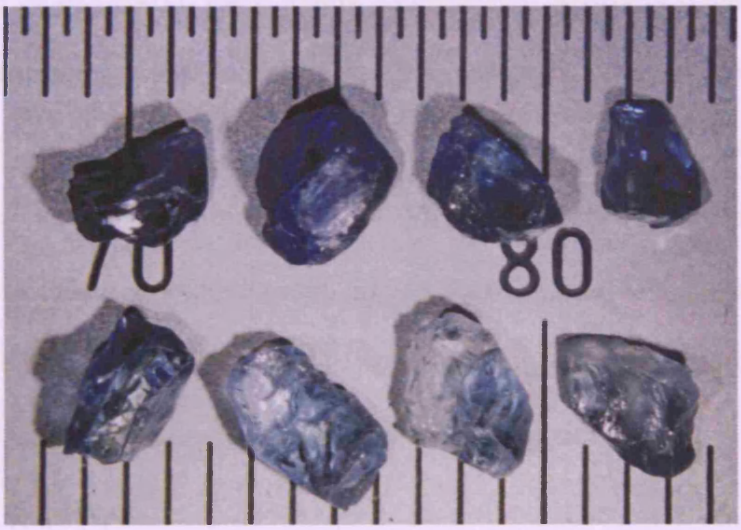

Figure 2.2 Photographs of representative rough crystals and colour variations among corundum from the Bo Ploi deposit.

Pleochroism: Pleochroism is manifest among those samples with intense colour with the pleochroic formula; $\omega > \varepsilon$, ω - blue, ε - pale blue or greenish yellow.

Luminescence: Most of samples are inert in both short wave (254 nm) and long wave (365 nm) ultraviolet light. Rarely, some samples weakly glow with a whitish blue fluorescence in a long wave ultraviolet light.

Refractive indices: ε 1.760-1.762; ω 1.768-1.772; δ 0.008 -0.009

Internal features: A diversity of inclusions is observed in Bo Ploi sapphires, which can be divided into four groups; structural related inclusions, mineral inclusions, fluid inclusions, and silicate-melt inclusions. The structural related inclusions are those inclusions which occur as growth zones, which appear as colour zoning, twin planes, and negative crystals. The mineral inclusions comprise of alkali feldspar ((Na, K) $AlSi_3O_8$), zircon ($ZrSiO_4$), spinel ($MgAl_2O_4$), rutile (TiO_2), boehmite ((AlO(OH)), nepheline ((Na,K)$AlSiO_4$), pyrochlore ($(Na,Ca)_2$ (Nb, Ta),$_2O_6$(O,OH,F)), and monazite $(Ce,La,Y,Th)PO_4$). A similar mineral inclusion suite has been reported found in corundum from basaltic terrains in the Chanthaburi gem field, Thailand (Intasopa *et al.*, 1998, Sutthirat *et al.*, 2001), Lava Plains, Queensland, Australia (Guo *et al.*, 1996a); Barrington, Australia (Sutherland *et al.*, 1998b); Pailin, Cambodia (Sutherland *et al.*, 1998b). The CO_2-rich inclusions and CO_2 + hypersaline brine are among the common fluid inclusions trapped in these samples. The last group, namely the silicate-melt inclusions, is the most remarkable group among these internal features since it provides direct evidence of a magmatic origin for at least some of the Bo Ploi corundum. The detailed studies of these inclusions are presented in Chapter 3.

2.2 Chemistry of sapphires from the Bo Ploi Deposit.

The sapphires were carefully graded by their colour for geochemical analyses and optical spectroscopic study. They were classified into four major colour ranges; deep blue, pale blue, dark blue, and greyish blue (Fig. 2.3). These sapphires were later prepared as doubly polished thin sections by mounting in Araldite epoxy resin. The blocks of mounted sapphires were polished by alumina powder of various grain sizes; 300μm, 600μm, and 1000μm respectively. The polished blocks of sapphires were finished with 0.6μm and 0.1μm diamond paste in order to obtain an optimum polish.

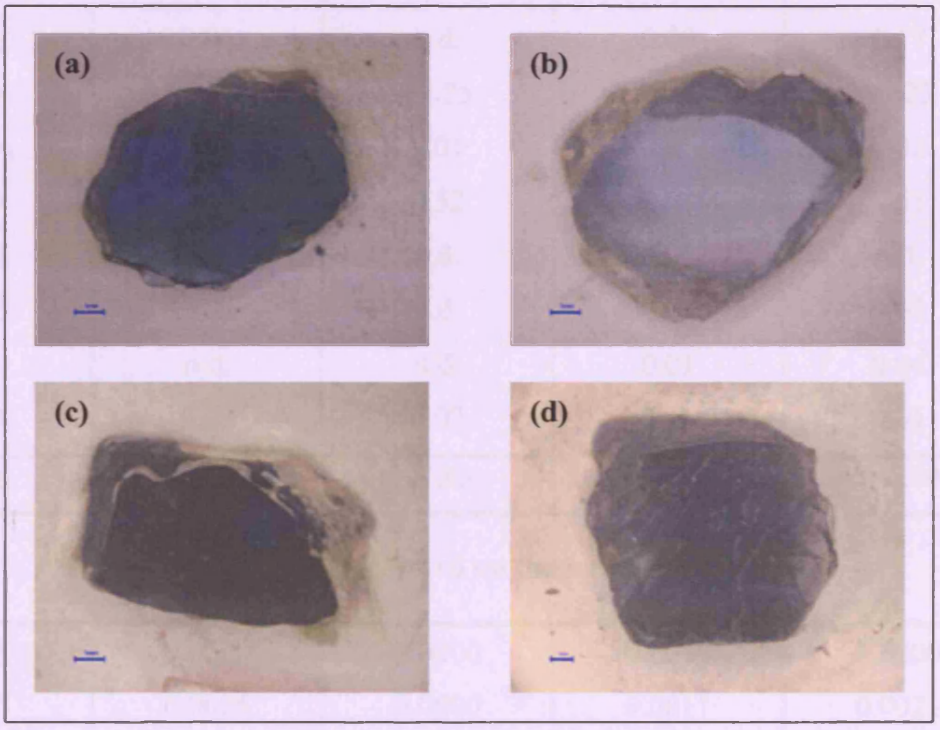

Figure 2.3 Photomicrographs of selected analysed samples that represent the colour of the four classified groups. The scale bar is 1.00 millimetre.
(a) Deep blue or intense blue (b) Pale blue (c) Dark blue (d) Greyish blue

Twelve sapphire samples were analysed for their chemical compositions by using the electron microprobe (JEOL-733 Superprobe equipped with Link Systems EDS) at Birkbeck College, University of London. An accelerating voltage of 15 kV and a count time of 100s were used. The major oxide composition of Bo Ploi sapphires are

Al_2O_3 99.25-99.88 wt%, FeO 0.40-0.61 wt%, and TiO_2 0.04-0.17 wt%. They may contain Cr_2O_3 and V_2O_5 upto 0.02 and 0.01 wt%, respectively. SiO_2, MnO and MgO contents are normally below the detection limits, however, SiO_2 in dark blue sapphires have an average value of 0.06 wt%. The oxide compositions of Bo Ploi sapphires are presented in Table 2.1

Table 2.1 Average oxide compositions (wt%) of sapphires from the Bo Ploi deposit by EPMA

Colour of sapphires				
Oxide	Intense blue	Pale blue	Dark blue	Greyish blue
SiO_2	n.d.	n.d.	0.06	n.d.
TiO_2	0.04	n.d.	0.09	0.17
Al_2O_3	99.79	99.25	98.88	99.25
Cr_2O_3	0.01	0.01	0.01	0.02
FeO	0.40	0.52	0.61	0.53
V_2O_5	n.d.	n.d.	0.01	n.d.
MnO	n.d.	n.d.	0.02	0.02
MgO	n.d.	n.d.	0.01	0.04
CaO	0.03	0.02	0.05	0.01
Total	100.27	99.83	99.73	100.04
Number of cations calculated on the basis of 3 oxygens				
Si^{4+}	0.0000	0.0000	0.0010	0.0000
Ti^{4+}	0.0005	0.0000	0.0011	0.0021
Al^{3+}	1.9949	1.9943	1.9901	1.9908
Cr^{3+}	0.0002	0.0001	0.0001	0.0002
Fe^{2+}	0.0056	0.0074	0.0087	0.0075
V^{5+}	0.0000	0.0000	0.0000	0.0000
Mn^{2+}	0.0000	0.0000	0.0002	0.0002
Mg^{2+}	0.0000	0.0000	0.0002	0.0010
Ca^{2+}	0.0005	0.0003	0.0009	0.0001
total	2.0017	2.0025	2.0023	2.0019

n.d. = not detected

Preliminary X-Ray microprobe analyses was made by Adrian P Jones (unpublished) of Bo Ploi sapphire using the facility GSECARS at the synchrotron in Chicago, Illinois. The work performed at GeoSoilEnviroCARS (Sector 13), Advanced Photon Source (APS), Argonne National Laboratory. GeoSoilEnviroCARS is supported by the National Science Foundation - Earth Sciences (EAR-0622171), Department of Energy - Geosciences (DE-FG02-94ER14466) and the State of Illinois. Use of the Advanced Photon Source was supported by the U. S. Department of Energy, Office of Science, Office of Basic Energy Sciences, under Contract No. DE-AC02-06CH11357. The calculated data from the X-Ray microprobe analyses are illustrated in table 2.2 and figure 2.4.

Table 2.2 Element concentrations in the Bo Ploi sapphire obtained from X-Ray microprobe analyses and quantified to ppm.

Elements	Synthetic diamond (counts)	Sapphire core (counts)	Sapphire core (ppm)	Sapphire rim (counts)	Sapphire rim (ppm)
Ca	10	260	*8.7*	100	*3.3*
Ti	10	230	*7.7*	700	*23.3*
Cr	110	10	*0.3*	10	*0.3*
Mn	20	50	*1.7*	50	*1.7*
Fe	370	60000	*1944.4*	110000	*3500*
Ni	260	30	*1*	10	*0.3*
Cu	10	45	*1.5*	180	*6*
Zn	10	35	*1.2*	10	*0.3*
Ga	10	9450	*315*	20000	*666.7*
Ge	10	10	*0.3*	90	*3*
Al	10	290	*9.7*	370	*12.3*
Si	10	355	*11.8*	1350	*45*
Ar	2750	710	*23.7*	1950	*65*

The result confirmed the relatively high levels of Ga and variations of Ga between core and rims of grains corresponding to different intensities of colour. The data was not calibrated but comparison with Fe count containing in microprobe (0.25 – 0.45 wt%) and the background set to about 10 cps suggested that concentrations of approximately 305-645 ppm Ga. Additional possible trace elements included transition metals of Cu and Zn but at much lower levels, and again then could not be quantified. Instrumental machine noise was discounted on the basis of diamond samples run sequentially between the sapphire, for which no Ga, Cu, and Zn peaks were observed.

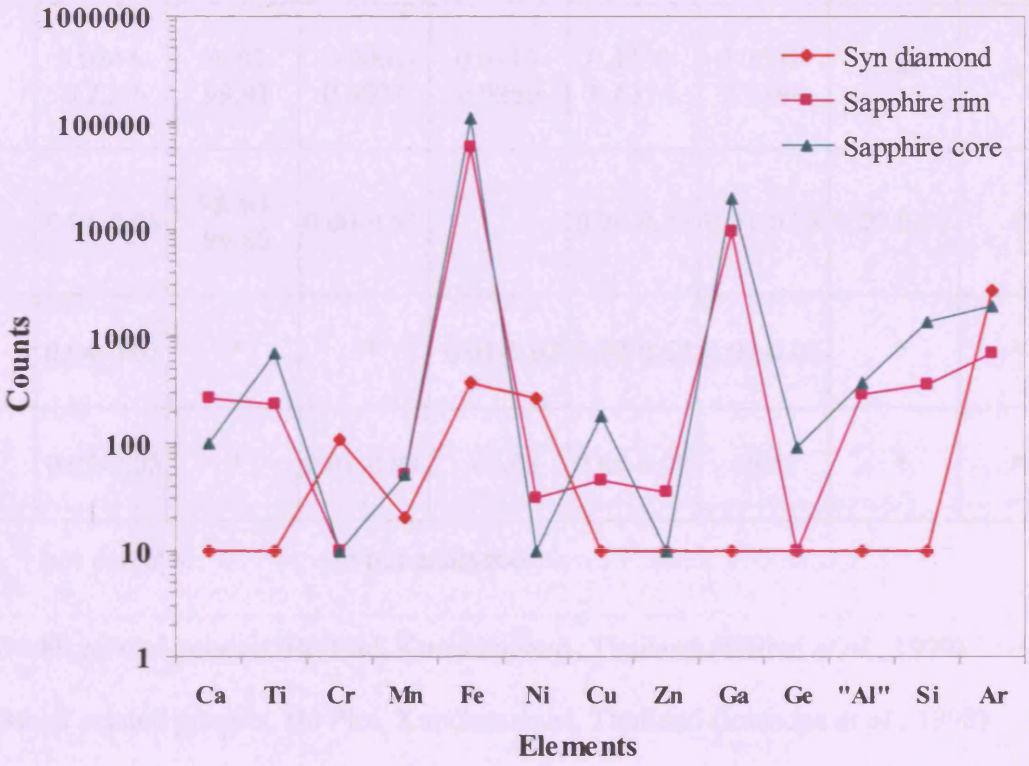

Figure 2.4 Relative comparison of trace elements abundance in sapphire (core and rim) and synthetic diamond standard obtained from X-Ray microbe analyses.

Note See appendix-I for X-Ray microprobe spectra and a calculation method

A comparison of chemical compositions of corundum, particularly for sapphires (blue corundum), from different occurrences and localities is shown in Table 2.3.

Table 2.3 Minor-trace oxide analyses (wt%) of gem-corundum from various deposits.

	TiO_2	Al_2O_3	Cr_2O_3	Ga_2O_3	FeO	V_2O_5	MnO	CaO
a	0.04-0.18	99.30-99.71	n.d.	*	0.27-0.46	n.d.-0.03	n.d.-0.01	0.00-0.01
b	0.01-0.10	*	*	0.04-0.16	0.13-1.06	0.01-0.03	*	*
c	0.00-0.04	*	0.05	0.02-0.04	0.70-1.60	<0.01	*	*
d	0.0344-0.2256	98.07-99.91	0.0001-0.0007	0.0113-0.0250	0.4938-0.6374	0.0004-0.0168	*	*
e	0.06-0.08	98.40-99.80	0.00-0.03		0.20-0.23	0.01-0.03	0.00-0.01	*
f	0.04-0.05	*	*	0.01-0.02	0.29-0.64	0.02-0.03	*	*
g	0.02-0.05	*	0.01-0.04	<0.01	0.60-1.00	<0.01	*	*

n.d. = not detected * not analysed

a: Basalt related genesis, Bo Ploi, Kanchanaburi, Thailand (Srithai *et al.*, 1999)

b: Basalt related genesis, Bo Ploi, Kanchanaburi, Thailand (Intasopa *et al.*, 1998)

c: Basalt related genesis, Barrington, Australia (Sutherland *et al.*, 1998b)

d: Basalt related genesis, Den Chai, Phrae, Thailand (Limtrakun *et al.*, 2001)

e: Pegmatitic related genesis, Andranondambo, Madagascar (Kiefert *et al.*, 1996)

f: Metamorphic related genesis, Mogok, Myanmar (Intasopa *et al.*, 1998)

g: Metamorphic related genesis, Barrington, Australia (Sutherland *et al.*, 1998b)

2.3 Optical spectroscopy

Spectroscopy is the study of the changing energy level of electrons in a certain material after being induced by certain type of incident radiation. As a result, the material absorbs and emits the incident energy and could be observed in the form of radiation that corresponds to particular involved energy levels. There are various methods of spectroscopy; however, the principle rules are in common. The energy and wavelength relation can be explained in terms of equation as

$$E = h\upsilon = hc/\lambda$$

Where h is Planck's constant (6.6×10^{-34} J s)

c is the velocity of light (3×10^{8} m s^{-1})

υ is the frequency (Hertz or cycles/s)

λ is the wavelength (centimetres)

E is the energy in joules

The energy difference between the ground state and excited state span the whole range of the electromagnetic spectrum, which has relation in terms of energy-wavelength absorption phenomena. The certain wavelength, or the certain energy, that is produced from an excited atom can reveal specific information about the involved mechanisms and hence has lead to various applications of spectroscopy such as crystallography and remote sensing.

Optical spectroscopy is concerned with the mechanism that involves the electronic transition of the outermost energy levels of atomic structure. The absorption and emission of energy, light, causes the energy perturbation to yield spectra range from Near-Infra-Red (NIR) through Visible (VIS) and through Ultraviolet (UV) regions corresponding to the cause of colour in minerals.

The causes of colour in minerals, in particular those related to gemstones, have been investigated for many decades. The extensive research as well as the robust advance in technology allows us to understand in more detail the mechanism behind the generation of specific colours in minerals and their prominence in attractive economic gemstones. There are several explanations for the colour mechanism in minerals, which are summarised as follows:

2.3.1 Conventional approach

The cause of colour in minerals is explained in terms of the presence of 'colouring elements', which is classified as

(a) Idiochromatic colour (self-coloured)

The colour of idiochromatic minerals comes from elements that are an essential part of their chemical composition. These minerals generally display one colour or only a limited range of colour. Olivine $(Mg, Fe)_2SiO_4$, or azurite $Cu_3(CO_3)_2(OH)_2$, for example, show olive green and azure blue because of the presence of iron (Fe^{2+}) and copper (Cu^{2+}), respectively. These elements are essential constituents in their chemical formulae.

(b) Allochromatic colour (other-coloured, as from an impurity)

The cause of colour in allochromatic minerals is a consequence of impurities or trace elements that are not an essential part of their chemical composition. These impurities usually refer to the transition or lanthanide elements, which habitually substitute in the structure of minerals. For example, pure corundum (Al_2O_3) is colourless; however, the presence of impurities like chromium, titanium, iron or a combination of these elements can cause the different colours in corundum. In the same way, the presence of cobalt (Co) in the spinel structure can cause a blue colour.

(c) Pseudochromatic colour (false-coloured, as caused by optical effects)

The colour mechanism can be explained by physical and optical effects. The observed phenomena such as iridescence, opalescence, sheen or more sophisticated features such as chatoyancy and asterism are the results of the interaction of minerals, crystallographic structure or the surface, with light such as interference of light, diffraction of light, and dispersion of light. For instance, the interference and diffraction of light on the surface and structure of regular orientation of cryptospheres of silica gel cause the colour effect in opal, known as opalescence.

2.3.2 Modern Approach

Modern approach explains the cause of colour in relation to crystal chemistry, particulary, the crystal field theory and the relationship between the chemical bonds. The mechanisms have been proposed by many researchers (Nassau, 1978; 1983; 2001; Fritsch and Rossman, 1987; 1988a, 1988b; Burns 1993). However, the general concepts of modern theory can be explained principally by electron transfer, particularly, those electrons that belong to the transition metals.

Atoms and Transition elements and Crystal Field theory

The contents according to this topic are summarised from Klein and Hurlbut Jr., (1999); Burns (1993); Putnis (1992); Nassau (2001). It is a general concept of the atomic structure, the transition metals and mechanism of transition elements and the crystal field theory relevant to mineral sciences.

An atom is the smallest unit of a substance that still retains the characteristics of the element. It consists of nucleus that made up of proton and neutrons and surrounded by electrons. The first generally accepted-concept of atom was depicted by Neils Bohr, a Danish physicist (Fig. 2.5a and 2.5b). In an atom, electrons are accommodated in different energy level, each known as a 'shell'; K, L, M, N with increased energy level, respectively. However, Bohr's model of atom does not satisfactorily explain a number of important observations, and does not fit well with elements of higher atomic

numbers, subsequently, a more precise and closer model had been proposed and modified. Nowadays, an atom is treated according to quantum theory, where the behaviours of atomic particles are explained. An atom of the new model is composed of various types of quantum numbers, which are including *principle quantum numbers, n,* which is designated the electrons distributed in shells. Each shell can be divided into a sub-shell, and the number of sub-shells are assigned by the principal quantum number (*n*: 1, 2, 3, 4,…). Each sub-shell has its own quantised energy level, and it is a measure of the energy of an electron, hence, n=1 is the lowest energy orbital level. A sub-shell is also further divided into orbitals, designated as *s, p, d,* and *f*. The letters *s, p, d,* and *f* are spectroscopic terms for sharp, principal, diffuse, and fundamental, respectively. The number of possible orbitals in each sub-shell equals $(2l+1)$, where $l = (n-1) = 0, 1, 2, 3,$ and so on. For examples, the s sub-shell has 1 orbital, the p sub-shell has 3 orbitals, *d* sub-shell has 5 orbitals.

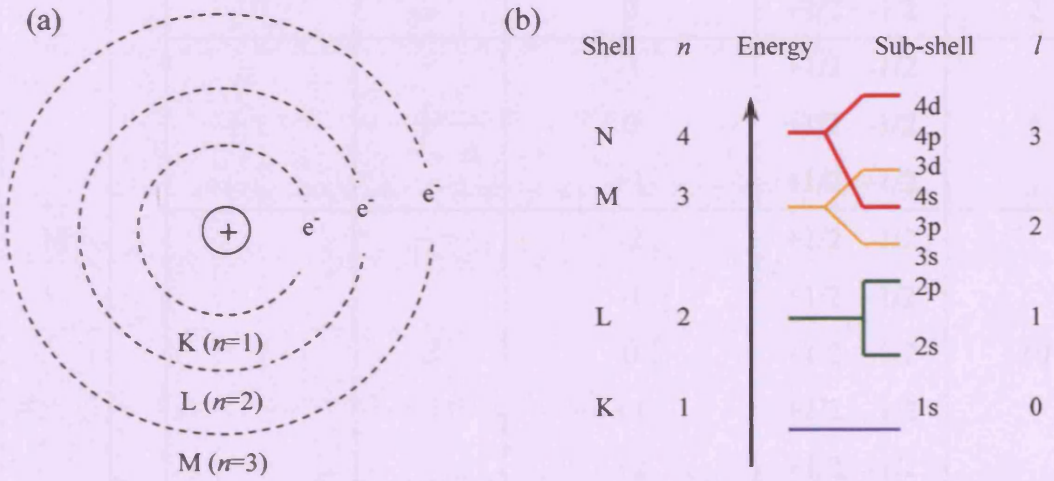

Figure 2.5 Schematic diagrams show the structure of an atom

(a) An atom and its electron shells depicted by Niels Bohr, Electrons travel along specific orbits of fixed energy levels known as K, L, M, N,… shells, with principal quantum number n=1, 2, 3, 4,…,∞)

(b) Diagram illustrates the internal component and properties of an atom.

In summary, electrons allocate themselves surrounding the nucleus of an atom in these orbitals, according to the certain parameters, which include the *principle quantum number (n)*, *azimuthal quantum number (l)*, *magnetic quantum number (m)*, and *spin quantum number (s)*. Each orbital allows two opposite spinning electrons to locate. Electrons will fill up the orbitals from the lowest energy level first to the higher energy level, which is summarised in Table 2.4

Table 2.4 Summary of the electron configuration in relation to atomic structure

Shell	n	l = 0,1,..n-1	Sub-shell	Magnetic quantum number (m=-l,..+l)	Spin quantum number (±½)	Maximum number of electrons
K	1	0	*s*	0	+1/2 -1/2	2
L	2	0	*s*	0	+1/2 -1/2	2
		1	*p*	-1	+1/2 -1/2	6
				0	+1/2 -1/2	
				+1	+1/2 -1/2	
M	3	0	*s*	0	+1/2 -1/2	2
		1	*p*	-1	+1/2 -1/2	6
				0	+1/2 -1/2	
				+1	+1/2 -1/2	
		2	*d*	-2	+1/2 -1/2	10
				-1	+1/2 -1/2	
				0	+1/2 -1/2	
				+1	+1/2 -1/2	
				+2	+1/2 -1/2	

Element	**Atomic number**	**Electronic configuration**
K	19	$1s^2\ 2s^2\ 2sp^6\ 3s^2\ 3p^6\ 4s^1$
Ca	20	$1s^2\ 2s^2\ 2sp^6\ 3s^2\ 3p^6\ 4s^2$
Sc	21	$1s^2\ 2s^2\ 2sp^6\ 3s^2\ 3p^6\ 3d^1\ 4s^2$
Fe	26	$1s^2\ 2s^2\ 2sp^6\ 3s^2\ 3p^6\ 3d^6\ 4s^2$
Co	27	$1s^2\ 2s^2\ 2sp^6\ 3s^2\ 3p^6\ 3d^7\ 4s^2$
Ni	28	$1s^2\ 2s^2\ 2sp^6\ 3s^2\ 3p^6\ 3d^8\ 4s^2$

Transition elements, *sensu stricto*, are the elements that *d* or *f* shells are partially occupied, consequently, the valance of oxidation can exist in more than one state. In the periodic table, the first series of transition group begins from Sc to Ge. The second transition series are from Y to Ag and the third series are from Hf to Au. They also include the lanthanide group ranging from La to Lu. The electronic configuration of the first series is characterised by the partially occupied 3d orbital, where partly filled in *4d* and *5d* orbitals characterise the second and the third transition series, respectively. The lanthanide group is recognised by partly filled *4f* and/or *5d* orbitals. The shapes and orientations of the d-orbital are illustrated in figure 2.6.

The most stable oxidation states in minerals at near surface environments include Ti^{4+}, V^{3+}, V^{5+}, Cr^{3+}, Cr^{4+}, Mn^{2+}, Mn^{3+}, Fe^{2+}, Fe^{3+} Co^{2+}, Co^{3+}, Ni^{2+}, Cu^{2+} and Cu^{+} (Burns, 1993). They can form 'coordination complexes', where a transition metal cation is surrounded by a number of ligands, and anions, which can be O^{2-}, OH^{-}, $(CO_3)^{2}$, $(SO_4)^{2-}$, non-bridging oxygen in silicates, or dipolar molecular species such as H_2O, NH_3, and bridging oxygen in silicate.

The coordination of a cation is determined by radius ratio rules. The coordination number represents the number of ligands surrounding the cation. In a cubic coordination polyhedron, for example, there are eight ligands surrounding a central cation, so the coordination number is eight. Also other polyhedra and coordination numbers, which are illustrated in Fig 2.7, these coordinations influence the electron orientation and electron splitting depends on the symmetry and the coordination of the cation.

The outer shell of the transition metals can accommodate between 0 to 10 electrons. These electrons are in the d-orbital, which have five different shapes according to their orientation with respect to the x, y, and z reference axes, as well as the environmental conditions.

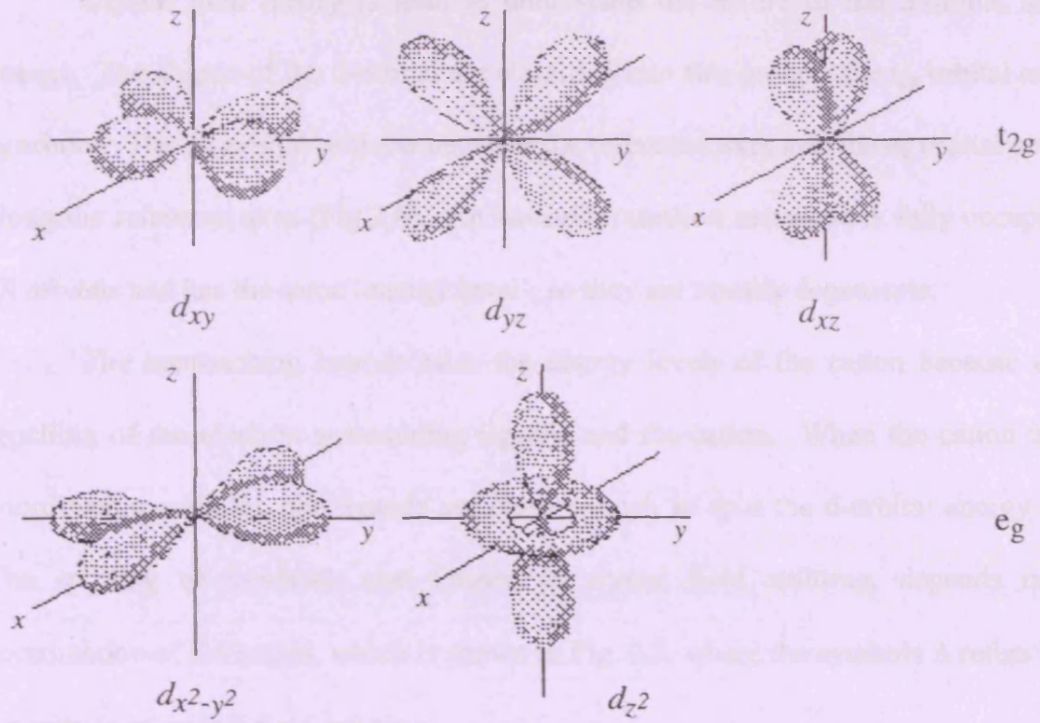

Figure 2.6 The shapes of d-orbital, which are divided into two groups; t_{2g} and e_g

(After Putnis, 1992)

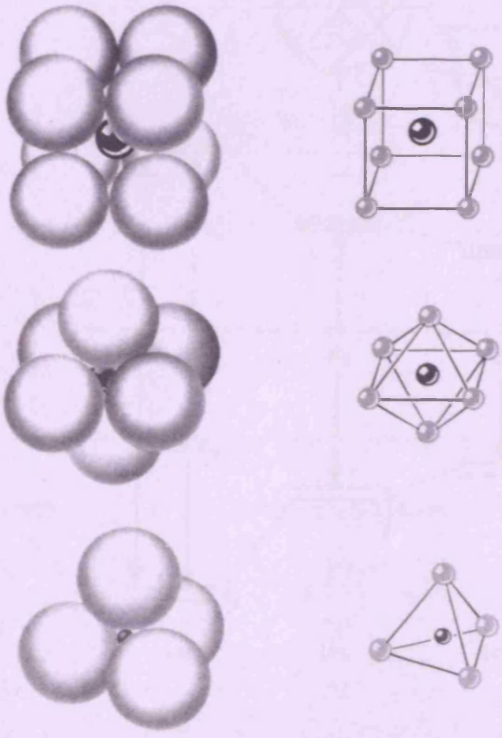

Cubic coordination (C.N. = 8)

Octahedral coordination (C.N. = 6)

Tetrahedral coordination (C.N. = 4)

Figure 2.7 Polyhedra and their coordination numbers

Crystal field theory is used to understand the nature of the d-orbital and its energy. The shapes of the d-orbital are classified into two groups: the t_{2g} orbital and the e_g orbital. The t_{2g} orbital projects between the reference axes and the e_g orbital projects along the reference axes (Fig.2.6). An isolated transition metal ion is fully occupied in all orbitals and has the same 'energy level', so they are equally degenerate.

The approaching ligands raise the energy levels of the cation because of the repelling of the electron surrounding ligands and the cation. When the cation is in a coordination complex, the ligands are close enough to split the d-orbital energy level. The splitting of d-orbital, also known as crystal field splitting, depends on the coordination of the cation, which is shown in Fig. 2.8, where the symbols Δ refers to the magnitude of crystal field splitting.

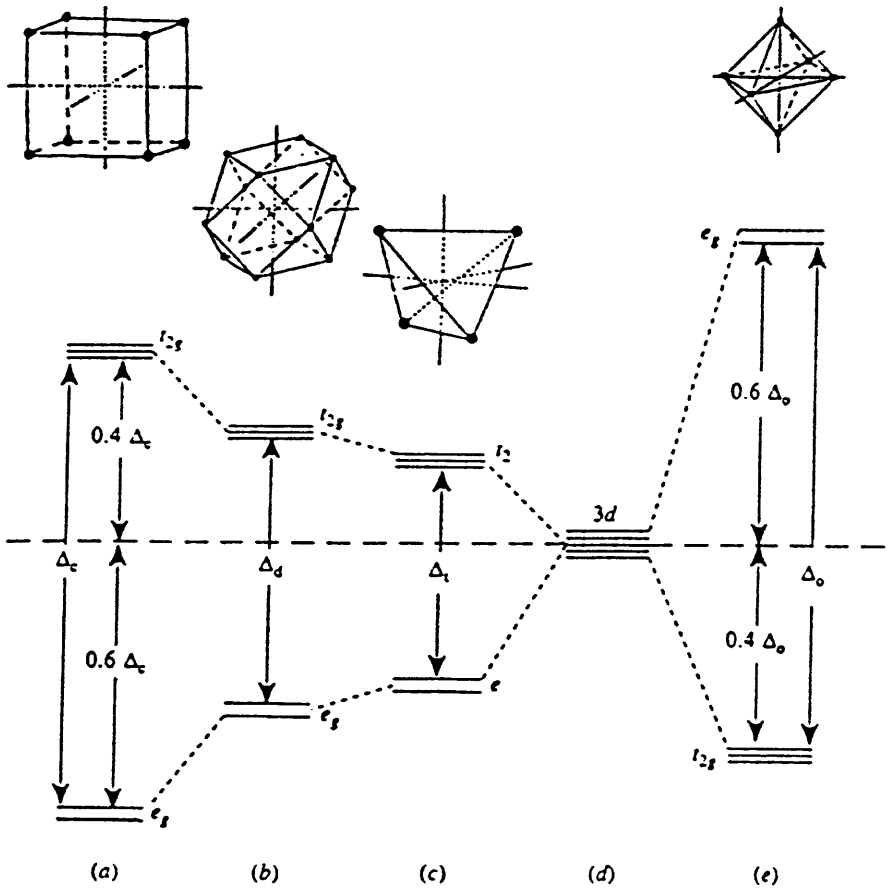

Figure 2.8 Crystal field splitting of 3d-orbitals in (a) cubic (b) dodecahedral (c) tetrahedral (d) spherical and (e) octahedral coordinations (Burns, 1993)

Crystal field splitting in 3d-orbital in different coordinations of cations

(1) Octahedral Coordination

Ligands approach the d-orbital parallel to the x, y, and z reference axes, therefore, repel the e_g orbitals more than t_{2g} orbitals. This repulsion causes a higher energy level in the e_g orbital. The height of the two levels is at centre about a baricentre, the centre of gravity. The total energy separation is called Δ_0. There are 2/5 Δ_0 below baricentre for t_{2g} orbital and 3/5 Δ_0 above baricentre for e_g orbital.

(2) Tetrahedral Coordination

The t_2 orbitals lobes are repelled by ligands greater than the e orbital lobes (subscript g is omitted due to lacks of centre of gravity in the system). Crystal field splitting parameter is Δ_t. The d-orbital of e group is stabilised by 0.6 Δ_t and the t_2 groups are destabilised by $0.4\Delta_t$.

(3) Cubic and dodecahedral coordination

The crystal field splitting of cubic and dodecahedral coordinations is the same as the d-orbital splitting in tetrahedral coordination. The splitting parameter is, however, denoted as Δ_c, which is larger than Δ_t.

According to Burns (1993), the mechanisms of crystal field transitions are the main contributor for the cause of colour in minerals. Additionally, similar works were also reported by Nassau, (1978; 2001). The colour mechanisms can be explained as three categories based on the types of transitions.

(1) Crystal Field Transitions

This transition occurs when an electron in one orbital absorbs the incident light and transfers to a higher energy level in the same atom. The processes take place within the d-orbital and involves transition element, which is partially, filled the d-orbital.

(2) Intervalence Charge Transfer Transitions

Similar to the crystal field transitions, but the mechanism involves the transition of an electron from one orbital that gains energy to the higher energy orbital of the neighbouring atom. The processes can be achieved in two ways:

(i) Homonuclear intervalence transitions

The transitions occur between different oxidation states, but within the same elements, for example, the transition of $Fe^{2+}$and Fe^{3+}or between $Ti^{3+}$and Ti^{4} as well as between Mn^{2+} and Mn^{3+}.

(ii) Heteronuclear intervalence transitions

The transitions occur between different oxidation states and different elements, for instance, Fe^{2+} and Ti^{4+} or Mn^{2+} and Fe^{3+} or Fe^{2+} and Mn^{3+}.

(3) Oxygen and metal charge transfer

The transitions usually occur in transition metals that have high valencies. Consequently, it involves a higher energy level and the absorption/emission will be in the region of ultra-violet and somehow extend to the visible region. The colours from this mechanism are distinctively intense, for example, crocoite ($PbCrO_4$) that exhibits bright hyacinth-red, has transitions of Cr^{6+} and O^{2-}, or Vanadinite ($Pb_5(VO_4)_3Cl$) whose colour is bright orange-red to yellow has transitions of V^{5+} and O^{2-}, or permanganate has Mn^{7+} and O^{2-} transitions.

2.4 Optical spectroscopic study of the Bo Ploi Sapphires

The optical absorption spectra of sapphires from the Bo Ploi deposit were analysed by a Bruker IFS 88 FTIR spectrometer fitted with a Bruker IR microscope in the Mineral Physics Unit, Department of Earth Sciences, University College London. Typically, 250 scans were accumulated between 9000 to 24000 wavenumber (cm^{-1}), with 8 cm^{-1} resolution using CaF_2 and quartz beam splitters, tungsten source, and silicon diode detector at room temperature. The analyses were done using orientated

specimens carefully prepared to be perpendicular and parallel to the C-axes of the samples.

Table 2.5 Summary of optical absorption spectra data of Bo Ploi corundum

	⊥C-axis		//C-axis	
Sample number	Peak position (cm^{-1})	Intensity (absorbance unit)	Peak position (cm^{-1})	Intensity (absorbance unit)
BPS01	11111.6	0.49		
	13648.5	0.41		
	17128.7	0.70		
BPS02	11201.7	0.74	10419.1	0.12
	13175.2	0.12	12640.1	0.18
	14660.6	0.28	16257.7	0.11
	17570.9	0.26		
BPS03	11106.6	0.25	10978.7	0.20
	13755.5	0.27	13935.9	0.12
	17570.6	0.53	17558.8	0.09
	22200.4	0.08		
BPS04	11123.1	0.25	10824.5	0.46
	13852.0	0.22	13333.7	0.36
	17334.8	0.08	15526.3	0.06
	17664.0	0.10	16779.6	0.21

The prominent absorption can be observed at two positions; first, at around 17000-17500 cm^{-1}, second, around 11100-11200 cm^{-1}, however, the peak positions vary slightly among these samples. In three samples, the absorbance intensities in the direction perpendicular to the C-axis are clearly higher than those intensities in the

direction parallel to the C-axis, except the sample BPS04. The absorption in the region of 17000-17500 cm^{-1} is consistent with the Fe^{2+} → Ti^{4+} intervalence charge transfer, while the absorptions in around 11100-11200 cm^{-1} is refered to the Fe^{2+} - Fe^{3+} charge transfer (Ferguson and Fielding, 1971, 1972; Smith, 1978; Schmetzer and Bank, 1980; Burns 1981, 1993; Nassau, 2001). The absorption spectra are displayed in Fig. 2.9–2.12. The inner curves represent the fitted curves for each spectrum.

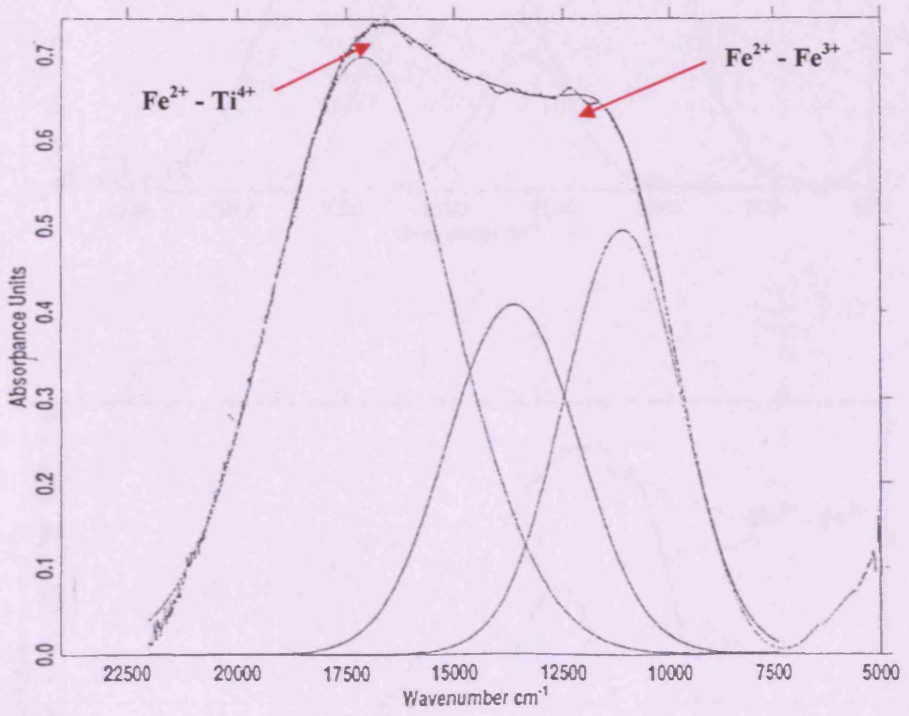

Figure 2.9 VIS-NIR absorption spectrum of Bo Ploi sapphire (BPS-01) in the orientation perpendicular to C-axis

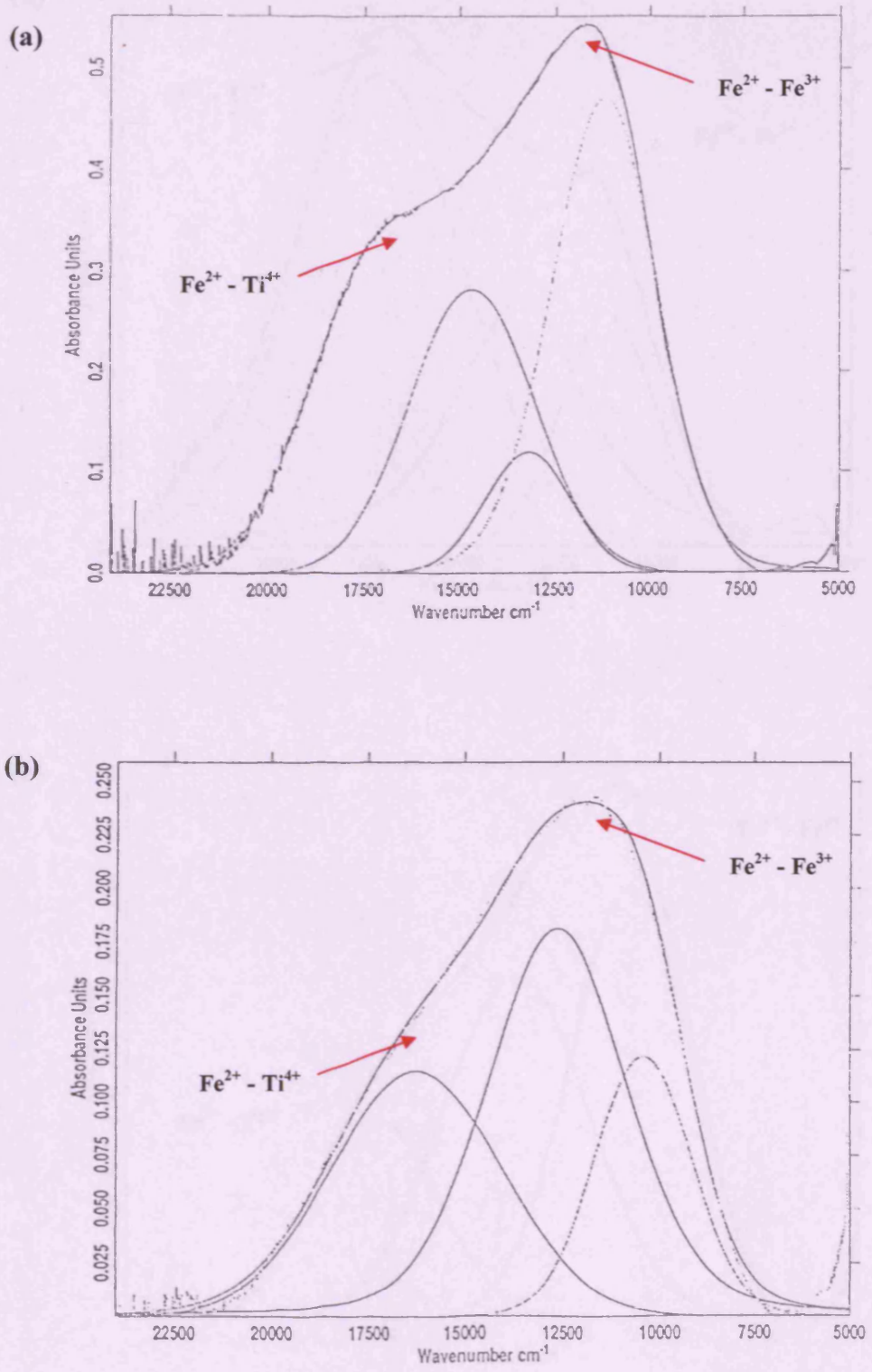

Figure 2.10 VIS-NIR absorption spectrum of Bo Ploi sapphire (BPS-02) in the orientation ⊥C-axis (a) and // C-axis (b), respectively.

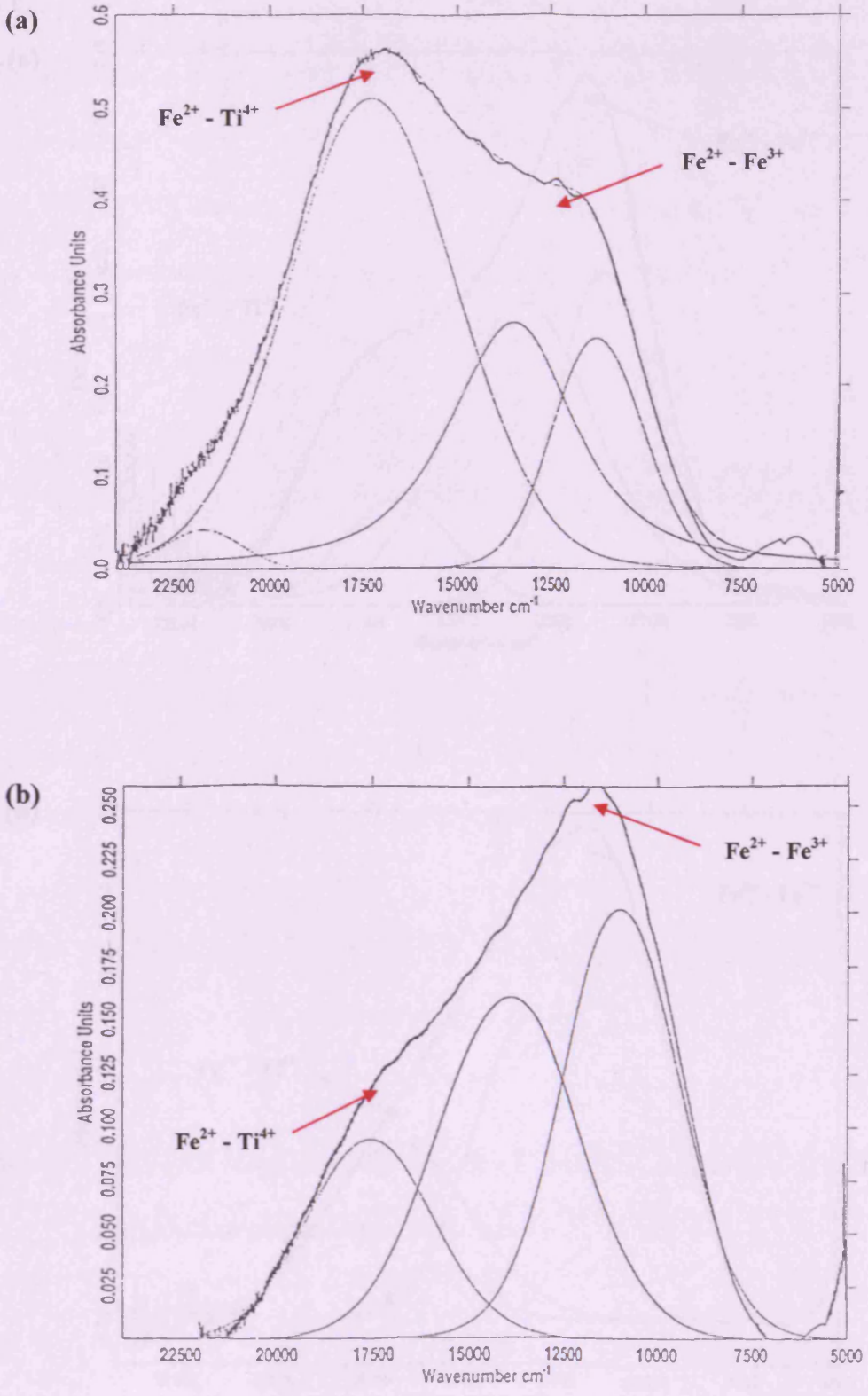

Figure 2.11 VIS-NIR absorption spectrum of Bo Ploi sapphire (BPS-03) in the orientation ⊥C-axis (a) and // C-axis (b), respectively.

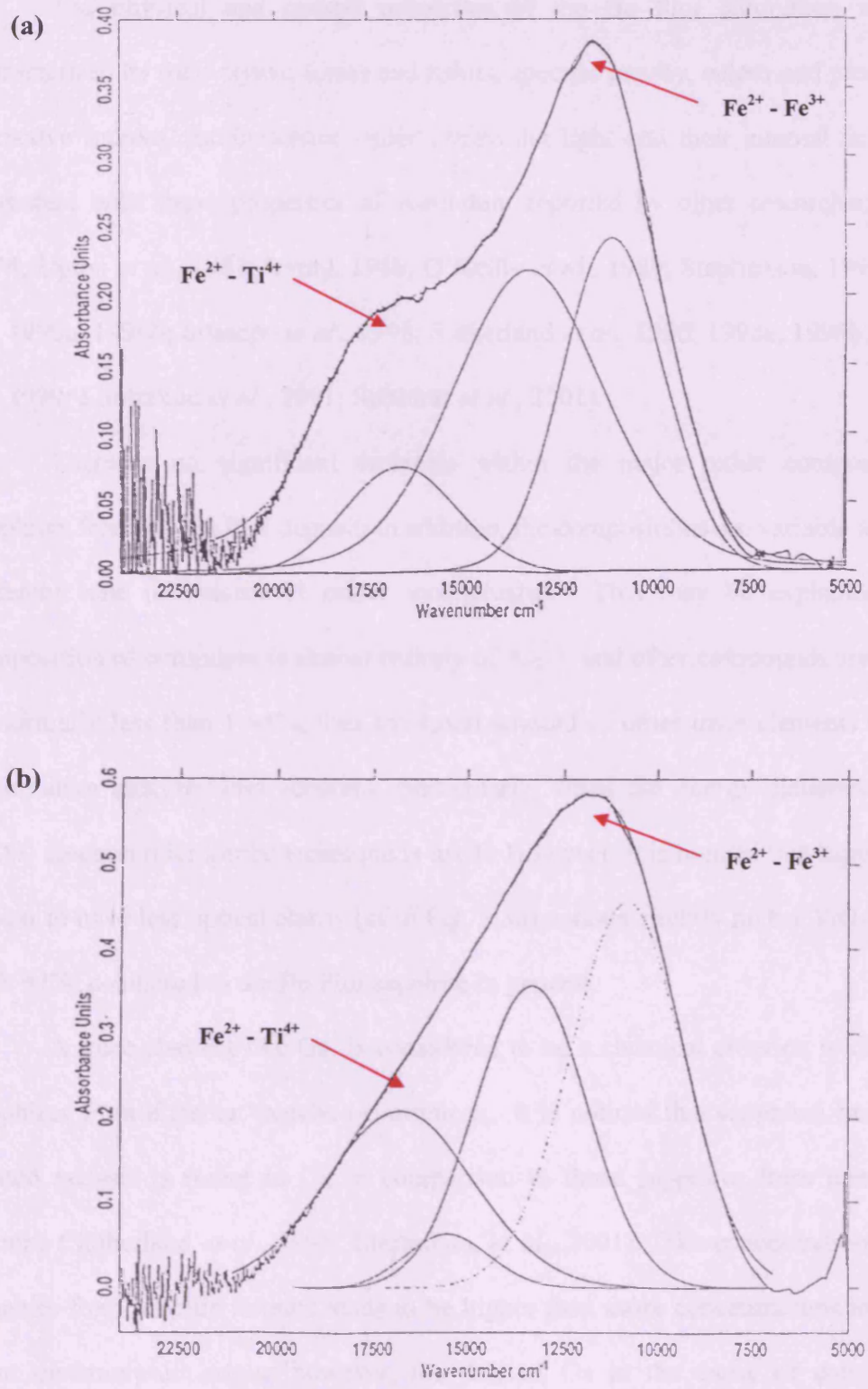

Figure 2.12 VIS-NIR absorption spectrum of Bo Ploi sapphire (BPS-04) in the orientation ⊥C-axis (a) and // C-axis (b), respectively.

2.5 Discussion of compositional and optical data

The physical and optical properties of the Bo Ploi corundum, which are characterised by their crystal forms and habits, specific gravity, colour and pleochroism, refractive indices, luminescence under ultraviolet light and their internal features are consistent with those properties of corundum reported by other researchers (Irving, 1974; Upton *et al.*, 1983; Irving, 1986; O'Reilly *et al.*, 1989; Stephenson, 1990; Guo *et al.*, 1996a; 1996b; Intasopa *et al.*, 1998; Sutherland *et al.*, 1996; 1998a; 1998b; Upton *et al.*, 1999; Limtrakun *et al.*, 2001; Sutthirat *et al.*, 2001).

There is no significant variation within the major oxide compositions of sapphires from the Bo Ploi deposit; in addition, the compositions are variable among the different tone of colours is rather inconclusive. This may be explained by the composition of corundum is almost entirely of Al_2O_3 and other compounds are made up of normally less than 1 wt%, thus the small amount of other trace elements cause the quantitative analyses less accuracy, particularly, when the energy dispersive spectra (EDS) electron microprobe technique is used. However, it is noticed that sapphires that appear to have less optical clarity (as in Fig. 2.3d) contain slightly higher TiO_2 contents, 0.18 wt%, compared to the Bo Ploi sapphire in general.

A trace element like Ga, is considered to be a chemical criterion to distinguish sapphires from different genetic occurrences. It is noticed that sapphires from basalt-related genesis is richer in Ga in comparison to those sapphires from metamorphic terrains (Sutherland *et al.*, 1998; Limtrakun, *et al.*, 2001). The concentration of Ga in sapphire from basaltic terrains tends to be higher than those concentrations in sapphire from metamorphic origin; however, the role of Ga in the cause of colour is still inconclusive.

The colour mechanism of blue sapphires has been proposed by many researchers and it is generally agreed that the presence of trace elements, iron (Fe) and titanium (Ti), produce blue colour in corundum (Ferguson and Fielding, 1971; 1972; Smith, 1978; Schmetzer and Bank, 1980; Burns 1981; 1993; Nassau, 2001). Burns also reported that the presence of Fe^{3+} in corundum yields yellow or pale green-blue shades, while Ti^{3+}-doped corundum displays a pink colour although Nassau (2001) argued that pink colouration in corundum may result from the small amount of Cr contamination and Ti gives, in his view, no colour in corundum. Both elements, Fe and Ti, replace Al in the corundum structure and reside in the octahedron coordination (Fig. 2.13).

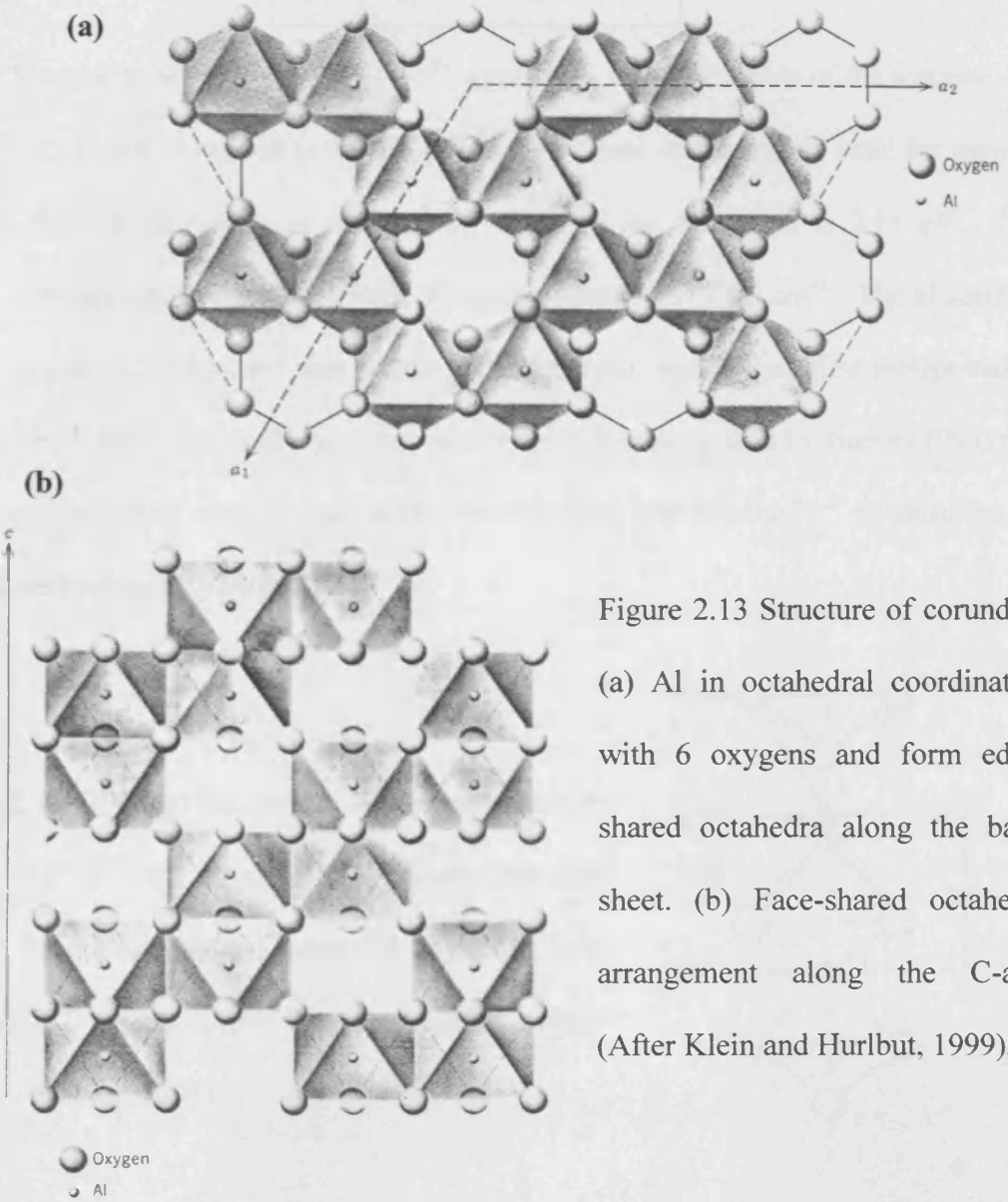

Figure 2.13 Structure of corundum (a) Al in octahedral coordination with 6 oxygens and form edge-shared octahedra along the basal sheet. (b) Face-shared octahedra arrangement along the C-axis (After Klein and Hurlbut, 1999).

Substitution of Al^{3+} by Fe could be either Fe^{2+} or Fe^{3+}, while Ti^{4+} normally substitutes for Al. The latter substitution is not straightforward, since charge neutrality has to be retained; this may occur by coupled substitution, like Fe^{2+} and Ti^{4+} substitution for two Al^{3+} sites. The Fe^{2+} - Ti^{4+} coupled substitution for Al^{3+} in the corundum structure normally takes place on the adjacent octahedra and causes the face-shared octahedra distortion (Fig.2.14) as a result the Fe^{2+} and Ti^{4+} are only 2.65Å away from each other and it is close enough for their d_{z^2} orbitals to be overlapped thus allowing an electron to transfer from one to the other. This is the so called intervalence charge transition (IVCT) and the reaction can be simplified as

$$Fe^{2+} + Ti^{4+} \rightarrow Fe^{3+} + Fe^{3+}$$

In order to achieve the Fe^{2+} + Fe^{3+} state in the right-hand side of the reaction, the energy of 2.11 eV is needed to be taken into the system or the energy used for transfer electron from ground state to the excited state in blue corundum is 2.11 eV. This energy corresponds to the wavelength of about 588 nm or 17000 cm^{-1}. The absorption in the region of 11150 cm^{-1} was additionally observed, which was first interpreted as Fe^{2+} and Fe^{3+} intervalence charge transfer, however, it is suggested by Burns (1993) that the more appropriate transition should be the transition between the Fe^{2+} substituting for Al^{3+} in the structure of corundum.

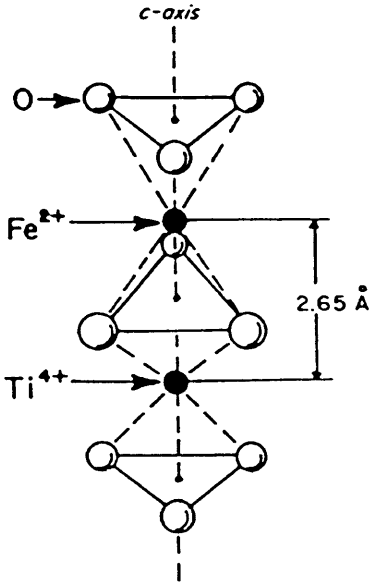

Figure 2.14 Diagram shows the coupled substitution of Fe^{2+}- Ti^{4+} for Al^{3+} and causes distortion to the face-shared octahedra. The Fe^{2+} and Ti^{4+} are at 2.65Å from each other. (After Nassau, 2001)

The less common absorption spectra which occur at 18450 and 20300 cm^{-1} likely represent the crystal field transitions within Ti^{3+} ions. The weaker broad band near 12500 cm^{-1} may represent a Ti^{3+} and Ti^{4+} intervalence charge transfer between the cations in face-shared octahedra (Burns, 1993).

The absorption spectra in the direction parallel to the C-axis of all these Bo Ploi corundum occur at similar positions, but the intensities of their absorbance were lower than those of the absorbance in the direction perpendicular to the C-axis. This can be explained by the dissimilarity of the position where the Fe^{2+} + Ti^{4+} intervalence charge transfer takes place. Unlike the direction parallel to the C-axis, the assembly of Al-octahedra in the corundum structure are characterised by edge-shared arrangement, as a result, the distance between the adjacent Al-octahedra after couple-substituted by Fe^{2+} + Ti^{4+} is about 2.79Å, which is slightly farther than the distance of face-shared octahedron in the direction along the C-axis, 2.65Å. The further distance the two atoms are apart causes less overlap of the electron orbitals thus leads to the lower intensities of Fe^{2+} - Ti^{4+} intervalence charge transfer spectra.

Schmetzer and Bank (1980) studied the absorption spectra of natural and synthetic corundum containing Fe-Ti and found that absorption spectra around 18500 and 20300 cm^{-1} can be produced by Ti-doping of synthetic sapphire. Only Fe-doped sapphire provided absorption spectra at 14500, 22200, 25800 and 26600 cm^{-1}. The Fe-Ti doped corundum always presented extra absorption spectra in the region of 17880 and 14300 cm^{-1}, which also occurs in natural blue corundum. Occasionally, the band at 11500 cm^{-1} may be observed and is interpreted as the Fe^{3+} - O^{2-} - Fe^{2+} electron charge transfer, with the process of transition of electron t_2-orbital on Fe^{2+} to the *e*-orbital on Fe^{3+} (Ferguson and Fielding, 1971; 1972).

Electron transfer only between the ferric and ferrous ions is another idea proposed to generate blue colour in sapphires (Nikolskaya *et al.*, 1978; Matson and

Rossman, 1988). This seems reasonable because both ferric and ferrous ions are intrinsic components in natural sapphires albeit at low levels. The exchange of electron pairs between the same valency like Fe^{2+} and Fe^{2+} or Fe^{3+} and Fe^{3+} could normally occur, as well as the electron transfer of the different valency: Fe^{2+} and Fe^{3+}. According to Nikolskaya *et al.*, (1978) the colour of sapphire has a close relationship to the concentration of iron and the Fe^{2+}/Fe^{3+} ratio and their number of exchange-coupled pairs. Colourless corundum shows no Fe pairs undergoing charge exchange. Green sapphire contains mainly exchange-coupled pairs of Fe^{3+} - Fe^{3+}, with the Fe^{2+}/Fe^{3+} ratio about 0.5. With the Fe^{2+}/Fe^{3+} ratio close to unity, together with equal activities of the two exchange-coupled pairs Fe^{2+} - Fe^{2+} and Fe^{3+} - Fe^{3+} produces blue sapphire coloured corundum.

The chemical compositions of the Bo Ploi sapphires are consistent with their optical spectroscopy confirming the blue colouration is due to the presence of Fe and Ti and in zoned crystals composition data from A.P.Jones (unpublished). A fairly good correlation was made between the absorption intensities at the position represent Fe-Ti colouration and the quality of blue colour e.g. the absorption intensity of intense blue colour sapphire (BPS-01) obviously high, reflects the Fe-Ti intervalence charge transfer. Unlike the absorption spectra of greyish blue sapphire (BPS-04), where the absorption intensity in the region of Fe-Ti intervalence charge transfer is significantly low and it is implied that either the availabilities Fe and Ti in the system are not sufficient or exceed of those elements in the system, therefore, the magnificent blue colour is not accomplished but the greyish blue instead.

Conclusions

1. Corundum from the Bo Ploi deposit, Kanchanaburi, Thailand is characterised by its physical and optical properties as stubby prismatic with tapering to ends shape or spindle shape - barrel shape with average specific gravity of 4.0 ± 0.5. Their colours are mainly blue with varieties of tone and saturation as well as their clarity. Colour zoning perpendicular to the C-axis is very common. Their refractive indices are ε 1.760-1.762; ω 1.768-1.772 and birefringence of 0.008 -0.009. Internal features that were observed including twin lamellae and growth zones (colour zones). Mineral inclusions (alkali feldspar, zircon, spinel, rutile, boehmite, nephiline, pyrochlore and monazite), fluid inclusions and silicate melt inclusions are also common.

2. The Bo Ploi corundum is composed of Al_2O_3 99.30-99.71 wt%, FeO 0.27-0.46 wt% and TiO_2 0.04-0.18 wt% with the negligible amount of Cr_2O_3 and V_2O_5, while SiO_2, MnO, MgO and CaO contents, generally, could not be detected except X-Ray microprobe data from A. P. Jones (unpublished).

3. The optical spectroscopy of the Bo Ploi corundum reveals that the causes of blue colour are due to the Fe^{2+}-Ti^{4+} intervalence charge transfer in the coupled substitution of Fe^{2+}-Ti^{4+} as an evidence of absorption at about 17000 cm^{-1}. Additional absorption observed around 11000 cm^{-1} region corresponds to either the crystal field transition of Fe^{3+}-Fe^{2+} within the same Fe^{3+} atom or the substitution of Fe^{3+} for Al^{3+} in corundum structure.

Chapter 3

Fluid inclusions

Fluid inclusions usually mean minute amounts of liquid and/or gas trapped in a crystal during a crystallisation or recrystallisation process. A solid phase, called daughter mineral, sometimes present with these fluid inclusions, which formed by two processes; a mineral trapping process where a mineral(s) may be trapped together with the fluid at the same time of the fluid inclusion formed and a fluid-host mineral interaction process which involves the reaction between the trapped fluid and the host mineral or precipitation of crystals from fluid upon cooling (Roedder, 1984; Shepherd *et al.*, 1985). The formation of fluid inclusions is principally based on the nature of crystal imperfection caused by defects in crystal structure, which affect the crystal growth and leads to diversity of crystal characteristics. While the crystals are growing, each face grows at a competitive rate of each favourable condition and they may occlude liquid or vapour at the growing interfaces and finally resulted in fluid inclusions trapped in the crystal structure. Geologists, particularly mineralogists, have been beneficial from studying fluid inclusions including, fluid compositions and their isotopic chemistries. A flow pattern chronology observing under microscopic study leads to the classification of fluid inclusions as *primary inclusions* as if they appear syngenetic in relation to the host crystal or *secondary inclusions*, where fluids were trapped after the formation of crystals. Thirdly, multi-phase fluid inclusions can often be re-homogenised by heating experiments in order to obtain the entrapment temperature. The trapping temperature is used for the fluid density calculation that leads to a pressure estimate of a formation, subsequently, these physical properties can be used as a geothermobarometer of the system.

There are always problems in ensuring that inclusions have behaved as closed systems during the long time interval since their formation, and a number of ways in

which this ideal behaviour can be corrupted or degrade which should be borne in mind. These include, fracture, segregation, leakage, recrystallisation, diffusion, etc. Nonetheless, in order to make progress, optimum inclusions can be selected based on established criteria relating to morphology, and these will be used.

A range of solid, fluid and melt inclusions have been reported in corundum (both rubies and sapphires) from various deposits (Coenraads, *et al.* 1990; Coenraads, 1992; Kammerling, *et al.*, 1994; Menon, *et al.*, 1994; Peretti, *et al.*, 1996; Milisenda and Henn, 1996; Kiefert, *et al.*, 1996; Smith, *et al.*, 1997; Sutherland, *et al.*, 1998b; Srithai *et al.*, 1999; Upton, *et al.*, 1999; Limtrakun, *et al.*, 2001; Giuliani *et al.*, 2003; Pakhomova, *et al.*, 2006; Pin, *et al.*, 2006). The solid inclusions have been most intensely studied by, mostly, gemmologist because they are thought to be useful in the identification of a particular province or mine from which a stone has been produced. For example, Thai sapphire/ruby was reported to contain hercynite, biotite, monazite, nepheline, feldspar, zircon, ilmenite, rutile and spinel (Aspen *et al.*, 1990; Coenraads *et al.*, 1990; Guo *et al.*, 1996a; Oakes, *et al.*, 1996; Sutherland, 1996; Intasopa, *et al.*, 1998; Srithai *et al.*, 1999; Upton, *et al.*, 1999; Limtrakun, *et al.*, 2001, Sutthirat, *et al.*, 2001; Saminpanya, 2001). Sutherland (1999) has used the range of mineral inclusions to help distinguish corundum derived from basalt versus corundum of metamorphic origin. In comparison with solid inclusions, little research has been carried out on melt and fluid inclusions (Amour and Linnen, 1999; Srithai *et al.*, 1999; Limtrakun, *et al.*, 2001; Saminpanya, 2001; Santosh, *et al.*, 2006). In theory, if fluid inclusions are presenting they should provide important information in combination with other independent geothermometers and geobarometers on PT conditions of crystallisation (Roedder, 1984; Bodnar, 1999; Diamond, 2001) and of the composition of melts and other fluids, including CO_2 and brine fluids responsible for crystallisation. However, there are some limitations for employing fluid inclusions as a tool to understand

geological problems. The inclusions must be primary in their original context and possess suitable sizes for analysis. Inclusions should be in perfect condition and any evidence of leakage has to be carefully considered since it can affect the accuracy of the microthermometric study. Sapphire from the Bo Ploi deposit meets these conditions, as will be demonstrated. Consequently, detailed Laser-Raman Microprobe, FTIR, EDS, SIMS and microthermometric studies were carried out in silicate-melt inclusions and to a lesser extent on the CO_2 and brine inclusions. These studies were supplemented by identification of solid inclusions. The results obtained from this chapter suggest that the Bo Ploi corundum formed from SiO_2-saturated melts in the presence of a CO_2-brine at the high temperature indicative of a magmatic origin.

This chapter, firstly, describes the inclusion phases including, mineral inclusions, fluid inclusions and silicate-melt inclusions. Secondly, the microthermometric studies on the fluid inclusions and silicate-melt inclusions are reported. Finally, the silicate-melt inclusions are analysed for their geochemical compositions. Subsequently, the genesis process of the Bo Ploi corundum is discussed using physiochemical conditions obtained from the inclusions studying.

3.1 Description of inclusions in the Bo Ploi corundum

Sapphire from the Bo Ploi deposits is characterised by a dense population of inclusions. The inclusions vary greatly in size, quantity and species. The inclusions that have been studied are sub-divided into mineral inclusions, fluid inclusions and silicate-melt inclusions.

3.1.1 Mineral inclusions

The Bo Ploi sapphire hosts several types of mineral inclusions. Only inclusions that occurred as primary inclusions are of interest hence they imply the environment and conditions during the crystallisation of sapphire. However, the secondary origins that form in healed fractures of the sapphire crystals are also briefly reported.

1. Alkali feldspar group

Mineral inclusions in Bo Ploi sapphires are perhaps dominated by the alkali feldspar group. By using Laser Raman Microprobe technique, they were identified as albite, sanidine and anorthoclase. Albite and sanidine usually randomly distributed in clusters, or sometimes as isolated crystals along the growth zones. They are euhedral, rounded crystals with stubby to elongate prismatic shapes; twinned crystals are commonly observed. Their sizes range from 20-100μm. and they could form a cluster of up to 70 grains of various sizes within a single sapphire crystal.

Anorthoclase appears as euhedral, stubby shaped crystals with relatively large sizes, ranging from 50-100μm. They are found only occasionally and tend to be distributed as isolated grains along sapphire growth zones. (Fig. 3.1a)

2. Zircon

Zircon is relatively abundant in Bo Ploi sapphire, with sizes ranging from 100-200μm. They are euhedral crystals with characteristic brown staining surrounding the zircon grain, known as zircon halos, as the result of radioactive decay of uranium and/or thorium within the zircon; this causes damage to the crystal structure of the host sapphire (Fig 3.1b). They are randomly distributed and can also form aggregates of crystals. Various forms of crystal are observed including as stubby, elongate and prismatic crystals. Twining of larger zircon crystals with smaller crystals at perpendicular orientation is commonly observed in polycrystalline inclusions.

3. Spinel

Spinel occurs as dark brown to black euhedral crystals. It exhibits stubby habit with crystal sizes of 50-100μm. It is relatively common and randomly distributed as isolated grains and also as aggregated grains (Fig. 3.1c). Spinel also displays rounded elongate crystals that tend to line up in rows of gradually changing size.

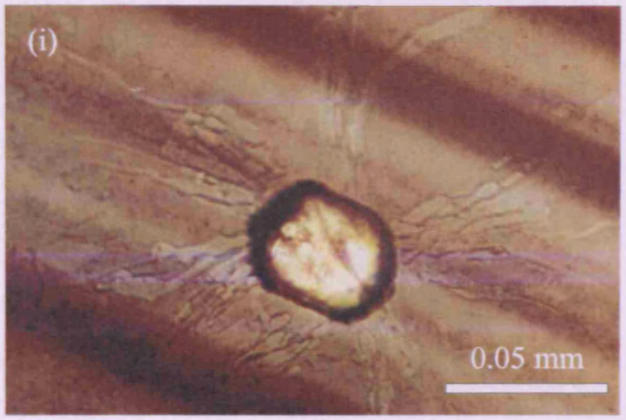

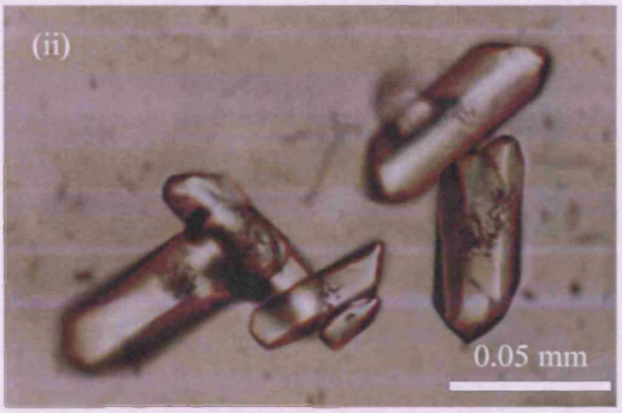

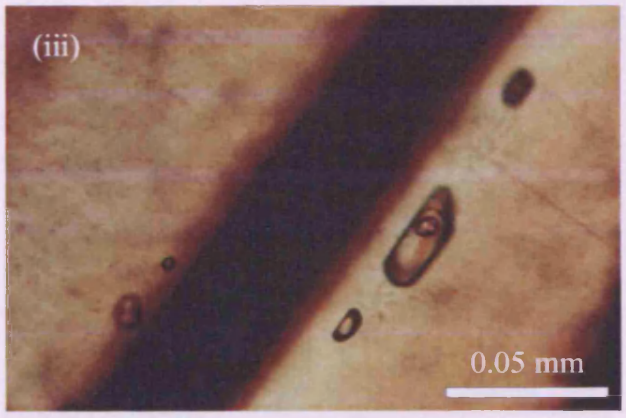

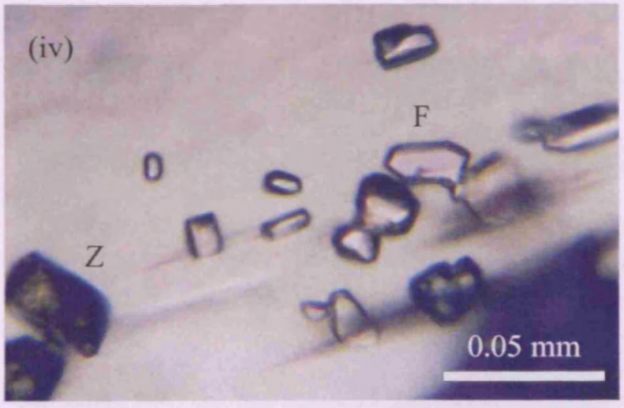

Figure 3.1(a) Photomicrographs of the morphology and distribution of feldspar inclusions in sapphire from the Bo Ploi deposit

(i) Anorthoclase feldspar with radiating features, cross-cutting growth zones of acicular micro inclusions.

(ii), (iii) Clusters of sanidine and albite feldspar, which exhibit euhedral to rounded euhedral crystals. The dark band of corundum growth zone is clearly seen in (iii), in which the feldspar grains show preferential orientation parallel to the growth zone.

(iv) Cluster of feldspar (F) associated with zircons (Z) in random orientation to corundum growth zones.

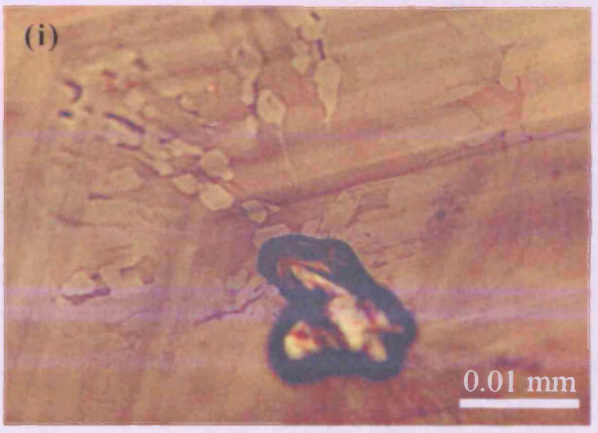

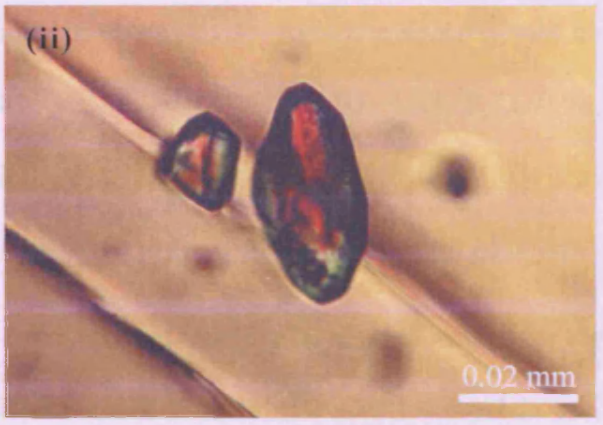

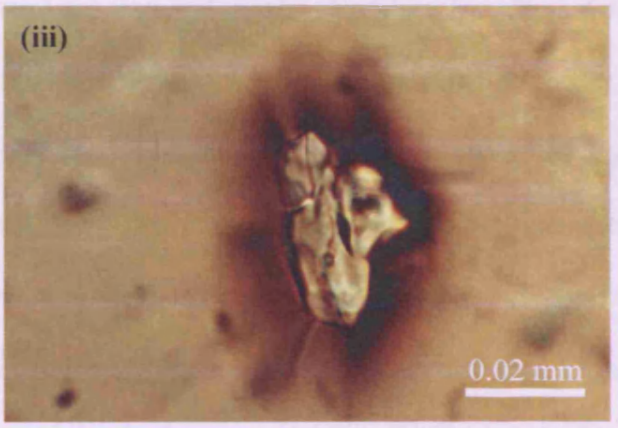

Figure 3.1(b) Photomicrographs of the morphology and distribution of zircon inclusions in sapphires from the Bo Ploi deposit. Note also the dark brown aureoles, zircon halos, which resulted from the radioactive decay that damaged the sapphire host.

(i) Trapped zircon crystal with cross-cutting radiate features across sapphire growth zone. Note also the small planar subhedral-euhedral polygonal forms along the radiating feature (top left corner).

(ii) Slightly rounded euhedral crystals of zircon with a diagonal micro-fracture.

(iii) Irregular (resorbed) crystals of zircon surrounded by zircon holos.

(iv) Typical form of a zircon crystal; tetragonal prism and dipyramids.

4. Monazite

Monazite is occasionally observed. It is euhedral with approximate size 20-50 μm. It also occurs as rounded and elongated crystals randomly distributed or found as aggregated crystals. (Fig. 3.1 d)

5. Pyrochlore (variety: columbite)

Pyrochlore (columbite) appears as a euhedral, opaque crystal of prismatic habit with tapering at the ends. Its size ranges from 100-500μm. (Fig. 3.1e). Electron microprobe analysis gives the approximate chemical composition in wt%; Na_2O 0.31, MgO 1.22, Al_2O_3 0.18, SiO_2 1.68, P_2O_5 0.98, CaO 0.20, TiO_2 4.06, V_2O_5 0.43, MnO 3.65, FeO 12.32, ZrO_2 0.89, Nb_2O_5 74.08. It is observed as an isolated grain. However, they sometimes form pairs or cluster of crystals that resemble twins.

6. Unidentified needles (boehmite or rutile?)

Unidentified dark brown acicular crystals are observed in almost every crystal. They are very tiny and maybe densely aggregated with approximate sizes of up to 2μm. The acicular inclusions form a mesh-like structure. Three sets of these inclusions show preferential orientation at approximately 120 degrees to each other (Fig. 3.1f). They are regularly distributed and form epitaxial growth along sapphire growth zones. In the section perpendicular to the c-axis of sapphire crystals, these growth zones are conspicuously seen as regular or distorted hexagonal bands, also recognised as colour zoning. Hughes (1999) reported in his book that the needle-like cloudy inclusions that found in ruby and sapphire are exsolved crystals, which formed under high pressure and boehmite. Rutile usually forms three sets of needle-crystals crossing at 60/120° and parallel to the basal plane. Boehmite may resemblance rutile, but only two sets of inclusions are in the same plane. This plane is at approximately 30/60° to C-axis and the other set of inclusions intersects this plane at 86.1/93.9°. It is, therefore, concluded that the unidentified needle-inclusions are rutile.

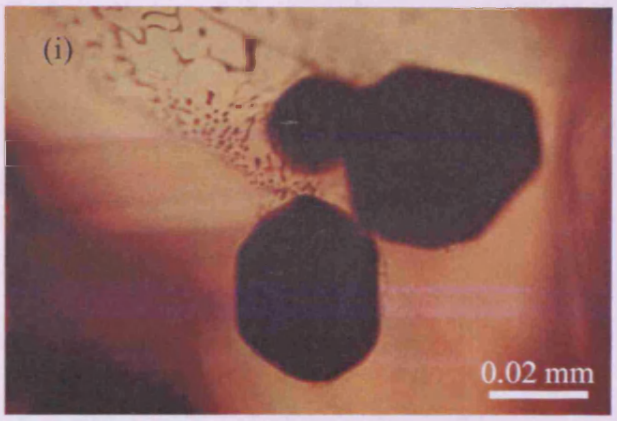

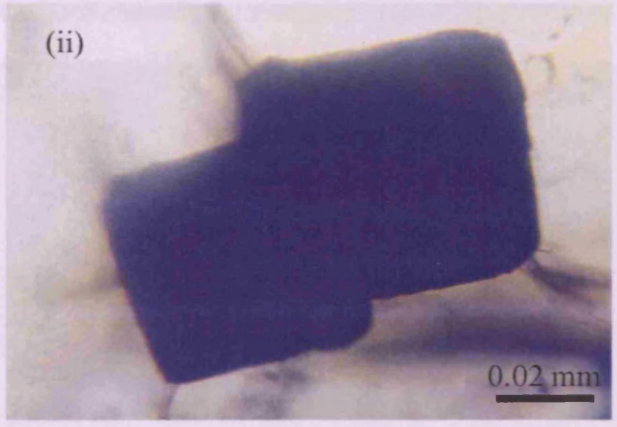

Figure 3.1(c) Photomicrographs of morphology and distribution of spinel inclusions in sapphires from the Bo Ploi deposit.

(i) Euhedral spinel associated with feather-like inclusions of necked inclusion of melt (?)

(ii) Common form of spinel and twinning.

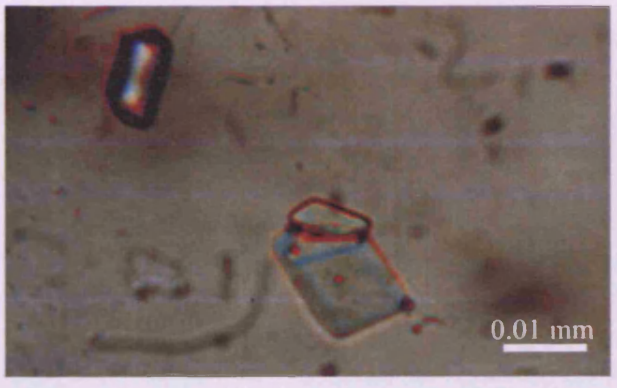

Figure 3.1(d) Photomicrograph of euhedral monazite and its twinning. Top left corner is a crystal of feldspar.

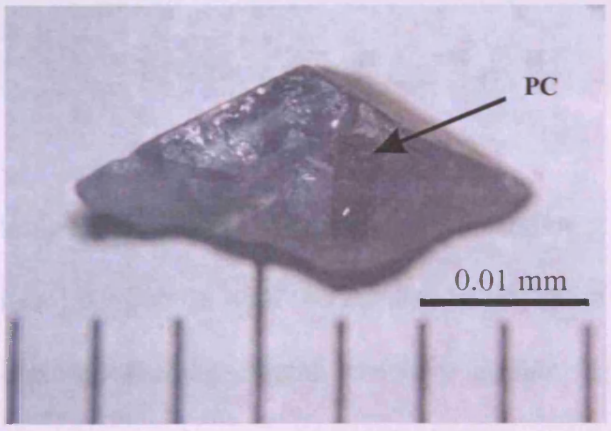

Figure 3.1(e) Photomicrograph of rough crystal sapphire with inclusion of pyrochlore (PC), in the dull black prismatic shape.

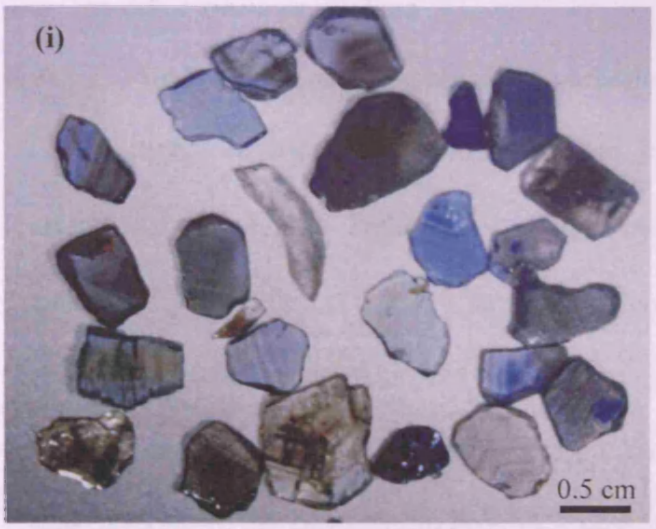

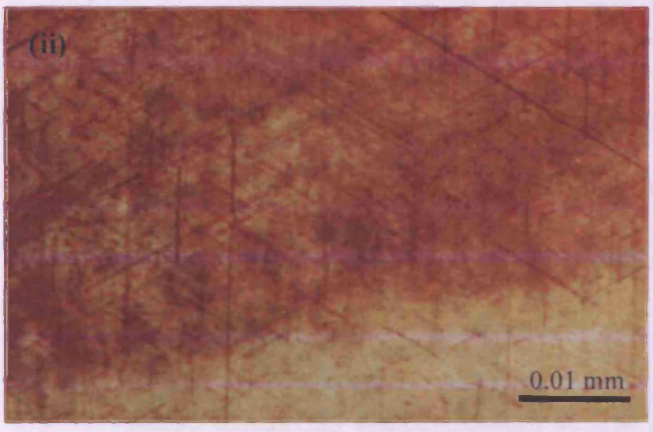

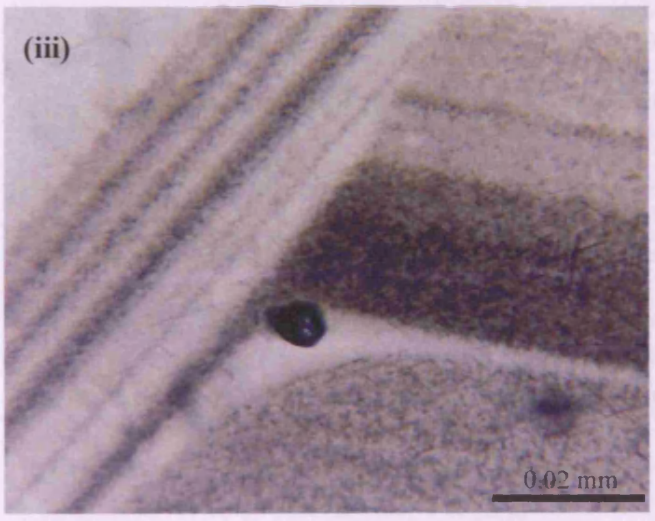

Figure 3.1f Photomicrographs of colour banded of unidentified needle inclusions.

(i) Doubly polished wafers of sapphire show clearly colour zoning

(ii) The dark acicular inclusions form a mesh-like structure. Three sets of these intersections show preferential orientations approximately 120 degree to each other.

(iii) The intersection of colour zoning, decorated by acicular formed inclusions. Note the thickness of colour bands are uneven, which may imply fluctuating conditions during the crystal growth.

temperature during the growth of corundum. It is difficult to distinguish between the needles of rutile with the needles of boehmite since the shape; size and appearance of these needle-like crystals are very similar. However, he suggested that by using the orientation of the sets of needle-crystals, one should be able to distinguish rutile from

3.1.2 Fluid inclusions

Fluid inclusions in sapphire are variable in terms of their size, distribution and composition. Many sample wafers contain informative inclusions, while some are effectively devoid of inclusions. Large inclusions, between 50-100 μm, occur sporadically. The exceptionally large inclusions, 150-170μm, are rare. They usually exhibit rounded, negative crystal shapes and less common amoeboid or irregular or polygon shapes. Many occur within and parallel to, separate colour growth bands and thus interpreted as primary inclusions. Less commonly, the larger inclusions occur along healed fractures and are either secondary or pseudosecondary in origin. Clusters of very small inclusions (<5μm) surrounding larger inclusions are a distinctive feature of Bo Ploi sapphire. Based on the optical and microthermometric properties, the fluid inclusions are divided into two broad compositional types.

1. Type 1 CO_2-rich inclusions

These inclusions appear monophase at room temperature but easily form two phases on cooling. Microthermometric study indicates pure CO_2 composition and was also confirmed by Laser Raman Microprobe. The only other phase detected was a tiny amount of water on the margins of the inclusions optical and microthermometric data support this identification. Aureoles of micro inclusions are observed in many samples. However, it was not possible to determine their composition, because their small sizes made the observations extremely difficult. The morphologies and distribution of type 1 CO_2-rich inclusions are illustrated in figure 3.2.

2. Type 2 Multiphase inclusions

Multiphase inclusions, containing vapour + aqueous + solid phase, are ovoid to negative-crystal-shaped. They commonly occur parallel to the growth zones and occasionally cross cut the growth zones. They are often associated with aureoles and curved planes of micro-inclusions (<2μm), which appear clearly before the heating

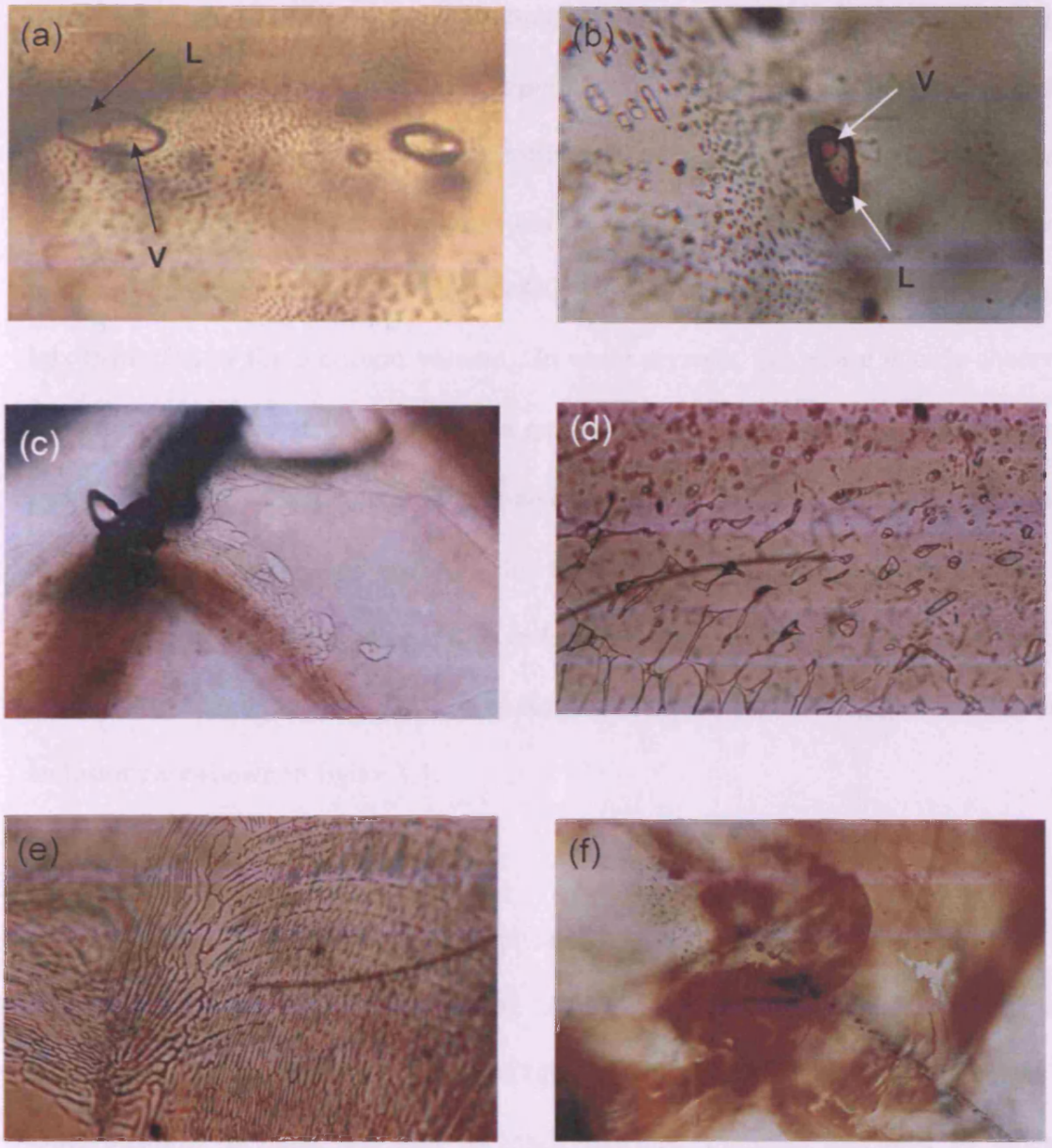

Figure 3.2 Photomicrographs display morphology and distribution of type 1 CO_2-rich inclusions. (a) and (b) Rare large primary ovoid CO_2-rich inclusions, which contain liquid (L)and vapour (V) phase. Note the plane of micro-inclusions surrounded the large inclusion. (c), (d), (e) and (f) The variety of patterns of CO_2-rich inclusions that form a network of CO_2 veinlets also known as feathers, veils and fingerprints. Note the necking down developed in (d). These inclusions are interpreted as secondary origin, where CO_2-rich fluid was trapped in sapphire structure as healed fracture.

experiment. They are characterised by large daughter minerals of halite and usually an additional cubic daughter mineral probably sylvite, according to microthermometric study. Smaller amounts of other isotropic and anisotropic daughter minerals are also present but could not be positively identified. The vapour bubble typically occupies about 20-25% of the inclusion volume, but the other ratio is 30-50%. The bubbles are probably composed of pure, low density CO_2-rich vapour. The aqueous phase occupies less than 15% of the inclusion volume. In some crystals, this phase is only observed from the appearance of CO_2 clathrate, a gas hydrate substance ($CO_2 \cdot 5.75H_2O$) resulted from interaction of aqueous and non-aqueous phases (Shepherd *et al*, (1985) and hydrohalite ($NaCl \cdot 2H_2O$) on cooling. However, the individual temperatures of clathrate and hydrohalite formation were not recorded accurately because of the closely packed of the assemblage phases. The morphologies and distribution of type 2 Multiphase inclusions are shown in figure 3.3.

3.1.3 Silicate-melt inclusions

This group of inclusions is complicated and difficult to interpret. They illustrate negative-crystal-shaped and are rounded. At room temperature, they appear to contain an isotropic or weakly anisotropic phase (glass), with or without immobile bubbles. In some samples, acicular and thin prismatic daughter minerals that may be slightly birefringence or opaque are present. This group of inclusions is usually associated with the planar and polygonal planar micro-inclusions, which was interpreted to be silicate-melt that leaked through the perfect parting of corundum. The inclusions were analysed by Laser Raman Microprobe, from which a broad curved was obtained and is an indicative of silicate glass (Fig. 3.4). However, the minute daughter crystals were not positively identified. The relative proportional volume occupied by these phases varied slightly among the samples. Typically, the vapour bubble is approximately 10-15%, daughter minerals are less than 5% and isotropic glass occupies approximately 50-90%

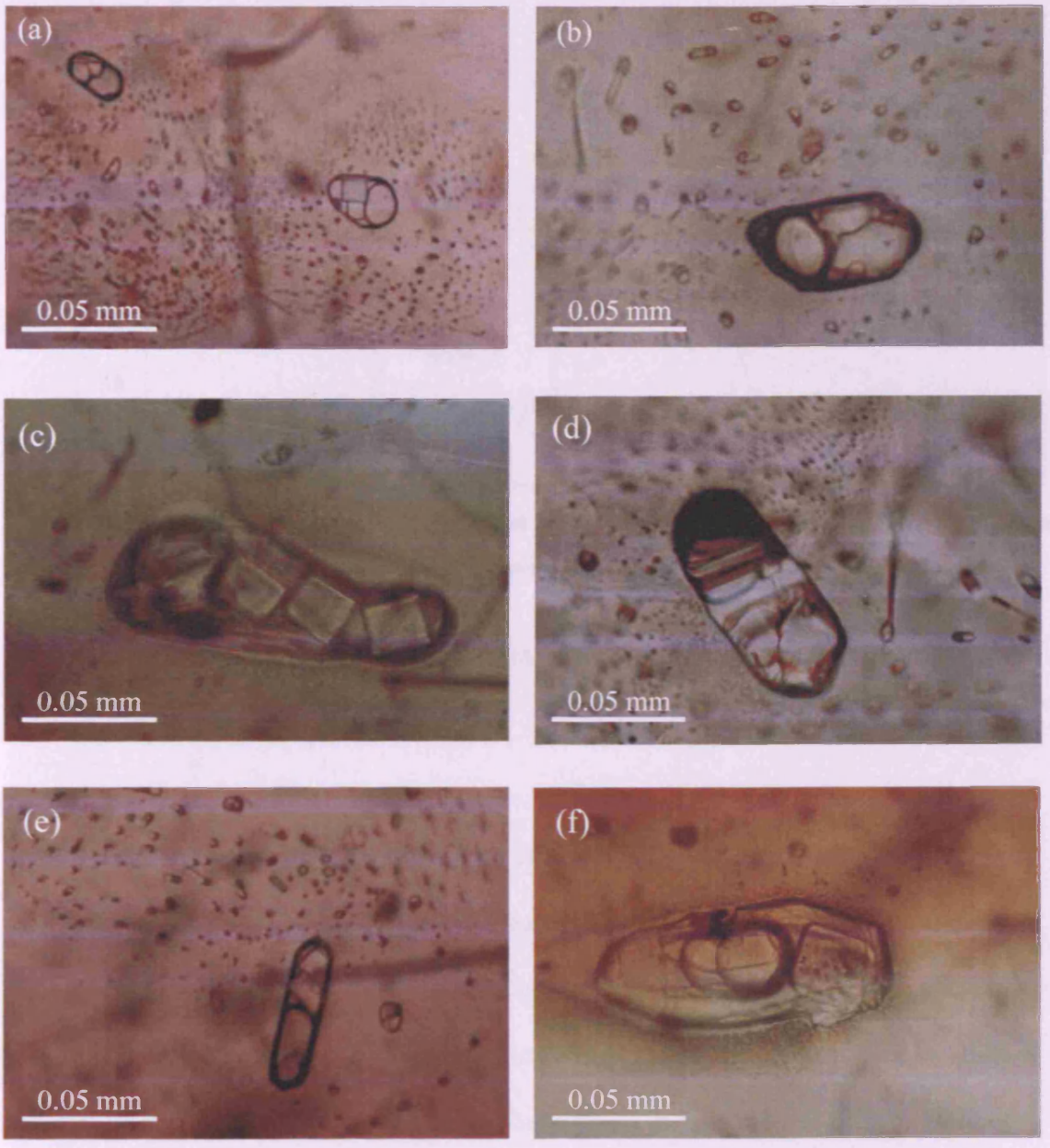

Figure 3.3 Photomicrographs (a-f) representative type 2 Multiphase inclusions. Typically, the inclusions are composed of a vapour bubble, hypersaline brine and cubic daughter minerals, especially well shown in (c). Note the different volume proportion of vapour phase and the aureoles of micro inclusions, which seem to swirl around the large inclusions.

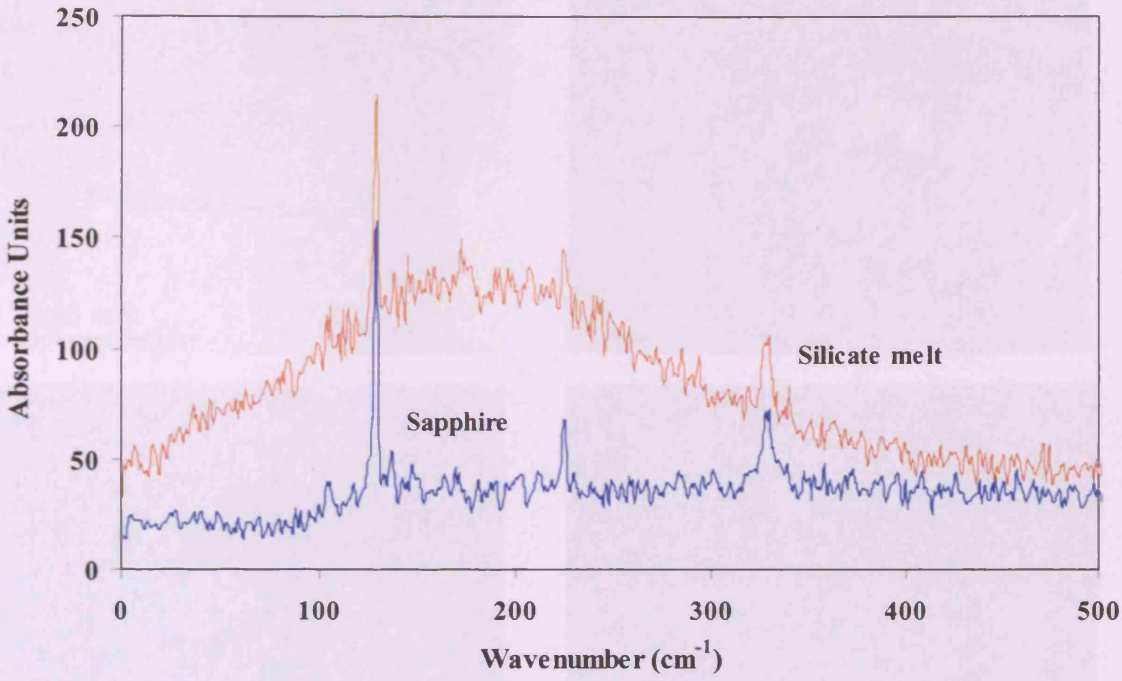

Figure 3.4 Laser Raman Microprobe spectra of trapped silicate melt compared with the host sapphire

of the inclusions volumes (Fig. 3.5). The bubbles, which occupied different proportion of the inclusions, were identified using Fourier Transform Infrared microscopy, where H_2O molecules and CO_2 molecules are found in the samples (Fig. 3.6). The coexisting phases in the vapour bubble of trapped silicate melts were distinguished by location of absorption regions; CO_2 molecules show sharp peaks in the range of 1200 to 1400 cm^{-1} and around 2400 cm^{-1}, while H_2O molecules display distinct absorption at 1595 cm^{-1} (bending mode) together with broad absorption around 3600 – 3700 cm^{-1} region (symmetrical and asymmetrical stretching mode).

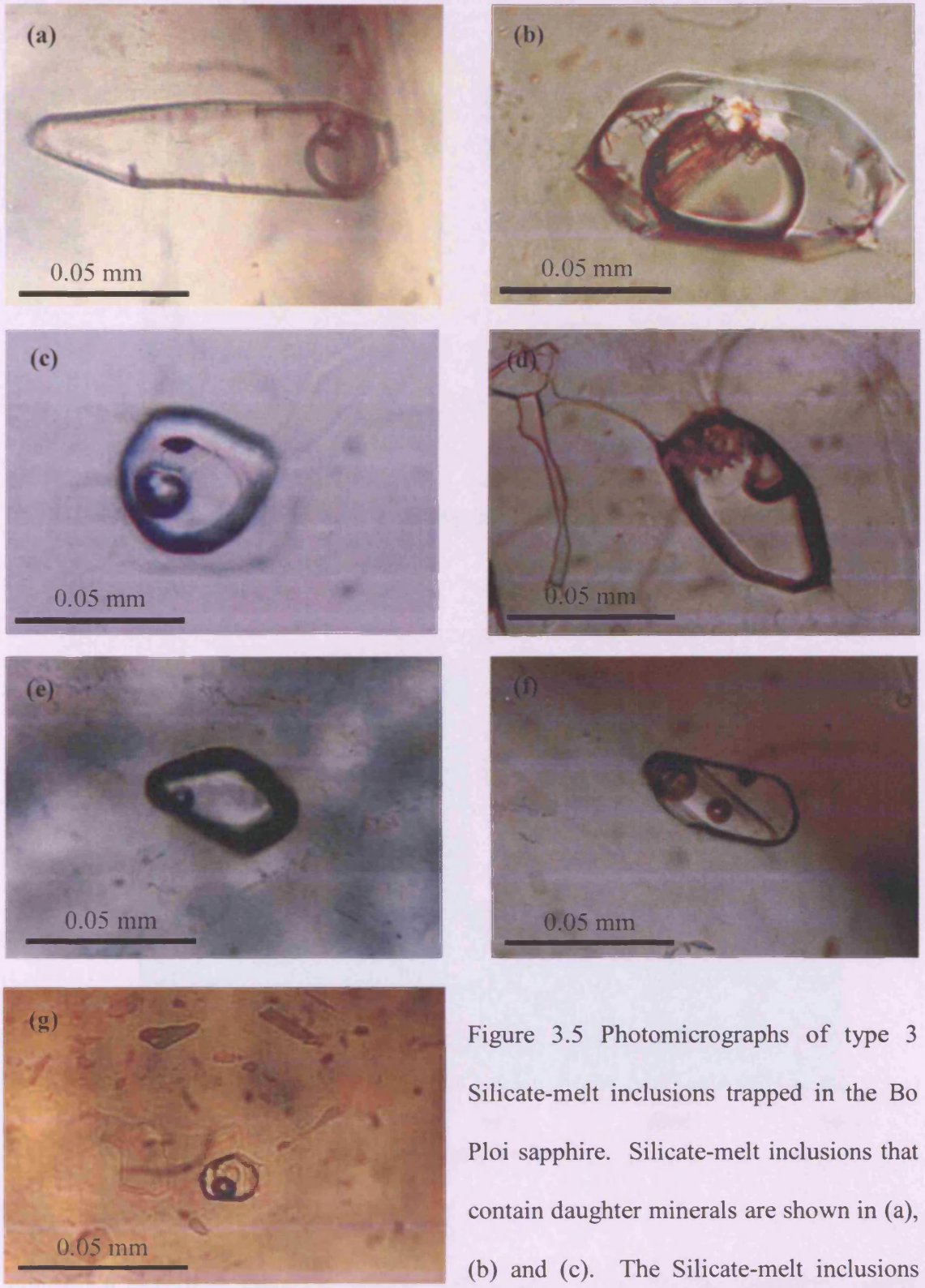

Figure 3.5 Photomicrographs of type 3 Silicate-melt inclusions trapped in the Bo Ploi sapphire. Silicate-melt inclusions that contain daughter minerals are shown in (a), (b) and (c). The Silicate-melt inclusions that devoid daughter crystal are shown in (d) (e), (f) and (g). Note also flat, irregular shaped, with swirl-liked planar inclusions surrounding melt inclusions, which is interpreted as leakage/decrepitation of the melt inclusions after the entrapment.

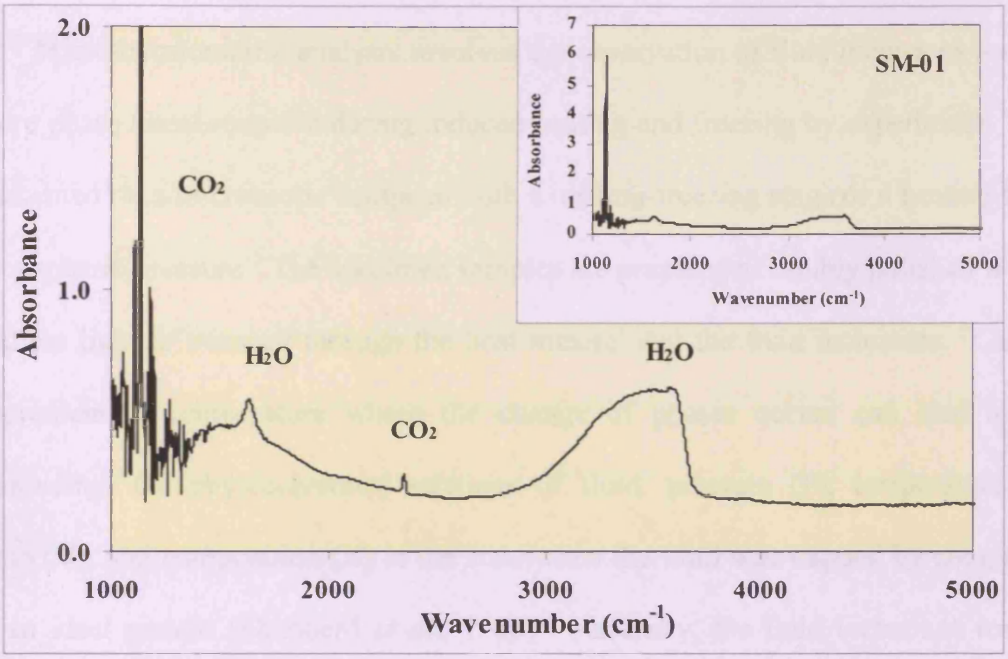

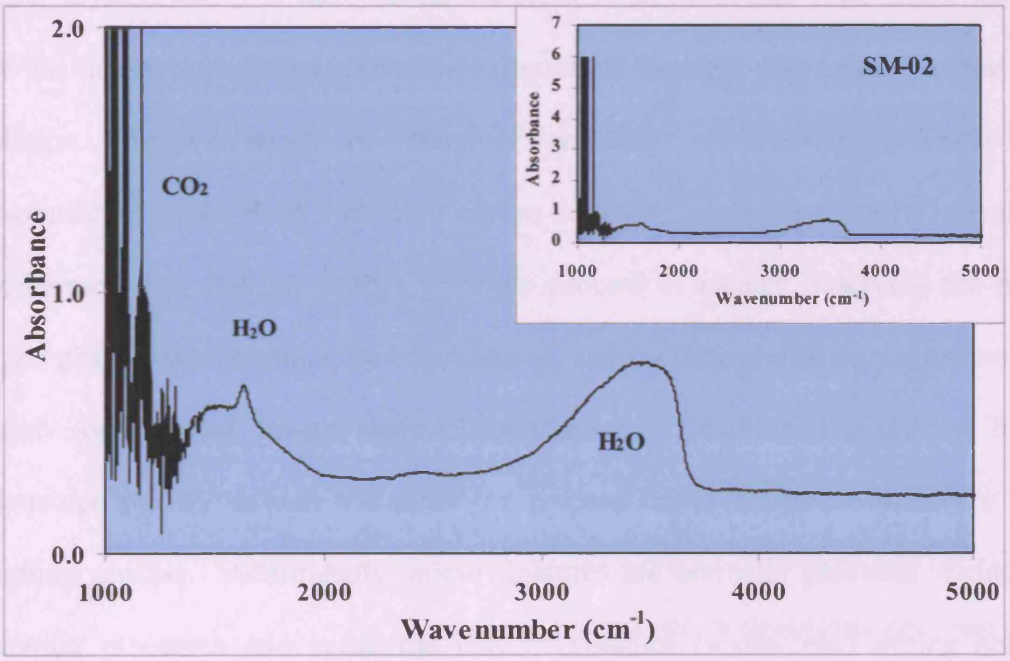

Figure 3.6 Infra-Red spectra of silicate melt trapped in the Bo Ploi corundum sample SM-01 and SM-02 show the presence H_2O and CO_2 molecules. The inset spectra are full scale of each analysis, where CO_2 is prominent with high absorbance units.

3.2 Microthermometric Analyses

Microthermometric analysis involves the observation of fluid inclusions for one or more phase transformation during induced heating and freezing by experiment. This is performed on a microscope equipped with a heating-freezing stage or a heating stage at atmospheric pressure. The specimen samples are prepared as doubly polished wafers that allow light to transmit through the host mineral and the fluid inclusions. Careful measurement of temperature where the change of phases occurs can lead to the determination the physiochemical relations of fluid: pressure (P), temperature (T), volume (V), and composition (X) at the state when the fluid was trapped by comparing with an ideal system (Shepherd *et al.*, 1985). Naturally, the fluid inclusions tend to comprise multiple phases such as vapour and liquid, or vapour, liquid, and solid daughter crystals and it is rare that an inclusion is single phase. The phase changes where the vapour bubbles dissolve into the liquid (or the other way round) and the total dissolution (disappearance) of daughter minerals on heating indicates the homogenisation of the fluid inclusions and re-homogenisation for the melt inclusions. Microthermometric analysis allows a simple process of closely observing the phase changes, phase transformation, homogenisation, and re-homogenisation via microscope or more sophisticated image analysis apparatuses. However, the method has a disadvantage mainly due to the need for preparation of wafers, which is a time consuming process. Additionally, micro fractures are normally produced during the preparation processes and cause the loss of volatiles (water, etc.) during heating experiment. In addition, the heating stages are very small so the wafers must be even smaller and that only limited number of inclusions will be examined at a time.

There is an alternate microthermometric analysis, particularly for melt inclusions, in which inclusions are incinerated in a special drop-quenched furnace. The vertical furnace is designed with an enormous difference in temperature between the

two ends that allow a rapid quench rate to achieve. The samples are suspended on a platinum wire in the optimum position of heating filaments and heated to the target temperature and duration. After the heating experiment the platinum wire is melted by remote electrical current and the whole sample container is dropped into the cooler part of the furnace or into the cooling medium such as liquid nitrogen to allow rapid quenching. The furnace can be modified for performing the heating experiment under pressure by installing additional apparatus for gas flow that allow the variation of pressure to be controlled. The manifest advantages of heating experiment in a drop-quenched furnace are the flexibility of the sizes of samples as well as inclusions. Many samples can be heated at the same time, while the experiment is performed. The hydrothermal furnace increases a chance for homogenisation, particularly for the melt inclusions, thus the introduction of pressure would, theoretically, reduce the homogenisation temperature of the system. On the other hand, the major disadvantage of heating the inclusions in a drop-quenched furnace concerns the accuracy thus the homogenisation temperature is estimated after recovering the samples from the experiments and frequently that the samples were wasted.

In this work, sapphire crystals were prepared for microthermometric study as doubly polished sections with approximately 0.4mm thickness. This thickness, which is thicker than conventional fluid inclusion wafers, was chosen in order to minimise the loss of the rare larger inclusions during the polishing. However, a temperature correction was done in order to assure the accuracy and it is concluded that negligible variation of temperature to the thickness of the sample. This may be explained by the excellent heat conductivity of corundum. Linkam TH600 heating/freezing and TH1500 heating stages at the School of Geological Sciences, Kingston University were used for the microthermometric studying. The TH600 heating/freezing stage has a working temperature range of –180°C to +600°C, and it was primarily used for identifying the

assemblage phases in the inclusions. It is noticed that all of the cubic daughter minerals from type 2 Multiphase inclusions were completely dissolved on the TH600 heating/freezing stage, however the total homogenisation were greater than 600°C and were carried out on the TH1500 heating stage as were type 3 Silicate-melt inclusions.

On heating, the inclusions were heated until the temperature reached approximately 50 to 55°C and retained at that point for a minute in order to eliminate moisture. The inclusions were then cooled down to room temperature, where the original phases were verified. The inclusions were then gradually heated and any phase changes were observed via the microscope. The temperature of homogenisation (Th) is recorded on heating at the point where the inclusions visually homogenise, which can be classified into two types of homogenisation; homogenisation to liquid, denoted by the subscript *l*, $Th_{(l)}$, and homogenisation to vapour where subscript *v*, $Th_{(v)}$, is indicated. Homogenisation into liquid is that when the volumes of vapour bubble are smaller and finally disappeared into liquid phase on heating. In contrast, homogenisation into vapour is characterised by the expansion of the vapour bubble until the whole inclusion is occupied by the vapour phase or the liquid phase vanished on heating. It is noticed that most of the type 1 CO_2-rich inclusions show homogenisation into liquid, while all of the type 2 Multiphase inclusions homogenised into vapour.

In the freezing experiments, liquid nitrogen (boiling point of -196°C), was used as a cryogenic liquid because the extremely low boiling point of liquid nitrogen allows a wide range of possible trapped gasses to be identified. Pure O_2-free nitrogen gas was fed directly to the "heating stage" to cool the inclusions until the temperature reach -196°C. The phase changes were observed via optical microscope. The diagnostic features of phase changes include straightening of boundaries of rounded vapour bubbles, the changing location of the vapour phases, and the changing colour (the observation must be done particularly caution as it could be a result from artefact). In

addition, the morphologies and crystal faces change in reaction between aqueous fluids with the vapour, in type 2 Multiphase inclusions are also noteworthy recorded. Subsequently, the inclusions were gradually heated up and carefully observed the melting of phases and the temperatures of melting (T_M), where the frozen phases completely melted, were recorded.

The microthermometric analyses of trapped inclusions in corundum from the Bo Ploi deposit are presented as follow;

3.2.1 Type 1 CO_2-rich inclusion

One hundred and thirty four CO_2-rich inclusions, which appeared primary and pseudo-secondary in origin, were used in the heating/freezing experiments. On heating, the CO_2 bubbles disappeared and homogenised into both liquid and vapour (Fig. 3.7). The temperature of homogenisation (Th) into liquid is between 10.9°C and 31°C, which corresponds to a density of 0.5 to 0.84g/cm^3. The temperature of homogenisation into vapour ranges from 26.6°C to 31°C and indicates a density of 0.45 - 0.27 g/cm^3. The densities are obtained from FLINCOR programme (Brown *et al.*, 1989). The high density CO_2 inclusions (0.84 g/cm^3) corresponds to the pressure 9-10 kbar (Brown and Lamb, 1989) at temperature 1000 - 1200°C, however, the estimate pressure is rather less accurate since inclusions appear to leak. Histograms exhibit the relationships between homogenisation temperature and the numbers of inclusions are shown in figure 3.8.

On freezing, the only phase change occurs between a temperature -56°C to-57°C, which indicates pure a CO_2 composition.

3.2.2 Type 2 Multiphase inclusions

Eleven samples of relatively large (60 to 170μm) multiphase inclusions were selected for microthermometric study. It is found that six of them could be totally

homogenised at the temperature range from 920-1000°C, while the rest of samples could not be homogenised.

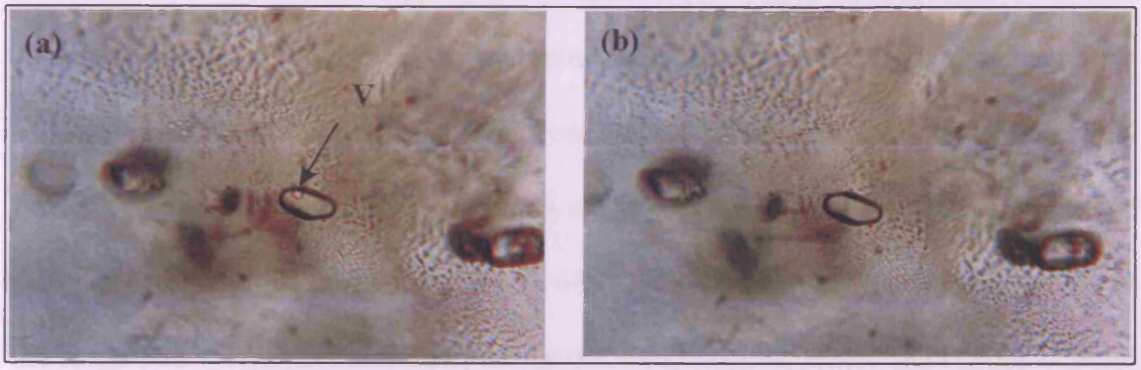

Figure 3.7 Photomicrographs show heating experiment of type 1 CO_2-rich inclusions

(a) At room temperature before heating experiment

(b) At 29°C, note the vapour bubble (v) disappeared on heating.

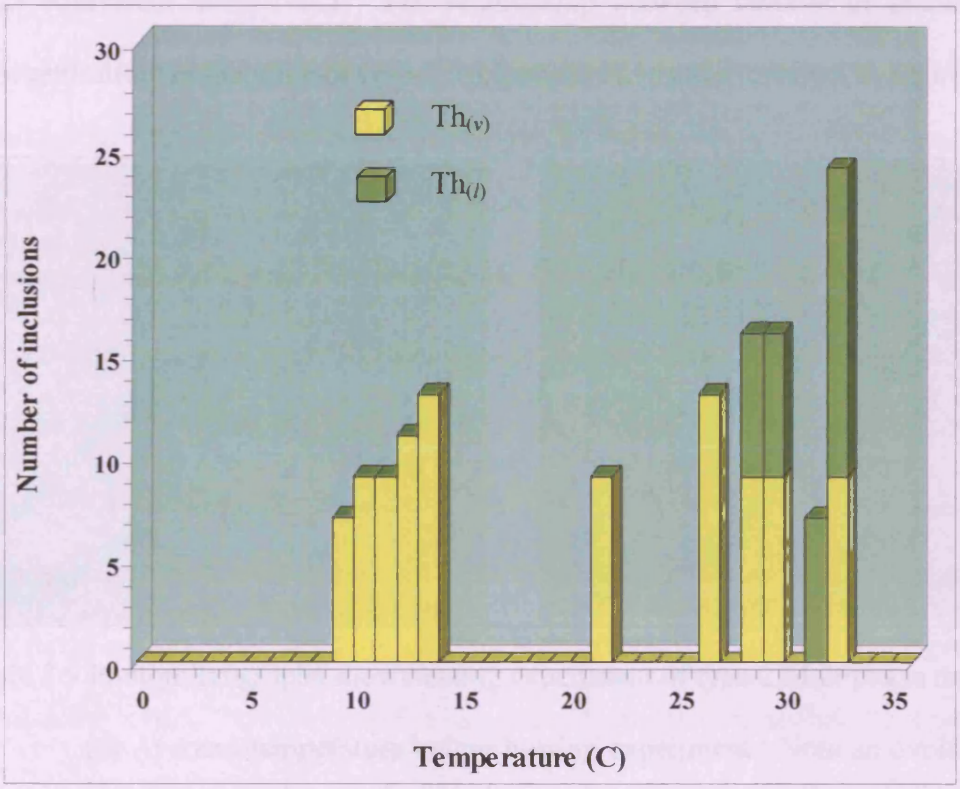

Figure 3.8 Histogram shows numbers of type-1 CO_2-rich inclusions and the homogenization temperatures. $Th_{(v)}$ is a temperature of homogenisation into vapour and $Th_{(l)}$ is a temperature of homogenisation into liquid.

On heating, the vapour phases showed homogenisation temperatures range between 13.5 to 31°C, which indicates the composition of low density CO_2 (0.15 to 0.47 g/cm^3). Some of type-2 Multiphase inclusions contain two different solid phases, cubic daughter minerals (Fig.3.9), which exhibit a distinctive phase change at two temperatures. At around 240 to 400°C, some of the cubic daughter minerals, probably sylvite, was completely dissolved. The larger cubic daughter minerals, halite, disappeared at higher temperatures range from 530 to 625°C. Total homogenisation temperature in the range 920 to 1000°C was observed in the six inclusions where the vapour bubbles occupied approximately 20-25% of the volume. In contrast, the samples that failed to homogenise generally contain vapour bubbles of about 35-50% volume. Based on the dissolution temperature of halite, the salinity of these inclusions is estimated between 64-73 equivalent Wt% NaCl. The relationship between number of inclusions and homogenisation temperature of type-2 Multiphase inclusions is shown in figure 3.10.

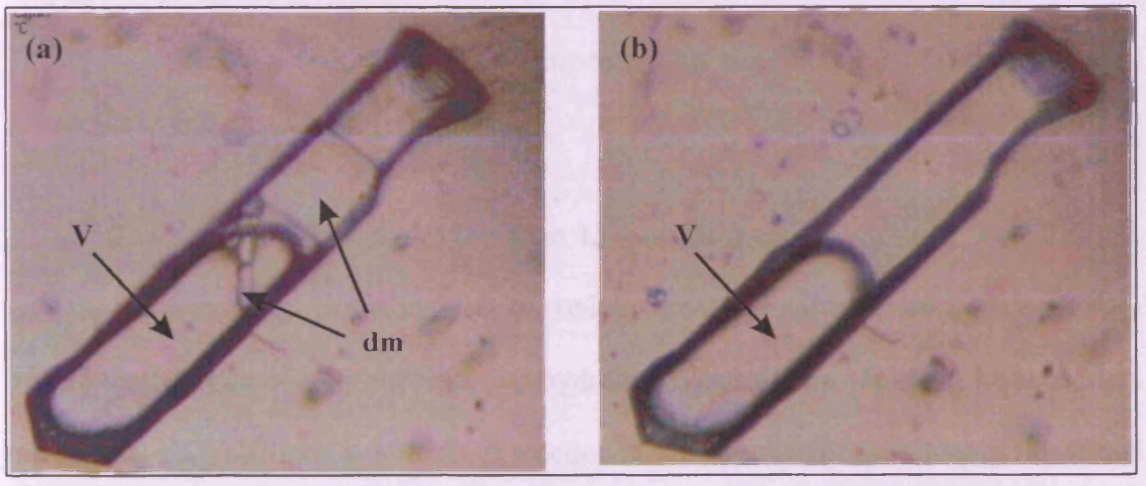

Figure 3.9 Photomicrographs show heating experiment of type 2 Multiphase inclusions

(a) At room temperature before heating experiment. Note an ovoid shape of vapour bubble (v) and large cubic and prismatic daughter minerals (dm).

(b) At 531°C, the daughter minerals were totally dissolved. Note changing location and shape of vapour bubble (v). The total homogenisation of this inclusion, where a vapour bubble disappeared is at 1064°C.

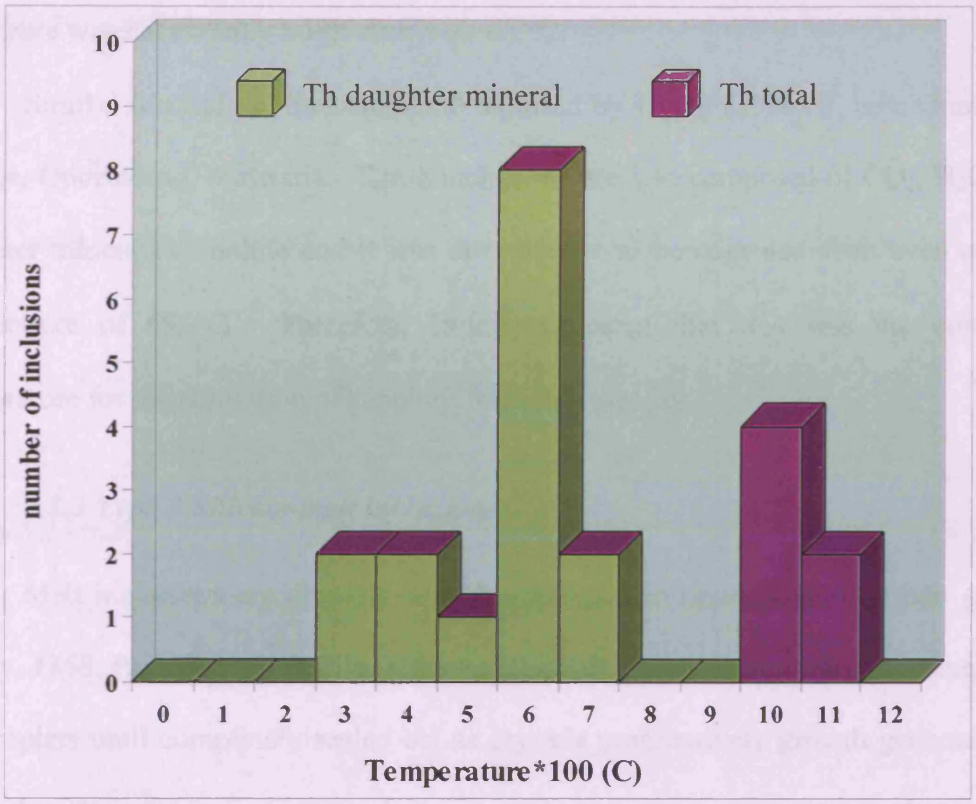

Figure 3.10 Histogram shows of type-2 Multiphase inclusions showing melting temperatures of daughter minerals (Th daughter mineral) and the total homogenisation temperature.

The liquid phase occupies less than 15% of the inclusion volume. The presence of CO_2 clathrate and hydrohalite were the only evidence of the co-existing phases. As a result, temperature of CO_2 clathrate and hydrohalite dissolution could not be accurately measured. CO_2 clathrate is a result of reaction at the interface of the aqueous liquid and the CO_2-rich liquid or gas bubble during cooling. Clathrate will freeze out prior to the freezing of the remaining aqueous fluid to ice (Collins, 1979). It occurs in the CO_2 bubbles and gradually reaches the aqueous surface and displays colourless aggregates of platy grains that look cloudy. It was extremely difficult to record the accurate temperature of onset of the clathrate nucleation, because the appearances of ice and CO_2 clathrate are very similar. Also the close proximity of other phases, however, the

decomposition of clathrate around 6°C is a confirmation of the presence of clathrate since pure water ice totally melts at or below 0°C.

Similar Multiphase inclusions are reported by Irving (1986) in corundum from Anakie, Queensland, Australia. These inclusions are also composed of CO_2, H_2O, and daughter minerals of halide and it was not possible to homogenise them even up to a temperature of 685°C. Therefore, Irving suggested that this was the minimum temperature for the formation of sapphire from that locality.

3.2.3 Type 3 Silicate-melt inclusions

Melt inclusions are droplets of melt entrapped in minerals during their growth (Sorby, 1858; Roedder, 1979; 1984) this begins with crystallisation interfaces engulfing the droplets until completely sealed off as crystals progressively growth generating an isolated melt inclusion. Unlike glasses in volcanic matrix that almost always have experienced volatiles loss during eruption processes, melt inclusions are pre-eruption volatile-contained samples of magmas, accordingly, these informative melt inclusions allow a specific stage of magma compositions and their evolutions to be reconstructed by re-heating the inclusion on a microscope heating stage until the inclusion is homogenised (Roedder, 1984; Shepherd, *et al.*, 1985; Sinton, *et al.*, 1993; Danyushevsky, *et al.*, 1997; Sours-Page, *et al.*, 1999; Kress and Ghiorso, 2004) where the temperature at which a homogenisation takes place is also regarded as a trapping temperature. The homogenised melt inclusions are later quenched and analysed for their chemical compositions. Nonetheless, this is based on the postulation that trapped melt inclusions are in closed system after the entrapment and have their own evolutions without any influence from the host minerals or the surrounding lava.

A number of works on melt inclusions are reported with a general focus on inclusion characteristics, their formation mechanisms and evolution, and sometimes

having economic implications (Sobolev and Shimizu, 1993; Neilson *et al.*, 1995; Barclay *et al.*, 1996; Sobolev and Chaussidon, 1996; Webster *et al.*, 1996; Chupin *et al.*, 1998; Nakamura and Shimakita, 1998; Nielsen *et al.*, 1998; Shimizu, 1998; Tsuruta and Takahashi, 1998; Yapnik, 1998, Danyushevsky *et al.*, 2000; Schiano *et al.*, 2000; Andersen and Neumann, 2001; Scambelluri, and Philippot, 2001; Borisoya *et al.*, 2002; Massare *et al.*, 2002; Grancea *et al.*, 2003; Schiano, 2003; Schiano *et al.*, 2004). Studying techniques on melt inclusions are commonly referred to the works of Sheperd *et al.*, (1985); Touret and Frezzotti, (1993); Halter *et al.*, (2002). Information obtained from melt inclusions on Magmatic immiscibility processes in the light of melt inclusions are discussed by Roedder (1992); Loferski and Arculus (1993); Morogan and Lindblom (1995); Kogarko *et al.*, (2001); Frezzotti *et al.*, (2002); Nielsen and Veksler, (2002); Bakker and Elburg, (2006). Application of silicate-melt inclusions on volatile magmatism and petrological information from silicate-melt inclusions are comprehensively reviewed by Lowenstern (1995); Sobolev (1996); Frezzotti (2001). Volcanologists have applied information from melt inclusions to elucidate the pre-eruptive conditions in the magma chambers that leads to further understanding the nature of eruption (Wallace *et al.*, 1985; Belkin *et al.*, 1998; Michaud *et al.*, 2000) or the potential hazard of the eruption, where the report on the estimation of sulphur dioxide released into the atmosphere from eruptive volcanoes were obtained from melt inclusions studying (Stoiber *et al.*, 1987; Kamenetsky and Clocchiatti, 1996; Streck and Wacaster, 2000).

Melt inclusions trapped in phenocrysts of volcanic and plutonic igneous rocks, particularly olivine, pyroxene, spinel, feldspar and quartz, are among the most commonly studied. However, re-homogenisation of melt inclusions in corundum is novel, and there is little information on melt inclusions in corundum. This work provides new information obtained from both the TH1500 heating stage and the 3 kbar

drop-quench furnace in attempts to homogenise the silicate melt inclusions trapped in corundum from Bo Ploi. Inclusions that appear to contain vapour bubbles were examined for the composition of the vapour phase by heating/freezing experiments. These inclusions showed no movement of bubbles on heating/freezing. They were re-examined using the LRM, which yielded the compositions of silicate glasses (Fig. 3.5). In addition, the vapour phase was examined by FTIR technique, where H_2O and CO_2 molecules were detected (Fig 3.6).

Silicate-melt inclusions that contain daughter minerals tend to possess larger sizes (70 to 120μm) than daughter mineral-free silicate-melt inclusions (10 to 50μm). On heating, the daughter minerals exhibited the first phase change around 500°C, where they began to melt and changed their morphologies to, for example, rounded, necking, ovoid or drop-like forms. The morphology changed progressively as the temperature was increased and with the duration of the experiment. The phase change of the silicate glass was recorded at a temperature of 850°C, where mobilisation of the bubble was observed, indicating that the solid silicate glass was remelted. The final temperature before the remnant of daughter minerals was totally melted was around 1200°C. Samples were further heated gradually to even higher temperature, approximately 1350°C, and retained at that temperature for up to 24 hours, but homogenisation was still not achieved (i.e. bubble vapour not dissolved). Similarly, the inclusions that contain no daughter mineral exhibited the first phase change where the silicate glass became liquefied around 800°C, as indicated by the mobilisation of the bubble. Temperature was also gradually raised and maintained at each temperature for up to an hour in order to allow the glass inclusions to reach their equilibrium, however, they failed to homogenise. Nevertheless, the small size and the locations of these inclusions made the observation extremely difficult hence it is not a totally accurate record and, therefore, only the silicate melt inclusions that contain daughter minerals were further

analysed for their chemical compositions.

Two samples of glass melt inclusions were heated under high pressure by using a hydrothermal furnace (drop-quench furnace) at the Institute of Mineralogy, University of Hannover. The samples were placed on the furnace container, which was hung on a platinum wire. Argon gas was fed to the sample apparatus to control the pressure. The experimental conditions were a pressure of 3 kbar and temperature of 1250°C for 100 minutes. Then the samples were quenched at the rapid cooling rate (more than 200K/s) by melting the platinum wire to allow the sample container to drop to the bottom part of the furnace, which is cold. However, the homogenisation of the inclusions was still not obtained although the inclusions were reached their melting points still the location of gas bubbles varied. The example of silicate-melt inclusion on heating experiments are illustrated in the figures 3.11

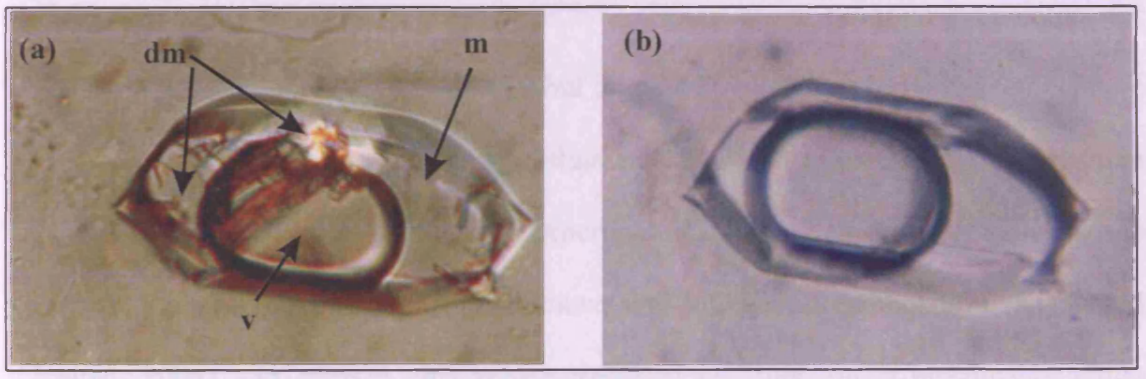

Figure 3.11 Photomicrographs show heating experiment of type 3 Silicate melt inclusions

(a) At room temperature before the heating experiment. The melt inclusion composed of vapour bubble (v), silicate glass (m), and acicular to prismatic shaped and slightly birefringence daughter minerals (dm).

(b) After heating and quenching to room temperature. Daughter minerals disappeared and the vapour bubble changed its size and locality.

3.3 Geochemistry of silicate-melt inclusions

The discovery of silicate melt inclusions in the Bo Ploi corundum may shed a light in answering the genesis enigma of corundum in basaltic terrain; however, the compositions obtained from geochemical analyses must be carefully treated because of a well recognised feature of post-entrapment crystallisation that can modify the composition of the trapped melt inclusion (Roedder, 1979; Qin *et al.*, 1992; Sinton *et al.*, 1993; Sobolev and Shimizu, 1993; Nielsen *et al.*, 1998; Danyushevsky *et al.*, 2000; Kress and Ghiorso, 2004). As the trapped melt inclusions cool down, they are no longer in equilibrium with the host crystal, which means diffusion into and out off the melt could take place and therefore varying their original compositions. The formation of crystals, daughter minerals, on the wall of the silicate-melt inclusions, on slow cooling (Frezzotti, 2001), is familiar and a routine heating experiment on a heating stage can efficiently correct this post-entrapment effect. However, an accurate temperature for the heating experiment is very important but hindered by kinetics; too low a temperature will not dissolve all post-entrapment crystals and may lead to incomplete composition of the melt and likewise an overheating experiment can induce the host components into the melt inclusion resulting in oversaturated and unrealistic composition (Kress and Ghiorso, 2004). In general, this post-entrapment modification is presumably either insignificant or can easily be assessed by carefully design an optimum temperature for an annealing experiment (Roedder, 1984; Michaud *et al.*, 2000; Kress and Ghiorso, 2004; Streck and Wacaster, 2006). In addition, microbeam technologies have been vigorously improved thus anaccuracy and precision of chemical determinations are higher and more information can be obtained from melt inclusions.

Sample preparations

Doubly polished sapphire wafers that contain melt inclusions were carefully polished by 600μm then 1000μm grain size alumina polishing powder until the

inclusions were exposed at the surface and finished by 0.6μm alumina polishing solution. These lengthy processes were employed in order to minimise the loss of relatively soft silicate glass materials. However, there are several factors that prevented the achievement of optimal quality of polishing these inclusions, such as the contrast in hardness between the host sapphire and the softer silicate glass inclusions. In addition, the perfect parting along the face 0001, perpendicular to the c-axis, that tends to cleave the crystal face and pull the inclusions away. Consequently, there is almost always a surface relief between the host corundum and the trapped silicate glass that leads to slightly irregular polished surfaces. These might possibly affect the precision and accuracy of the geochemical analyses. The irregular surface of silicate-melt inclusions after final polishing is illustrated in figure 3.12.

Five silicate-melt inclusions in Bo Ploi sapphires were analysed for major oxide elements by JEOL-733 Superprobe equipped with Link Systems EDS at Birkbeck College, University of London. An accelerating voltage of 15 kV and a count time of 30s were used to obtain the optimal results and prevent the loss of easily volatile elements, like sodium.

3.3.1 Major oxide analyses

The chemical compositions of trapped silicate-melt inclusions are slightly variable, which can be characterised by 57.0 to 62.8 wt% of SiO_2, with an average value of 58.5 wt%. The Al_2O_3 content ranges from 24.2 to 27.1 wt%, with an average of 26.0 wt%. The total alkali content: Na_2O and K_2O ranges from 8.7 to 9.5 wt% with 8.6 wt% on average. However, it is likely that the alkali content will be lower than the original composition of the melt as the heating experiment could directly affect the mobile elements like Na_2O although the analysis condition was carefully selected to minimise this (Webster, *et al.*, 1996; Chabiron, *et al.*, 2001). The silicate-melt inclusions have a mean aluminium saturation index, (A.S.I.), [molecules $Al_2O_3/(CaO + Na_2O+K_2O)$] value

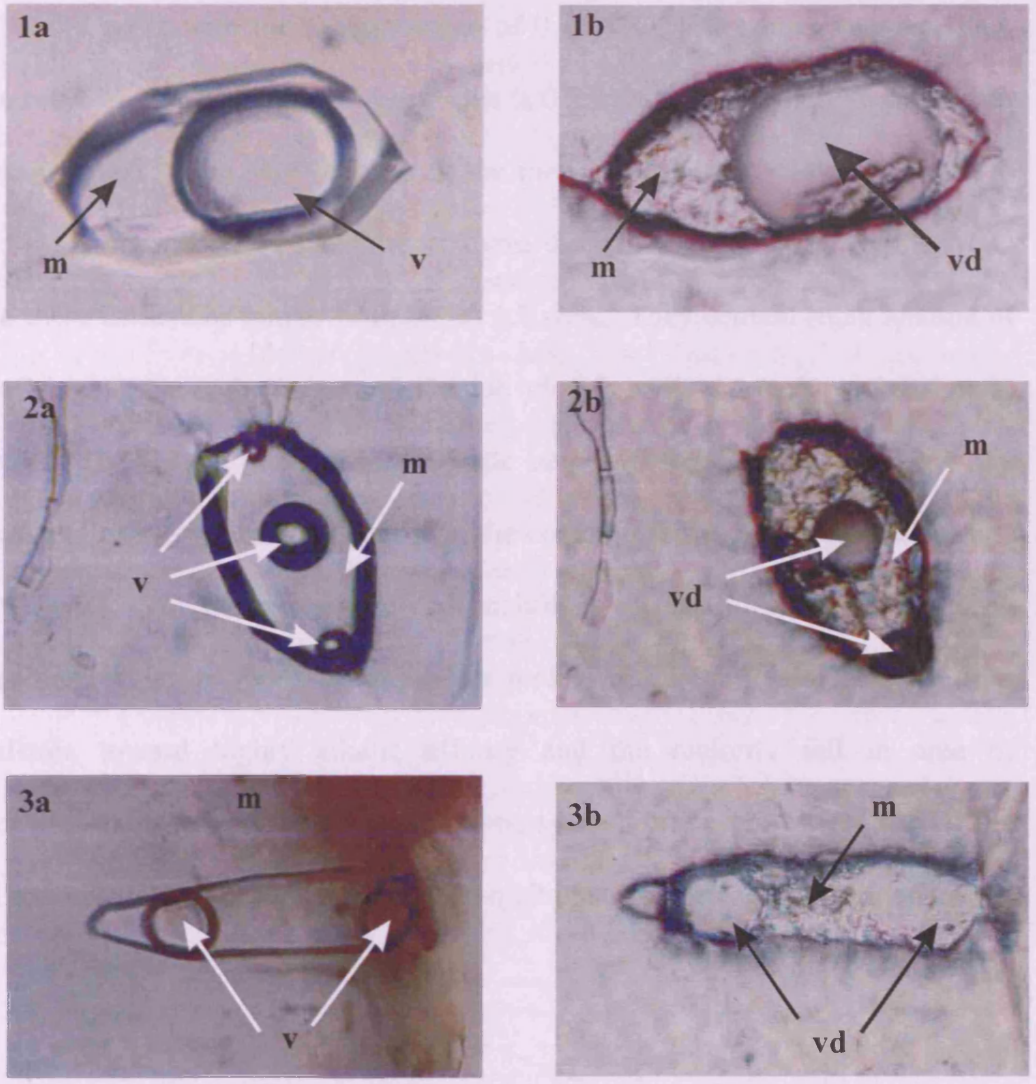

Figure 3.12 Photomicrographs of three silicate-melt inclusions that were chosen for SIMS analyses. The photos in the left column represent the sample after heating experiment and quenching to room temperature. The photos in the right column show the same samples where the silicate melt is exposed at the surface. Although the polishing was carried out with extremely care, however, the partial loss of silicate glass was not avoidable. Note v: vapour bubble, vd: void remnant of vapour bubble and m: silicate melt

of 2.83, which is classified as peraluminous melt. They contain small amounts of FeO from 0.3 to 0.6 wt%, with the average value of 0.4 wt%. In a similar manner, TiO_2 ranges from 0.1 to 0.3wt % and the mean value is 0.2 wt%, which is fairly common for felsic igneous rocks. The MgO content in the melt inclusions is below the detection limit of the microprobe; however, the analyses from SIMS showed that the MgO content in these inclusions ranges from 0.8 to 1.8 wt%. They contain small amount of CaO, MnO and SrO, with the average value of 0.6 wt%, 0.2 wt% and 0.4 wt% respectively. The P_2O_5 content shows a wide range of variability, nevertheless the average content of P_2O_5 is rather higher than the common felsic rocks with the average value of 0.5 wt%. The trapped silicate-melt inclusions are alkali intermediate to felsic in composition, which in terms of equivalent rock nomenclature would extend from mildly alkalic toward highly alkalic affinity and the majority fall in area of trachyandesites-trachyte or equivalent to plutonic syenodiorite-syenite (Fig. 3.13). The chemical composition of these trapped silicate-melt inclusions are presented in table 3.1

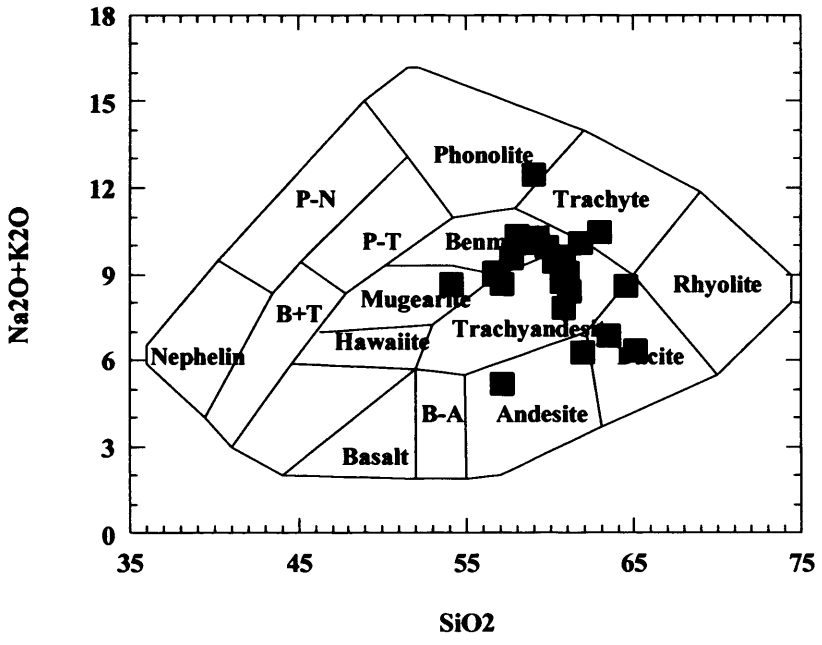

Figure 3.13 Plots of SiO_2 content *vs.* total alkali content of melt inclusions trapped in corundum from the Bo Ploi deposit (after Cox *et al.*, 1979).

Table 3.1 Representative major oxide compositions of the silicate-melt inclusions

Oxide	SM-01	SM-02	SM-03	SM-04	SM-05
SiO_2	62.77	58.08	56.25	57.47	56.96
TiO_2	0.26	0.28	0.26	0.08	0.23
Al_2O_3	25.90	24.22	27.09	25.86	27.14
FeO	0.37	0.27	0.43	0.28	0.60
MnO	0.16	0.30	0.24	0.06	0.25
MgO	<dl	<dl	<dl	<dl	<dl
CaO	0.33	0.74	0.69	0.72	0.32
SrO	0.41	0.30	0.41	0.30	0.30
Na_2O	4.25	4.34	3.81	4.57	4.13
K_2O	4.48	4.62	3.09	4.90	4.92
P_2O_5	0.79	0.92	0.43	0.13	0.20
total	99.72	94.07	92.71	94.28	95.09

Table 3.2 Trace and REE concentrations (ppm) of the silicate-melt inclusions and the normalised values

Element	SM-01	SM-02	SM-03	M-norm01	M-norm02	M-norm03	C-norm01	C-norm02	C-norm03
Li	49.96	48.42	1600.14	31.2	30.3	1000.1	31.8	30.8	1019.2
Be	55.42	55.70	40.37	n.a	n.a	n.a	n.a	n.a	n.a
B	126.73	122.38	78.37	n.a	n.a	n.a	n.a	n.a	n.a
Mg	914.23	835.41	115.63	n.a	n.a	n.a	n.a	n.a	n.a
Rb	403.81	270.83	163.20	630.69	423.2	255.0	174.1	116.7	70.3
K	3726.70	4174.90	2639.40	14.9	16.7	10.6	6.8	7.7	4.8
P	344.44	427.28	222.36	3.6	4.5	2.3	0.3	0.4	0.2
Ti	1558.70	1798.50	1558.70	1.2	1.4	1.2	3.5	4.0	3.5
Sr	1.16	8.03	7.37	0.1	0.4	0.3	0.2	1.1	1.0
Y	93.38	71.44	72.55	20.5	15.7	15.9	59.5	45.5	46.2
Zr	152.86	111.08	151.62	13.6	9.9	13.5	39.5	28.7	39.2
Ba	22.22	78.75	11.02	3.2	11.3	1.6	9.2	32.7	4.6
La	8.58	7.84	34.27	12.4	11.4	49.7	36.2	33.1	144.6
Ce	46.67	30.30	115.22	26.2	17.0	64.7	76.3	49.5	188.3
Nd	30.48	14.33	40.63	22.6	10.6	30.1	65.3	30.7	87.0
Sm	6.93	4.18	11.30	15.7	9.5	25.7	45.3	47.3	73.8
Eu	0.02	0.26	1.00	0.1	1.5	5.9	0.4	4.5	17.2
Dy	15.06	10.56	11.11	20.3	14.3	15.0	59.3	41.6	43.8
Er	10.75	8.16	9.90	22.4	17.0	20.6	65.0	49.3	59.8
Yb	13.54	11.48	11.20	27.6	23.4	22.9	79.7	67.5	65.9
Lu	2.08	1.79	1.54	29.7	25.6	22.0	82.0	70.4	60.6
Hf	8.16	7.37	8.48	26.3	23.8	27.4	76.6	69.1	79.5

M-norm = trace element concentrations normalised by primordial mantle

C-norm = trace element concentrations normalised by chondrite

Note: The primordial mantle and chondrite values after Sun and McDonough (1989)

The major oxide elements are plotted on Harker variation diagram, which and generally define a series of coherent trends on these variation diagrams; suggesting a common origin (Fig.3.14). The Al_2O_3, Na_2O, K_2O, CaO and MnO form well-defined negative correlations with the increasing of SiO_2, while FeO and TiO_2 form broad negative coherent trends. In contrast, P_2O_5, Cr_2O_3 and SrO show increasing tendency with the increasing of SiO_2 thus indicate incompatible manner of these elements.

3.3.2 Trace elements and Rare Earth Elements analyses

Three large samples of trapped melt inclusions, 120-150 μm, were chosen for trace elements and rare earth element (REE) analysis by Secondary Ion Mass Spectroscopy (SIMS) at the GeoForschungZentrum Potsdam, Germany, with the assisted of Dr Michael Wiedenbeck, SIMS laboratory supervisor. The Cameca ims 6f SIMS was used. Because of differing requirements for the analytical conditions, it was necessary to conduct separate analyses for light versus heavy elements. The secondary ion yields for all elements were determined using NIST SRM612 glass, where the preferential average concentrations have been given by Pearce *et al*, 1997. The samples were cleaned in an ultrasonic bath of ethanol fluid then dried at 75°C and coated with a conducting gold film prior to analyses. A 20nA beam was initially raster over a 50×50 μm area of the sample for five minutes in order to remove any surface contamination. The diameter of the 22.5 kV ^{16}O primary probe beam is approximately 15 μm. SIMS measurements were conducted at a moderately high mass resolution of M/dM = circa 1675 which resolves all major isobaric interference. The peak stepping sequence included: 6.5 background (1s) ^{7}Li (10s), ^{9}Be (20s), ^{24}Mg (10s), ^{27}Al (2s), ^{30}Si (2s). All peaks were detected using an ion counting system except ^{27}Al, which were detected by Faraday cup. A total of 12 cycles of the peak stepping sequence were conducted, consequently, a total time was 14 minute peranalysis/spot. The field of view of the sample was 39μm. During the first analytical session a total of six analyses were

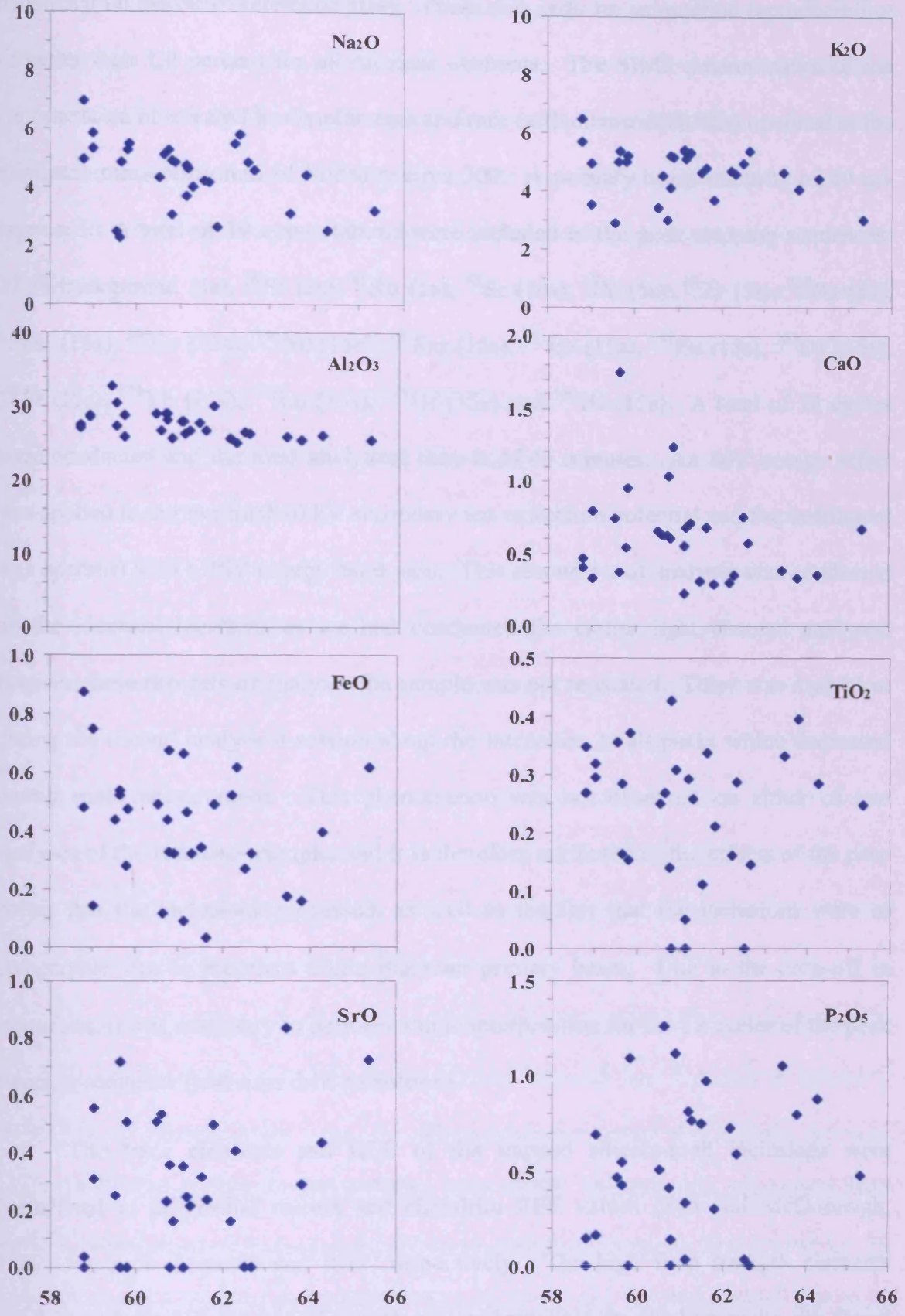

Figure 3.14 Variation diagrams of major oxides versus SiO_2(wt%) in the trapped silicate-melt inclusions in the Bo Ploi corundum.

conducted on the NIST reference glass. These data indicate an external reproducibility of better than 1.0 percent for all of these elements. The SIMS determination of the concentration of selected heavy elements and rare earth elements (REEs) operated at the minimum mass resolution of M/dM = circa 300. A primary beam intensity of 40 nA was used. A total of 19 mass stations were included in the peak stepping sequences: 27.75 background (1s), ^{30}Si (2s), ^{85}Rb (5s), ^{88}Sr (10s), ^{89}Y (5s), ^{90}Zr (5s), ^{138}Ba (5s), ^{139}La (15s), ^{140}Ce (15s), ^{146}Nd (15s), ^{147}Sm (15s), ^{151}Eu (15s), ^{153}Eu (15s), ^{163}Dy (15s), ^{167}Er (15s), ^{174}Yb (15s), ^{175}Lu (15s), ^{179}Hf (15s) and ^{180}Hf (15s). A total of 12 cycles were conducted and the total analytical time is of 45 minutes. An 80V energy offset was applied to our nominal 10 kV secondary ion extraction potential and the instrument was operated with a 25V energy band pass. This second set of analyses was conducted on the identical locations as we had conducted the earlier light element analyses; between these two sets of analyses the sample was not re-coated. There was a problem during the second analytical session about the intensities of all peaks which decreased during each measurement. This phenomenon was not observed on either of two analyses of the reference sample, and it is therefore attributed to the effects of the poor polish that the inclusions possessed, as well as the fact that the inclusions were of comparable size to the circa 20μm diameter primary beam. Due to the drop-off in intensities, it was necessary to perform a time interpolation for the 12 cycles of the peak stepping sequence (real time drift correction).

The trace elements and REE of the trapped silicate-melt inclusions were normalised to primordial mantle and chondrite REE values (Sun and McDonough, 1989) for trace elements and REE, respectively. The high field strength elements (HFSE) such as Hf, Zr and Y, which are incompatible in alkaline melts are found relatively enriched compare to primordial mantle, with the concentrations in the range of 111 to 153ppm, narrow range of 7 to 8ppm and 71 to 93ppm for Zr, Hf and Y,

respectively. Unlike the other HFSE, Ti shows comparatively depleted concentration. The large ion lithophile elements (LILE), including Ba (11 to 79ppm), K (2640 to 4175ppm) and Rb (163 to 403ppm) are enriched compared to the primitive mantle, but not for Sr (1 to 8ppm), which is notably lower than primitive mantle value.

The plots of incompatible trace elements normalised to primitive mantle compositions are presented in figure 3.15 where it is found that mobile highly incompatible trace elements like Sr show the expected negative anomalies and relatively depleted contrasts with Ba and Rb which shows a positive anomaly. Less incompatible trace elements from La, Ce to Y display relatively constant concentrations, while P and Ti both show slightly negative anomalies. Sr and Ba likely reflect the segregation of plagioclase and K-feldspar, which means the relatively depletion of these elements might be explained by fractionation of plagioclase from the melts, or the parental magma contains low Sr concentration. The enrichment of Rb and relatively high K in the melt could reflect the mineralogical control of biotite. Similarly, the crystallisation/fractionation of biotite contributes to the enrichment of K, Rb to the melts and can decrease Sr contents (Downes *et al.*, 1997). The deeper negative Ba, Sr, P and Ti anomalies might suggest a further of fractionation of feldspar, apatite and ilmenite in the melt (Ngounouno *et al.*, 2000)

The consistent trend of the chondrite-normalised REE patterns for the three representative silicate-melt inclusions (Fig. 3.16) indicates that the melt is relatively homogeneous and the REEs were not selectively incorporated into specific minerals during crystallisation (Gibson, 1988; Wilson *et al.*, 1995). The chondrite-normalised REE patterns of the silicate melt inclusions show remarkably flat patterns from La-Nd and all show a prominent negative Eu anomaly. The $(La/Yb)_N$ and $(Sm/Nd)_N$ ratios vary from 0.45 to 2.19 and from 0.69 to 0.89, respectively. La is slightly depleted relative to Ce as a result $(La/Ce)_N$ is less than 1 in all samples. Sm/Nd ratios varied from 0.23 to 0.27.

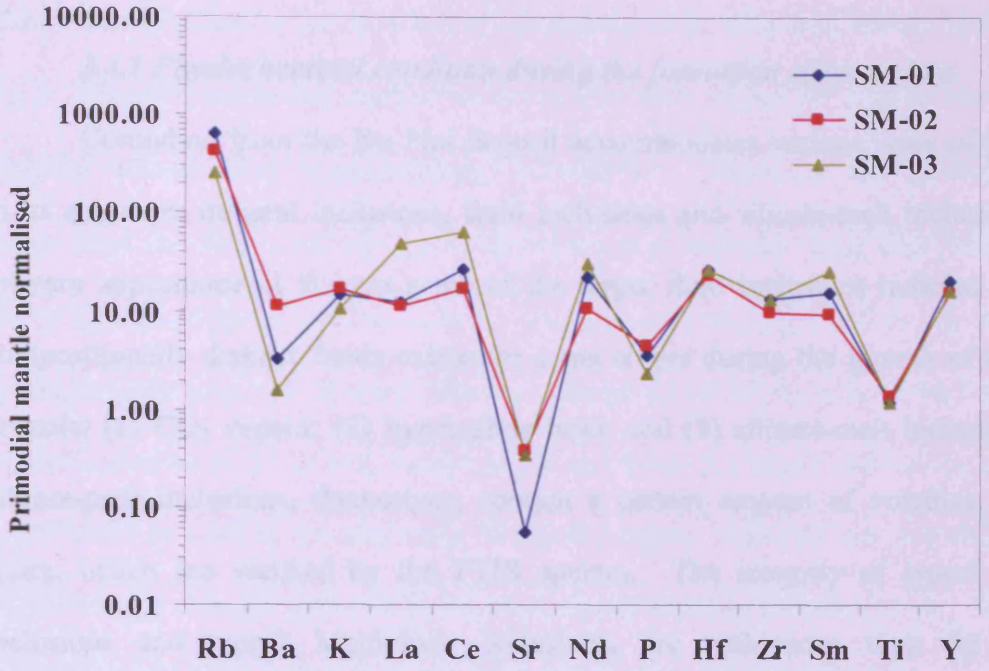

Figure 3.15 Patterns of incompatible elements in trapped silicate melts normalised to the primordial mantle composition (Sun and Mcdonough, 1989).

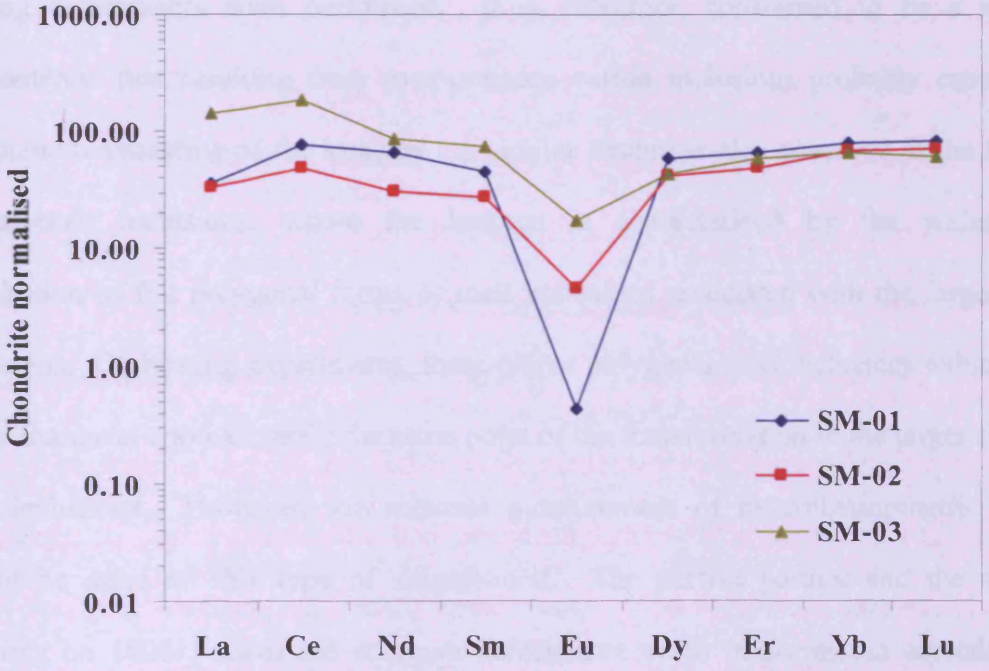

Figure 3.16 Patterns of incompatible elements in trapped silicate melts normalised to chondrite meteorite composition (Sun and Mcdonough, 1989).

3.4 Discussion and conclusion

3.4.1 Physiochemical condition during the formation of corundum

Corundum from the Bo Ploi deposit accommodates various types of inclusions in its structure; mineral inclusions, fluid inclusions and silicate-melt inclusions. The primary appearance of at least some of the larger fluid inclusions indicate that three compositionally distinct fluids existed at some stages during the growth of corundum crystals; (1) CO_2 vapour, (2) hypersaline brine and (3) silicate-melt inclusions. The silicate-melt inclusions, themselves, contain a certain amount of volatiles, CO_2 and water, which are verified by the FTIR spectra. The integrity of type-1 CO_2-rich inclusions and type-2 Multiphase inclusions, are ambiguous thus the common appearance of aureoles of smaller inclusions around the larger ones, which indicate leakage or decrepitation processes (Sterner and Bodnar, 1989; Rankin, 2002; Rankin and Edwards, 2003; Schiano, 2003). The aureoles were clearly observed before the heating experiments were performed. It is, therefore, considered to be a natural phenomenon that resulting from over-pressure within inclusions probably caused by magmatic overheating of the samples. A similar feature is also observed in the type-3 silicate-melt inclusions, where the leakage is characterised by the widespread distribution of flat polygonal forms of melt inclusions associated with the larger melt inclusions. On heating experiments, these planar polygonal melt inclusions exhibited a phase change at approximately the same point of the transformation in the larger silicate melt inclusions. However, the accurate measurement of microthermometric study cannot be done on this type of silicate-melt. The perfect parting and the simple twinning on {0001} faces are common defects that occur in corundum crystals and, naturally, these defects tend to cause weak zones in their structures, especially between (0001) layers. When corundum crystals are under strain, trapped melt inclusions may simply leak through micro-fracture and form flat polygonal shaped of melt inclusions

along these planes. The apparent leakage in primary silicate-melt inclusions is, therefore, interpreted as an evidence of incorporation of corundum into the host basalt.

Microthermometric studies on the silicate melt inclusions suggest the minimum trapping temperatures approximately 800-850°C. However, the homogenisation temperature of multiphase inclusions (solid-aqueous-vapour) range 930-1000°C might imply higher temperature of formation. The temperature ranges and durations used for heating experiments can directly affect the compositions of the silicate-melt inclusions. The miscalculation of heating temperature can drive the liquid composition from the equilibrium as well as incompletely dissolve daughter minerals and possibly that the liquid was in re-equilibrium with the host zoned crystals (Nielsen *et al.*, 1998), as a result, the re-homogenised compositions of melt inclusions may not represent the original compositions of the melt. The question about overheating the silicate-melt inclusions is also concerned, hence the temperatures of intermediate to felsic magma are normally in the range of 900-1000°C and can be as low as 700-800°C in a condition that saturated by water (Wylie and Wolf, 1993; Hall, 1996). The minimum trapping temperatures of silicate-melt inclusions are relatively consistent with those reported by other researchers like Limtrakun *et al.*, (2001) who reported that the first phase change at about 770°C on heating experiment of silicate-melt inclusions in corundum from Denchai deposit, Thailand. Likewise, temperature in the range of 750-850°C is a minimum trapping temperature of silicate-melt inclusions in corundum from Changle district, Shangdong province, China (Liu *et al.*, 2006) and 685°C for those silicate-melt inclusions from Dak-Nong corundum, Central Vietnam (Smirnov *et al.*, 2006). At these temperatures, however, is only the beginning of the melting or the silicate-melt inclusions starting to liquefy while the transformation of these trapped silicate-melt inclusions gradually occurred until the temperature up to 1200°C, where the last phase changed took place as the daughter minerals were completely dissolved. There are

slightly differences in the last recorded temperatures on heating the silicate-melt inclusions are including 1200-1250°C for Denchai corundum (Limtrakun *et al.*, 2001); while the final temperature recorded at 1150°C and 930-1100°C are for heating melt inclusions from Changle corundum (Liu *et al.*, 2006) and Dak-Nong corundum (Smirnov *et al.*, 2006), respectively. The heating experiments were carried on after the last phase changed to the temperature 1350°C in order to ensure that the temperature range is sufficient for homogenise the silicate-melt inclusions. If the samples were overheated, this may result in a loss of mobile elements as well as volatile components and definitely change the composition of the melt. The volatile-rich silicate-melt inclusions liquefy at the lower temperature compare to volatile-poor silicate-melt inclusions because liquidus temperatures are lowered by the volatile pressure.

Although, there is no clear evidence that the silicate-melt inclusions were overheated, nonetheless, it is suggested that further heating experiments should be done with an alternative strategy in order to investigate this issue. A set of heating experiments should be conducted by heating silicate-melt inclusions at different temperatures, for example, 700, 800, 900, 1000, 1100 and 1200°C. Quenched glasses from each experiment will be analysed for their compositions, then the element behaviours with increasing of temperature should be able to establish.

3.4.2 Petrogenesis of the trapped silicate-melt inclusions

The trachyandesitic composition of the trapped silicate-melt inclusions in the Bo Ploi sapphire has an average composition as SiO_2 61.4 wt%, TiO_2 0.24 wt%, Al_2O_3 27.4 wt%, Cr_2O_3 0.06 wt%, FeO 0.4 wt%, MnO 0.2 wt%, CaO 0.5 wt%, Na_2O 4.5 wt%, K_2O 4.5 wt%, P_2O_5 0.6 wt% and SrO 0.4 wt%. The MgO content, however, was not detected by electron microprobe but the values of 0.8-1.8 wt% are obtained from SIMS analyses. It is noticed that some analyses yielded rather poor total (less than 90 wt% in total) and the data was, subsequently, normalised to 100 prior a geochemical

interpretation. A low total on microprobe analyses indicates the loss of volatile contents including, H_2O, CO_2, F, Cl and perhaps a lesser extent of S (Anderson, 1973; Sommer, 1977; Chabiron *et al.*, 2004), in addition, it is generally agreed that H_2O and/or H_2 diffusion between melt inclusions and the host mineral after entrapment can lead to water loss from melt inclusions although it is complicated to accurately constrain the process (Roedder, 1984; Qin *et al.*, 1992; Webster *et al.*, 1996). The poor quality of microprobe section is also a factor that causes a low total analysis because of a significant hardness different between the two materials. Although the samples were carefully polished until the silicate-melt inclusions exposed to the surface, but there is always a surface relief between the harder corundum and the softer silicate-melt inclusion. It is noticed that the Al_2O_3 content is unusually high, average 27.4 wt% and the possibility of contamination by the host corundum is considered. However, it is thought to be minimal, since the diameter of the microprobe beam is 2μm and covers much less area than the size of the melt inclusion fleshes. The negative correlation between Al_2O_3 and SiO_2 also suggests a normal fractionation trend. On balance, it is likely that the Al_2O_3 contents of the glasses obtained from the microprobe analyses are genuine constituents.

In nature, the high-alumina magmas such as high-alumina basalts have been regarded as a typical melts erupted in volcanic arc environments (Nicholls and Ringwood, 1973; Arculus and Wills, 1980; Uto, 1986; Sisson and Layne, 1993; Kersting and Arculus, 1994; Schiano and Bourdon, 1999; Johnston, 1986; Crawford *et al.*, 1987; Schiano *et al.*, 2004). Although a genesis model is a controversial matter, it is generally agreed that it is a process in the crustal or crustal-mantle boundary level with a significance role of water in the generation and differentiation of high-alumina basalts (Bartel *et al.*, 1991; Beard and Lofgren, 1992; Sisson and Grove, 1993a; 1993b). The high-alumina magma is considered to be a primary magma generated by a high degree

of partial melting of the subducted oceanic crust (Marsh, 1976; Brophy and Marsh, 1986; Myers, 1988) and also by the fractionation of olivine and clinopyroxene of peridotitic melts at crustal level (Nicholsls and Ringwood, 1973; Perfit *et al.*, 1980; Kay and Kay, 1985; Nye and Reid, 1986; Uto, 1986; Kersting and Arculus, 1994). Crawford *et al.*, (1987) proposed that the accumulation of plagioclase in less aluminous magmas can produce high-alumina melts, alternatively, Keleman, (1990) suggested that the genesis of high-alumina magmas resulted from an extensive contamination of ascending magmas with refractory mantle. Concurrently, researches on experimental petrology investigating the high-alumina melts have also been performed. These include an eclogitic source hypothesis (Baker and Eggler, 1983; Johnston, 1986) where melting of eclogite from subducted oceanic crust is responsible for the generation of high-alumina basalts since olivine is not present in liquidus phase at any studied pressure but garnet and/or clinopyroxene are liquidus phase at the pressure greater than 25 kbar (Baker and Eggler, 1983; Johnston, 1986). This means fractionation of olivine from peridotites or even more primitive melt cannot generate high-alumina melts. Gust and Perfit (1987) proposed that fractionation of augite and olivine at the lower pressure (less than 10 kbar) can produce high-alumina melts from high Mg, low-Al mantle-derived arc basalts. Alternatively, plagioclase can be a liquidus phase of high-alumina melts at 1 atm to 20 kbar (Baker and Eggler, 1983; 1987) thus strengthened the plagioclase accumulation as a cause of high-alumina composition (Crawford *et al.*, 1987).

From this point view, these mechanisms that caused high-alumina compositions in arc volcanisms is assumed to be partly analogous to those mechanisms for high alumina concentration in the studied trapped silicate-melt inclusions. It can be depicted by an extensive fractionation during the ascending of the more primitive magma by, the earliest, iron- and magnesium-based minerals, including olivine and pyroxenes thus causing depletion of MgO and FeO in the melt residue. Clinopyroxene may be the next

phase to crystallize, which in turn depleted CaO content, then crystallisation of magnetite, which control FeO and partly TiO_2 content in the melts. The gradually decreasing TiO_2 content is a result of the ilmenite fractionation, with minor contributions from magnetite and sphene crystallisation. The Al_2O_3 contents in the melt should be gradually increased and there must be a process preventing the crystallisation of plagioclase that drives the melt compositions toward the high-alumina magma. Crawford *et al.*, (1987) suggested that a small but significant amount of water may play a role in retarding the nucleation of plagioclase until the earlier crystallised phases like olivine and clinopyroxene had driven the residual liquid to Al_2O_3 content of about 17.5wt%. Schiano *et al.*, (2004) reported in their work on basaltic-andesitic compositions melt inclusions trapped in olivine and clinopyroxene grains of cumulate xenoliths from Adak island, Aleutian arc, which are characterised by high Al_2O_3 (18.5-26.3 wt%), SiO_2 (47.1-56.4 wt%), MgO (0.1-6.5 wt%) and FeO (0.3-6.5 wt%) that the high-alumina melts originated from low alumina with water and MgO-rich magma by fractionation process. The presence of water can delay the plagioclase crystallisation and resulting in a smaller plagioclase field and the proportion of earlier fractionated phases including, olivine, clinopyroxene and/or amphibole had been increased thus forced the liquid residue to become richer in Al_2O_3. This is supported by experimental petrology on CaO-MgO-Al_2O_3-SiO_2 (CMAS) at 7 kbar anhydrous system (Presnall *et al.*, 1979) and 15 kbar water-saturated systems (Kushiro, 1974), which is clearly demonstrated that the plagioclase liquidus volume is smaller in a water-saturated system and leads to the higher proportion of olivine and pyroxene stability field.

The crystallisation of corundum through a fractional crystallisation process may ambiguously explain the trace element variations, particularly, the REE patterns of these trapped silicate-melt inclusions, which show relatively flat pattern (unfractionated), except the prominent negative Eu anomalies usually indicating a removal of plagioclase

from the melt, although a negative Eu anomaly can also be produced by other minerals like apatite, nepheline and other feldspathoids. This feature is consistent with the Sr and Ba depletion since Sr can be readily substituted for Ca in plagioclase and also for K in K-feldspar, while Ba prefers K-bearing minerals like K-feldspar, hornblende and biotite. This reflects that the accumulated alumina had been consumed in a crystallisation of plagioclase and perhaps including other Eu-compatible minerals like apatite, nepheline and feldspathoid minerals, then alumina content in the melt should be depleted and the melt is moved away from peraluminous composition. Consequently, an alternate process that promotes alumina content in the melt is needed and the best contender is an assimilation of alumina-rich crustal materials in the melt.

The role of crustal contamination to the trapped silicate-melt is strengthened by oxygen stable isotope analyses of the Bo Ploi corundum, where the studied samples provided oxygen stable isotope in the range of $\delta^{18}O$ of 6.5-9.6‰ (detailed in chapter 4). These $\delta^{18}O$ values indicate that the oxygen used in the forming of corundum has both crustal and mantle signatures (Taylor and Sheppard, 1986; Price *et al.*, 2003; Pandit *et al.*, 2003; Giuliani *et al.*, 2005) supporting the idea of Al_2O_3 contribution from crustal materials. The country rock in the Bo Ploi area satisfies this criterion since it is dominated by aluminous sedimentary and metamorphic rocks such as shale, phyllite, gneiss and biotite schist (Bunopas and Bunjitradulaya, 1975). In addition, the crustal xenoliths found entrained in the host Bo Ploi basalt suggests that the deeper crust beneath the Bo Ploi area is composed of, at least, coarse-grained nepheline syenite and granitic rocks, (detailed in chapter 6), which are compositionally alkali intermediate to alkali felsic that similar to the composition of the trapped silicate-melt, therefore, they are prone to assimilate into the melt (Wilson, 1989; Hall, 1996). Although the heat activities of the magma with the country rocks in the area are not well constrained, it is believed that the latent heat released from crystallisation, a temporal and spatial process,

in the magma chamber is sufficient for melting country rocks and assimilates it in the melt. Carmichael, (1974) estimated the energy required for dissolving a crystal, which can be quantified based on a thermodynamic equation. This latent heat released from crystallisation prevents magma from cooling. Approximately the same amount of heat energy is required to dissolve a crystal of comparable silicate supplying the required latent heat of melting, in other words; the latent heat of crystallisation is about the same as latent heat for fusion (melting). The waste heat, which is lost through convection and conduction, however, has to be accounted for and this means the melted crust would remain frozen in situ and not transport to the crust thus it is called underplating.

One may argue that contamination of aluminous materials from country rock may result in light REE enrichment since crustal rocks generally exhibit light REE enrichment pattern (Taylor and McLennen, 1981; Gromet, *et al.*, 1984; Rollinson, 1993), but the present of monazite as a syngenetic inclusion in corundum shed a light on the answer to this feature. It is believed that light REE may reside in their preferential minerals like in monazite; although only small amount of monazite occurred in corundum, its very high partition coefficient causes a great influence on the melt REE patterns (Rollinson, 1993). Likewise, other syngenetic mineral inclusions, particularly, feldspar and zircon accommodate REE in their structures for example middle REE, Eu in particular, is favourable for feldspar and result in negative Eu anomaly. Zircon is expected to deplete heavy REE, but instead, a relatively flat heavy REE is observed. Hokada and Harley (2004) reported the relatively flat heavy REE zircon occurs in feldspathic leucosomes resulting from melt injection into garnet-bearing paragneiss in the Napier Complex, East Antarctica. The further reaction of leucosomes with the country rock, garnet-bearing gneiss, causes decreasing of Zr and Hf from garnet to an equivalent value of the melt and crystallised zircon on the pre-existed ones (overgrowth) thus produced zoned zircons. The REE also distributed from garnet

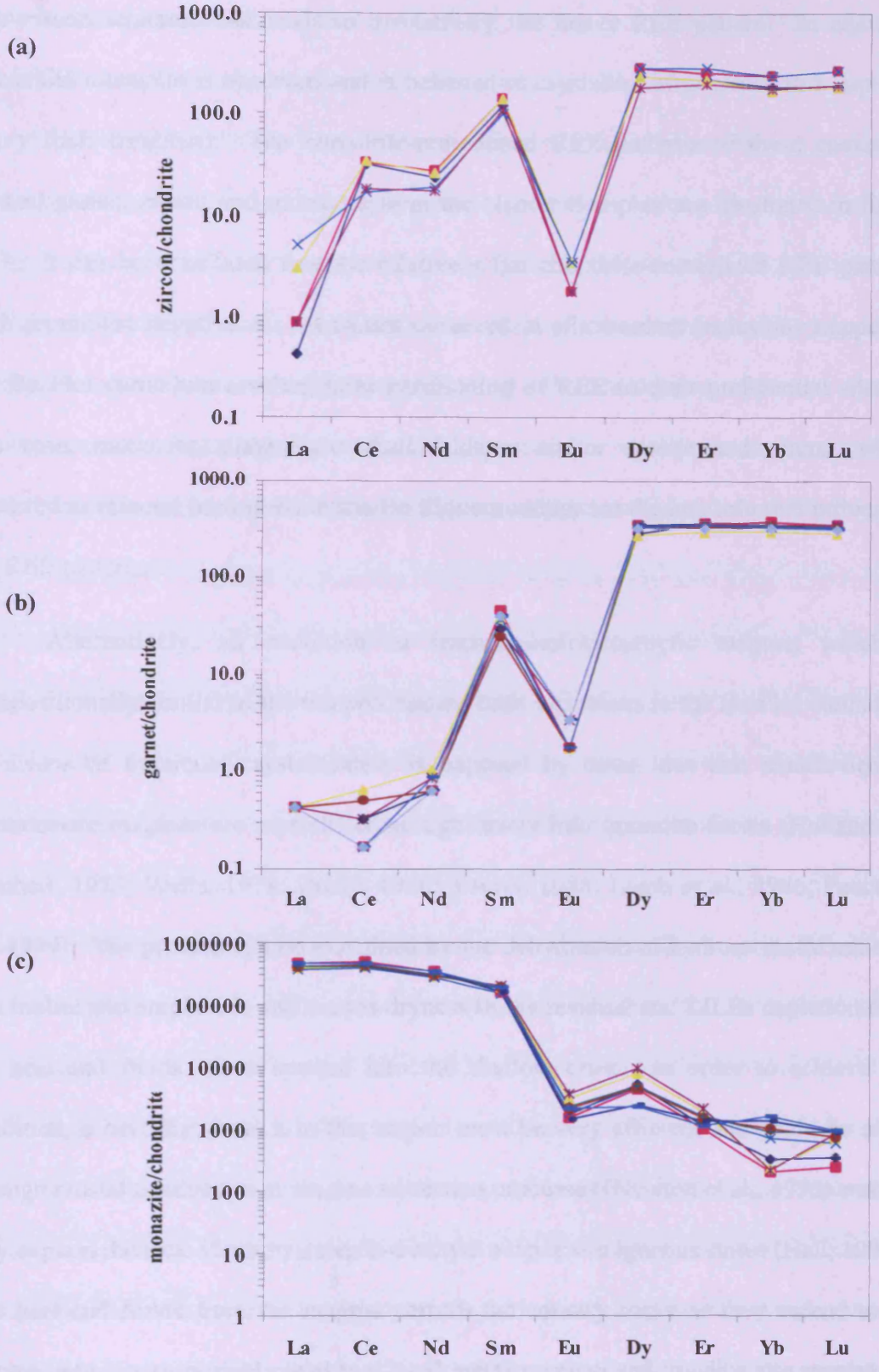

Figure 3.17 Chondrite-normalised REE patterns of (a) zircon (b) garnet and (c) monazite coexist in feldspathic leucosomes from the Napier Complex, East Antarctica (Modified after Hokada and Harley, 2004).

into zircon structure and leads to a relatively flat heavy REE pattern. In addition, interstitial monazite is observed and is believed to crystallise after zircon in a depleted heavy REE condition. The chondrite-normalised REE patterns of these coexisting phases; garnet, zircon and monazite from the Napier Complex are illustrated in figure 3.17. It can be concluded that the relatively flat chondrite-normalised REE patterns with prominent negative Eu anomalies observed in silicate-melt inclusions trapped in the Bo Ploi corundum resulted from partitioning of REE to their preferential sites, in this case; monazite, plagioclase-alkali feldspar and/or apatite and zircon, which occurred as mineral inclusions in the Bo Ploi corundum are the key role that influenced the REE patterns.

Alternatively, an evolution of trachyandesitic/trachytic magma, which is compositionally similar to the trapped silicate-melt inclusions in the Bo Ploi corundum, by means of fractional crystallisation is opposed by other idea that mantle-derived intermediate magmas are crystallised straight away into granulite facies (Holland and Lambert, 1975; Wells, 1978; Drury, 1980; Touret, 1985; Lamb *et al.*, 1986; Peucat *et al.*, 1989). The process can be explained by the dehydration of hydrous mafic minerals like biotite and amphibole and causes dryness in the residual and LILEs depletion since the heat and fluids move upward into the shallow crust. In order to achieve this condition, a heat distribution in that region must be very efficient and could be either through crustal conduction or magma advection processes (Newton et al., 1998) and this may explain the lack of trachyandesite-trachyte outcrops in igneous suites (Hall, 1996a). The heat and fluids from the magma perturb the country rocks as they ascend to the surface, which also possibly lead to a local metasomatism and, readily, the magma has undergone alkali loss through this process. A process of desilication may take place if the magma interacts with particular type of wall rocks such as carbonaceous rocks. The composition of the magma gradually changes toward peraluminous and leads to the

crystallisation of corundum.

Amour and Linnen (1999) studied trapped silicate-melt inclusions in sapphires from the Bo Ploi deposit, which they interpreted as nepheline syenite composition. They concluded that corundum originally crystallised from a nepheline syenite (pegmatite?) and was later entrained as xenoliths in the Bo Ploi basalt (nepheline hawaiite; Barr and Dostal, 1986) thus it is in a good agreement with this work, nonetheless, homogenisation was not achieved in their trapped nepheline syenite glasses, even though temperatures of heating experiments were in the range of 1200 to 1300°C and the sample was retained at the last temperature for five hours. Their partial composition of the trapped glass is summarised as SiO_2 51.31%, TiO_2 0.10%, Al_2O_3 27.73%, Cr_2O_3 0.03%, FeO 0.26%, MnO 0.24%, MgO 0.04, CaO 0.50, Na_2O 8.74, K_2O 5.18% and P_2O_5 0.32%. Most of the major oxide elements are in good agreement with this work, except the lower SiO_2 content and higher total alkali content. However, there is only one nepheline syenite glass found trapped in sapphire becaused of the limitation of samples. The higher alkaline content comparing with this work may be explained by the shorter duration of heating experiment employed in their work. In addition, the analyses time using when probing the glass samples from different laboratories tends to yield different values of sensitive elements like Na, as a result, the longer analyses, the lower Na-content.

3.4.3 Do the trapped silicate melt inclusions represent the composition of corundum parental melt?

The chemical compositions of trapped silicate-melt inclusions may not always represent the original composition of silicate melts for a number of reasons (Albarède and Bottinga, 1972; Watson, 1996; Kennedy *et al.*, 1997; Webster and Rebbert, 2000; Schiano, 2003; Faure and Schiano, 2005). Principally, crystals of a rapid growth rate

are very likely to have a boundary layer at their crystal-melt interface since the interchange rate between element uptake and remove is much higher than the diffusion rate in the melt. If the crystal-melt equilibrium does exist at the interface, the composition of melt in the interface proximity will certainly differ from the bulk composition. Melt inclusions trapped during this kind of boundary layer formation cannot represent the parental melt, even performing re-homogenisation experiment (Watson *et al.*, 1982; Bacon, 1989; Lowenstern, 1995; Gasparik and Hutchison, 2000; Webster and Rebbert, 2000; Faure and Schiano, 2005). This effect causes an uneven distribution of elements, particularly, the large and highly charged ions like Sr, Zr and Nb in the boundary layer proximity to the growing crystal faces. However, it is accepted that the incompatible trace elements are more ready to diffuse compared to silica in silicate melts (Lu *et al.*, 1995; Watson, 1996); accordingly, the effect of boundary layer also varies on the type chemical elements and less effect on incompatible trace elements.

After entrapment, the composition of the silicate-melt inclusions may change by chemical diffusion or exchange with the host corundum as they continue growing. Post-entrapment processes, including, the formation of daughter minerals inside the trapped silicate-melt inclusions as well as the progression of the host crystal growth could decrease the concentrations of certain elements and increase the concentration of others elements. For example, the crystallisation of iron oxide as daughter minerals in the trapped melt inclusions will reduce the FeO and/or TiO_2 content; consequently, the concentration of other constituents will be raised. The heating experiments were performed at atmospheric condition, therefore water contents could lost from the silicate-melt inclusion (Massare *et al.*, 2002; Solovova *et al.*, 2005). It was reported by several researchers that the loss of volatile components, particularly, H_2O, could occur by the diffusion of H_2 and/or H_2O in the host crystal after entrapment (Roedder, 1984;

Qin *et al.*, 1992; Bacon *et al.*, 1992) and it is calculated basis on thermodynamic properties (Roedder and Coombs, 1967) that the loss of H_2O would occur if the trapped melt inclusions had lasted at magmatic temperatures for 24 hours or longer. The abundance of primary and pseudo-secondary inclusions of type-1 CO_2-rich inclusions and type-2 Hypersaline brine as well as H_2O-CO_2 coexist with type-3 Silicate-melt inclusions reflect that they experienced little of volatile loss. In addition, the duration that they were entrained in the alkali basalt must be a short period of time thus the presence of mantle and crustal xenoliths and at least phenocrysts/xenocrysts of corundum in the Bo Ploi alkali basalt are strong evidences indicating a rapid ascending of the magma to the surface, therefore, the loss of volatiles after entrapment in the alkali basalt, again, should be minimal.

In conclusion, the trapped silicate-melt inclusion found in the Bo Ploi corundum should represent the intermediate stage of the melt that crystallised corundum, although not the theoretical parental melt, since there are various factors that could modify the original compositions and prevent an accurate P/T trapping condition to be established. Further microthermometric studies should be done on the other assemblage minerals coexisting with corundum, including spinel, clinopyroxene, alkali feldspar, in order to confirm the relationship among these phases and pin point the actual parental magma that yields corundum. Experimental petrology on the crystallisation of corundum can be simulated from the available results including physiochemical conditions during the entrapment, the composition of the silicate-melt, the phase transformation and the homogenisation temperatures, in order to postulate the genesis of corundum from this deposit.

Conclusion

1. The Bo Ploi corundum contains variety of inclusions including mineral inclusions, fluid inclusions and silicate-melt inclusions. The mineral inclusions are dominated by alkali feldspar, zircon, spinel, monazite, pyrochlore, boehmite and rutile. The trapped fluid inclusions are CO_2-rich inclusions and hypersaline multiphase inclusions (gas-liquid-solid). The silicate-melt inclusions are either with or without daughter minerals.
2. Microthermometric study of these fluid inclusions indicates that the trapping temperature is approximately 920-1000°C, while a slightly lower but wider trapping temperature was obtained from the silicate-melt inclusions (850-1200°C).
3. The corundum originated from trachyandesitic magma by extensive fractional crystallisation of Mg-Fe based minerals under conditions that prevented or slowed down the crystallisation of plagioclase so the melt became saturated with alumina. An additional alumina source from Al-rich crustal material, confirmed by oxygen isotope analyses, was introduced to the magma and caused peraluminous composition that allowed corundum to crystallise.
4. A particular type of syngenetic mineral inclusions like feldspar, monazite and zircon had an influence on the chondrite-normalised REE patterns of the Bo Ploi corundum by flattened light REE and heavy REE and caused negative Eu anomalies.
5. The Bo Ploi corundum is magmatic in origin crystallised from trachyandesitic melt under an environment that was composed of, at least, CO_2, H_2O and hypersaline brine. It was brought up to the surface by the later eruption of Bo Ploi basalt (basanites), this is supported by aureoles of smaller inclusions around the larger ones, which indicate leakage or decrepitation processes as the corundum incorporated into the ascendant alkali basaltic magma.

Chapter 4

Oxygen stable isotope

The study of oxygen stable isotope is reported in this chapter. The aim of the study is to distinguish oxygen stable isotope signatures among the studied materials, including, the Bo Ploi corundum, the Bo Ploi basalt and its entrained crustal xenoliths. Since mantle and crustal materials have different oxygen isotope characteristics, the technique can be employed to discriminate between mantle and crustal signatures, which is relevant to the genesis of Bo Ploi corundum.

4.1 Introduction

Oxygen stable isotope chemistry is a useful tool to explain the geological processes on the basis of isotopic fractionation both in low- and high-temperature geological processes (Clayton *et al.*, 1996; Eiler *et al.*, 1996; Demény *et al.*, 1997; Downes, *et al.*, 1997; Zheng, 1997; Dobosi *et al.*, 1998; Chen *et al.*, 1999; Zheng *et al.*, 2001; Hu and Clayton, 2003). In addition, most common rock-forming minerals have been analysed for their oxygen isotopic fractionations that take place between mineral-pair assemblages, minerals and water fluid and minerals and melts (Chiba *et al.*, 1989, Zheng, 1991, 1993; Nabelek *et al.*, 1992; Vennemann and Smith, 1992; Palin *et al.*, 1996; Macpherson and Matty, 1998; Tennie *et al.*, 1998; Zhao and Zheng, 2002; Appola, *et al.*, 2003; Matthews, *et al.*, 2003; Bindeman, *et al.*, 2006). One of the common application of the oxygen stable isotope determination is to use for distinguish crustal from mantle materials according to the abundance of the $^{18}O/^{16}O$ stable isotope ratio. Mantle materials have an average restricted range of $\delta^{18}O$ value of 5.7±0.3‰. Nonetheless $\delta^{18}O$ may be slightly enriched or depleted relative to this mean value and this variation is a result of the different diffusion rates of isotopic exchange and possibly isotopic heterogeneities in the mantle (Graham and Harmon, 1983). On the other hand,

$\delta^{18}O$ values of crustal materials exhibit a much wider variable range, from depleted $\delta^{18}O$ of less than 4.5‰ to $\delta^{18}O$-enriched with values higher than 7.5‰ (Taylor and Sheppard, 1986). Additionally, oxygen isotope geothermometry can be used to quantify closure temperatures, which is principally based on the thermal sensitivity and pressure insensitivity of isotopic exchanges between the coexisting phases. Theoretically then, in combination with other independent geothermometry such as from fluid and melt inclusions studies, the PT conditions during the crystallisation of corundum might be established. The great advantage of oxygen isotope geochemistry is that most materials contain oxygen molecules in their structure, which can be analysed for their $\delta^{18}O$ values. Thus, for example, corundum (Al_2O_3) consists of nearly pure Al_2O_3 which represent (48/102) wt% oxygen (~47%). From there, the determination of the $\delta^{18}O$ value in corundum and the host alkali basalt should also be a sensitive method to evaluate the relationship between corundum and host alkali basalt.

However, unlike rock-forming silicate minerals, there are few references on the determination of $\delta^{18}O$ for corundum, nonetheless, these works represent corundum from different modes of occurrence; therefore, the likely variability of $\delta^{18}O$-fractionation can be estimated (Kerrich *et al.*, 1987; Virag *et al.*, 1991; Fallick *et al.*, 1995-unpublished data; Upton *et al.*, 1999; Lowry *et al.*, 2003; Yui *et al.*, 2003, 2006; Giuliani *et al.*, 2005; Mariga *et al.*, 2006). A $\delta^{18}O$ of 3.5-4.8‰ for corundum phenocrysts from O'Briens Claims rock, Zimbabwe, which is located in a close proximity to greenstone belt basement schists was reported by Kerrich *et al.*, (1987). The host rock is volcanic schists, where lenses of corundum are associated with dissemination of Cr-muscovite. The authors proposed that corundum crystallised from a low pH hydrothermal solution that interacted with ultramafic rock at high temperature. Fallick *et al.*, 1995 (unpublished data) showed that the $\delta^{18}O$ of corundum from Yogo Gulch, Montana ranges from 5.4 to 6.8‰ compared with the host dyke rock, which varies from 5.1 to

12.1‰. They also noticed that the higher Al_2O_3 content in the Yogo Gulch dyke correlated with a higher $\delta^{18}O$ value. Upton *et al.,* (1999) described corundum from Loch Roag, Scotland where corundum megacrysts occur in alkali basaltic hosts together with a suite of megacrysts (phenocrysts) including zircon, anorthoclase, apatite, clinopyroxene, Fe-rich biotite and magnetite. They reported $\delta^{18}O$ of 4.65 to 5.25‰ for the corundum megacrysts and although the $\delta^{18}O$ of the host rock was not presented, they concluded that the $\delta^{18}O$ of corundum is in the range of the sub-continental mantle of Scotland. Therefore, they proposed that the Loch Roag corundum megacrysts originated from the mantle. Lowry *et al.*, (2003) worked on an ultramafic layer of Early Archean, in SW Greenland, and found ruby corundum, with $\delta^{18}O$ of 4.27‰, occurring in gabbro anorthosite bands in close proximity to a gneiss vein, which they interpret as a product of metamorphism. $\delta^{18}O$ analyses for sapphires from the Denchai deposit, northern Thailand (Yui, *et al.*, 2003) give $\delta^{18}O$ of 4.7 to 6.1‰ with one sample showing $\delta^{18}O$ of 8.4‰. The sapphire with $\delta^{18}O$ higher than 5.5‰ is believed to have a crustal signature in their origin. Subsequently, they proposed a hybrid genetic model, with interaction of fractionated partial melt from metasomatised mantle with Al-rich rock of lower/mid crustal rock. Another corundum deposit in Thailand in Chanthaburi-Trat province also yields magnificent gem quality rubies and sapphires, which have been analysed for $\delta^{18}O$; the rubies have low $\delta^{18}O$ of 1.3-4.2‰, while sapphires $\delta^{18}O$ are higher in the range of 5.1-6.2‰ (Yui *et al.*, 2006). They propose a complex model for the genesis of corundum in the Chanthaburi-Trat deposit; magmatic crystallisation from evolved mantle magmas are responsible for sapphire, while mafic metamorphic rock such as garnet pyroxenite in sub-continental mantle are thought to represent parental source to crystallisation of the ruby. In the Voisey's Bay intrusion, Labrador, Canada, corundum occur in xenoliths of plagioclase - corundum - hercynite ± magnetite assemblage found scattered in gabbroic to troctolitic intrusive bodies. This corundum

has $\delta^{18}O$ values of 1.9-6.1‰ ($\delta^{18}O$ 5.0‰ average; Mariga *et al.*, 2006).

4.2 Methodology of oxygen stable isotopes

There are three isotopes of oxygen, ^{16}O, ^{17}O and ^{18}O with relative abundance in nature of 99.763%, 0.037% and 0.200% respectively (Gill, 1996). The isotopic ratio for oxygen stable isotope of interest in this study is $^{18}O/^{16}O$. *Isotope Fractionation* refers to the partitioning of stable isotopes for a certain element amongst the different coeval phases. There are two types of isotope fractionation processes, termed *kinetic* and *equilibrium* isotope fractionation.

Kinetic isotope fractionation occurs in rapid or dynamic system, usually with more than one phase, for instance; evaporation, diffusion and dissociation processes. In the case of evaporation and diffusion, fractionation occurs due to the different velocities of isotopic molecules that are mobilised within and between the phases. The kinetic energy (K.E.) for a certain molecule is the same for all ideal gases at a stated temperature. In the CO_2 system, the possible isotopic components could be $^{12}C^{16}O$ and $^{12}C^{18}O$, with molecular weights of 28 and 30 respectively. The kinetic energy can be obtained from the equation: K.E. = 1/2 mv^2 for both isotopic species. Therefore, the ratio of velocities of the light isotope to the heavy isotope in this system is $(30/28)^{1/2}$, which equals 1.035. That means the lighter isotope compound, $^{12}C^{16}O$, has a velocity approximately 3.5% faster than the heavier isotope counterpart, $^{12}C^{18}O$, for the given temperature. Hence the light isotope tends to escape from the system and leave the system enriched in the heavy isotope. In evaporation, the higher translational velocities of lighter isotopic molecules enable them to pass through the liquid surface easily, as a result of isotopic fractionation between liquid and vapour. For instance, $\delta^{18}O$ value of water vapour above the ocean ($\delta^{18}O = 0$) is typically around -13‰, however the value of -9‰ is obtained at equilibrium depending on the temperature of the evaporation. As

the vapour phase reaches saturation, the process of isotopic fractionation is reduced to the value of the equilibrium fractionation (see below), where the rate of molecular exchange between liquid into vapour and vapour into liquid are the same. Similarly, the chemical bonds of ^{12}C-H or ^{32}S-O are easier to separate than those bonds of ^{13}C-H or ^{34}S-O, therefore, it is implied that lighter isotopes have lower dissociation energies than heavier isotopes. In the same sense, light isotopes are less stable than heavy isotopes. It is the rate dependent differences in molecular velocities or dissociation energies that allow kinetic isotopic fractionation to occur. Kinetic processes can yield large isotopic differences, however, such processes are less effective at the high temperatures of many natural processes (O'Neil, 1986), which are dominated by equilibrium fractionation.

Equilibrium isotope fractionation is directly related to thermodynamic equilibrium. The fractionation occurs due to different atomic mass and bonding energies of each isotope. In theory, the substitution of a light isotope by a heavy isotope has no effect on charges and electronic distribution of the molecules. That means the potential energy curve remains unchanged. Figure 4.1 shows the relationship between different hydrogen isotopes and the potential energy of the atoms. The vibrational energy levels are expressed as $E = \left(n + \frac{1}{2}\right)h\upsilon$

Where n = energy levels (0, 1, 2, 3,...)

h = Planck's constant (6.624×10^{-27} erg^{-sec})

υ = Frequency (sec^{-1})

At ground energy level (n = 0) and $E = (\frac{1}{2})h\upsilon$ which gives the energy of molecules even at the absolute zero (zero point energy-ZPE). The ZPE represents the energy difference between the potential energy and the zeroeth vibrational energy level as shown in figure 4.1. The frequency is related to mass by Hooke's Law

$$\upsilon = \frac{1}{2\pi}\sqrt{\frac{k}{\mu}}$$

Where k = force constant (dyne/cm)

μ = Reduced mass, $\mu = \frac{M_A M_B}{M_A + M_B}$ for molecule AB whose atomic weights are M_A and M_B.

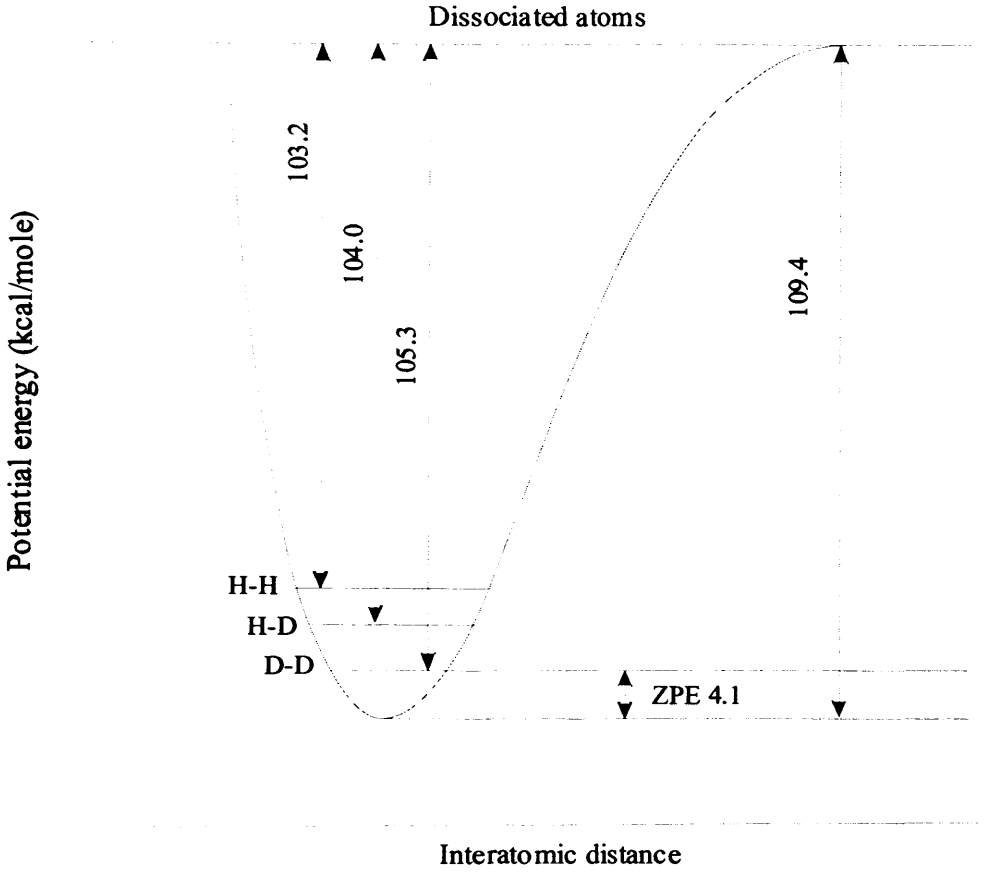

Figure 4.1 Potential energy diagram of hydrogen molecule shows three different isotopes H_2, HD and D_2. The molecules of the heavier isotope are more stable than those molecules with lighter isotopes hence they require higher energy to dissociate. All of these isotopes have the same spectroscopic dissociation energy (109.4 kcal/mole) but have varied chemical dissociation energies and zero point energies (ZPE). Modified after Taylor and Sheppard, (1986)

Frequency is also expressed in terms of wave number (ω), with unit (cm^{-1}), particularly in spectroscopic and thermodynamic calculations; $\omega = \frac{\upsilon}{c}$, and c = light velocity. In isotopic exchange, K remains unchanged, as the only shape of the potential energy curve would be influenced, nevertheless, μ changes. If A is substituted by its heavier isotope A′, therefore,

$$\mu > \mu'$$

$$\upsilon' < \upsilon$$

$$E' < E$$

The molecules with heavy isotope are more stable i.e. their bonding energies are higher than those molecules of lighter isotope, which means that the molecules of heavier isotopes have higher dissociation energy and are more difficult to dissociate. However, the isotopic substitution is also related to the temperature and at higher temperature where molecules are activated and vibrate at higher vibrational energy levels as a result the energy differences between isotopic species is lessened until dissociation occurs. The free energy differences associated with isotope effects are very small when compared to the typical bond energies or heat capacities released from chemical reactions. For example in the system of $\frac{1}{2}C^{16}O_2 + H_2{}^{18}O = \frac{1}{2} C^{18}O_2 + H_2{}^{16}O$ the system has an equilibrium constant of 1.0412 at 25°C and free energy change is only –23.9 cal/mole, which is very normal value of isotopic fractionation at low temperature. The low free energy difference such as (–23.9) cal/mole is not adequate to activate the chemical reactions. In contrast, it is equitable that isotopic equilibrium fractionation should be formed during the reaction that are chemically or mineralogical in equilibrium.

A + B′ = A′ + B; as in example $^{12}CH_4 + {}^{13}CO_2 = {}^{13}CH_4 + {}^{12}CO_2$

Then the equilibrium constant; $K_{AB} = \frac{[A']/[A]}{[B]/[B']} = \frac{[A']/[B]}{[A]/[B']}$ and *ln* K is a function of temperature. Fractionation of isotopes causes the variations of concentrations of stable isotopes in nature. It is usually described as ***Isotope ratios, R***

Where $R = \frac{Isotopic\ \ heavy}{Isotopic\ \ light}$ *or* $\frac{Rare\ \ isotope}{Abundant\ \ isotope}$

For instance, (D/H), ($^{13}C/^{12}C$), ($^{18}O/^{16}O$)

In Earth sciences, the isotope ratio determination is described in the ***Delta (δ) per mil (‰)*** unit, which is derived from $\delta_{sample\text{-}standard} = \delta_{sample} - \delta_{s\tan dard} = \left(\frac{R_{sample}}{R_{s\tan dard}} - 1\right) \times 10^3$

$$\delta_{sample} - \delta_{s\tan dard} = \left(\frac{R_{sample} - R_{s\tan dard}}{R_{s\tan dard}}\right) \times 10^3$$

Where the standard for Hydrogen is SMOW (Standard Mean Ocean Water): δD

Carbon is PDB (Peedee Belemnite); $\delta^{13}C$

Oxygen is SMOW, PDB; $\delta^{18}O$

Nitrogen is Air; $\delta^{15}N$

Sulphur is CDT (Canyon Diablo Troilite); $\delta^{34}S$

The operations of isotope fractionations are defined by an ***Isotope fractionation factor*, α.** Therefore, for a specific system, isotopes of the elements are distributed throughout the system and can be expressed as a simple equation:

$$\alpha_{AB} = \frac{R_A}{R_B} = \frac{[A']/[A]}{[B']/[B]} = \frac{[A'][B]}{[A][B']}$$

The above equation can also be expressed in the form of δ values as:

$R_{sample} = R_{s\tan dard}\left(1 + 10^3 \delta_{sample-s\tan dard}\right)$ and wherever the same standard is used

$R_A = R_{std}\left(1 + 10^{-3}\delta_A\right)$ and $R_B = R_{std}\left(1 + 10^{-3}\delta_B\right)$

$\alpha_{AB} = \frac{R_A}{R_B} = \frac{\left(1 + 10^{-3}\delta_A\right)}{\left(1 + 10^{-3}\delta_B\right)}$, In which $\ln\alpha_{AB} = \ln\left(1 + 10^{-3}\delta_A\right) - \ln\left(1 + 10^{-3}\delta_B\right)$

For the small values of δ_A and δ_B the approximation of the operation ln (1+x) ≈ x, which means $\ln\alpha_{AB} = 10^{-3}\delta_A - 10^{-3}\delta_B$ or $\delta_A - \delta_B = 10^3 \ln\alpha_{AB}$

At equilibrium, isotopes are distributed throughout the whole molecule and isotope fractionation factor (α) is related to the equilibrium constant (K) in terms of;

$\alpha_{AB} = K_{AB}$ and $\alpha = K^{\frac{1}{n}}$ Where *n* represents exchangeable atoms.

For the system $^{12}CH_4 + {}^{13}CO_2 = {}^{13}CH_4 + {}^{12}CO_2$, the equilibrium constant (K) for the isotope exchange reaction can be described as $K = \frac{(^{13}CO_2)(^{12}CH_4)}{(^{12}CO_2)(^{13}CH_4)}$. Similar to equilibrium constants of all reactions, the equilibrium constants of isotopic exchange depend on temperature. This leads to the useful application of stable isotope thermometry. Isotopic fractionation factors are also reported in the various different mathematical operations including, α, lnα, 10^3lnα, Δ and ε. However, the final values from each of these mathematical operations are very close.

4.3 Oxygen stable isotope determination

4.3.1 Sample preparation

$^{18}O/^{16}O$ determinations were performed on individual sapphire samples, host alkali basalt, and the entrained crustal xenoliths. Optically clear sapphire crystals were carefully selected using a binocular microscope and immersion method, where the rough stones were immersed in the water to be examined through the binocular microscope. This method allows the different materials, for example, mineral inclusions, fluid inclusions, and the host sapphire; to be easily identified base on the appearances of relief due to their reflective index differences. The samples were then crushed in an alumina piston prior to being ground in an agate mortar until approximate size of 200 mesh. The fresh host alkali basalt was crushed into small

pieces of approximately 0.5 centimetres and hand picked for the material that was free from obvious phenocrysts, megacrysts, mantle or crustal materials, and secondary minerals. The selected pieces of basalt were then ground into a powder using a tungsten carbide Tema mill. The entrained crustal xenoliths were sawn from the host alkali basalt and crushed into coarse chips and carefully hand picked for only the crustal material avoiding the alteration or reaction rim, which results from reaction of the host alkali basalt and the crustal nodules. The selected pieces of crustal xenoliths were ground in an agate mortar to size of 200 mesh. In order to minimise the contamination that may occur during sample preparation, these sample powders were leached by acetone. The laser fluorination technique was employed for $^{18}O/^{16}O$ determinations, and the processes were performed at the Scottish University Research and Reactor Centre (SURRC), East Kilbride, Glasgow. Using a laser fluorination set-up based on that of Sharp (1990); oxygen was extracted from approximately 1.5 mg of purified sample by reaction with BrF_5 at 609°C over night. The purified oxygen was converted to CO_2 by reaction with a hot carbon rod. The yielded CO_2 was then analysed, on-line, using a VG PRISM III mass spectrometer. Oxygen isotope $\delta^{18}O$ values are reported in the standard permil-notation relative to Standard Mean Ocean Water (SMOW) as defined by Craig (1961). The NBS28 quartz standard gave values of 9.6±0.2‰ (per mil) SMOW during the course of analyse; a reproducible precision of ±0.2‰ (1σ) was obtained.

4.3.2 Oxygen stable isotope determination

It is found that sapphires from the Bo Ploi deposits have $\delta^{18}O$ range from 6.5 to 9.6‰. The Bo Ploi basalt contains oxygen isotope signatures that indicate mantle origin with the $\delta^{18}O$ value range from 6.0 to 6.9‰, while $\delta^{18}O$ of the crustal xenoliths range from 2.4 to 10.3‰. The results for $\delta^{18}O$ determinations for Bo Ploi sapphires are illustrated

in Table 4.1, while $\delta^{18}O$ analyses for the basalt and entrained crustal xenoliths are shown in Table 4.2 and 4.3.

Table 4.1 The $\delta^{18}O$ determinations for sapphires from the Bo Ploi deposit.

Number	Sample	Colour - Clarity	$\delta^{18}O$ (‰V-SMOW)
1	A01-01	deep intense blue, transparent	7.3
2	A01-02	deep intense blue, transparent	6.9
3	A02-01	deep blue, transparent	6.8
4	A03-01	deep blue with greyish, yellowish tint	6.5
5	B01-01	light blue to mauve, transparent	6.8
6	B-pB01-01	pale light blue, transparent	9.6
7	B-dB01-01	darker light blue, semi-transparent	6.5
8	C-pB01-01	pale greyish blue, translucent	8.4
9	C-dB01-01	dark greyish blue, translucent	7.1
10	D01-01	dark cornflower blue, semi-translucent	7.9
		average	7.38
		STDEV	0.9875

Table 4.2 The $\delta^{18}O$ determination of the Bo Ploi alkali basalt.

Sample	Description	$\delta^{18}O$ (‰V-SMOW)
N 4.2-01	alkali basalt	6.7
N 4.2-02	alkali basalt	6.9
C 01-01	alkali basalt	6.2
T 02-01	alkali basalt	6.0
N01-01	alkali basalt	6.1
N02-01	alkali basalt	6.3
	average	6.36
	STDEV	0.3559

Table 4.3 The $\delta^{18}O$ determination of entrained crustal xenoliths in the Bo Ploi basalt.

Sample	Description	$\delta^{18}O$ (‰V-SMOW)
a	nepheline syenite	7.4
b	nepheline syenite	6.6
c	quartzite	2.4
d	nepheline syenite	6.5
e	quartzite	2.3
f	granitic rock	4.4
g	quartzite	3.6
h	granitic rock	4.8
i	nepheline syenite	9.9
j	nepheline syenite	10.3
	average	5.82
	STDEV	2.8354

4.4 Oxygen stable isotope thermometry

Isotope Geothermometry is established using the partition fractionation of stable isotopes of an element (O, C, S, H, etc.) between two minerals and these partitioning processes do not depend, as far as is known, on pressure. Together with the facts that the higher temperature, the lower isotope fractionations and the relative consistency of isotope abundant among the coexisting phases as well as the magnitude of fractionations are still significant when compared with analytical errors. All of these factors allow the isotope thermometry to be established. The essential condition of isotope thermometry is that the interesting system must have isotope equilibrium. Basically, systems in chemical and mineralogical equilibrium should be in isotopic equilibrium (O'Neil, 1986, Hoefs, 1997). Isotope fractionation ratios of light elements such as D/H, $^{13}C/^{12}C$, $^{18}O/^{16}O$ and $^{34}S/^{32}S$ have been employed in various geologic problems. The remarkable usage is among the thermal activities as in evaluating P-T conditions of metamorphic terrains, determining high and low temperatures of mineral assemblages and temperature constraints in geothermal and ore deposits. The works in palaeoclimatology, oceanography, sedimentology and even hydrogeology have regularly applied isotope thermometry as a wizardry tool to solve the study enigmas thus the isotope fractionation ratio is sensitive to temperature, in particular at low temperature. Nevertheless, the isotope fractionation ratios of hydrogen, carbon and sulphur may manifest a powerful tool in geothermometry studies, still oxygen isotope thermometry demonstrate greater applications. In this study, only the oxygen isotope thermometry will be examined.

It is commonly accepted that fractionation factor (α) for an isotope partitioning between minerals is a function of $1/T^2$, where T is temperature in Kelvin. At temperature lower than 500°C, the partitioning of O-isotope between a coexisted

mineral pair can be stated as $1000\ln\alpha = \frac{A}{T^2}$. It is more common under the expression

$$10^3 \ln\alpha = A\left(\frac{10^6}{T^2}\right) + B$$

Unlike the low temperature, for the temperature higher than 500°C the above relation can be expressed as $1000\ln\alpha = \frac{A}{T^2} + B$. Similarly, it can be expressed as

$$10^3 \ln\alpha = A\left(\frac{10^3}{T}\right) + B$$

The factor A and B are constant values, which need to obtain for calculating the temperature of equilibrium. These equilibrium constant values have been determined by two major methods. Firstly, the ***theoretical calculations***, which have been performed by many researchers (Kieffer, 1982, O'Neil, 1986, Zheng, 1991). It was primarily favourable for fractionation equilibrium in gas. Then the development of ideal gas theory leads to the application on the solid phases, as they still employ the same principle of the relationship between vibrational frequencies and fundamental modes of vibration (O'Neil, 1986, Hoefs, 1997). The thermodynamic properties of minerals i.e. elasticity, structural and spectroscopic properties were evaluated and applied for calculation of oxygen isotope fractionation ratios for common silicate minerals by Kieffer, (1982). Her classical calculation method is a foundation stone for further development on calculations of isotope fractionation factors that are available nowadays. Nonetheless, the accuracy in calculations is limited as a result of estimated values that are required in the equation and the errata from spectroscopic data. In the last decade, calculations of fractionation factors were extensively developed. The relationship between the nature of chemical bonding and oxygen isotope fractionation was regarded earlier by Garlick (1966) and Taylor (1968). They noticed that the ^{18}O-enrichment in the group of coexisting silicate minerals have direct relation to the bond

strengths in the minerals. From this observation Schütze (1980; 1986) also in Hoefs, (1997) attempted to quantify fractionation by considering the effects of type of bond and its strength and the effects to cation mass due to isotopic substitution. They, therefore, introduced an incremental method for estimation of the fractionation of oxygen isotopes in silicate minerals. Zheng (1991, 1993) further modified this incremental method, where he demonstrated that the crystallographic parameters; the difference of crystal structure and cation distribution has significant influence on the oxygen isotopic fractionation factors. These calculations were designed to perform from 0°C to 1200°C; consequently, the $10^3 ln\alpha$ values and fractionation curves can be established across all of my range of interest.

Secondly, ***experimental determination***, where the isotopic fractionation factors are determined in the laboratories under controlled conditions. The experiments have been carried out usually between temperatures of 250°C to 800°C, which the capacity of the experimental apparatus and the rate of reaction are the main factors limiting the temperature (Hoefs, 1997). Experiments can be divided into two categories; two-direction approach partial exchange techniques and three-isotope method. *Two-direction approach* only works in the case of real exchange reactions. Basically, the platinum or gold capsule is filled with mineral powder (10-20 mg) sealed with water (200 mg) of different isotopic ratio. The capsules are heated in a hydrothermal furnace with confining pressure of 1-2 kbar for duration of days to months. Piston cylinder can also be used but the amounts of the contents have to be reduced, typically 5-10 mg for each element. The experiments run at s pressure of 15-20 kbar. At the end of each experiment, the $\delta^{18}O$ value of the products will be established by material balance or can be directly measured. The equilibration from the two-way approach can be proved using Arhenius plots. The starting materials of minerals powdered and the isotopic difference of starting water (e.g. –5.0‰, +5.0‰ and +15.00‰) demonstrate accurately

the equilibrium fractionation, which has been confirmed by fractionation trends of the isotopic shifts toward the same value of $\Delta^{18}O_{(mineral\text{-}water)}$ (Fig. 4.2).

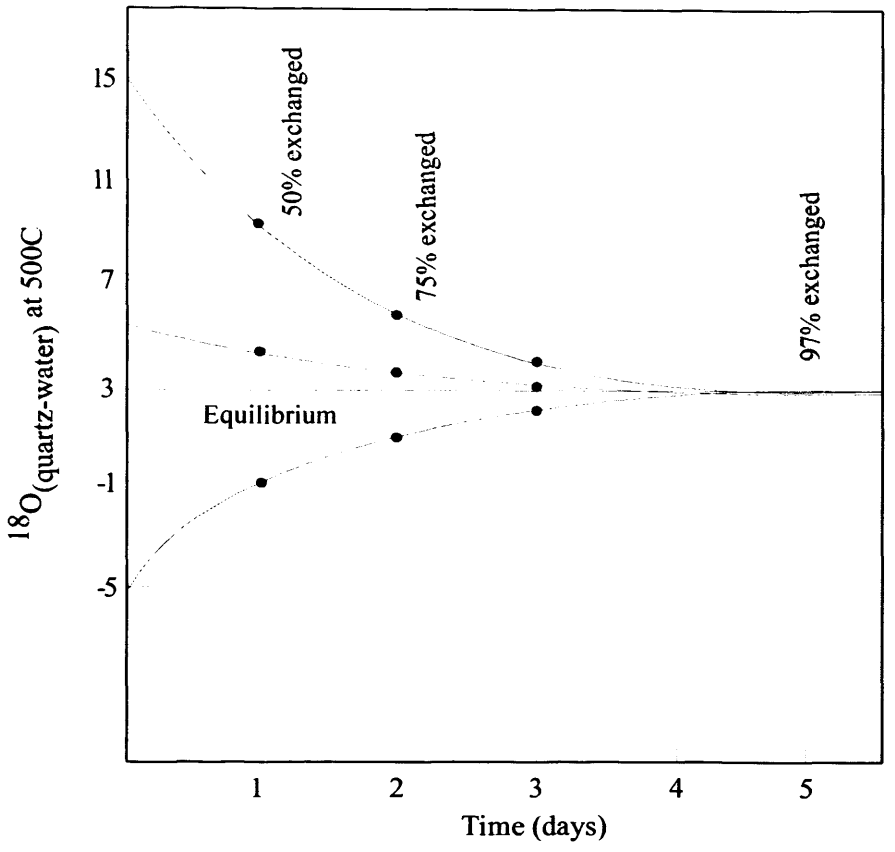

Figure 4.2 Diagram of two-direction experimental approach method for equilibrium fractionation shows an exchange isotope between quartz – water. The $\delta^{18}O$ of starting materials are 10.0‰ (quartz); -5.0‰ (water-A); 5.0‰ (water-B); 15.0‰ (water-C). The values of $\delta^{18}O$ become the same after about a week and indicates that $\Delta^{18}O$ = 3.0, which is the equilibrium fractionation. (Modified after Taylor and Shepperd, 1986)

However, the two-direction experimental approach has some limitations. The rates of isotope exchange between the experimental elements are low thus they are ruled by the diffusion and recrystallization rates. Conventional hydrothermal furnace may induce recrystallization on quenching the experiment hence the quenching time could take several minutes. Besides, the length of experiment capsules could cause the

variation of temperature within the bomb or thermal gradient, which prevent the experiment from reaching thermodynamic equilibrium. The introduction of piston cylinder apparatus can reduce the problem of thermal gradients in the hydrothermal bomb. Nevertheless, the capsules for piston cylinder apparatus are much smaller that those capsules performed on conventional hydrothermal furnace, which means that much smaller amounts of materials are produced. Additionally, considerable skill is necessary for removal of the final products from the capsule and transfer to the analytical instrument for analysis. *Partial Exchange Technique* is introduced to solve the problem where the isotope exchange rates are low. It is based on the postulation that the rates of isotope exchange of two or more identical counterpart experimental conditions run at the same time should be equivalent. Basically, several sample capsules are run together in a single bomb in order to minimise the variation of conditions during an experiment such as heating and quenching rates. The experimental conditions and the capsule preparations are kept the same in terms of capsule volumes, grain sizes of mineral powder, samples loading technique, duration of experiment and temperature of the experiment. Each individual capsule from the experiment presents products to be compared and calculated for the percentage of the isotopic exchange, which can be expressed in terms of Δ-value as:

$$\% \text{ exchange} = \frac{\Delta_i - \Delta_f}{\Delta_i - \Delta_e}$$ where Δ_i, Δ_f *and* Δ_e are the Δ-values at initial composition, final composition and equilibrium composition respectively. The Δ-values from each experiment will be substituted in the equation and then the two equations are solved in order to find Δ_e. Higher percentage means the experiments are more productive reliable. Another useful relation based on the kinetics of isotope exchange, can be generalised as $\ln\alpha_i = \ln K + B(\ln\alpha_f - \ln\alpha_i)$ best illustrated by using graphic method (plot of $\ln\alpha_i$ against $(\ln\alpha_f - \ln\alpha_e)$. Three different $\ln\alpha_i$ values from the companion

experiments produce a straight line on the plot against the ($\ln \alpha_f - \ln \alpha_e$). The slope of the line represents B and the intercept represents ln K. Nonetheless, there is a disadvantage that the fractionation values established from the partial exchange approach tend to produce higher values compared to equilibrium fractionation, particularly when dealing with low temperature systems where the rate of isotope exchange is low. At that point, the plot of $\ln \alpha_i$ against ($\ln \alpha_f - \ln \alpha_e$) illustrates a straight line with negative slope. The lower rate of isotope exchange increases the gradient of this slope, which means more difficult to control the precision in the plot and leads to the error in the interception.

Lastly, the ***Three-isotope method***, which all isotopes such as in oxygen; ^{16}O, ^{17}O and ^{18}O are used to solve the problem by determining $^{17}O/^{16}O$ and $^{18}O/^{16}O$ of an equilibrium system. Starting materials: mineral (M_o) and water (W_o) are chosen. Mo is located on the Primary Mass Fractionation line (PF). W_o must have $\delta^{17}O$ far from equilibrium to M_o, but has $\delta^{18}O$ in close equilibrium with M_o. During the experiment, $\delta^{17}O$ change dramatically and the percentage of equilibrium attained can be calculated (as if in partial exchange technique). Assuming that $^{17}O/^{16}O$ and $^{18}O/^{16}O$ have the same exchange rates, an accurate $\Delta^{18}O$ at equilibrium ($\Delta^{18}O_e$) can be extrapolated from $\Delta^{18}O$. The compositions of partially exchanged isotopes (M_f and W_f) move toward the equilibration (M_e and W_e), that lie on the Secondary Mass Fractionation line (SF). A schematic diagram of the three-isotope method is displayed in figure 4.3.

Information about the oxygen isotope behaviour in corundum is restricted; for the corundum-H_2O or corundum - mineral fractionations, moreover, it has not been experimentally established. The only substitution oxygen isotope fractionations in corundum - water and corundum - quartz have been done by theoretical modelling (Zheng, 1991) whereas the fractionation and the temperature dependence are expressed as the following equations

$$10^3 \ln\alpha = A \times \frac{10^6}{T^2} + B \times \frac{10^3}{T} + C$$

Where, for quartz-corundum, A = 2.00, B = 9.94, C = (-5.32)

for corundum-water, A = 2.24, B = (-13.71), C = 4.28

T = Temperature in Kelvin

Therefore, $10^3 \ln \alpha_{(quartz-cor)} \approx \delta^{18}O_{quartz} - \delta^{18}O_{cor}$

or $10^3 \ln \alpha_{(cor-water)} \approx \delta^{18}O_{cor} - \delta^{18}O_{water}$

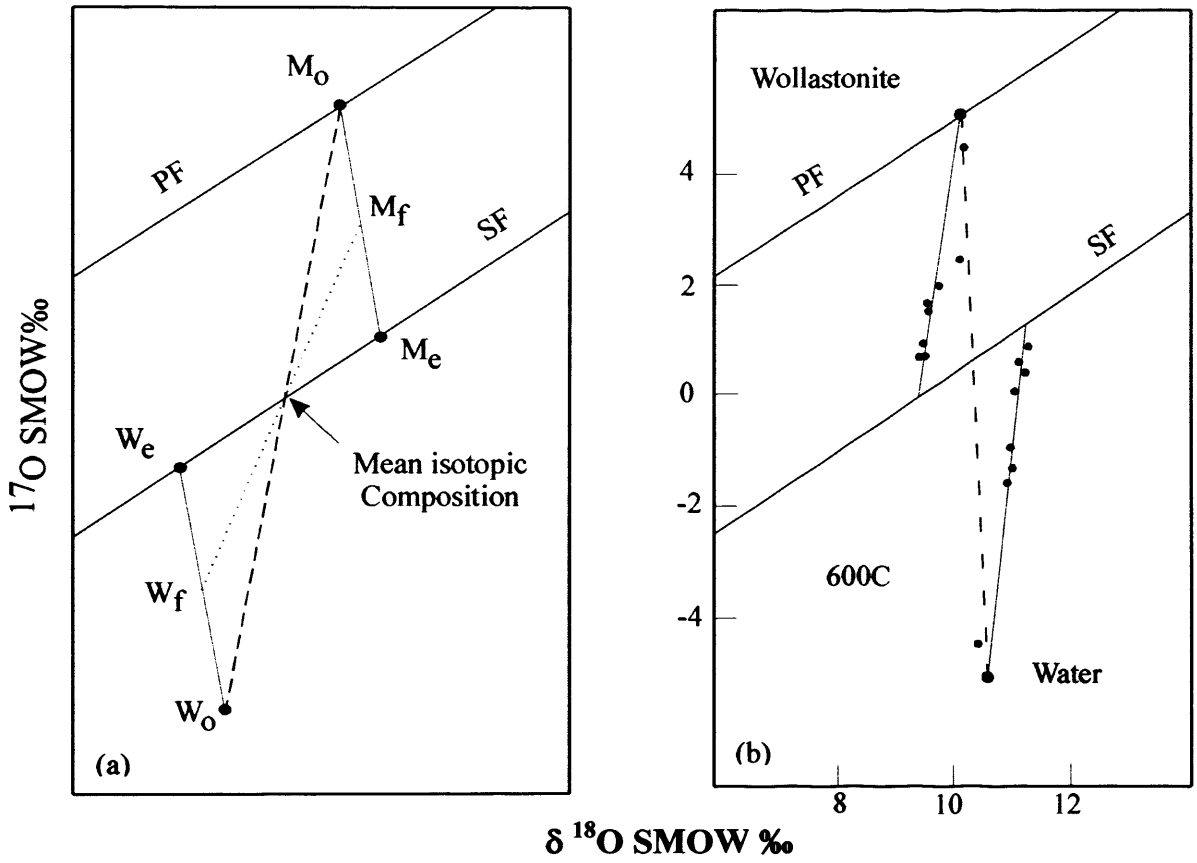

Figure 4.3 (a) In this example the isotopic compositions of the starting materials (M_o) lie on the primary fractionation line (PF) whereas the starting water (W_o) do not. M_f and W_f are isotopic compositions after partial exchange and M_e and W_e represent isotopic equilibrium where both compositions are linked by a tie-line of secondary fractionation line (SF).

(b) Three-isotope plot for wollastonite-water exchange at 600°C.

The average $\delta^{18}O$=7.38‰ of Bo Ploi sapphire (Table 4.2) was substituted in the above equations for isotopic fractionation for quartz-corundum and for corundum-water. The calculations are displayed in tables 4.3 and 4.4, where the fractionation curves are illustrated in figure 4.4 and 4.5. The estimated minimum trapping temperatures were taken to be from the homogenisation temperature of the multiphase inclusions and the silicate melt inclusions are in the range of 1,000 to 1,200°C. Supposing that these temperatures are the locus of high temperature isotope fractionation, where the oxygen in the sapphire structure isotopically exchanges with the precursor materials. It is found that Bo Ploi sapphire ($\delta^{18}O$ = 7.38‰) would have isotopic equilibrium with pure water of $\delta^{18}O$ range 11.38 to 12.49‰. Similarly, the calculation was carried out for isotope fractionation of quartz – corundum, where Bo Ploi sapphire is in equilibrium with quartz of $\delta^{18}O$ = 9.73 to 11.10‰. Theoretically, the $\delta^{18}O$ of water or quartz in equilibrium with sapphire of $\delta^{18}O$ 7.38‰ has a crustal signature. This leads to the interpretation that the materials, which provide oxygen for corundum structures must contain a crustal signature. That means either they resided in proximity to the surface where oxygen is abundant and enriched them with ^{18}O or these materials may be in contact with sedimentary rocks. Otherwise they were interacted with hydrothermal fluid and other possible crustal processes that take place at low temperature, where isotope fractionation may also easily have occurred.

Table 4.4 Calculations of oxygen isotope fractionation for corundum in equilibrium with quartz.

t (°C)	T (K)	$10^6/T^2$	$10^3/T$	$10^3\ln\alpha_{(qtz\text{-}cor)}$	$\delta^{18}O(qtz)$
25	298	11.26	3.36	50.56	57.94
50	323	9.59	3.10	44.62	52.00
100	373	7.19	2.68	35.70	43.08
200	473	4.47	2.11	24.63	32.01
300	573	3.05	1.75	18.12	25.50
400	673	2.20	1.49	13.87	21.25
500	773	1.67	1.29	10.89	18.27
600	873	1.31	1.15	8.69	16.07
700	973	1.06	1.03	7.01	14.39
800	1073	0.87	0.93	5.68	13.06
900	1173	0.73	0.85	4.61	11.99
1000	1273	0.62	0.79	3.72	11.10
1100	1373	0.53	0.73	2.98	10.36
1200	1473	0.46	0.68	2.35	9.73

Equation from Zheng, (1991): $10^3\ln\alpha = 2.00(10^6T^{-2}) + 9.94(10^3T^{-1}) - 5.32$

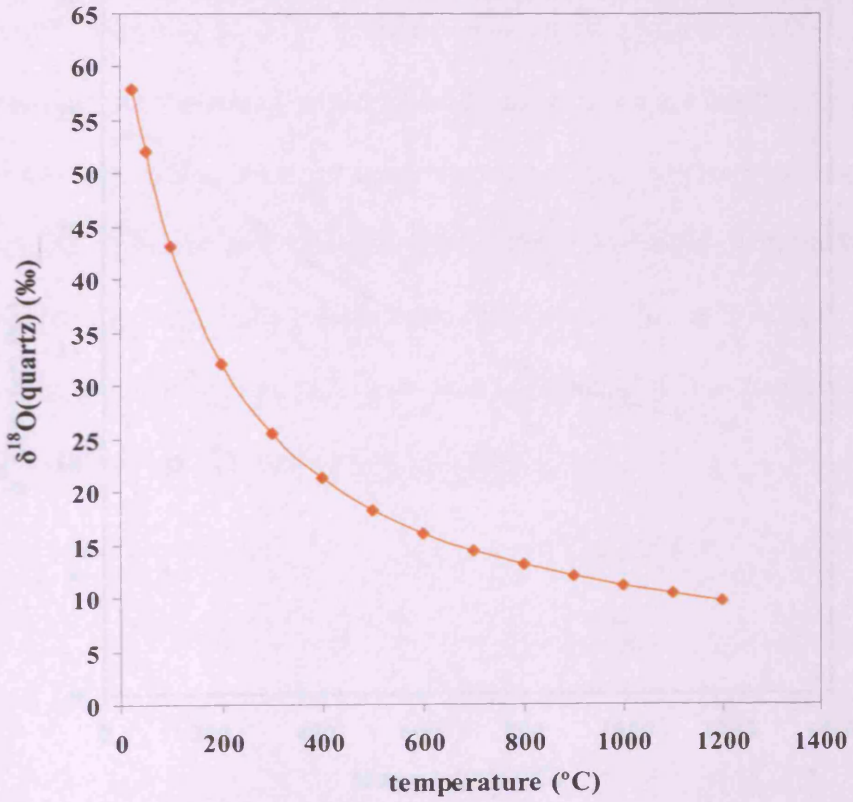

Figure 4.4 Locus of quartz $\delta^{18}O$ in isotopic equilibrium with corundum of $\delta^{18}O$ =7.38‰ as a function of temperature (°C)

Table 4.5 Calculations of oxygen isotope fractionation for corundum in equilibrium with water.

t (°C)	T (K)	$10^6/T^2$	$10^3/T$	$10^3\ln\alpha_{(qtz\text{-}cor)}$	$\delta^{18}O(qtz)$
25	298	11.26	3.36	-16.50	23.88
50	323	9.59	3.10	-16.70	24.08
100	373	7.19	2.68	-16.38	23.76
200	473	4.47	2.11	-14.69	22.07
300	573	3.05	1.75	-12.82	20.20
400	673	2.21	1.49	-11.15	18.53
500	773	1.67	1.29	-9.71	17.09
600	873	1.31	1.15	-8.49	15.87
700	973	1.06	1.03	-7.44	14.82
800	1073	0.87	0.93	-6.55	13.93
900	1173	0.73	0.85	-5.78	13.16
1000	1273	0.62	0.79	-5.11	12.49
1100	1373	0.53	0.73	-4.52	11.90
1200	1473	0.46	0.68	-4.00	11.38

Equation from Zheng, (1991): $10^3\ln\alpha = 2.24(10^6T^{-2}) - 13.71(10^3T^{-1}) + 4.28$

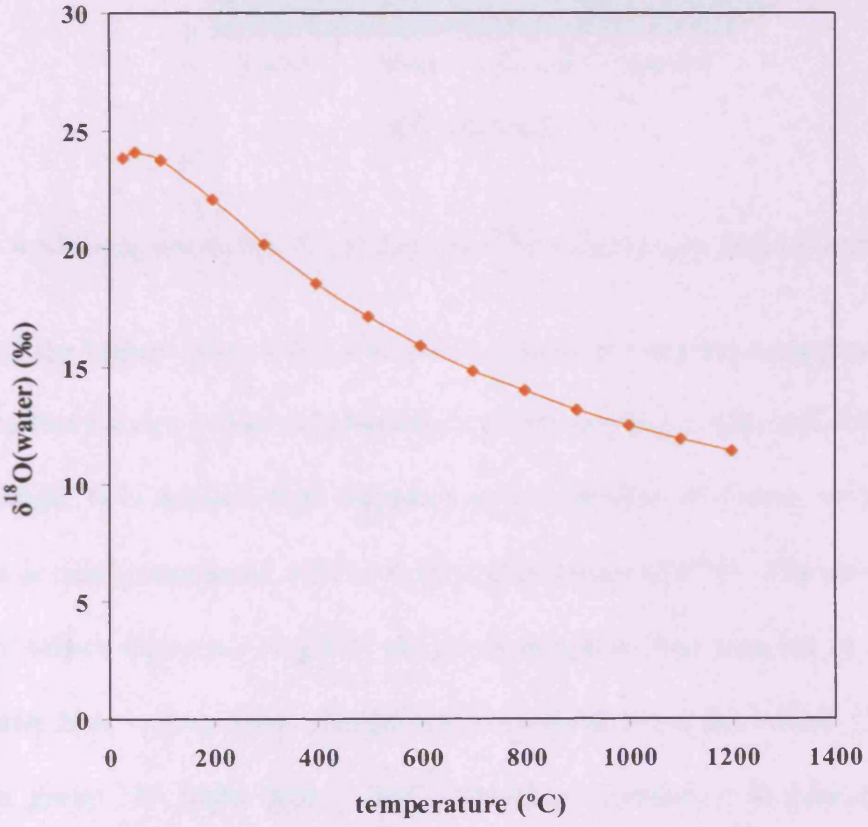

Figure 4.5 Locus of water $\delta^{18}O$ in isotopic equilibrium with corundum of $\delta^{18}O$ =7.38‰ as a function of temperature (°C)

4.5 Discussion and conclusion

4.5.1 The $\delta^{18}O$ of the Bo Ploi corundum

The $\delta^{18}O$ determinations of sapphire from the Bo Ploi deposit range from 6.5 to 9.6‰, with standard deviation of 0.99‰. However, the majority of $\delta^{18}O$ determinations of five samples have $\delta^{18}O$ 6.5 to 6.9‰, three samples with $\delta^{18}O$ 7.1 to 7.9‰ and two samples with $\delta^{18}O$ higher than 8.0‰ (Fig.4.6).

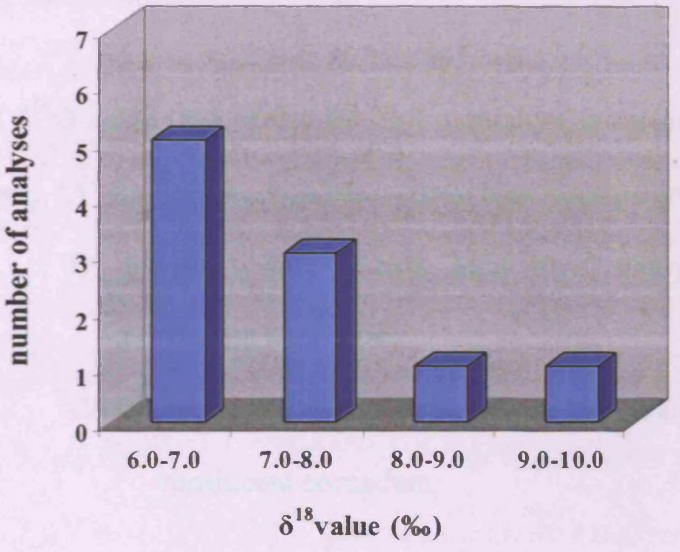

Figure 4.6 Histogram shows distribution of $\delta^{18}O$-value (‰) in Bo Ploi corundum

Still, the higher values 7.9, 8.4 and 9.6‰ obtained from these samples are rather random and there is not a clear relationship between sapphire colour and the values of $\delta^{18}O$, although, it is noticed that sapphires of low quality of clarity, which appear translucent or semi-transparent, tend to yield higher values of $\delta^{18}O$. The plots of $\delta^{18}O$-value with colour variations (Fig.4.7) clearly demonstrate that samples of group 'A' (deep intense blue – deep blue, transparent corundum) have the lowest $\delta^{18}O$, while samples in group 'B' (light blue – dark light blue, transparent to semi-transparent corundum) and group 'C' (greyish blue – dark greyish blue, translucent to semi-translucent corundum) show higher and more variable $\delta^{18}O$ values. The $\delta^{18}O$ values indicate both mantle and crustal geochemistry among the Bo Ploi corundum.

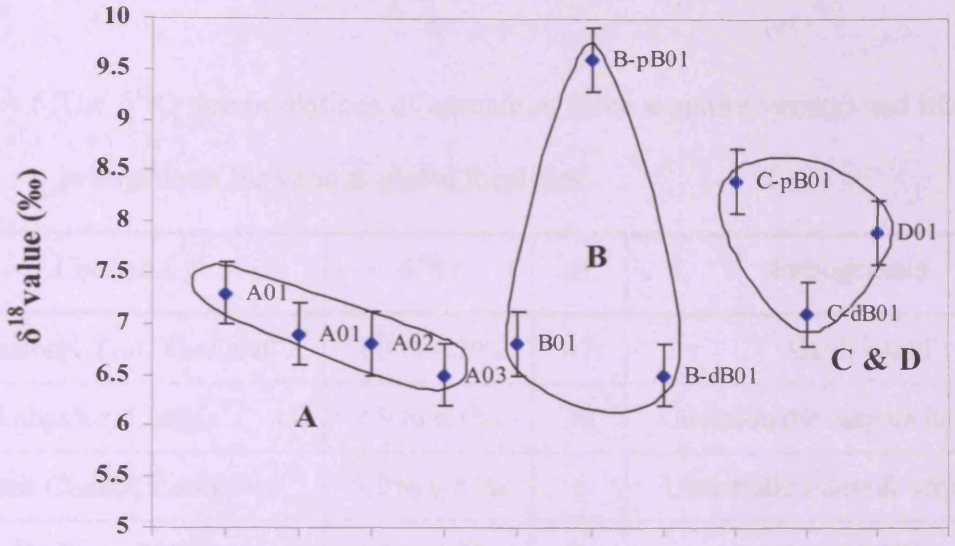

Figure 4.7 Plots of δ^{18}O-value (‰) of the Bo Ploi corundum grouping to their colour variations. 'A' for deep intense blue – deep blue, transparent corundum

'B' for light blue – dark light blue, transparent to semi-transparent corundum

'C&D' for greyish blue – dark greyish blue, translucent to semi-translucent corundum

In comparison with corundum from different localities, which are shown in Table 4.6, it is noticed that δ^{18}O values of corundum, both rubies and sapphires, could be as low as 1.3‰ and as high as 22.3‰, which reflect a diversity of genetic models entailing various geological processes. Summarising all of the available data, δ^{18}O values can be interpreted in terms of geological occurrence into four modes as follows; (1) alkali basalt-related occurrences (2) mafic-metamorphic rock related occurrences (3) syenite – anorthoclasite related occurrences and (4) skarn-related occurrences.

The δ^{18}O values of corundum of the alkali basalt-related occurrences, are in the range of 1.3 to 9.6‰ and include the Bo Ploi deposit (this work), Denchai deposit (Yui *et al.*, 2003) and the Chanthaburi-Trat deposit (Yui *et al.*, 2006), which are all renowned gem quality corundum deposits from Thailand. They were recovered along paleo-channels, as alluvial secondary deposits as well as in situ in weathered basaltic soil, in

Table 4.6 The $\delta^{18}O$ determinations of corundum (blue sapphire variety) and interpreted petrogenesis for various global localities

Location	$\delta^{18}O$	*n**	Petrogenesis
Chanthaburi-Trat, Thailand[6-1]	1.3 to 4.2‰	47	Alkali basalt
Labrador, Canada[7]	1.9 to 6.1‰	30	Gneiss-mafic magma interaction
O'Briens Claims, Zimbabwe [1]	3.5 to 4.8 ‰	6	Ultramafic schist & serpentinite
Kashmir, India[5]	4.2 to 4.9‰	2	Amphibolite
Umba Valley, Tanzania[5]	4.2-7.5‰	3	Amphibolite & serpentinite
Loch Roag, Scotland [3]	4.65 to 5.25‰	4	Syenite- anorthoclasite
Denchai, Thailand [4]	4.7 to 8.4‰	16	Alkali basalt
Chanthaburi-Trat, Thailand[6-2]	5.1-6.2‰	15	Alkali basalt
Yogo Gulch, USA [2]	5.4 to 6.8‰	16	Lamprophyres
Bo Ploi, Thailand	**6.5 to 9.6 ‰**	**10**	**Alkali basalt**
Grenville Province, Canada[1]	7.5 to 7.8 ‰	3	Syenite
Various deposits, Sri Lanka[5]	7.7 to 10.7‰	4	Marble skarn
Kashmir, India[5]	10.9 to 11.2‰	2	Desilicated pegmatite
Andranondambo, Madagascar[5]	10.7 & 14.0‰	2	Marble skarn
Mogok, Myanmar[5]	15.5 to 15.9‰	2	Desilicated pegmatite
Chumar, Nepal[5] Luc Yen, Vietnam Mong Hsu, Myanmar	16.3 to 22.3‰	3	Marble skarn

Note: [1] Kerrich *et al.*, 1987; [2] from Fallick, Taylor and Groat, 1995 (unpublished data); [3] from Upton *et al.*, 1999; [4] from Yui *et al.*, 2003; [5] Giuliani *et al.*, 2005; [6-1] ruby variety from Yui *et al.*, 2006; [6-2] sapphire variety from Yui *et al.*, 2006; [7] Mariga *et al.*, 2006.

*n** = number of samples.

a close proximity to the Caenozoic alkali basalts. The ages of the associated alkali basalt are: Bo Ploi basalt (3.14 ± 0.17 to 4.17 ± 0.11 Ma); the Denchai basalt (5.64 ±0.28 Ma.); and for the Chanthaburi-Trat area including Khao Wua basalt (3.00 ± 0.19 Ma.), Thamai basalt (0.44 ± 0.11 to 2.57 ± 0.2 Ma.) and Ban Ta Bad basalt (1.13 ± 0.17 Ma.). It is generally agreed that corundum could not be a phenocryst phase crystallised from basalts, however, if the genesis involved magmatic or metamorphic processes is still a controversy. The feature that reflects both crustal and mantle isotopic nature is also reported from the Denchai deposit, Thailand (Yui *et al.,* 2003), where the majority of sapphire has $\delta^{18}O$ values ranging from 4.7 to 6.1‰ and one sample shows higher value of 8.4‰. Both Bo Ploi and the Denchai sapphire share several similarities such as, their occurrence since they are associated with Caenozoic alkali basalt, as well as their mineral assemblages, fluid inclusions and silicate-melt inclusions (Srithai *et al.,* 1999; Limtrakun *et al.,* 2001). The Denchai sapphire was, therefore, interpreted as a product of crystallisation from CO_2-rich alkaline magmatism (Limtrakun *et al.*, 2001; Yui *et al.*, 2003). Nonetheless, the Chanthaburi-Trat corundum gem field shows a more complicated petrogenesis with both ruby and sapphire having crystallised from different genetic processes. The $\delta^{18}O$ values of 1.3 to 4.2‰ obtained from ruby (Yui *et al.*, 2006) correspond with previous ideas that Chanthaburi-Trat ruby originated from mafic metamorphic rock under upper mantle conditions, with an approximate temperature range of 800-1150°C at 10-25 kbar pressure (Sutthirat *et al.*, 2001; Saminpanya *et al.*, 2003). These were then transported to the surface via the Caenozoic basalt in that area. The more restricted $\delta^{18}O$ values, 5.1 to 6.2‰ reported for sapphire from the Chanthaburi-Trat deposit (Yui *et al.*, 2006) are consistent with the assumed oxygen isotope composition of the upper mantle, so it is suggested that the genesis of Chanthaburi-Trat sapphire should be monogenetic and of magmatic origin. Sapphire from Yogo Gulch, Montana; has a very consistent $\delta^{18}O$ values in the range of 5.4 to

6.8‰, unlike the lamprophyres dyke host, that give $\delta^{18}O$ varies from 5.1 to 12.1‰ (Fallick *et al.*, 1995-unpublished data).

The second group of mafic metamorphic rock-related corundum, typically has $\delta^{18}O$ values in the range of 3.5 to 7.5‰ and often in a narrow range of 3.5 to 4.9‰. Minerals with $\delta^{18}O$ values lower than 4.5‰ are oxygen isotope-depleted and generally regarded as crustal in origin. This is because oxygen isotope fractionation takes place easily at low temperatures in crustal environment and drives crustal materials towards depleted in $\delta^{18}O$ values. Kerrich *et al.*, (1987) combined wholerock geochemistry with mineral isotope data and interpreted depleted $\delta^{18}O$ (3.5 to 4.8‰) for corundum at the O'Briens claims, Zimbabwe, as a consequence of alteration ultramafic rocks by low pH hydrothermal solutions. Here, lenses of purplish to grey corundum with approximate sizes 16x50 meter are found in a rock of corundum – andalusite - Cr muscovite - chlorite assemblage. Sapphire from Kashmir is another example of a complex metamorphic crustal origin (Giulianni *et al.*, 2005). In this locality, the sapphire crystallised during desilication and exchange reactions between pegmatite and host ultramafic rock, giving two families of corundum; one in the amphibolite - serpentinite and the other in the pegmatite. The $\delta^{18}O$ in the restricted range of 4.2 to 4.9‰ were obtained for corundum occurring in amphibolite-serpentinite while much higher values of 10.9 and 11.2‰ occur in corundum within the pegmatite (Giulianni *et al.*, 2005).

The occurrence of corundum that is categorized in the third group, syenite-anorthoclasite related, shows a $\delta^{18}O$ value ranging from 4.65 to 8.2‰. The corundum from Loch Roag, Scotland, was found as both megacrysts and xenolith of composite anorthoclasite, which is made up of corundum and anorthoclase, in alkali basaltic host. The sapphires from Loch Roag, Scotland and from the Bo Ploi deposits are similar in that they are both hosted by alkali basalt. Nevertheless, the Loch Roag corundum has $\delta^{18}O$ in the range of 4.65-5.25‰, which is a lower and a narrower range than corundum

from Bo Ploi. This is also an indicative of isotopic dissimilarity of the lithospheres between these two localities. Upton *et al.*, (1999) suggested that the $\delta^{18}O$ values of the Loch Roag corundum (4.65 to 5.25‰) correspond to the $\delta^{18}O$ value of the Scottish sub-continental mantle, which further depends on their assumption that the corundum and coexisting megacrysts such as zircon, biotite and feldspar, are magmatic in origin. It is noticed that both the $\delta^{18}O$ value of sapphires and of the host alkali basalt representative of the mantle in the Bo Ploi area, 6.0-6.9‰, are slightly higher than those $\delta^{18}O$-value determinations on the Loch Roag sapphire as well as the Scottish sub-continental mantle. The relatively higher $\delta^{18}O$ values and wider range of variation of sapphires from the Bo Ploi deposit suggests several possible mechanisms, such as the original magma that crystallised corundum was richer in $\delta^{18}O$. Additionally, the wider variation of $\delta^{18}O$ values is consistent with polygenic crystallisation of the Bo Ploi from a mixed mantle and crustal transitional region, so that both crustal and mantle isotopic signatures are presented. Kerrich *et al.*, (1987) also reported corundum associated with syenite and pegmatite from Grenville Province, Canada with $\delta^{18}O$ in the range 7.6-7.8‰, where they further demonstrated that isotope fractionation among the mineral assemblages as plagioclase-corundum ($\Delta = 2.3 - 2.5$) and muscovite – corundum ($\Delta = 1.2$ to 1.4), which they match with the expected range of isotopic fractionation in a magmatic system. Elsewhere $\delta^{18}O$ values from ruby bearing rock, anorthite-edenite from South Africa, have an average of 8.2‰ while $\delta^{18}O$ of the rock itself is much lower (3.8‰) and isotope fractionations between plagioclase – corundum are 3.6 to 3.7‰, which are approximately 1.2‰ higher than those of associated with syenite. Based on their available example, they assumed that isotope fractionations between anorthitic plagioclase – corundum ($\Delta_{\text{plagioclase- corundum}}$) are about 2.5 to 3.7‰ at high grade metamorphic to magmatic temperatures.

The last type of corundum deposits, skarn rocks and skarn-related occurrences, have mostly higher $\delta^{18}O$ values ($\delta^{18}O$ 7.7 to 22.3‰). This is consistent with depletion in the heavy isotope that should be a consequence from the processes in crustal region or contamination with meteoric water or a hydrothermal solution. The corundum deposits in this group can be sub-divided into two subgroups according to the host rock types in which the corundum is deposited. The first subgroup is characterised by corundum developed in pegmatite, or endoskarn, by a process of desilication of pegmatite as reaction of pegmatite with low silica country rocks such as carbonate rocks or basic rocks. The deposits that belong to this subgroup including the famous finest sapphire from Kashmir, India; Jegdalek, Afghanistan; some parts of Mogok, Myanmar; and some parts of Andranondambo, Madagascar. The latter subgroup is corundum crystallised in marble, or exoskarn, which include sapphires from Sri Lanka; Mogok and Mong Hsu, Myanmar; Luc Yen, northern Vietnam; and Chumar, Nepal. It is noticed that sapphires of the first subgroup, deposited in pegmatite, show a narrower range of $\delta^{18}O$ (10.9-15.9‰), while those sapphires form in marble have a much wider range of $\delta^{18}O$ (7.7 to 22.3‰).

4.5.2 The $\delta^{18}O$ of the Bo Ploi basalt

The host alkali basalt $\delta^{18}O$ value ranges from 6.0 to 6.9‰. These numbers are in the normal range of basalt, which implies that the magma itself had not been greatly affected by a process of contamination and/or hydrothermal alteration, which normally cause a substantial effect on the range and variability of ^{18}O in igneous rocks. According to Taylor and Sheppard (1986), the $\delta^{18}O$ value of Mid Oceanic Ridge Basalt (MORB) shows an astoundingly narrow variation around 5.7 ± 0.3‰ and the maximum isotope fractionation accompanying the fractional crystallisation processes is merely 1‰. Hence, it is generally accepted that for all relatively enriched or depleted $\delta^{18}O$

values in silicate melts i.e. magmatic systems with $\delta^{18}O \geq +7.5‰$ or $\delta^{18}O \leq +4.5‰$, must either have partially derived from or have interchanged with a material that resided at or near the Earth's surface (i.e. crust) to allow the large $^{18}O/^{16}O$ fractionation to occur (Taylor and Sheppard, 1986). Oxygen isotope fractionation between melt and minerals has been investigated by many researchers using both experimental and theoretical calculation (Anderson *et al.,* 1971; Muehlenbachs and Kushiro, 1974; Kyser *et al.,* 1982; Sheppard and Harris, 1985). It is found that ^{18}O fractionation occurs only to an extremely small magnitude at high temperature; for example, basaltic melts are merely slightly enriched in ^{18}O relative to their precursor peridotites. Dobosi *et al.,* (1998) reported the $\delta^{18}O$ determination in alkali basalt and its phenocrysts from the Pannonian Basin where the whole rock ($\delta^{18}O$ 6.0-7.2‰) is richer in ^{18}O in relative to olivine phenocrysts ($\delta^{18}O$ 5.0-5.5‰). Nevertheless, it is noticed that the $\delta^{18}O$ values from the whole rock alkali basalt yield approximately 1‰ higher than their phenocrysts such as olivine or pyroxene (Dobosi *et al.*, 1998). In their work, $\delta^{18}O$ value of phenocrysts and megacrysts from the Pannonian Basin alkali basalts such as olivine, pyroxene and amphibole are in the range of 5.0 to 5.5‰, whereas the $\delta^{18}O$ value of the bulk rock is higher and more variable in the range 6.0-7.2‰ (Embey-Isztin *et al.*, 1993) and a similar feature is also reported by Garlick (1966) and Kyser *et al.*, (1982). It is, therefore, explained that although such igneous basaltic rock samples look fresh, the groundmass may have experienced some degree of low temperature alteration by surface water during cooling (Dobosi *et al.*, 1998). The phenocrysts and megacrysts still preserve their original magmatic oxygen isotope signature because of their better ability to withstand low temperature isotopic alteration. The oxygen isotope behaviour in alkali basalt and its phenocrysts from the Pannonian Basin is compared with the Bo Ploi alkali basalt. Although the phenocrysts in the Bo Ploi alkali basalt have not been analysed for their oxygen isotopes, it is reasonable to believe that the alkali basalt

groundmass should have higher $\delta^{18}O$ value to its phenocrysts. Thus, minerals reach their isotopic equilibrium differently, within the sequence of plagioclase, magnetite, pyroxene and olivine, respectively; $\delta^{18}O$ value increasing, respectively (from theoretical calculation after Kieffer, 1982 and Zheng, 1991). So that the isotope exchange occurs among the constituent minerals in basalt groundmass and the lower resistance of low temperature alteration by surface atmosphere/water causes $\delta^{18}O$ in the groundmass to be higher than in the phenocrysts. Since the range of $\delta^{18}O$ in Bo Ploi corundum is higher than the $\delta^{18}O$ value of whole rock basalt, which is in contrast to other phenocrysts in host basalt elsewhere, it is, therefore implied that corundum from the Bo Ploi deposit may possibly occur as xenocrysts in the host Bo Ploi alkali basalt.

The $\Delta^{18}O$ difference between alkali basalt and corundum ($\delta^{18}O_{basalt}$ - $\delta^{18}O_{corundum}$) varies from 0.5 to 2.4 for the majority of corundum, which indicates that the fractionations are within the igneous temperature (Kerrich *et al.*, 1987 and references therein). However, the maximum value $\delta^{18}O$ of 9.6‰ is outside this range ($\Delta^{18}O$ = 3.6‰) and possibly resulted from lower temperature crystallisation or recrystallisation, in which isotope fractionation takes place more easily. Otherwise, the parental materials that provided oxygen to form corundum (Al_2O_3) of high $\delta^{18}O$ value must themselves have been enriched in ^{18}O, which implies that they resided in the crust, where isotope fractionation or isotope contamination with high $\delta^{18}O$ value are endemic. Some variation in the $\delta^{18}O$ values may reflect different sources (depths) in the middle or lower crust, which imposed a range of temperature fractionation effects. The associated megacrysts of pyroxene, feldspar, zircon and spinel were not analysed for their $\delta^{18}O$ values. It is encouraged that in the future, additional the $\delta^{18}O$ determinations should be performed on these other relevant materials coeval with the Bo Ploi sapphire in order to confirm the isotope geothermometry and the isotope fractionation among them. This should also extend to crustal xenoliths in the future (although no relic corundum-

bearing rocks were found so far).

4.5.3 The $\delta^{18}O$ of the entrained crustal xenoliths in the Bo Ploi basalt

The wide range of $\delta^{18}O$ (2.3 to 10.3‰) in crustal xenoliths is quite common for the crust in volcanic areas, nonetheless, the values can be considered as $\delta^{18}O$-depleted and $\delta^{18}O$-enriched relative to the $\delta^{18}O$ value of mantle (= 5.5). The $\delta^{18}O$-'depleted' crustal xenoliths ($\delta^{18}O$ 2.3-4.8‰) are generally characterised by felsic crustal silica-rich rocks like granites and quartzite and often show petrographic textures indicative of partial melting; howevet a coarse-grained nepheline syenite is $\delta^{18}O$-'enriched' (δ^{18}6.5-10.3‰). It is generally accepted that meteoric water and surface oxygen are responsible for the depletion of $\delta^{18}O$ in crustal rocks, while the enrichment in $\delta^{18}O$ crustal rocks results from hydrothermal alteration or groundwater alteration genetically related to sedimentary rocks (Hoefs, 1997). It is, then, interpreted that the crust beneath the Bo Ploi vicinity is made up of high-grade metamorphic basement with coexisting plutonic intrusive bodies (Yaemniyom, 1986). The $\delta^{18}O$ data also suggest that hydrothermal activity played a role in the formation of the crust in this area. These crustal nodules had the opportunity to exchange bulk oxygen with other materials in the host basalt, including corundum. This explains the variation of $\delta^{18}O$ in the corundum.

The combination of isotope geothermometry and geothermometry from microthermometric studies of fluid- and melt-inclusions reveal that the Bo Ploi corundum ($\delta^{18}O$ 7.38‰), which crystallised at temperature in the range of 1,000 to 1,200°C has an isotopic equilibrium equivalent to pure H_2O with a $\delta^{18}O$ value of 11.4 to 12.5‰. Similarly, if tested for isotopic equilibrium with quartz at the same temperature values of 9.7 to 11.1‰ are obtained. This means that the parent materials which provided oxygen to the Al_2O_3 (corundum) have oxygen isotope signatures of 11.4 to 12.5‰, meaning corundum likely crystallised from fluid-bearing systems with oxygen

isotope signatures of $\delta^{18}O$ = 11.4 to 12.5‰. These high $\delta^{18}O$ values are typical of geological systems in the crust where hydrothermal fluid and/or sedimentary rocks occur or are dominant materials.

Conclusions

1. Oxygen isotope determinations on Bo Ploi basalt and entrained crustal xenoliths and corundum found associated with the basalt yield $\delta^{18}O$ = 6.0 to 6.9‰, 2.3 to 10.3‰ and 6.5 to 9.6‰ respectively.
2. The $\delta^{18}O$ of host alkali basalt are slightly high (6.0 to 6.5‰) compared with upper mantle worldwide (5.5‰) and this could be the mantle heterogeneity or minor crustal contamination in the analysed samples.
3. Calculated isotope geothermometry suggested that the corundum (average $\delta^{18}O$ = 7.38‰) was in isotopic equilibrium with H_2O of $\delta^{18}O$ value of 11.4 to 12.5‰ or with quartz of $\delta^{18}O$ of 9.7 to 11.1‰ at temperature range of 1,000 to 1,200°C. This indicates that the parental materials of this corundum are from crustal region.
4. The $\delta^{18}O$ of alkali basalt and corundum are different and variable ($\Delta^{18}O$ = 0.5 to 3.6‰) suggesting a disequilibrium, which implies that there is no genetic relationship; i.e. the corundum is a xenocrystic phase.
5. The entrained crustal xenoliths ($\delta^{18}O$ 2.3 to 10.3‰) are among the potential sources of $\delta^{18}O$-rich materials that yield the high $\delta^{18}O$ value to Bo Ploi corundum. Some entrained xenoliths of nepheline syenitic/pegmatitic origin, are particularly interesting and may represent the sort of host rocks (high Al or Al-saturated) in which corundum could have formed in the crust. This is quite similar to the analysed melt compositions (chapter 3) except for alkalies, assuming magmatic crystallisation.

Chapter 5

Mantle xenoliths

The entrainment of mantle-derived xenoliths, particularly peridotites, in Caenozoic continental alkali volcanic rock is common. The further association between these xenolithic alkali basalts and corundum and/or diamond is however, quite rare, and has lead to considerable research in a few classic areas such as SE Australia (Tertiary: reference), and N Scotland (Menzies *et al.*, 1987; Upton *et al.*, 1999) including whether or not the corundum could be megacrysts of xenocrysts. The indications from previous chapters is that the corundum is likely to be crustal in origin (chapters 3 and 4), but study of the mantle xenoliths provides some useful additional constraints. The occurrence of mantle xenoliths is commonly associated with two different tectonic settings: active tectonic regimes, where xenoliths occur in alkali basalt-basanite-nephelinite magma series; and stable tectonic regions, where mantle nodules are found in kimberlite and its derivatives (Harte and Hawkesworth, 1989). In general, research into mantle xenoliths has concentrated on their texture, geochemistry and petrogenesis (Eastern China; Cao and Zhu, 1987; Chen *et al.*, 2003, Massif Central France; Downes, (1987), British Isles (Upton *et al.*, 1983, 1993) Pannonian Basin, Eastern Central Europe (Embeyisztin *et al.*, 1992, Downes *et al.*, 1992), Australia (O'Reilly and Griffin, 1985,1988; Yaxley *et al.*, 1991). Meanwhile, a parallel body of research has been undertaken in the field of experimental petrology and experimental geochemistry for better understanding the mantle conditions as represented by mantle xenoliths, which are the best representative samples of the upper mantle environment. (Draper and Green, 1997; Brey *et al.*, 1999; Conceição and Green, 2004; Klemme, 2004).

The occurrence of corundum in association with peridotites is relatively uncommon compared to the occurrence of diamond associated with peridotites,

however, it has been reported from some localities, for example; Beni Bousera, Spain (Kornprobst *et al.*, 1990; Horoman peridotite complex in Japan (Morishita and Arai, 2007). Euhedral to subhedral corundum crystals are found as an accessory mineral in these peridotites. The Bo Ploi basalt is also packed with peridotite nodules, therefore, it is interesting to evaluate whether they could be a potential source of corundum and whether they may provide other information which could constrain the genesis of the Bo Ploi corundum. The entrained mantle xenoliths in the Bo Ploi basalt were briefly mentioned in the works of Yaemniyom (1982) and Barr and Macdonald (1978; 1981). In this chapter, the texture, geochemistry and mineral chemistry of the entrained mantle xenoliths in the Bo Ploi basalt is used to derive pressure and temperature through an application of geothermometry and geobarometry. This provides a fortuitous opportunity to derive the local geotherm, based on equilibration and closure temperatures between peridotite minerals. The P-T estimates provide a minimum depth of origin for the host basalt, which must be deeper than the entrained xenoliths. In turn, this can also provide a depth estimate for formation of corundum, accepting that there are assumptions to be made about the crustal thickness and geotherm at the time when the corundum formed (see chapter 7 for more detail).

5.1 Petrography of the mantle xenoliths

In hand specimens, the mantle xenoliths are distributed randomly in the host Bo Ploi basalt. They usually range from 1-2 cm in size with some larger specimens up to 5 cm across and xenoliths size up to 15 cm across are also observed at outcrops (Fig. 5.1-5.2). The common shapes of these mantle xenoliths are rounded, rectangular or ovoid. Some have partly angular shapes, with sharp edged triangular or even point-end shapes, where the host lava mineral alignment tends to display a flow around the xenolith. The xenoliths are very fresh and have a clear and distinctive contact with the host basalt. In some cases, however, minor traces of reaction of the mantle xenolith

with the host basalt were observed. The primary mineral constituents of the mantle xenoliths are olivine, orthopyroxene, clinopyroxene, and spinel. Their modal compositions range from harzburgite, through lherzolite, to dunite.

Olivine displays a typical olive green colour with slightly brownish yellow on the grains around the edge of the nodules that are in contact or closer to the basalt, which may be the effect of heat from the basalt to these mantle xenoliths. Orthopyroxene has a yellowish-brown colour and clinopyroxene is dark bottle green. Dark brown to black is a common colour for the spinel. Frequently one or several grains of these same minerals appear in the adjacent area of the host basalt as a megacryst or xenocryst, and usually also show remnants such as necking down of the xenoliths, or veinlets that cut into the mantle nodules. It is, therefore, interpreted that parts of the xenoliths were carried away in the host alkali basalt.

Figure 5.1 Photograph of a group of mantle xenoliths entrained in the Bo Ploi basalt outcrop. The film cartridge lid diameter is 3.5 cm

Figure 5.2 General size and shape of the studied mantle xenoliths from Bo Ploi basalt. Note also a white nodule of felsic crustal xenolith at the top left corner

Microscopically, ***Olivine*** is colourless in plane-polarised light with or without brownish staining that is caused by slightly alteration along the fractures. It has subhedral to anhedral crystals. Olivine has two distinctive grain sizes: the coarser up to 3 mm in diameter and the smaller up to 1 mm depending on the texture of the rocks (Fig.5.3). It is generally accepted that the smaller grains are the products of recrystallisation of the larger grains. However, the chronological sequences of deformation and/or partial melting or recrystallization is more complicated, hence, the xenoliths have often undergone one or more metamorphic episodes (Pike and Schwarzman, 1977) and this leads to a superimposed texture. Olivine displays both curvilinear grain boundaries and straight boundaries, particularly, in association with polygonal grains. Most of them are optically homogeneous, rarely crystals show undulate extinction. Strain bands, so called "kink bands" were observed in most of the large olivine grain. The kink bands may

appear as single straight lines or several lines in one olivine, particularly in those elongate shapes olivine, depend on the degree of deformation. They are characterised by sharp, multiple, narrow bands, in higher degrees of deformation whereas the less number and wider bands represent lower degrees of deformation (Fig. 5.4). The smaller olivine forms subhedral, "neoblasts" and is usually strain-free. They are sometimes polygonal with straight grain boundaries and form near perfect triple junctions with 120° angles. Ovoid shaped olivine "poikiolitic" enclosed in larger olivine, spinel or orthopyroxene are frequently seen, however, it cannot be an indicator of any texture because poikiolitic textures can occur in both igneous and metamorphic rocks (Pike and Schwarzman, 1977).

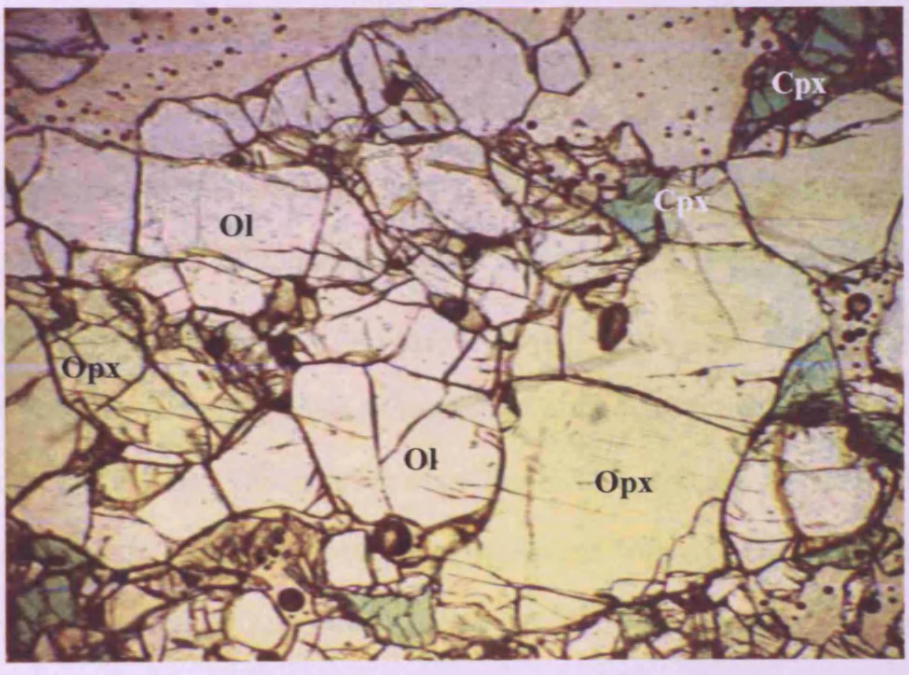

Figure 5.3 Sample BPX-01 shows general appearance of mineral constituents; large patch of yellowish brown orthopyroxene, colourless with fractured of olivine and green stubby clinopyroxene.

Cpx: clinopyroxene Opx: orthopyroxene, , Ol: olivine

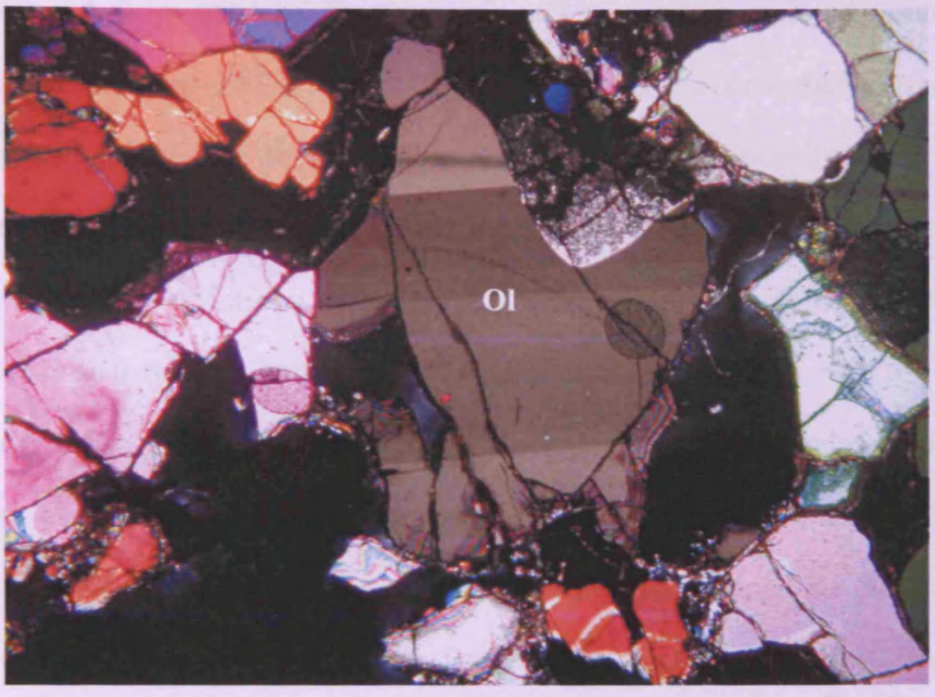

Figure 5.4 Photomicrograph shows multiple strained bands or kinked bands in olivine crystal (Ol) of sample BPX-04

Orthopyroxene is colourless or very pale brown in plane-polarized light. It usually forms large patches of anhedral crystals with clearly defined cleavages. The sizes range from 3-4 mm in diameter for the protogranular texture, and up to 1.5×5 mm for elongated porphyroclasts. The last generation of orthopyroxene exhibits subhedral crystals up to 1 mm in size. The undulate extinction, which indicates zoning or strain, was observed in one in sample BPX-02. Orthopyroxene with exsolution lamellae of clinopyroxene composition is occasionally observed. The strained bands present in orthopyroxene are different from those which occur in olilvine, as they are curved lines.

Clinopyroxene is pale green to medium green in plane-polarized light (Fig.5.3), although very weak pleochroism of the same shade is observed. They exhibit subhedral to anhedral crystals. The average grain size is approximately 0.7-1 mm in diameter, with rarely larger grain sizes up to 4 mm found. They occurred as a single grains or small clusters disseminated in the rock and amoeboid shape interlocked with other

silicate minerals. A large patch of clinopyroxene of 4 mm, which enclosed a small neoblast of olivine, was found in sample BPX-07. In addition, the occurrence as small irregular interstitial grains was observed. Simple twinning is occasionally found in clinopyroxene grains. Many grains of clinopyroxene demonstrate undulate extinction. Porous or spongy grain boundaries were frequently observed in most of pyroxene grains (Fig.5.5), which is an indicative of melting (Kleeman *et al.*, 1960).

Spinel is yellowish brown to dark brown in plane-polarized light with anhedral crystal outlines, except in the sample BPX-01 where chrome-rich spinel is black in colour and displays subhedral crystal morphology. Their sizes and shapes are variously dependent on the texture of the xenoliths. Spinel occurs in association with larger pyroxene crystals. It usually occurs in bleb-like or thin globules inside or in between pyroxene grains. The "vermicular spinel" in which spinel resembles exsolution from enstatite, was observed in many samples (Fig.5.6-5.7) and was employed as a criterion for protogranular texture (Mercier and Nicolas, 1975). Many samples contain bleb-shaped spinel, it was noticed that this spinel was rimmed by layers of small pyroxene crystals. The host spinel was, however, juxtaposed against orthopyroxene. The 'holly shape' spinel (Mercier and Nicolas, 1975) was prominent in sample BPX-12 (Fig.5.8) with a texture suggesting it formed after the silicate recrystallization. In addition, spinel was found in stubby rounded form as an inclusion in olivine or in rock fabric triple junctions. Mercier and Nicolas (1975) employ this form of spinel as a mark of equigranular texture. In sample BPX-14, spinel appears as a relic, which is rimmed and resorbed by plagioclase. Pike and Schwarzman (1977) suggest that it is a result from a melting event, which occurred along the clinopyroxene and spinel grains and generated olivine + plagioclase or plagioclase + spinel of different compositions.

(a)

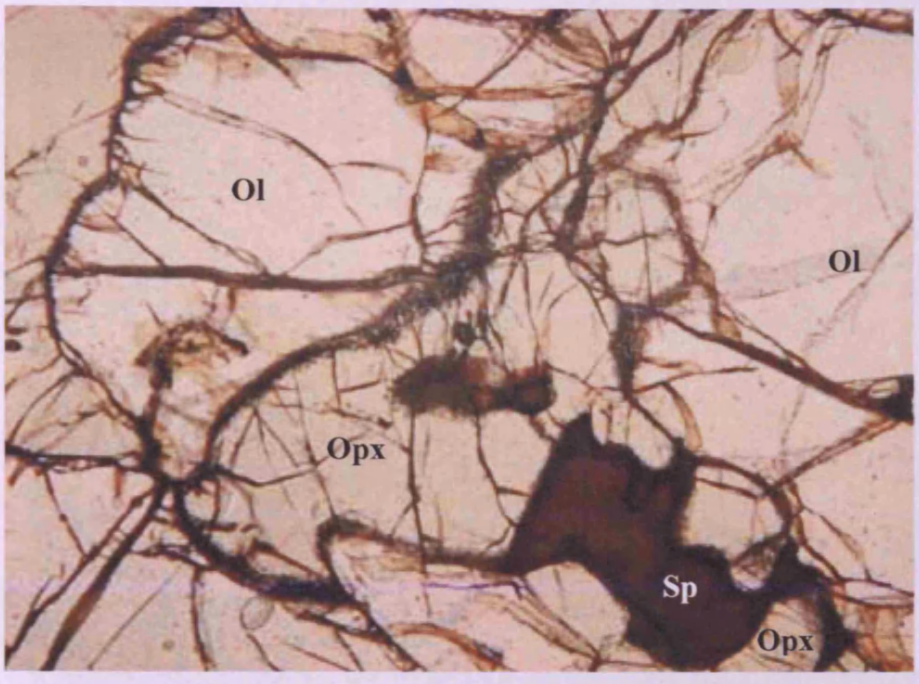

(b)

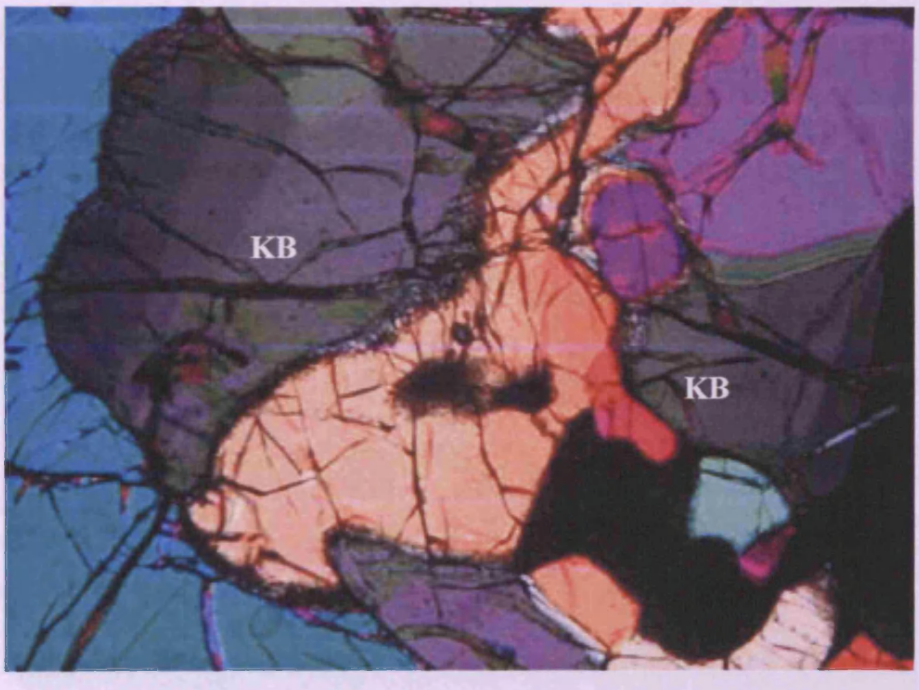

Figure 5.5 Sample BPX-05 shows protogranular texture with bleb shaped spinel rimmed by layers of tiny pyroxene crystals. Multiple kink bands are also observed in olivine grains. Orthopyroxene grain boundaries show spongy or cloudy look. (a) Plane polarised light (b) Crossed polarised light

Opx: orthopyroxene, Ol: olivine, Sp: spinel, KB: kink band

(a)

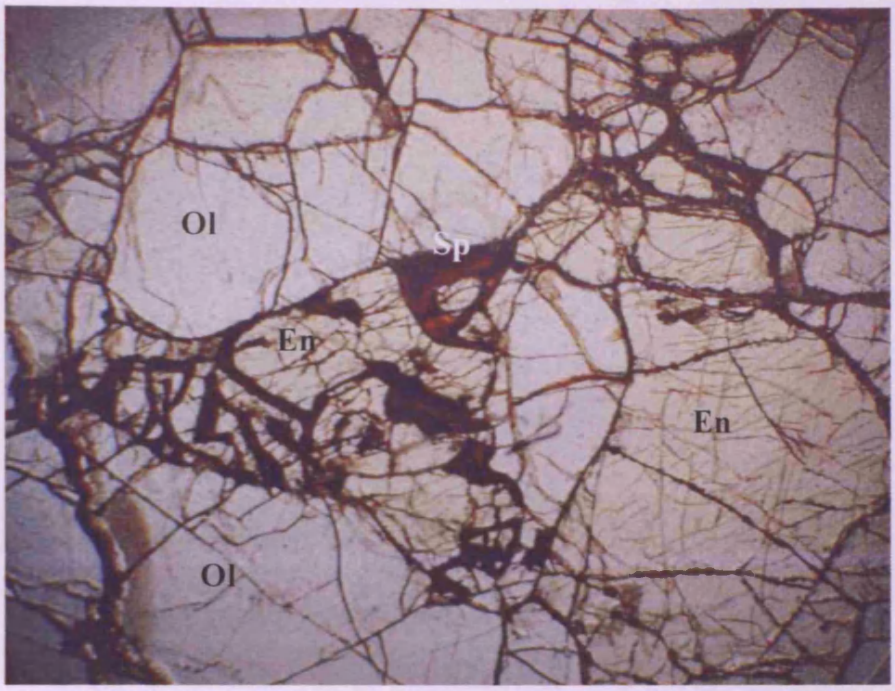

(b)

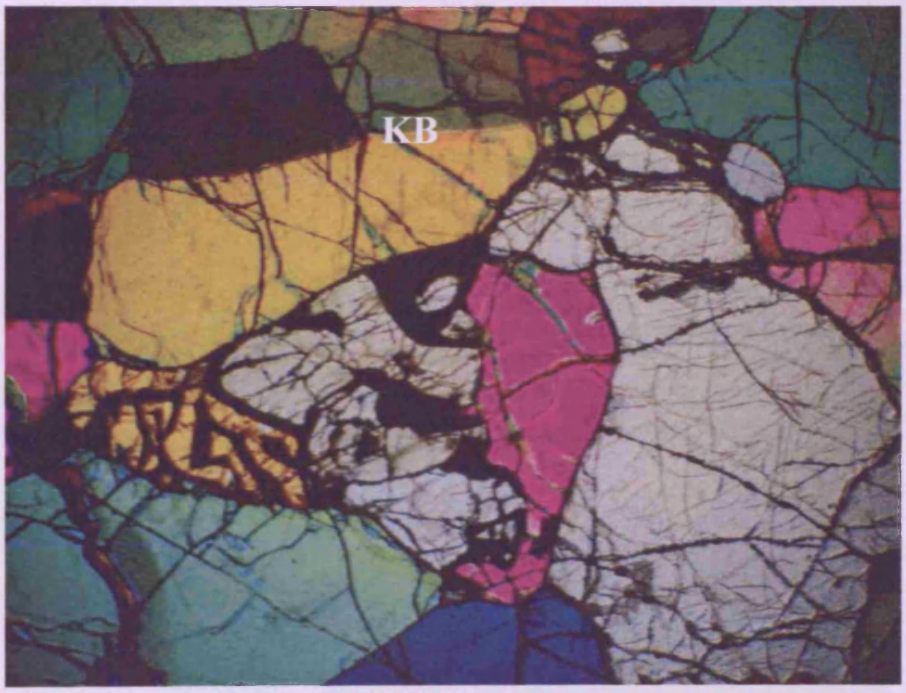

Figure 5.6 Sample BPX-03 shows spinel vermicular intergrowth with enstatite grain. Note also the curved kink band (KB) in the olivine grain. (a) Plane-polarized light (b) Cross-polarized light. En: Enstatite, Sp: Spinel, Ol: Olivine, KB: Kink band

(a)

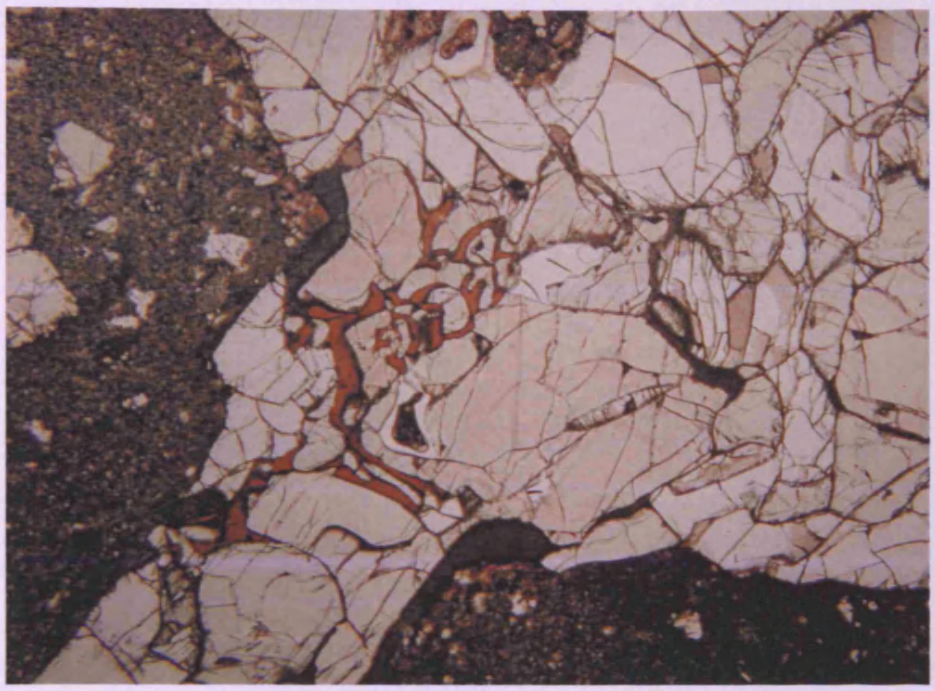

(b)

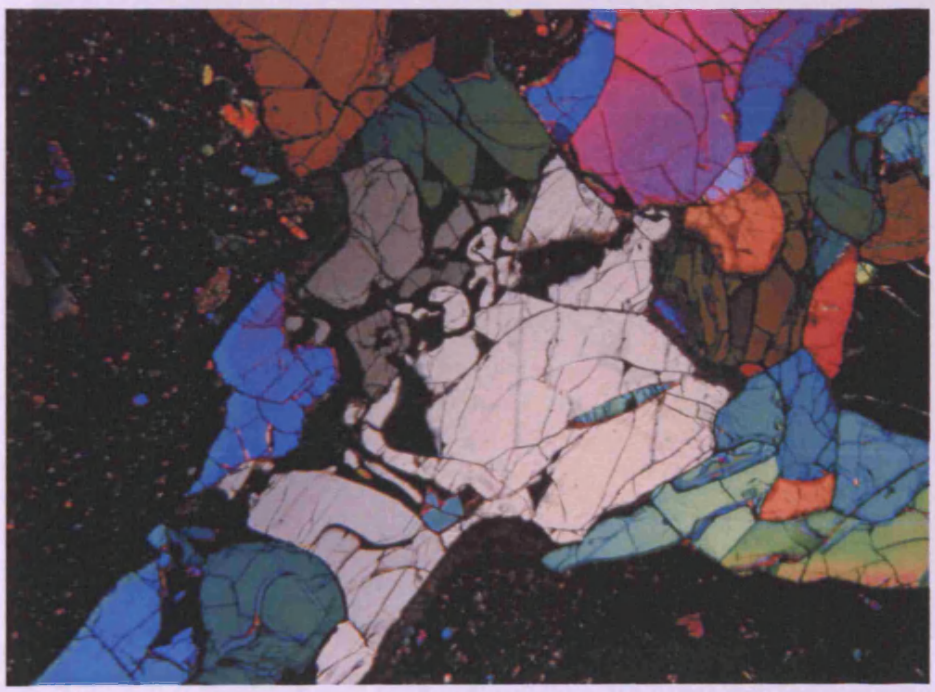

Figure 5.7 Spinel shows vermicular intergrowth with the enstatite grain. Note also olivine neoblast enclosed in the large patch orthopyroxene.

(a) Plane polarised light (b) Crossed polarised light

Opx: orthopyroxene, Sp: spinel, Ol: olivine, KB: kink band

(a)

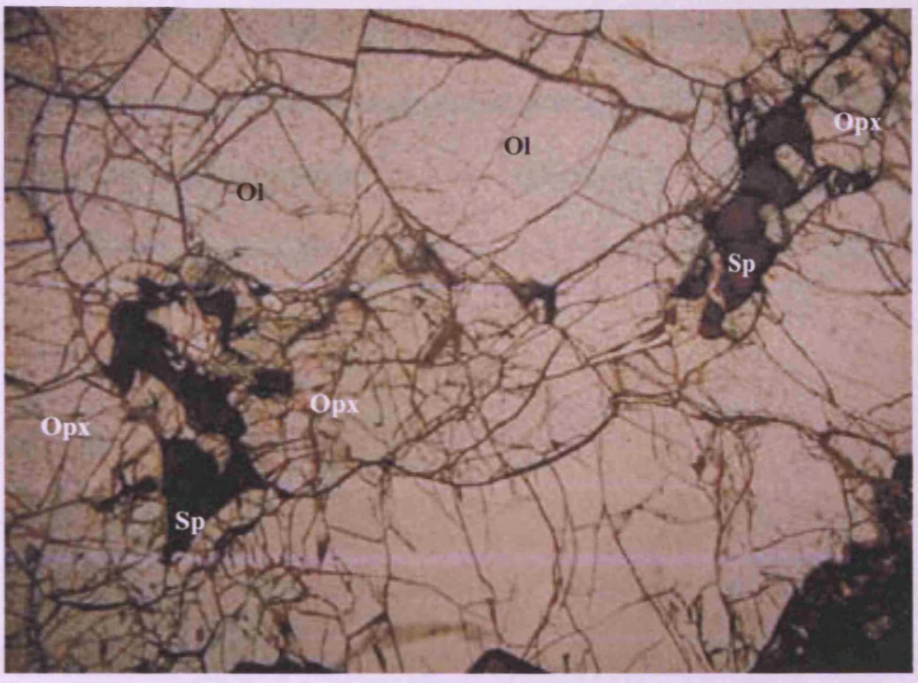

(b)

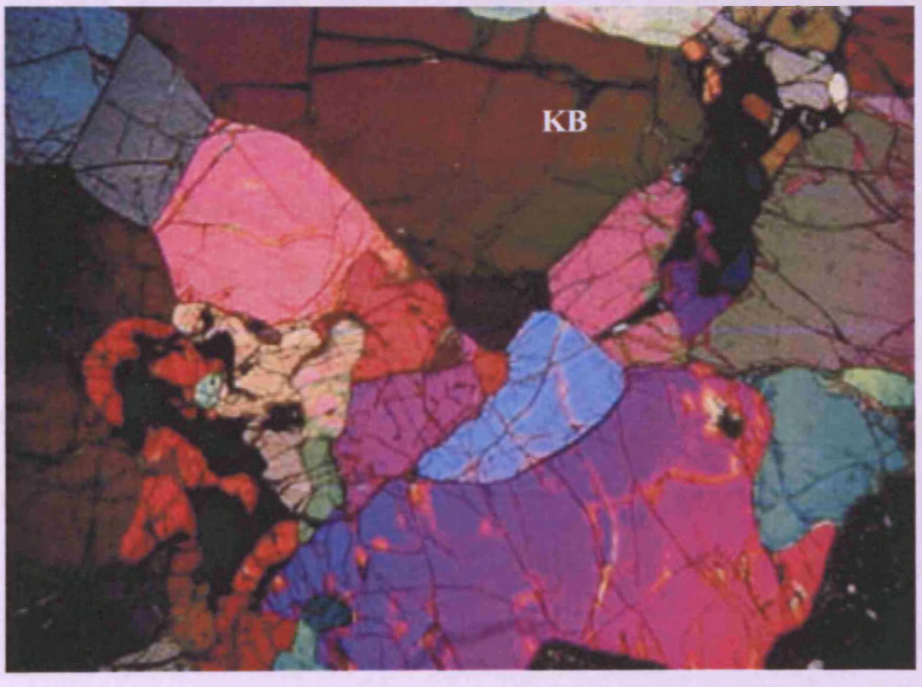

Figure 5.8 Spinel displays 'holly shape' form associates with other silicate minerals. A curved kink band (KB) is observed in olivine.

(a) Plane polarised light (b) Crossed polarised light

Cpx: clinopyroxene, Opx: orthopyroxene, Ol: olivine, Sp: spinel, KB: kink band, w-Cpx: worm-like clinopyroxene

Sixteen samples of mantle xenoliths were selected for detailed study of their petrography and for petrological interpretation. The samples are divided into three major groups as protogranular texture, transitional protogranular to porphyroclastic texture, and modified transitional protogranular to porphyroclastic texture, according to their texture by modifying the criteria of Mercier and Nicolas (1975) and Pike and Schwarzman (1977).

5.1.1 Protogranular texture

The samples in this group are BPX-03, BPX-04, BPX-05, BPX-11, BPX-12, BPX-13 and BPX-15, which are characterised by coarse grained fabrics, with approximate grain size of olivine and orthopyroxene (enstatite) 3-4 mm in diameter, whereas clinopyroxene (diopside) and spinel are smaller, up to 1 mm in diameter. Pike and Schwarzman (1977) proposed a texture classification for ultramafic xenoliths in relation to their genetic processes. The term pyrometamorphic was introduced to describe xenoliths which show evidence of solidification of partial melting. The xenoliths that belong to this group show the least degree of partial melting.

Olivine displays coarse grains with curvilinear grain boundaries, however polygonal and smaller recrystallized grains also occur. This is the result of local recrystallization of larger crystals (Mercier and Nicolas, 1975). Strained band or kink band was frequently found in the larger grains of olivine, while smaller grains were strained free. The polygonal olivine exhibited straight grain boundaries and occasionally formed locally mosaic-like fabric.

The enstatite commonly displays exsolution lamellae, but no strained band was observed. Diopside occurs as small crystals disseminated among other silicate minerals and usually in a close association with larger crystals of enstatite. The porous or spongy grain boundary was noticed in some pyroxene grains, which is an indicative of melting, similar to the occurrence of interstitial glass

Spinel shows a typical vermicular or blebby form, bleb shaped takes place in the remnant of pyroxene. In addition, the corona layers of tiny pyroxene crystals rimmed spinel grains were observed as shown in figure 5.9.

5.1.2 Transitional protogranular to porphyroclastic texture

The xenoliths that illustrate transitional protogranular to porphyroclastic texture are BPX-01, BPX-02, BPX-06, BPX-07, BPX-08, BPX-09, and BPX-10.

BPX-01, BPX-02, BPX-06, BPX-07, BPX-08, BPX-09, and BPX-10 are mainly composed of coarse-grained minerals that form coarse fabrics, nonetheless, the crystals have well developed elongation and flattening. Consequently, lineation/foliation and deformation of grains were observed. The coarse elongated crystals of olivine and enstatite are 1×3 to 1.5×4 mm in sizes. The recrystallised, neoblasts, appear in the form of polygonal, tabular, or ovoid crystals. Their sizes range from 0.5 to 1 millimetre in diameter. The grain boundaries transformed from curvilinear, which was typically found in protogranular texture, to less curvature and straight line. Olivine was severely strained and multiple kink bands were found in the majority of coarse-grained olivine.

Pyroxene exhibited lamellae (orthopyroxene host with clinopyroxene lamellae) and some grains showed strain. Clinopyroxene occurred as small-scattered subhedral to anhedral crystals. However, most of them were in direct contact with enstatite crystals or occur as interstitial phase among the olivine grains.

Spinel was found in various shapes, including the 'holly leaf form' (Mercier, and Nicolas, 1975), which exhibits irregular shaped spiney points (Fig.5.8). Besides, the primitive forms of vermicular spinel exsolved from enstatite, it also occurs as blebs or lobate forms interstitial between pyroxene.

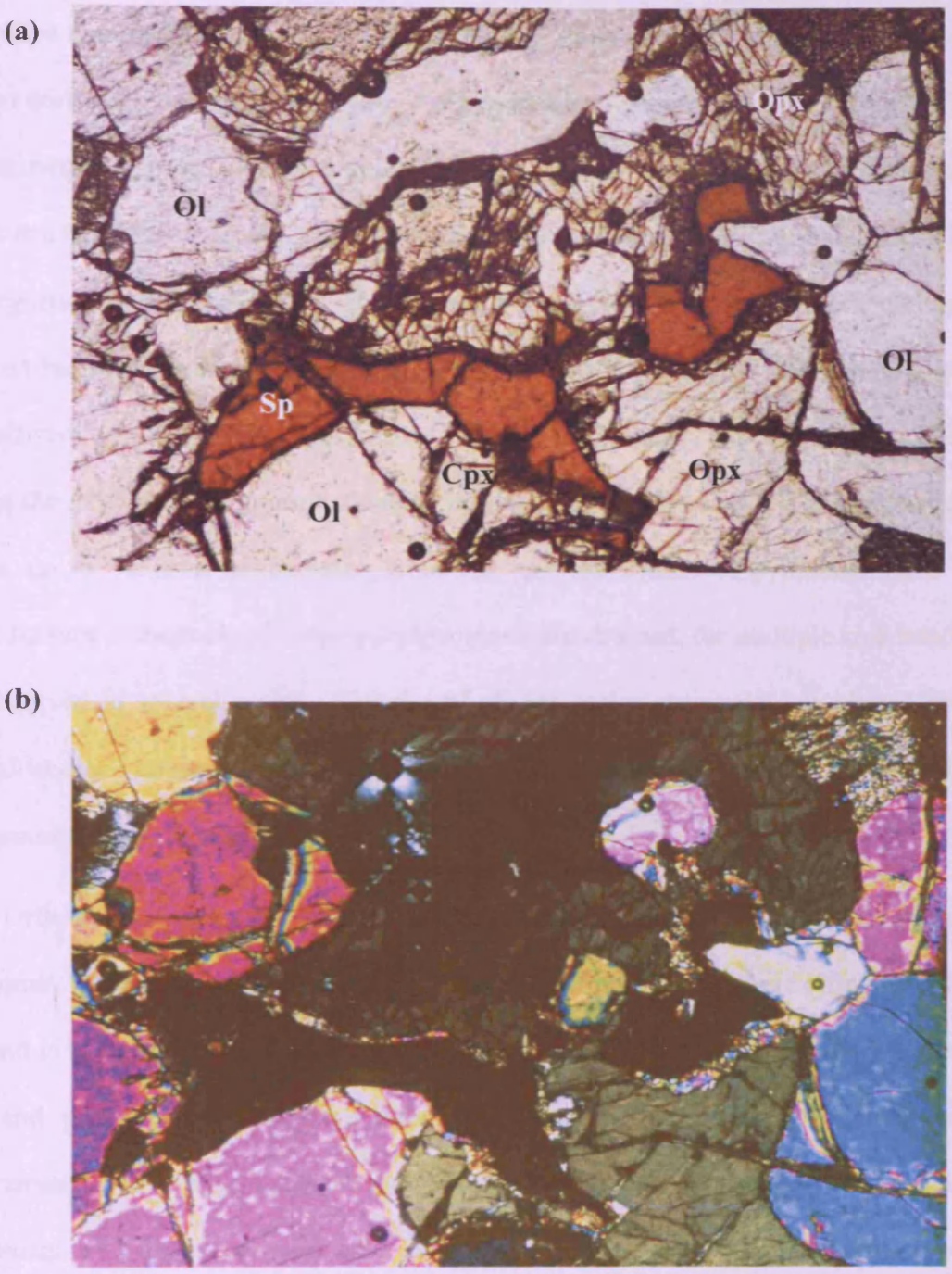

Figure 5.9 Sample BPX-11 shows bleb-shape spinel surrounded by corona layers of tiny pyroxene crystals. (a) Plane polarised light (b) Crossed polarised light

Opx: orthopyroxene, Cpx: clinopyroxene, Sp: spinel, Ol: olivine

5.1.3 Modified transitional protogranular to porphyroclastic texture

This texture is interpreted as a result from various degree of partial melting that occurred during the entrapment in the host alkali basalt. Their distinguished character is the coexistence of plagioclase and spinel although the calculated pressure estimates of 18 kbar consistent to the spinel stability field. Only two samples: BPX-14 and BPX-16 are categorised in this group. Sample BPX-14 is dominated by a coarse fabric and the deformed large minerals of olivine and enstatite sit in a matrix of very fine-grained recrystallised pyroxene and plagioclase. The porphyroclasts are 1-5 mm in size, whereas the neoblasts are approximately 1 mm across. The smaller and near euhedral crystals, up to 0.3 mm in diameter, from the recrystallization of pyroxenes form a graphic texture in the rock. Olivine porphyroclasts are strained, the multiple kink bands were observed in several grains. The rim of olivine grains are commonly altered and recrystallised as vermicular shape interlocked with vermicular plagioclase, particularly in the grains that are adjacent to pyroxene.

Orthopyroxene shows pyroxene exsolution and appears cloudy, particularly the large grains. Symplectitic intergrowth of pyroxene with plagioclase was observed (Fig 5.10) and it is explained as a result of partially recrystallization (Mercier and Nicolas, 1975) and probably resulted from slow cooling of partial melt pools (Pike and Schwarzman, 1977). The pyroxene symplectitic intergrowth texture was observed as the remnant of a large enstatite core surrounded by tiny crystals of clinopyroxene intergrown with plagioclase. The extensive recrystallization of pyroxene forms a mosaic interlocking pattern in the nodule. In addition, the enstatite crystals also show pyroxene exsolution. Spinel displays a vermicular to bleb-like shape associated with pyroxene and has rims replaced by small feldspar crystals (Fig.5.11).

Xenolith sample BPX-16 is characterised by two generations of minerals, but a high proportion of recrystallised crystals and their mineral compositions indicate a

higher degree of deformation of this xenoliths. Olivine and enstatite porphyroclasts are 1-5 mm in sizes and show grain elongation and flattening. It was noticed that the strained olivine porphyroclasts display multiple, curved or wavey, kink bands. The enstatite porphyroclasts show pyroxene exsolution and have curved kink band, which is an indication of strain. The neoblasts of olivine, pyroxenes, and feldspar are smaller, less than 1 millimetre in diameter. They occur as subhedral to euhedral crystals, which usually show straight grain boundaries and form 120° triple junctions. Occasional sharp straight kink bands were seen in the olivine neoblasts.

Spinel occurs as rounded stubby to thin lobate grains both inside and interstitial to olivine grains. According to Mercier and Nicolas (1975), this dual spinel form is an indicator of classic equigranular texture.

It seems that many of the xenoliths have modified textures compared with normal mantle xenoliths. For example, the coexisting both spinel and plagioclase indicate a more complicated pathway and history of the xenoliths. The grain size distribution, also, suggests the transitional texture of porphyritic to equigranular texture. Also the graphic or sieve texture pyroxene indicates recrystallisation of partial melts.

(a)

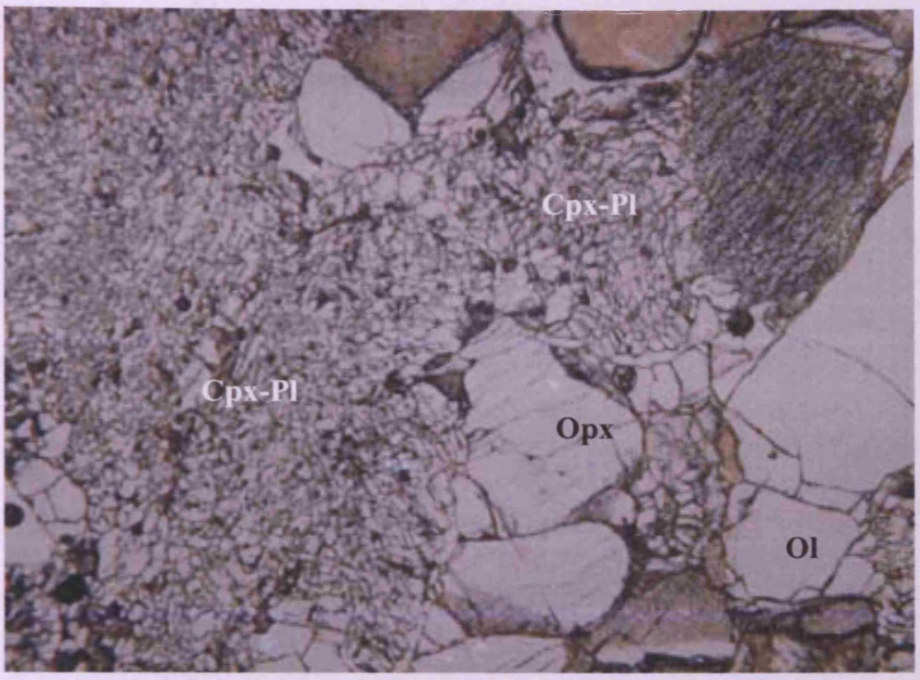

(b)

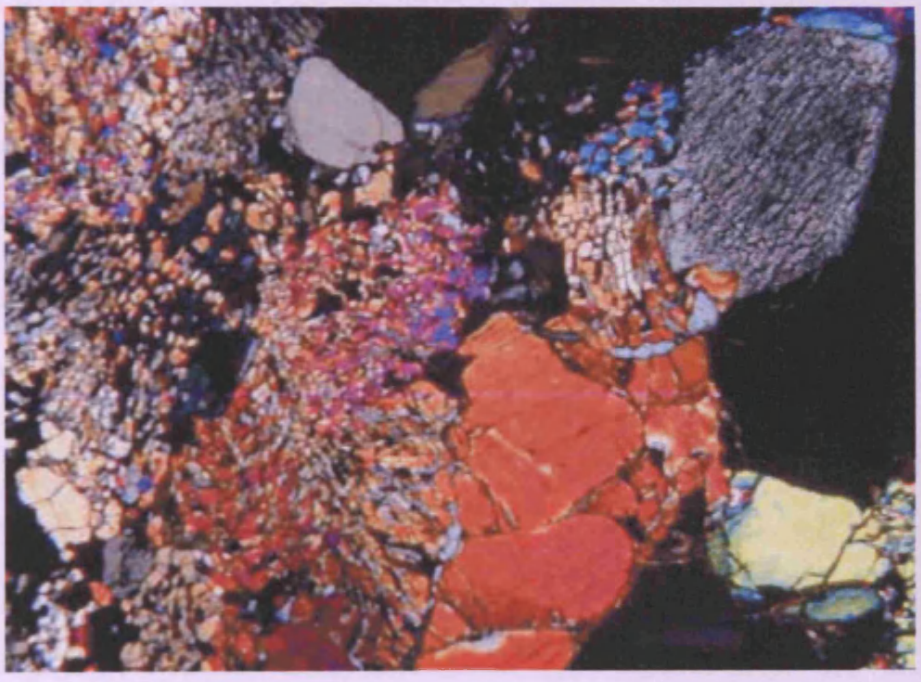

Figure 5.10 Sample BPX-14 shows pyroxene simplectitic intergrowth with plagioclase advancing into intact orthopyroxene patches, which may display exsolution texture (top right corner).

(a) Plane polarised light (b) Crossed polarised light.

Cpx: clinopyroxene, Opx: orthopyroxene, Ol: olivine, Pl: plagioclase, Cpx-Pl: worm-like clinopyroxene-plagioclase intergrowth

(a)

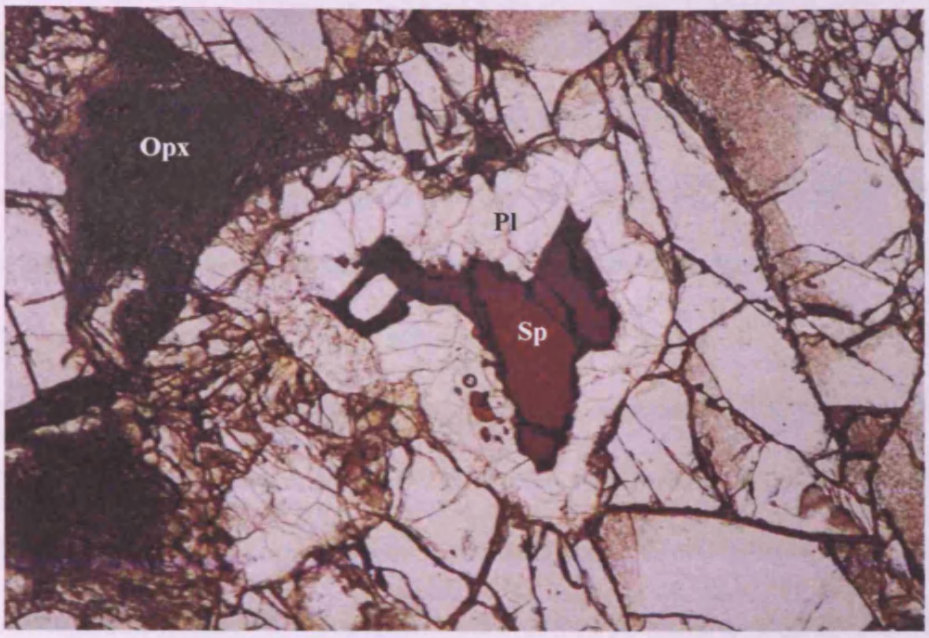

(b)

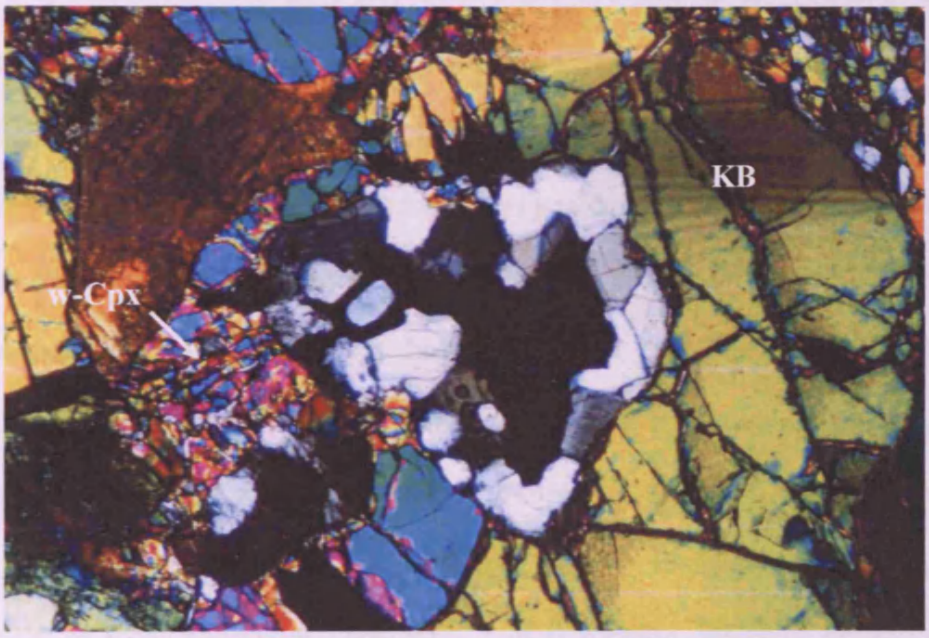

Figure 5.11 Sample BPX-14 shows spinel rimmed by plagioclase and also partly formed worm-like intergrowth with clinopyroxene (w-Cpx). Orthopyroxene is heavily exsolved thus appears cloudy. Olivine with kink-band is easily noticed. (a) Plane polarised light (b) Crossed polarised light

Cpx: clinopyroxene, Opx: orthopyroxene, Ol: olivine, Pl: plagioclase, Sp: spinel, KB: kink band, w-Cpx: worm-like clinopyroxene

5.2 Modal Variation

The approximation modal compositions of the mantle nodules were estimated by point estimating. There are factors that constrained the effectiveness of the modal analyses; the small size of the xenoliths and the variable grain size distribution. The modal analysis was done by point counter. The mineral "bins" were set for olivine, orthopyroxene, clinopyroxene, spinel and other minerals. The counting points were varied according to the sizes of the mantle nodules, from 200 points to 400 points. The modal composition of the mantle xenoliths from the Bo Ploi Basalt varies widely and includes dunite, harzburgite, and spinel lherzolite. In almost every sample, olivine is the most abundant mineral, except sample 2 where orthopyroxene is slightly higher. Olivine present up to 88% in dunite, where harzburgite contains up to 77%, and the lherzolite has rather wide range of 40 to 83%. Orthopyroxene occur up to 6% and 15% in dunite and harzburgite respectively, while those in lherzolite that far more vary from 6 to 36%. Similarly, clinopyroxene in lherzolite ranges from 2-13%, with narrower range of up to 5% in dunite and harzburgite. Spinel is present in all type of the xenoliths, it is noticed that the relatively high amount of 3-6% occurs in dunite. Lherzolite contains a wide range of spinel from 1-8%. Other phases and minerals include interstitial glass, plagioclase, and opaque minerals. In sample BPX-14, the exceptionally high amount of another phase (plagioclase): 11% was found. It is, therefore, thought to have undergone substantial partial melting, which is consistent with the resorbed texture of spinel by plagioclase. The modal variation of mineral constituents in relation to texture is summarised in Table 5.1 and the rock classification is illustrated in figure 5.12.

Table 5.1 Summary of modal variation of mineral composition and the nomenclature of mantle xenoliths from the Bo Ploi basalt

No.	Sample	Point counted	Texture	Modal variation of mineral compositions (%)					Rock type
				Ol	Opx	Cpx	Sp	Pl	
1	BPX-03	400	protogranular	66	18	16	-	-	lherzolite
2	BPX-04	400	protogranular	89	6	2	3	-	dunite
3	BPX-05	400	protogranular	67	17	14	2	-	lherzolite
4	BPX-11	200	protogranular	43	8	41	8	-	lherzolite
5	BPX-12	200	protogranular	88	1	5	6	-	dunite
6	BPX-15	400	protogranular	83	10	5	2	-	lherzolite
7	BPX-01	400	transitional	70	18	11	1	-	lherzolite
8	BPX-02	400	transitional	41	44	12	3	-	lherzolite
9	BPX-06	400	transitional	78	11	8	3	-	lherzolite
10	BPX-07	200	transitional	76	13	10	1	-	lherzolite
11	BPX-08	400	transitional	57	27	11	5	-	lherzolite
12	BPX-09	200	transitional	76	17	2	5	-	harzburgite
13	BPX-10	400	transitional	72	8	17	3	-	lherzolite
14	BPX-13	400	transitional	81	7	7	5	-	lherzolite
15	BPX-14	400	modified	39	36	13	1	11	lherzolite
16	BPX-16	400	modified	76	15	2	4	3	harzburgite

Note Ol: Olivine, Opx: Orthopyroxene, Cpx: Clinopyroxene, Sp: Spinel, Pl: Plagioclase

protogranular = protogranular texture

transitional = transitional protogranular to porphyroclastic texture

modified = modified transitional protogranular to porphyroclastic texture

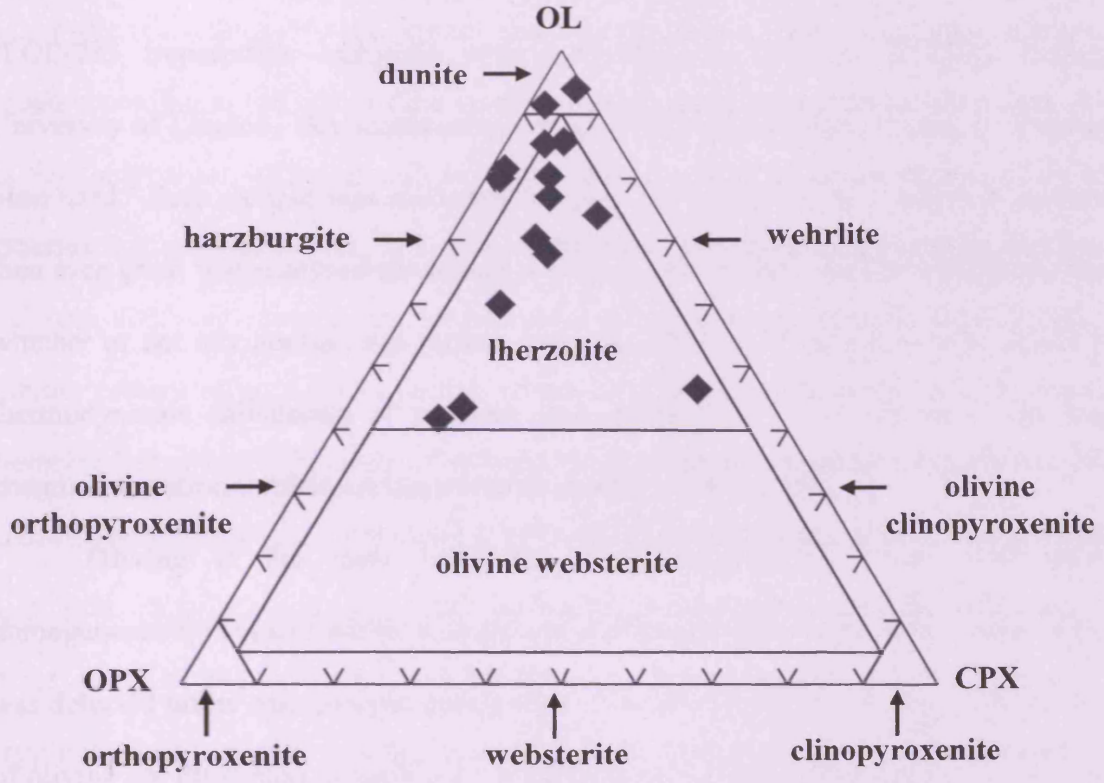

Figure 5.12 Discrimination diagram of mafic plutonic rock shows the composition of mantle xenoliths entrained in the Bo Ploi basalt. Modified after Streckeisen, 1976. (OL = olivine, OPX = orthopyroxene, CPX = clinopyroxene)

5.3 Mineral chemistry

The mineral chemistry of the mantle xenoliths from the Bo Ploi basalt were analysed using an electron microprobe, the spectra were analysed by energy dispersive methods (EDS), to determine the major oxides of individual grains of the constituent minerals; olivine, orthopyroxene, clinopyroxene and spinel. The instrument used is a JEOL-733 Superprobe equipped with Link Systems EDS at Birkbeck College, University of London. An accelerating voltage of 15 kV and a count time of 100s have been used. Each sample was randomly selected for 4-6 grains of constituent minerals, then each grain was analysed traversing, 4-6 spots, from rim to core in order to ascertain whether or not any zoning was present since equilibrium compositions are needed for thermodynamic calculation of pressure and temperature found that there are slight chemical variations within certain minerals among these samples.

Olivine is the most consistent in chemical composition, with almost homogeneous Fo content within a single grain although very rarely slight optical zoning was detected under microscopic observation. The major oxides chemical compositions of olivine are illustrated in table 5.2. It has $Fo_{88.3-90.8}$, with average of $Fo_{89.4}$. This Fo-content or the Mg#, (Mg/Mg + Fe), are in the range of primitive mantle, Mg# 84-92, (Glücklich and Mercier, 1989 and Xu *et al.*, 1998). Cr_2O_3 and TiO_2 are in the range of 0.01 to 0.03%. MnO contents range from 0.07 to 0.19 wt% and an inverse correlation is observed in the plots of MnO versus Fo content in olivine (Fig. 5.13). The plots of Cr/(Cr + Al), Cr# in spinel versus Fo content in olivine are in the olivine-spinel mantle array, which indicates mantle origin for the coexisting phases (Fig. 5.14).

Orthopyroxene, enstatite, has near end member composition as $En_{87.1-89.9}Wo_{1.1-1.3}Fs_{8.8-10.6}$. Its Mg# falls within the narrow range of 0.90-0.94, which is the highest Mg# among the constituent minerals. The Al_2O_3, FeO, CaO, and Na_2O contents range from 2.06-6.28%, 5.73-6.80%, 0.56-1.38%, and 0.13-0.59%, correspondingly.

Table 5.2 Representative EPMA analyses of olivine from the Bo Ploi xenoliths

Oxides	BPX-01	BPX-02	BPX-03	BPX-04	BPX-05	BPX-06	BPX-07	BPX-08
SiO_2	41.69	41.51	41.26	40.92	41.06	40.96	40.96	40.86
TiO_2	0.02	0.00	0.01	0.00	0.00	0.01	0.01	0.00
FeO	8.93	10.26	10.35	10.35	10.30	10.36	10.41	10.71
MnO	0.14	0.07	0.13	0.13	0.10	0.13	0.11	0.15
CaO	0.02	0.04	0.08	0.09	0.12	0.05	0.07	0.06
MgO	49.15	48.21	48.03	48.59	48.64	48.69	48.67	48.28
Cr_2O_3	0.00	0.00	0.02	0.01	0.02	0.01	0.03	0.02
Total	99.95	100.09	99.88	100.09	100.24	100.21	100.26	100.08

Olivine cation numbers on the basis of 4 oxygen atoms

Si	1.015	1.015	1.013	1.003	1.005	1.003	1.003	1.003
Ti	0.000	0.000	0.000	0.000	0.000	0.000	0.000	0.000
Fe	0.182	0.210	0.212	0.212	0.211	0.212	0.213	0.220
Mn	0.003	0.001	0.003	0.003	0.002	0.003	0.002	0.003
Ca	0.001	0.001	0.002	0.002	0.003	0.001	0.002	0.002
Mg	1.784	1.757	1.757	1.776	1.774	1.778	1.776	1.768
Cr	0.000	0.000	0.000	0.000	0.000	0.000	0.001	0.000
total	2.985	2.984	2.987	2.996	2.995	2.997	2.997	2.996
Fa:	9.25	10.67	10.78	10.67	10.62	10.66	10.71	11.06
Fo:	90.75	89.33	89.22	89.33	89.38	89.34	89.29	88.94

Table 5.2 (continued)

Oxides	BPX-09	BPX-10	BPX-11	BPX-12	BPX-13	BPX-14	BPX-15	BPX-16
SiO_2	40.95	40.72	41.00	40.85	41.44	41.36	41.37	41.23
TiO_2	0.01	0.00	0.02	0.01	0.00	0.01	0.00	0.00
FeO	10.47	11.28	10.21	10.81	10.04	10.96	9.86	9.46
MnO	0.15	0.19	0.14	0.12	0.11	0.15	0.11	0.12
CaO	0.06	0.05	0.09	0.08	0.11	0.05	0.09	0.03
MgO	48.28	47.84	48.65	48.27	48.26	47.42	48.77	49.42
Cr_2O_3	0.02	0.01	0.01	0.03	0.01	0.03	0.03	0.01
Total	99.94	100.09	100.12	100.17	99.97	99.98	100.23	100.27

Olivine cation numbers on the basis of 4 oxygen atoms

Si	1.004	1.003	1.004	1.003	1.014	1.016	1.010	1.005
Ti	0.000	0.000	0.000	0.000	0.000	0.000	0.000	0.000
Fe	0.215	0.232	0.209	0.222	0.206	0.225	0.201	0.193
Mn	0.002	0.004	0.003	0.002	0.002	0.003	0.002	0.002
Ca	0.001	0.001	0.002	0.002	0.003	0.001	0.002	0.001
Mg	1.773	1.756	1.776	1.766	1.760	1.737	1.774	1.795
Cr	0.000	0.000	0.000	0.001	0.000	0.001	0.001	0.000
total	2.995	2.996	2.994	2.996	2.985	2.983	2.990	2.996
Fa:	10.8	11.68	10.53	11.16	10.45	11.48	10.19	9.69
Fo:	89.2	88.32	89.47	88.84	89.55	88.52	89.81	90.31

The plots of Al_2O_3 against Mg# and Cr/(Cr+Al) ratio against Mg# exhibit negative correlation as the increasing of Mg#, which also indicates that the higher Al_2O_3 content, the higher degree of partial melting (Fig. 5.15 and 5.16). The chemical composition of orthopyroxene is showed in table 5.3.

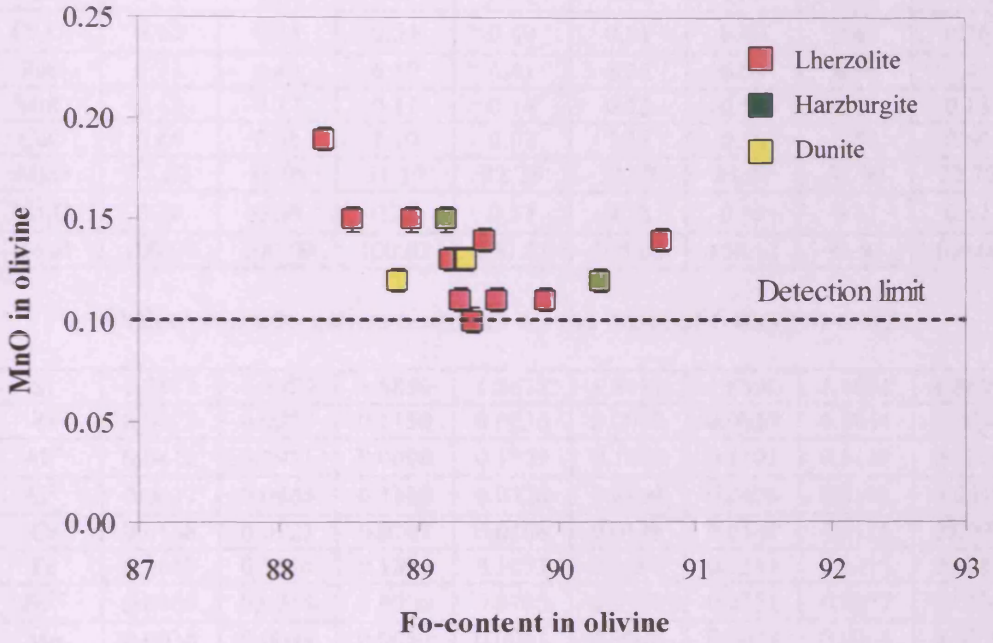

Figure 5.13 Plots of MnO versus Fo content in olivine from mantle xenoliths trapped in the Bo Ploi basalt

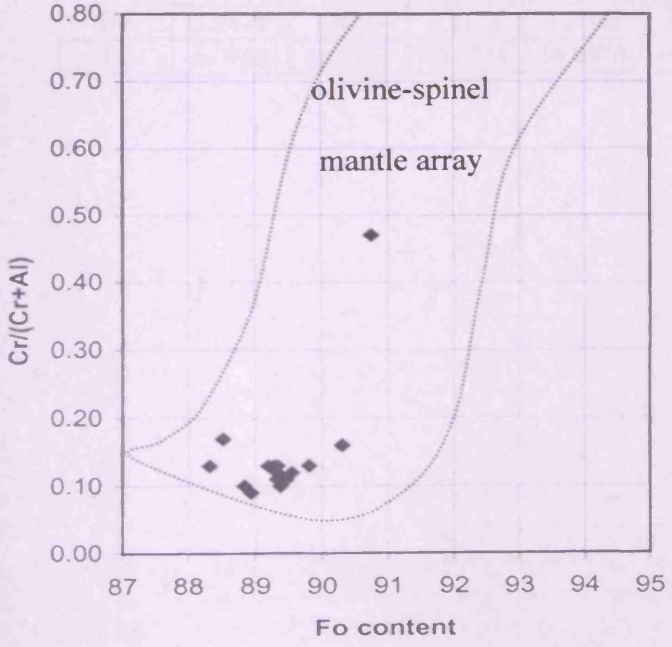

Figure 5.14 Plots of spinel Cr# [Cr/(Cr+Al)] against Fo content of coexisting olivine. The dashed area, mantle peridotite, is modified after Unimo, *et al.*, 1996.

Table 5.3 Representative EPMA analyses of orthopyroxene from the Bo Ploi xenoliths

Oxide	BPX-1	BPX-2	BPX-3	BPX-4	BPX-5	BPX-6	BPX-7	BPX-8
SiO_2	56.88	55.15	54.42	54.22	53.39	54.93	54.74	54.72
TiO_2	0.09	0.23	0.17	0.14	0.19	0.15	0.17	0.14
Al_2O_3	2.06	4.38	5.56	5.05	6.28	3.84	3.99	4.41
Cr_2O_3	0.62	0.45	0.54	0.40	0.51	0.40	0.43	0.36
FeO	5.73	6.43	6.59	6.41	6.36	6.59	6.56	6.43
MnO	0.12	0.17	0.11	0.14	0.12	0.13	0.15	0.13
CaO	0.66	0.85	1.10	0.92	1.38	0.56	0.58	0.60
MgO	33.62	31.98	31.17	32.26	31.27	33.07	32.90	32.79
Na_2O	0.30	0.36	0.37	0.53	0.58	0.45	0.41	0.42
Total	100.08	100.00	100.03	100.07	100.08	100.12	99.93	100.00

Orthopyroxene cation numbers on the basis of 6 oxygen atoms

Si	1.9582	1.9079	1.8850	1.8671	1.8417	1.8899	1.8881	1.8850
Ti	0.0023	0.0059	0.1150	0.0036	0.0049	0.0039	0.0044	0.0036
Al^{4+}	0.0418	0.0921	0.0000	0.1329	0.1583	0.1101	0.1119	0.1150
Al^{6+}	0.0417	0.0864	0.1120	0.0720	0.0969	0.0455	0.0503	0.0640
Cr	0.0168	0.0123	0.0147	0.0108	0.0138	0.0108	0.0116	0.0098
Fe	0.1649	0.1814	0.1879	0.1073	0.1080	0.1145	0.1215	0.1246
Fe^{3+}	0.0000	0.0045	0.0030	0.0772	0.0754	0.0751	0.0677	0.0606
Mn	0.0034	0.0049	0.0032	0.0041	0.0035	0.0038	0.0044	0.0038
Mg	1.7252	1.6490	1.6092	1.6558	1.6077	1.6958	1.6914	1.6837
Ca	0.0243	0.0315	0.0408	0.0339	0.0510	0.0206	0.0214	0.0221
Na	0.0200	0.0241	0.0248	0.0354	0.0388	0.0300	0.0273	0.0280
total	3.9986	4.0000	4.0010	4.0001	4.0000	4.0000	4.0000	4.0002
Mg#	0.91	0.90	0.90	0.94	0.94	0.94	0.93	0.93
En	89.9572	88.1206	87.2628	88.1542	87.1099	88.7946	88.7222	88.8590
Wo	1.2671	1.6833	2.2123	1.8048	2.7633	1.0786	1.1225	1.1664
Fs	8.7757	10.1961	10.5249	10.0410	10.1268	10.1267	10.1553	9.9747

Table 5.3 (continued)

Oxide	BPX-9	BPX-10	BPX-11	BPX-12	BPX-13	BPX-14	BPX-15	BPX-16
SiO_2	51.22	51.55	51.47	51.43	51.36	52.85	51.95	51.94
TiO_2	0.81	0.76	0.57	0.54	0.73	0.78	0.49	0.52
Al_2O_3	5.86	5.42	7.26	7.17	6.58	4.34	6.52	5.82
Cr_2O_3	1.03	1.01	0.90	0.82	0.95	1.11	1.06	1.23
FeO	2.94	2.99	3.19	3.40	3.53	2.46	3.12	2.50
MnO	0.09	0.08	0.08	0.08	0.10	0.08	0.07	0.09
CaO	21.51	21.68	19.15	19.52	20.13	21.65	19.61	21.13
MgO	15.00	15.17	15.67	15.49	15.25	15.17	15.63	15.49
Na_2O	1.45	1.39	1.76	1.71	1.40	1.53	1.53	1.30
Total	99.91	100.05	100.05	100.16	100.03	99.97	99.98	100.02

Orthopyroxene cation numbers on the basis of 6 oxygen atoms

Si	1.8577	1.8677	1.8517	1.8508	1.8599	1.9163	1.8759	1.8790
Ti	0.0221	0.0207	0.0153	0.0145	0.0199	0.0212	0.0133	0.0141
Al^{4+}	0.1423	0.1323	0.1483	0.1492	0.1401	0.0837	0.1241	0.1210
Al^{6+}	0.1081	0.0991	0.1595	0.1548	0.1407	0.1017	0.1533	0.1271
Cr	0.0294	0.0289	0.0256	0.0233	0.0271	0.0318	0.0303	0.0351
Fe	0.0280	0.0308	0.0419	0.0420	0.0772	0.0610	0.0744	0.0552
Fe^{3+}	0.0612	0.0597	0.0541	0.0603	0.0296	0.0135	0.0198	0.0204
Mn	0.0027	0.0024	0.0024	0.0024	0.0030	0.0024	0.0021	0.0027
Mg	0.8108	0.8192	0.8403	0.8308	0.8232	0.8199	0.8412	0.8353
Ca	0.8358	0.8416	0.7382	0.7526	0.7811	0.8411	0.7586	0.8190
Na	0.1019	0.0976	0.1227	0.1193	0.0983	0.1075	0.1070	0.0911
total	4.0000	4.0000	4.0000	4.0000	4.0001	4.0001	4.0000	4.0000
Mg#	0.97	0.96	0.95	0.95	0.91	0.93	0.92	0.94
En	46.6379	46.7127	50.1103	49.2151	48.0252	47.1776	49.5961	48.2108
Wo	48.0759	47.9900	44.0217	44.5827	45.5691	48.3975	44.7261	47.2700
Fs	5.2862	5.2974	5.8680	6.2022	6.4057	4.4249	5.6777	4.5192

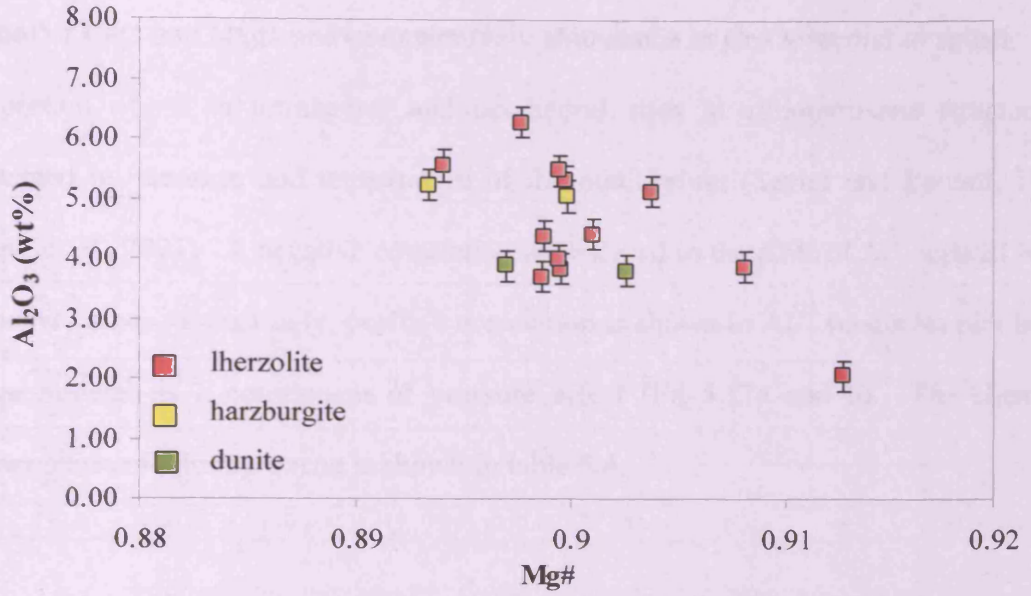

Figure 5.15 Plots of Al_2O_3 versus Mg# in orthopyroxene from mantle xenoliths trapped in the Bo Ploi basalt.

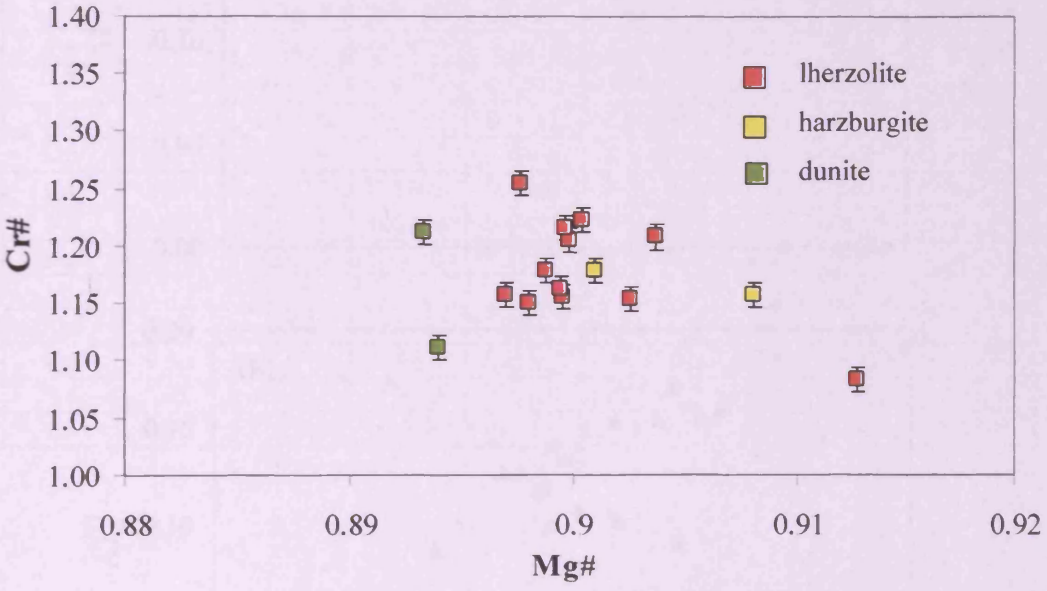

Figure 5.16 Plots of Cr# versus Mg# in orthopyroxene from mantle xenoliths trapped in the Bo Ploi basalt

The counterpart, clinopyroxene, is Cr-diopside and Na-Al-Cr-Mg-rich augite in composition. They have end member trend $En_{46.6-48.7}Wo_{45.5-48.6}Fs_{4.2-6.0}$ for diopside and $En_{49.2-50.1}Wo_{44-45}Fs_{5.6-6.2}$ for augite. The Mg# is restricted in the range of 0.89-0.91. Al_2O_3 (4.43-7.26%), Cr_2O_3 (0.80-1.83), and TiO_2 (0.28-0.80) contents in clinopyroxene

are usually higher than those contents in coexist orthopyroxene. In general, diopside is a pool of CaO and Na_2O and comparatively abundance in Cr_2O_3 second to spinel. The proportion of Al in tetrahedral and octahedral sites in clinopyroxene structure is governed by pressure and temperature of the equilibrium (Seyler and Bonatti, 1994; Chen, *et al.*, 2001). A negative correlation is observed in the plots of Al^{IV} against Na in clinopyroxene, contrastingly, positive correlation is shown in Al^{VI} versus Na plot in the same mineral as a consequent of pressure effect (Fig.5.17a and b). The chemical composition of clinopyroxene is shown in table 5.4.

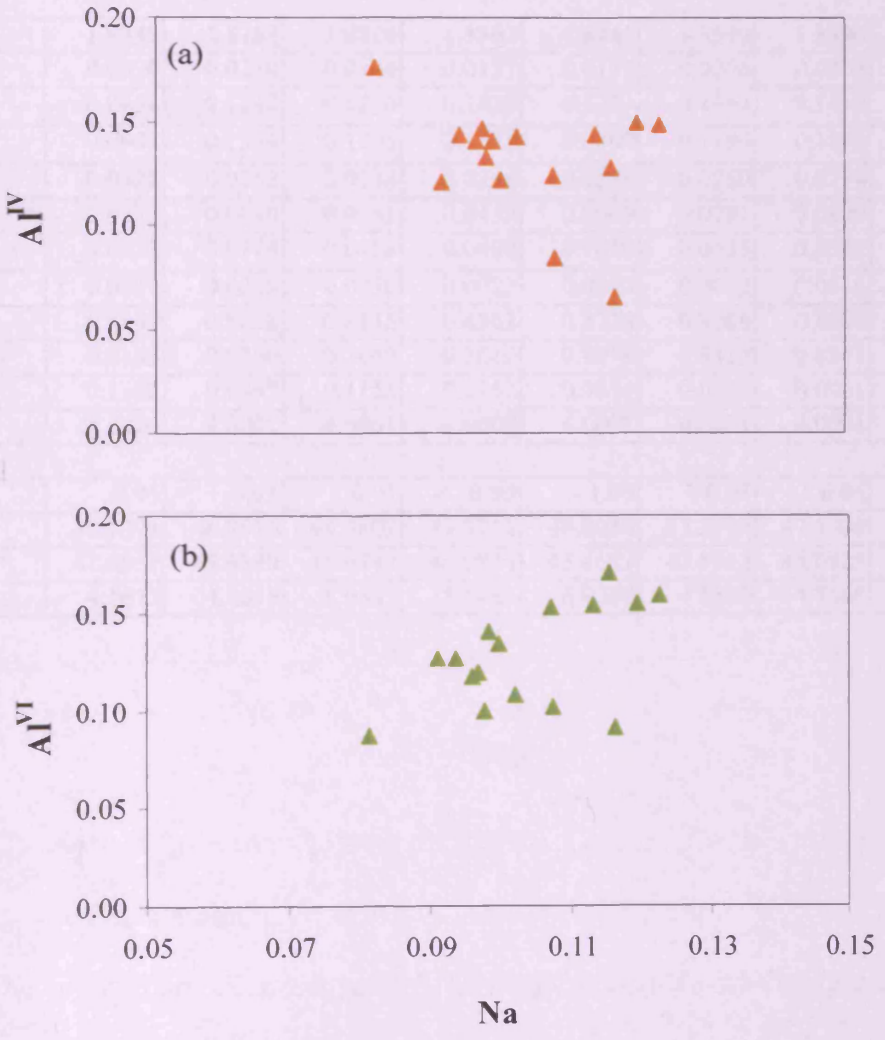

Figure 5.17 Plots of (a) tetrahedral Al versus Na in clinopyroxne

(b) octahedral Al versus Na in clinopyroxene

Table 5.4 Representative EPMA analyses of clinopyroxene from the Bo Ploi xenoliths

Oxide	BPX-1	BPX-2	BPX-3	BPX-4	BPX-5	BPX-6	BPX-7	BPX-8
SiO_2	53.56	51.85	51.83	51.45	50.81	51.25	51.36	51.42
TiO_2	0.28	0.80	0.53	0.51	0.66	0.76	0.75	0.63
Al_2O_3	3.66	6.00	7.00	7.00	6.21	6.22	6.05	6.35
Cr_2O_3	1.83	0.88	0.87	0.90	0.91	0.98	0.96	0.78
FeO	2.30	2.59	3.19	3.08	3.46	2.73	2.69	2.65
MnO	0.09	0.06	0.10	0.09	0.13	0.04	0.05	0.08
CaO	21.09	21.54	19.74	19.71	21.00	21.45	21.56	21.65
MgO	15.69	14.87	15.07	15.55	16.31	15.22	15.20	15.25
Na_2O	1.66	1.42	1.65	1.62	1.17	1.38	1.37	1.34
Total	100.16	100.01	99.98	99.91	100.66	100.03	99.99	100.15

Clinopyroxene cation numbers on basis of 6 oxygen atoms

Si	1.9349	1.8783	1.8724	1.8562	1.8241	1.8539	1.8590	1.8564
Ti	0.0076	0.0218	0.0144	0.0137	0.0177	0.0206	0.0204	0.0170
Al^{4+}	0.0651	0.1217	0.1276	0.1438	0.1759	0.1461	0.1410	0.1436
Al^{6+}	0.0907	0.1344	0.1705	0.1538	0.0869	0.1190	0.1171	0.1266
Cr	0.0522	0.0252	0.0248	0.0256	0.0258	0.0280	0.0274	0.0222
Fe	0.0473	0.0610	0.0781	0.0439	0.0000	0.0291	0.0309	0.0265
Fe^{3+}	0.0222	0.0174	0.0183	0.0490	0.1039	0.0535	0.0505	0.0535
Mn	0.0027	0.0018	0.0030	0.0027	0.0039	0.0012	0.0015	0.0024
Mg	0.8448	0.8028	0.8115	0.8362	0.8728	0.8206	0.8200	0.8206
Ca	0.8163	0.8360	0.7640	0.7619	0.8078	0.8313	0.8362	0.8375
Na	0.1162	0.0997	0.1155	0.1132	0.0814	0.0968	0.0961	0.0938
total	4.0000	4.0001	4.0061	4.0000	4.0002	4.0001	4.0001	4.0001
Mg#	0.95	0.93	0.91	0.95	1.00	0.97	0.96	0.97
En	48.7394	46.7016	48.4807	49.3712	48.8034	47.2778	47.1508	47.1474
Wo	47.0951	48.6329	45.6147	44.9844	45.4689	47.8942	48.0823	48.1184
Fs	4.1655	4.6655	5.9347	5.6444	6.0277	4.8280	4.7668	4.7343

Table 5.4 (continued)

Oxide	BPX-9	BPX-10	BPX-11	BPX-12	BPX-13	BPX-14	BPX-15	BPX-16
SiO_2	51.22	51.55	51.47	51.43	51.36	52.85	51.95	51.94
TiO_2	0.81	0.76	0.57	0.54	0.73	0.78	0.49	0.52
Al_2O_3	5.86	5.42	7.26	7.17	6.58	4.34	6.52	5.82
Cr_2O_3	1.03	1.01	0.90	0.82	0.95	1.11	1.06	1.23
FeO	2.94	2.99	3.19	3.40	3.53	2.46	3.12	2.50
MnO	0.09	0.08	0.08	0.08	0.10	0.08	0.07	0.09
CaO	21.51	21.68	19.15	19.52	20.13	21.65	19.61	21.13
MgO	15.00	15.17	15.67	15.49	15.25	15.17	15.63	15.49
Na_2O	1.45	1.39	1.76	1.71	1.40	1.53	1.53	1.30
Total	99.91	100.05	100.05	100.16	100.03	99.97	99.98	100.02

Clinopyroxene cation numbers on basis of 6 oxygen atoms

Si	1.8577	1.8677	1.8517	1.8508	1.8599	1.9163	1.8759	1.8790
Ti	0.0221	0.0207	0.0153	0.0145	0.0199	0.0212	0.0133	0.0141
Al^{4+}	0.1423	0.1323	0.1483	0.1492	0.1401	0.0837	0.1241	0.1210
Al^{6+}	0.1081	0.0991	0.1595	0.1548	0.1407	0.1017	0.1533	0.1271
Cr	0.0294	0.0289	0.0256	0.0233	0.0271	0.0318	0.0303	0.0351
Fe	0.0280	0.0308	0.0419	0.0420	0.0772	0.0610	0.0744	0.0552
Fe^{3+}	0.0612	0.0597	0.0541	0.0603	0.0296	0.0135	0.0198	0.0204
Mn	0.0027	0.0024	0.0024	0.0024	0.0030	0.0024	0.0021	0.0027
Mg	0.8108	0.8192	0.8403	0.8308	0.8232	0.8199	0.8412	0.8353
Ca	0.8358	0.8416	0.7382	0.7526	0.7811	0.8411	0.7586	0.8190
Na	0.1019	0.0976	0.1227	0.1193	0.0983	0.1075	0.1070	0.0911
total	4.0000	4.0000	4.0000	4.0000	4.0001	4.0001	4.0000	4.0000
Mg#	0.97	0.96	0.95	0.95	0.91	0.93	0.92	0.94
En	46.6379	46.7127	50.1103	49.2151	48.0252	47.1776	49.5961	48.2108
Wo	48.0759	47.9900	44.0217	44.5827	45.5691	48.3975	44.7261	47.2700
Fs	5.2862	5.2974	5.8680	6.2022	6.4057	4.4249	5.6777	4.5192

Spinel compositions can be distinctively divided into two groups; the first group is of spinels end member ($MgAl_2O_4$ 78.7-82.1) and slightly variable proportion of other compositions, including, hercynite-jacobsite – ulvöspinel – chromite – magnetite. The spinel of this group contain 9.70-14.93 wt% Cr_2O_3, 55.1-59.5 wt% Al_2O_3, 17.7-21.6 wt% MgO, 9.64-11.59 wt% FeO, and 0.09-0.17 wt% MnO. Nonetheless, spinel from sample BPX-1 is different hence its end member is in spinel $_{(51.9)}$ – magnesioferrite – magnesiochromite – picotite – chromite, where the major composition is characterised by 38.61 wt% Cr_2O_3, 29.62 wt% Al_2O_3, 15.35 wt% MgO, 14.16 wt% FeO, and 0.19 wt% MnO. They have a restrict variation in Cr/(Cr+Al) ratio, Cr#, in the range of 0.09-0.17. The only exceptionally high Cr# was found in spinel from sample BPX-1, where the value of 0.47 was determined. The Mg# in spinel is the most variable compared to other mineral constituents; they range from 0.69 to 0.81. The ratio of Cr/(Cr+Al) in spinel and in the coexist clinopyroxene can be used as an indicator of partial melting; the higher Cr/(Cr+Al) ratio, the higher degree of partial melting of the xenolith (Mysen and Kushiro, 1977; Jaques and Green, 1980; Dick and Bullen, 1984; Seyler and Bonatti, 1994; Chen *et al.*, 2001). In addition, the relationship between Cr# and Mg# in spinel can be an indicative of a partial melting trend as the lower Cr# or the higher Mg# reflects the less degree of partial melting of the xenoliths protolith. The relationship between the Cr# in spinel and coexisting clinopyroxene and the correlation of Cr# in spinel with Mg# in spinel are shown in figure 5.18-5.19. The chemical compositions of spinel and their end member calculations are illustrated in Table 5.5.

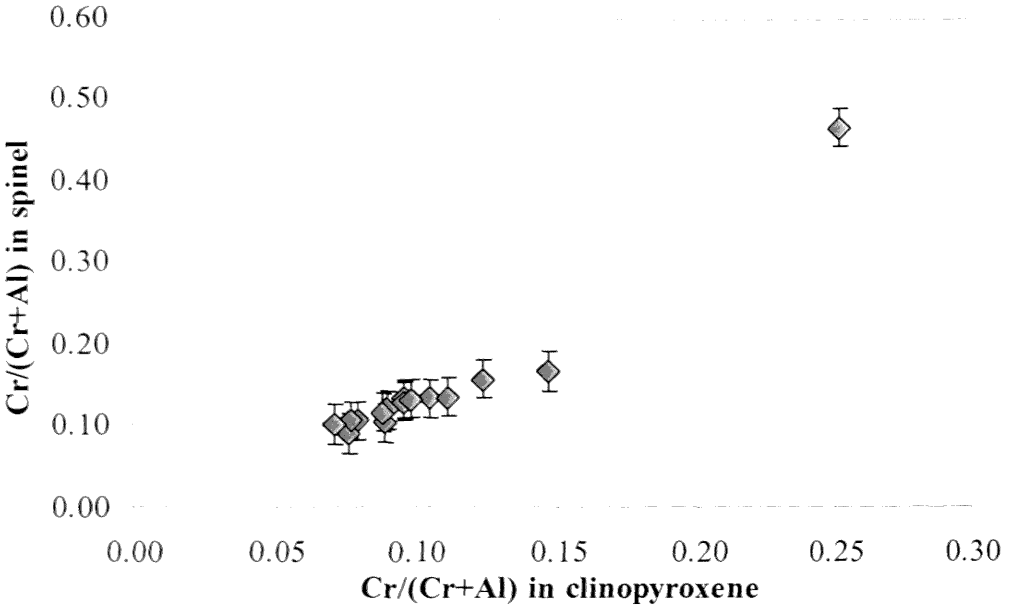

Figure 5.18 Plots of Cr/(Cr+Al) ratio in spinel versus Cr/(Cr+Al) in pyroxene

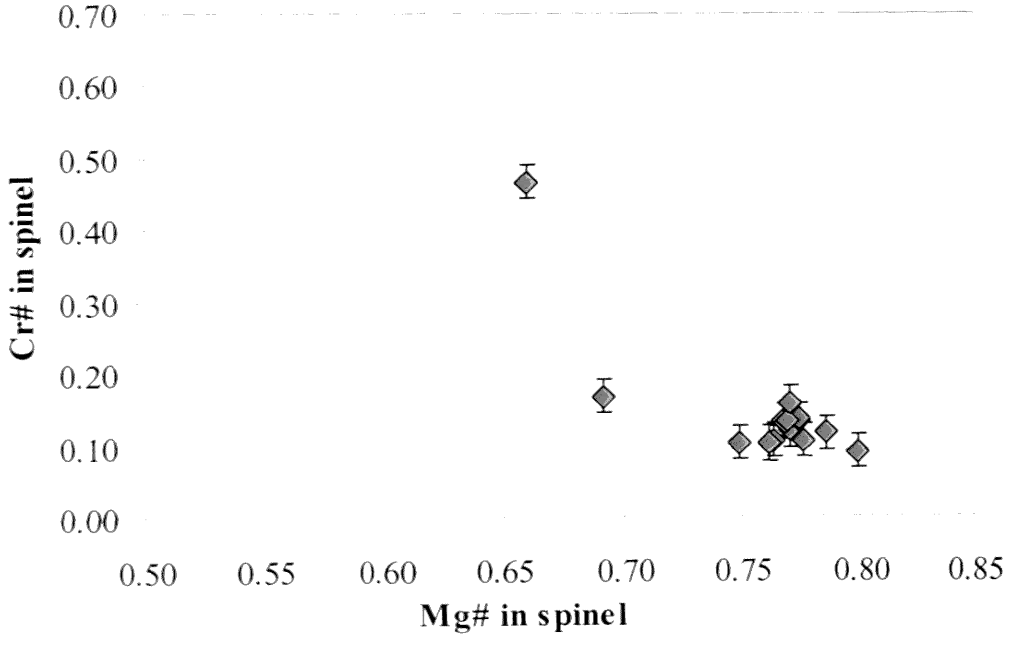

Figure 5.19 Plots of Cr# versus Mg# in spinel

Table 5.5 Representative EPMA analyses of spinel from the Bo Ploi xenoliths

Oxide	BPX-1	BPX-2	BPX-4	BPX-5	BPX-6	BPX-7	BPX-8
SiO_2	0.29	0.28	0.18	0.21	0.20	0.14	0.23
TiO_2	0.33	0.10	0.15	0.26	0.11	0.11	0.11
Al_2O_3	29.62	56.77	57.55	57.14	55.39	55.80	59.53
Cr_2O_3	38.61	11.57	10.19	9.76	12.73	12.44	8.82
FeO	14.16	10.66	10.79	11.04	11.01	10.98	9.64
MnO	0.19	0.11	0.10	0.12	0.15	0.12	0.17
MgO	15.35	20.36	20.97	21.40	20.37	20.45	21.57
CaO	0.03	0.02	0.02	0.03	0.02	0.01	0.00
Total	98.58	99.87	99.95	99.96	99.98	100.05	100.07
Fe_2O_3 calc.	0.94	0.51	1.58	2.54	1.28	1.28	0.99
FeO	13.32	10.21	9.37	8.76	9.86	9.83	8.75
New Total	98.67	99.92	100.11	100.21	100.11	100.18	100.17

Spinel cation numbers on basis of 32 oxygen atoms

Si	0.0680	0.0568	0.0360	0.0424	0.0408	0.0280	0.0456
Ti	0.0576	0.0144	0.0224	0.0392	0.0160	0.0160	0.0160
Al	8.3048	13.8696	13.9672	13.8472	13.5832	13.6552	14.2944
Cr	7.2624	1.8960	1.6584	1.5856	2.0936	2.0416	1.4200
Fe	2.6488	1.7680	1.6128	1.5056	1.7152	1.7056	1.4912
Mn	0.0368	0.0184	0.0160	0.0200	0.0256	0.0200	0.0280
Mg	5.4432	6.2904	6.4360	6.5584	6.3176	6.3288	6.5496
Ca	0.0064	0.0032	0.0032	0.0056	0.0032	0.0008	0.0000
Fe^{3+} calc.	0.1680	0.0784	0.2440	0.3920	0.1992	0.1992	0.1504
total	23.9960	23.9952	23.9960	23.9960	23.9944	23.9952	23.9952
Mg#	0.67	0.78	0.80	0.81	0.79	0.79	0.81
Cr#	0.47	0.12	0.11	0.10	0.13	0.13	0.09

Spinel end member calculation

Spi	51.9420	78.7301	80.5536	82.1088	79.0500	79.1913	81.9130
Her	-	8.0099	6.7984	4.4848	5.8786	6.2202	7.4707
Qua	1.5869	-	-	-	-	-	-
Mfe	1.0512	-	-	-	-	-	-
Jac	-	0.2398	0.2093	0.2585	0.3291	0.2594	0.3593
Usp	-	0.9094	0.7476	1.0342	0.7280	0.5686	0.7885
Mnc	0.4691	-	-	-	-	-	-
Pic	12.0079	-	-	-	-	-	-
Chr	32.9430	11.8575	10.3720	9.9193	13.0936	12.7696	8.8830
Mag	-	0.2532	1.3191	2.1943	0.9208	0.9910	0.5855
Total	100.00	100.00	100.00	100.00	100.00	100.00	100.00

Spi = Spinel, Her = Hercynite, Qua = Qandilite, Mfe = Magnesioferrite, Jac = Jacobsite, Usp = Ulvöspinel, Mnc = Magnesiochromite, Pic = Picotite, Chr = Chromite, Mag = Magnetite

Table 5.5 (continued)

Oxide	BPX-9	BPX-10	BPX-11	BPX-12	BPX-13	BPX-14	BPX-15	BPX-16
SiO_2	0.18	0.15	0.20	0.16	0.21	0.26	0.34	0.18
TiO_2	0.11	0.15	0.18	0.16	0.19	0.75	0.22	0.12
Al_2O_3	55.29	55.10	57.13	57.58	57.52	51.86	55.22	53.66
Cr_2O_3	12.75	12.80	10.14	9.70	11.26	15.51	12.56	14.93
FeO	10.79	10.84	11.51	11.59	10.04	14.10	11.00	10.78
MnO	0.13	0.17	0.15	0.13	0.09	0.13	0.13	0.06
MgO	20.72	20.80	20.79	20.74	20.67	17.74	20.55	20.29
CaO	0.03	0.02	0.03	0.02	0.01	0.05	0.00	0.00
Total	100.00	100.03	100.13	100.08	99.99	100.40	100.02	100.02
Fe_2O_3 calc.	1.62	1.88	2.09	2.08	0.15	0.00	1.21	1.05
FeO	9.33	9.15	9.63	9.72	9.90	0.00	9.91	9.83
New Total	100.16	100.22	100.34	100.29	100.01	86.30	100.14	100.13

Spinel cation numbers on basis of 32 oxygen atoms

Si	0.0360	0.0304	0.0400	0.0350	0.0424	0.0552	0.0696	0.0368
Ti	0.0160	0.0224	0.0272	0.0240	0.0280	0.12	0.0336	0.0176
Al	13.5352	13.4888	13.8768	13.975	13.9864	13.0280	13.5288	13.2424
Cr	2.0928	2.1008	1.6520	1.5784	1.8360	2.6136	2.0640	2.4704
Fe	1.6208	1.5888	1.6584	1.6728	1.7080	2.5128	1.7224	1.7208
Mn	0.0216	0.0288	0.0248	0.0216	0.0144	0.0232	0.0216	0.0096
Mg	6.4144	6.4384	6.3864	6.3656	6.3560	5.6360	6.3672	6.3320
Ca	0.0056	0.0032	0.0056	0.0032	0.0008	0.0104	0.0000	0.0000
Fe^{3+} calc.	0.2528	0.2928	0.3240	0.3224	0.0232	0.0000	0.1888	0.1656
total	23.9952	23.9944	23.9952	23.9982	23.9952	23.9992	23.9960	23.9952
Mg#	0.80	0.80	0.79	0.79	0.79	0.69	0.79	0.79
Cr#	0.13	0.13	0.11	0.10	0.12	0.17	0.13	0.16

Spinel end member calculation

Spi	80.3176	80.5796	79.9562	79.6662	79.5186	70.6253	79.6336	79.1937
Her	4.3408	3.7695	6.8239	7.7247	7.9519	10.8404	4.9677	3.6174
Qua	-	-	-	-	-	-	-	-
Mfe	-	-	-	-	-	-	-	-
Jac	0.2791	0.3685	0.3186	0.2787	0.1467	-	0.2763	0.1297
Usp	0.6678	0.6772	0.8561	0.7167	0.9002	2.1911	1.3068	0.6985
Mnc	-	-	-	-	0.0434	0.2901	-	-
Pic	-	-	-	-	-	-	-	-
Chr	13.0922	13.1411	10.3330	9.8749	11.4393	16.0530	12.9082	15.4525
Mag	1.3024	1.4640	1.7122	1.7387	-	-	0.9045	0.9081
Total	100.00	100.00	100.00	100.00	100.00	100.00	100.00	100.00

Spi = Spinel, Her = Hercynite, Qua = Qandilite, Mfe = Magnesioferrite, Jac = Jacobsite, Usp = Ulvöspinel, Mnc = Magnesiochromite, Pic = Picotite, Chr = Chromite, Mag = Magnetite

5.4 Geothermobarometry

Geothermometer and geobarometer obtained from equilibrium pressure-temperature calculation on the coexisting mineral pairs is one of the most useful application of mineral chemistry and petrography of mantle xenoliths, which simply allows the geothermal gradient of the studied areas to be constructed. This works on the basis of partitioning elements between coexisting minerals and are an integral part of research on the upper mantle. A major advance in P-T calculation resulted from experiments utilizing natural composition mantle xenoliths. The behaviour of pyroxene, particularly, those involving enstatite and diopside solid solution or Fe-Mg ion exchanges among ferromagnesian minerals are among the more useful equilibria for temperature estimation (Wood and Banno, 1973; Wells (1977); Mercier, 1980, Brey and Köhler, 1990; Sachtleben and Seck, 1981). However, unlike temperature, pressure estimation is far more complicated and less certain. Geobarometry calculation using garnet as an indicator of pressure, however, have been successfully exploited for understanding the mantle, such as in the garnet peridotite systems (Bertrand *et al*, 1986; Carswell and Gibb, 1987; Finnerty and Boyd, 1987). The pressure dependence of Al-content in orthopyroxene co-existing with garnet is a key for the answer but these rocks do not contain garnet therefore, this is not applicable to the garnet-free assemblages systems. Mercier (1980) proposed pressure estimation using an empirical barometer dependant on the Al-content in pyroxenes coexistence with spinel.

Temperature estimation

Temperature estimation of the mantle xenoliths from Bo Ploi basalt is done by various equations based on the equilibrium of coexisting orthopyroxene-clinopyroxene pairs and other mineral phases, such as spinel. The results are summarised in Table 5.6. It is found that temperature estimation calculated after Wood and Banno (1973) are about 100°C higher (960-1150°C) compared to the temperature range (844-1046°C),

after Wells (1977). However, both calculations are in good agreements for sample BPX-10, which has the highest calculated temperature and the lowest temperature estimate is for sample BPX-13. Similarly, the role of Al-solubility in orthopyroxene thermometry, which was calculated after Sachtleben & Seck (1981), yields generally lower temperatures (826-1103°C). Brey and Köhler (1990) proposed a temperature method based on the pyroxene mineral pairs and on Ca in orthopyroxene. This thermometry provides a similar trend, however, the range of temperature is much wider (797-1101°C). Alternately, pyroxene-spinel geothermometry of Mercier (1980), using diopside/spinel gives temperatures in the range of 834-1076°C; and his enstatite/spinel thermometer gives higher and narrower temperatures in the range 1012-1189°C.

Pressure estimation

The thermodynamic equations proposed by Mercier (1980) were used to estimate the pressure of the Bo Ploi mantle xenoliths (Table 5.6), which is principally based on the role of chromium on aluminium solubility in pyroxene relative to coexisting spinel. This relation allows us to determine the pressure of the xenoliths by using pyroxene-spinel pairs: diopside/spinel and enstatite/spinel mineral pairs. It is found that the pressure estimates of these mantle peridotites are in the range of 17.6 to 23.8 kbar on the enstatite/spinel pair calculations, which in a good agreement with the stability field of spinel in peridotite (O'Hara *et al*, 1971), however, the exceptionally low value of 11.0 kbar is obtained from the sample BPX-01. Sample BPX-03, although does not contain spinel, but spinel may not actually be present in the spinel lherzolite stability field if there is a small amount of Al_2O_3 in the rock and the temperature is close to solidus (Hall, 1996). At this point, pyroxenes allow all of Al_2O_3 contents into their structures so that spinel cannot develop. On the other hand, the pressure estimates using a diopside/spinel mineral pair yield much lower and widely variable values (3.4 to 17.8 kbar).

Table 5.6 Temperature and pressure estimates of the Bo Ploi xenoliths

Sample	Rock type	Temperature (°C)							Pressure (kbar)	
		a	*b*	*c*	*d*	*e*	*f*	*g*	*A*	*B*
BPX-01	Lherzolite^{T}	1000	884	932	877	954	975	1032	4.5	11.0
BPX-02	lherzolite^{T}	986	878	990	855	1014	863	1079	5.6	20.9
BPX-03	Lherzolite^{P}	-	-	-	-	-	-	-	-	-
BPX-04	dunite^{P}	1127	1020	985	1066	1033	1042	1098	15.7	22.0
BPX-05	lherzolite^{P}	1117	1010	1103	1008	1144	989	1189	12.4	23.8
BPX-06	lherzolite^{T}	1024	901	833	885	919	870	1005	5.1	18.3
BPX-07	lherzolite^{T}	1011	889	855	866	927	857	1012	4.6	17.6
BPX-08	lherzolite^{T}	1012	891	902	868	934	848	1018	5.0	18.2
BPX-09	lherzolite^{T}	995	866	826	843	938	834	1019	3.4	19.2
BPX-10	lherzolite^{T}	990	864	831	832	941	848	1022	5.1	17.9
BPX-11	lherzolite^{P}	1150	1046	1019	1101	1052	1076	1114	17.8	22.0
BPX-12	dunite^{P}	1124	1022	999	1069	1045	1050	1107	16.5	21.6
BPX-13	lherzolite^{P}	1099	1003	1083	1043	1052	1033	1113	15.0	20.4
BPX-14	Lherzolite^{M}	960	844	995	797	930	884	1015	9.2	18.2
BPX-15	lherzolite^{P}	1125	1031	1047	1082	1054	1073	1112	17.7	20.4
BPX-16	harzburgite^{M}	1060	944	843	962	996	958	1063	10.2	18.9

Note: Temperature estimation by
a Wood & Banno, 1973
b Wells, 1977
c Sachtleben & Seck, 1991
d Brey & Kohler, 1990 (BKN)
e Brey & Kohler, 1990 (Ca-op)
f Mercier, 1980 (di/sp)
g Mercier, 1980 (en/sp)

Pressure estimation by
A Mercier, 1980 (di/sp)
B Mercier, 1980 (en/sp)

Sample BPX-03 does not contain spinel

^{P} = Protogranular texture

^{T} = Transitional protogranular to porphyroclastic texture

^{M} = Modified transitional protogranular to porphyroclastic texture

5.5 Discussion and conclusion

The entrained mantle xenoliths, peridotites, from Bo Ploi Basalt range from spinel lherzolite to clinopyroxene-poor lherzolite, harzburgite and dunite. The variation of rock types indicates the evolution of these mantle materials as a remnant after several episodes of basaltic magma segregation and also implies that the upper mantle beneath the study area is anomalous and may be partly composed of spinel-plagioclase lherzolite (Xu *et al.*, 1998; Nasir and Safarjalani, 2000; Kühn *et al.*, 2000). It was suggested by Xu *et al.*, (1998) that this is because the upper mantle may locally constitute layers of undeformed and fertile peridotites, which were overlaid by deformed-depleted ones. There is a weak relationship between the texture of these mantle nodules and the temperature/pressure estimation. Xenoliths of protogranular texture have higher temperature estimates than the other groups and this similar feature have been observed in peridotitic xenoliths from young volcanic regions in the Massif Central (Brown *et al.*, 1980) and the xenoliths from Rhenish Massif, Germany (Witt-Dickschen and Seck, 1991).

5.5.1 Variations of the temperature-pressure estimates

The temperature-pressure estimates using various geothermobarometers are generally variable (Downes *et al.*, 1992; Hsu and Chen, 1998; Chen *et al.*, 2003) so as the P-T estimates from this work, however, the variation is systematic. It is noteworthy that xenoliths of protogranular texture tend to give higher temperature than xenoliths of transitional protogranular to porphyroclastic texture and modified transitional protogranular to porphyroclastic texture. The highest temperature estimate from the seven thermodynamic equations (Table 5.6) is well consistent, since the highest temperature estimate is obtained from either BPX-05 or BPX-11, which are protogranular texture. The temperature estimates for BPX-05 are 1103°C (Sachtleben

and Seck, 1981); 1144°C (Ca-orthopyroxene: Brey and Köhler, 1990) and 1189°C (enstatite-spinel: Mercier, 1980), while other equations giving BPX-11 the highest temperature estimation including 1150°C (Wood and Banno, 1973); 1046°C (Wells, 1977), 1101°C (BKN: Brey and Köhler, 1990) and 1076°C (diopside-spinel: Mercier, 1980). The lowest temperature estimates are more variable, however, all of them are those xenoliths of transitional protogranular to porphyroclastic texture and modified transitional protogranular to porphyroclastic texture, including BPX-06 which a temperature of 919°C (Ca-orthopyroxene: Brey & Kohler, 1990) and 1005°C (enstatite-spinel: Mercier, 1980), BPX-09 with minimum temperature of 826°C (Sachtleben and Seck, 1981) and 834°C (diopside-spinel: Mercier, 1980) and BPX-14 with temperature estimates 797°C (BKN: Brey and Köhler, 1990), 844°C Wells, (1977) and 960°C (Wood and Banno, (1973). In addition, temperature estimates using equilibrium of enstatite-spinel mineral pairs (Mercier, 1980) give the highest values on every sample, while the lowest temperature estimates are mostly obtained from the equation of Sachtleben and Seck, (1981).

The temperature estimates obtained from enstatite-spinel thermometer of Mercier, (1980) were compared with those estimate by other thermometers are illustrated in Figure 5.20. The BK-Ca temperature shows an excellent correlation with enstatite-spinel thermometer. The temperature estimate obtained from clinopyroxene-orthopyroxene thermometer, two pyroxene thermometer, which are proposed by Wood and Banno, (1973), Wells, (1977) and Brey and Köhler, 1990 (BKN), show general correlation with enstatite-spinel thermometer with R^2 in the range of 0.6-0.7. The temperature from diopside – spinel thermometer shows more scatter.

The variation in pressure estimates is greater than the temperature. Although both methods; diopside-spinel and enstatite-spinel thermobarometer, show a good positive correlation on P-T diagram, the diopside-spinel barometer gives unrealistic

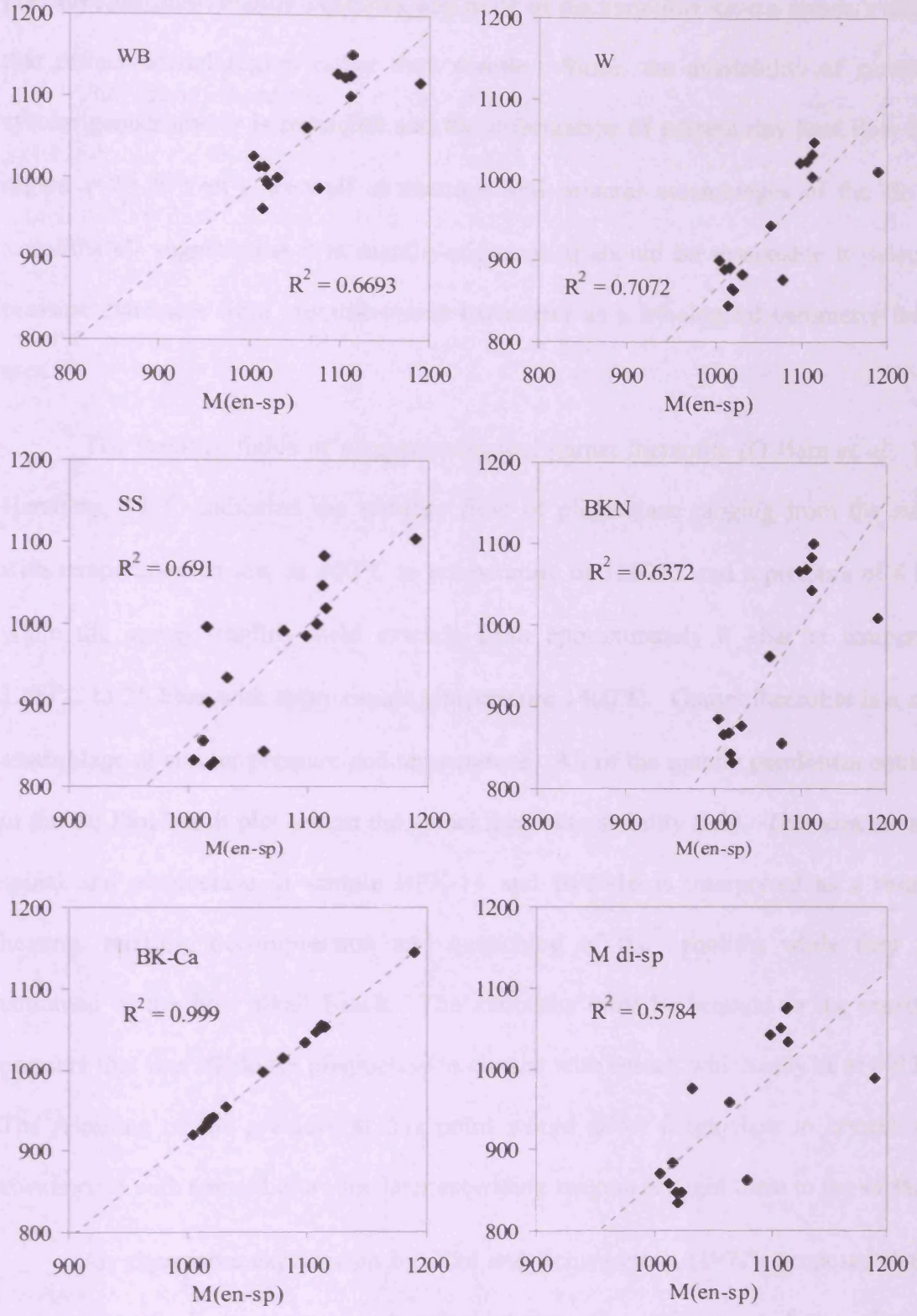

Figure 5.20 Comparison between temperature estimated by enstatite-spinel thermometer and other thermometers. WB = Wood & Banno, 1973; W = Wells, 1977; SS = Sechtleben & Seck, 1991; BKN and BK-Ca = Brey and Köhler, 1990; M (di-sp) and M (en-sp) = Mercier, 1980.

pressures for these mantle xenoliths and most of the xenoliths have a pressure estimate that reflect crustal region rather than mantle. Since, the availability of garnet-free system geobarometer is restricted and the information of present day heat flow in the region (~70 mW/m^2), as well as textures and mineral assemblages of the Bo Ploi xenoliths all suggest that it is mantle origin, so it should be reasonable to select the pressure estimates from enstatite-spinel barometer as a lithological barometry for this area.

The stability fields of plagioclase-spinel-garnet lherzolite (O'Hara *et al.*, 1971; Herzberg, 1978) indicated the stability field of plagioclase ranging from the surface with temperature as low as 400°C to temperature of 1200°C and a pressure of 8 kbar, while the spinel stability field extends from approximately 8 kbar at temperature 1200°C to 25 kbar with approximate temperature 1400°C. Garnet lherzolite is a stable assemblage at greater pressure and temperature. All of the mantle peridotites entrained in the Bo Ploi basalt plot within the spinel lherzolite stability field. The coexistence of spinel and plagioclase in sample BPX-14 and BPX-16 is interpreted as a result of heating, melting, decompression and quenching of the xenoliths while they were entrained in the host alkali basalt. The xenoliths must be brought to the maximum pressure that was stable for plagioclase to coexist with spinel, which may be at 8-9 kbar. The retaining of the pressure at this point would allow plagioclase to crystallise in coexistence with spinel before the later ascending magma brought them to the surface.

An alternative explanation by Pike and Schwarzman (1977), proposed that the interaction of clinopyroxene and spinel during the melting produces olivine + plagioclase or plagioclase + spinel of a different composition. The textural feature of plagioclase bordering the spinel core is the results from slow cooling rate of partial melting, while the xenoliths were entrained in the host alkali basalt. It is noticed that the position of the coexisting spinel-plagioclase assemblages in sample BPX-14 and

BPX-16 are relatively close to contact with the host alkali basalt, so it is possible that texture of the xenoliths are perturbed by the heat from the host magma

Dautria and Girod, (1987 and the references therein), reported spinel rimmed by plagioclase in peridotites from Adamawa, Cameroon. A model of coexisting plagioclase and spinel was proposed as, initially, the peridotites were partially melted and yielded the peridotite in spinel lherzolite stability field, later on the cooling and pressure release, which possibly related to the upper mantle uplifting, to the maximum pressure of plagioclase lherzolite stability field. Finally, spinel and diopside were partially melted, consequently, plagioclase crystallised as rims around spinel grains and veinlets in the nodules.

5.5.2 Geotherm beneath the Bo Ploi area

The pressure estimation for the Bo Ploi xenoliths ranges from 11.0 to 23.8 kbar, in which all of the spinel lherzolite essential phases: olivine-orthopyroxene-clinopyroxene-spinel are stable. The absence of water-bearing or hydroxyl minerals such as phlogopite and amphiboles implies dry condition during the formation of the xenoliths, which is consistent with the relatively high heat flow in the region. The palaeogeotherm of this area from the maximum P-T estimation is compared with mantle xenoliths from alkali province geotherm, mostly from the East Aferican rift (Jones *et al.*, 1983) as shown in figure 5.21. It is found that these mantle xenoliths lie in between the boundaries of the alkali province geotherm. The Bo Ploi mantle xenolith geotherm, however, shows a more gentle slope compared to the South-eastern Australian xenolith geotherm (O'Rielly and Griffin, 1985) and both geotherms intersect at approximately 25 kbar. The relatively high geothermal gradient in this area, which was recorded in the xenoliths, is interpreted as a result from thermal perturbation either by the uprising of hot magma diapirs in the lithosphere or a regional intrusion of hot asthenosphere as a result of crustal extension. There is no direct heat flow measurement available in this

area, however, the heat flow records from bore holes logging in Suphanburi oil field, which is located 50 km east of the Bo Ploi basalt, is appropriated for comparison purpose.

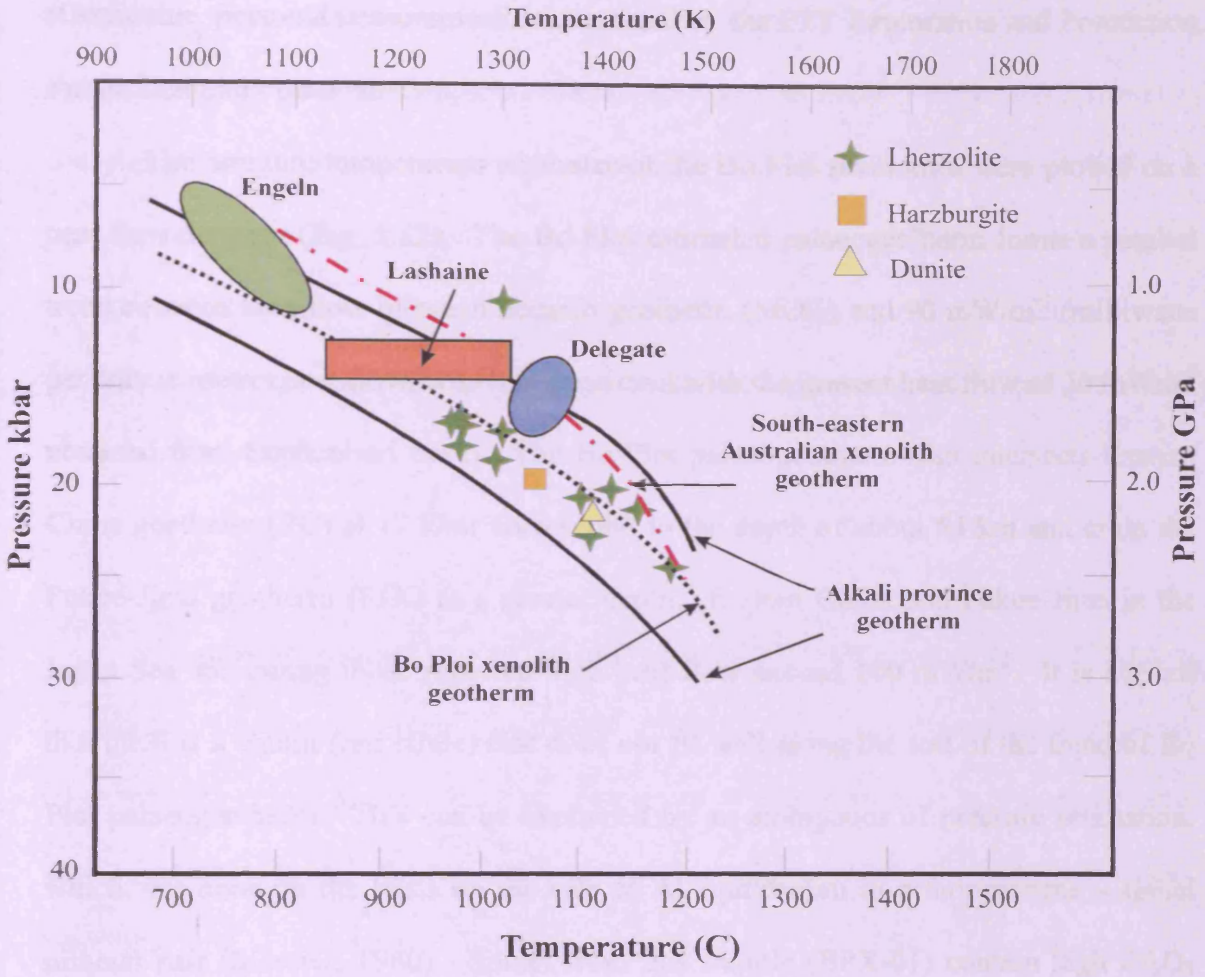

Figure 5.21 Thermodynamic calculations for pressures and temperatures on equilibrium of enstatite-spinel (Mercier, 1980). The P-T of lower crustal granulites is from Jones *et al.*, (1983a). South-eastern Australian xenolith geotherm is from O'Reilly and Griffin, (1985).

Suphanburi oil field or Suphanburi basin is one of onshore Tertiary basins in Thailand with the basin axis nearly north/south in orientation covers an area of approximately 800 km^2. This half graben basin is a result from the movement of the Mae Ping fault in the north of basin and the dextral Three Pagoda fault in the south

(Remus *et al.*, 1993; Pisutha-Arnond *et al.*, 1997). The basin is about 3 km thick filled with sediment of fluvial-lacustrine and fan-delta environment sediment in the 1 km thickness upper part. The heat flow of 70 mW/m^2 is obtained from bore hole logging (Gonecome, personal communication) operated by the PTT Exploration and Production Public Company Limited.

The pressure-temperature estimates of the Bo Ploi peridotites were plotted on a heat flow diagram (Fig. 5.22). The Bo Ploi estimated palaeogeotherm forms a parallel trend between heat flow of mean oceanic geotherm (MOG) and 90 mW/m^{-2} (milliwatts per square metre) heat flow, which is consistent with the present heat flow of 70 mWm^{-2} obtained from Suphanburi basin. The Bo Ploi palaeogeotherm also intersects Eastern China geotherm (EC) at 17 kbar correspond to the depth of about 55 km and cross the Fukue-Jima geotherm (FJX) at a greater depth. Eastern China and Fukue-Jima in the Japan Sea are among those reported high heat flow exceed 100 mW/m^2. It is noticed that there is a datum (red circle) that does not fit well along the rest of the trend of Bo Ploi palaeogeotherm. This can be explained by an ambiguous of pressure estimation, which was done on the basis on the role of Al equilibrium in orthopyroxene – spinel mineral pair (Mercier, 1980). Spinel from this sample (BPX-01) contain high Cr_2O_3 content (38.61wt%) with Cr# 0.47, as a result, the Al_2O_3 content in this spinel is much lower and could reduce the pressure estimation enormously.

Crustal extension, which can cause lithosphere thinning, is believed to play a role in the replacement of the continental lithosphere by the upwelling of hot asthenosphere, which in turn elevates the geothermal gradient (Nicolas *et al.*, 1987; Witt and Seck, 1987; Umino and Yoshizawa, 1996). It was suggested by Xu *et al.*, (1998) that the difference in temperature estimates among mantle nodules, which appeared to show higher temperatures in the protogranular textured group and gradually lower temperatures for the more deformed xenoliths, was caused by the different position of

the nodules situated in an upwelling body of mantle. The undeformed protogranular xenoliths are likely to be situated in the inner part of upwelling body. The temperature of the hotter diapir and the cooler peridotite nodules were retained and readjusted to their equilibrium. In contrast, the more deformed xenoliths are likely to reside in the peripheral part of the mantle diapir, where they are more susceptible to deformation and interaction (possibly metasomatism) with wall rocks that are rich in exotic elements.

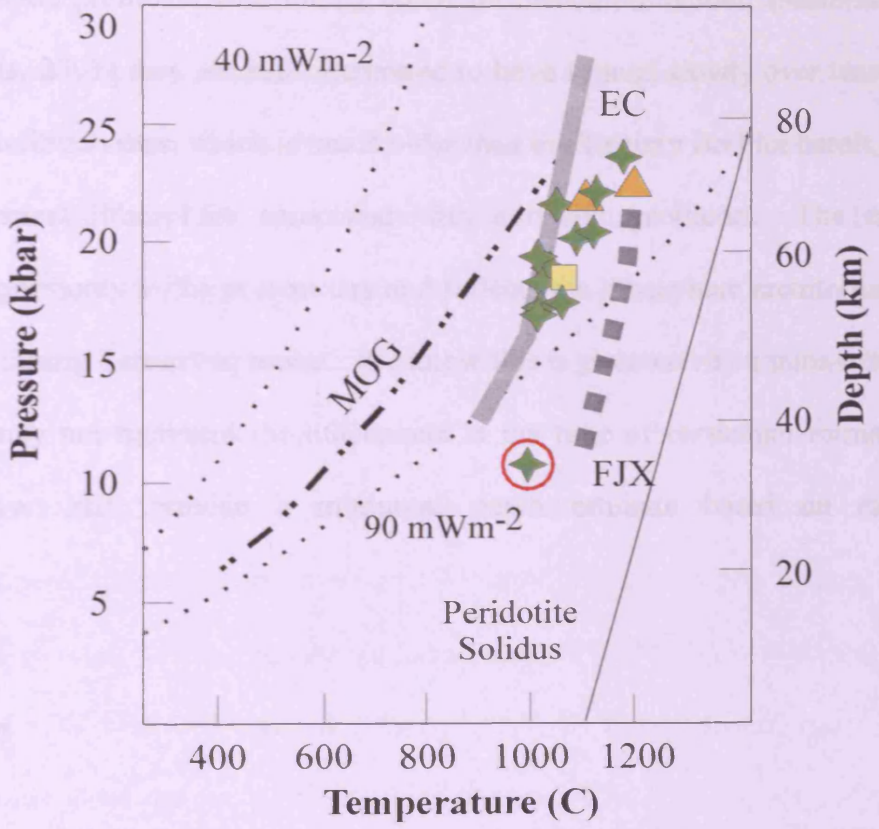

Figure 5.22 The Bo Ploi xenoliths geotherm plot on P-T diagram with 40-90 mW/m^2 heat flows (modified after Unimo & Yoshizawa, 1996, Nasir & Safarjalani, 2000, Al-Mishwat & Nasir, 2004), compare with those geotherm from Eastern China (EC: grey solid line; Fan&Hooper, 1989) and Fukue-Jima, Japan (FJX: grey dash line; Unimo & Yoshizawa, 1996). Symbols are in Fig.5.22.

The mineral constituents of these mantle peridotites are typical for spinel lherzolite mineral assemblages. Corundum is not found associated with these peridotites. The P-T estimates of these xenoliths indicated that they originated from the upper mantle and were not involved in the genesis of corundum, which was more likely to have taken place in the (lower) crust. In addition, relatively wide pleochroic halos (10-30 microns) around zircon inclusions in the Bo Ploi corundum suggest that they were trapped in the corundum long before the corundum crystal was brought to the surface. Despite problems with dating based on pleochroic haloes, (Meldrum *et al.*, 1998; Nasdala, 2001) they are still interpreted to have formed slowly over tens or even hundreds of million years, which is much older than the Tertiary Bo Ploi basalt, perhaps under an ancient lithosphere associated with a cooler geotherm. The estimated geotherm applies only to the present day and reflects the lithosphere architecture of the Bo Ploi area during Tertiary to recent. We know this is governed by a trans-extensional regime but may not represent the lithosphere at the time of corundum formation. It does, however, still provide a minimum depth estimate based on calculated temperatures.

Conclusion

1. The mantle xenoliths entrained in the Bo Ploi basalt are consisted of spinel lherzolite, harzburgite and dunite. Texturally, they are classified into three main groups including protogranular texture, transitional from protogranular to porphyroclastic texture and modified transitional protogranular to porphyroclastic texture.
2. The P-T estimates basis on equilibrium of enstatite-spinel mineral pairs suggest that these xenoliths originated from pressure 18 to 24 kbar and temperature range from 1000 to 1200°C, which is compatible to the depth of 59 to 79 km in

the upper mantle region. One spinel lherzolite yielded 11 kbar pressure estimate due to higher Cr_2O_3 and lower Al_2O_3 content of spinel in this sample, which may not suitable for pressure estimate using Al_2O_3 sensitivity.

3. The coexisting of spinel – plagioclase in some mantle xenoliths indicates a decompression, melting and re-crystallisation of the xenoliths. This may have occurred when the xenoliths were lifted to spinel – plagioclase transition region that allows coexistence of both mineral and later brought to the surface by later ascending magma.
4. The Bo Ploi xenolith geotherm suggests high heat flow in the study area corresponding to the present day heat flow of 70 mWm^{-2} and the extensional regime in the vicinity.

Chapter 6

Geochemistry and Petrogenesis of the Bo Ploi Basalt

This chapter approaches the origin of corundum from the Bo Ploi deposits by considering the geochemical analyses of all samples potentially related to corundum. These include the host basalt whole rock geochemistry petrography, phenocryst mineral chemistry and comparison with minerals associated with corundum in the placer deposits, including pyroxene, spinel and zircon. The aim of the study is to characterise all potential sample domains using all the data available to understand the geochemistry and ultimately to explain the petrogenesis of Bo Ploi basalts.

6.1 Occurrence and Petrography of the Bo Ploi basalt

The subaerial Bo Ploi basalt occurs as a single small volume unit, where outcrops and boulders spread over an area of approximately 1 km^2, which is known locally as basalt Khao Lan Tom, in the vicinity of Bo Ploi district, Kanchanaburi province. The basalt forms a group of small reddish brown hills (Fig.6.1a-b) that resemble an intrusive volcanic plug remnant. The eruption cuts through country rocks of the Silurian-Devonian metamorphic basement of the Tanao Sri Group, where the rocks are dominated by quartzite, phyllite, tuffaceous sandstone and tuffaceous shale (Bunjitradulya and Prapaitrakul, 1973, Bunopas and Bunjitradulya, 1975). Aranyakanond, (1988) suggested that the Bo Ploi basalt effused along the fractured zones, so called Huai Ma Kha and yielded a volume of lava that accumulated higher than 100 metres above the present outcrops. It flowed westward only across the hill to the Lam Ta- Phoen basin, since there is no evidence of basalt rocks on the eastern flank of the fractured zone. The basaltic flows and, perhaps, pyroclastic debris have been weathered and decomposed and as a result, the reddish brown soil with some *in situ* basalt floats are commonly observed. It is impossible for the number of flows to be

resolved because of fairly heavy weathering. The internal structures such as platy joints and columnar joints are fairly common and are used to make pavement stones. The total volume of the Bo Ploi basalt is very small, probably < 1 km^3.

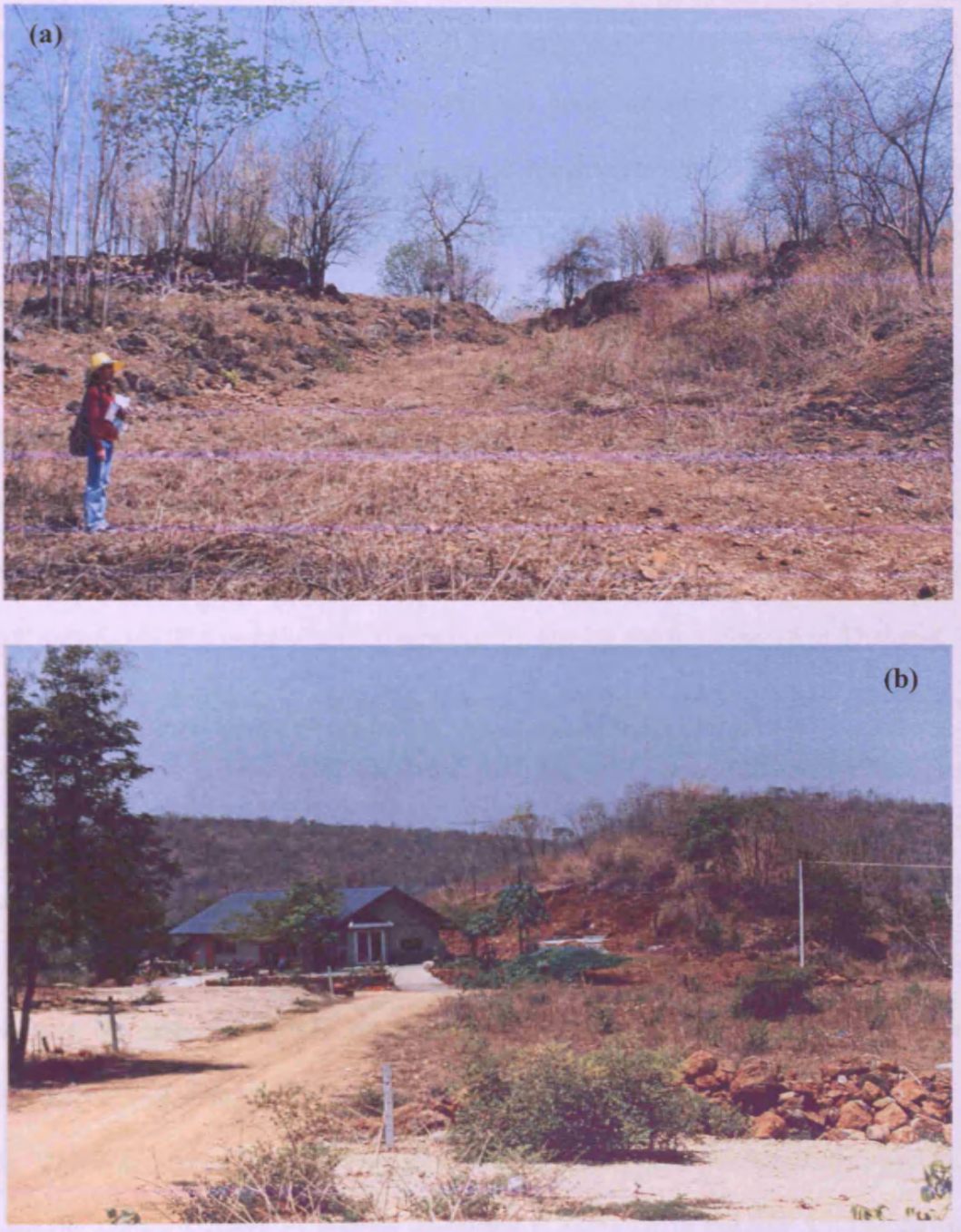

Figure 6.1 Photographs show the Bo Ploi basalt forms small hills that covered by reddish brown soil and scant vegetation (a) look N60E (b) look S15W

In hand specimens, the fresh Bo Ploi basalt is black and dark in colour, weathered colour is yellowish brown. It is fine-grained and porphyritic texture. The rock contains numbers of phenocrysts, crustal xenoliths, mantle xenoliths and amygdale minerals. The phenocrysts occur in two size ranges, phenocrysts and megacrysts. The phenocrysts are variable in size, but average approximately 0.5×1 mm to 1×2 mm. They are olive-green olivine, deep green to black pyroxene, with occasionally black spinel and orange brown zircon is observed. The most common megacrysts are black spinel, black pyroxenes (Fig. 6.2) and vitreous feldspars (Fig.6.3), which range from 1×3 cm to 3×5 cm and rarely that the larger size of 3×10 cm megacrysts of black pyroxene were also found. In addition, megacrysts of magnetite (1×3 cm in size) have been recovered associated with other megacrysts in the reddish brown basaltic soil that covers the foothill of the outcrops. Jewellery made from these megacrysts, particularly, black spinel, black pyroxene and magnetite are among the best known in Thailand.

The basalt contains abundant crustal and mantle xenoliths of various species, shapes and sizes. The crustal xenoliths were identified as nepheline syenite, granitic rocks and quartzite. Some crustal xenoliths display a distinct contact with the host basalt, where the dark green minerals rimmed the crustal nodules and they are interpreted as reaction rims of the crustal nodules with the host basalt (Fig. 6.4). Similarly, the mantle xenoliths are rounded to ovoid shaped with sizes from 1-2 cm and some larger specimens up to 5 cm across and rarer xenoliths up to 15 cm across (Fig 6.5). These peridotite nodules are classified as spinel lherzolite, harzburgite and dunite, where the detailed study of mantle xenoliths is reported in chapter 5. The amygdale minerals that formed in the void spaces as secondary minerals are calcite and analcite.

Figure 6.2 Photograph shows black pyroxene megacryst above the coin (2 cm) in the Bo Ploi basalt

Figure 6.3 Photograph shows glassy sanidine megacryst in the Bo Ploi basalt

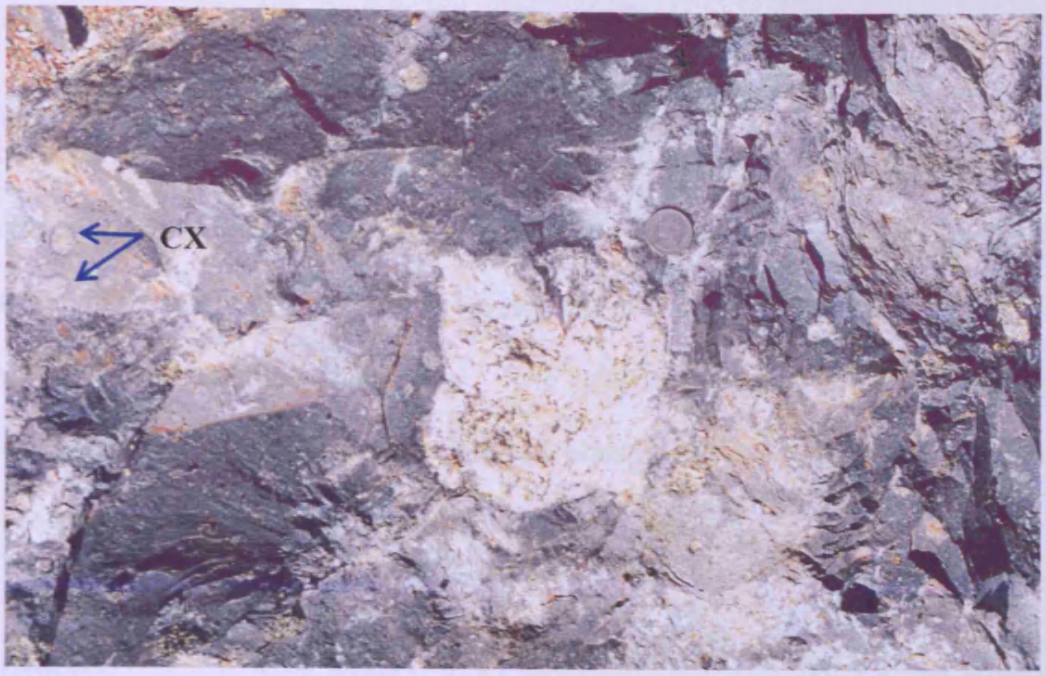

Figure 6.4 Photograph shows a large felsic-rich crustal xenolith (white) in the middle and crustal xenoliths (CX) with distinctive greyish-green reaction rim against the basalt.

Figure 6.5 Photograph shows a basalt outcrop with a group of large mantle xenoliths (MX). Note that the dark reddish brown weathered surface was peeled of from the road cutting process.

Microscopically, the Bo Ploi basalt displays petrographic variations, which mainly result from recrystallisation and the degree of alteration. It is holocrystalline to hypocrystalline and porphyritic. The basalt carried various species of mantle and crustal materials, therefore, there are several complicated textures present and extra precaution on interpretation is essential. The mineral constituents of Bo Ploi basalt were categorised and identified as groundmass, phenocrysts, amygdale minerals, crustal xenoliths and mantle xenoliths.

Groundmass

The groundmass is principally composed of plagioclase laths, clinopyroxene, augite, magnetite granules and brownish patches of glasses and devitrified glasses. Additionally, sanidine and anorthoclase, analcite and calcite were observed as minor components. The major mineral constituents, plagioclase and augite, form seriate texture with sub-parallel alignment manner. ***Plagioclase*** displays euhedral to subhedral crystals, where lath-shaped is common. Repeated albite twinning is most common for groundmass plagioclase. Occasionally, combined albite-pericline twinning, which exhibits cross-hatch pattern, is observed. Some grains of plagioclase groundmass were optically determined for their An-content and it is in the range of $An_{25} - An_{40}$, therefore, the composition of plagioclase is quite evolved and ranges from oligoclase to andesine. ***Augite*** is subhedral to anhedral and exhibits a wide range of crystal forms including needle-like, prismatic, bladed and equidimensional forms. The crystals dimension is < 0.3 mm. Augite sometimes exhibits subophitic texture. ***Magnetite*** is readily identified by its opaque euhedral square section and silver grey colour under reflected light. It is scattered throughout the rocks with size range from 0.02 to 0.3 mm.

Phenocrysts

Bo Ploi basalt has two distinguish generations of phenocrysts. They are identified as megacrysts for crystals that larger than 5 mm in diameters and as phenocrysts for grains that smaller than 5 mm in diameter. The phenocrysts are dominated by olivine, clinopyroxene (augite), spinel and sanidine, respectively.

Olivine megacrysts are usually not larger than 1.2 cm in diameter. They possess subhedral to anhedral short prismatic rounded crystals with characteristic fractures. The brownish staining along the fractures is common identified as iddingsite and serpentine alteration. Some olivine grains were suspected as xenocrysts disintegrated from mantle peridotites. Olivine phenocrysts exhibit varieties of crystal shapes, where the common forms range from typical euhedral olivine crystal, rounded subhedral short prismatic crystals, rounded triangular shaped. Skeletal olivine is occasionally seen. Most of olivine grains show marginal zoning, where higher birefringence is observed at the rim of crystal surrounding the lower birefringence in the core. The higher birefringence area indicates richer iron content. Grain boundaries of olivine habitually display sieve texture, concurrent with the intergrowth of feldspar and opaque minerals from the groundmass. Trails of complicated fluid inclusions and melt inclusions were observed in some large olivine grains. Photomicrographs of olivine phenocrysts are illustrated in figure 6.6-6.7.

Clinopyroxene megacrysts are brown and slightly reddish brown. They occur as large single crystals from 5 mm to 40 mm in size. The common forms of clinopyroxene megacrysts are stubby and short prismatic forms. Clinopyroxene phenocrysts are euhedral to anhedral crystals. They display eight-sided shape on crossed sections. The rectangular shape on long sections is also often observed. The other common forms are bladed and lamellar shaped, nonetheless, rounded subhedral crystals are also found. Simple twin and marginal zoning are frequently observed. Augite occasionally exhibits

(a)

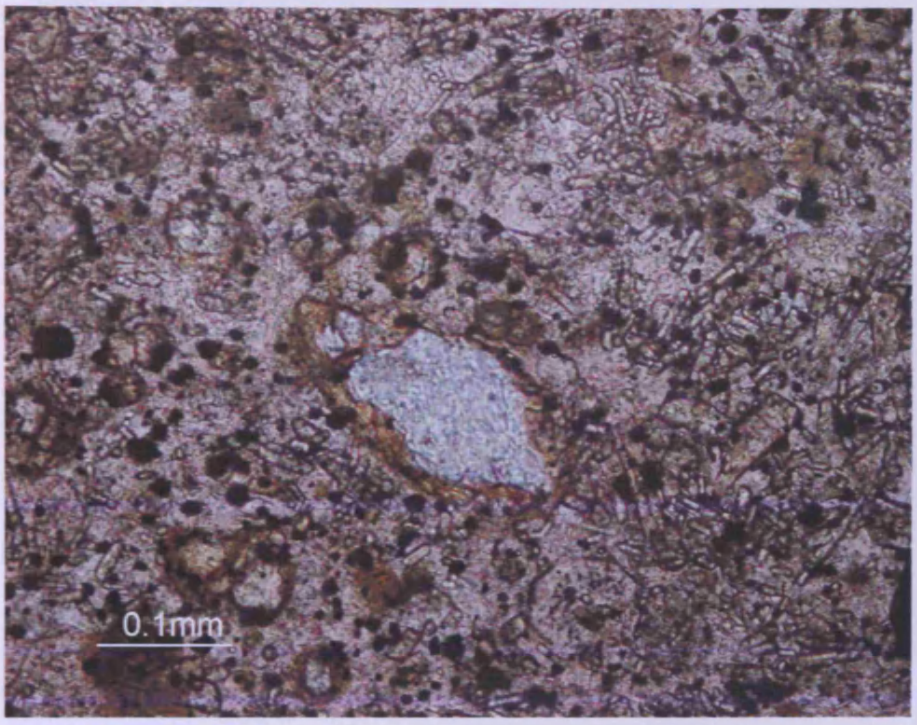

(b)

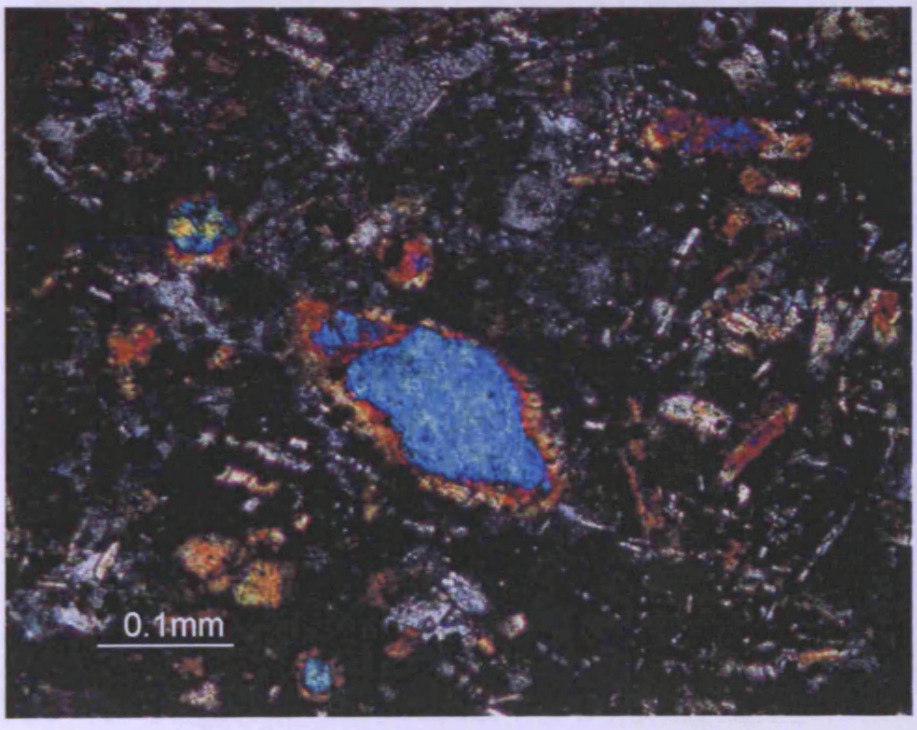

Figure 6.6 Photomicrographs show marginal alteration in anhedral olivine phenocryst within a matrix dominated by plagioclase and clinopyroxene (a) plane polarized light (b) cross polarized light

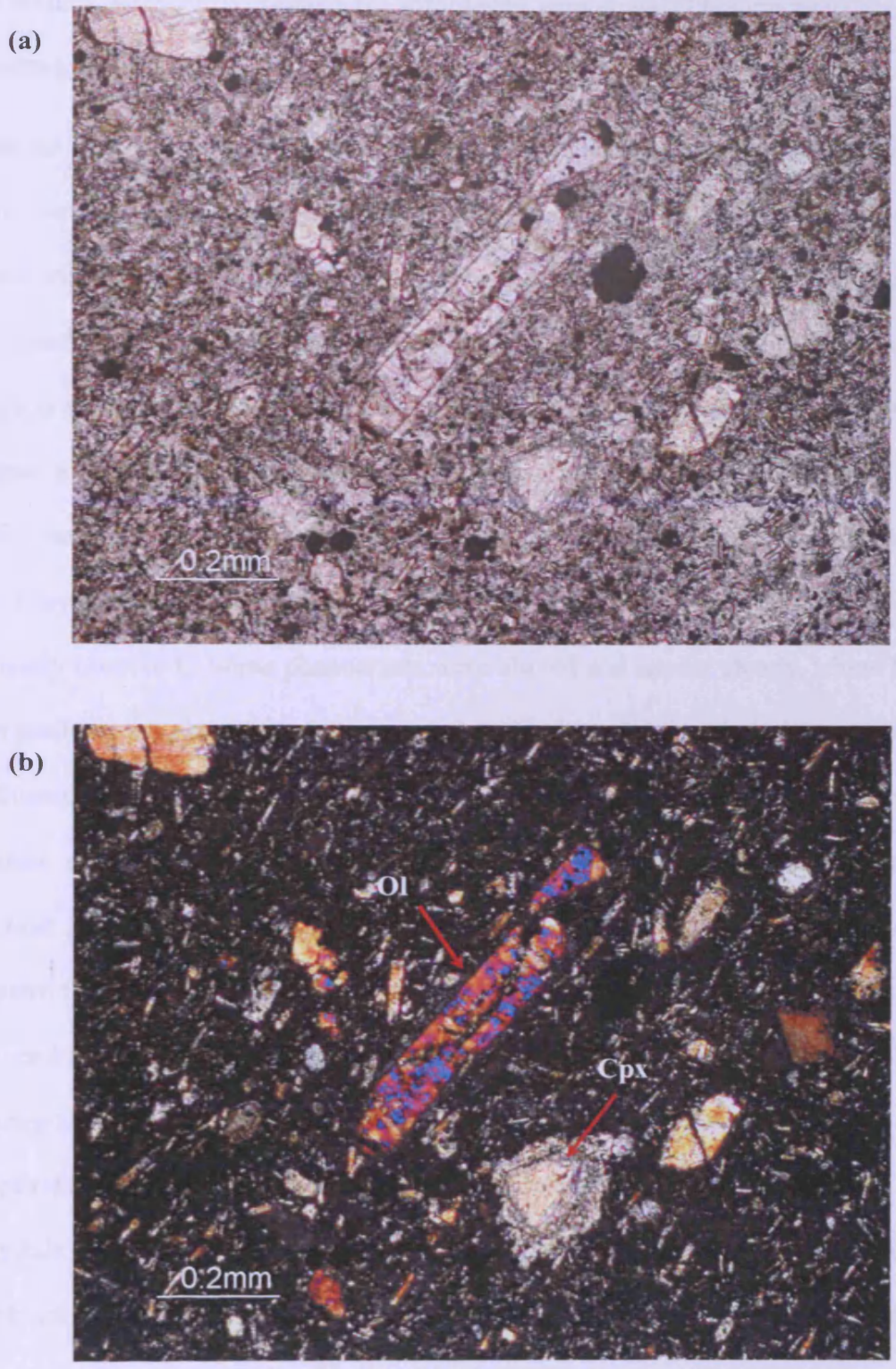

Figure 6.7 Photomicrographs show embayed texture of elongated olivine (Ol) phenocryst and subhedral spongy rimmed clinopyroxene (Cpx) in a felty texture groundmass. (a) plane polarized light (b) cross polarized light

a corona texture, where it is rimmed by hornblende amphibole. Photomicrographs of clinopyroxene phenocrysts are illustrated in Figure 6.8 - 6.13.

Alkali feldspar megacrysts are subhedral to anhedral forms. In some hand specimens, *sanidine* can be as large as 5 cm. They are colourless, transparent to sub-transparent, vitreous lustre or rarely with pearly lustre. Its two sets of cleavages are clearly noticed. The smaller megacrysts are generally 0.5 to 10.0 mm in dimension. The common form is elongate rounded bladed-shape. Crystals often display twinning. The degree of alteration on sanidine megacrysts is lower than the alteration on comparable sanidine phenocrysts. Sanidine phenocrysts are subhedral to anhedral crystals. They show rounded prismatic to near equidimensional crystals. Simple twins are commonly observed. Some phenocrysts were altered and appear cloudy, where the alteration products are clay minerals, e.g. sericite. Small scale of perthitic intergrowths were additionally seen on some grains. Similar to other phenocrysts, sanidine illustrates sieve texture along its grain boundary indicating resorption with host alkali basalt. *Anorthoclase* phenocrysts are rare, but subhedral crystals can be identified by their tartan-pattern twin. This subordinate constituent is believed to be a component of alkali feldspar end-member progressing from high albite towards sanidine. The photomicrographs of alkali feldspar phenocrysts are illustrated in figure 6.14-6.16.

Spinel is found only as megacrysts. Ifz sizes range from 0.5 mm to 3.0 cm. The rough crystals in hand specimens are euhedral octahedral spinel or partly fragmented. They are black, with vitreous lustre and conchoidal fracture. Under microscopic study, they appear dark brown to black subhedral to anhedral isotropic crystals. The common shape of spinel is rounded droplet-shape to amoeboid-shape. Photomicrographs of spinel are illustrated in figure 6.17.

(a)

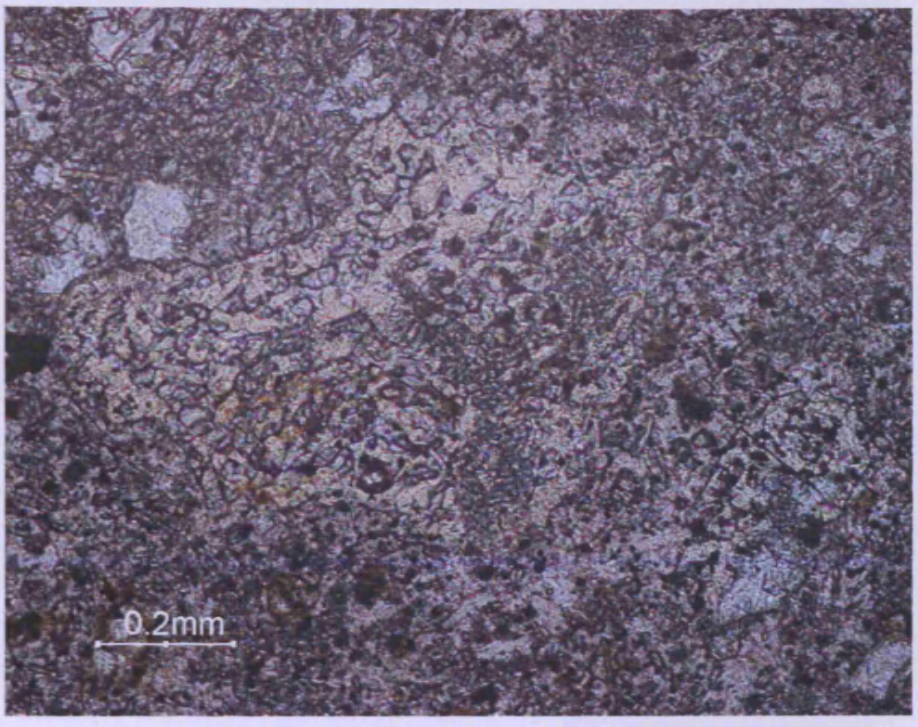

(b)

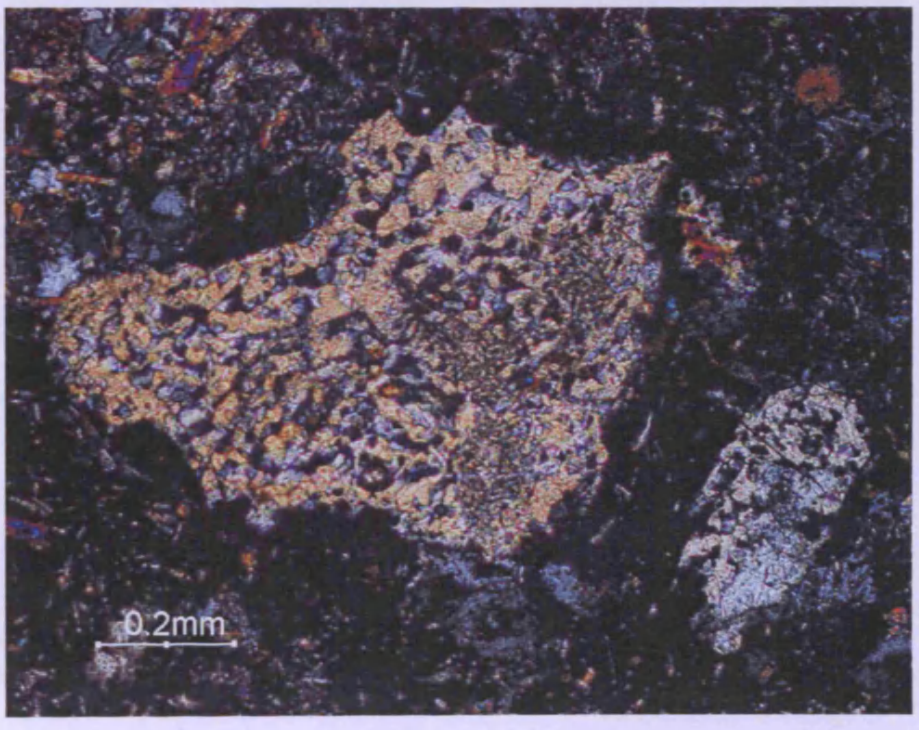

Figure 6.8 Photomicrographs show euhedral and anhedral pyroxene grains with sieve-texture. (a) plane polarized light (b) cross polarized light

(a)

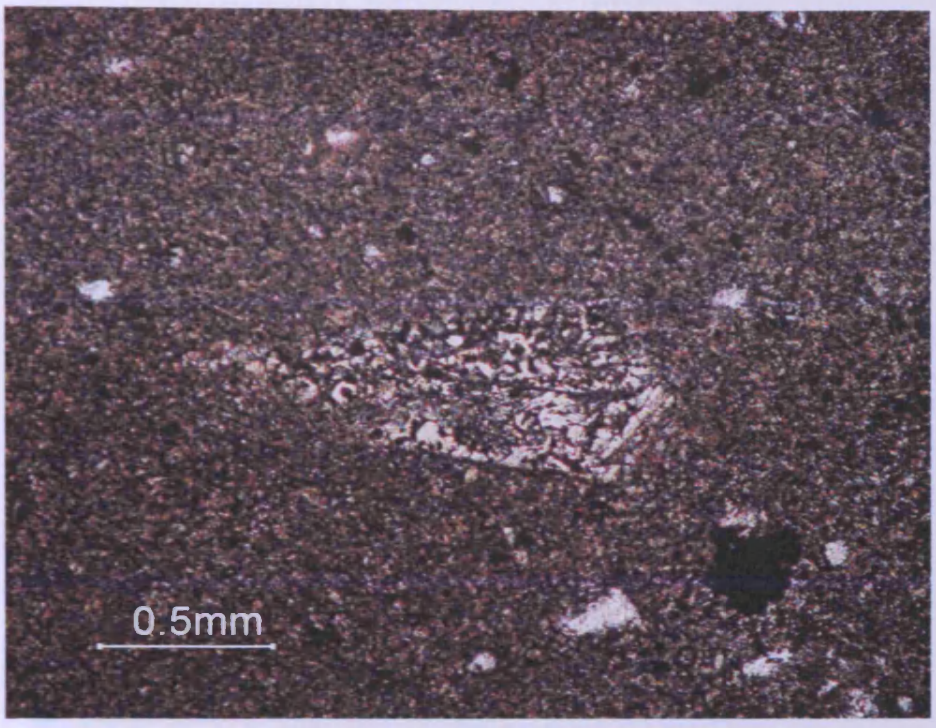

(b)

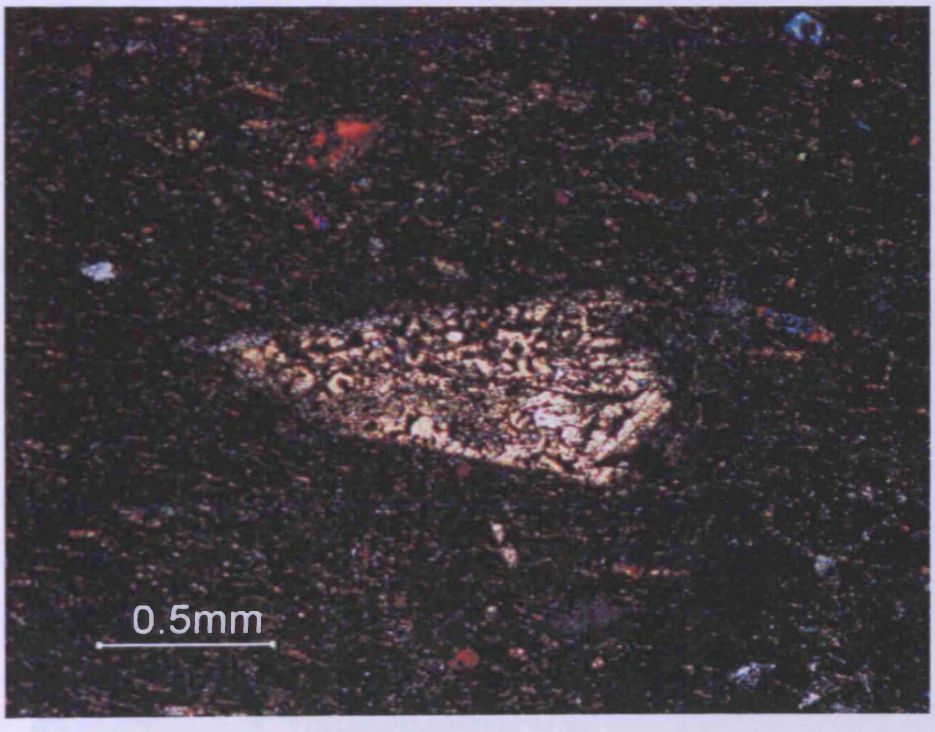

Figure 6.9 Photomicrographs show subhedral clinopyroxene crystal with sieve-texture.

(a) plane polarized light (b) cross polarized light

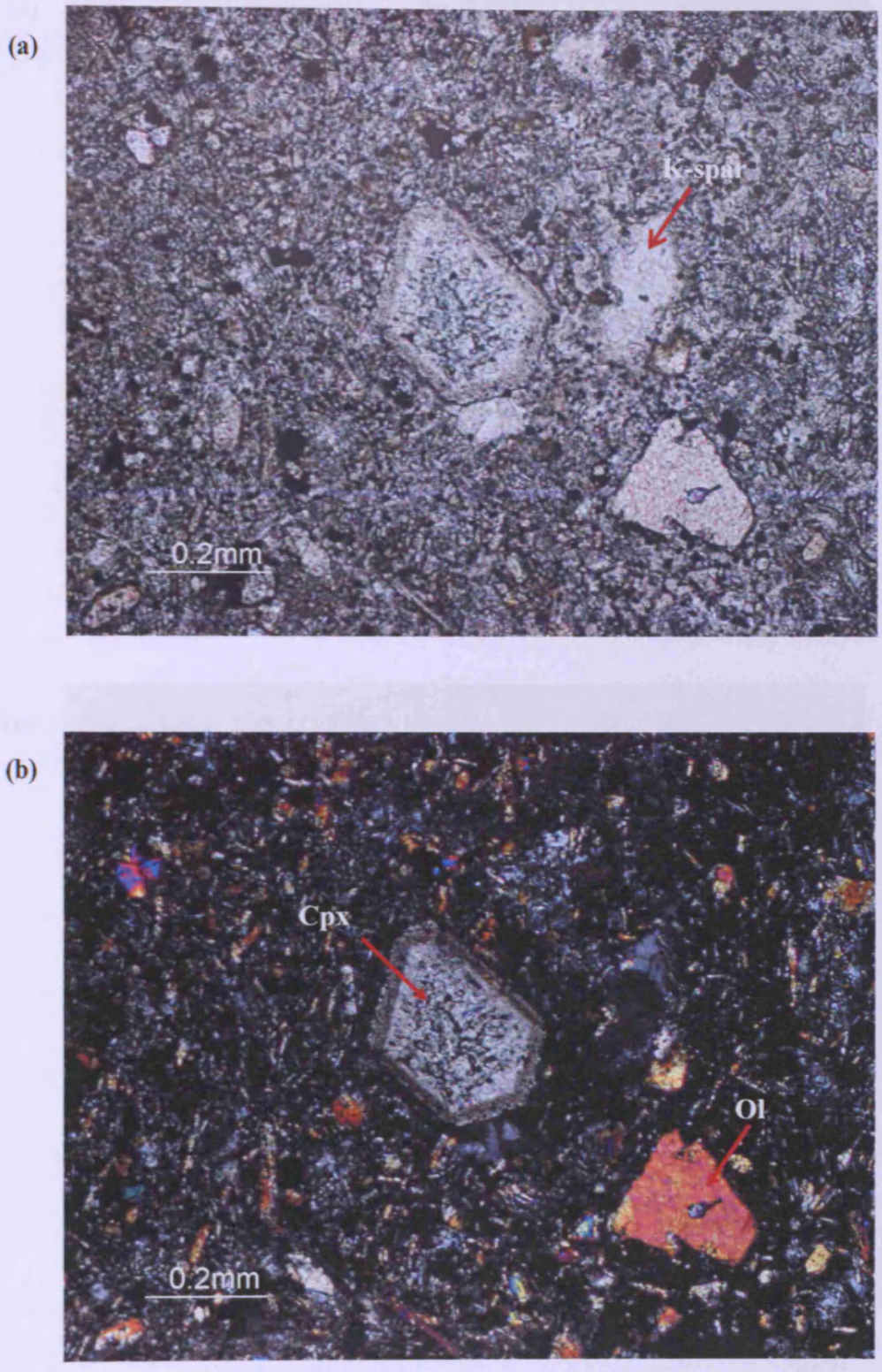

Figure 6.10 Photomicrographs show euhedral corona pyroxene (Cpx), anhedral sanidine (K-spar) and subhedral olivine (Ol) phenocrysts in a sub-ophitic texture. (a) plane polarized light (b) cross polarized light

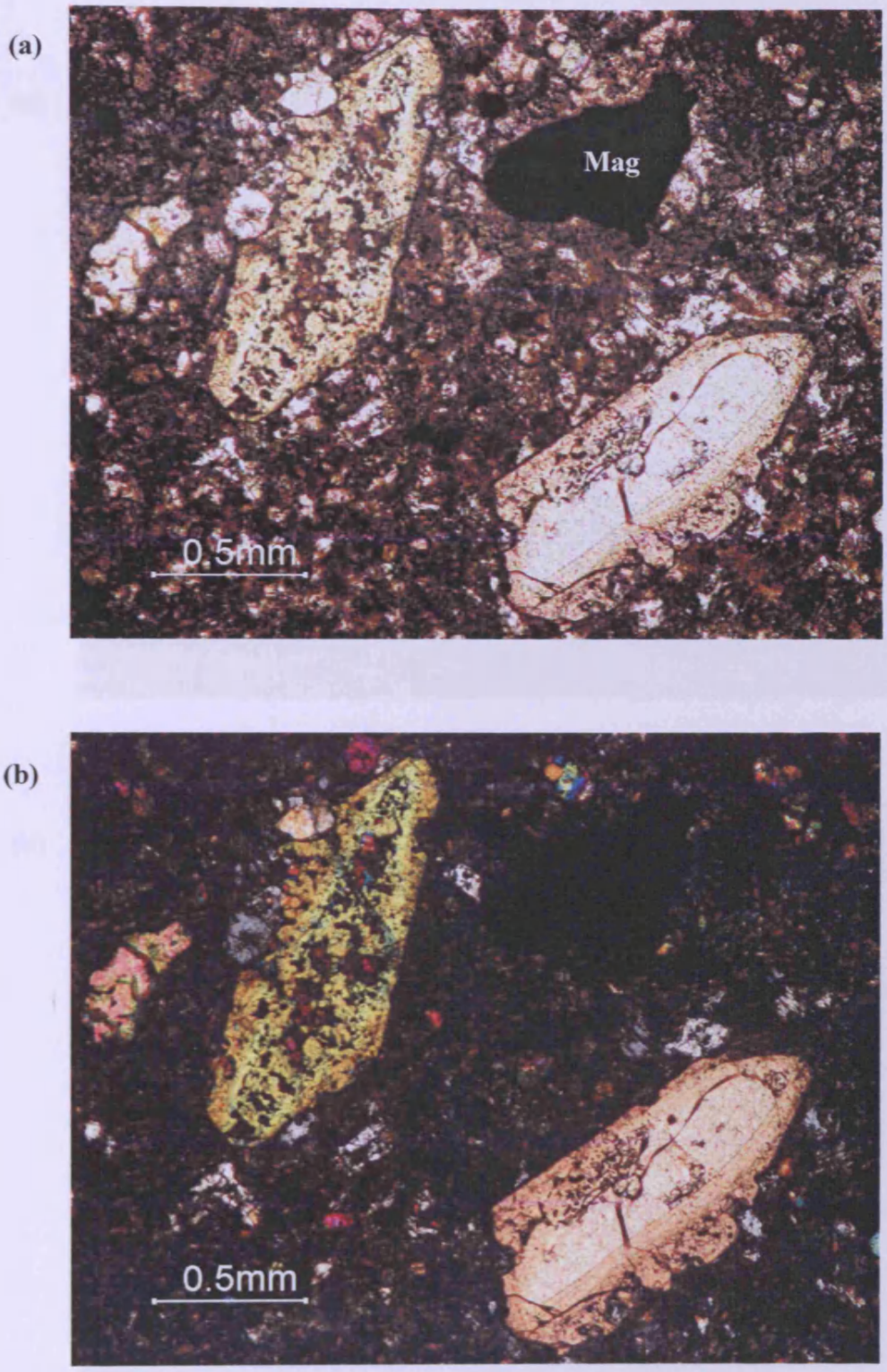

Figure 6.11 Photomicrographs of euhedral clinopyroxene crystals that exhibit zonal pattern with porous resorbed grain boundaries. The opaque minerals marked (Mag) is magnetite aggregate. (a) plane polarized light (b) cross polarized light

(a)

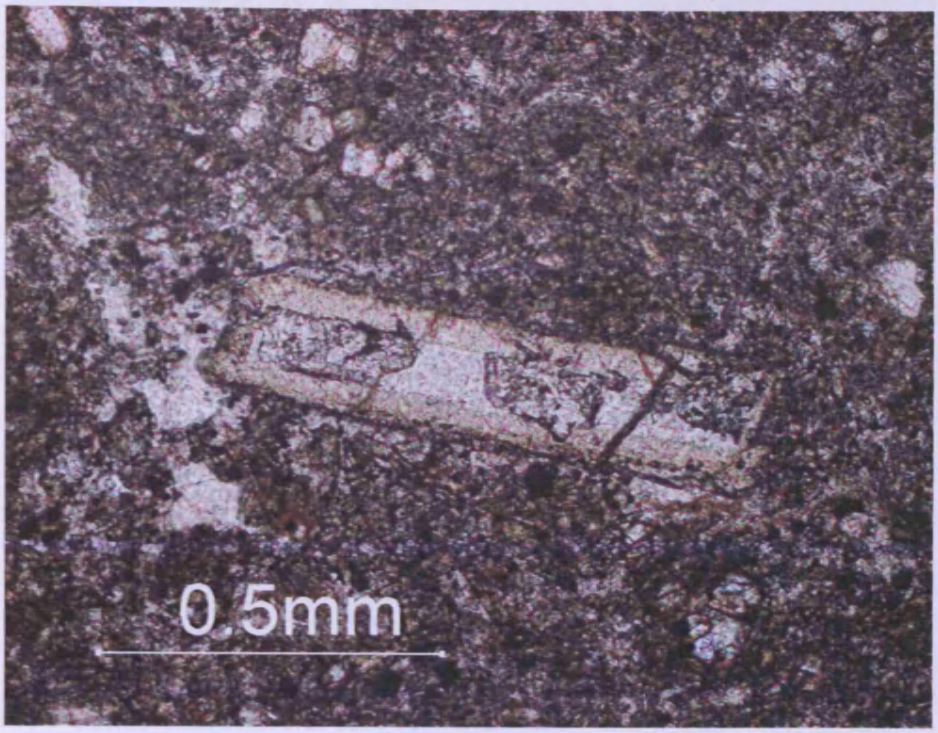

(b)

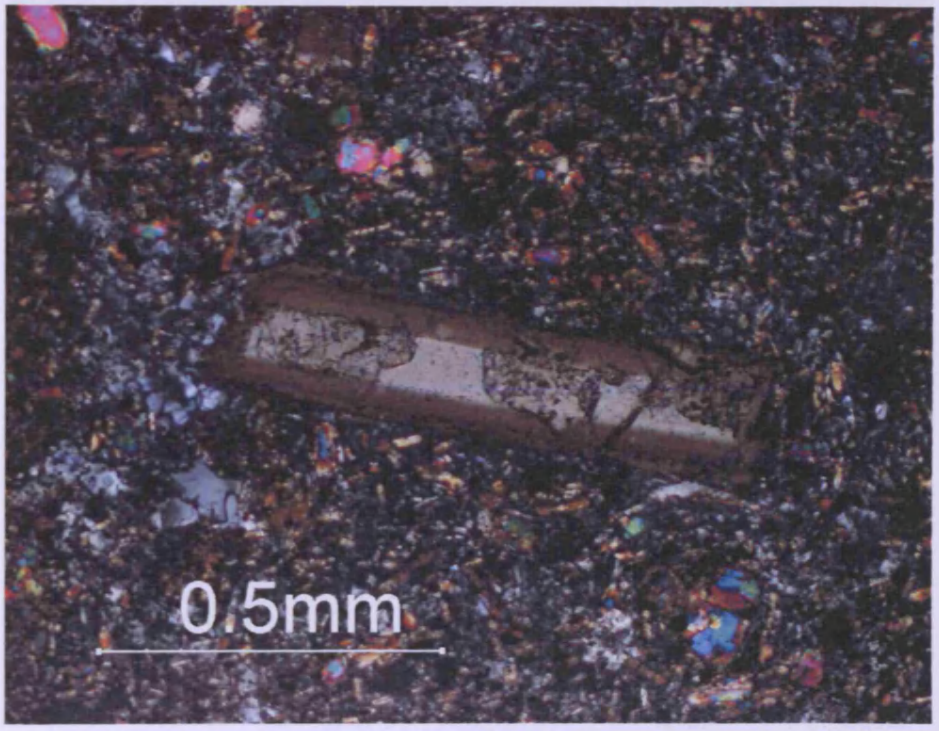

Figure 6.12 Photomicrographs of a zoned euhedral clinopyroxene megacryst that also shows partial-sieve texture.

(a) plane polarized light (b) cross polarized light

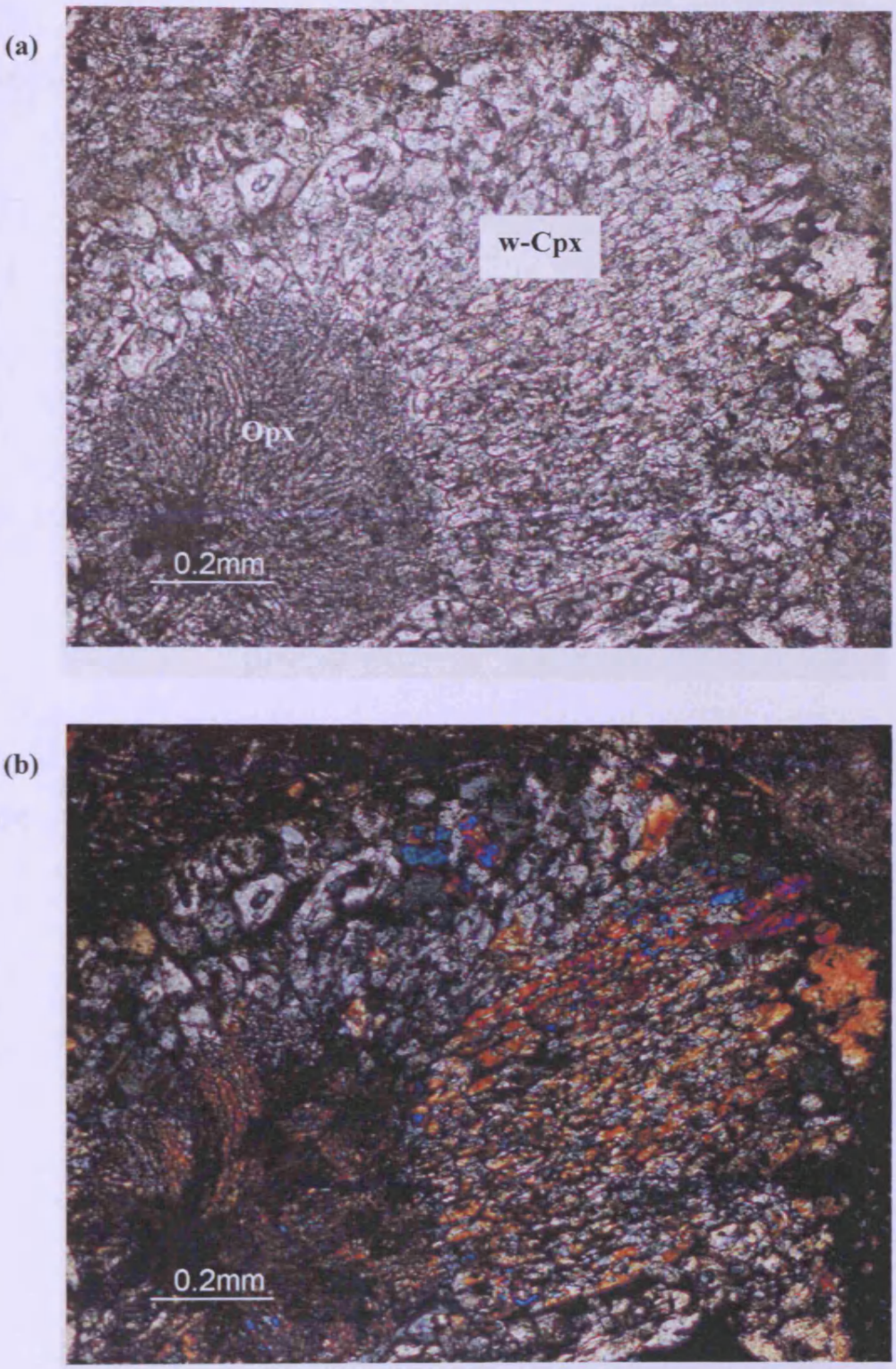

Figure 6.13 Photomicrographs show anhedral vermicular clinopyroxene and plagioclase intergrowth (w-Cpx) forming reaction rim surrounding vermicular orthopyroxene crystal (Opx), which is probable a xenocryst. (a) plane polarized light (b) cross polarized light

(a)

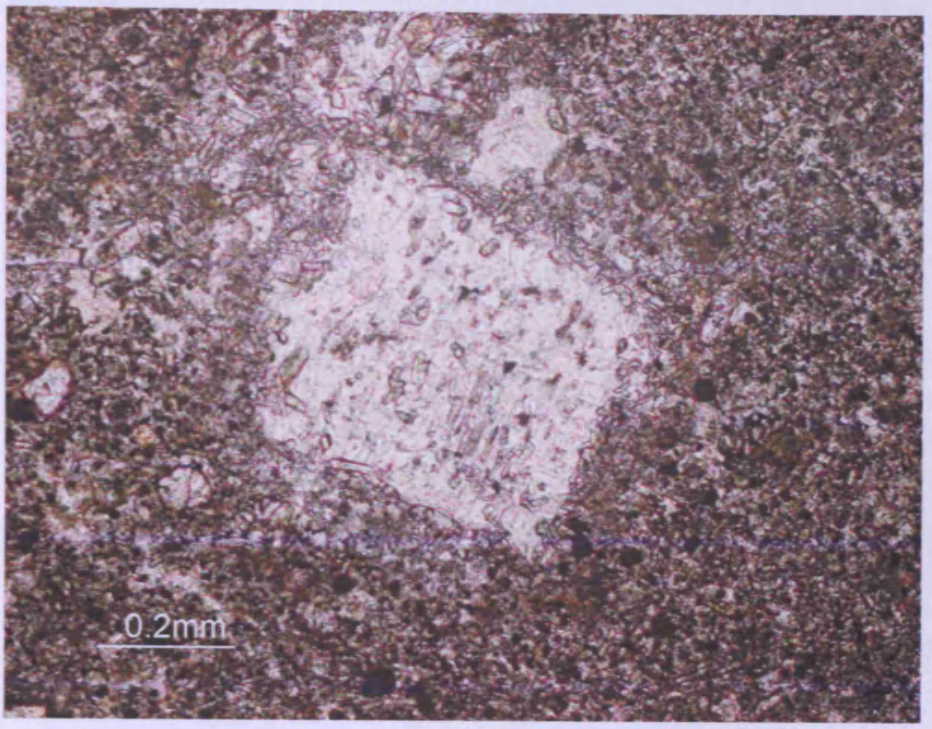

(b)

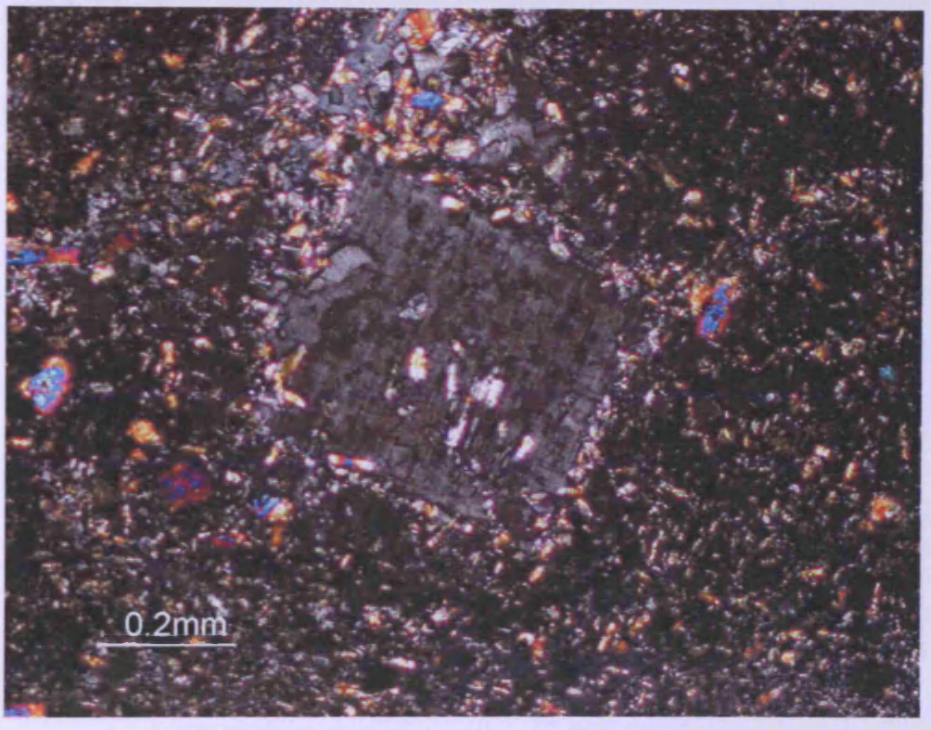

Figure 6.14 Photomicrographs show euhedral microcline with tartan twin that is rimmed by higher birefringence grains of pyroxene.

(a) plane polarized light (b) cross polarized light

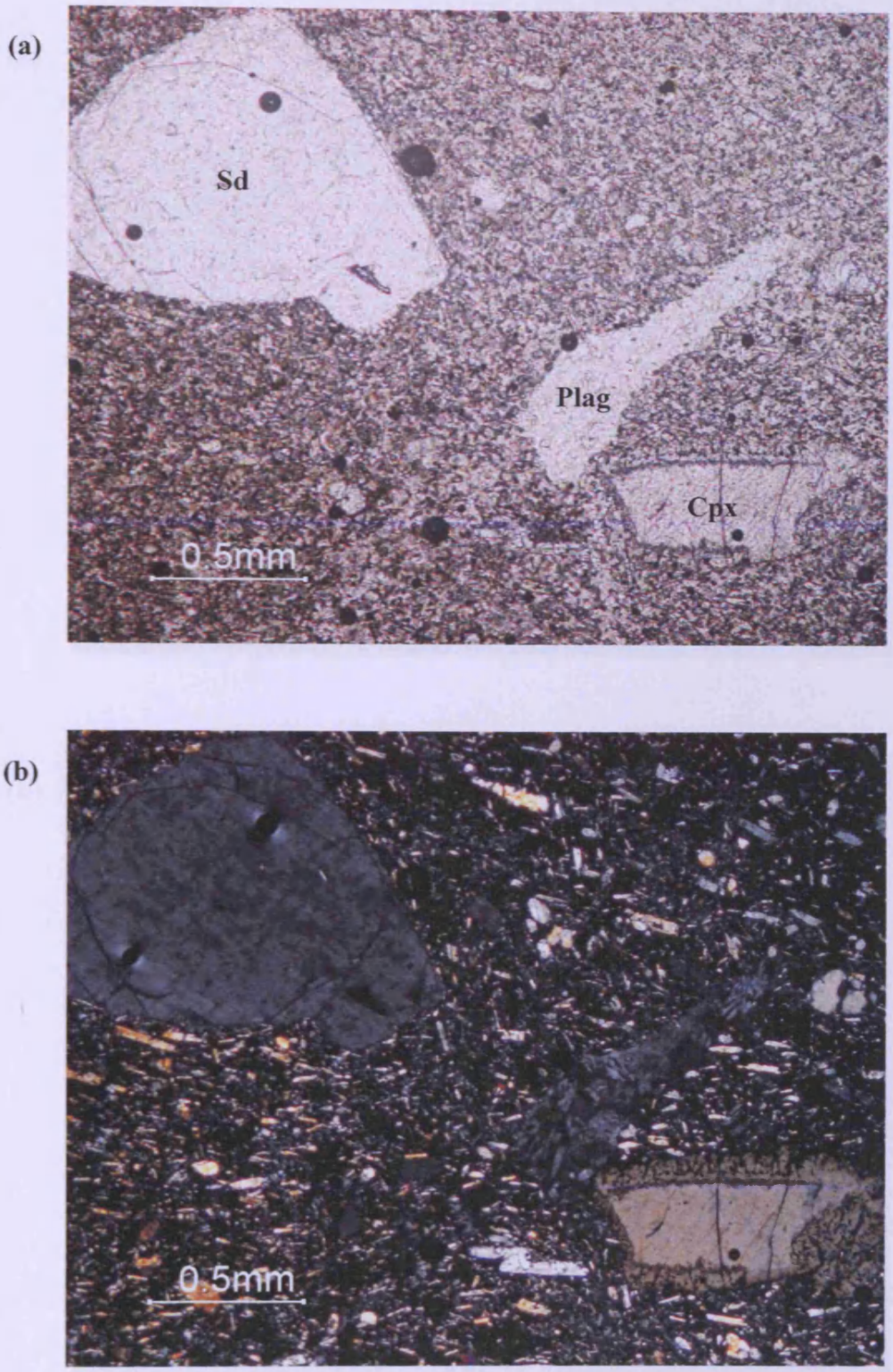

Figure 6.15 Photomicrographs of a subhedral sanidine (Sd) phenocryst, a porous (sieve) grain boundary clinopyroxene (Cpx) and a "vug" of plagioclase (Plag) in a matrix of sub-ophitic flow-aligned preferred orientation matrix.

(a) plane polarized light (b) cross polarized light

(a)

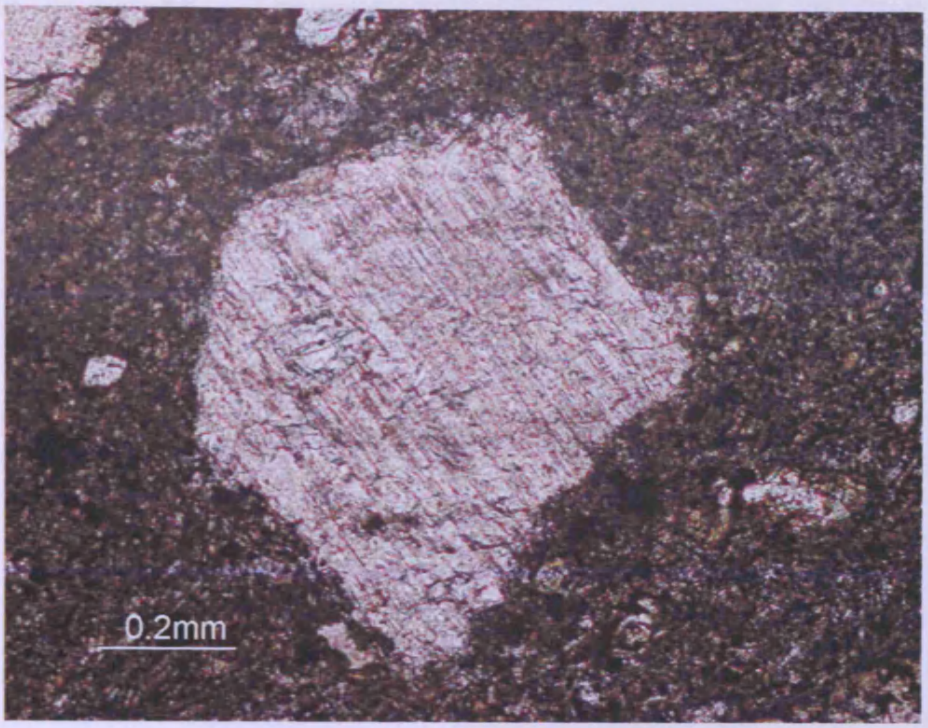

(b)

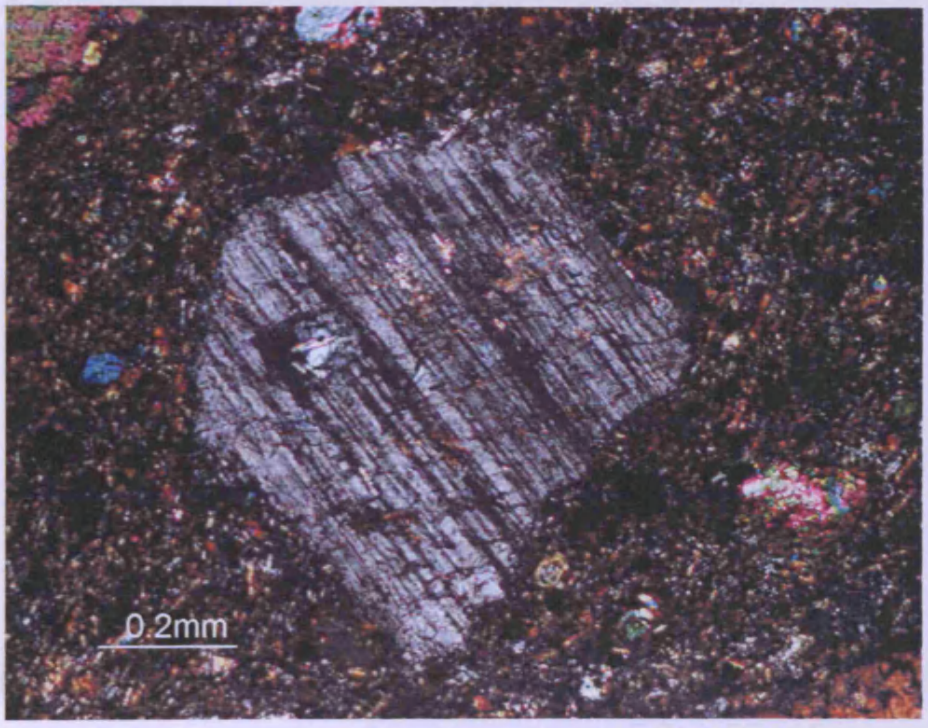

Figure 6.16 Photomicrographs show a euhedral plagioclase phenocrysts slightly altered to clay mineral or sericite.

(a) plane polarized light (b) cross polarized light

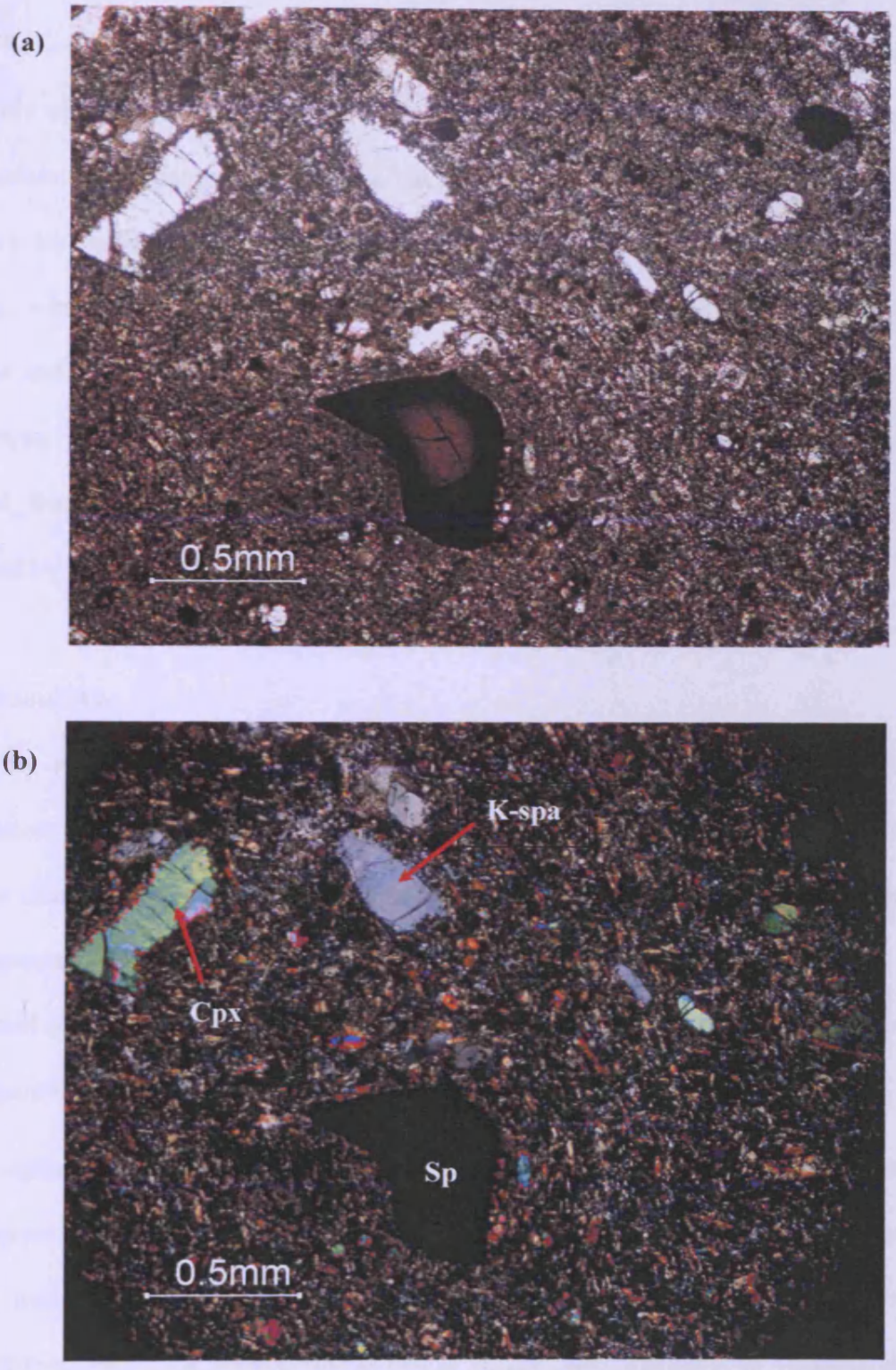

Figure 6.17 Photomicrographs show dark yellowish brown anhedral spinel phenocryst with marginal zone pattern. Clinopyroxene (Cpx) and alkali feldspar (K-spa) crystals with typical resorbed rim are at the top left corner.
(a) plane polarized light (b) cross polarized light

Amygdale minerals

The veins and veinlets in Bo Ploi basalt are filled by secondary minerals, which were solely optically identified as calcite, dolomite, tridymite and analcime. Calcite partly associated with dolomite formed a cavity filled texture. It is common for calcite and dolomite to exhibit perfect rhombohedral cleavages and tabulated multiple twinning, where twin lamellae may parallel to or bisect the rhombic cleavages. Analcime and perhaps other zeolite minerals formed patches of isotropic minerals in vein cavities. Sometimes the boundaries of analcime-filled veins cannot be distinctively identified from minerals extending from the groundmass. Tridymite is readily recognised by its wedge-shaped twinned crystals and its low relief.

Crustal xenoliths

The quenched texture rimming the crustal nodules probably resulted from solidification after partial melting of crustal rocks during the ascent of basalt to the surface is characteristic of crustal xenoliths. The entrained crustal xenoliths are lower crustal igneous rocks and metamorphic rocks. These rocks were later re-classified as fine-grained nepheline syenite, which was previously reported as diabase (Yaemniyom, 1982), granitic rocks and quartzite.

Coarse-grained nepheline syenite or malignite: the rock is porphyritic texture and composed of mainly nepheline and alkali feldspar with small amounts of mafic minerals including pyroxene and/or amphibole and opaque minerals. Nepheline displays distinct prismatic section that is nearly square, although lamellar shape is also common. Most square sections of nepheline contain dark, fine inclusions that radiate from the middle toward the corners of the crystals. Nepheline and alkali feldspar intergrowths are fairly common, particularly on smaller crystals. Alkali feldspar exhibits lath-shaped or sometimes more elongate crystals. Pyroxene is interpreted as

aegirine-augite according to its distinctive green to yellowish green pleochroism and very high relief. They are euhedral to subhedral equant crystals. The nepheline syenite nodules are essentially rimmed by layers of green pyroxene and possibly include amphibole and/or chlorite alteration as a reaction rim with the host alkali basalt. Typical photomicrographs of nepheline syenite crustal xenoliths are shown in Figure 6.18-6.22.

Granitic rocks: granitic xenoliths tend to be larger in size compared to other crustal xenoliths. They are slightly porphyritic to equigranular in texture. The mineral constituents are quartz, alkali feldspar, plagioclase and mafic minerals. Quartz is readily identified by its interlocking grain boundaries of low interference colour and the undulose extinction. Secondary quartz also occurs as intergrown crystals with larger grain minerals are also observed and believed to be a result from partial melting. Feldspar crystals are usually heavily altered with cloudy appearance and can be recognised by their twinning. The mafic minerals are chiefly amphibole and occasionally a mica remnant is found. They exhibit various degree of alteration to chlorite group minerals that can be clearly seen as brownish green or brownish yellow along the perfect cleavages. Melting texture is, again, very common and is associated with yellowish-brown to dark-brown interstitial. Spinifex texture of devitrified crystals is commonly noticed in these glass pools (Fig. 6.23-6.24).

Quartzite (?): These quartz-feldspar rich xenoliths are composed almost entirely of quartz with minor amounts of feldspar with mildly porphyritic to granoblastic textures. Relatively large patches of interstial glass with its devitrication products are commonly observed, which many of these glass sags connected to each other and appear as an alternating series of darker and lighter band.

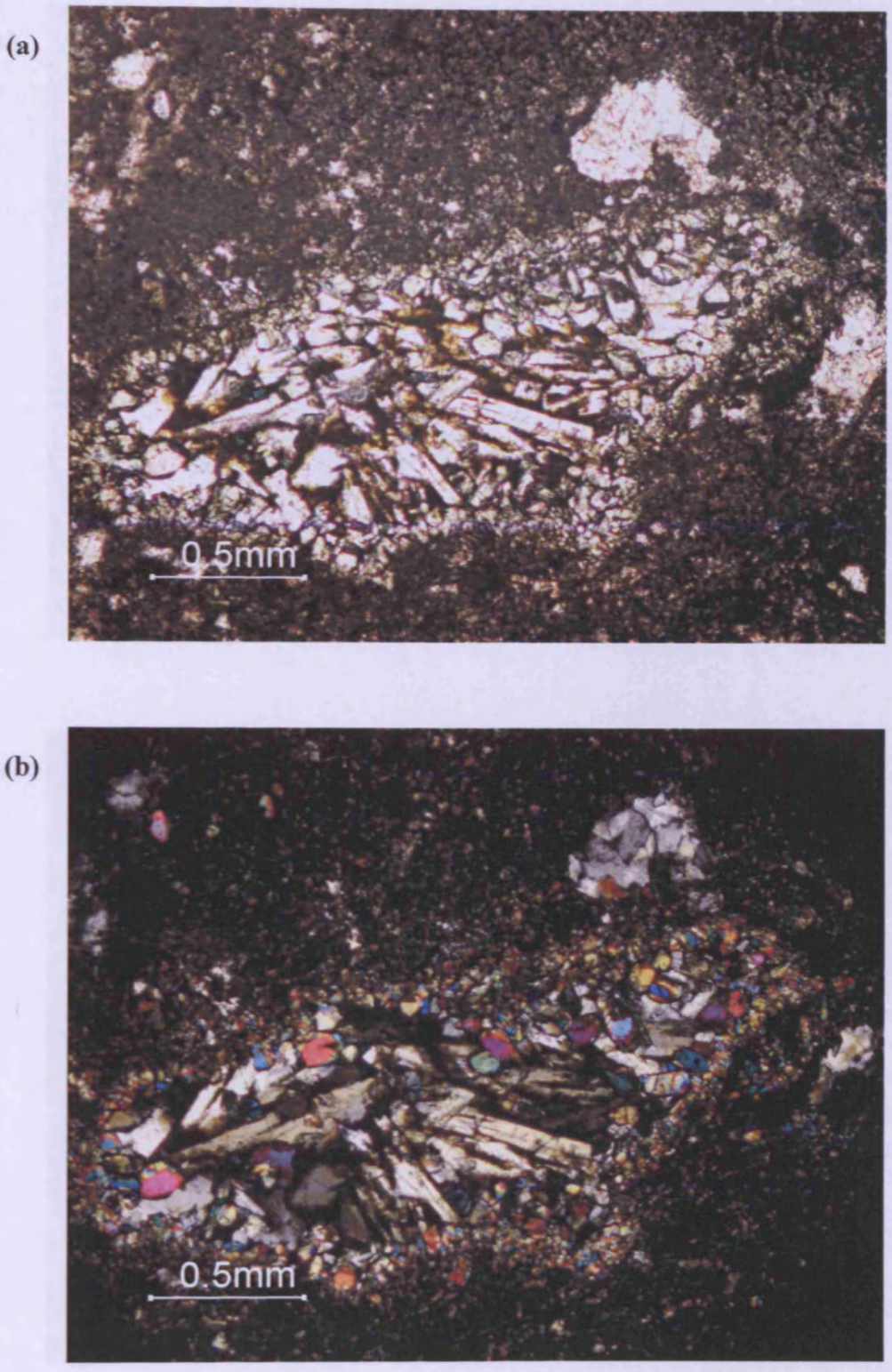

Figure 6.18 Photomicrographs show crustal nodule of nepheline syenite composition. The distinctive reaction rim with the host basalt is defined by layers of equant pyroxene crystals.

(a) plane polarized light (b) cross polarized light

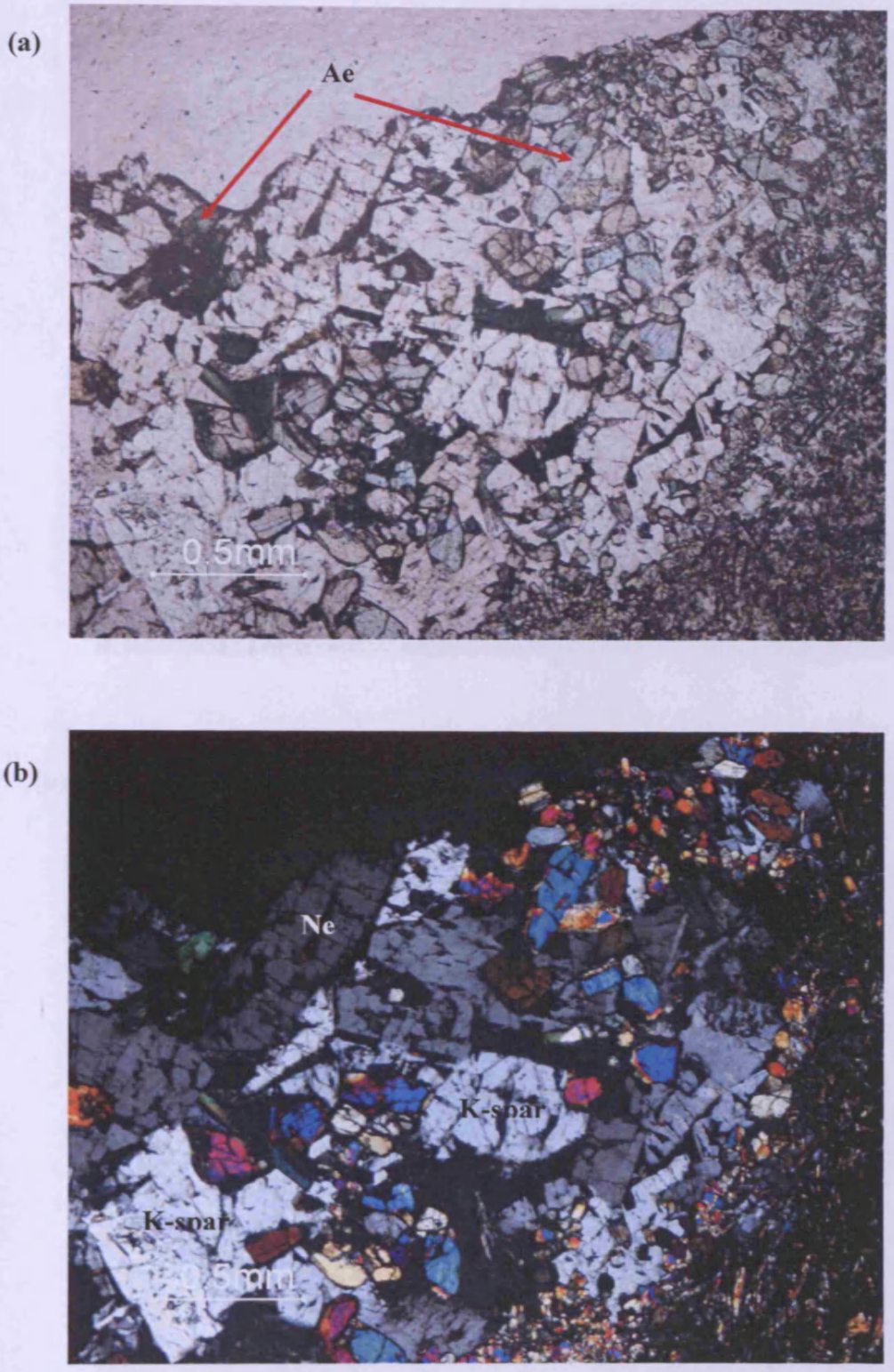

Figure 6.19 Photomicrographs of malignite xenolith shows subhedral to equant green clinopyroxene (Ae) crystals disseminated in the matrix of nepheline (Ne) and alkali feldspar (K-spar).

(a) plane polarized light (b) cross polarized light

(a)

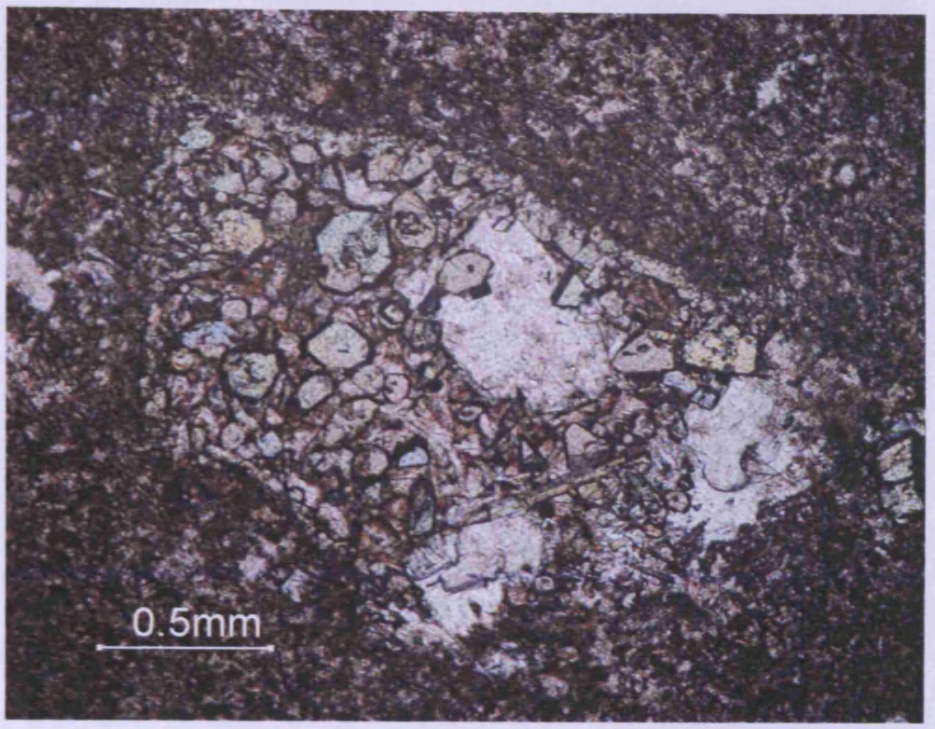

(b)

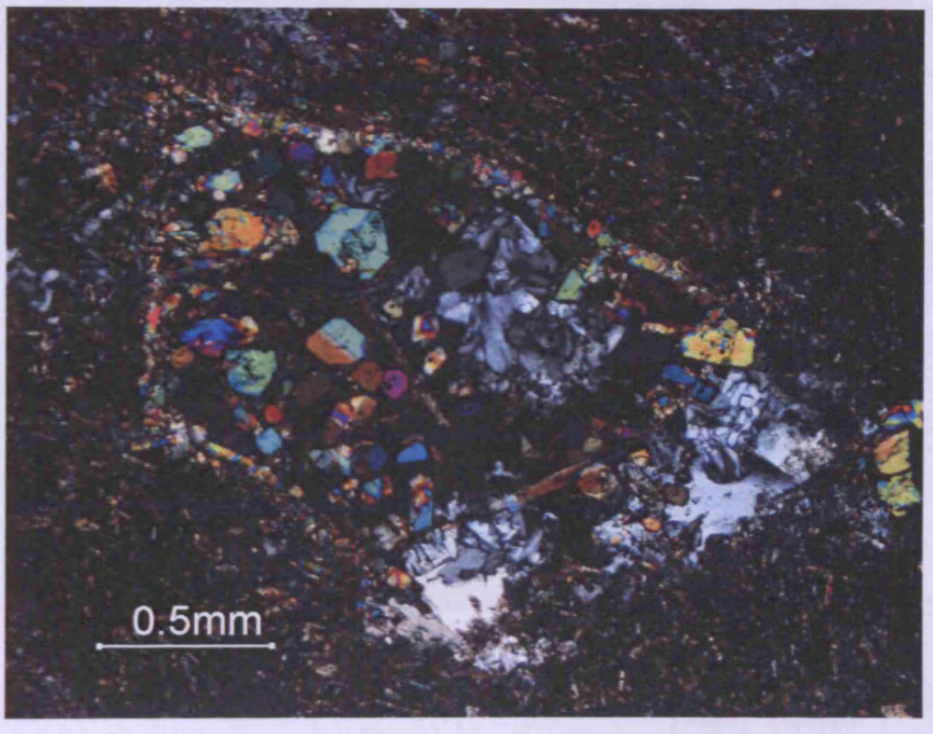

Figure 6.20 Photomicrographs of nepheline syenite xenolith shows euhedral equant green clinopyroxene crystals disseminated in the matrix of greyish nepheline and alkali feldspar. The ovoid vugs are filled with tridymite-cristobalite. (a) plane polarized light (b) cross polarized light

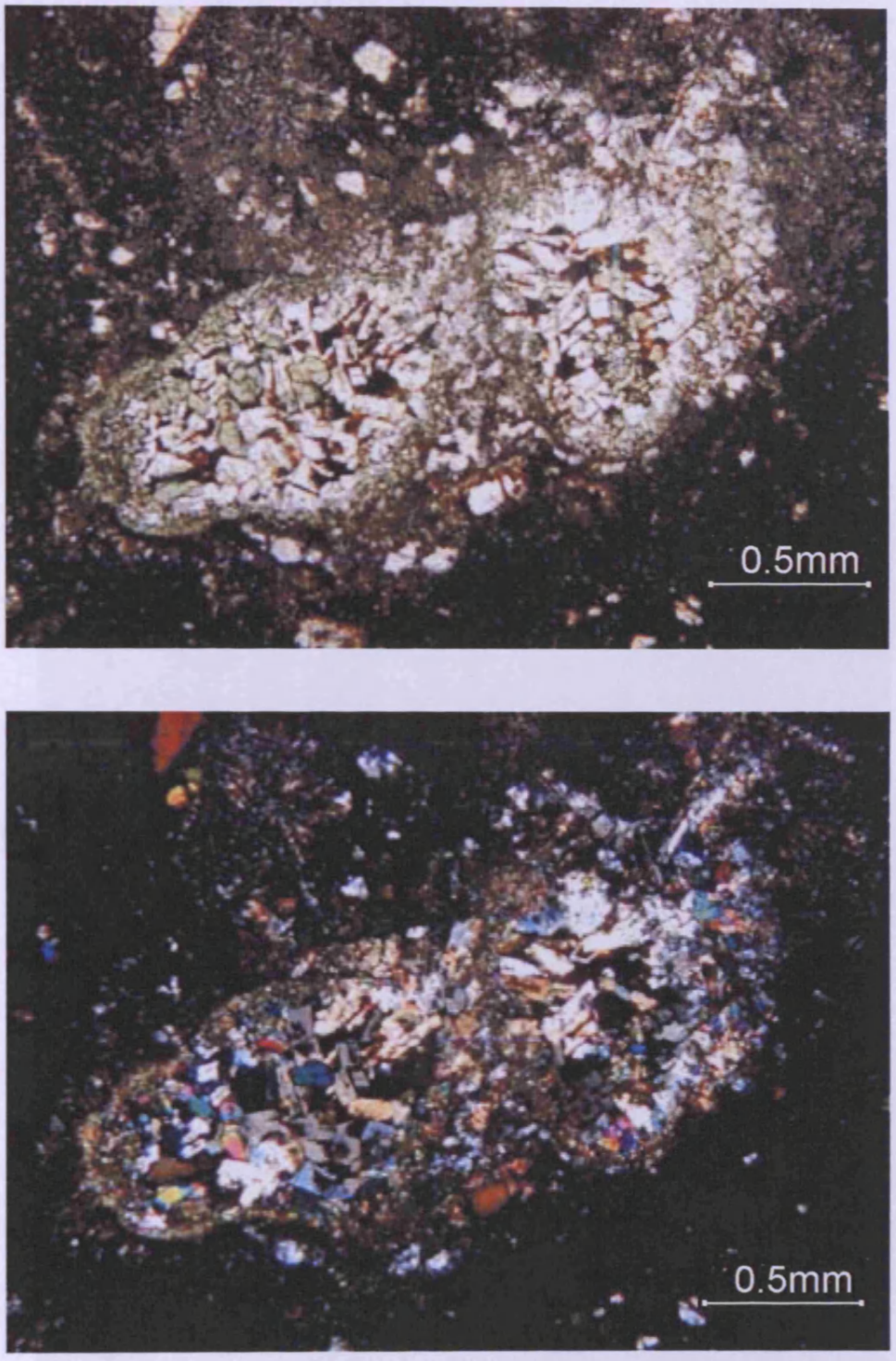

Figure 6.21 Photomicrographs of composite nepheline syenite xenoliths show euhedral equant green clinopyroxene crystals disseminated in the matrix of nepheline and alkali feldspar. The brownish green of pyroxene layers marked a distinctive boundary of the xenolith. (a) plane polarized light (b) cross polarized light

(a)

(b)

Figure 6.22 Photomicrographs of spheroid nepheline syenite xenolith show euhedral equant green clinopyroxene crystals in the matrix of euhedral-subhedral prismatic nepheline and alkali feldspar.

(a) plane polarized light (b) cross polarized light

(a)

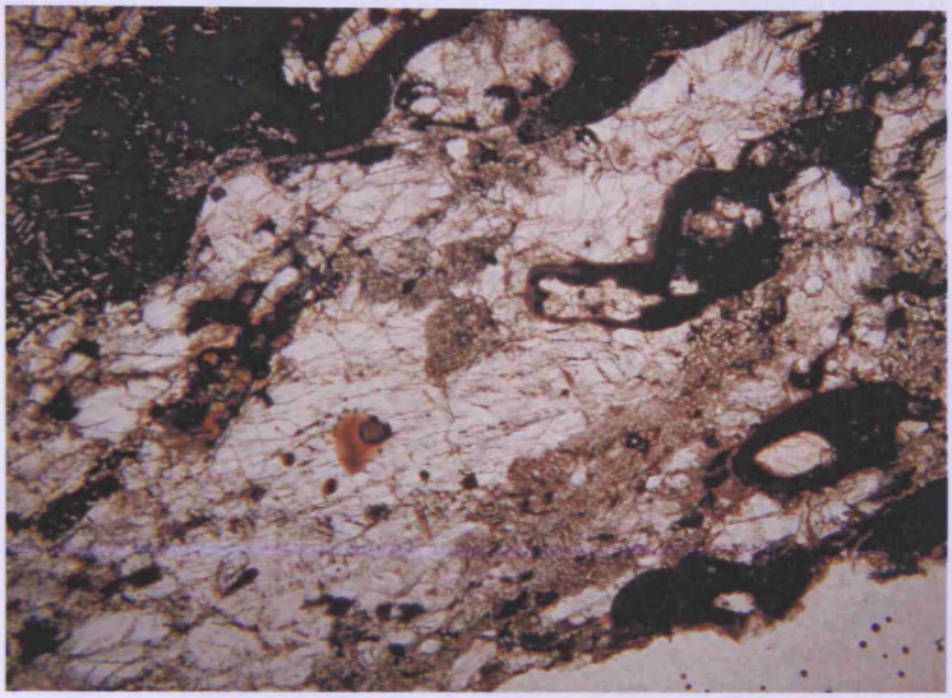

(b)

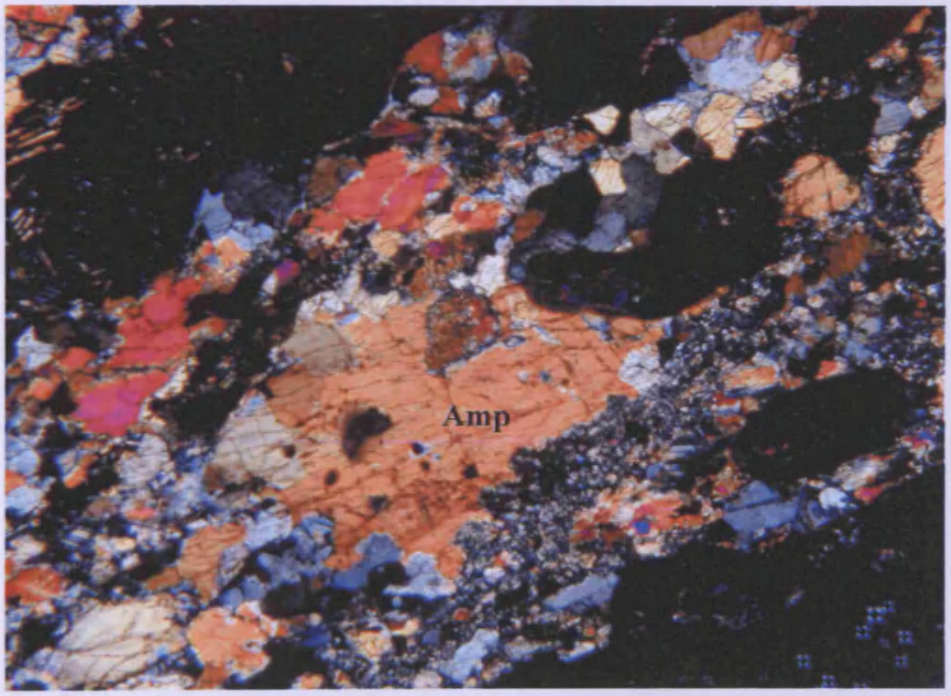

Figure 6.23 Photomicrographs of granitic xenolith shows partially melted texture with brownish patches of glass invaded from grain interfaces inward. Large amphibole (Amp) contains zircon halo.

(a) plane polarized light (b) cross polarized light

(a)

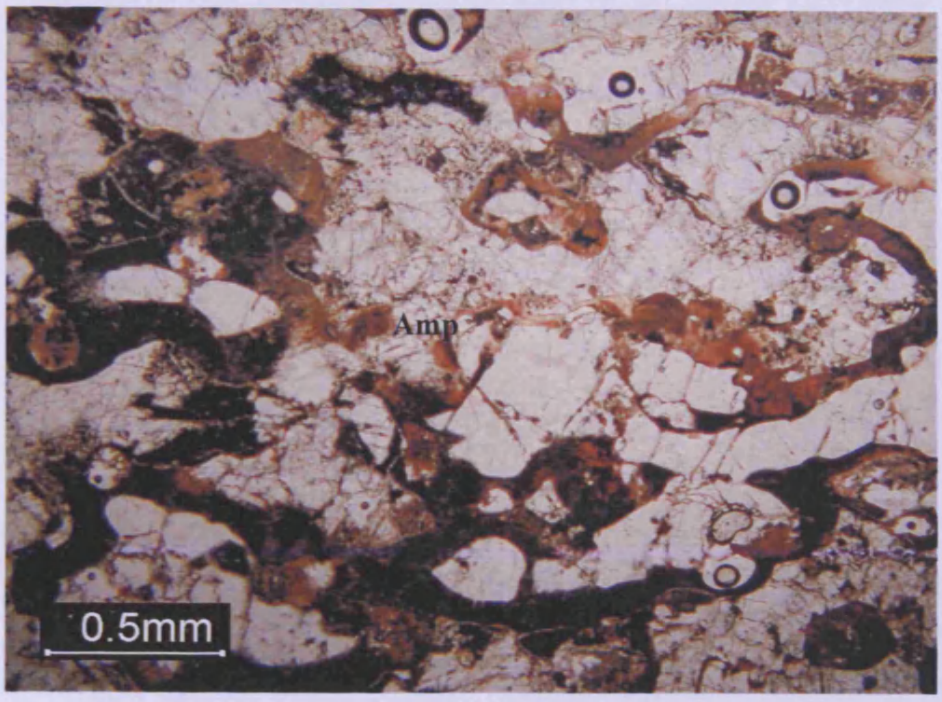

(b)

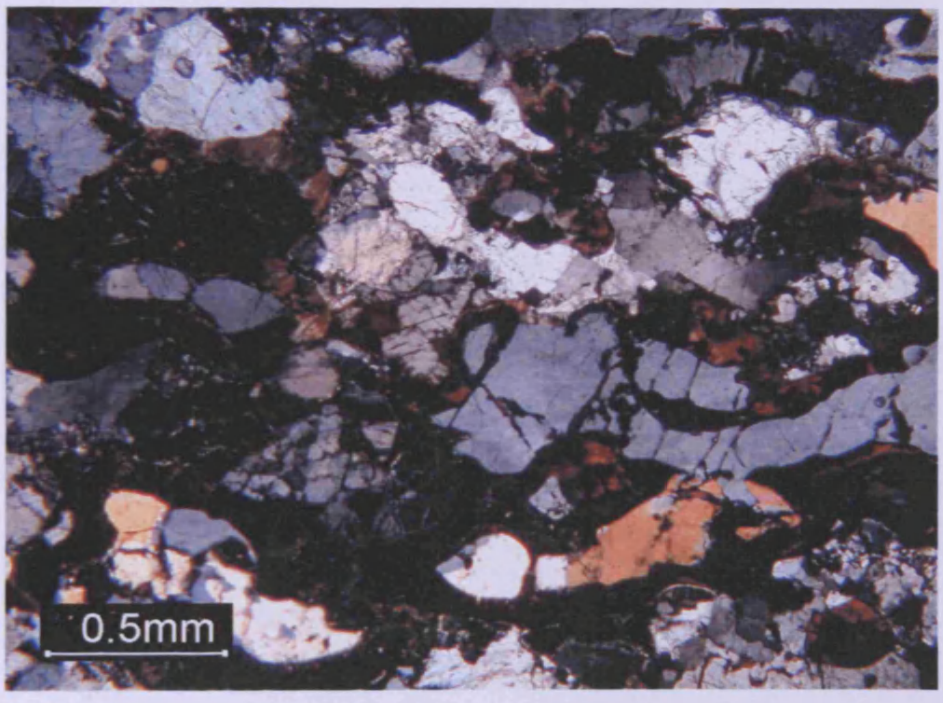

Figure 6.24 Photomicrographs show glass whirlpool in granitic xenolith that also causes dark-light bands in the rock. Thin prismatic anisotropic crystals are found in some glass pools. A group of amphibole crystals (Amp) can be seen in the middle of the field. (a) plane polarized light (b) cross polarized light

6.2 Geochemistry of the Bo Ploi basalt

6.2.1 Whole rocks analyses for major oxide and trace elements content

Sample preparation and analytical techniques

Representative samples of fresh Bo Ploi basalt were selected for whole rock analyses. The rocks were crushed into small pieces of approximately 0.5 mm in diameter by using a jaw crusher. They were then hand picked to avoid phenocrysts, xenoliths, amygdale minerals and the weathered materials. The selected chips were ground into powder by using TEMA tungsten carbide mill. The powder was dried at 110°C for 24 hours. The volatile contents were eliminated by igniting the samples at 1100°C for 20 minutes. The lost on ignition was calculated by the difference from original and final weights of each sample after ignition. The whole rock analyses were performed by using X-Ray Fluorescence analysis for major oxides, including, SiO_2, Al_2O_3, FeO, MgO, CaO, Na_2O, K_2O, TiO_2, MnO and P_2O_5. Additionally, the trace elements Pb, Th, Rb, Sr, Y, Zr, Nb, Cl, Ga and Ti, were determined at the Department of Geological Sciences, Royal Holloway, University of London. The major oxide analyses were carried out on fused glass discs, while the trace element analyses was performed on pressed pellets prepared at University College London according to the standard laboratory procedures for the XRF analysis. Raw trace element analyses were then corrected for mass absorption effects by using coefficients calculated from the major element analyses.

Magmatic affinity and rock types

The major oxides, minor oxides and trace element analyses of the Bo Ploi basalt, presented in Table 6.1, were utilised as a tool to attest magmatic affinity and rock types. The rocks are compositionally basic with SiO_2 content range from 46.7 to 47.8 wt%,

Table 6.1 XRF analyses for major oxides (wt%), trace elements (ppm) and CIPW normative calculation of the Bo Ploi basalt.

Sample	BPB-01	BPB-02	BPB-03	BPB-04	BPB-05	BPB-06	BPB-07
SiO_2	47.36	46.96	46.88	46.78	46.67	47.82	46.98
Al_2O_3	16.43	16.01	15.62	16.40	16.52	15.58	14.84
Fe_2O_3	8.46	8.88	9.22	8.91	9.01	9.02	9.28
MgO	7.08	6.84	7.07	7.06	7.03	7.23	8.36
CaO	7.25	7.76	8.23	8.24	8.26	8.05	9.29
Na_2O	5.66	5.60	5.29	5.09	4.94	4.87	4.68
K_2O	3.99	3.99	3.61	3.57	3.59	3.46	2.56
TiO_2	1.78	1.90	1.89	1.89	1.90	1.80	1.90
MnO	0.19	0.20	0.20	0.20	0.21	0.20	0.19
P_2O_5	0.86	0.87	0.97	0.87	0.87	0.97	0.89
total	99.06	99.01	98.98	99.01	99.00	99.00	98.97
LOI	0.96	1.18	1.39	1.61	1.72	2.04	2.13
Rb	103	77	74	104	114	73	49
Th	15	14	15	14	14	16	12
Nb	121	114	116	116	118	113	102
K	3312	3312	2996	2963	2980	2872	2125
Sr	1067	980	1095	1051	1077	1010	918
P	375	379	423	379	379	423	388
Zr	319	299	302	305	308	304	271
Ti	10671	11391	11331	11331	11391	10791	11391
Y	28	27	29	27	29	29	27
Pb	8	7	8	7	7	9	6
Ga	22.0	19.5	22.2	21.9	21.6	22.2	19.2
			CIPW normative				
or	23.58	23.58	21.33	21.10	21.22	20.45	15.13
ab	6.25	4.26	6.41	6.38	6.29	11.41	10.89
an	7.64	6.76	8.21	11.36	12.30	10.43	11.92
ne	**22.56**	**23.37**	**20.78**	**19.88**	**19.24**	**16.14**	**15.56**
cpx	18.47	21.23	21.43	19.41	18.74	18.87	23.01
di	12.28	13.75	13.80	12.69	12.17	12.31	15.65
hd	6.18	7.48	7.63	6.73	6.57	6.56	7.35
ol	**13.69**	**12.61**	**13.34**	**13.70**	**13.99**	**14.42**	**15.15**
fo	8.36	7.47	7.85	8.20	8.32	8.62	9.50
fa	5.32	5.14	5.48	5.50	5.68	5.81	5.64
mt	1.62	1.70	1.77	1.71	1.73	1.73	1.78
il	3.38	3.61	3.59	3.59	3.61	3.42	3.61
ap	2.04	2.06	2.30	2.06	2.06	2.30	2.11
SI	-33.58	-34.73	-31.30	-29.82	-28.92	-24.77	-23.78
K_2O/Na_2O	0.70	0.71	0.68	0.70	0.73	0.71	0.55
CaO/Al_2O_3	0.44	0.48	0.53	0.50	0.50	0.52	0.63
Na_2O/Al_2O_3	0.34	0.35	0.34	0.31	0.30	0.31	0.32
Mg#	62.86	60.90	60.81	61.58	61.22	61.86	64.57
Ti/Y	375.74	415.71	392.06	419.65	398.27	367.04	425.02
Rb/Sr	0.10	0.08	0.07	0.10	0.11	0.07	0.05
Zr/Nb	2.63	2.62	2.61	2.64	2.60	2.68	2.65
Th/Pb	1.99	1.86	1.77	2.04	1.99	1.67	2.11
Th/Y	0.54	0.50	0.51	0.51	0.47	0.53	0.44
Nb/Y	4.26	4.16	4.01	4.29	4.14	3.85	3.81

Table 6.1 XRF analyses for major oxides (wt%), trace elements (ppm), and CIPW normative calculation of the Bo Ploi basalt (continued).

Sample	BPB-08	BPB-09	BPB-10	BPB-11	BPB-12	BPB-13
SiO_2	47.50	47.48	47.64	46.92	47.11	47.47
Al_2O_3	14.78	14.69	15.15	14.85	16.29	15.56
Fe_2O_3	9.03	9.21	8.95	9.33	8.82	9.04
MgO	8.22	8.42	8.38	8.42	7.28	7.12
CaO	8.37	9.42	8.90	8.91	8.56	8.75
Na_2O	4.94	4.19	4.34	4.67	5.15	4.91
K_2O	3.23	2.61	2.78	2.83	2.85	3.09
TiO_2	1.86	1.88	1.80	1.92	1.81	1.88
MnO	0.20	0.19	0.19	0.20	0.20	0.20
P_2O_5	0.87	0.89	0.88	0.91	0.95	0.98
total	99.00	98.98	99.01	98.96	99.02	99.00
LOI	1.56	2.05	2.21	1.41	1.73	2.10
Rb	69	79	62	39	81	64
Th	12	11	12	12	15	15
Nb	100	100	101	105	112	108
K	2681	2166	2307	2349	2366	2565
Sr	947	1008	1009	984	1046	1035
P	379	388	384	397	414	427
Zr	267	268	274	274	294	285
Ti	11151	11271	10791	11510	10851	11271
Y	26	26	28	27	28	28
Pb	6	6	7	5	8	8
Ga	18.8	19.7	20.4	18.1	20.7	20.8
CIPW normative						
or	19.09	15.42	16.43	16.72	16.84	18.26
ab	9.61	12.73	12.98	10.01	11.38	11.19
an	8.62	13.57	13.65	11.20	12.92	11.29
ne	**17.44**	**12.31**	**12.86**	**15.99**	**17.44**	**16.45**
cpx	22.09	22.19	20.07	21.96	19.00	20.95
di	15.08	15.16	13.80	14.95	12.55	13.64
hd	7.01	7.02	6.27	7.01	6.45	7.31
ol	**15.00**	**15.49**	**15.97**	**15.67**	**14.24**	**13.41**
fo	9.45	9.77	10.14	9.84	8.63	7.99
fa	5.55	5.72	5.83	5.84	5.61	5.42
mt	1.73	1.76	1.71	1.79	1.69	1.73
il	3.53	3.57	3.42	3.65	3.44	3.57
ap	2.06	2.11	2.08	2.16	2.25	2.32
SI	-26.39	-19.21	-19.97	-24.43	-26.56	-25.22
K_2O/Na_2O	0.65	0.62	0.64	0.61	0.55	0.63
CaO/Al_2O_3	0.57	0.64	0.59	0.60	0.53	0.56
Na_2O/Al_2O_3	0.33	0.29	0.29	0.31	0.32	0.32
Mg#	64.81	64.91	65.45	64.60	62.54	61.45
Ti/Y	430.53	430.18	392.40	429.49	387.53	408.36
Rb/Sr	0.07	0.08	0.06	0.04	0.08	0.06
Zr/Nb	2.68	2.67	2.71	2.61	2.62	2.63
Th/Pb	1.97	1.98	1.86	2.17	1.81	1.80
Th/Y	0.47	0.42	0.44	0.44	0.52	0.55
Nb/Y	3.85	3.82	3.68	3.91	4.01	3.93

with an average of 47.0 ± 0.36 wt%. The *mg*-numbers 100*[Mg/(Mg + Fe^{2+} + Fe^{3+})] are in the range of 61 to 65 with an average value of 62.9 ± 1.73. The rock contains relatively variable total alkali content (Na_2O+K_2O) from 6.8 to 9.6 wt% (8.2±0.89 on average). The rocks are sodic with K_2O/Na_2O ratio range from 0.5 to 0.7. The ratios of Nb/Y of the rocks range from 3.8 to 4.1, which is near the upper range for alkalic rocks (Floyd and Winchester, 1975; Winchester and Floyd, 1976 & 1977). According to calculated CIPW norms, the rock contains 12 to 22% normative nepheline (Ne) and 12 to 16% normative olivine (Ol) without the presence of hypersthene (Hy).

Plots of the total alkali content against SiO_2 show that the host rock is alkalic compositionally mildly alkalic to highly alkalic. These alkalic basaltic rocks are hawaiites, basanites (Ol > 10%), or mugearites toward phonolitic tephrites with mostly basanitic composition (Fig. 6.25). This is consistent with the plot on variation diagrams using Zr/TiO_2*0.0001 versus Nb/Y (Winchester and Floyd, 1977), which the plots are in the basanite – nephelinite region (Fig.6.26). Further tests were carried out on other minor and trace elements variation diagrams; P_2O_5 versus Zr (Winchester and Floyd, 1976) and TiO_2 versus $Zr/(P_2O_5$*10000) from Winchester and Floyd, (1976), which are all indicate alkali basalt affinity as illustrated in figure 6.27-6.28, respectively.

Major and minor oxides

The Bo Ploi alkali basanite shows coherent, rather small chemical variations. Generally, it is agreed that igneous rocks that are evolved by crystal fractionation process without extensive contamination by crustal materials should exhibit linear trends on variation diagrams. Accordingly, the major and minor oxides are plotted against MgO as a fractionation parameter (Fig 6.29). It is found that the plots of TiO_2, Fe_2O_3 and CaO show negative correlations with MgO, while SiO_2, Al_2O_3, Na_2O and K_2O form well-defined negative coherent trends with increasing MgO content. MnO, however, show neither positive nor negative correlation with MgO. In addition,

fractional crystallisation vectors were annotated, here the position of vectors were located on the composition of the most primitive magma, (BPB-10) with Mg# 65.4. The pattern of these major oxide variation trends reflects successive proportion of minerals crystallized from the melt. The decreasing trends indicate the fractionation of Fe-Ti oxide minerals, olivine and pyroxene at the earlier stage followed by plagioclase and alkali feldspar. The presence of olivine, clinopyroxene and Fe-Ti oxide phenocrysts/megacrysts is consistent with the interpretation.

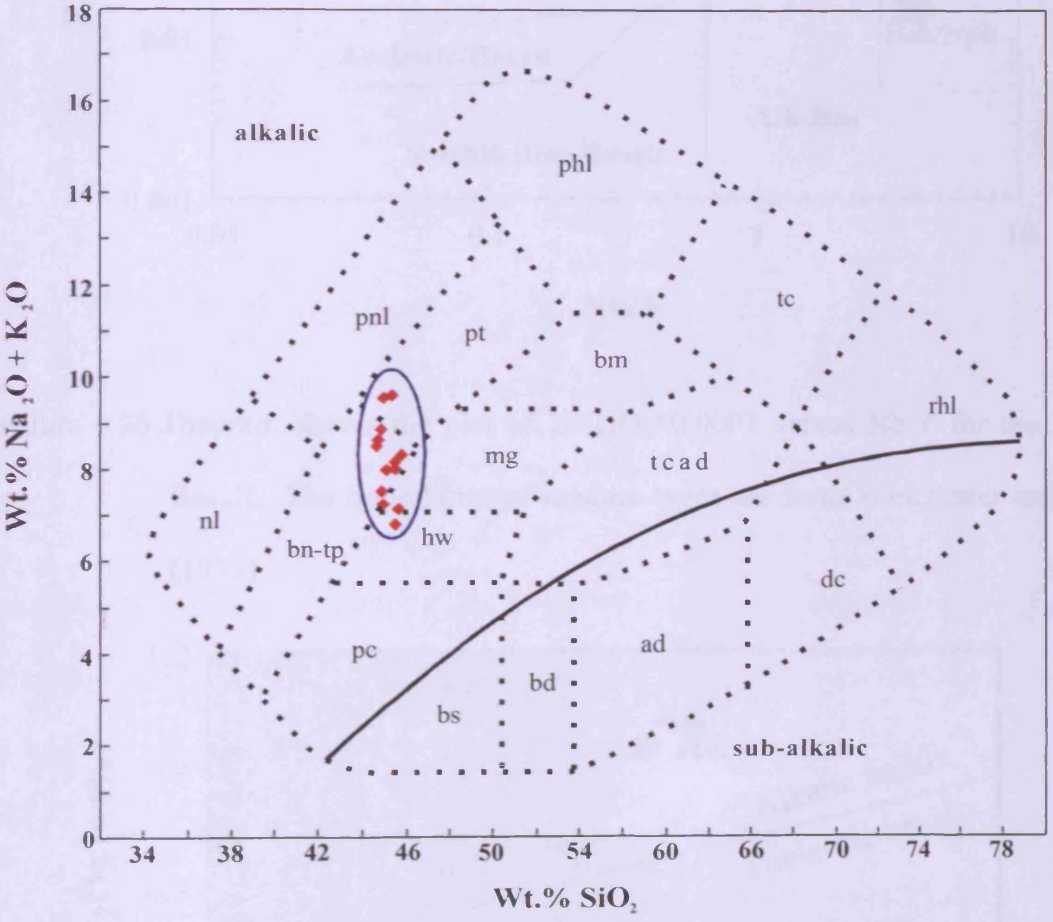

Figure 6.25 Diagram shows the plots of SiO_2 content against total alkali content of the Bo Ploi basalt (modified after Cox *et al.*, 1979 and Miyashiro, 1978).

Note: ad=andesites, bd=basaltic andesites, bm=benmoreites, bn-tp=basanites and tephrites, bs=basalts, dc=dacites, hw=hawaiites, mg=mugearites, nl=nephelinites, pt=phonolitic tephrites, pc=picrite, phl=phonolites, pnl=phonolitic nephelinites, rhy=rhyolite, tc=trachytes, tcad=trachyandesites

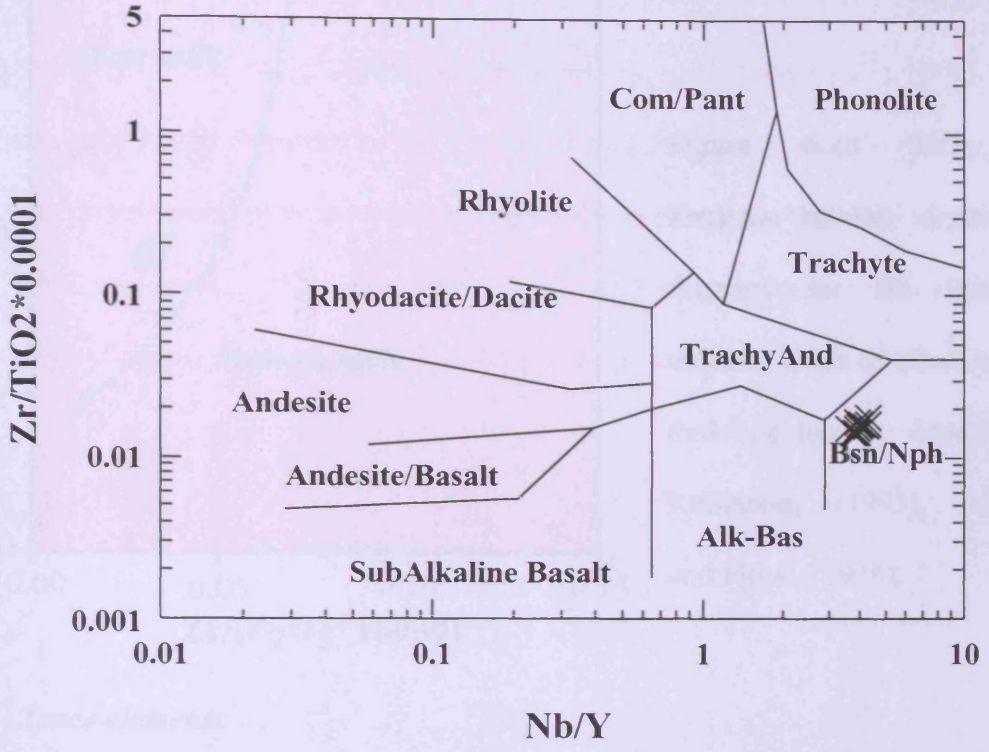

Figure 6.26 Diagram shows the plot of $Zr/TiO_2*0.0001$ versus Nb/Y for the Bo Ploi Basalt. The boundaries of magma types are from Winchester and Floyd, (1977)

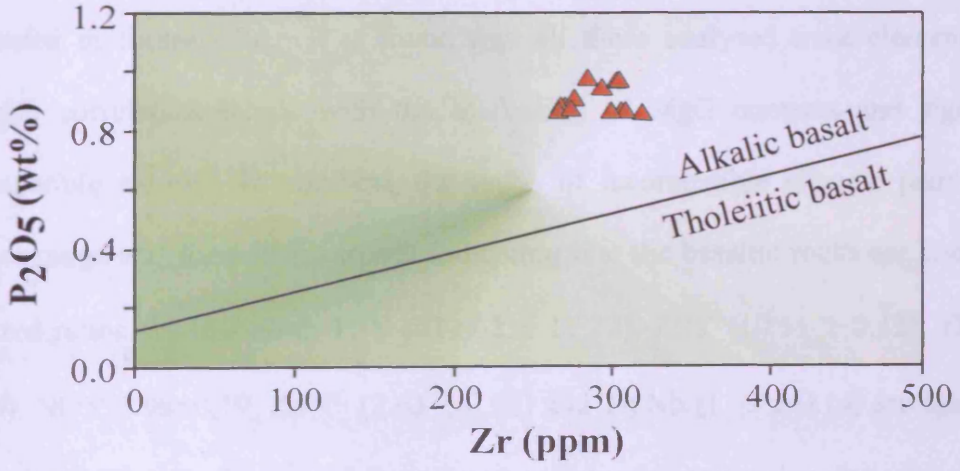

Figure 6.27 Plots of the Bo Ploi basalt on P_2O_5 versus Zr discrimination diagram.

(Modified afer Rollinson, 1993; Winchester and Floyd, 1976)

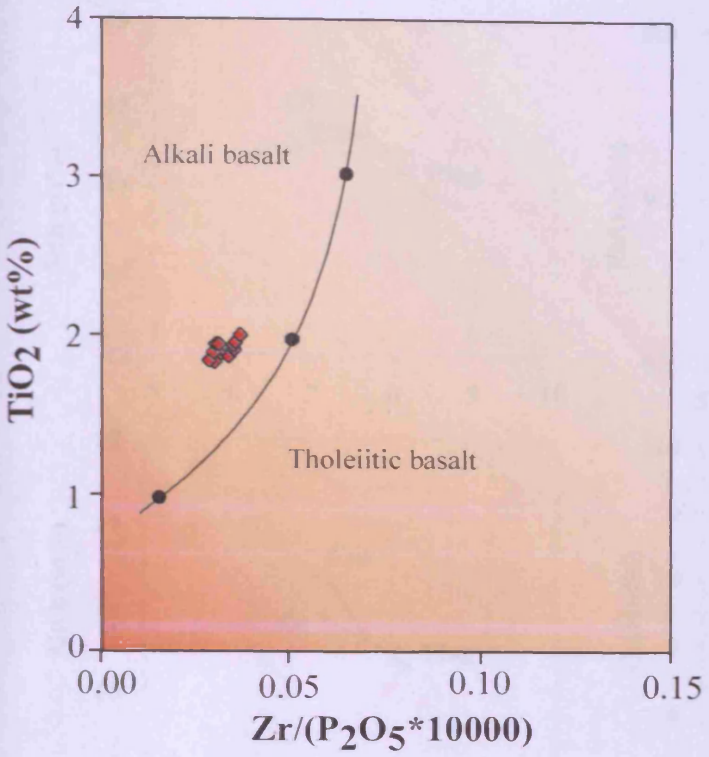

Figure 6.28 TiO_2 versus $Zr/(P_2O_5*10000)$ discrimination diagram for Bo Ploi basalt exhibits fields of alkali basalt and tholeiitic basalt. Modified after Rollinson, (1993), Winchester and Floyd, (1976).

Trace elements

The basanite contains Ga (18 to 22 ppm), Sr (918 to 1095 ppm), Rb (39 to 114 ppm), Zr (267 to 319 ppm), Nb (100 to 121 ppm), Pb (5 to 9 ppm), Th (11 to 16 ppm) and Y (26 to 29 ppm). These trace elements were studied for their behaviour during the fractionation process by using the same fractionation parameter, MgO, which is illustrated in figure 6.30. It is found that all these analysed trace elements exhibit negative correlation trends with the increasing of MgO contents and signify their incompatible nature. In addition, the ratios of incompatible element pairs are in a narrow range and form linear trends indicating that the basaltic rocks are comagmatic. Selected ratios are including Ti/Y (412.62 ± 12.72), Zr/Y (10.51 ± 0.42), Th/Y (0.49 ±0.04), Nb/Y 3.98±0.19, Zr/Nb (2.63 ± 0.03) and Th/Nb (1.92 ± 0.14) are illustrated in figure 6.31. The consistency of these incompatible elements ratios also suggest that the rock is unlikely to be subjected to major crustal contamination. This is in good agreement with the oxygen stable isotope analyses, where the representative samples yield $\delta^{18}O$ 6.0-6.9‰ indicating ordinary mantle-derived basalt (basanite).

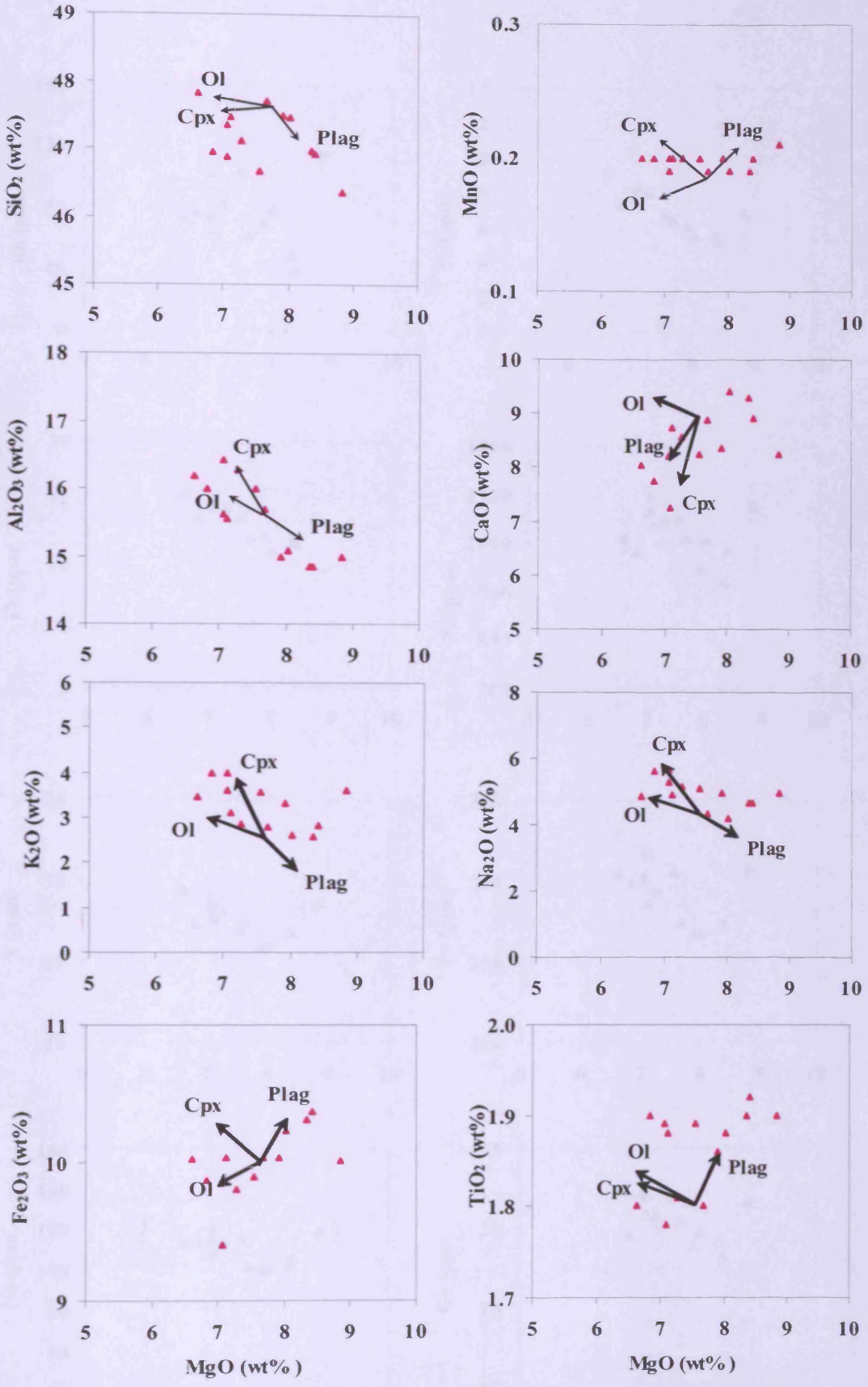

Figure 6.29 Variation diagrams of major oxides versus MgO for the Bo Ploi basalt with crystal fractionation vectors, where the position of vectors corresponds to the most primitive composition (BPB-10).

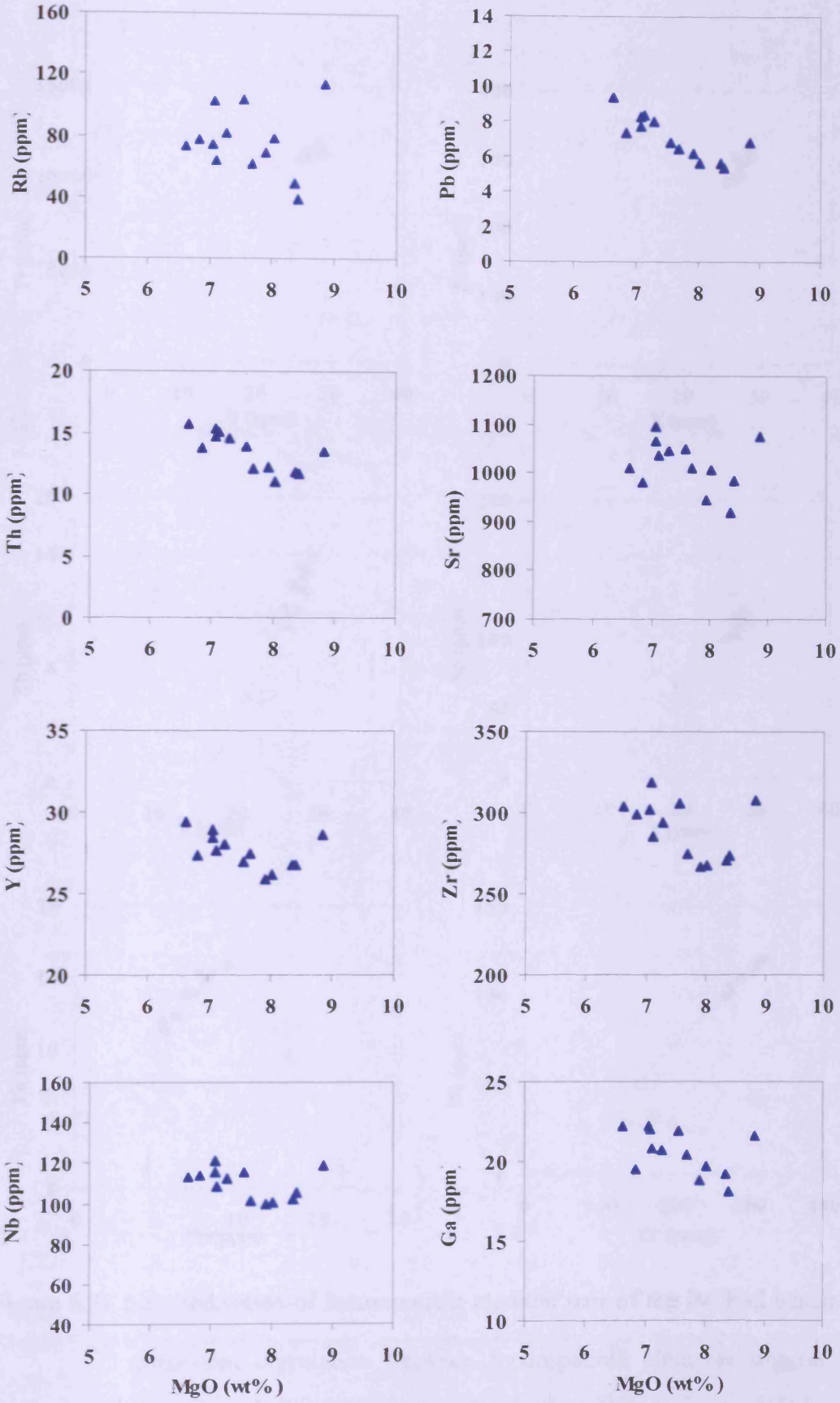

Figure 6.30 Variation diagrams of trace elements versus MgO for the Bo Ploi basalt

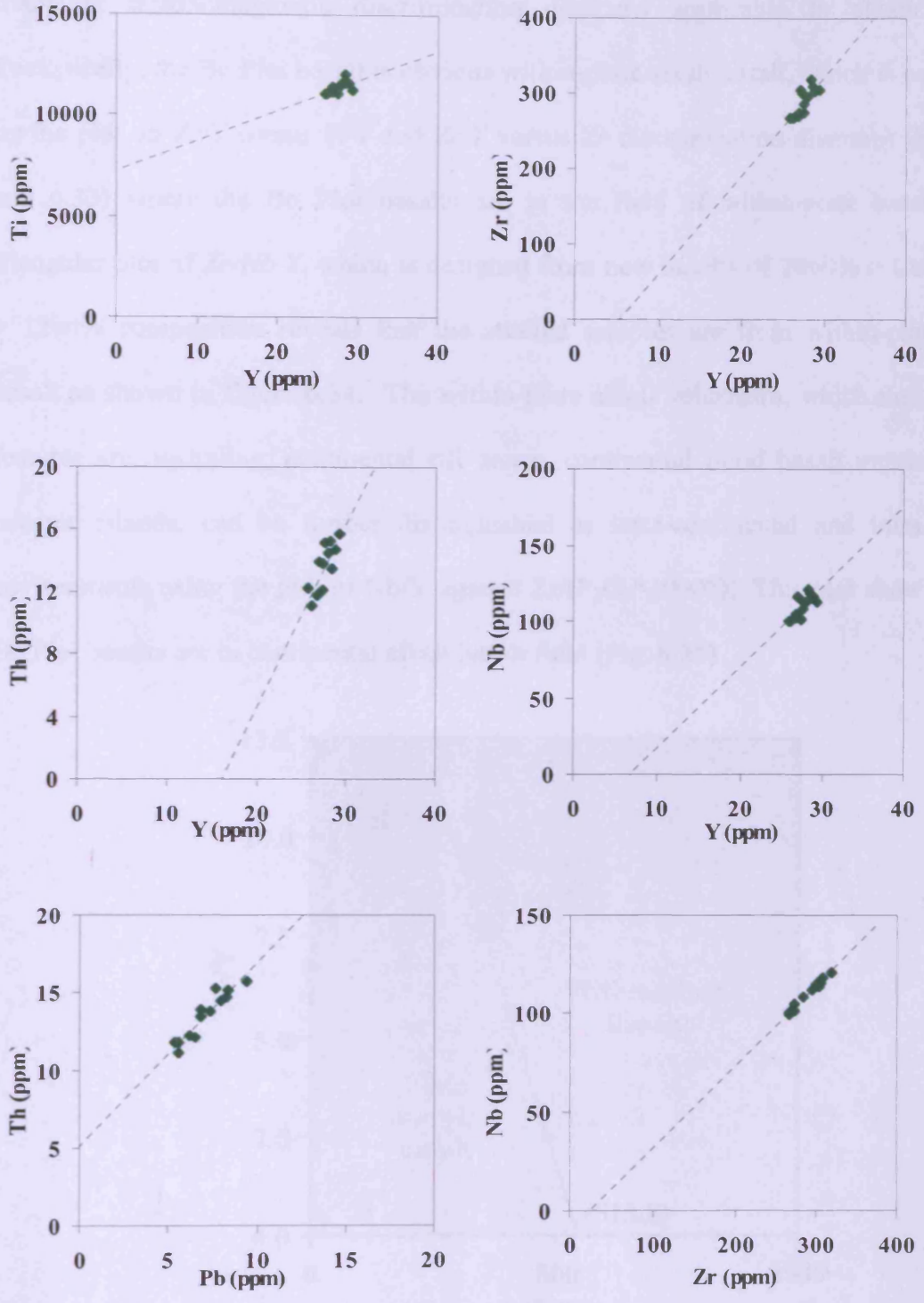

Figure 6.31 Selected ratios of incompatible element pair of the Bo Ploi basalt showing consistent correlation between incompatible elements suggest a closed system fractionation.

Tectonic setting of eruption

Major and minor oxides and trace elements analyses are utilised in bivariate and triangular tectonomagmatic discrimination diagrams applicable to alkalic basalt. Tectonically, the Bo Ploi basalt is obvious within-plate alkali basalt, which is confirmed by the plot on *Zr/Y versus Ti/Y* and *Zr/Y* versus *Zr* discrimination diagrams (Fig. 6.32 and 6.33) where the Bo Ploi basalts are in the field of within-plate basalt. The triangular plot of *Zr-Nb-Y*, which is designed from new basalts of 20wt% > CaO+MgO > 12wt% composition reveals that the studied samples are from within-plate alkali basalt as shown in figure 6.34. The within-plate alkali volcanism, which the volcanic features are, including, continental rift zones, continental flood basalt provinces and oceanic islands, can be further distinguished as intra-continental and intra-oceanic environments using the plot of Nb/Y against $Zr/(P_2O_5*10000)$. This plot show that the Bo Ploi basalts are in continental alkali basalt field (Fig. 6.35)

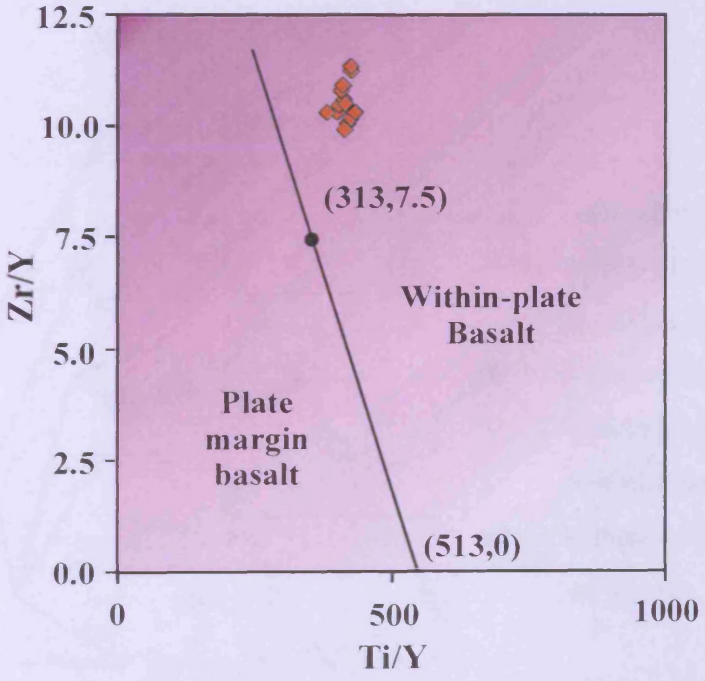

Figure 6.32 The Zr/Y versus Ti/Y discrimination diagram exhibits that the Bo Ploi basalt is plotted in a field of within-plate basalt. Modified after Rollinson, (1993) and Pearce, (1982)

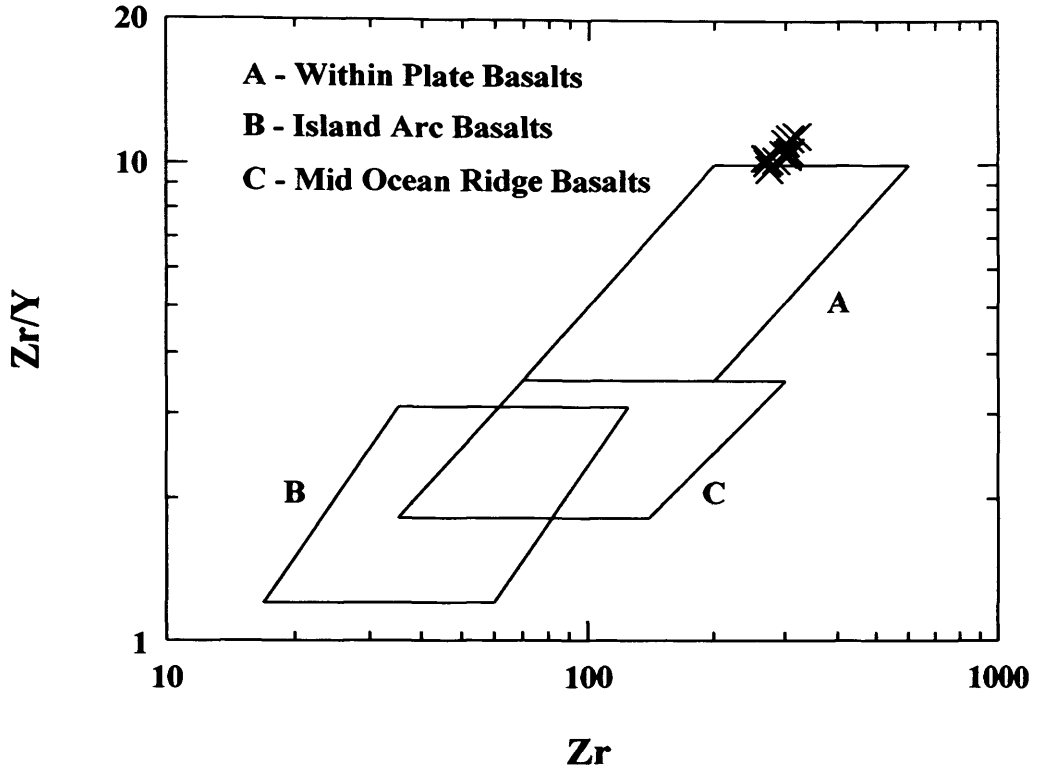

Figure 6.33 The Zr/Y versus Zr diagram shows that the Bo Ploi basalt is close to the within plate field. Modified after Pearce and Norry, (1979).

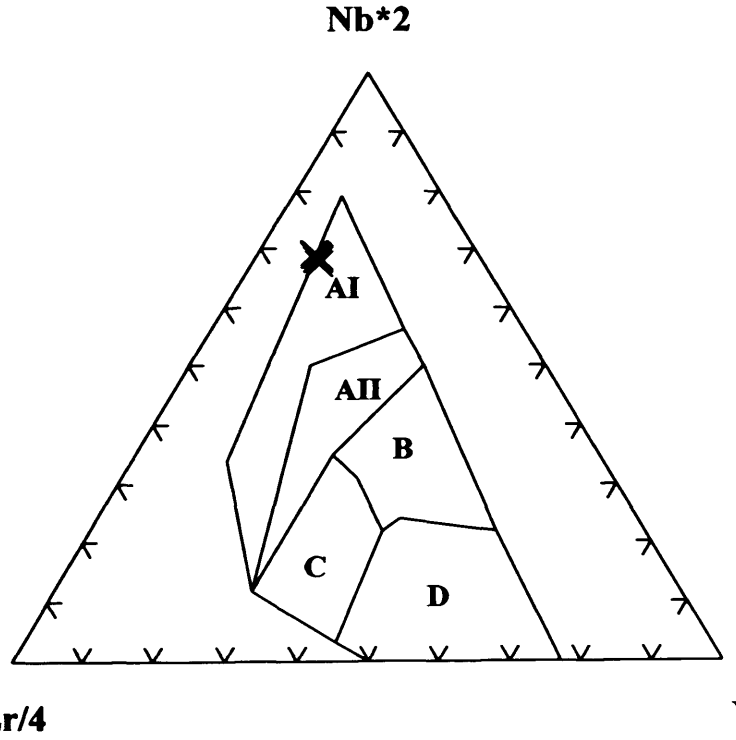

AI: within-plate alkali basalts

AII: within-plate alkali basalts & within-plate tholeiites

B: E-type MORB

C: within-plate tholeiites & volcanic-arc basalts

D: N-type MORB & volcanic arc basalts

Figure 6.34 The Nb-Zr-Y discrimination diagram for Bo Ploi basalt. Modified after Meschede, (1986)

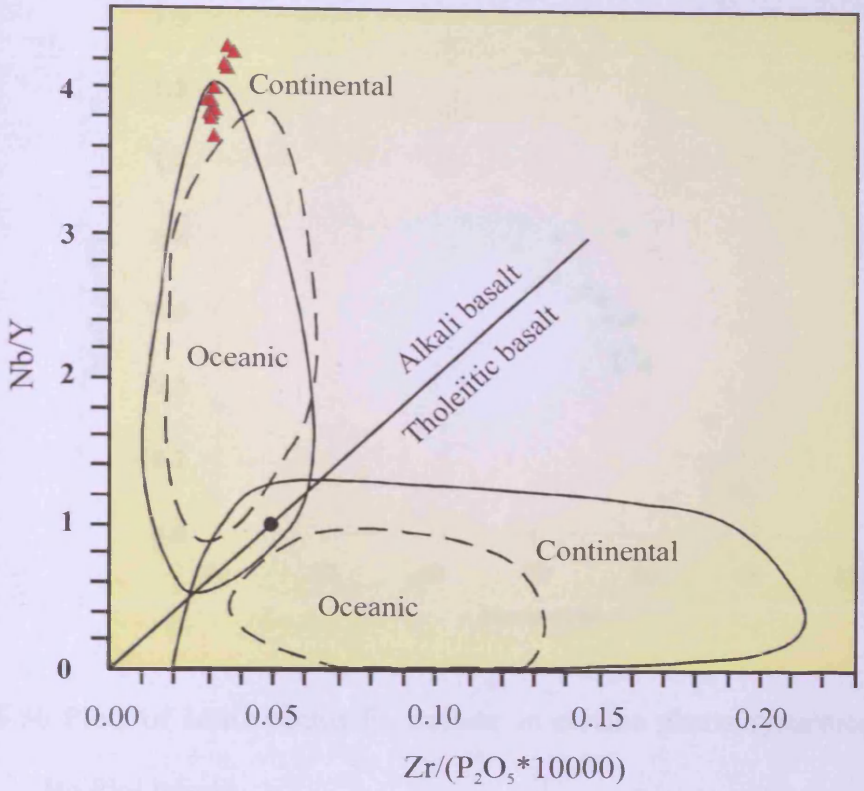

Figure 6.35 Plots of Nb/Y versus $Zr/(P_2O_5*10000)$ for the Bo Ploi basalt. Modified after Rollinson, (1993) and Pearce, (1982)

6.2.2 Mineral Chemistry

Phenocrysts, including megacrysts, were selected petrographically to determine for chemical compositions using EDS technique. The analyses were performed on olivine, clinopyroxene, spinel, alkali feldspar and nepheline, which are the most abundant phases. The instrument conditions are JEOL-733 Superprobe equipped with Link Systems EDS at Birkbeck College, University of London. An accelerating voltage of 15 kV and a count time of 100s have been used.

Olivine is the most abundant phenocrysts in the Bo Ploi basalt. Their megacrysts range in composition from Fo_{71} to Fo_{90} and are more Mg-rich compared to phenocrysts which range from Fo_{68} to Fo_{80}. Minor elements contents are CaO (0.1 to 0.3wt%) and MnO (0.5 to 0.8wt%). Olivine Fo contents are plotted against MnO, where they form a negative correlation trend (Fig. 6.36) reflecting a comagmatic origin.

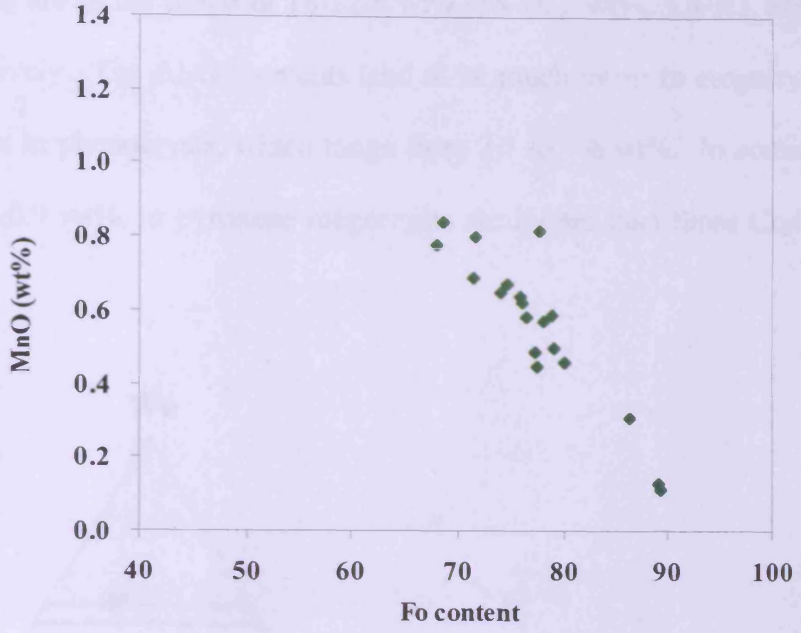

Figure 6.36 Plots of MnO versus Fo content in olivine phenocrysts/megacrysts of the Bo Ploi basalt

Clinopyroxene phenocrysts and megacrysts are characterised by 20-22 wt% CaO, 11.8-13wt% MgO, 5.8-6.7 wt% FeO and 0.1-0.2 wt% MnO. The Al_2O_3 and Cr_2O_3 contents range between 6.2-9.4 wt% and 0.03-0.1wt%, respectively. The alkali contents were found in a significant amount only of Na_2O range from 1.4-1.7 wt%. The end-member compositions projected into the Wo-En-Fs triangle of phenocrysts are in the range of $En_{30.2\text{-}34.4}$ $Wo_{50.3\text{-}52.9}$ $Fs_{14.9\text{-}17.1}$. The majority compositions correspond to IMA nomenclature as sodian aluminian ferroan diopside with subordinate aluminian ferroan diopside and sodian aluminian subsilicic ferroan diopside. The atomic percent of Ca, Mg and total Fe (Fe^{2+}+Fe^{3+}+Mn) content of both clinopyroxene phenocrysts and megacrysts were plotted on composition ranges and nomenclature diagram modified after Morimoto (1988), in addition, the coexisting olivine phenocrysts/megacrysts were plotted on the same diagram which are illustrated in figure 6.37. The compositions of clinopyroxene megacrysts are slightly different from those compositions of phenocrysts. They have a higher SiO_2 content from 50.4 to 51.9 wt%. The CaO, MgO, FeO and

MnO contents are in the range of 18-22.5 wt%, 14-16.2 wt%, 3.4-5.1 wt% and 0.1-0.3 wt%, respectively. The Al_2O_3 contents tend to be much lower in megacrysts than those Al_2O_3 content in phenocrysts, which range from 3.1 to 7.6 wt%. In contrast, the Cr_2O_3 contents, 0.2-0.9 wt%, in pyroxene megacrysts are higher than those Cr_2O_3 contents in phenocrysts.

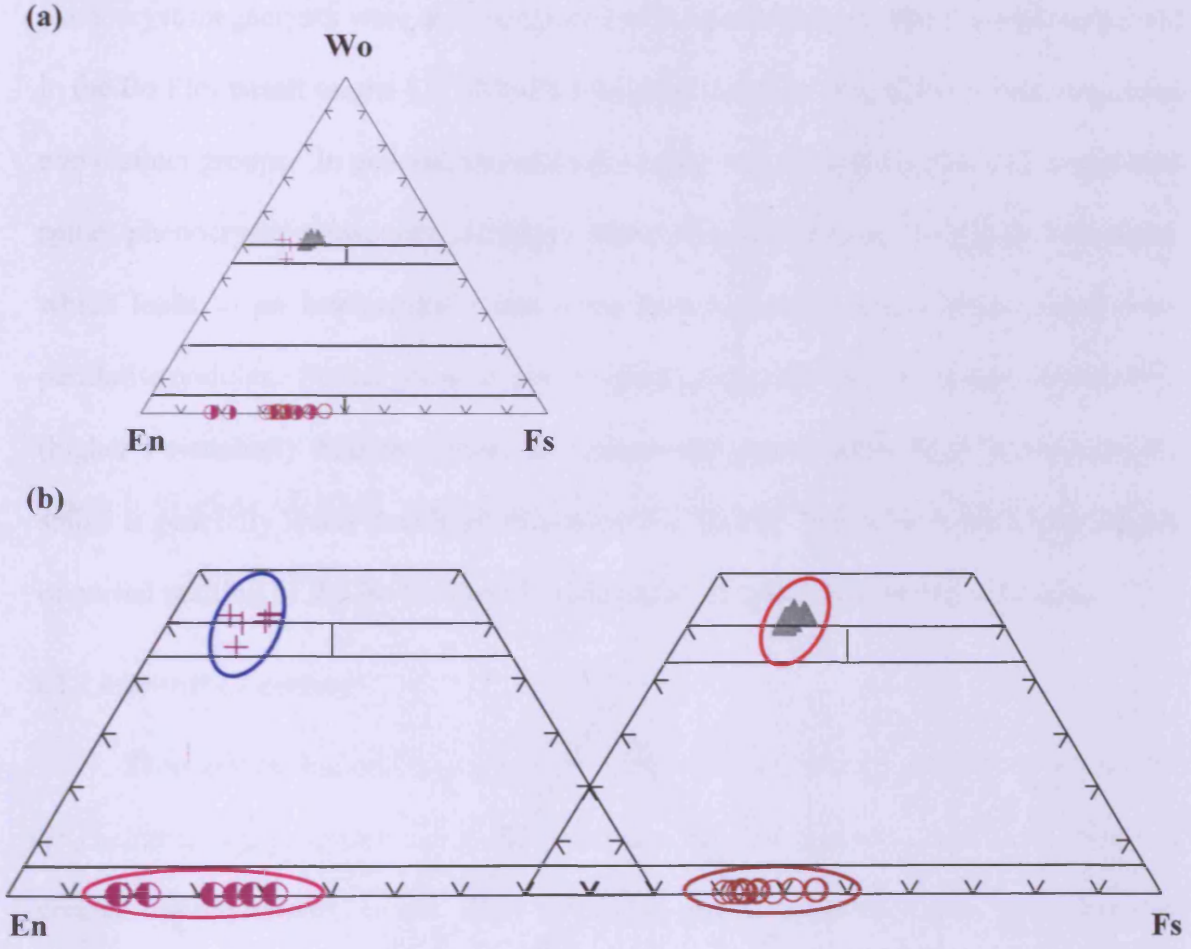

Figure 6.37 (a) Pyroxene nomenclature diagram shows the compositions of clinopyroxene and coexisting olivine of the Bo Ploi basalt.
(b) Enlargement of the polygonal compositional diagram for megacrysts of clinopyroxene (blue circle) and olivine (pink circle) and phenocrysts of clinopyroxene (red circle) and olivine (brown circle)

Spinel phenocrysts, though less common than megacrysts, consist of 53.9 to 59.6 wt% Al_2O_3, 16.1 to 18.8 wt% MgO and 14.7 to 18.2 wt% FeO. Minor components

include 0.1 to 0.2 wt% SiO_2, 0.1 to 0.7 wt% TiO_2 and 0.1 to 0.3 wt% MnO. There is a wide variation in Cr_2O_3 content among these spinels, where phenocrysts may contain up to 10.6 wt% Cr_2O_3, contrast to spinel megacrysts that contain merely up to 1 wt% of Cr_2O_3. Other constituents of spinel megacrysts are 58.5-60.5 wt% Al_2O_3, 19.1-23.5wt% FeO, 0.5-0.7 wt% TiO_2, up to 0.1 wt% for SiO_2 and up to 0.2 wt% for MnO. Spinel phenocryst/megacrysts were also compared with spinel from mantle xenoliths entrained in the Bo Ploi basalt on the Cr^{2+}-Mg-Fe triangular diagram (Fig. 6.38), where they form two distinct groups. In general, spinel from mantle xenoliths has higher Cr-content than spinel phenocrysts/megacrysts, although some phenocrysts also have high Cr-content, which leads to an interpretation that these spinel grains possibly disintegrated from peridotite nodules. Spinel phenocrysts are compositionally more hercynite end member (higher Fe-content) than the spinel of xenocrystic phase, while Mg# in phenocrystic spinel is generally lower than Mg# in xenocrystic spinel. This reflects the higher degree of partial melting of the Bo Ploi basalt compare to its entrained mantle peridotites.

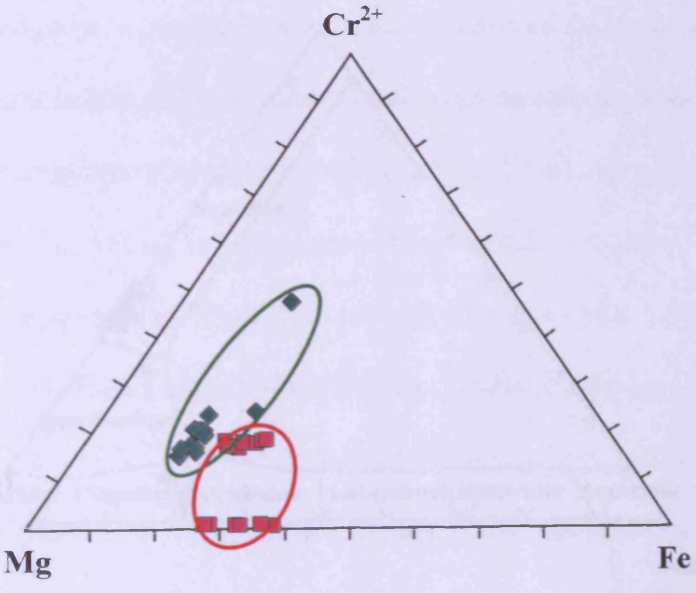

Figure 6.38 Plots of spinel phenocrysts (red square) of the Bo Ploi basalt in comparison with spinel from the entrained spinel peridotites (green diamond).

Feldspar phenocrysts/megacrysts are compositionally fairly consistent though their compositions can be distinctively classified on the basis of their end members into alkali feldspar and plagioclase. The K-rich end member has been found more often than the Na-rich end member and the plagioclase. The alkali feldspar of the first group is characterised by higher SiO_2 (66.4 to 67.6 wt%) and higher alkali contents (Na_2O and K_2O) range from 12.4 to 14.4 wt% but lower Al_2O_3 (17.5 to 19.0 wt%) CaO (up to 0.1 wt%) contents than another group. The plagioclase phenocrysts/megacrysts are oligoclase with SiO_2 60.3 to 62.0 wt%, lower Al_2O_3 (23.5 to 25.3 wt%), K_2O (upto 1.7 wt%) but higher CaO (4.9 to 5.9 wt%) contents. The other elements are very much less variable. Their end-members are calculated as $Or_{40.7\text{-}47.5}$ $Ab_{52.4\text{-}58.8}$ $An_{0\text{-}0.5}$ and $Or_{5.5\text{-}9.7}$ $Ab_{64.8\text{-}66.8}$ $An_{23.5\text{-}28.4}$. Alkali feldspar phenocryst chemical compositions are shown in table 6.5 and also plotted on Or-Ab-An diagram for their nomenclature (Fig.6.39).

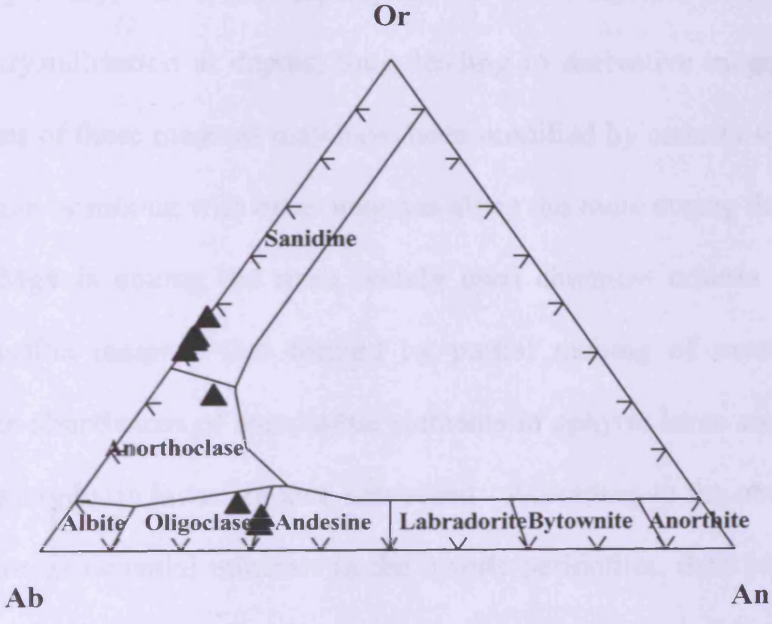

Figure 6.39 Feldspar nomenclature diagram shows end member compositions of feldspar phenocrysts from the Bo Ploi basalt.

Nepheline phenocryst chemical compositions show slightly variations and are summarised in table 6.6. They composed of 43.2 to 44.2 wt% SiO_2, 33.1 to 34.1 wt% Al_2O_3, 15.4 to 16.8 wt% Na_2O, 0.8 to 2.1 wt% CaO and 3.7 to 4.4 wt% K_2O. The subordinate constituents of TiO_2, FeO and MgO are less than 1 wt%. The general compositions of nepheline phenocrysts are $Ne_{80.0\text{-}82.4}\,Ks_{14.0\text{-}15.6}\,Qz_{2.6\text{-}5.7}$.

6.3 Petrogenesis of the Bo Ploi basalt

6.3.1 Primary Magma or Derivative Magma

It is generally agreed that the genesis of basaltic melts is resulted from variable degrees of partial melting of mantle peridotites at various depths (Yoder, 1976; Wilson, 1989; Zhou and Mukasa, 1997; Kimura *et al.*, 2002). The major mineral constituents of mantle peridotites are olivine, orthopyroxene, clinopyroxene and the minor constituents are garnet, spinel and plagioclase. The magmas derived directly to peridotite are designated primary, which may rapidly ascend to the surface, otherwise they undergo fractional crystallisation at depths, thus, leading to derivative magmas. The original compositions of these magmas may have been modified by country rock assimilation or contamination or mixing with other magmas along the route during the ascending path.

The Mg# is among the most widely used chemical criteria for distinguishing primary basaltic magmas that formed by partial melting of mantle peridotite. In addition, the abundances of compatible elements in aphyric lavas and glassy rocks and phenocrysts in phyric lavas are also accounted. According to the abundance of olivine and pyroxene as essential minerals in the mantle peridotites, then primary magma that formed by partially melt of peridotite should be equilibrated with these phases at the depths where magmas segregated and these phases should be present at liquidus of melting experiments of certain pressures (Wilson, 1989). One of the most remarkable works on these equilibria is the distribution coefficient of mantle olivine to liquid, also

written as $K_D^{Ol\text{-}Liq}$. The equation expresses the distribution of elements in terms of ratio of FeO/MgO in olivine to FeO/MgO in liquid. The value of $K_D^{Ol\text{-}Liq}$ in the range of 0.30 ± 0.03, which is derived from experiments (Roeder and Emslie, 1970; Grove, *et al.*, 1973) is generally accepted. The $K_D^{Ol\text{-}Liq}$ value of 0.30 ± 0.03 would equal Mg# of olivine in the range of 0.66-0.75 (Irving and Green, 1976), likewise, slightly higher Mg# of olivine in the range of 0.68-0.75 was proposed by Frey *et al.*, (1978) for the primary basaltic magmas that are evolved by crystal fractionation and/or crustal contamination as well as high concentration of compatible elements like Ni and Cr. Subsequently, a summary of concentrations in primary basaltic magmas that are in equilibrium with upper mantle peridotites was proposed by Wilson (1989) that the magmas should have Mg# over 0.7, Ni (400-500 ppm) and high Cr (>1000 ppm) with SiO_2 not excess 50 wt%. The porphyritic texture of the Bo Ploi basalt causes difficulty when separating microphenocrysts or even some phenocrysts from the rocks during the sample preparation for the whole rock chemical analyses, as a result, the analyses are unlikely to represent the primary magma composition. Taking the porphyritic character into account and assuming that the analyses correspond to magma compositions, the Mg# of the Bo Ploi basalt is in the range of 0.60-0.65, which is below the Mg# of typical primary magma compositions.

6.3.2 The role of partial melting

The Bo Ploi alkali basalt shows compositional variation from hawaiite to mugearite to basanite to phonolitic tephrite (Fig.6.25) is suggesting the role of partial melting of mantle source materials at different pressures (Wilson, 1989; Zhou and Mukasa, 1997; Kimura, *et al.*, 2002). Alkali basaltic rocks are generally regarded to be diverse in geochemistry and origins (White, 1985; Allégre *et al.*, 1987; Hart, 1988; Gibson *et al.*, 1997; Frey *et al.*, 2000; Abdel-Rahman and Nassar, 2004), nonetheless, the chemical nature of the mantle sources are reflected in the compositions of the basaltic

lavas, for example, whether the source related with materials of exotic origin such as recycled oceanic crust or recycled sedimentary rocks as well as the differentiation processes that the magmas had undergone of which a partial melting is one of the most common process that magmas had experienced Some highly to moderately incompatible element ratios are useful for indicating the degree of partial melting, for example Ba/Y, Ba/Zr and P_2O_5/TiO_2 ratios should decrease as the degree of partial melting is increased (Pankhurst, 1977). The partial melting of magma, which diversifies the magma compositions, is a pressure dependent process. The SiO_2 in a melt is pressure sensitivity and normally shown an inverse correlation with a pressure. If extensive decompression takes place, the degree of partial melting of mantle source materials will increase (Jaques and Green, 1980; Liu *et al.*, 1994; Zhou and Musaka, 1997; Kimura *et al.*, 2002). For this reason, partial melting of deep mantle material at a smaller degree is responsible for the enrichment of alkali and incompatible trace elements and relatively deficiency of SiO_2, in contrast, higher SiO_2 with lower alkalis and incompatible elements concentrations are explained by higher degree of partial melting of shallower mantle materials. Jaques and Green, (1980) proposed experimental models that suggest the alkali basalt is generated from small degree of partial melting (2-10%) of enriched lherzolite at pressure greater than 15 kbar (Fig. 6.40). In a similar manner, alkali magmas are thought originate at depths of approximately 60-100 km, whereas tholeiitic and calc-alkaline magmas form at much higher level (Neumann and Ramberg, 1978; Takahashi and Kushiro, 1983; Hirose and Kushiro, 1993; Baker *et al.*, 1995). The melts produced by partial melting of a depleted spinel lherzolite at low pressures are highly aluminous (17-18 wt.% Al_2O_3: Jaques & Green, 1980) and in this respect are dissimilar to the basanitic rocks erupted in the Bo Ploi area (14.7-16.5 wt.% Al_2O_3)

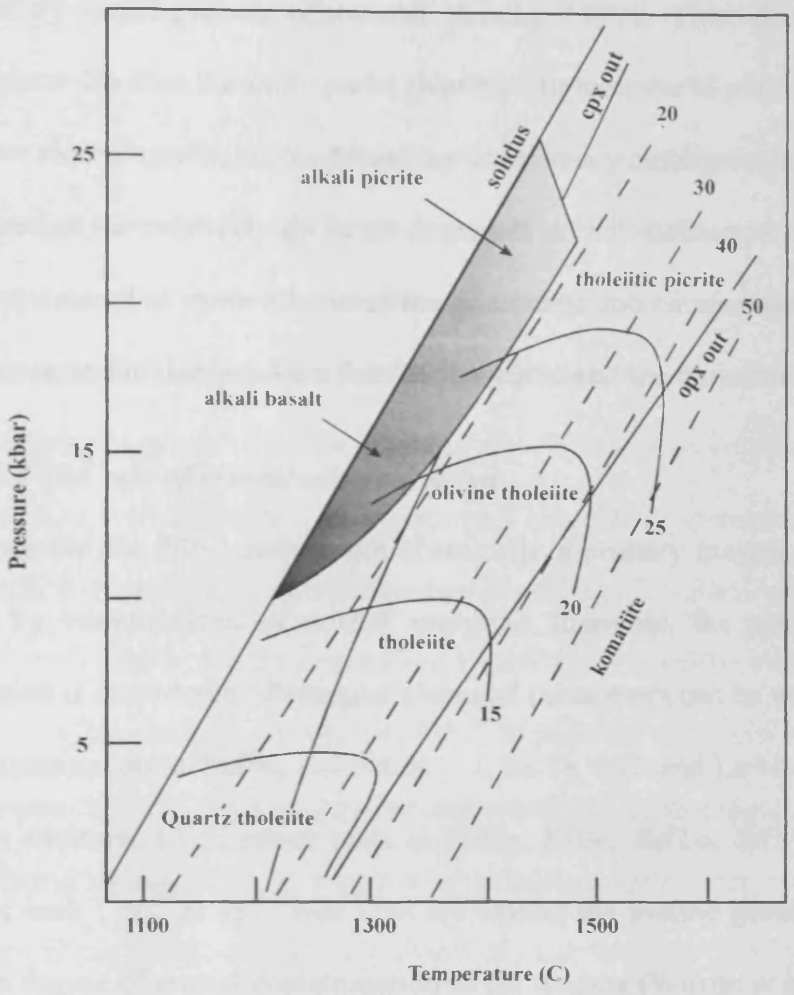

Figure 6.40 Experimental demonstrated the generation of alkali basaltic magmas from partially melted of an enriched lherzolite. Dashed lines represent percent of partial melting. The curved contours indicate olivine normative content in the melt. Solid lines denoted cpx-out and opx-out outline the point where cpx and opx are completely melted, respectively. Modified after Jaques and Green, (1980).

The covariation of incompatible elements as displayed in figure 6.31 suggesting different degrees of partial melting of compositionally similar mantle source (Parlak *et al.*, 2001). In addition, highly – moderately incompatible trace elements (Th, Sr, Rb, Nb, Zr, Y) and alkalis in the Bo Ploi basanites show a decreasing tendency with the increasing of SiO_2 content and this cannot be explained by fractional crystallisation

process but by partial melting (Zhou and Musaka, 1997). This allows the conclusion that the diverse Bo Ploi basanitic rocks (hawaiite to basanite to phonolitic tephrite) but evolved in a closed system, as confirmed by consistency among incompatible elements, are generated at the relatively different degree of partial melting at relatively different pressure regimes. The more alkalic of the phonotephritic compositions is generated at smaller degree and higher pressure than the basanitic and the hawaiitic compositions.

6.3.3 The role of crustal contamination

Since the Bo Ploi basalt is not chemically a primary magma and also densely populated by various types of crustal xenoliths, therefore, the possibility of crustal contamination is considered. Particular chemical parameters can be utilised to attest the crustal contamination including K/P ratios > 7, La/Ta > 22 and La/Nb >1.5 (Hart *et al.*, 1989). In addition, LILE ratios such as K/Rb, K/Ba, Ba/La, Sr/Nd and radiogenic isotopes of such $^{87}Sr/^{86}Sr$ vs $^{143}Nd/^{144}Nd$ are among the routine geochemical ratios for assessing a degree of crustal contamination in the magma (Wilson *et al.*, 1997; Hsu and Chen, 1998; Shinjo, 1998; Kimura *et al.*, 2002; Ingle *et al.*, 2002; Shaw *et al.*, 2003). In order to investigate the role of crustal contamination in the samples a ratio plot of Th/Y against Nb/Y was used since Th tends to be concentrated in continental crust and Nb is generally depleted (Kempton *et al*, 1991; Rogers *et al.*, 1992; Seyitoğlu *et al.*, 1997; Wilson *et al*, 1997; Parlak *et al.*, 2001). The Bo Ploi basanites cluster in the region of OIB on the Th/Y versus Nb/Y diagram with a restricted range of Th/Nb ratios close to 0.1 (Fig. 6.41). Higher Th/Nb ratios such as those in Vulsini lavas, Central Italy, indicate the role of crustal in the genesis of this magma. The Vulsini lavas are low in Nb/Y and Ti/Y ratios, which are recognised as a subduction related feature (Rogers, 1992; Peate *et al.*, 1999; Barley *et al.*, 2000: Arakawa *et al.*, 2003), therefore, the crustal contamination in these rocks, are interpreted as a result of subduction process (Rogers *et al., 1985).* The ratio plot of Th/Y versus Nb/Y clearly exhibits two distinguishable

trends that represent different processes, first, the subduction enrichment trend that features the increase of Th/Y relative to Nb/Y, second, the melt enrichment vector, showing the increasing tendency of both Th/Y and Nb/Y as a result of small degree of partial melting. The Bo Ploi lavas are compared with Cenozoic basalt from Southeast Asia, which alkali basaltic rocks from the Khorat Plateau, Thailand (Zhou and Mukasa, 1997) and alkali basalts from Dien Bien Phu, Vietnam (Koszowska *et al.*, 2006). The basaltic rocks from the Khorat Plateau, although, form a narrow trend along the melt enrichment array with the Th/Nb ratio (average 0.09) slightly lower than those of the Bo Ploi thus indicates that the basaltic rocks from the Khorat Plateau have an insignificance influenced by crustal materials in their genesis, which is in accord with Zhou and Mukasa (1997), that the lavas originated in the continental asthenosphere then ascended through the lithosphere without much contamination. The Dien Bien Phu basalts, Vietnam, form a dissimilar trend toward subduction enrichment vector with Th/Nb ratios range from 0.13-0.22 and this suggests a heterogeneous mantle beneath the Southeast Asia. The Dien Bien Phu basalts are similar to other Vietnamese basalts in that they underwent contamination by crustal materials (Hoang *et al.*, 1996; Hoang and Flower, 1998; Koszowska *et al.*, 2006) although the contamination mechanism is still a matter of debate. In the case of Dien Bien Phu basalts contamination is thought to have been by assimilation of sedimentary wallrock and by selective enrichment of mobile elements derived from these wallrock and mobilised by hydrous fluids (Koszowska *et al.*, 2006).

According to the available geochemical analyses, the Bo Ploi basanites have low values of these element ratios; K/P from 5.5 to 8.8 with an average value of 6.88; Nb/Y ratios from 3.7 to 4.3 (average 3.9); Th/Nb ratios of 0.11 to 0.14 (average 0.12), together with low silica content (average 47.2 wt%) and the stable oxygen isotope analyses, $\delta^{18}O$ 6.0 to 6.9‰V-SMOW, which reflects a normal range of mantle derived

magma. In addition, the presence of mantle peridotites in the Bo Ploi basalt indicates that magma ascended to the surface at a rapid rate thus residence time at a crustal level is minimal, therefore, all the criteria lead to the conclusion that the crustal contamination to the basalt is insignificant.

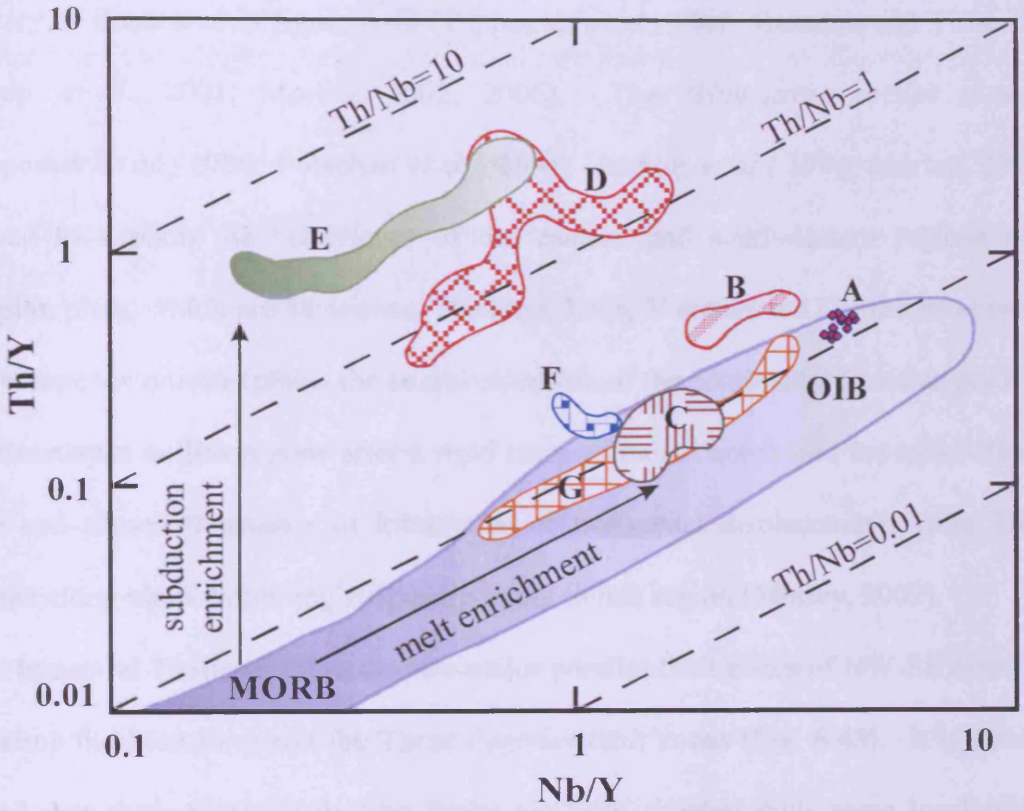

Figure 6.41 The plots of Th/Y versus Nb/Y for the Bo Ploi basalt compared with selected volcanic provinces. (Modified after Seyitoğlu *et al.*, 1997 and Wilson *et al.*, 1997 field of MORB, OIB and Basin&Range Province are from Kempton *et al.*, 1991).

A= Bo Ploi basalt; B, D = Rio Grande rift axis and Rio Grand frank (Gibson *et al.*, 1993); C= Basin&Range Province (Kempton *et al.*, 1991); E= Vulsini, Central Italy (Rogers *et al.*, 1985); F= Khorat Plateau, Thailand (Zhou and Mukasa, 1997); G= Dien Bien Phu basalt, Vietnam (Koszowska *et al.*, 2006).

6.3.4 Geodynamic implications

The major active tectonic regime in the mainland Southeast Asia is dominated by transtensional regime, large strike-slip faults and related rift systems, resulted from a colliding of India subcontinent with the massive Eurasia plate during late Cretaceous to Tertiary as illustrated in figure 6.42 (Tapponier *et al.*, 1986; Bunopas and Vella, 1992; Leloup *et al.*, 2001; Morley, 2002; 2006). The "*Himalayan escape tectonics*" (Tapponier *et al.*, 1986; Polachan *et al.*, 1991; Huchon *et al.*, 1994; Morley, 2002) is utilised to explain the behaviours of the eastern and south-eastern regions of the Eurasian plate, which are Myanmar, Thailand, Laos, Vietnam and Cambodia at present. The escape tectonics explains the lateral extrusion of the continental Eurasian plate from the Himalayan collision zone after a rigid mass of Indian notch into the softer Eurasian plate and causes thousands of kilometres of horizontal displacements from Tibetan Plateau along block-bounding strike-slip faults in this region (Morley, 2002).

In central Thailand, there are two major parallel fault zones of NW-SE orientation including the Mae Ping and the Three Pagodas fault zones (Fig. 6.43). It is generally agreed that these major strike-slip faults are both sinistral with some local scale of dextral movements (Morley, 2002) but their connection with other blocks is a controversial issue (Hall, 1996; Leloup *et al.*, 2001; Morley, 2002). The fault movements and the major rifting episode occurred during the Miocene-Oligocene ended in the opening of the Gulf of Thailand, at the same time, the localised tensional regime caused the forming of NS elongate sedimentary basins of Miocene-Oligocene closely associated with these strike-slip fault systems. The Bo Ploi area situated in the Three Pagodas fault zone and on the western flank of the Suphan Buri basin (Fig.6.43). The late Caenozoic Bo Ploi basanitic lavas (3.14±0.17 – 4.17 ± 0.11 Ma by Barr & Macdonald, 1981 and Sutthirat *et al.*, 1994, respectively) are compositionally consistent with a magma generation in an extension regime similar to others lithospheric rifting

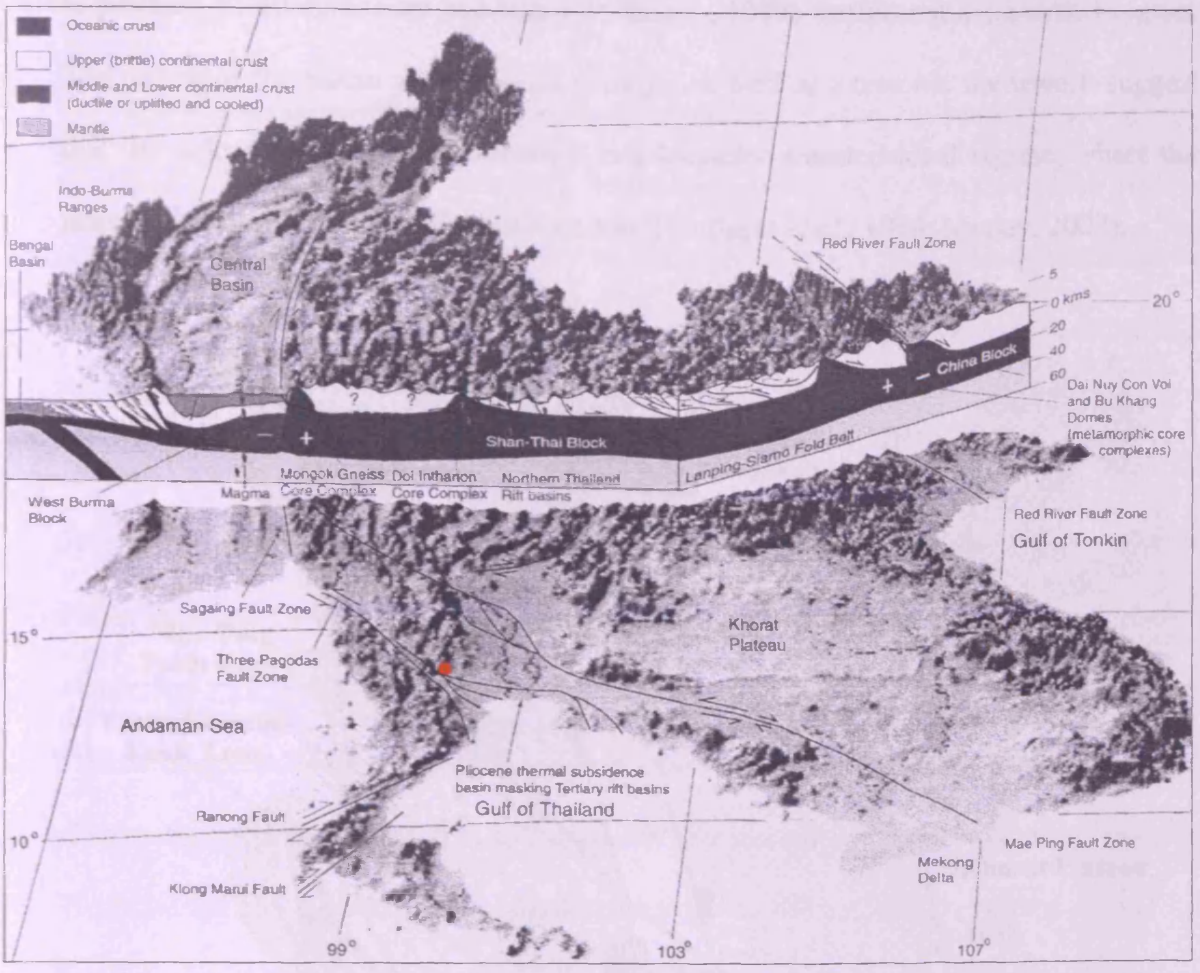

Figure 6.42 A digital elevation model (DEM) combined topographic and Tertiary geologic features of the mainland Southeast Asia modified from Morley (2002) and references therein, showing the metamorphic core complexes and the associated major strike-slip fault zones. The red circle represents the location of the Bo Ploi basalt.

and thinning related to within-plate volcanisms in many locations, for example, the East African Rift, the Baikal Rift (south central Siberia), the Rio Grande Rift and the Basin and Range province (western USA) and the Rhine Graben (north-western Europe). The Bo Ploi basalt, although, is chemically within-plate consistent with a generic of magma in an extensional regime but its very small voluminous and the lack of trending caused a doubt in its 'rifting genesis'. The possibility of mantle plume related in the generation of the Bo Ploi basanitic magma is far from unrealistic since mantel plumes are thought

to produce 20-40 stationary hotspots (Hoffmann, 1997) that do not exist in this region. The nature of the basalt and regional geology as well as a tectonic framework suggest that the volcanism may have occurred in a localised transtensional regime, where the mantle may be activated by the fault activity (Sutthirat *et al.*, 1994; Morley, 2002).

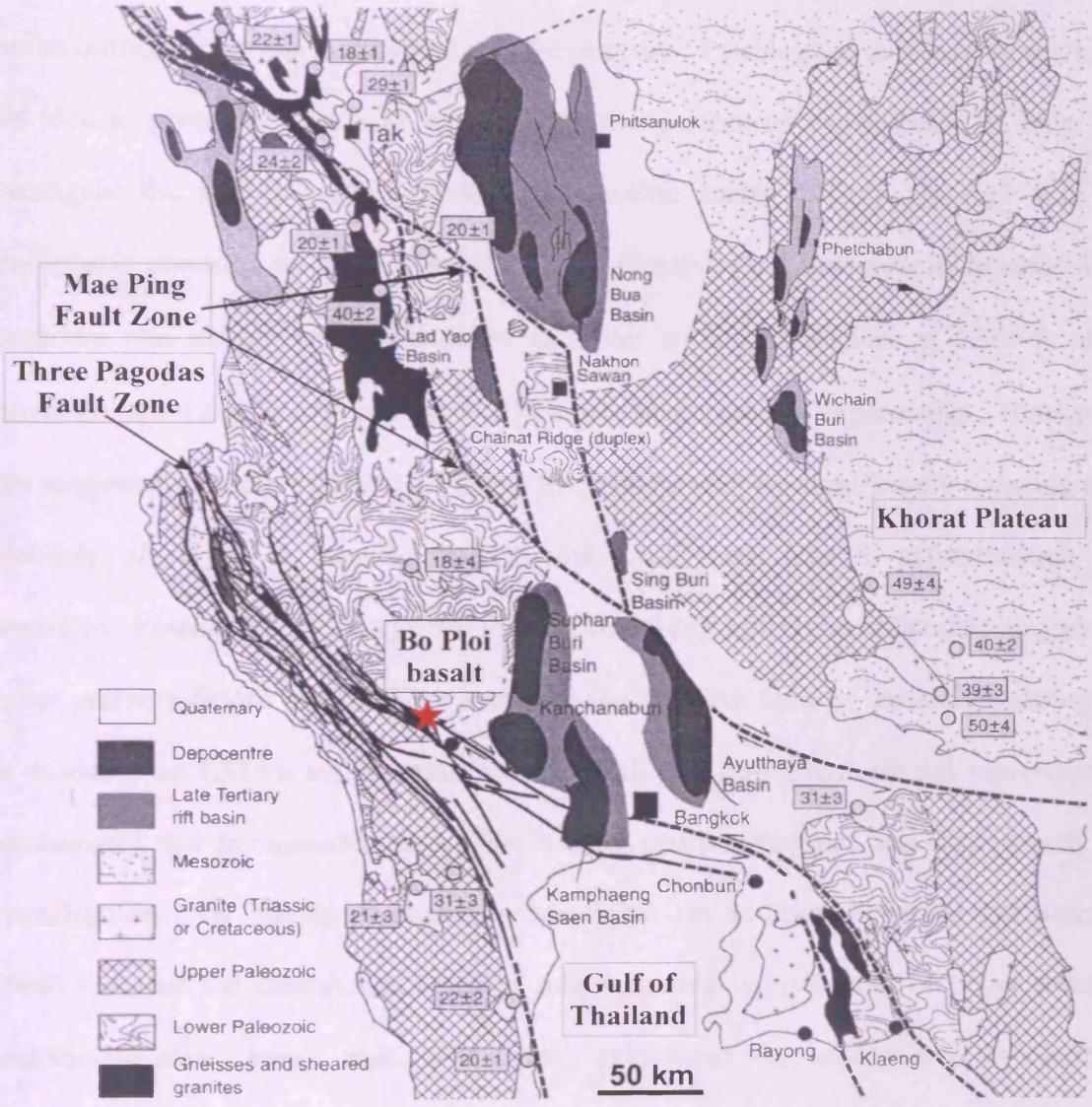

Figure 6.43 A geologic map shows the two main strike-slip faults in central Thailand, the Mae Ping and the Three Pagodas faults and the location of the Bo Ploi basalt (red star), which is closely related to the Three Pagodas fault zone. Number in boxes are fission-track age dating. (Modified after Morley, 2002 and references therein)

6.4 Experimental petrology: dissolution of corundum in the Bo Ploi basalt

The occurrences of corundum associated with alkali basalt from worldwide distributions are generally considered as a xenocrystic phase (Guo *et al.*, 1996, Oak *et al.*, 1996, Upton *et al.*, 1999; Srithai *et al.*, 1999; Limtrakun *et al.*, 2001) that could not crystallise directly from the host alkali basalt but accidentally incorporated into the basalts during the eruption ascending to the surface. Petrological evidence supporting this idea is given by Green *et al.*, (1978) who performed experiments in order to investigate the stability of corundum in basaltic melts. They reported that at atmospheric pressure, up to 2 - 8 wt% of Al_2O_3 dissolved in basalt near its liquidus and corundum was almost totally dissolved in basalt within 30 minutes at 1270°C; also corundum could not be crystallised at 10 kbar in their hydrous experiments. However, they suggested the role of CO_2 will affect the silicate melt by significantly reducing the solubility of Al_2O_3 in basaltic magma and could then lead to crystallisation of corundum. Presnall (1999) suggested that fractional crystallisation of basaltic magma at higher pressure (more than 2 GPa) increases the stability field of corundum, although his model is on CMAS components, where alkali and Fe-content are not represented. Additionally, the fractionation at 3 GPa is more complicated and can only present as crystallisation path instead of algebraic equations. In addition, Brearley and Scarfe, (1986) reported the dissolution rates of major mineral constituents of upper mantle xenoliths in alkali basalt melt, where they performed the experiments on olivine, clinopyroxene, orthopyroxene, spinel and garnet at high-pressure (5, 12 and 30 kbar) and superliquidus temperature (1300 to 1500°C). It is found that, at 12 kbar, the dissolution rate of these minerals are 4.21×10^{-8}cm s^{-1} for spinel to 1.67×10^{-5} cm s^{-1} for garnet, where most of the minerals have dissolution rate in the range of 10^{-7} to 10^{-6} cm s^{-1}. These dissolution rates are not comparable to the dissolution in nature like partial melting occur in magma chambers, but only applicable to the resorption rate of minerals

in alkali basalt magma during its rapid ascending to the surface, which is believed that the mantle materials have a residence time in alkali basalts during their eruption probably less than 50 hours (Kushiro *et al.*, 1976). These petrology experiments have provided information for better understanding the physiochemical condition and the genesis of corundum in basaltic terrains and I had the opportunity to directly test for dissolution of Bo Ploi corundum in the associated host alkali basalt by using high-pressure experiments.

6.4.1 Experimental procedures

Sample preparation

Corundum crystals were selected and examined to avoid uneven colour and oscillatory zoning. The crystals were, then, prepared as mineral beads using a sphere-making machine designed by Bond (1951) to the required sizes of approximately 1.0 mm in diameter. The volume of corundum beads is approximately 1.0 mm^3, where the uncertainty of ±30% is applied to the volume (Fig. 6.44-6.45). The beads were cleaned with distilled water in an ultrasonic bath. The powder sample of the Bo Ploi basalt (BPB-12), which has chemical composition of SiO_2 47.11 wt%, $Al_2O_3$16.29 wt%, Fe_2O_3 8.82wt%, MgO 7.28wt%, CaO 8.56wt%, Na_2O 5.15wt%, K_2O 2.85wt%, TiO_2 1.81wt%, MnO 0.20wt% and P_2O_5 0.95wt%. The powder was stored at 110°C until use. A corundum bead and basalt powder was loaded into the graphite capsule. With practice it was possible to centralise the bead in the middle of the capsule. The sample was compressed to remove air and packed with more basalt powder. The capsule was then sealed and the completed piston cylinder assemblage, then further placed in a 70°C drying furnace overnight before the experiment.

Experimental method

Experiments were performed in solid-media piston-cylinder apparatus in the Haskel High Pressure Laboratory (Department of Earth Sciences, University College

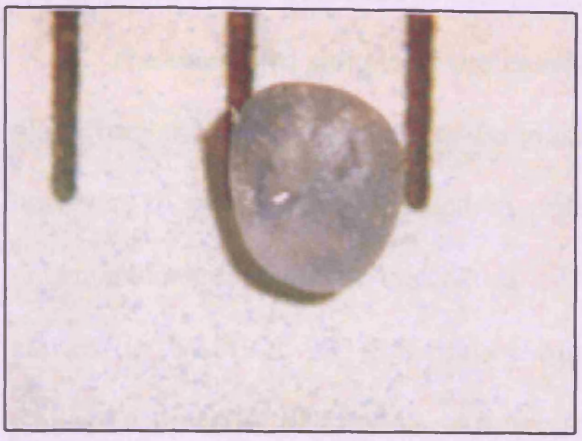

Figure 6.44 Photomicrograph shows morphology of corundum bead preparing for high-pressure experiment. Note scale in millimetre.

London). The capsule assemblies are 10 mm in diameter and made of pyrophyllite and Pyrex. The samples, corundum bead and basalt powder, were filled in 2.3 × 5.0 mm graphite capsules for the experiments. The temperatures were monitored and controlled by a Tungsten-Rhenium thermocouple (W3Re97/W25Re75) with variation of ±20°C. The experiments were performed at 10 kbar pressure and temperatures of 1200 and 1400°C for 60 minutes. The experiments were terminated with an isobaric quench and the quenched rates were approximately 125°C per second by switching off the power supply to the graphite heater. The experimental conditions are summarised in table 6.2.

The capsules were loaded in the piston cylinder apparatus then pressure was gradually applied to 10 kbar, meanwhile a temperature was raised from the beginning to the target temperatures (1200°C and 1400°C for the first and the second experiment, respectively) and maintained the experiment condition for 60 minutes then isobaric quenched.

Table 6.2 High-pressure experimental conditions and results

Run	P (kbar)	T (°C)	Starting assemblage	Time (mins)	Result
EXP 01	10.0	1200±20	Alkali basalt + cor	60	Brown gl + cor*
EXP 02	10.0	1400±20	Alkali basalt + cor	60	Brown gl + cor*

* Corundum sphere delaminated into discs due to quenching

Analytical procedures

The quenched samples were carefully recovered and sectioned. The quenched glass from each run was mounted on glass slide and prepared for microprobe analysis, however, they were not polished in order to minimise the loss of material due to delaminated nature of the corundum. The analyses for major oxide elements were carried out by JEOL-733 Superprobe equipped with Link Systems EDS at Birkbeck College, University of London. An accelerating voltage of 15 kV and a count time of 30s were used. The beam diameter is approximately 2 micron and chemical variation profiles were carried out across the samples with the analyses spacing of 100 microns.

6.4.2 Experimental results

Corundum beads were recovered from the middle part of the capsule surrounding by dark brown basalt glass, which indicates the experiment temperatures are high enough to reach the melting temperature of the basalt. Nonetheless, trails of black spots were clearly observed on thin edge of basalt glass, which was believed to be the residue of basalt powder. The swirling pattern of these trails reflects melt convection in the cell, which occurred during the high-pressure experiment. The beads were exfoliated and shattered in form of thin concave-film, therefore, it is not possible to accurately measure the dimension of corundum sphere after experiments. The photomicrographs of the capsule recovered from the experiments are shown in figure 6.46 – 6.50. Basalt glass has similar chemical composition to original basalt powder, although the analysed totals are not as good as those analyses from XRF. The corundum bead is partly resorbed in the alkali basalt of which 40 to 50 microns from the contact boundaries. In this area, there is a sharp change of Al_2O_3 and SiO_2 contents, also some other oxide components like MgO and CaO. The analyses are illustrated in tables 6.3 and 6.4. The concentration profiles of the quenched samples are shown in figure 6.51 and 6.52 for sample EXP01 and EXP02, respectively.

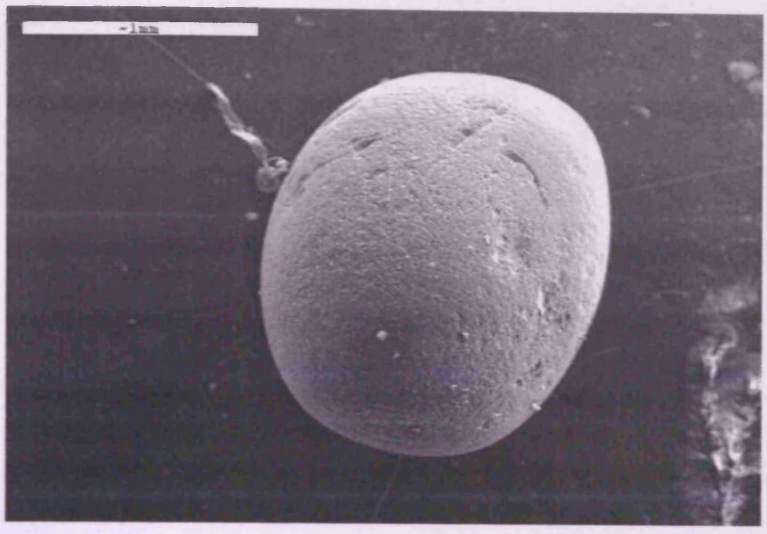

Figure 6.45 SEM image shows morphology and surface of corundum bead preparing for high-pressure experiment.

(Scale 1 millimetre)

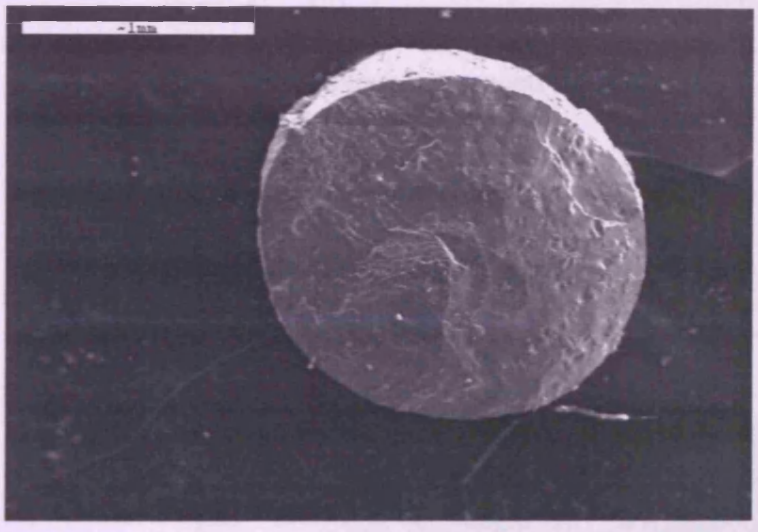

Figure 6.46 SEM images of quenched sample after a high-pressure experiment showing

(a) Morphology and surface of the charge.

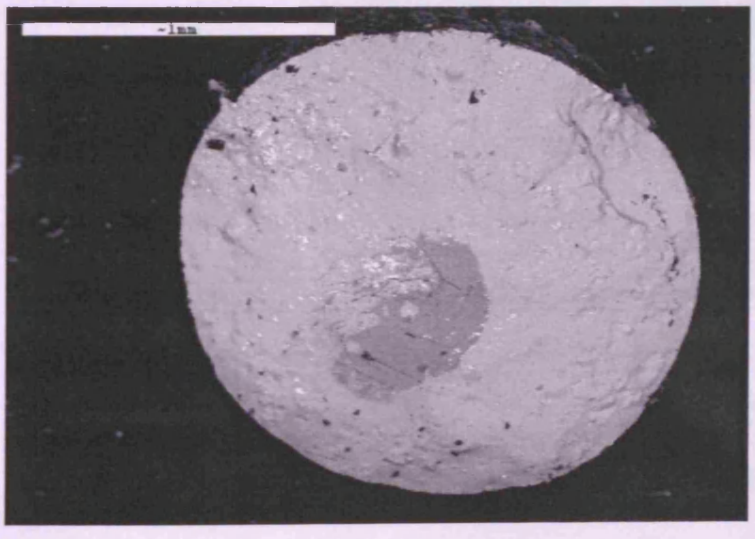

(b) Secondary electron image of the charge indicates compositionally different of the darker area is corundum and the lighter area is basaltic glass.

(Scale 1 millimetre)

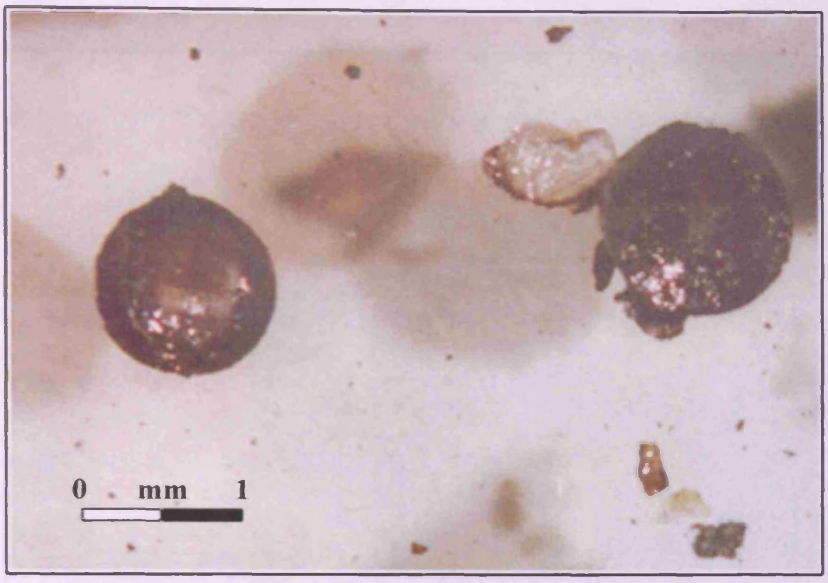

Figure 6.47 Photomicrograph shows cross-section of the capsule assemblages recovered from the experiment. (a) Corundum bead coated by layer of basalt glass (brown). (b) A piece of corundum exfoliated from corundum seed as a result from exceeding speed of quenching. (c) Graphite capsule (dull) with the remnant of dark basalt glass (shiny)

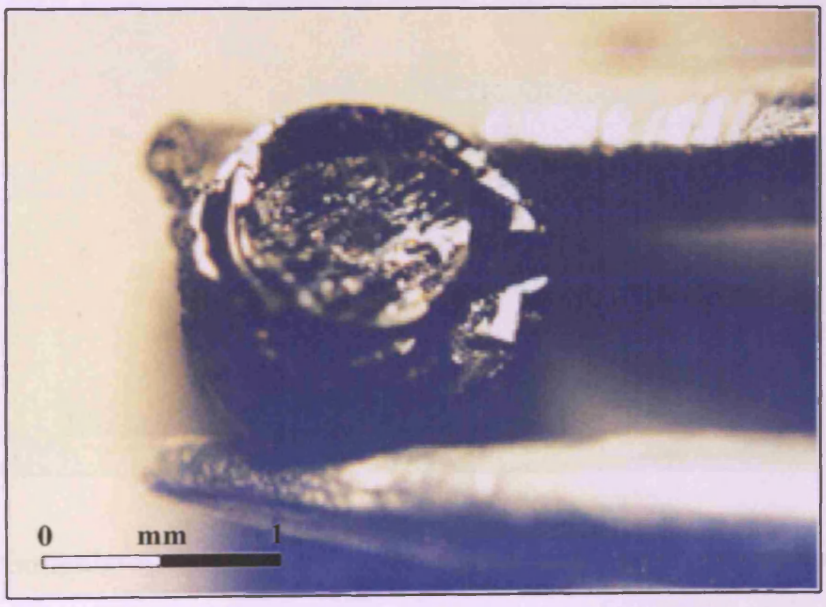

Figure 6.48 The bottom part of the capsule at higher magnification. Note the concave fracture in colourless corundum bead that engulf by dark basalt glass.

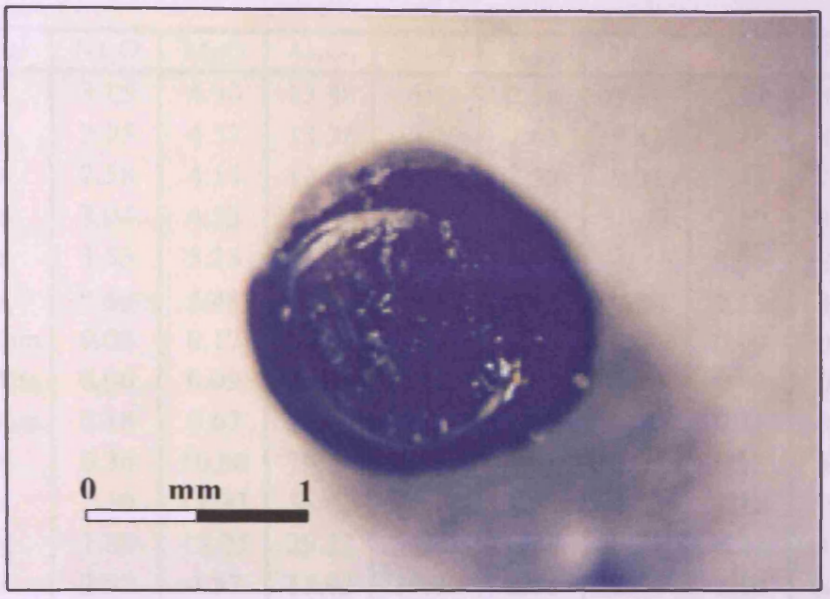

Figure 6.49 Photomicrograph of cross-section of capsule recovered from experiment, the colourless corundum sphere is in the middle surrounded by black basalt glass. Note the fracture lines on corundum bead

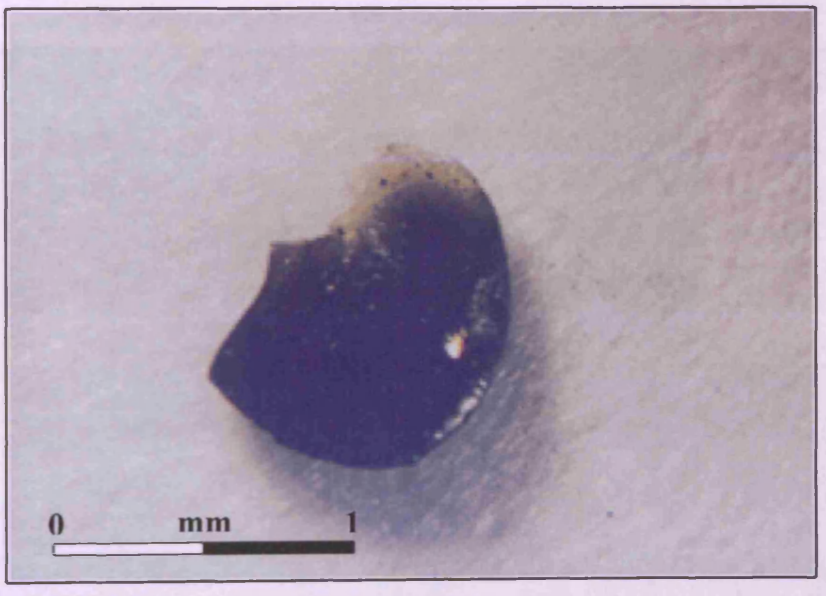

Figure 6.50 Photomicrograph of a piece of dark brown basalt glass recovered from experiment. Note the microscopic trail of black dots clearly seen on the thin translucent edge of the glass which may represent the residue of basalt powder that was not completely melted in the experiment.

Table 6.3 Major oxides variation across sample EXP01 after high-pressure experiment.

Point	Material	Na_2O	MgO	Al_2O_3	SiO_2	K_2O	CaO	TiO_2	FeO	Total
1	Glass	3.15	4.90	13.48	43.65	2.58	9.67	2.13	8.08	87.64
2	Glass	2.95	4.57	13.25	42.20	2.63	9.42	2.18	8.22	85.42
3	Glass	2.58	4.14	12.61	39.40	2.58	9.31	1.86	7.74	80.22
4	Glass	3.04	4.52	14.57	42.89	2.74	10.23	2.20	8.16	88.35
5	Glass	3.53	5.25	17.51	45.81	2.88	10.46	2.06	8.34	95.84
6	Glass	3.68	5.48	18.27	47.80	3.01	10.91	2.15	8.70	100.00
7	Corundum	0.08	0.17	96.56	0.20	0.08	0.00	0.00	0.43	97.52
8	Corundum	0.06	0.09	99.75	0.18	0.00	0.00	0.09	0.72	100.89
9	Corundum	0.18	0.67	97.55	0.39	0.06	0.00	0.11	0.68	99.64
10	Glass	0.36	10.60	79.65	0.64	0.03	0.09	0.13	6.49	97.99
11	Glass	2.10	11.97	38.01	24.19	1.23	4.65	1.12	9.15	92.42
12	Glass	1.88	17.05	29.22	35.41	0.74	0.85	0.25	1.12	86.52
13	Glass	2.93	4.37	15.03	39.84	2.56	9.74	2.18	8.04	84.69
14	Glass	3.39	4.91	16.61	43.31	2.55	9.94	2.09	8.03	90.83
15	Glass	3.05	4.72	15.00	41.42	2.44	9.76	2.18	7.70	86.27
16	Glass	2.67	4.20	13.67	39.94	2.54	9.63	2.28	7.87	82.80
Av.glass		2.72	6.67	22.84	37.42	2.19	8.05	1.75	7.51	89.15

Note: Av.glass = Average composition of glass

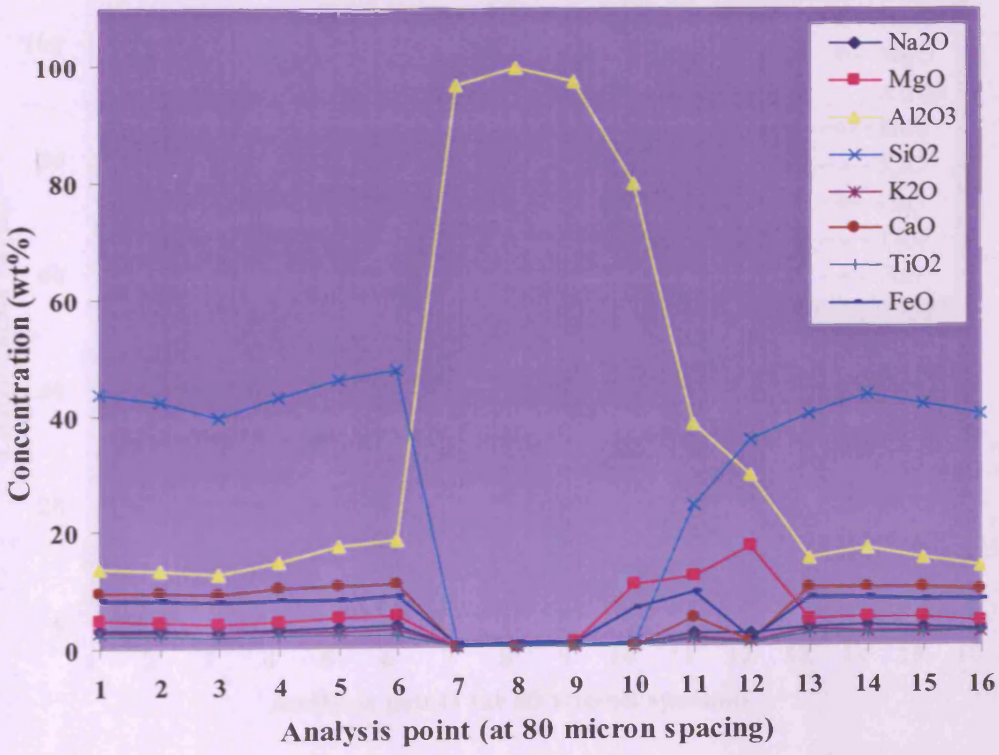

Figure 6.51 Chemical variations profile of sample EXP01 after high-pressure experiment

Table 6.4 Major oxides variation across sample EXP02 after high-pressure experiment

Point	Material	Na_2O	MgO	Al_2O_3	SiO_2	K_2O	CaO	TiO_2	FeO	Total
1	Glass	3.44	5.16	14.70	45.10	2.34	9.98	2.12	7.88	90.72
2	Glass	3.15	4.88	14.96	44.07	2.55	9.74	2.13	8.44	89.92
3	Glass	2.72	5.57	13.52	43.65	2.38	9.83	1.88	8.37	87.92
4	Glass	3.08	5.24	12.96	43.70	2.58	10.11	1.97	7.94	87.58
5	Glass	1.54	14.77	22.89	42.61	1.11	4.35	0.87	6.32	94.46
6	Glass	1.67	16.71	29.74	39.37	0.87	3.45	0.43	4.54	96.78
7	Corundum	0.07	0.09	99.25	0.15	0.00	0.00	0.07	0.66	100.29
8	Corundum	0.18	0.07	97.55	0.39	0.06	0.00	0.11	0.68	99.04
9	Corundum	0.00	0.05	96.88	0.32	0.00	0.00	0.07	0.70	98.02
10	Corundum	0.05	0.09	97.23	0.41	0.02	0.02	0.11	0.57	98.50
11	Glass	2.23	6.72	55.40	17.08	1.11	6.32	1.04	7.56	97.46
12	Glass	3.53	5.25	19.12	42.78	3.10	10.26	2.23	8.44	94.71
13	Glass	2.89	4.70	15.00	43.67	2.55	10.12	2.15	8.05	89.13
14	Glass	3.13	4.89	15.45	43.70	2.55	9.87	2.10	8.12	89.81
15	Glass	3.15	4.78	15.00	42.95	2.45	9.95	2.24	7.98	88.50
16	Glass	2.98	4.53	14.11	44.60	2.60	9.73	2.30	8.21	89.06
Av.glass		2.79	6.93	20.24	41.11	2.18	8.64	1.79	7.65	91.34

Note: Av.glass = Average composition of glass

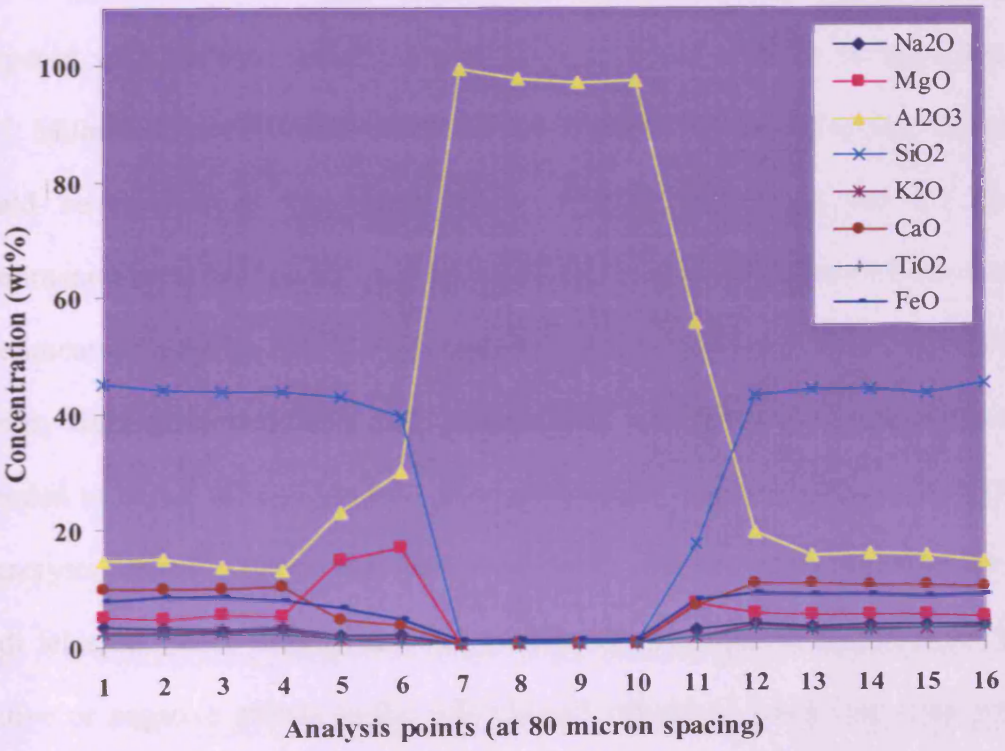

Figure 6.52 Chemical variations profile of sample EXP02 after high-pressure experiment

6.4.3 Discussion

The results from two high-pressure experiments indicated that corundum withstands the condition at 10 kbar, although the temperature differences (1200 and 1400°C) do not significantly affect the dissolution of corundum. The present of a swirl of basalt powder residue in the basalt glass after the experiment was an evidence of a small convection cell within the capsule, however, there was possibly a problem with heat distribution during the experiment and caused incomplete melting of basalt powder. It is considered that the basalt powder residue could be entirely melted if the run duration was longer. Corundum beads in these experiments were dissolved in alkali basalt merely by a few hundreds of microns from the surface; by contrast, the experiment at 1 atm by Green *et al.*, (1978) showed that added Al_2O_3 was completely dissolved in basalt near its liquidus temperature. The simplest interpretation is that the rates of dissolution of corundum in basalts were much slower at 10 kbar compared with 1 atm. This is consistent with the enhanced stability of corundum at high pressure, compared with basaltic mineral phase fields at lower pressure (O'Hara and Yoder, 1967; Milholland and Presnall, 1998; Pressnall, 1999). There are several factors, which should be considered for interpretation of dissolution rates and for the future experimental investigation of the stability of corundum in alkali basalt melt. Firstly, the experiments should be extended to higher-pressure conditions where theoretically the stability field of corundum is still larger. Also the experimental duration should be extended to check for equilibrium. It is worthwhile to consider the role of coexisting megacrysts phases in the natural host alkali basalt such as spinel, pyroxene, olivine and alkali feldspar, hence these phases have different dissolution rates that could be either positive or negative effects to the solubility of corundum when they react with alkali basalt. Thus the effect of bulk composition is not well known, including H_2O. The appropriate ratio of corundum bead and capsule, by inference, the amount of basalt

powder should be considered. The capsule loading should be carried out with careful practice in order to ensure that the basalt powder is evenly distributed. Lastly, the accuracy on the measurement of the sphere dimension can be improved by measuring with sophisticated equipment. The texture at the contacted area of corundum and basalt glass, corundum/melt reaction, at different experimental conditions should be a systematic study, hence the variation of textures indicates relative stability of corundum at various pressures.

Dissolution rate

A preliminary estimate for the solubility and dissolution rate of corundum in alkali basalt from these experiments was quickly established, although insufficient experiments were performed to discriminate between the competing phases. Corundum is not a common rock-forming mineral and there is limited knowledge about its physiochemical properties, for instance, diffusion coefficients, crystal-melt temperature distribution, latent heat of fusion of corundum and temperature gradient in the melt surrounding the sphere. However, the size of the sphere is small (~1.0mm in diameter), it should be practical to assume that the effect from those variation factors is minimal and the interaction of basaltic melt on corundum sphere is hydrostatic and isotropic. Therefore, ideally the dissolution rate should be obtainable from a simple arithmetic calculation together with the graphic diagram of chemical variation profile in figure 6.48 and 6.49. The experimental charges display a distinctive composition profile between corundum (bead) and the basaltic glass, so the initial radius and final radius of the bead can be estimated and summarised in table 6.3. The initial radii of the beads are taken from the chemical variation profiles, which can be clearly distinguished between corundum and glass at the last point where Al_2O_3 or SiO_2 sharply change their contents. The final radii of the beads are assumed from the length across corundum bead at the points where Al_2O_3 are at their highest contents (corundum composition without

reaction with the melt). Dissolution rate, which is a function of radial change with time, can be ideally simplified in an equation as $\Delta r/t$, where Δr is the changing of sphere radii (centimetre) and t represents time (second), although in reality a radial change is a non-linear function but the beads are small and the experiment duration is rather short so he other physiochemical factors should not significantly affect their dissolution rates in alkali basaltic melt thus using an equation $\Delta r/t$ for the dissolution rate should be satisfactory. The radius change of corundum bead (Δr) is approximately 0.018 to 0.025 cm for experiment at 1200 °C and 1400 °C, respectively. The dissolution rate of corundum in alkali basalt melt at 10 kbar is in the range of 5.0×10^{-6} to 6.94×10^{-6} cm s^{-1}. These approximate dissolution rates are consistent with the work of Brearley and Scarfe, (1986) that most of the mantle minerals have dissolution rates in alkali basaltic melt in the range of 10^{-7} to 10^{-6} cm s^{-1} (at 12 kbar), however, there are some factors that might vary the dissolution rate of corundum in nature. These include, speed of eruption/emplacement/transport that could control high temperature residence time of corundum in host basanites. Additionally, the location where corundum was incorporated into the host basanite, if it takes place at a greater depth, this should result in slower dissolution rate since the stability field of corundum is larger at higher pressure (Presnall, 1999), but countered by higher temperatures the completing effects are impossible to estimate. Small crystals will disappear preferentially due to surface area to volume ratios.

Table 6.5 Results of dissolution experiments

Run no	P (kbar)	T (°C)	r_i (cm)	r_f (cm)	Δr (cm)	t (s)
EXP01	10	1200	0.028	0.01	0.018	3600
EXP02	10	1400	0.032	0.012	0.025	3600

Note: P = pressure, T = temperature, r_i = initial radius, r_f = final radius, Δr = change in sphere radius, t = time

Chapter 7

Synthesis of data and genesis model

This chapter synthesises the data from previous chapters with the chapter lay out basis on the type of samples; the Bo Ploi corundum, the Bo Ploi basalt and the entrained mantle xenoliths. In the first part, a general review of the facts discovered from the studies and their interpretations are presented for each sample types. The second part demonstrates a connection and relation among these samples, which leads to the genesis of the Bo Ploi corundum.

7.1 Characterisation and interpretation of samples from the Bo Ploi deposit

7.1.1 The Bo Ploi corundum

The Bo Ploi corundum, gem quality blue sapphire, in this study has similar physical and optical properties to sapphires from other deposits worldwide. Its chemical composition, particularly the trace element concentrations, reflects 'basaltic type' nature consistent with its occurrence. Particular elements have an influence on the colour of these sapphires, which are Fe and Ti. A small amount but significant content of Fe and Ti in sapphire structure can produce an adorable blue colour thus the Fe^{2+} - Ti^{4+} intervalence charge transfer is responsible for the colour mechanism in blue sapphire, which is supported by a fairly good relationship between Ti content and a blue colour of sapphire. In this study, sapphires of a similar amount of FeO (about 0.5-0.6 wt%) though contain a relatively higher Ti content are darker or exhibit a tint of greyish colour and less transparency. The sapphires are mostly zoned and contain various species and abundances of mineral inclusions, including alkali feldspar (albite, sanidine, and anorthoclase), zircon, spinel, monazite, pyrochlore, and rutile. They also accommodate fluid inclusions, which were identified as CO_2-rich inclusions, multiphase inclusions that consisted of hypersaline aqueous (64 to 73 equivalent wt% NaCl),

although the isochore cannot be accurately established as the appearance of inclusions suggested leakage. A novel discovered of primarily appearance trapped silicate-melt inclusions indicated that the Bo Ploi corundum is magmatic origin. The trapping temperature obtained from microthermometric studies of the Type-II Multiphase fluid inclusions is in the range of 900 to 1000°C but the trapped silicate-melt inclusions give a wider range of 850 to 1200 °C. High density CO_2 (up to 0.84 g/cm^3) of the Type-I CO_2-rich fluid inclusions corresponds to pressure in the range of 9-10 kbar (Brown and Lamb, 1989) if the trapping temperature is at 1000 - 1200°C.

The re-homogenised silicate-melt inclusions are alkali intermediate or trachyandesitic composition with high Al_2O_3 content (average 27.4 wt%). Their chondrite normalised REE patterns show relatively flattened LREE and HREE patterns suggesting an unfractionated nature with prominent negative Eu anormalies indicating a segregation of Eu-containing minerals such as feldspar, apatite and nepheline from the melt. The Bo Ploi corundum was further analysed for its oxygen isotope chemistry, where a rather wide variation of $\delta^{18}O$ value, 6.5 to 9.6‰, was acquired. These $\delta^{18}O$ values overlap both with crust and mantle oxygen isotope values suggesting the involvement of crust in the genesis of the Bo Ploi corundum.

7.1.2 The Bo Ploi basalt and the entrained xenoliths

The dark, dense and highly porphyritic basaltic rocks outcropped in the study area are compositionally basanite. The rock also accommodates numbers of megacrysts/phenocrysts including olivine, pyroxene, alkali feldspar and spinel. Its Mg# ranges from 60.8 to 65.5 indicates that it is not a primary magma, additional whole rock chemical analysis signifies that this derivative magma originated from small degree partial melting of mantle materials and the melt evolved through fractional crystallisation without an involvement of crustal contamination process. This is confirmed by its oxygen isotope chemistry, where it yielded $\delta^{18}O$ values of 6.0 to 6.9‰,

which is a normal range of mantle oxygen isotope. In addition, the Bo Ploi basanite accommodates numbers of crustal xenoliths, including granitic rocks, coarse-grained nepheline syenite and quartzite and also mantle peridotites. These mantle xenoliths are dominated by spinel lherzolite and were utilised as a geothermobarometer based on the equilibrium of mineral pairs which they provided temperature estimate in a range of 1000 to 1200°C and the pressure ranges from 18 to 24 kbar corresponds to the depth of 60 to 79 km in the upper mantle region. These palaeogeotherms form a trend along the 70 mWm^{-2} heat flow line consistent with the present day heat flow in the study area.

The high-pressure experiments on dissolution of the Bo Ploi corundum in the Bo Ploi basanitic melt revealed the estimate dissolution rate at 10 kbar in the range of 5.0×10^{-6} to 6.94×10^{-6} cm s^{-1}, which is in relatively the same range of dissolution rate of mantle minerals (10^{-7} to 10^{-6} cm s^{-1}). This may imply that corundum and other mantle minerals originated or entrapped in the Bo Ploi basanite from a closed proximity region.

7.2 Genesis of the Bo Ploi corundum

To date, it can be concluded that the Bo Ploi corundum is a xenocrystic phase in the Bo Ploi basanites since the composition of the basanites are not Al_2O_3 saturated that allows corundum to crystallise. A discovery of silicate-melt inclusions in the Bo Ploi demonstrates that this corundum is definitely a magmatic origin. An oscillatory zoning or colour zoning observed in these sapphire crystals suggests chemical disequilibrium between the melt and the growing crystals and this feature often occurs in crystallisation from melt or magmatic origin. The physiochemical analyses of the silicate-melt inclusions, including their chemical compositions and oxygen isotopes, indicate the role of crustal material involvement in the genesis of the Bo Ploi corundum, therefore, the process of corundum crystallisation should take place in the crustal region, particularly in the lower crust.

The microthermometric studies of fluid and silicate-melt inclusions suggest that the temperature of crystallisation ranges from 800 to 1000°C, though a wider range (800 to 1200°C) was observed but the re-homogenisation had been successfully in the narrower range of 800-1000°C, therefore, it is more reliable in this range of temperature.

In principle, combining these trapping temperatures on the Bo Ploi geotherm should be able to establish the pressure of crystallisation, however, the lithologic geotherm from the entrained mantle xenoliths is likely to represent rather recent lithosphere architecture of the Bo Ploi area since the palaeogeotherm and the present day geotherm are the same, thus, this mantle xenolith geotherm may not reflect the right pressure of corundum crystallisation that took place millions of years before as an evidence from the thickness of zircon halo. The intrusion of the trachyandesitic melt into the lower crust should perturb the lithosphere architecture beneath the Bo Ploi area by introducing a high heat flow circulation in the vicinity and the geotherm at that time should be higher than the present day geotherm. Temporally, the lithosphere should gradually cool down until the next eruption of the Bo Ploi basanites in Tertiary, while the region was governed by a transtensional tectonic regime and the lithosphere was again perturbed by the new heat influx feeding from the magma.

Taking this into account, an average crustal thickness in this region of 30-40 km, the mantle xenolith barometer gives the crust-mantle boundary at the depth of 36.3 km (11 kbar). Assuming the same thermal gradient, this should be the maximum depth and/or pressure for majority of the Bo Ploi corundum to crystallise. The trapping temperature range of 800 to 1000°C is the temperature of crystallisation, therefore, the P-T of corundum crystallisation can be extrapolated (Fig. 7.1). The homogenisation temperature over 1000°C may corresponds to the pressure greater than 11 kbar or deeper than 36.3 km, which is rather ambiguous since the inclusions could not be re-homogenised and the appearance leakage of inclusions resulting from incorporating of

corundum in the hotter basanitic magma. The pressure beyond 11 kbar and temperature over 1000°C are presented by dashed line with question marks (?). The genesis of the Bo Ploi corundum can be established as follow;

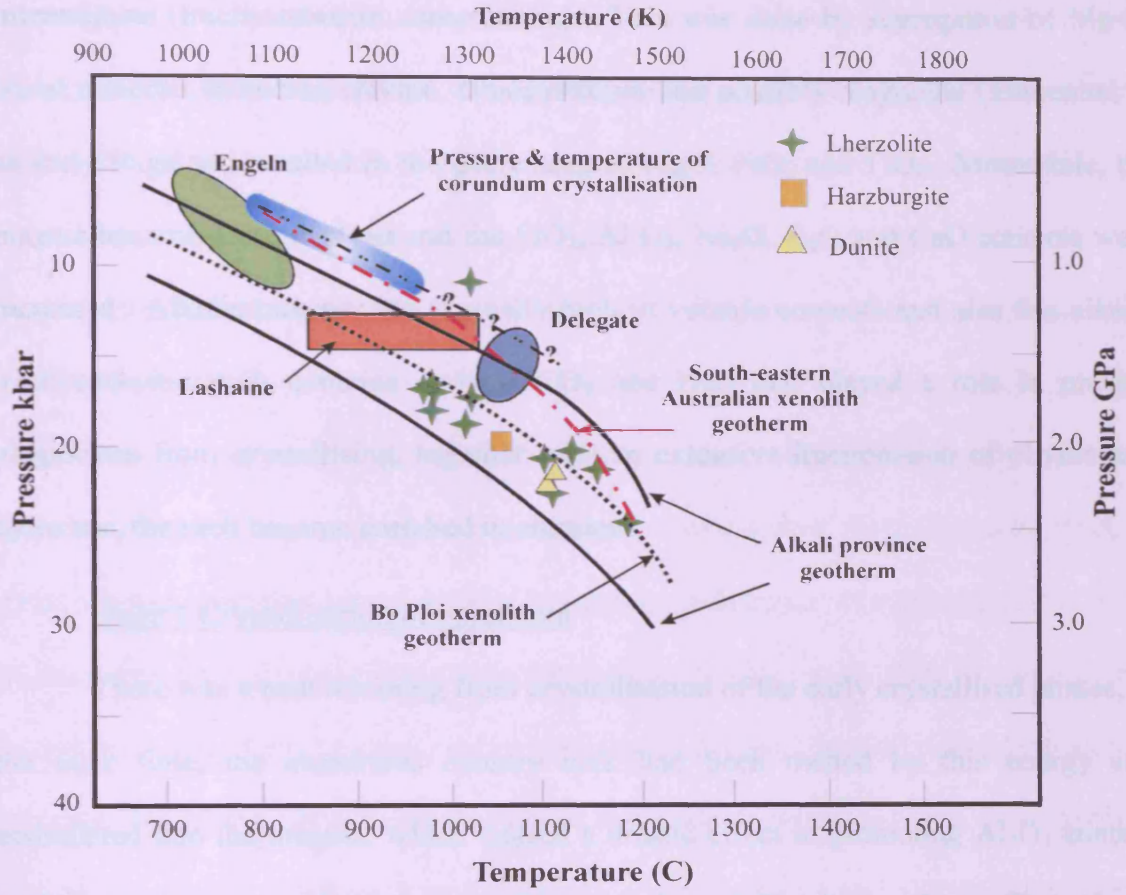

Figure 7.1 Pressure-temperature diagram showing an approximate crystallisation field of the Bo Ploi corundum (dashed line with blue shaded) taken from the homogenisation temperature range of 800-1000°C and the maximum pressure of 11 kbar (a pressure at crust-mantle boundary obtained from mantle xenolith geotherm). The palaeogeotherm of the Bo Ploi area (dashed line) is constructed from thermodynamic calculations on equilibrium of enstatite-spinel (Mercier, 1980) of the Bo Ploi mantle peridotites. Engeln-Lashaine-Delegate represents lower crustal granulites from East African Rift (Jones *et al.*, 1983a), which is on the upper range of alkali province geotherm (solid line). South-eastern Australian xenolith geotherm (pink dash line) is from O'Reilly and Griffin, 1985.

Stage 1 A formation of trachyandesitic melt

A trachyandesitic melt was generated by fractional crystallisation of alkali mafic magma such as alkali basalt until the composition gradually changed to alkali intermediate (trachyandesitic composition). This was done by segregation of Mg-Fe based minerals including olivine, clinopyroxene and possibly magnetite (±ilmenite) at an early stage and resulted in the decreasing of MgO, FeO, and TiO_2. Meanwhile, the magma became more evolved and the SiO_2, Al_2O_3, Na_2O, K_2O and CaO contents were increased. Alkalic magmas are normally high in volatile contents and also this alkalic trachyandesitic melt contains at least CO_2 and H_2O that played a role in prevent plagioclase from crystallising, together with an extensive fractionation of olivine and pyroxene, the melt became enriched in alumina.

Stage 2 Crystallisation of corundum

There was a heat releasing from crystallisation of the early crystallised phases, at the same time, the aluminous country rock had been melted by this energy and assimilated into the magma, which caused a drastic effect in promoting Al_2O_3 content until the melt became alumina oversaturated and crystallised corundum. The role of aluminous country rocks assimilated in the melt is confirmed by $\delta^{18}O$ values, 6.5 to 9.6‰, of the Bo Ploi corundum that indicates crustal signature in this corundum. The mineral inclusions in the Bo Ploi corundum suggests that this melt not only crystallised corundum but also include, feldspar, zircon, spinel, rutile, monazite and pyrochlore. These syn-genetic minerals share their roles in the chemistry of the melt, particularly partitioning the REE patterns. It is likely that the P-T of crystallisation is in the range of 8 to 11 kbar (26.4 to 36.3 km) and the temperature of 800 to 1000°C.

Stage 3 Entrapment of corundum in the later erupted Bo Ploi basanite

After corundum crystallised from trachyandesitic melt, this corundum formation might be disseminated in the lower crust and upper mantle region, according to the PT

of crystallisation. The later eruption of the Bo Ploi basanite brought these corundum crystals to the surface. This is confirmed by, at least, three major evidences indicating the xenocrystic phase of corundum in the Bo Ploi basanite, including, firstly, corundum crystals normally exhibit corroded surfaces, which are interpreted as a result of interaction of corundum and basalt hosts (Coenraads *et al.*, 1990; Guo *et al.*, 1996; Sutherland, 1996; Sutherland *et al.*, 1998a, 1998b). Secondly, an appearance of micro inclusions surrounded larger inclusions resulted from thermal-pressure strained while they were incorporating in the hotter basaltic magma. The internal pressure within inclusions was increased tremendously until the inclusions burst out and leaked then formed aureoles of smaller fluid inclusions surrounded the larger ones. This thermal strain has been observed in heat-treated sapphires from deposits in Madagascar (Rankin, 2002; Rankin and Edwards, 2003), which are metamorphic related deposits. They reported that the micro-inclusion aureoles do not present in untreated stones but this feature is found in heat-treated stones, which means the metamorphic fluids cannot withstand the heat-treatment temperature that is usually performed at 1200 to 1600°C (Hansawek, 1996). Thirdly, a zircon halo can determine a relative age of corundum since it takes hundred of million year to form a thick aureole like those aureoles occurred around zircon inclusions in corundum, which means corundum formed million of years before they were brought with the Bo Ploi basanite (3.14±0.17 to 4.17±0.11 Ma by Barr and Macdonald, (1981) and Sutthirat *et al.*, (1994), respectively) to the surface or cold corundum incorporated in hot basanitic magma.

The Bo Ploi basanite erupted to the surface at a rapid rate since all the foreign materials including corundum xenocrysts, crustal rocks such as granite, coarse-grained nepheline syenite and quartzite and mantle peridotites still survived the pressure difference from their originated sources. In addition, it is expected that there is possibly CO_2 in the basanite that functioned as a medium that stop corundum from dissolving in

the magma similar to experiments demonstrated by Green *et al.*, (1978). It is noteworthy that plagioclase-spinel coexist in some spinel lherzolite nodules entrained in the Bo Ploi basanite, which indicates a decompression of the xenoliths that led to melting of spinel and recrystallised as a plagioclase mantle. This suggests that there was an interruption in the eruption of the Bo Ploi basanite, which brought the spinel lherzolites to spinel – plagioclase transition region thus both spinel and plagioclase were allowed to crystallise together.

Stage 4 Recovering of the Bo Ploi corundum

The Bo Ploi corundum bearing basanites flowed from a surface topographic high where it erupted westward to the lower plain of palaeo-stream channel. The tropical climates as in Thailand is advantageous for both physical and chemical weathering and erosion processes that gradually changed the rock into reddish basaltic soil. Corundum crystals and the associated megacrysts such as spinel, pyroxene, and zircon that can withstand physical and chemical weathering processes better than the host rock are carried away to deposit extended from the source rock, in particular, transported by water. A high concentration of corundum in the Bo Ploi gem fields have been recovered along the palaeo-stream channel not far from where the Bo Ploi outcrop located.

7.3 Cartoon showing a genesis model of the Bo Ploi corundum

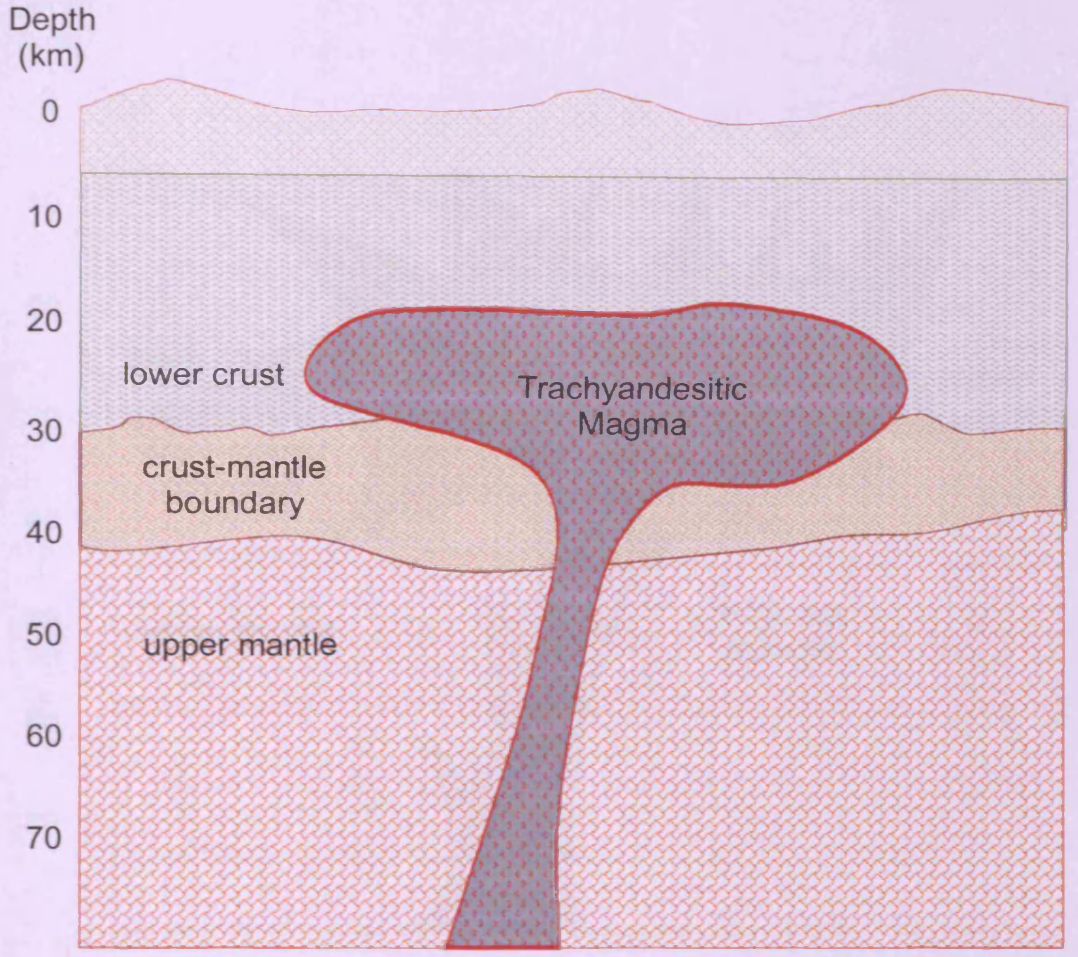

Figure 7.2 Cartoon shows the eruption of trachyandesitic magma to shallow level in the lower crust. The activity within the magma chamber may be dominated by extensive fractionation of the early phases like olivine and clinopyroxene. The H_2O in the magma retarded crystallisation of plagioclase and elevated Al_2O_3 content in the melt. The crust-mantle boundary (approximately 36 km) is obtained from the P-T estimates of the entrained mantle peridotites in the host Bo Ploi basanites. This is consistent with an estimate crustal thickness in this region ranging from 30 to 40 km (Mooney *et al.*, 1998).

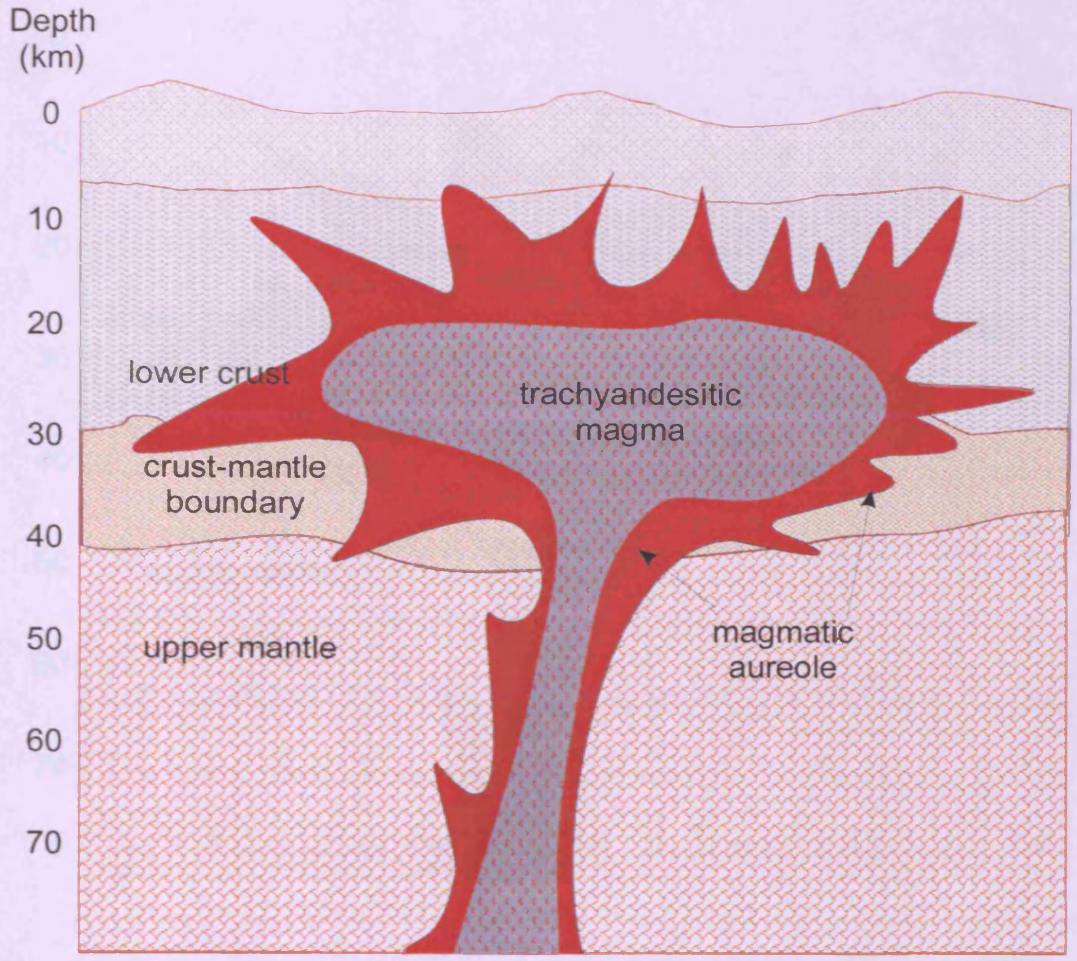

Figure 7.3 Cartoon showing the interaction of trachyandesitic magma with the country rocks, which are composed of at least granite and coarse-grained nepheline syenite, presented as magmatic aureole. The volatiles in the magma effused and distributed heat into country rock that led to melting and assimilation of country rocks in the melt then drove the composition to alumina oversaturated thus corundum can be crystallised.

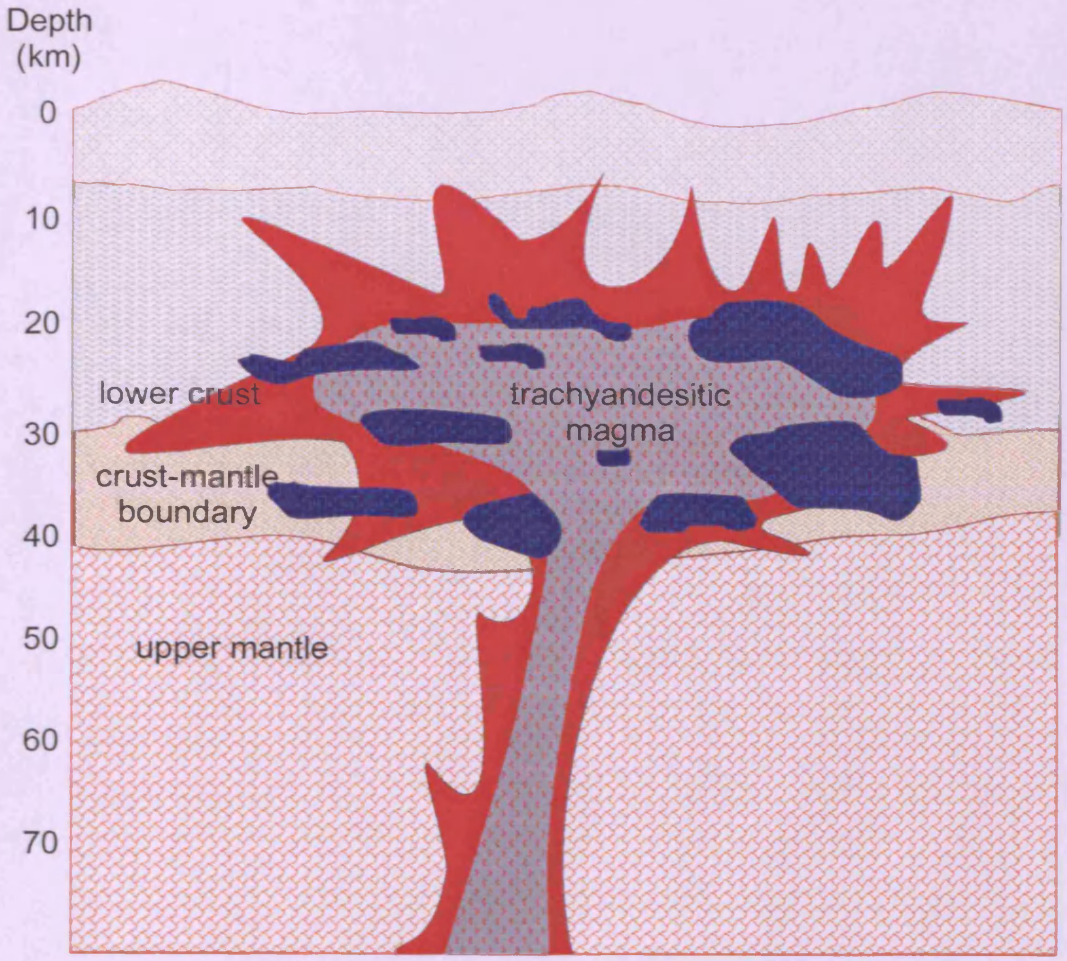

Figure 7.4 Cartoon showing crystallisation of corundum, presented as deep blue lens, from alumina oversaturated melt that evolved through fractional crystallisation and contaminated with crustal materials (confirmed by corundum $\delta^{18}O$ 6.5-9.6‰). The estimate P-T for majority of corundum crystallisation corresponds to the depth of approximately 26 to 36 km and the temperature of 800 to 1000°C. The P-T of crystallisation at the temperature higher than 1000°C cannot be accurately established since the inclusions could not be homogenised.

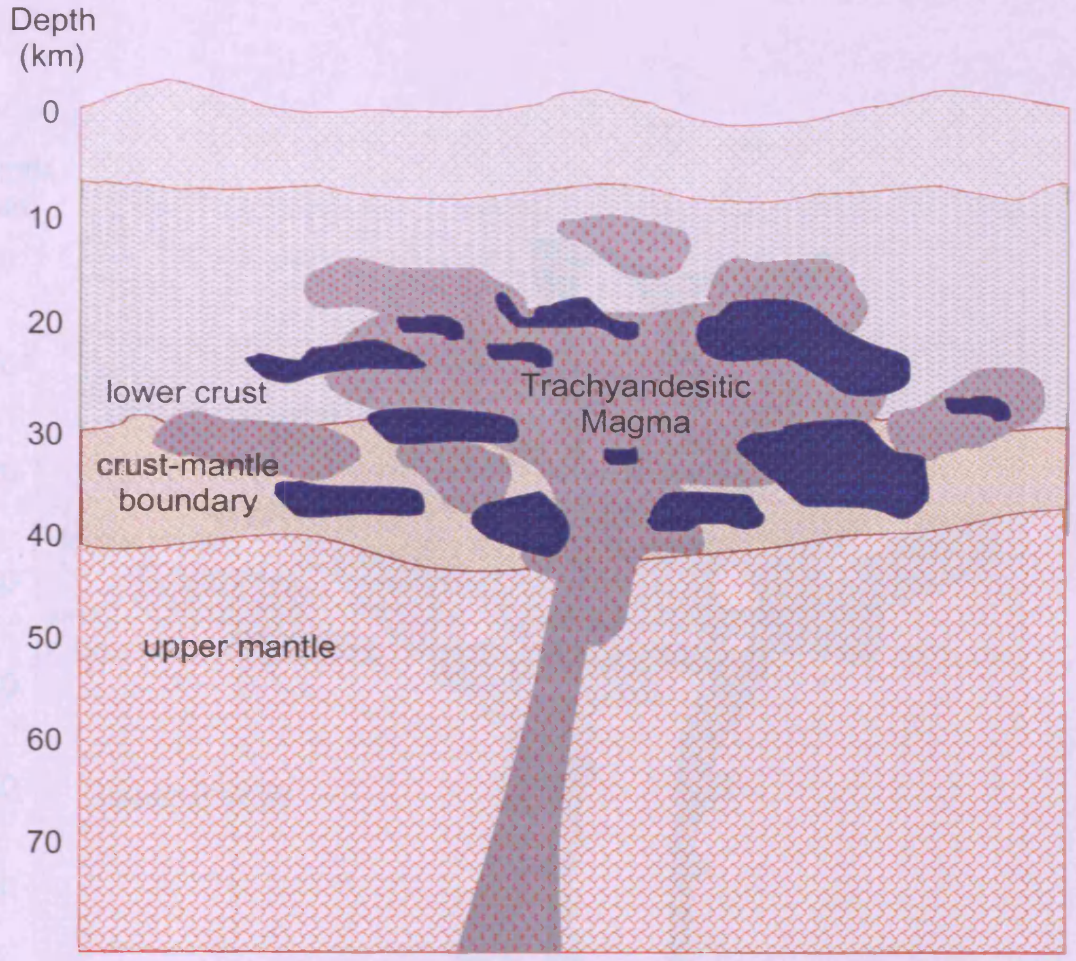

Figure 7.5 The evolved trachyandesitic magma cooled down and underplated with corundum deposited scattering around the crust-mantle region. As a matter of time, this event must take place long before the eruption of the Bo Ploi Tertiary basanites or the cold corundum incorporated into hot basanitic melt, where supporting evidences are discussed in Section 7.2.

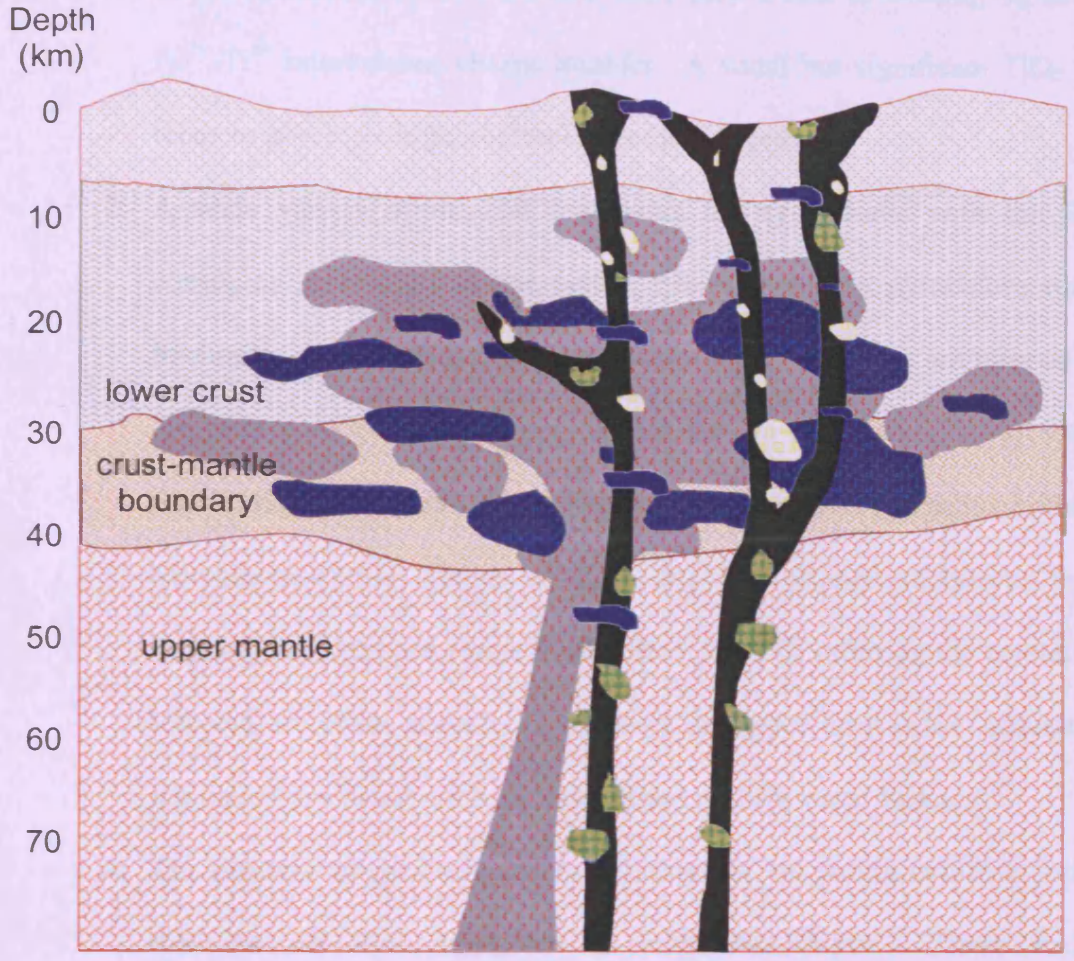

Figure 7.6 Cartoon showing the later rapid eruption of the Bo Ploi basanitic magma brought corundum to the surface together with numbers of mantle xenoliths (green) and crustal xenoliths (yellow). Corundum has been recovered from palaeo-stream channel deposits and in situ in the basanitic soil.

7.4 Conclusions

1. The studies of gem quality corundum from the Bo Ploi deposit demonstrate that a major composition of this corundum is almost entirely Al_2O_3 with a minor concentration of FeO and TiO_2 play a role in causing its colour by Fe^{2+}-Ti^{4+} intervalence charge transfer. A small but significant TiO_2 content tends to provide a high quality blue colour sapphire.
2. A wide variety of mineral inclusions are syn-genetic with the Bo Ploi corundum including feldspar, zircon, spinel, monazite, pyrochlore, rutile and boehmite. In addition, fluid and silicate-melt inclusions are trapped during the growth of corundum suggests that the Bo Ploi corundum growth from melt in the environment that consist of CO_2-rich and hypersaline brine.
3. Microthemometric studies of fluid and silicate-melt inclusions provided trapping temperatures range from 800 to 1200°C, inferring the crystallisation temperature of the corundum, however the upper limit is less accurate since the inclusions could not be homogenised and appeared leakage.
4. The primary trapped silicate-melt inclusions are strong evidence indicating that the Bo Ploi corundum is magmatic origin. These melts are trachyandesitic compositions that yielded corundum by fractional crystallisation and gained excess alumina from assimilation of high alumina crustal material.
5. The oxygen isotope chemistry of the Bo Ploi corundum is in the range of 6.5 to 9.6‰ reflecting both crust and mantle oxygen isotope chemistry thus confirming the involvement of crustal material in the genesis of the corundum.
6. The 'Bo Ploi basalt' is a within-plate alkalic magma of basanitic composition generated by a small degree partial meting of mantle materials

and modified through fractional crystallisation without a significant crustal contamination, which is confirmed by their $\delta^{18}O$ values of 6.0 to 6.9‰.

7. The mantle xenoliths entrained in the Bo Ploi basanites are spinel lherzolite, harzburgite and dunite. The estimated P-T based on the equilibrium of enstatite-spinel mineral pairs is in the range of 18 to 24 kbar and temperature of 1000-1200°C thus these xenoliths are from the upper mantle region. The Bo Ploi xenolith palaeogeotherm is consistent with the present day geotherm of heat flow approximately 70mW/m^2.
8. The Bo Ploi geotherm is used for extrapolating the crystallisation field of the Bo Ploi corundum by combining with the temperatures of crystallisation taken from homogenisation temperatures of fluid and silicate-melt inclusions (800 to 1000°C). The pressure of crystallisation should be in the range of 8 to 11 kbar. The homogenising temperature above 1000°C cannot accurately demonstrate the pressure of crystallisation.
9. The high-pressure experiments on the dissolution of Bo Ploi corundum in basanitic melt show that corundum has a dissolution rate in same range as most of the mantle minerals, 10^{-7} to 10^{-6} cm s^{-1}, implying that they may originate or entrain in the basanites from a closed proximity.
10. The Bo Ploi basanites erupted as a result of a localised tensional regime, the movement of minor faults in the Three Pagodas Fault zone. The magma conveyed mantle peridotites from upper mantle together with corundum that formed and disseminated in lower crust - upper mantle region and the lower crustal xenoliths of granitic, coarse-grained nepheline syenite and quartzite to the surface.

References

Abdel-Rahman, A.H. and Nassar, P.E. 2004. Cenozoic volcanism in the Middle East: petrogenesis of alkali basalts from northern Lebanon. *Geological Magazine*, **141**, 545-563.

Albarède, F. and Bottinga, Y. 1972. Kinetic disequilibrium in trace element partitioning between phenocrysts and host lava. *Geochimica et Cosmochimica Acta*, **36**, 141-156.

Allégre, C.J., Hamelin, B., Provost, A. and Dupré, B. 1987. Topology in isotopic multispace and origin of mantle chemical heterogeneities. *Earth and Planetary Science Letters*, **81**, 319-337.

Al-Mishwat, A. and Nasir, S.J. 2004. Composition of the lowere crust of the Arabian Plate: a xenolith perspective. *Lithos*, **72**, 45-72

Altermann, W. 1986. The Upper Palaeozoic pebbly mudstone facies of peninsular Thailand and Western Malaysia-continental margin deposits of Palaeoeurasia. *Geologische Rundschau*, **75**, 79-89.

Altermann, W. 1991, Structural evolution of Mesozoic Peninsular Malaysia- Discussion. *Journal of Geological Society London*, **148**, 417.

Amour, N.St. and Linnen, R.L. 1999. Microprobe Analysis of Melt Inclusions in Sapphires from Bo Phloi, Thailand. *In*: Lüders, V., Schmidt-Mumm, A. and Thomas, R. (eds) *Terra Nostra*, **99/6:** *European Current Research on Fluid Inclusions XV, Programme and Abstracts*, 6.

Andersen, T. and Neumann, E-R. 2001. Fluid inclusions in mantle xenoliths. *Lithos*, **55**, 301-320.

Anderson, A.T. 1973. The before-eruption water content of some high alumina magmas. Bulletin of Volcanology, **37**, 530-552.

Anderson, A. T., Clayton, R. N. and Mayeda, T. K. 1971. Oxygen isotope thermometry of mafic igneous rocks. *Journal of Geology,* **79,** 715–729.

Appora, I., Eiler, J.M., Matthews, A. and Stolper, E.M. 2003. Experimental determination of oxygen isotope fractionations between CO_2 vapor and soda-melilite melt. *Geochimica et Cosmochimica Acta,* **67**, 459-471.

Arakawa, Y., Park, K.H., Kim, N.H., Song, Y.S. and Amakawa, H. 2003. Geochemistry and tectonic implications of Proterozoic amphibolites in the northeastern part of the Yeongnam massif, SouthKorea. *The Island Arc*, **12**, 180-189.

Aranyakanond, P. 1988. Sapphire Deposit, Amphoe Bo Phloi, Kanchanaburi. *Supplementary document for Royal Institute of Thailand conference, Bangkok, Thailand, 25-37.* (in Thai)

Arculus, R.J. and Wills, K.J. 1980. The petrology of plutonic blocks and inclusions from the Lesser Antilles island arc. *Journal of Petrology*, **21**, 743– 799.

Asnachinda, P. 1978. Tin mineralization in the Burmese-Malayan Peninsula: a plate tectonic. *In*: Nutalaya, P. (editor in chief) *Proceedings of the Third Regional Conference on Geology and Mineralogy Resources of Southeast Asia,* Bangkok, Thailand, 193-199.

Aspen, P., Upton, B.G.J. and Dickin, A.P. 1990. Anorthoclase, spinel and associated megacrysts in Scottish alkali basalts: high-pressure syenitic debris from upper mantle sources? *European Journal of Mineralogy*, **2**, 503-517.

Audley-Charles, M.G. 1988. Evolution of the southern margin of Tethys (North Australian region) from Early Permian to Late Cretaceous. *In*: Audley-Charles, M.G. and Hallam, M.G. (eds) *Gondwana and Tethys*. Geological Society Special Publication, **37**, 79-100.

Bacon, C.R., Newman, S. and Stopler, E. 1992. Water, CO_2, Cl and F in melt inclusions in phenocrysts from three Holocene explosive eruptions, Crater Lake, Oregon. *American Mineralogist*, **77**, 1021-1030.

Baker, D.R. and Eggler, D.H. 1983. Fractionation paths of Atka (Aleutians) high-alumina basalts: constraints from phase relations. *Journal of Volcanology and Geothermal Research*, **18**, 387-404.

Baker, D.R. and Eggler, D.H. 1987. Compositions of anhydrous and hydrous melts coexisting with plagioclase, augite and olivine or low-Ca pyroxene from 1 atm to 8 kbar: application to the Aleutian volcanic center of Atka. *American Mineralogist*, **72**, 12– 28.

Baker, J.M., Hirschmann, M.M., Ghiorso, M.S. and Stolper, E.M. 1995. Compositions of near-solidus peridotite melts from experiments and thermodynamic calculations. *Nature*, **375**, 308-311.

Bakker, R.J. and Elburg, M.A. 2006. A magmatic-hydrothermal transition in Arkaroola (northern Flinders Ranges, South Australia): from diopside-titanite pegmatites to hematite-quartz growth. *Contributions to Mineralogy and Petrology*, **152**, 541-569.

Barclay, J., Carroll, M.R., Houghton, B.F. and Wilson, C.J.N. 1996. Pre-eruptive volatile content and degassing history of an evolving peralkaline volcano, *Journal of Volcanology and Geothermal Research*, **74**, 75-87.

Barley, M. E., Kerrich, R., Reudavy, I. and Xie, Q. 2000. Late Archaean Ti-rich, Al-depleted komatiites and komatiitic volcaniclastic rocks from the Murchison Terrane in Western Australia. *Australian Journal of Earth Sciences*, **47**, 873.

Barr, S.M. and Dostal, J. 1986. Petrochemistry and origin of megacrysts in Upper Cenozoic basalts, Thailand. *Journal of Southeast Asian Earth Sciences*, **1**, 107-116.

Barr, S. M. and James, D. E. 1990. Trace element characteristics of Upper Cenozoic basaltic rocks of Thailand, Kampuchea and Vietnam. *Journal of Southeast Asian Earth Sciences*, **4**, 233-242.

Barr, S.M. and Macdonald, A.S. 1978. Geochemistry and petrogenesis of Late Cenozoic alkaline basalts of Thailand. *Geological Society of Malaysia Bulletin*, **10**, 25-52.

"----------" 1981. Geochemistry and geochronology of late Cenozoic basalts of Southeast Asia. *Geological Society of America Bulletin; part II*, **92**, 1096-1142.

"----------" 1987. Nan River Suture zone, northern Thailand. *Geology*, **15**, 907-910.

"----------" 1991. Toward the late Palaeozoic- early Mesozoic tectonic model of Thailand. *Journal of Thai Geosciences*, **1**, 11-22.

Barr, S.M., Macdonald, A.S., Dunning, D.R., Ounchanum, P. and Yaowanoiyothin, W. 2000. U-Pb (zircon) age and paleotectonic setting of the Lampang volcanic belt, northern Thailand. *Journal of Geological Society*, **157**, 553-563.

Barr, S.M., Macdonald, A.S., Haile, N.S. and Reynolds, P.H. 1976. Paleomagnetism and age of the Lampang basalts (northern Thailand) and age of the underlying pebble tools. *Journal of Geological Society of Thailand*, **2** (no.1-2), 1-10.

Barr, S.M., Macdonald, A.S., Yaowanoiyothin, W. and Panjasawatwong, Y. 1985. Occurrence of blueschist in the Nan River mafic-ultramafic belt, northern Thailand. *Warta Geologi*, **11**, 47-50.

Barr, S.M., Tantisukrit, C., Yaowanoiyothin, W. and Macdonald, A.S. 1990. Petrology and tectonic implications of Late Paleozoic volcanic rocks of the Chiang Mai belt, northern Thailand. *Journal of Southeast Asian Earth Sciences*, **4**, 37-47.

Bartels K.S., Kinzler, R. J. and Grove, T.L. 1991. High pressure phase relations of primitive high-alumina basalt from Medicine Lake volcano, northern California. *Contributions to Mineralogy and Petrology*, **108**, 253-270.

Beard, J.S. and Lofgren, G.E. 1992. An experiment-based model for the petrogenesis of high-alumina basalts. *Science*, **256**, 112-115.

Belkin, H.E., DeVivo, B., Torok, K. and Webster, J.D. 1998. Pre-eruptive volatile content, melt-inclusion chemistry and microthermometry of interplinian Vesuvius lavas (pre-AD1631). *Journal of Volcanology and Geothermal Research*, **82**, 79-95.

Bertrand, P., Sotin, C., Mercier, J-C.C. and Takahashi, E. 1986. From the simplest chemical system to the natural one: garnet peridotites barometry. *Contributions to Mineralogy and Petrology*, **93**, 168-178.

Bindeman, I.N., Sigmarsson, O. and Eiler, J. 2006. Time constraints on the origin of large volume basalts derived from O-isotope and trace element mineral zoning and U-series disequilibria in the Laki and Grímsvötn volcanic system. *Earth and Planetary Science Letters*, **245**, 245-259.

Bodnar, R.J. 1999. Melt-volatile evolution in porphyry-type ore deposits. *In*: Lüders, V., Schmidt-Mumm, A. and Thomas, R. (eds) *Terra Nostra*, **99/6:** *European Current Research on Fluid Inclusions XV, Programme and Abstracts*, 40-42.

Borisoya, A.Y., Nikogosian, I.K., Scoates, J.S., Weis, D., Damasceno, D., Shimizu, N and Touret, J.LR. 2002. Melts, fluids and crystal inclusions in olivine phenocysts from

Kerguelen plume-derived picritic basalts: evidence for the interaction with the Kerguelen Plateau lithosphere. *Chemical Geology*, **183**, 195-220.

Brearley, M. and Scarfe, C.M. 1986. Dissolution Rates of Upper Mantle Minerals in an Alkali Basalt Melt at High Pressure: An Experimental Study and Implications for Ultramafic Xenolith Survival. *Journal of Petrology*, **27**, 1157-1182.

Brey, G.P. and Köhler, T. 1990. Geothermobarometry in four-phase lherzolites II. New thermobarometers and practical assessment of existing thermobarometers. *Journal of Petrology*, **31**, 1353-1378

Brey, G.P., Doroshev, A.M., Girnis, A.V. and Turkin, A.I. 1999. Garnet-spinel-olivine-orthopyroxene equilibria in the FeO-MgO-Al_2O_3-SiO_2-Cr_2O_3 system: I. Composition and molar volumes of minerals. *European Journal of Mineralogy*, **11**, 599-617.

Brophy, J.G. and Marsh, B.D. 1986. On the origin of high-alumina arc basalt and the mechanics of melt extraction. *Journal of Petrology*, **27**, 763-789.

Brown, G.F., Buravas, S., Charaljavanaphet, J., Jalichandra, N., Johnston, W.D. Sresthaputra, V. and Taylor, G.C. 1951. Geologic reconnaissance of the mineral deposits of Thailand. *United States Geological Survey Bulletin*, **984**, 183p.

Brown, G.M., Pinsent, R.H.and Coisy, P. 1980. The petrology of spinel-peridotites from the Massif Central, France. *American Journal of Science*, **280-A**, 471-498.

Brown, P.E. and Lamb, W.M. 1989. P-V-T properties of fluids in the system $H_2O \pm CO_2 \pm$ NaCl: New graphical presentations and implications for fluid inclusion studies. *Geochimica et Cosmochimica Acta*, **53**, 1209-1221.

Bunjitradulya, S. and Prapaitrakul, N. 1973. *Geologic map of Amphoe Bo-Phloi and its vicinities, scale 1:50,000.* Geological Survey Division, Department of Mineral Resources, Bangkok, Thailand. *Geologic Map of Changwat Suphan Buri, scale 1: 250,000.* Geological Survey Division, Department of Mineral Resources, Bangkok, Thailand.

Bunopas, S. 1977. *Geologic Map of Changwat Suphan Buri, scale 1: 250,000.* Geological Survey Division, Department of Mineral Resources, Bangkok, Thailand.

Bunopas, S. 1981. Palaeogeographic history of western Thailand and adjacent part of Southeast Asia: A plate tectonics interpretation. PhD thesis. Victoria University of Wellington, New Zealand. (Reprinted 1982 as Geological Survey Paper 5), Department of Mineral Resources, Thailand, 810p.

Bunopas, S. and Bunjitradulya, S. 1975. Geology of Amphoe Bo Phloi north Kanchanaburi with special notes on the 'Kanchanaburi Series'. *Journal of Geological Society of Thailand*, **1**, 51-67. (in Thai)

Bunopas, S. and Vella, P. 1978. Late Palaeozoic and Mesozoic structural evolution of northern Thailand, a plate tectonics model. *In*: Nutalaya, P. (editor in chief) *Proceedings of the Third Regional Conference on Geology and Mineralogy Resources of Southeast Asia,* Bangkok, Thailand, 133-140.

Bunopas, S. and Vella, P. 1983. Tectonic and geologic evolution in Thailand. *In*: Nutalaya, P. (ed) *Proceeding of Workshop on Stratigraphic Correlation of Thailand and Malaysia,* Haad Yai, Thailand, 213-232.

Bunopas, S. and Vella, P. 1992. Geotectonics and geologic evolution of Thailand. *In* Piancharoen, P. (editor-in-chief) *Proceeding of a National Conference on Geological Resources of Thailand: Potential for Future Development, Bangkok, Thailand.*

Burns, R.G. 1993. *Mineralogical Applications of Crystal Field Theory Second Edition,* Cambridge University Press, Cambridge.

Burton, C.K. 1985. The tectonic framework of mainland Southeast Asia. *The Conferences on applications of geology and the national development,* Chulalongkorn University, Bangkok, Thailand, Supplementary volume, 255-268.

Cao, R.-L. and Zhu, S.-H. 1987. Mantle xenoliths and alkali-rich host rocks in eastern China. *In*: Nixon, P.H. (ed) *Mantle Xenoliths*. John Wiley, New York, 167–180

Carbonel, J.P., Duplaix, S. and Selo, M. 1972. La methode des traces de fission de l'uranium appliquee a la geochronologie, datation du magmatisme recent de l'Asie du Sudest. *Reuu De Geographic Physique Et De Geologic Dynamique*, **14(1)**, 29-46.

Carey, S.P., Burret, C., Chaodumrong, P., Wongwanich, T. and Chonglakmani, C. 1995. Triassic and Permian conodonts from the Lampang and Ngao Groups, Northern

Thailand. Sonderdruck aus CFS-Courier 142, Frankfurt am Main, **142**, 497-513.

Carswell, D.A. and Gibb, F.G.F. 1987. Garnet lherzolite xenoliths in the kimberlites of northern Lesotho: revised P-T equilibrium conditions and upper mantle palaeogeotherm. *Contributions to Mineralogy and Petrology*, **97**, 473-387.

Cawthorn, R.G., Strong, D.F. and Brown. 1976. Origin of corundum-normative intrusive magma. *Nature*, **259**, 102-104.

Chabiron, A., Alyoshin, A.P., Cuney, M., Deloule, E., Golubev, V.N., Velitchkin, V.I. and Poty, B. 2001. Geochemistry of rhyolitic magmas from the Streltsovka caldera (Transbaikalia, Russia): melt inclusion study. *Chemical Geology*, **175**, 273-290.

Charaljavanaphet, C. 1951. Bo-Phloi placers, Kanchanaburi. *In*: Brown, G.F. *et al.*, (eds). *Geological Reconnaissance of the Mineral deposits of Thailand, United States Geological Survey Bulletin*, **984.**

Chen, C, Nakada, S., Shieh, Y. and DePaolo, D.J. 1999. The Sr, Nd and O isotopic studies of the 1991–1995 eruption at Unzen, Japan. *Journal of Volcanology and Geothermal Research*, **89**, 243-253

Chen, S., O'Reilly, S.Y., Zhou, X., Griffin, W.L., Zhang, G., Sun, M., Feng, J. and Zhang, M. 2001. Thermal and petrological structure of the lithosphere beneath Hannuoba, Sino-Korean Craton, China: evidence from xenoliths. *Lithos*, **56**, 267-301.

Chen, J., Hsu, C. and Ho, K., 2003. Geochemistry of Cenozoic volcanic rocks and related ultramafic xenoliths from the Jilin and Heilongjian provinces, northeast China, *Journal of Asian Earth Sciences*, **21**, 1069-1084.

Chiba, H., Chacko, T., Clayton, R.N. and Goldsmith, J.R. 1989. Oxygen isotope fractionations involving diopside, frosterite, magnetite and calcite: application to geothermometry. *Geochimica et Cosmochimica Acta*, **53**, 2985-2995.

Chuaviroj, S., Chaturongkawanich, S. and Sukkawattananun, S. 1980. *Report on Geology of Geothermal Resources of Northern Thailand: Part I San Kampaeng.* Department of Mineral Resources, Bangkok, Thailand, 45p.

Chupin, S.V., Chupin, V.P., Barton Jr, J.M. and Barton, E.S. 1998. Archean melt inclusions in zircon from quartzite and granitic orthogneiss from South Africa: Magma compositions

and probable sources of protoliths. *European Journal of Mineralogy*, **10**, 1241-1251.

Clayton, R.N. and Mayeda, T.K. 1996. Oxygen isotope studies of achondrites. *Geochimica et Cosmochimica Acta,* **60**, 1999-2017.

Coenraads, R.R., Sutherland, F.L. and Kinny, P.D. 1990. The origin of sapphires: U-Pb dating of zircon inclusions shades new light. *Mineralogical Magazine*, **54**, 113-122.

Coenraads, R.R. 1992. Sapphires and rubies associated with volcanic provinces: inclusions and surface features shed light on their origin. *Australian Gemmology*, **18**, 70-80.

Collins, P.L.F. 1979. Gas hydrates in CO2-bearing fluid inclusions and the use of freezing data for estimation of salinity. *Economic Geology*, **72**, 1435-1444.

Conceição, R.V. and Green, D.H. 2004. Derivation of potassic (shoshonitic) magmas by decompression melting of phlogopite+pargasite lherzolite. *Lithos*, **72**,209-229.

Cooper, M.A., Herbert, R. and Hill, G.S. 1989. The structural evolution of Triassic intermontane basins in northeastern Thailand. *In* Thanasutthipitak, T. and Ounchanum, P. (eds) *Proceeding of Intermontane basins: geology and resources*, Chiang Mai, Thailand, 231-242.

Cox, K.G., Bell, J.D. and Pankhurst, R.J. 1979. *The interpretation of igneous rocks*. Allen and Unwin, London, 450pp.

Craig, H., 1961. Isotopic variations in meteoric waters, *Science*, **13**, 1702-1703.

Crawford, A.J., Falloon, T.J. and Eggins, S. 1987. The origin of island arc high-alumina basalts. *Contributions to Mineralogy and Petrology*, **97**, 417– 430.

Crawford, A.J. and Panjasawatwong, Y. 1996. Ophiolite, ocean crust and the Nan suture in NE Thailand. *In*: Lee, T-Y. (ed) *International Symposium on Lithosphere Dynamics of East Asia: Geology, Energy and Mineral Resources of the Indochina Region,* Taipei, Taiwan, R.O.C., *Program and Extended Abstracts*, 84-89.

Danyushevsky, L.V., Carroll, M.R. and Fanning, J.C. 1997. Origin of high-An plagioclase in Tongan high-Ca boninites: implications for plagioclase-melt equilibria at low $P(H_2O)$. *Canadian Mineralogist*, **35**, 313-326.

Danyushevsky, L.V., Della-Pasqua, F.N. and Sokolov, F. 2000. Re-equilibration of melt inclusions trapped in magnesian olivine phenocrysts from subduction-related magmas:

petrological implications. *Contributions Mineralogy and Petrology*, **138**, 68-83.

Dautria, J.M. and Girod, M. 1987. Cenozoic volcanism associated with swells and rifts. *In* Nixon, P.H. (ed) *Mantle Xenoliths*, New York, John Wiley, 195-214

Demémy, A., Sharp, Z.D. and Pfeifer, H-D. 1997. Mg-metasomatism and formation conditions of Mg-chlorite-muscovite-quartzphyllites (leucophylittes) of the Eastern Alps (W.Hungary) and their relations to Alpine whiteschists. *Contributions Mineralogy and Petrology*, **128**, 247-260.

Diamond, L.W. 2001. Review of the systematics of CO_2-H_2O fluid inclusions. *Lithos*, **55**, 69-99.

Dick, H.J.B. and Bullen, T. 1984. Chromian spinel as a petrogenetic indicator in abyssal and alpine-type peridotites and spatially associated lavas. *Contributions to Mineralogy and Petrology*, **86**, 54-76.

Dobosi, G., Downes, H., Mattey, D. and Embey-Isztin, A. 1998. Oxygen isotope ratios of phenocrysts from alkali basalts of the Pannonian basin: Evidence for an O-isotopically homogeneous upper mantle beneath a subduction-influenced area. *Lithos*, **42**, 213-223

Downes, H., Embey-Isztin, A. and Thirlwall, M.F. 1992. Petrology and geochemistry of spinel peridotite xenoliths from the western Pannonian Basin (Hungary): evidence for an association between enrichment and texture in the upper mantle. *Contributions Mineralogy and Petrology*, **109**, 340-354

Downes, H., Shaw, A., Williamson, B.J. and Thirlwall, M.F. 1997. Sr, Nd and Pb isotopic evidence for the lower crustal origin of Hercynian granodiorites and monzogranites, Massif Central, France. *Chemical Geology*, **136**, 99-122.

Draper, D.S. and Green, T.H., 1999. P-T phase relations of silicic, alkaline, aluminous liquids: new results and applications to mantle melting and metasomatism. *Earth and Planetary Sciences Letters*, **170**, 255–268

Drury, S.A. 1980. Lewisian pyroxene gneisses from Barra and the geochemistry of the Archaean lower crust. *Scottish Journal of Geology*, **16**, 199-207.

Eiler, J.M., Farley, K.A., Valley, J.W., Hofmann, A.W. and Stolper, E.M. 1996. Oxygen isotope constraints on the sources of Hawaiian volcanism. *Earth and Planetary Science Letters,* **144**, 453-467.

Embey-Isztin, A., Downes, H., James, D.E., Upton, B.G.J., Dobosi, G, Ingram, G.A., Harmon, R.S. and Scharbert, H.G. 1993. The petrogenesis of Pliocene alkaline volcanic rocks from the Pannonian basin, Eastern Central Europe, *Journal of Petrology*, **34**, 317-343.

Ewart, A. and Stipp, J.J. 1968. *Geochimica et Cosmochimica Acta*, **32**, 699-735.

Fan, Q. and Hooper, P.R. 1989. The mineral chemistry of ultramafic xenoliths of eastern China: implications for upper mantle composition and the palaeogeotherms. *Journal of Petrology*, **30**, 1117-1158.

Faure, F. and Schiano, P. 2005. Experimental investigation of equilibrium conditions during forsterite growth and melt inclusion formation. *Earth and Planetary Sciences Letters*, **236**, 882-898.

Ferguson, J. and Fielding, P.E. 1971. The origins of the colours of yellow, green and blue sapphires. *Chemical Physics Letters*, **10**, 262-265

"----------" 1972. The origins of colours of natural yellow, blue and green sapphires. *Australian Journal of Chemisty*, **188**, 1371-1385.

Finnerty, A.A. and Boyd, F.R. 1987. Thermobarometry for garnet peridotites xenoliths: a basis for upper mantle stratigraphy. *In*: Nixon, P.H. (ed) *Mantle Xenoliths*. John Wiley, New York, 381-402.

Floyd, P.A. and Winchester, J.A. 1975. Magma-type and tectonic setting discrimination using immobile elements. *Earth and Planetary Sciences Letters*, **27**, 211-218.

Frey, F.A., Green, D.H. and Roy, S.D. 1978. Integrated models of basalt petrogenesis: A study of quartz tholeiites to olivine melilitites from SE Australia utilizing geochemical and experimental petrological data. *Journal of Petrology*, **19**, 463-513.

Frey, F.A., Clague, D., Mahoney, J.J. and Sinton, J.M. 2000. Volcanism at the edge of the Hawaiian plume: petrogenesis of submarine alkalic lavas from the North Arch Volcanic Field. *Journal of Petrology*, **41**, 667-691.

Frezzotti, M-L., 2001. Silicate-melt inclusions in magmatic rocks: application to petrology. *Lithos*, **55**, 273-299.

Frezzotti, M-L. andersen, T., Neumann, E-R. and Simonsen, S.L. 2002. Carbonatite-melt CO_2 fluid inclusions in mantle xenoliths from Tenarife, Canary Island: a story of trapping, immiscibility and fluid-rock interaction in the upper mantle. *Lithos*, **64**, 77-96.

Fritsch, E. and Rossman, G.R. 1987. An update on color in gems. Part 1: Introduction and colors caused by dispersed metal ions. *Gems and Gemology*, **23**(3), 126-139.

Fritsch, E. and Rossman, G.R. 1988a. An Update on Color in Gems. Part 2: Colors involving multiple atoms and color centers. *Gems & Gemology*, **24**(1), 3-15.

Fritsch, E. and Rossman, G.R. 1988b. An Update on Colors in Gems. Part 3: Colors caused by band gaps and physical phenomena. *Gems & Gemology*, **24**, (2), 81-102.

Garlick, G.D. 1966. Oxygen isotope fractionation in igneous rock. *Earth and Planetary Sciences Letters*, **1**, 361-368.

Garson, M.S., Young, B., Mitchell, A.H.G. and Tait, B.A.R. 1975. The geology of tin belt in Peninsular Thailand around Phuket, Phangnga and Takua Pa. *Institute of Geological Sciences Overseas Memoir*, **1**, 1-112.

Gasparik, T. and Hutchison, M.T., 2000. Experimental evidence for the origin of two kinds of inclusions in diamonds from deep mantle. *Earth and Planetary Sciences Letters*, **181**, 103-114.

Gatinski, Y. G., Mishina, A.V., Vinogradov, I.V. and Kovalev, A.A., 1978. Metallogenic belts of Southeast Asia as a result of different geodynamic conditions interference. *In*: Nutalaya, P. (ed) *Proceeding of the Third Regional Conferences on Geology and Mineral Resources Southeast Asia*, 313-318.

German Geological Mission. 1972. Final report of the German Geological Mission to Thailand 1965-1971, unpublished report, Bundesanstalt für Bodenforschung, Hannover, 94p.

Ghiorso, M.S. and Sack, R.O. 1995. Chemical mass transfer in magmatic processes IV. A revised and internally consistent thermodynamic model for the interpolation and extrapolation of liquid-solid equilibria in magmatic systems at elevated temperatures and pressures. *Contributions to Mineralogy and Petrology*, **119**, 197-212.

Gibson, S. A. 1988. The Geochemistry, Mineralogy and Petrology of the Trotternish Sill Complex, Northern Skye, Scotland, Ph.D. Thesis, Kingston University.

Gibson, S. A., Thompson, R.N., Leat, P.T., Morrison, M.A., Hendry, G.L, Dickin, A.P. and Mitchell, J.G. 1993. Ultrapotassic magma along the flanks of the Oligo-Miocene Rio Grande Rift, USA: Monitor of the zone of lithospheric mantle extension and thinning beneath a continental rift. *Journal of Petrology*, **34**, 187-228.

Gibson, S. A., Thompson, R.N., Weska, R. K., Dickin, A. P. and Leonardos, O.H. 1997. Late Cretaceous rift-related upwelling and melting of the Trinidade starting mantel plume head beneath western Brazil. *Contributions to Mineralogy and Petrology*, **126**, 303-314.

Giuliani, G., Dubessy, J., Banks, D., Vinh, H. Q., Lhomme, T., Pironon, J., Garnier, V. Trinh, P. T., Long, P.V., Ohmenstetter, D. and Schwarz, D. 2003. CO_2-H_2S-COS-S_8-AlO(OH)-bearing fluid inclusions in ruby from marble-hosted deposits in Luc Yen area, North Vietnam. *Chemical Geology*, **194**, 167-185.

Giuliani, G., Fallick, A.E., Garnier, V., France, L.C., Ohnenstetter, D. and Schwarz, D. 2005. Oxygen isotope composition as a tracer for the origins of rubies and sapphires. *Geology*, **33**, 249-252.

Grancea, L., Fulop, A., Cuney, M., Liroy, J. and Pironon, J. 2003. Magmatic evolution and ore-forming fluids involved in the origin of the gold/base metals mineralization in the Baia Mare province, Romania. *Journal of Chemical Exploration*, **78**, 627-630.

Green, T.H. and Ringwood, A.E. 1968. Genesis of the calc-alkaline igneous rock suite. *Contributions to Mineralogy and Petrology*, **18**, 105-162.

Green, T.H., Wass, S.Y., Ferguson, J. 1978. Experimental study of corundum stability in basalts (abstract). *Abstract Programme 3rd Australia Geological Convention*, Townsville, 34.

Graham, C.M. and Harmon, R.S. 1983. Stable isotope evidence on the nature of crust-mantle interactions. *In* Hawkesworth, C.J. and Norry, M.J.(eds.), *Continental basalts and mantle xenoliths*. Shiva, Nantwich, 20-45.

Gromet, L.P., Dymek, R.F., Haskin, L.A. and Korotev, R.L. 1984. The 'North American Shale Composite': its application, major and trace element characteristics. *Geochimica et Cosmochimica Acta*, **48**, 2469-2482.

Grove, T.L., Walker, D., Longhi, J., Stolper, E. and Hays, J.F., 1973. Petrology of rocks 12002 and origin of picritic basalts at Oceanus Procellarum. *Geochimica et Cosmochimica Acta*, **1**, 955-1011.

Guo, J., Griffin, W.L. and O'Rielly, S.Y. 1994. A cobalt-rich spinel inclusion in a sapphire from Bo Ploi, Thailand. *Mineralogical Magazine*, **58**, 247-258.

Guo, J., O'Reilly, S.Y. and Griffin, W.L. 1996a. Corundum from basaltic terrains: a mineral inclusion approach to the enigma. *Contributions to Mineralogy and Petrology*, **122**, 368-386.

"----------" 1996b. Zircon inclusions in corundum megacrysts: I. Trace element geochemistry and clues to the origin of corundum megacrysts in alkali basalts. *Geochimica et Cosmochimica Acta*, **60**, 2347-2363.

Guo, J., Wang, F. and Yakoumelos, G. 1992. Sapphires from Changle, in Shandong province, China. *Gems and Gemology*, **28**(4), 225-260.

Gust, D.A. and Perfit, M.R. 1987. Phase relations of a high-Mg basalt from the Aleutian Island Arc: implications for primary island arc basalts and high-Al basalts. *Contributions to Mineralogy and Petrology*, **97**, 7– 18.

Hada, S. 1990. Geology of the Nan-Chanthaburi suture zone: (I) Stratigraphy and geologic structure. *In:* Charusiri, P. (editor-in-chief) *The Technical Conference on Development Geology for Thailand into the Year 2000, Abstract.* Bangkok, Thailand, 13-14.

Hada, S, Bunopas, S., Salyapongs, S., Thitisawan, V., Panjasawatwong, Y., Yaowanoiyothin, W., Ishii, K. and Yoshigura, S. 1991. *The Seventh Regional Conference on Geology, Mineral and Energy Resources of Southeast Asia,* Abstract, Bangkok, 40.

Hada, S., Bunopas, S., Ishii, K. and Yoshikura, S. 1999. Rift-drift history and the almalgamation of Shan Thai and Indochina/East Malaya blocks. *In* Metcalfe, I. (ed.) *Gondwana Dispersion and Asian Accretion.* Balkema, Rotterdam, 67-87

Hahn, L., Koch, K.E. and Wittekindt, H. 1986. Outline of the geology and the mineral potential of Thailand. *Geologische Jahrbuch*, **59**, 3-49.

Hall, A. 1996. *Igneous Petrology, second edition.* Longman Group Limited, England

Hall, R. 1996. Reconstructing Cenozoic SE Asia. *In* Hall, R. and Blundell, D. (eds) *Tectonic Evolution of Southeast Asia, Geological Society Special Publication*, **106**, 153-184.

Halter, W.E., Pettke, T. Heinrich, C.A. and Rothen-Rutishauser, B. 2002. Major to trace element analysis of melt inclusions by laser-ablation ICP-MS: methods of quantification. *Chemical Geology*, **183**, 63-86.

Hansawek, R. and Pattamalai, K. 1996. Kanchanaburi Sapphire Deposits. *Economics Geology Division Annual Report*, Department of Mineral Resources, 24p. (in Thai)

Hart, S.R. 1988. Heterogeneous mantel domains signatures, genesis and mixing chronologies. *Earth and Planetary Sciences Letters*, **90**, 273-296.

Hart, W.K., Wolde, G.C., Walter, R.C. and Mertzman, S.A. 1989. Basaltic volcanism in Ethiopia: constraints on continental rifting and mantle interactions. *Journal of Geophysical Researches*, **94**, 7731-7748.

Hayashi, M. 1989. The Hydrocarbon potential and tectonics of Indochina. *Geological Society of Malaysia Bulletin*, **25**, 65-78.

Helmcke, D. 1985. The Permo-Triassic "Paleotethys" in mainland southeast- Asia and adjacent part of China. *Geologische Rundshcau*, **74**, 215-228.

Helmcke, D. and Lindenberg, H.G. 1983. New data on "Indosinian" orogeny from central Thailand. *Geologische Rundschau*, **72**, 317-328.

Heming, R.F. and Carmichael, I.S.E. 1973. High-temperature pumice flows from the Rabaul caldera Papua, New Guinea. *Contributions to Mineralogy and Petrology*, **38**, 1-20.

Herzberg, C.T. 1978. Pyroxene geothermometry and geobarometry: experimental and thermodynamic evaluation of some subsolidus phase relation involving pyroxenes in the system CaO-MgO-Al_2O_3-SiO_2. *Geochimica et Cosmochimica Acta*, **42**, 945-957.

Hess, A. and Koch, K.E. 1979. *Geologic Map of Northern Thailand, sheet 4 (Chiang Dao), scale 1: 250,000.* Federal Institute of Geosciences and Natural Resources, Germany.

Hirose, K. and Kushiro, I. 1993. Partial melting of dry peridotites at high pressure: determination of compositions of melt segregated from peridotite using aggregates of diamond. *Earth and Planetary Sciences Letters*, **114**, 477-489.

Hisada, K., Charusiri, P. and Ueno, K. 2005. Suture line in collision zone: a case of northern Thailand. *In* Wannakao, L, Youngme, W, Srisuk, K. and Lertsirivorakul, R. (eds) *Proceeding of the International Conference on Geology, Geotechnology and Mineral Resources of INDOCHINA*, Khon Kaen, Thailand, 466-467.

Hoang, N. and Flower, M.F.J. 1998. Petrogenesis of Cenozoic basalts from Vietnam: implication for origins of a 'diffuse igneous province'. *Journal of Petrology*, **39**, 369-395.

Hoang, N., Flower, M.F.J. and Carlson, W.W. 1996. Major, trace element and isotopic compositions of Vietnamese basalts: interaction of hydrous EM-1-rich asthenosphere with thinned Eurasian Lithosphere. *Geochimica et Cosmochimica Acta*, **60**, 4329-4351.

Hoefs, J. 1997. *Stable Isotope Geochemistry, Fourth Completely Revised, Updated and Enlarged Edition*. Springer-Verlag, Germany.

Hofmann, A. W. 1997. Mantle geochemistry: the message from oceanic volcanism. *Nature*, **385**, 219–229.

Hokada, T. and Harley, S.L. 2004. Zircon growth in UHT leucosome: constraints from zircon-garnet rare earth elements (REE) relations in Napier Complex, East Antarctica. *Journal of Mineralogical and Petrological Sciences*, **99**, 180-190.

Holland, J.G. and Lambert, R.St.J. 1975. The chemistry and origin of the Lewisian gneisses of the Scottish Mainland: the Scourie and Inver assemblages and sub-crustal accretion. *Precambrian Research*, **2**, 161-188.

Hughes, R.W. 1997. *Ruby and Sapphires*. KWH Publishing, Boulder, 511.

Hsu, C. and Chen, J., 1998. Geochemistry of late Cenozoic basalt from Wudalianchi and Jingpohu areas, Heilongjiang Province, northeast China, *Journal of Asian Earth Sciences*, **16**, 385-405.

Hu, G. and Clayton, R.N. 2003. Oxygen isotope salt effects at high pressure and high temperature and the calibration of oxygen isotope geothermometers. *Geochimica et Cosmochimica Acta*, **67**, 3227-3246.

Hutchison, C.S. 1989. *Geological Evolution of Southeast Asia.* Oxford University Press, Oxford.

Hutchon, P., Le Pichon, X. and Rangin, D. 1994. Indo-China peninsular and the collision of India and Eurasia. Journal of Geology,

Ingavat, R. and Douglas, R.C. 1981. Fusuline fossils from Thailand, Part xiv: The fusulinid genus *Monodiexodina* from northwest Thailand. *Geology and Palaeontology of Southeast Asia*, **22**, 23-34.

Ingle, S., Weis, D. and Frey, F.A. 2002. Indian Continental Crust Recovered from Elan Bank, Kerguelan Plateau (ODP Leg 183, Site 1137). Journal of Petrology, **43**, 1241-1257.

Intasopa, S. 1993. Petrology and Geochronology of the Volcanic Rocks of the Central Thailand Volcanic Belt, PhD Thesis, University of New Brunswick.

Intasopa, S. and Dunn, T. 1994. Petrology and Sr-Nd isotopic systems of basalts and rhyolites, Loei, Thailand. *Journal of Asian Earth Science*, **9**, 167-180.

Intasopa, S., Atichat, W. and Pisutha-Arnond, V. 1998. A comparative study on corundums from Southeast Asia: their application to origin determination. *Ninth Regional Congress on Geology, Mineral and Energy Resources of South East Asia.* Kuala Lumpur, Malaysia, Absrtact, 220-222.

Irving, A.J. 1974. Megacrysts from the Newer Basalts and other basaltic rocks of Southeaster Australia. *Geological Society of America Bulletin*, **85**, 1503-1514.

Irving, A.J. 1986. Polybaric magma mixing in alkalic basalts and kimberlites: Evidence from corundum, zircon and ilmenite megacrysts. *4th International Kimberlite Conference, Abstracts*, 262-264.

Irving, A.J. and Green,D.H. 1976. Geochemistry and petrogenesis of the newer basalts of Victoria and South Australia, *Journal of Geological Society of Australia*, **23**, 45-66

Jaques, A.L and Green, D.H. 1980. Anhydrous melting of peridotite at 0-15 kbar pressure and the genesis of tholeiitic basalts. *Contributions to Mineralogy and Petrology*, **73**, 287-310.

Javanaphet, J.C. 1969. *Geologic map of Thailand, scale 1:1,000,000.* Department of Mineral Resources, Bangkok, Thailand

Johnston, A.D. 1986. Anhydrous P–T phase relations of near-primary high-alumina basalt from the South Sandwich Islands. Implications for the origin of island arcs and tonalite–trondhjemite series rocks. *Contributions to Mineralogy and Petrology*, **92**, 368– 382.

Jones, A.P., Smith, J.V., Dawson, J.B. and Hansen, E.C. 1983. Metamorphism, partial melting and K-metasomatism of garnet-scapolite-kyanite granulite xenoliths from Lashaine, Tanzania. *Journal of Geology*, **91**, 143-165

Jungyusuk, N. and Khositanont, S. 1992. Volcanic rocks and associated mineralization in Thailand: *In*: Piancharoen, C. (editor-in-chief) *Proceeding of a National Conference on Geological Resources of Thailand: Potential for Future Development*, Bangkok, Thailand, 151-156.

Jungyusuk, N. and Sinsakul, S. 1989. Geology of Ban Na Chaliany, Amphoe Nong Phai and Amphoe Wichianburi. *Geological Survey Report, Department of Mineral Resources,* Bangkok, Thailand, **127**, 97p.

Jungyusuk, N. and Sirinawin, N. 1983. Cenozoic basalts of Thailand. *Conference on Geology and Mineral Resources of Thailand*, 9p.

Kaewbaidhoon, S. and Potisat, S. 1974. Sapphire deposit at Bo-Phloi, Kanchanaburi. *In: Sapphire*, Department of Mineral Resources, Bangkok, Thailand. 43-47. (in Thai)

Kamenetsky, V. and Clocchiatti, R. 1996. Primitive magmatism of Mt. Etna: insights from mineralogy and melt inclusions. *Earth and Planetary Sciences Letters*, **142**, 553 – 572.

Kammerling, R.C., Scaratt, K., Bosshart, G., Jobbins, E.A., Kane, R.E., Gübelin, E.J. and Levinson, A.A. 1994. Myanmar and its gems – an update. *Journal of Gemmology*, **24**, 3-40.

Kay, S.M. and Kay, R.W. 1985. Aleutian tholeiitic and calc-alkaline magma series: I the mafic phenocrysts. *Contributions to Mineralogy and Petrology*, **90**, 276-290.

Kelemen, P.B. 1990. Reaction between ultramafic rock and fractionating basaltic magma: I. Phase relations, the origin of calc-alkaline magma series, and the formation of discordant dunite. *Journal of Petrology*, **31**, 51–98.

Kempton, P.D., Fitton, J.G., Hawkesworth, C.J. and Ormerod, D.S. 1991. Isotopic and trace element constrains on the composition and evolution of the lithosphere beneath the southwestern United States. *Journal of Geophysical Researches*, 96, 13713-13735.

Kerrich, R., Fyfe, W.S., Barnett, R.L., Blair, B.B. and Willmore, L.M. 1987. Corundum, Cr-muscovite rocks at O'Briens, Zimbabwe: the conjunction of hydrothermal desilication and isotope evidence. *Contributions to Mineralogy and Petrology*, 95, 481-498.

Kersting, A.B. and Arculus, R.J. 1994. Klyuchevskoy volcano, Kamchatka, Russia: the role of high-flux recharged, tapped and fractionated magma chamber(s) in the genesis of high-Al_2O_3 from high-MgO basalt. *Journal of Petrology*, **35**, 1-41.

Kiefert, L., Schmetzer, K, Krezemnicki, M.S., Bernhardt, H. and Hänni, H.A. 1996. Sapphires from Andranondambo area, Madagascar. *Journal of Gemmology*, **25**, 185-209.

Kieffer, S.W. 1982. Thermodynamics and lattice vibrations of minerals: 5. Application to phase equilibria, isotopic fractionation and high-pressure thermodynamics properties. *Reviews in Geophysics and Space Physics*, **20**, 827-849.

Kimura, J-I., Manton, W.I., Sun, C-H., Iizumi, S., Yoshida, T. and Stern, R.J. 2002. Chemical Diversity of the Ueno Basalts, Central Japan: Identification of Mantle and Crustal Contributions to Arc Basalt. *Journal of Petrology*, **43**, 1923-1946.

Klein, C. and Hurlbut Jr, C.S. Manual of Mineralogy revised 21st Edition, John Wiley&Sons, New York

Klemme, S. 2004. The influence of Cr on the garnet-spinel transition in the Earth's mantle: experiments in the system MgO-Cr_2O_3-SiO_2 and thermodynamic modelling. *Lithos*, **77**, 639-646.

Kogarko, L., Kurat, G. and Ntaflot, T. 2001. Carbonate metasomatism of the oceanic mantle beneath Fernando de Noronha Island, Brazil. *Contributions to Mineralogy and Petrology*, **140**, 577-587.

Kosuwan, P. 2004. Petrochemistry and tectonic setting of mafic volcanic rocks in the Khlong Tha Dan Dam area, Nakhon Nayok province, Thailand. M.S. thesis, Chiang Mai University, Thailand.

Koszowska, E., Wolska, A., Zuchiewicz, W., Cuong, N.Q. and Pécskay, Z. 2006. Crustal contamination of Late neogene basalts in the Dien Bien Phu Basin, NW Vietnam: Some insights from petrological and geochronological studies. *Journal of Asian Earth Sciences*, **xx**, 1-17 (article in press)

Kress, V.C. and Ghiorso, M.S. 2004. Thermodynamic modelling of post-entrapment crystallization in igneous phases. *Journal of Volcanology and Geothermal Research*, **137**, 247-260.

Kornprobst, J., Piboule, M., Roden, M. and Tabit, A. 1990. Corundum-bearing garnet clinopyroxenites at Beni Boursera (Morocco): original plagioclase-rich gabbros recrystallized at depth within the mantle? *Journal of Petrology*, **31**, 717-745.

Kühn, A., Glodny, J., Iden, K. and Austrheim, H. 2000. Retention of Precambrian Rb/Sr phlogopite ages through Caledonian eclogite facies metamorphism, Bergen Arc Complex, W-Norway. *Lithos*, **51**, 305–330.

Kushiro, I. 1972. Effect of Water on the Composition of Magmas Formed at High Pressures. *Journal of Petrology*, **13**, 311-334.

Kushiro, I. 1974. Melting of hydrous upper mantle and possible generation of andesitic magma: an approach from synthetic systems. *Earth and Planetary Sciences Letters*, **22**, 294-299.

Kushiro, I. and Yoder, H.S. 1972. *Annual Report of the Director Geophysical Laboratory 1979-1980*, Carnegie Institution, 290-296.

Kushiro, I., Yoder, H.S. and Mysen, B.O. 1976. Viscosities of basalt and andesite melts at high pressures. *Journal of Geophysical Researches*, **81**, 6351-6356.

Kyser, T.K., O'Neil, J.R. and Carmichael, S.E. 1982. Genetic relations among basic lavas and ultramafic nodules: evidence from oxygen isotope compositions. *Contributions to Mineralogy and Petrology*, **81**, 88-102.

Laccasin, R., Hinthong, C., Siribhakdi, K., Chauviroj, S., Charoenpravat, A., Maluski, H., Leloup, P.H. and Tapponier, P. 1997. Tertiary diachronic extrusion and deformation of western Indochina: structure and $^{40}Ar/^{39}Ar$ evidence from NW Thailand. *Journal of Geophysical Research*, **102**(B5), 10013-10037.

Lamb, R.C., Smalley, R.C. and Field, D. 1986. PT conditions for the Arendal granulites, southern Norway, implications for the roles of P, T and CO_2 in deep crustal LILE-depletion. *Journal of Metamorphic Petrology*, **4**, 143-160.

Leloup, P.H., Arnaud, N., Lacassin, R., Kienast, J.R., Harrison, T.M., Trong, T.T.P., Replumaz, A. and Tapponnier, P. 2001. New constraints on the structure, thermochronology and timing of the Ailao Shan-Red River shear zone, SE Asia. *Journal of Geophysical Research*, **66**, 1083-6732.

Levinson, A.A. and Cook, F.A. 1994. Gem corundum in alkali basalt: Origin and occurrence. *Gems and Gemology*, **30**(4), 253-262.

Limtrakun, P., Zaw, K., Ryan, C.G. and Mernagh, T.P. 2001. Formation of the Denchai gem sapphires, northern Thailand: evidence from mineral chemistry and fluid/melt inclusion characteristics. *Mineralogical Magazine*, **65**(6), 725-735.

Liu, C., Masuda, A. and Xie, G. 1994. Major- and trace-element compositions of Cenozoic basalts in eastern China: petrogenesis and mantle source. *Chemical Geology*, **114**, 19-42.

Liu, J., Ni, P., Ding, J. and Pan, L. 2006. Immiscibility of magma recorded in melt inclusion within corundum megacrysts from alkali basalt. *In* Pei, N. and Zhaolin, L. (eds) *Abstracts volume of First International Conference on Asia Current Research on Fluid Incluion*, Nanjing, China, 122-123

Loferski, P.J. and Arculus, R.J. 1993. Multiphase inclusions in plagioclase from anothosites in the Stillwater Complex, Montana: implications for the origin of the anorthosites. *Contributions to Mineralogy and Petrology*, **114**, 63-78.

Lowenstern, J.B. 1995. Applications of silicate melt inclusions to the study of magmatic volatiles. *In* Thompson J.F.H. (ed), *Magmas, Fluids and Ore deposits*, Mineralogical Association of Canada, **23**, 71-99.

Lowry, D., Appel, P.W.U. and Rollinson, H.R. 2003. Oxygen isotopes of an Early Archaean layered ultramafic body, southern West Greenland: implications for magma source and post-intrusion history. *Precambrian Research,* **126**, 273-288.

Lu, F., Anderson, A.T. and Davis, A.M. 1995. Diffusional gradientsat the crystal/melt interface and their effect on the composition of melt inclusions. *Journal of Geology*, **103**, 591-597.

Luth, W.C., Jahns, R.H. and Tuttle, O.F. 1964. *Journal of Geophysical Researches*, **69**, 759-773.

Macdonald, A.S. and Barr, S.M. 1978. Tectonic significance of a Late Carboniferous volcanic arc in Thailand. *In*: Nuttalaya, P. (ed) *Proceedings of Third Regional Conference on Geology and Mineral Resources of Southeast Asia,* Pathumthani, Thailand, 151-156.

Macpherson, C.G. and Mattey, D.P. 1998. Oxygen isotope variations in Lau Basin lavas. *Chemical Geology,* **144**, 177-194.

Mariga, J., Ripley, E.M., Li, C., McKeegan, K.D., Schmidt, A. and Groove, M. 2006. Oxygen isotopic disequilibrium in plagioclase–corundum–hercynite xenoliths from the Voisey's Bay Intrusion, Labrador, Canada *Earth and Planetary Science Letter* (In Press)

Marsh, B.D. 1976. Some Aleutian andesites: their nature and source. *Journal of Geology*, **84**, 27-45.

Massare, D.N., Metrich, N., Clocchiatti, R. 2002. High-temperature experiments on silicate melt inclusions in olivine at 1 atm: inference on temperatures of homogenization and H_2O concentrations. *Chemical Geology*, **183**, 87-98.

Metcalfe, I. 1990. Stratigraphic and tectonic implications of Triassic conodonts from northwest Peninsular Malaysia. *Geology Magazine*, **127**, 567-578.

Matthews, A., Putlitz, B., Hamiel, Y. and Hervig, R.L. 2003. Volatile transport during the crystallization of anatectic melts: oxygen, boron and hydrogen stable isotope study on the metamorphic complex of Naxos, Greece. *Geochimica et Cosmochimica Acta,* **67**, 3145-3163.

Matson, S.M. and Rossman, G.R. 1988. Fe^{2+}-Ti^{4+} charge transfer in stoichiometric Fe^{2+}, Ti^{4+} minerals. *Physics and Chemistry of Minerals*, **16**, 76-82

Menon, R.D., Santosh, M., and Yoshida, M. 1994. Gemstone mineralization in southern Kerala, India. *Journal of Geological Society of India*, **44**, 241-252.

Menzies, M.A., Halliday, A.N., Palacz, Z., Hunter, R.H., Upton, B.G.J., Aspen, P. and Hawkesworth, C.J. 1987. Evidence from mantle xenoliths for an enriched lithospheric keel under the Outer Hebrides. *Nature*, **325**, 44-47.

Mercier, J-C.C. and Nicolas, A. 1975. Textures and Fabrics of Upper-Mantle Peridotites as Illustrated by Xenoliths from Basalts. *Journal of Petrology*, **16(2)**, 454-487.

Mercier, J-C.C. 1980. Single pyroxene thermobarometry. *Tectonophysics*, **70**, 1-37.

Metcalfe, I. 1999. Gondwana dispersion and Asian accretion: an overview. *In* Metcalfe, I. (ed.), *Gondwana Dispersion and Asian Accretion*, Balkema, Rotterdam, 9-28.

Metcalfe, I. 2000. The Bentong-raub Suture zone. *Journal of Asian Earth Sciences*, **18**, 691-712.

Michaud, V., Clocchiatti, R. and Sbrana, S. 2000. The Minoan and post-Minoan eruptions, Santorini (Greece), in the light of melt inclusions: chlorine and sulphur behaviour. *Journal of Volcanology and Geothermal Research*, **99**, 195-214.

Milholland, C.S. and Presnall, D.C. 1998. Liquidus phase relations in the CaO-MgO-Al2O3-SiO2 system at 3 GPa: the aluminous pyroxene thermal divide and high-pressure fractionation of picritic and komatiitic magmas. *Journal of Petrology*, **39**, 3-27.

Milisenda, C.C. and Henn, U. 1996. Compositional characteristics of sapphires from a new find in Madagascar. *Journal of Gemmology*, **25**, 177-184.

Michell, A.H.G., Young, B. and Jautaranipa, W. 1970. The Phuket Group, peninsular Thailand: a Palaeozoic geosynchlinal deposit. *Geoloical Magazine*, **107**, 411-428.

Mitchell, A.H.G., 1981. Phanerozoic plate boundary in mainland SE Asia, the Himalayas and Tibet. *Journal of Geological Society of London*, **138**, 109-122.

Miyashiro, A. 1978. Nature of alkalic volcanic rock series. *Contributions to Mineralogy and Petrology*, **66**, 91-104.

Morishita, T. and Arai, S. 2001. Petrogenesis of Corundum-Bearing Mafic Rock in the Horoman Peridotite Complex, Japan. *Journal of Petrology*, **42**, 1279-1299.

Mooney, W.D., Laske, G. and Masters, G. 1998. C RUST 5.1: A global crustal model at 5°x5°. *Journal of Geophysical Research*, **104**, 727-747.

Morley, C.K. 2002. A tectonic model for the Tertiary evolution of strike-slip faults and rift basins in SE Asia. *Tectonophysics*, **347**, 189-215.

Morley, C.K. 2006. Variations in Late Cenozoic–Recent strike-slip and oblique-extensional geometries, within Indochina: The influence of pre-existing fabrics. *Journal of Structural Geology*, **29**, 36-58.

Morogan, V. and Lindblom, S. 1995. Volatiles associated with the alkaline-carbonatite magmatism at Alnö, Sweden: a study of fluid and solid inclusions in minerals from the Långarsholmen ring complex. *Contributions to Mineralogy and Petrology*, **122**, 262-274.

Muehlenbachs, K. and Kushiro, I. 1974. Oxygen isotope exchange and equilibrium of silicates with CO_2 and O_2. *Carnegie Institution Washington Yearbook,* **73,** 232–236.

Myers, J.D. 1988. Possible petrogenetic relations between lowand high-MgO Aleutian basalts. *Geological Society of America Bulletin*, **100**, 1040–1053.

Mysen, B.O. and Kushiro, I. 1977. Compositional variations of coexisting phases with degree of melting of peridotite in the upper mantle. *American Mineralogist*, **82**, 52-67.

Nabelek, P. I., Nabelek, C. R. and Haeussler, G. T. 1992. Stable isotope evidence for the petrogenesis and fluid evolution in the Proterozoic Harney Peak leucogranite, Black Hills, South Dakota. *Geochimica et Cosmochimica Acta* **56**, 403-417.

Nakamura, M. and Shimakita, S. 1998. Dissolution origin and syn-entrapment compositional change of melt inclusion in plagioclase. *Earth and Planetary Science Letters*, **161**, 119-133.

Nassau, K. 1978. The origins of color in minerals. *American Mineralogist*, **63**, 219-229.

Nassau, K. 1983. *The Physics and Chemistry of Color: the Fifteen Causes of Color.* John Wiley&Sons, New York.

Nassau, K. 2001. *The Physics and Chemistry of Color: the Fifteen Causes of Color.* John Wiley&Sons, New York. 481p.

Nasir, S. and Safarjalani, A. 2000. Lithospheric petrology beneath the northern part of the Arabian plate in Syria: evidence from xenoliths in alkali basalts. *Journal of African Earth Sciences*, **30**(1), 149-168.

Neumann, E.R. and Ramberg, I.B. 1978. Paleorifts-concluding remarks. *In* Neumann, E.R. and Ramberg, I.B. (eds) *Tectonics and Geophysics of Continental Rifts*, D.Reidel, Dordrecht, 409-424.

Newton, R.c., Aranovich, L.Ya., Hensen, E.C. and Vandenheuvel, B.A. 1998. Hypersaline fluids in Precambrian deep-crustal metamorphism. *Precambrian Research*, **91**, 41-63.

Ngounouno, I. O., Déruelle, B., Montigny, R. and Demaiffe, D. 2000. Petrology and geochemistry of monchiquites from Tchircotché (Garoua rift, north Cameroon, Central Africa). *Mineralogy and Petrology*, **83**, 167–190.

Nicholls, I.A. and Ringwood, A.E. 1973. Effects of water on olivine stability in tholeiite and the productions of silica-saturated magmas in the island arc environment. *Journal of Geology*, **81**, 285-300.

Nicolas, A., Lucazeau, F. and Bayer, R. 1987. Peridotite xenoliths in Massif Central basalts: textural and geophysical evidence for asthenospheric diapirism. *In* Nixon, P.H. (ed) *Mantle Xenoliths*, New York, John Wiley, 563-574

Nielsen, R.L., Crum, J., Bougouis, R., Forsythe, L.M., Fisk, M.R. and Christie, D.M. 1995. Melt Inclusions in High-An Plagioclase from the Gorda Ridge: An Example of the Local Diversity of MORB Parent Magmas. *Contributions to Mineralogy and Petrology*, **122**, 34-50.

Nielsen, R.L., Michael, P.J. and Sours-Page, R. 1998. Chemical and physical indicators of compromised melt inclusions. *Geochimica et Cosmochimica Acta*, **62**, 831-839.

Nielsen, T.F. and Veksler, I.V. 2002. Is natrocarbonatite a cognate fluid condensate? *Contributions to Mineralogy and Petrology*, **142**, 425-435.

Nikolskaya, L.V., Terekhova, V.M. and Samoilovich, M.I. 1978. On the Origin of Natural Sapphire Color. *Physics and Chemistry of Minerals*, **3**, 213-224.

Nye, C.J. and Reid, M.R. 1986. Geochemistry of primary and least fractionated lavas from Okmok volcano, central Aleutians: implications for arc magma genesis. *Journal of Geophysical Researches*, **91**, 271-287.

Oakes, G.M., Barron, L.M. and Lishmond, S.R. 1996. Alkali basalts and associated volcaniclastic rocks as a source of sapphire in eastern Australia. *Australian Journal of*

Earth Sciences, **43**, 289-298.

O'Hara, M.J., Richardson, S.W. and Wilson, G. 1971. Garnet peridotite stability and occurrence in crust and mantle. *Contibutions to Mineralogy and Petrology*, **32**, 48-68.

O'Hara, M.J. and Yoder, H.S.Jr. 1967. Formation and fractionation of basic magmas at high pressures. *Scottish Journal of Geology*, **3**, 67-117.

O'Neil, J.R. 1986. Theoretical and experimental aspects of isotopic fractionation. p.1-36 in: *Reviews in Mineralogy Vol.16. Stable Isotopes in High Temperature Geological Processes.* (J.W.Valley, H.P.Taylor, Jr. and J.R.O'Niel eds). BookCrafters, Inc., Chelsea, Michigan, USA

O'Reilly, S.Y. and Griffin, W.L. 1985. A xenolith-derived geothem for south-eastern Australian and its geophysical implication. *Tectonophysics*, **111**, 41-63.

O'Reilly, S.Y. and Griffin, W.L. 1988. Mantle metasomatism beneath Victoria, Australia: I. Metasomatic processes in Cr-diopside lherzolites. *Geochimica et Cosmochimica Acta*, **52**, 433–447.

O'Reilly, S.Y., Nicholls, I.A. and Griffin, W.L. 1989. Xenoliths and megacrysts of eastern Australia. *In* Johnson, R.W. (ed.) *Intraplate Volcanism in Eastern Australia and New Zealand*, Cambridge University Press, 249-288.

Pakhomova, V.A., Zalishchak, B.L., Odarichenko, E.G., Lapina, M.I. and Karmanov, N.S. 2006. Study of melt inclusions in the Zezametnoye corundum deposit, Primorsky region of the Russian Far East: Petrogenetic consequence. *Journal of Geochemical Exploration*, **89**, 302-305.

Palin, J.M., Epstein, S. and Stolper, E.M. 1996. Oxygen isotope partitioning between rhyolitic glass/melt and CO_2: An experimental study at 550–950°C and 1 bar. *Geochimica et Cosmochimica Acta,* **60**, 1963-1973.

Pandit, M.K., Sial, A.N., Malhotra, G., Shekhawat, L.S. and Ferreira, V.P. 2003. C-, O-Isotope and Whole-rock Geochemistry of Proterozoic Jahazpur Carbonates, NW Indian Craton. *Gondwana Research*, **6**, 513-522.

Panjasawatwong, Y. 1983. Chemical variation within a single basalt flow at Denchai, Phrae. *Proceedings on Annual Technical Meeting*, Department of Geological Sciences, Chiang

Mai University, Chiang Mai, Thailand.

Panjasawatwong, Y. 1991. Petrology, Geochemistry and Tectonic Implication of Igneous Rocks in the Nan Suture, Thailand and an Empirical Study of the Effects of Ca/Na, Al/Si and H_2O on Plagioclase-Melt Equilibria at 5-10 Kb Pressure. PhD Thesis, University of Tasmania.

Panjasawatwong, Y. 1999. Petrology and tectonic setting of eruption of basaltic rocks penetrated in well GTE-1, San Kamphaeng geothermal field, Chiang Mai, northern Thailand. *In*: Ratanasthien B. & Rieb S. L. (eds.) *Proceedings of International Symposium on Shallow Tethys (ST5),* Chiang Mai, Thailand, 242-264.

Panjasawatwong, Y., Chantaramee, S., Limtrakun, P. and Pirarai, K. 1997. Geochemistry and tectonic setting of eruption of central Loei volcanics in the Pak Chom area, Loei, northeast Thailand. *In*: Nuttalaya, P. (ed) *Proceedings of International Conference on Stratigraphy and Tectonic evolution of Southeast Asia and the South Pacific*, Bangkok, Thailand, 225-234.

Panjasawatwong, Y., Kanpeng, K. and Ruangvatanasirikun, K. 1995. Basalts in Li basin, northern Thailand: Southern extension of Chiang Mai volcanic belt. *In*: Wannakao, L. (editor-in-chief) *Proceedings of the International Conference on Geology, Geotechnology and Mineral Resources of Indochina,* Khon Kaen, Thailand, 225-234.

Panjasawatwong, Y. and Yaowanoiyothin, W. 1993. Petrochemical study of post-Triassic basalts from the Nan suture, Northern Thailand. *Journal of Southeast Asian Earth Sciences*, **8**, 147-158.

Panjasawatwong, Y. and Youngsnong, M. 1996. Chiang Khong corundum-bearing basalt, Amphoe Chiang Khong, Changwat Chiang Rai. *Journal of Science Faculty, Chiang Mai University*, **23(1)**, 39-52.

Panjasawatwong, Y., Phajuy, B. and Hada, S. 2003. Tectonic setting of the Permo-Triassic Chiang Khong volcanic rocks, northern Thailand based on petrochemical characteristics. *Gondwana Research*, **6**, 743-755.

Pankhurst, R.J. 1977. Open system fractionation and implications of Ti, Zr, Y and Nb variations in volcanic rocks. *Nature,* **268**, 36-38.

Parlak, O., Delaloyeb, M., Demirkola, C. and Ünlügença, U.C. 2001. Geochemistry of Pliocene/Pleistocene basalts along the Central Anatolian Fault Zone (CAFZ), Turkey. *Geodinamica Acta*, **14**, 159–167.

Peate, D.W., Hawkesworth, C.J., Mantovani, M.S.M., Roders, N.W. and Turner, S.P. 1999. Petrogenesis and stratigraphy of the high-Ti/Y Urubici magma type in the Paraná flood basalt province and implications for the nature of 'Dupal'- type mantle in the South Atlantic region. *Journal of Petrology*, **40**, 451-473.

Peretti, A., Mullis, J. and Mouawad, F. 1996. The role of fluorine in the formation of colour zoning in rubies from Mong Hsu, Myanmar (Burma). *Journal of Gemmology*, **25**, 3-19.

Perfit, M.R., Gust, D.A., Bence, A.E., Arculus, R.J. and Taylor, S.R. 1980. Geochemical characteristics of island-arc basalts: implications for mantle sources. *Chemical Geology*, **30**, 227– 256

Peucat, J.J., Vidal, Ph., Bernard-Griffiths, J. and Condie, K.C. 1989. Sr, Nd and Pb isotopic systematics in the Archean low- to high-grade transition zone of souther India: syn-accretion vs. post-accretion granulites. Journal of Geology, 97, 537-550.

Phajuy, B. 2001. Geochemistry petrology and tectonic setting of Permo-Triassic mafic volcanic rocks in the northern part of Chiang Khong-Tak volcanic belt. MSc Thesis, Chiang Mai University.

Pike, J.E.N and Schwarzman, E.C. 1977. Classification of texture in ultramafic xenoliths. *Journal of Geology*, **85**, 49-61.

Pin, C., Monchoux, P., Paquette, J.L., Azambre, B., Wang, R.C. and Martin, R.F. 2006. Igneous albitite dikes in orogenic lherzolites, wester Pyrenees, France: A possible source for corundum and alkali feldspar xenocrysts in basaltic terranes. II. Geochemical and petrogenetic considerations. *Canadian Mineralogist*, **44**, 843-856.

Pisutha-Arnond, S., Ukkakimapan, J., Klan-Ngern, S., Pisutha-Arnond, V. and Taiyaqupt, M., 1997. Predicting oil and water interval in U-Thong field using thermal extraction–pyrolysis gas chromatography. *In*: Dheeradilok, P., Hinthong, C., Chaodumrong, P., Putthaphiban, P., Tansathien, W., Utha-aroon, C., Sattayarak, N., Nuchanong, T. and Techawan, S. (eds), *Proceeding of the International Conference on Stratigraphy and*

Tectonic Evolution of Southeast Asia and the South Pacific, Bangkok, Thailand, 543-559.

Pisutha-Arnond, V., Wathanakul, P., Intasopa, S. and Griffin, W.L., 1998. Corsilzirspite, a corundum-silimanite-zircon-hercynite rock: New evidence on the origin of Kanchanaburi sapphire, Thailand. *In*: Ninth Regional Congress on Geology, Mineral and Energy Resources of South East Asia, Kuala Lumpur, Malaysia, 95-96.

Piyasin, S. 1972. Geology of Lampang Sheet (NE 47-11), scale 1:250,000. Report on investigation, **14**, Department of Mineral Resources, Bangkok, Thailand, 98p. (in Thai with English abstract).

Piyasin, S. 1991. Tectonics events and radiometric dating of the basement rocks of Phitsanulok Basin, *Journal of Thai Geosciences*, **1**, 41-48.

Polachan, S., Pradittan, S., Tongtaow, C., Janmaha, S., Intarawijitr, K. and Sangsuwan, C. 1991. Development of Cenozoic basins in Thailand. *Marine Petroleum Geology*, **8**, 84-97.

Pongsapich, W., Charusiri, P. and Vedchakanchana, S. 1983. Reviews of metamorphic rocks of Thailand. *In*: Nutalaya, P. (ed) *Proceeding of Workshop on Stratigraphic Correlation of Thailand and Malaysia*, Haad Yai, Thailand, 224-252.

Presnall, D.C. and Bateman, P.C. 1973. *Bulletin of Geological Society of America*, **84**, 3181-3202.

Presnall, D.C., Dixon, J.R., O'Donnell, T.H. and Dixon, S.A. 1979. Generation of mid-ocean ridge tholeiites. *Journal of Petrology*, **20**, 3-35.

Price, R., Cooper, A.F., Woodhead, J.D. and Cartwright, A. 2003. Phonolitic Diatremes within the Dunedin Volcano, South Island, New Zealand. *Journal of Petrology*, **44**, 2053-2080.

Putnis, A. 1992. *Introduction to Mineral Sciences*, BAS Printers Ltd, Over Wallop, Hampshire.

Qin, Z., Lu, F. and Anderson, A.T-Jr. 1992. Diffusive reequilibration of melt and fluid inclusions. *Geochimica et Cosmochimica Acta*, **77**, 565-576.

Rankin, A. H. 2002. Natural and heat-treated corundum from Chimwadzulu Hill, Malawi: genetic significance of zircon clusters and diaspore-bearing inclusions. *Journal of Gemmology*, **28**, 65-75

Rankin, A. H. and Edwards, W. 2003. Some effects of extreme heat treatment on zircon inclusions in corundum. *Journal of Gemmology*, **28**, 257-264.

Remus, D., Webster, M. and Keawkan, K. 1993. Rift architecture and sedimentology of the Phetchabun intermontane basin, central Thailand. *Journal of Southeast Asian Earth Sciences*, **8**, 421-432.

Roedder, E. 1979. Origin and significance of magmatic inclusions. *Bulletin de Minéralogie*, 102, 487-510.

Roedder, E. 1984. *Fluid Inclusions*. Reviews in Mineralogy, **12**, Mineralogical Society of America, Washington.

Roedder, E. 1992. Fluid inclusion evidence for immiscibility in magmatic differentiation. *Geochimica et Cosmochimica Acta,* **56**, 5-20.

Roedder, E. and Coombs, D.S. 1967. Immiscibility in granite melts, indicated by fluid inclusions in ejected granite blocks from Ascension Island. *Journal of Petrology*, **8**, 417-451.

Roeder, P.L. and Emslie, R.F., 1970. Olivine-liquid equilibrium, *Contributions to Mineralogy and Petrology*, **29**, 275-289.

Rogers, N.W. 1992. Potassic magmatism as a key to trace element enrichment processes in the upper mantle. *Journal of Volcanology and Geothermal Research*, **50**, 85-99.

Rogers, N.W., De Mulder, M. and Hawksworth, C.J. 1992. An enriched mantle source for potassic basanites: evidence from Karisimbi volcano, Virunga province, Rwanda. *Contributions to Mineralogy and Petrology*, **111**, 543-556.

Rogers, N.W., Hawksworth, C.J., Parker, R.J. and Marsh, J.S. 1985. The geochemistry of potassium lavas from Vulsini Central Italy and implications for mantle enrichment processes beneath the Roman region. *Contributions to Mineralogy and Petrology*, **90**, 244-257.

Rollinson, H. 1993. *Using geochemical data: evaluation, presentation, interpretation.* Pearson Education Asia (Pte) Ltd., Singapore, 352pp.

Sachtleben, T.H. and Seck, A.A. 1981. Chemical control of Al-solubility in orthopyroxene and its implications on pyroxene geothermometry. *Contributions to Mineralogy and Petrology*, **111**, 543-556.

Sakagami, S. and Hatta, A. 1982. ON the Upper Permian Paleofusulina-Coranicella fauna from Khao Doi Pha Phlung, North Thailand. *Geology and Palaeontology of Southeast Asia*, **24**, 1-14.

Saminpanya, S., Manning, D.A.C., Droop, G.T.R. and Henderson, C.M.B. 2003. Trace elements in Thai gem corundums. *Journal of Gemmology*, **28**, 392-398.

Santosh, M., Tsunogae, T., Iki, T., Vansutre, S. and Hari, K.R. 2006. Petrology, fluid inclusions and metamorphic history of Bhopalpatnam granulites, central India. *Journal of Asian Earth Sciences*, **28(1)**, 81-98.

Sattayarak, N, Srigulwong, S. and Pum-Im, S. 1989. Petroleum potential of the Triassic pre-Khorat intermontane basins in Northeastern Thailand. *In*: Thanasuthipitak, T. and Ounchanum, P. (eds), *Proceedings of the International Symposium on Intermontane Basins: Geology and Resources*, Chiang Mai, Thailand, 43-58.

Sawata, H., Arpornsuwan, S. and Pisutha-Anond, V. 1975. Note on geology of Khao Phra, Ratchaburi, West Thailand. Journal of the Geological Society of Thailand, **1**, 31-49.

Scambelluri, M and Philippot, P. 2001. Deep fluids in subduction zones. *Lithos*, 55, 213-227.

Scarfe, C.M., Takahashi, E. and Yoder, Jr. H.S. 1980. Rates of dissolution of upper mantle minerals in an alkali-olivine basalt melt at high pressure. *Annual Report of the Director Geophysical Laboratory 1979-1980*, Carnegie Institution, 290-296.

Schiano, P. 2003. Primitive mantle magmas recorded as silicate melt inclusions in igneous minerals. *Earth Sciences Reviews*, **63**, 121-144.

Schiano, P. and Bourdon, B. 1999. On the preservation of mantle information in ultramafic nodules: glass inclusions within minerals versus interstitial glasses. *Earth and Planetary Sciences Letters*, **169**, 173-188.

Schiano, P., Clocchiatti, R., Bourdon, B, Burton, K.W. and Theiller, B. 2000. The composition of melt inclusions in minerals at the garnet-spinel transition zone. *Earth and Planetary Sciences Letters*, 174, 375-383.

Schiano, P., Clocchiatti, R., Boivin, P. and Medard, E. 2004. The nature of melt inclusions inside minerals in an ultramafic cumulate from Adak volcanic center, Aleutian arc: implications for the origin of high-Al basalts. *Chemical Geology*, **203**, 169-179.

Schmetzer, K. and Bank, H. 1980. Explanation of the absorption spectra of natural and synthetic Fe- and Ti-containing corundums. *Neues Jahrbuch für Mineralogie; Abhandlungen*, **139**, 216-225

Sengör, A.M.C. 1979. Mid-Mesozoic closure of Permo-Triassic Tethys and its implications. *Nature*, **279**, 590-593.

Seyitoğlu, G. anderson, D., Nowell, G. and Scott, B. 1997. The evolution from Miocene potassic to Quaternary sodic magmatism in western Turkey: implications for enrichment processes in the lithospheric mantle. *Journal of Volcanology and Geothermal Research*, **76**, 127-147.

Seyler, M. and Bonatti, E. 1994. Na, Al^4 and Al^6 in clinopyroxenes of continental and suboceanic ridge peridotites: a clue to different melting processes in the mantle? *Earth and Planetary Sciences Letters*, **122**, 281-289.

Shaw, J.E., Baker, J.A., Menzies, M.A., Thirwall, M.F. and Ibrahim, K.M. 2003. Petrogenesis of the Largest Intraplate Volcanic Field on the Arabian Plate (Jordan): a Mixed Lithosphere-Asthenosphere Source Activated by Lithospheric Extension. *Journal of Petrology*, **44**, 1657-1679.

Sheppard, S.M.F. and Harris, C. 1985. Hydrogen and oxygen isotope geochemistry of Ascension island lavas and granites: variation with crystal fractionation and interaction with sea water. *Contributions to Mineralogy and Petrology*, **91**, 74-81.

Shepherd, T.J., Rankin, A.H. and Alderton, D.H.M. 1985. *A Practical Guide to Fluid Inclusion Studies*. Blackie & Son Limited, Glasglow.

Shimizu, N. 1998. The geochemistry of olivine-hosted melt inclusions in a FAMOUS basalt ALV519-4-1. *Physics of the Earth and Planetary Interiors*, **107**, 183-201.

Shinjo, R. 1998. Petrochemistry and tectonic significance of the emerged late Cenozoic basalt behind the Okinawa Troughs, Ryukyu arc system. *Journal of Volcanology and Geothermal Research*, **80**, 39-53.

Singharajwarapan, S. and Berry, R., 2000. Tectonic implications of the Nan Suture Zone and its relationships to the Sukhothai Fold belt, Northern Thailand. *Journal of Asian Earth Sceinces*, **18**(6), 663-673.

Sinton, C.W., Christie, D.M., Coombs, V.L., Nielsen, R.L. and Fisk, M.R. 1993. Near primary melt inclusions in anorthite phenocrysts from the Galapagos platform. *Earth and Planbetary Sciences Letters*, **119**, 527-537.

Sirinawin, S. 1981. Geochemistry and genetic significance of gem-bearing basalt in Chantaburi-Trat area. M.Sc. thesis, Chiangmai University

Sisson, T.W. and Layne, G.D. 1993. H_2O in basalt and basaltic andesite glass inclusions from four subduction-related volcanoes. *Earth and Planetary Sciences Letters*, **117**, 619-635.

Sisson, T.W. and Grove, T.L. 1993a. Experimental investigations of the role of H2O in calc-alkaline differentiation and subduction zone magmatism. *Contributions to Mineralogy and Petrology*, **113**, 143-166.

Sisson, T.W. and Grove, T.L. 1993b. Temperatures and H2O contents of low-MgO high-alumina basalts. *Contributions to Mineralogy and Petrology*, **113**, 167-184.

Smirnov, S.Z., Izokh, A.E., Kovyazin, S., Hoa, C.C., Ngo, T.P., Kalinina, V.V. and Pospelova, L.N. 2006. Inclusions in the Dak-Nong placer sapphires: conditions of corundum crystallization in the Middle Vietnam Earth Crust. *In* Pei, N. and Zhaolin, L. (eds) *Abstracts volume of First International Conference on Asia Current Research on Fluid Incluion*, Nanjing, China, 200-202.

Smith, A.D. 1996. Intraplate volcanism in Asia and the origin of the DUPAL anomaly. *In:* Lee, T-Y. (ed) *International Symposium on Lithosphere Dynamics of East Asia: Geology, Energy and Mineral Resources of the Indochina Region,* Taipei, Taiwan, R.O.C., *Program and Extended Abstracts*, 40-43.

Smith, C.P., Gübelin, E.J., Basset, A.M., Manandhar, M.N. 1997. Rubies and fancies-color sapphires from Nepal. *Gems and Gemology*, **33**, 24-41.

Smith, G. 1978. Evidence for Absorption by Exchange-Coupled Fe2+-Fe3+ Pairs in the Near Infra-red Spectra of Minerals. *Physics and Chemistry of Minerals*, **3**, 375-383.

Sobolev, A.V. 1996. Melt inclusions in minerals as a source of principal petrological information. *Petrologiya* , **4**, 228-239.

Sobolev, A.V. amd Chaussidon, M. 1996. H_2O concentrations in primary melts from supra-subduction zones and mid-ocean ridges: implications for H_2O storage and recycling in the mantle. *Earth and Planetary Science Letters*, **137**, 45-55.

Sobolev, A.V. and Shimizu, N. 1993. Ultra depleted primary melt included in an olivine from the Mid-Atlantic Ridge. *Nature*, **363**, 151-154.

Solovova, I.P., Girnis, A.V., Kogarko, L.N., Kononkova, N.N., Stoppa, F. and Rosatelli, G. 2005. Compositions of magmas and carbonate-silicate liquid immiscibility in the Vuture alkaline igneous complex, Italy. *Lithos*, **85**, 113-128.

Sommer, M.A. 1977. Volatiles H_2O, CO_2 and CO in silicate melt inclusions in quartz phenocrysts from rhyolitic Bandelier air-fall and ash-flow tuff, New Mexico. *Journal of Geology*, **85**, 423-432.

Sorby, H.C. 1858. On the microscopical structure of crystal indicating the origin of rocks and minerals. *Journal of the Geological Society London*, **14**, 453-500.

Sours-Page, R., Johnson, K.T.M., Nielsen, R.L. and Karsten, J.L. 1999. Local and regional variation of MORB parent magmas: evidence from melt inclusions from the Endevour Segment of the Juan de Fuca Ridge. *Contributions to Mineralogy and Petrology*, **134**, 342-363.

Srithai, B., Rankin, A.H., Jones, A.P. and Price, G.D. 1999. Fluid inclusions characteristic of gem sapphires from Bo Ploi, Kanchanaburi, Thailand. *In*: Lüders, V., Schmidt-Mumm, A. and Thomas, R. (eds) *Terra Nostra*, **99/6:** *European Current Research on Fluid Inclusions XV, Programme and Abstracts*, 296-299.

Stauffer, P. and Mantajit, N. 1981. Later Paleozoic tilloids of Malaysia, Thailand and Burma. *In*: Humbrey, M.J. and Harland, W.B. (eds) *Earth's Pre Pleistocene Glacial Record*, Cambridge University Press, Cambridge, 331-337.

Stephenson, P.J. 1990. The geological context of corundum occurrences in the Anakie region, Central Queensland. *Abstract in 10th Australian Geological Convention*, 232-233.

Sterner, S.M. and Bodnar, R.J. 1989. Synthetic inclusions-VII. Re-equilibration of fluid inclusions in quartz during laboratory-simulated metamorphic burial and uplift. *Journal of Metamorphic Geology*, **7**, 100-120.

Stoiber, R.E., Williams, B. and Huebert, B. 1985. Annual contribution of sulfur dioxide to the atmosphere by volcanoes. *Journal of Volcanology and Geothermal Research*, **33**, 1-8.

Stokes, R.B., Lovatt Smith, P.E. and Soumphonphakdy, K. 1996. Timing of the Shan-Thai-Indochina collision: new evidence from the Pak Lay Foldbelt of the Lao PDR. *In* Hall, R. and Blundell, D. (eds) *Tectonic Evolution of Southeast Asia, Geoloical Society London Special Publication*, **106**, 225-232.

Streck, M.J. and Wacaster, S. 2000. Plagioclase and pyroxene hosted melt inclusions in basaltic andesites of the current eruption of Arenal volcano, Costa Rica. *Journal of Volcanology and Geothermal Research,* **157,** 236–253.

Sun, S.S. and McDonough, W.F. 1989. Chemical and isotopic systematics of oceanic basalts: implication for mantle composition and processes. *In* Saunders, A.D. and Norry, M.J. (eds) *Magmatism in Oceaninc Basins. Geological Soceity London Special Publication*, **42**, 313-345.

Sutherland, F.L. 1996. Alkaline rocks and gemstones, Australia: a review and synthesis. *In*: Sutherland, F.L. (ed) *The Nicholas Rock Symposium: Alkaline rocks and their associated mineralisation. Australian Journal of Earth Sciences*, **43**, 323-343.

Sutherland, F.L. 1999. Volcanism, Geotherms, Gemstones and Lithosphere since orogenesis, N.E. New South Wales: A synthesis. *In*: Flood, P.G. (ed) *New England Orogen - Regional Geology, Tectonics and Metallogenesis*, 355-364, University of New England, Armidale, New South Walse.

Sutherland, F.L., Hoskin, P.W.O., Fanning, C.M. and Coenraads, R.R. 1998a. Models of corundum origin from alkali basaltic terrains: a reappraisal. *Contributions to Mineralogy and Petrology*, **133**, 356-372.

Sutherland, F.L., Schwarz, D., Jobbins, E.A., Coenraads, R.R. and Webb, G. 1998b. Distinctive gem corundum suites from discrete basalt fields: a comparative study of Barrington, Australia and West Pailin, Cambodia, gemfields. *Journal of Gemmology*, **26**, 65-85.

Sutthirat, C. 1992. Petrochemistry of mafic igneous rocks at Khao Phu Fai, Amphoe Khun Han, Changwat Sri Sa Ket. B.S. senior project, Department of Geology, Chulalongkorn University, Thailand, 88p.

Sutthirat, C. 1995. Petrochemistry of Basalts in Amphoe Sop Prab and Amphoe Ko Kha, Changwat Lampang. M.S.thesis, Chulalongkorn University, 153p.

Sutthirat, C., Charusiri, P., Farrar, E. and Clark, A.H. 1994. New $^{40}Ar/^{39}Ar$ geochronology and characteristics of some Cenozoic basalts in Thailand. *In Proceedings of the Internationl Symposium on: Stratigraphic Correlation of Southeast Asia, Bangkok, Thailand*, 306-321.

Sutthirat, C., Saminpanya, S., Droop, G.T.R., Henderson, C.M.B. and Manning, D.A.C. 2001. Clinopyroxene-corundum assemblages from alkali basalt and alluvium, eastern Thailand: constrains on the origin of Thai rubies. *Mineralogical Magazine*, **65**, 277-295.

Seyler, M. and Bonatti, E., 1994. Na, Al^4 and Al^6 in clinopyroxenes of continental and suboceanic ridge peridotites: a clue to different melting processes in the mantle? *Earth and Planetary Sciences Letters*, **122**, 281-289.

Takahashi, E. and Kushiro, I. 1983. Melting of a dry peridotite at high pressures and basalt magma genesis. *American Mineralogist*, **68**, 859-879.

Taylor, S.R. and McLennen, S.M. 1981. The composition and evolution of the continental crust: rare earth element evidence from sedimentary rocks. *Philosophical Transactions of Royal Society*, London, **A301**, 381-399.

Tantiwanit, W., Raksakulwong, L., Bupasiri, V. and Kamchoo, A. 1985. *Geologic map of Amphoe Mae Ramat and Ban Mae La, scale 1:50,000.* Department of Mineral Resources, Bangkok, Thailand

Tapponnier, P., Peltzer, G. and Armijo, R. 1986. On the mechanism of collision between India and Asia. *In*: Coward, M.P. and Ries, A.C. (eds) *Collision Tectonics, Geological*

Society of London Special Publication, **19**, 115-157.

Taylor, H.P.Jr. and Sheppard, S.M.F. 1986. Igneous Rocks: I. Processes of Isotopic Fractionation and Isotopic systematics. *In*: Valley, J.W., Taylor, H.P.Jr. and O'Niel, J.R. (eds). *Stable Isotopes in High Temperature Geological Processes. Reviews in Mineralogy,* **16**, BookCrafters, Inc., Michigan, 227-271.

Tennie, A., Hoffbauer, R. and Hoernes, S. 1998. The oxygen isotope fractionation behaviour of kyanite in experiment and nature. *Contributions to Mineralogy and Petrology*, **133**, 346-355.

Thanasuthipitak, T. 1978. Geology of Uttaradit area and its implications on tectonic history of Thailand. *In* Nuttalaya, P. (ed) *Proceeding of the Third Regional Conferences on Geology and Mineral Resources of Southeast Asia*, 187-197.

Touret, J.L.R. 1985. Fluid regime in southern Norway, the record of fluid inclusion. *In*, Tobi, A.C. and Touret, J.L.R. (eds), *The Deep Proterozoic Crust in the North Atlantic Provinces*. Reidel, Dordrecht, 517-549.

Touret, J.L.R. and Fezzotti, M.-L. 1993. Magmatic remnants in plutonic rocks. *Bulletin of Society Geological of France*, **164**, 229-242.

Tsuruta, K. and Takahashi, E. 1998. Melting study of an alkali basalt JB-1 upto 1.2 GPa: behaviour of potassium in the deep mantle. *Physics of the Earth and Planetary Interiors*, **107**, 119-130.

Umino, S. and Yoshizawa, E. 1996. Petrology of ultramafic xenoliths from Kishyuku Lava, Fukue-jima, Southwest Japan. *Contributions to Mineralogy and Petrology*, **124**,154-166

Upton, B.G.J., Aspen, P. and Chapman, N.A. 1983. The upper mantle and deep crust beneath the British Isles: evidence from inclusions in volcanic rocks. *Journal of the Geological Society, London*, **140**, 105-121.

Upton, B.G.J., Hinton, R.W., Aspen, P., Finch, A. and Valley, J.W. 1999. Megacrysts and Associated Xenoltihs: Evidence for Migration of Geochemically Enriched Melts In the Upper Mantle beneath Scotland. *Journal of Petrology*, **40**, 935-956.

Uto, K., 1986. Variations of Al_2O_3 content in Late Cenozoic Japanese basalts: a reexamination of Kuno's High-Alumina Basalts. *Journal of Volcanology and Geothermal Research,*

29, 397-411.

Vennemann, T.W. and Smith, H.S. 1992. Stable isotope profile across the orthoamphibole isograd in the Southern Marginal Zone of the Limpopo Belt, South Africa. *Precambrian Research*, **55**, 365-397.

Vichit, P., Udompornvirat, S., Tritrangan, A. and Jariyawat, P. 1988. A report on gem deposits in Wichian Buri area, Changwat Phetchabun. *Economic Geology Report No.61/1988*, 145pp. (in Thai)

Vichit, P., Vudthichatvanich, S. and Hansawek, R. 1978. The distribution and some characteristics of corundum-bearing basalt in Thailand. *Journal of Geological Society of Thailand*, **3**, 1-8.

Vichit, P. 1992. Gemstones in Thailand. *In* Piancharoen, C. (editor-in-chief) *Proceeding of a National Conference on Geological Resources of Thailand: Potential for Future Development,* Bangkok, Thailand, 124-150.

Virag, A., Zinner, E., Amari, S. and Anders, E. 1991. An ion microprobe study of corundum in the Murchison meteorite: Implications for ^{26}Al and ^{16}O in the early solar system. *Geochimica et Cosmochimica Acta*, **55**, 2045-2062.

Wallace, P.J., Anderson Jr, A.T. and Davis, A.M. 1985. Quantification of pre-eruptive exsolved gas content in silicic magmas. *Nature*, **377**, 612-616.

Watson, E.B. 1982. Basalt contamination by continental crust: some experiments and results. *Contributions to Mineralogy and Petrology*, **80**, 73-87.

Watson, E.B., Sneeringer, M.A. and Ross, A. 1982. Diffusion of dissolved carbonate in magmas: Experimental results and applications. *Earth and Planetary Sciences Letters*, **61**, 346-358.

Webster, J.D., Burt, D.M. and Aguillon, R.A. 1996. Volatile and lithophile trace-element geochemistry of Mexican tin rhyolite magma dedeced from melt inclusions. *Geochimica et Cosmochimica Acta*, **60**, 3267-3283.

Webster, J.D. and Rebbert, C.R. 1998. Geochemical evidence of fluid saturation in felsic magma determined through experimental investigation of H_2O and Cl solubilities in F-rich rhyolite melts. *Contributions to Mineralogy and Petrology*, **132**, 198-207.

Wells, P.R.A. 1977. Pyroxene thermometry in simple and complex systems. *Contibutions to Mineralogy and Petrology*, **62**, 129-139.

"----------" 1978. Chemical and thermal evolution of archaean silicic crust, southern West Greenland. *Journal of Petrology*, **20**, 187-226.

White, W. M. 1985. Sources of oceanic basalts: radiogenic isotopic evidence. *Geology,* **13**, 115-118.

Wilson, M. 1989. *Igneous Petrogenesis: A global tectonic approach.* Chapman&Hall, London.

Wilson, M., Downes, H. and Cebria, J. 1995. Contrasting Fractionation Trends in Coexisting Continental Alkaline Magma Series, Cantal, Massif Central, France. *Journal of Petrology*, **36**, 1729-1753.

Wilson, M., Tankut, A. and Guleç, N. 1997. Tertiary volcanism of the Galatia province, north-west Central Anatolia, Turkey. *Lithos*, **42**, 105-121.

Winchester, J.A. and Floyd, 1976. Geochemical magma type discrimination; application to altered and metamorphosed basic igneous rocks. *Earth and Planetary Sciences Letters*, **28**, 459-469.

Winchester, J.A. and Floyd, 1977. Geochemical discrimination of different magma series and their differentiation products using immobile elements. *Chemical Geology*, **20**, 325-343.

Witt, G.E. and Seck, H.A. 1987. Temperature history of sheared mantle xenoliths from the west Eifel, West Germany: evidence for mantle diapirism beneath the Rhenish Massif. *Journal of Petrology*, **28**, 475-493

Witt-Dickschen, G.E. and Seck, H.A. 1991. Solubility of Ca and Al in orthopyroxene from spinel peridotite: an improved version of an empirical geothermometer. *Contributions to Mineralogy and Petrology*, **106**, 431-439.

Wolfart, R. 1987. Geology of Amphoe Sop Prap (4844-I) and Amphoe Wang Chin (4944-IV), Thailand, scale 1:50,000. *Geologisches Jahrbuch*, **65**, 3-52.

Wood, B.J. and Banno, S. 1973. Garnet-orthopyroxene and orthopyroxene-clinopyroxene relationships in simple and complex systems. *Contributions to Mineralogy and Petrology*, **42**, 102-124.

Wylie, P.J. and Wolf, M.B. 1993. Amphibolite dehydration-melting: sorting out the solidus. *In* Pritchard, H.M. *et al.* (eds) *Magmatic processes and plate tectonics*, Geological Society Special Publication, **76**, 405-416.

Xu, Y., Menzies, M.A., Vroon, P., Mercier, J-C and Lin, C. 1998. Texture-Temperature-Geochemistry Relationships in the Upper Mantle as Revealed from Spinel Peridotite Xenoliths from Wangqing, NE China. *Journal of Petrology*, **39(3)**, 469-493

Yamniyom, N. 1982. The petrochemical study of corundum-bearing basalts at Bo Phloi district, Kanchanaburi. M.Sc. thesis, Chulalongkorn University.

Yaxley, G.M., Crawford, A.J. and Green, G.H., 1991. Evidence for carbonatite metasomatism in spinel peridotite xenoliths from western Victoria, Australia. *Earth and Planetary Sciences Letters*, **107**, 305–317

Yoshikura, S. 1990. Geology of the Nan-Chanthaburi suture zone (II) – Petrology of basaltic rocks. *In:* Charusiri, P. (editor-in-chief) *The Technical Conference on Development Geology for Thailand into the Year 2000, Abstract.* Bangkok, Thailand, 11-12.

Yui, T.F., Zaw, K. and Limtrakun, P. 2003. Oxygen isotope composition of the Denchai sapphire, Thailand: a clue to its enigmatic origin, *Lithos*, **67**, 153-161.

Yui, T.F., Wu, C.M., Limtrakun, P., Sricharn, W. and Boonsoong, A. 2006. Oxygen isotope studies on placer sapphire and ruby in the Chanthaburi-Trat alkali basaltic gemfield, Thailand. *Lithos,* **86**, 197-211.

Zhao, Z.F. and Zheng, Y.F. 2002. Calculation of oxygen isotope fractionation in magmatic rocks. *Chemical Geology*, **193**, 59-80.

Zheng, Y.F. 1991, Calculation of oxygen isotope fractionation in metal oxides. *Geochemica et Cosmochimica Acta*, **55**, 2299-2307.

Zheng, Y.F. 1993, Calculation of oxygen isotope fractionation in anhydrous silicate minerals. *Geochemica et Cosmochimica Acta*, **57**, 1079-1091.

Zheng, Y.F. 1997. Prediction of high-temperature oxygen isotope fractionation factors between mantle minerals. *Physics and Chemistry of Minerals*, **24**, 356-364

Zheng, Y.F., Fu, -p;B., Li Y.L., Wei, C.S. and Zhou, J.B. 2001. Oxygen isotope composition of granulites from Dabie Shan in eastern China and its implications for geodynamics of

yangtze plate subduction. *Physics and Chemistry of the Earth,Part A: Solid Earth and Geodesy,* **26**, 673-684.

Zhou, P. and Mukasa, S.B. 1997. Nd-Sr-Pb isotopic and major- and trace-element geochemistry of Cenozoic lavas from the Khorat Plateau, Thailand: sources and petrogenesis. *Chemical Geology*, **137**, 175-193.

Appendix-I

X-Ray microprobe analyses of the Bo Ploi corundum

Secondary X-Ray pattern of elements in a synthetic yellow diamond

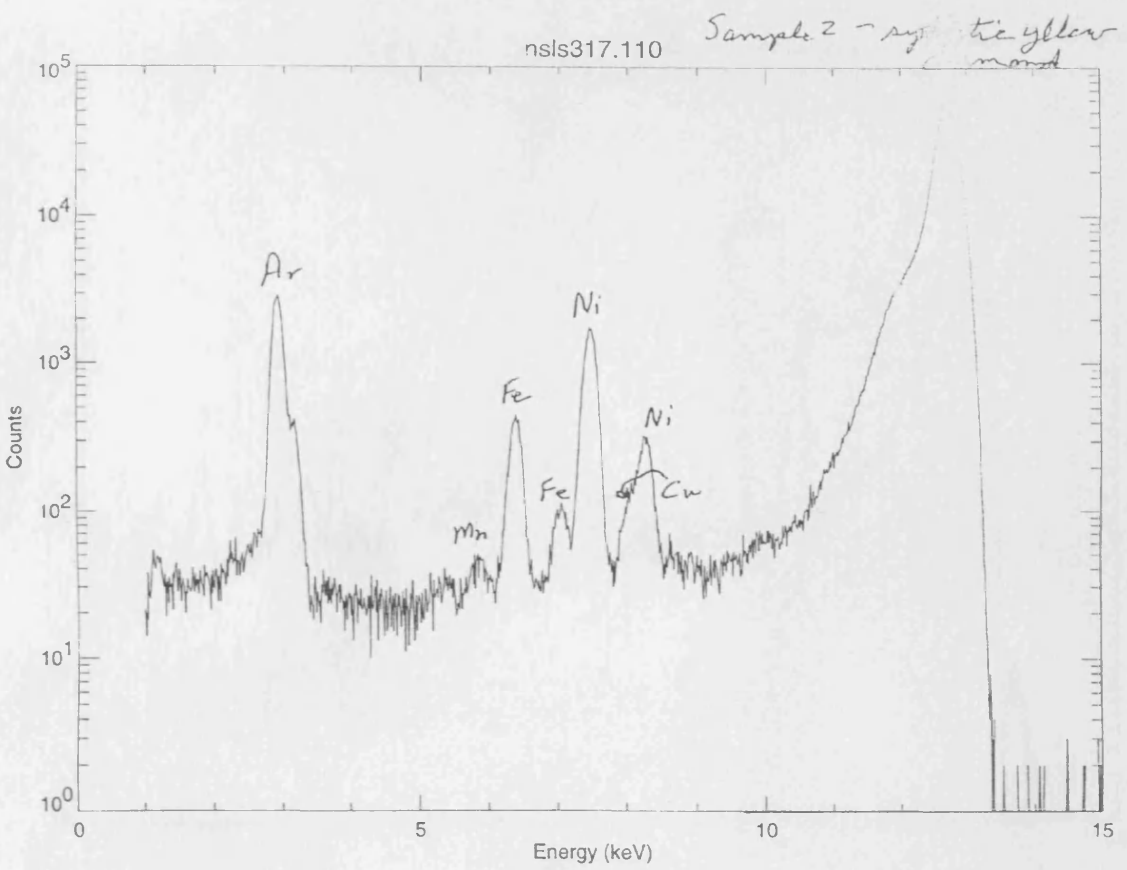

X-Ray microprobe analysis using the facility GSECARS at the synchrotron in Chicago, Illinois showing the spectrum on synthetic yellow diamond, which was used as a material background. It is noticed that spectrum assigned as Ar, Ni, Fe, Cu, and Mn are dominated the pattern.

Secondary X-Ray pattern of elements in a natural light blue sapphire

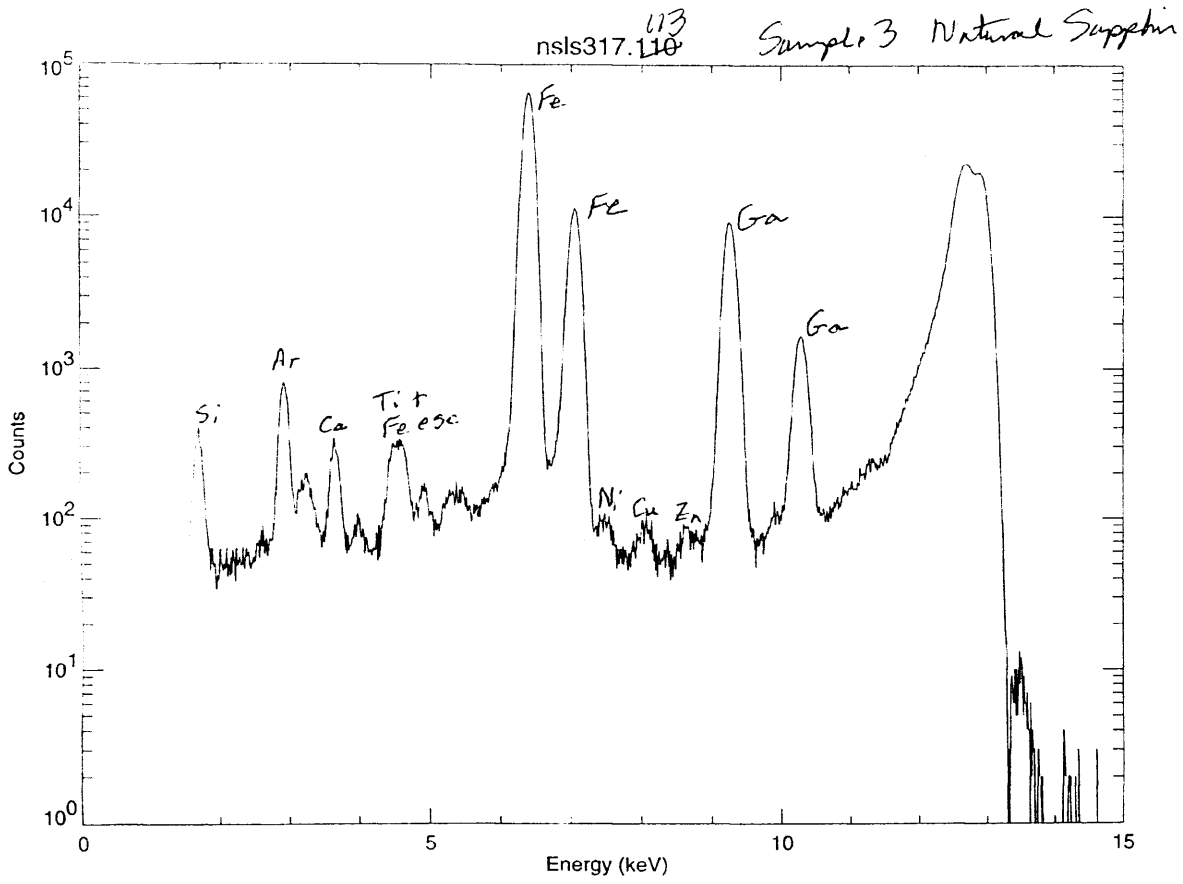

X-Ray microprobe analysis using the facility GSECARS at the synchrotron in Chicago, Illinois showing the spectrum on natural light blue sapphire. In this sample, the pattern is dominated by Fe, Ga, Ti , Ar and Si with minor peak of Ni, Cu and Zn.

Secondary X-Ray pattern of elements in a natural dark blue sapphire

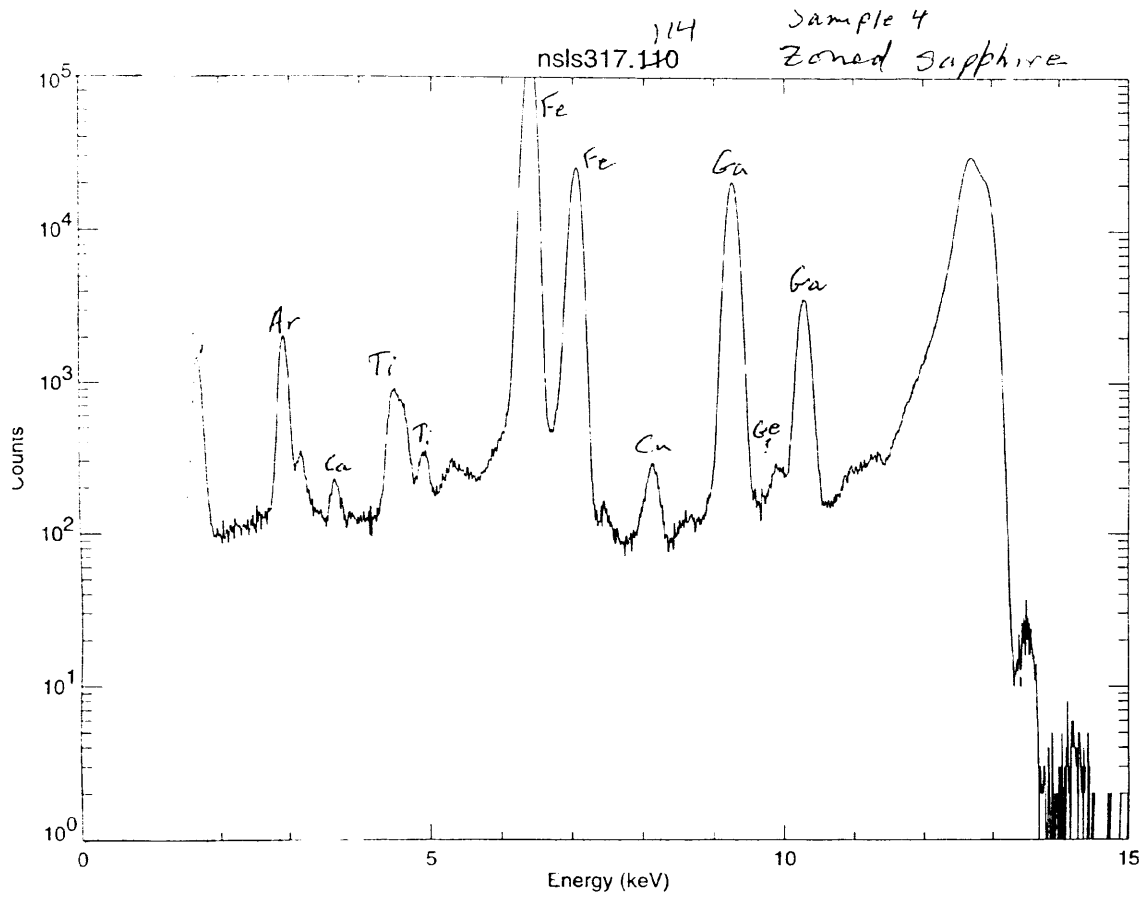

X-Ray microprobe analysis using the facility GSECARS at the synchrotron in Chicago, Illinois showing the spectrum on the natural dark blue sapphire. This pattern very much similar to the pattern obtained from light blue sapphire with prominent peaks assigned as Fe and Ga and relatively abundant of Ti, Ar and Si with slightly lower proportion of Cu. No Zn and Ni allocated in this pattern.

Appendix-II

Chemical composition of phenocryts in the Bo Ploi basalt

Major oxide analyses for selected olivine phenocrysts and megacrysts

Sample	OL-01	OL-02	OL-03	OL-04	OL-05	OL-06	OL-07	OL-08	OL-09	OL-10
SiO_2	39.03	38.46	38.14	39.12	37.64	37.61	39.14	39.5	38.11	40.69
TiO_2	0.01	0.01	0.07	0.00	0.1	0.02	0.03	0.07	0.04	0.03
FeO	20.23	23.4	25.28	20.72	27.64	28.07	19.44	18.38	20.48	20.26
MnO	0.57	0.65	0.8	0.45	0.84	0.78	0.5	0.46	0.82	0.49
MgO	40.57	37.47	35.61	40.02	33.78	33.5	41.01	41.16	39.92	38.7
CaO	0.12	0.18	0.33	0.09	0.31	0.33	0.18	0.2	0.34	0.11
Total	100.53	100.17	100.23	100.40	100.31	100.31	100.3	99.77	99.71	100.28
				Olivine cation numbers on the basis of 4 oxygens						
Si	1.000	1.005	1.006	1.005	1.004	1.005	1.002	1.010	0.990	1.039
Ti	0.000	0.000	0.001	0.000	0.002	0.000	0.001	0.001	0.001	0.001
Fe^{2+}	0.433	0.511	0.558	0.445	0.617	0.627	0.416	0.393	0.445	0.433
Mn	0.0 12	0.014	0.018	0.010	0.019	0.018	0.011	0.010	0.018	0.011
Mg	1.550	1.459	1.400	1.532	1.343	1.334	1.564	1.569	1.546	1.474
Ca	0.003	0.005	0.009	0.002	0.009	0.009	0.005	0.005	0.009	0.003
CAT	2.986	2.994	2.992	2.994	2.994	2.993	2.999	2.988	3.009	2.961
Fa	21.86	25.94	28.48	22.51	31.47	31.97	21.00	20.03	22.35	22.70
Fo	78.14	74.06	71.52	77.49	68.53	68.03	79.00	79.97	77.65	77.30

Sample	OL-11	OL-12	OL-13*	OL-14*	OL-15*	OL-16*	OL-17*	OL-18*	OL-19*	Average
SiO_2	40.73	38.01	38.54	38.12	38.92	39.81	40.83	40.25	40.88	39.62
TiO_2	0.08	0.08	0.03	0.04	0.05	0.06	0.04	0.05	0.03	0.04
FeO	21.06	22.14	22.97	25.48	19.43	21.15	10.36	13.12	10.45	17.57
MnO	0.62	0.64	0.67	0.69	0.59	0.58	0.11	0.31	0.13	0.44
MgO	37.48	38.77	37.88	35.77	40.7	38.32	48.48	46.04	48.49	42.24
CaO	0.16	0.31	0.21	0.24	0.24	0.19	0.12	0.12	0.08	0.17
Total	100.13	99.95	100.30	100.34	99.93	100.11	99.94	99.89	100.06	100.08
					Olivine cation numbers on the basis of 4 oxygens					
Si	1.046	0.992	1.004	1.005	1.001	1.026	1.003	1.003	1.003	1.006
Ti	0.002	0.002	0.001	0.001	0.001	0.001	0.001	0.001	0.001	0.001
Fe^{2+}	0.452	0.483	0.500	0.562	0.418	0.456	0.213	0.273	0.214	0.377
Mn	0.013	0.014	0.015	0.015	0.013	0.013	0.002	0.007	0.003	0.010
Mg	1.435	1.508	1.470	1.405	1.56	1.472	1.775	1.709	1.773	1.595
Ca	0.004	0.009	0.006	0.007	0.007	0.005	0.003	0.003	0.002	0.005
CAT	2.952	3.008	2.996	2.995	3.000	2.973	2.997	2.996	2.996	2.993
Fa	23.97	24.26	25.39	28.55	21.13	23.64	10.70	13.78	10.78	11.83
Fo	76.03	75.74	74.61	71.45	78.88	76.36	89.30	86.22	89.22	88.17

CAT = Total cation numbers

* is denoted to megacrysts

Major oxide analyses for selected clinopyroxene phenocrysts

Sample	CPX-01	CPX-02	CPX-03	CPX-04	CPX-05	CPX-06
SiO_2	48.05	48.26	48.28	48.56	48.6	48.76
TiO_2	1.45	1.54	1.52	1.59	1.46	1.51
Al_2O_3	8.99	9.07	9.04	8.77	8.89	8.98
Cr_2O_3	0.06	0.05	0.03	0.12	0.09	0.09
FeO	5.84	5.82	5.92	5.84	6.02	5.94
MnO	0.11	0.06	0.12	0.05	0.06	0.04
CaO	20.09	19.98	20.04	20.29	20.13	20.31
MgO	13.59	13.55	13.7	13.11	13.07	13.11
Na_2O	1.61	1.58	1.56	1.49	1.56	1.47
K_2O	0.04	0.04	0.02	0.00	0.00	0.00
Total	99.83	99.95	100.23	99.82	99.88	100.21

Clinopyroxene cation numbers on basis of 6 oxygens

T site						
Si^{4+}	1.7519	1.7586	1.7543	1.7776	1.7771	1.7781
Al^{4+}	0.2481	0.2414	0.2457	0.2224	0.2229	0.2219
Fe^{3+}	0.0000	0.0000	0.0000	0.0000	0.0000	0.0000
Total	2.0000	2.0000	2.0000	2.0000	2.0000	2.0000
M1 site						
$Al6^{+}$	0.1383	0.1481	0.1414	0.1560	0.1601	0.1640
Fe^{3+}	0.1432	0.1197	0.1300	0.0799	0.0893	0.0751
Ti^{4+}	0.0397	0.0422	0.0414	0.0437	0.0401	0.0413
Cr^{3+}	0.0017	0.0014	0.0008	0.0034	0.0026	0.0026
Mg^{2+}	0.6771	0.6886	0.6864	0.7153	0.7079	0.7125
Fe^{2+}	0.0000	0.0000	0.0000	0.0017	0.0000	0.0045
Total	1.0000	1.0000	1.0000	1.0000	1.0000	1.0000
M2 site						
Mg^{2+}	0.0615	0.0473	0.0556	0.0000	0.0044	0.0000
Fe^{2+}	0.0349	0.0576	0.0499	0.0971	0.0947	0.1014
Mn^{2+}	0.0034	0.0018	0.0037	0.0015	0.0018	0.0013
Ca^{2+}	0.7848	0.7800	0.7801	0.7958	0.7886	0.7935
Na^{+}	0.1155	0.1134	0.1108	0.1057	0.1106	0.1038
Total	1.0001	1.0001	1.0001	1.0001	1.0001	1.0000
CAT	4.0001	4.0001	4.0001	4.0001	4.0001	4.0000
Mg#	0.81	0.81	0.80	0.80	0.79	0.80
En	34.292	34.382	34.439	33.367	33.274	33.274
Wo	50.694	50.698	50.377	51.642	51.247	51.548
Fs	15.014	14.920	15.184	14.991	15.479	15.178

Table 6.2 Major oxide analyses for selected clinopyroxene phenocrysts (continued)

Sample	CPX-07	CPX-08	CPX-09	CPX-10	CPX-11	CPX-12
SiO_2	48.83	48.70	48.72	47.92	47.73	47.83
TiO_2	1.50	1.83	1.53	1.79	1.9	1.85
Al_2O_3	9.07	6.24	8.73	9.32	9.44	9.29
Cr_2O_3	0.07	0.08	0.06	0.04	0.03	0.06
FeO	5.87	6.28	5.77	6.73	6.74	6.57
MnO	0.04	0.09	0.17	0.11	0.02	0.06
CaO	20.22	22.07	20.38	20.59	20.71	20.69
MgO	13.28	13.25	13.24	11.88	12.04	11.9
Na_2O	1.44	1.14	1.41	1.54	1.57	1.66
K_2O	0.00	0.00	0.00	0.00	0.00	0.00
Total	100.32	99.68	100.01	99.92	100.18	99.91

Clinopyroxene cation numbers on basis of 6 oxygens

T site						
Si^{4+}	1.7775	1.7967	1.7802	1.7626	1.7494	1.7572
Al^{4+}	0.2225	0.2033	0.2198	0.2374	0.2506	0.2428
Fe^{3+}	0.0000	0.0000	0.0000	0.0000	0.0000	0.0000
Total	2.0000	2.0000	2.0000	2.0000	2.0000	2.0000
M1 site						
$Al6^{+}$	0.1665	0.0680	0.1561	0.1666	0.1571	0.1594
Fe^{3+}	0.0728	0.1117	0.0769	0.0793	0.0985	0.0970
Ti^{4+}	0.0410	0.0507	0.0420	0.0495	0.0524	0.0511
Cr^{3+}	0.0020	0.0023	0.0017	0.0011	0.0008	0.0017
Mg^{2+}	0.7177	0.7287	0.7210	0.6513	0.6578	0.6516
Fe^{2+}	0.0000	0.0386	0.0023	0.0522	0.0334	0.0392
Total	1.0000	1.0000	1.0000	1.0000	1.0000	1.0000
M2 site						
Mg^{2+}	0.0028	0.0000	0.0000	0.0000	0.0000	0.0000
Fe^{2+}	0.1059	0.0433	0.0971	0.0756	0.0747	0.0656
Mn^{2+}	0.0012	0.0028	0.0052	0.0034	0.0006	0.0018
Ca^{2+}	0.7886	0.8724	0.7979	0.8114	0.8133	0.8144
Na^{+}	0.1016	0.08145	0.0999	0.1098	0.1115	0.1182
Total	1.0001	1.0000	1.0001	1.0002	1.0001	1.0000
CAT	4.0001	4.0000	4.0001	4.0002	4.0001	4.0000
Mg#	0.80	0.82	0.81	0.81	0.79	0.80
En	33.697	31.782	33.468	30.221	30.473	30.342
Wo	51.307	52.938	51.517	52.379	52.417	52.754
Fs	14.996	15.279	15.015	17.400	17.110	16.905

Major oxide analyses for selected spinel phenocrysts and megacrysts

Sample	SP-01	SP-02	SP-03	SP-04	SP-05	SP-06
SiO_2	0.16	0.16	0.14	0.14	0.15	0.18
TiO_2	0.23	0.2	0.42	0.69	0.74	0.6
Al_2O_3	56.26	56.16	55.21	59.56	59.45	58.14
Cr_2O_3	9.88	10.07	10.54	0.09	0.08	0.06
FeO	14.88	14.68	15.28	21.69	21.41	24.77
MnO	0.1	0.18	0.24	0.22	0.16	0.08
MgO	18.29	18.81	17.96	17.6	17.67	16.09
CaO	0.02	0.01	0.03	0	0.05	0.03
total	99.82	100.27	99.82	99.99	99.71	99.95

Spinel cation numbers on basis of 32 oxygens

Si	0.033	0.033	0.029	0.029	0.038	0.038
Ti	0.035	0.030	0.066	0.107	0.115	0.094
Al	13.928	13.822	13.743	14.589	14.590	14.427
Cr	1.640	1.662	1.759	0.014	0.012	0.009
Fe^{2+}	2.329	2.183	2.403	2.652	2.635	3.071
Mn	0.017	0.031	0.042	0.038	0.027	0.014
Mg	5.726	5.854	5.654	5.451	5.483	5.049
Ca	0.003	0.001	0.006	0.000	0.010	0.006
calc.Fe^{3+}	0.284	0.379	0.294	1.117	1.092	1.290
Total	23.995	23.995	23.995	23.997	24.003	23.997
Mg#	0.71	0.73	0.70	0.67	0.68	0.62
Cr#	0.11	0.11	0.11	0.00	0.00	0.00

End-member for spinels

Spinel	71.666	73.236	70.798	68.176	68.738	63.225
Hercynite	15.429	13.192	15.155	23.040	22.521	26.995
Jacobsite	0.219	0.398	0.528	0.482	0.344	0.177
Ulvospinel	0.867	0.806	1.195	1.710	1.830	1.657
Mnc	-	-	-	-	-	-
Chromite	10.259	10.393	11.006	0.089	0.079	0.059
Magnetite	1.561	1.976	1.318	6.504	6.489	7.889
Sum	100.00	100.00	100.00	100.00	100.00	100.00

Mnc = Magnesiochromite

* is denoted to megacrysts

Table 6.5 Major oxide analyses for selected spinel phenocrysts and megacrysts (continued)

Sample	SP-07	SP-08	SP-09	SP-10*	SP-11*	SP-12*
SiO_2	0.15	0.11	0.10	0.09	0.13	0.13
TiO_2	0.19	0.17	0.14	0.59	0.67	0.47
Al_2O_3	55.58	54.60	53.94	60.39	60.54	58.50
Cr_2O_3	10.73	10.43	10.63	0.30	0.29	0.27
FeO	13.90	17.41	18.25	19.10	18.92	23.57
MnO	0.14	0.29	0.26	0.13	0.00	0.24
MgO	18.90	16.94	16.65	19.26	19.17	16.48
CaO	0.06	0.00	0.03	0.02	0.00	0.00
total	99.65	99.95	100.00	99.86	99.72	99.66
			Spinel cation numbers on basis of 32 oxygens			
Si	0.030	0.022	0.020	0.019	0.028	0.028
Ti	0.029	0.026	0.022	0.098	0.110	0.078
Al	13.760	13.682	13.562	15.714	15.746	15.434
Cr	1.782	1.753	1.792	0.052	0.050	0.047
Fe^{2+}	2.114	2.635	2.706	3.526	3.491	4.114
Mn	0.024	0.051	0.046	0.024	0.000	0.045
Mg	5.918	5.368	5.294	4.556	4.532	3.952
Ca	0.012	0.000	0.006	0.006	0.000	0.000
calc.Fe^{3+}	0.326	0.459	0.550	0.000	0.000	0.297
Total	23.995	23.997	23.996	23.996	23.958	23.995
Mg#	0.74	0.67	0.66	0.73	0.72	0.64
Cr#	0.11	0.11	0.12	0.00	0.00	0.00
			End-member for spinels			
Spinel	74.174	67.128	66.299	57.051	57.019	49.427
Hercynite	11.881	18.413	18.517	41.200	42.037	47.072
Jacobsite	0.309	0.646	0.585	-	-	0.568
Ulvospinel	0.757	0.626	0.536	1.448	0.944	1.344
Mnc	-	-	-	0.300	-	-
Chromite	11.145	10.960	11.210	-	-	0.299
Magnetite	1.736	2.228	2.854	-	-	1.291
Sum	100.00	100.00	100.00	100.00	100.00	100.00

Mnc = Magnesiochromite

* is denoted to megacrysts

Major oxide analyses for selected alkali feldspar phenocrysts and megacrysts

Sample	Kfd-01	Kfd-02	Kfd-03	Kfd-04	Kfd-05	Kfd-06	Kfd-07	Kfd-08	Kfd-09
SiO_2	66.61	66.38	67.07	60.29	60.88	62.01	66.90	67.42	67.56
TiO_2	0.13	0.03	0.04	0.03	0.01	0.02	0.01	0.14	0.10
Al_2O_3	18.10	19.06	17.41	25.20	24.60	23.46	17.71	17.47	17.46
FeO	0.97	0.02	1.21	0.11	0.00	0.20	1.21	0.86	0.97
CaO	0.08	0.01	0.10	5.86	5.83	4.94	0.03	0.01	0.09
MgO	0.02	0.02	0.01	0.03	0.00	0.01	0.05	0.10	0.10
Na_2O	6.63	6.06	6.72	7.52	7.45	7.76	6.52	6.51	6.33
K_2O	7.66	8.34	7.07	0.95	1.24	1.71	7.69	7.51	7.48
Total	100.20	99.92	99.63	99.99	100.01	100.11	100.12	100.02	100.09
alkali	14.29	14.40	13.79	8.47	8.69	9.47	14.21	14.02	13.81

Alkali feldspar cation numbers on basis of 32 oxygens

Si	12.000	11.948	12.116	10.748	10.852	11.044	12.004	12.128	12.140
Ti	0.016	0.004	0.004	0.004	0.000	0.004	0.000	0.020	0.012
Al	3.804	4.044	3.708	5.296	5.168	4.928	3.764	3.704	3.696
Fe^{2+}	0.144	0.004	0.184	0.016	0.000	0.028	0.168	0.128	0.144
Ca	0.016	0.000	0.020	1.120	1.112	0.944	0.004	0.000	0.016
Mg	0.004	0.004	0.004	0.008	0.000	0.004	0.012	0.028	0.028
Na	2.316	2.116	2.352	2.600	2.576	2.680	2.280	2.268	2.204
K	1.760	1.896	1.628	0.216	0.280	0.388	1.768	1.724	1.712
CAT#	20.060	20.016	20.016	20.008	19.988	20.020	20.000	20.000	19.952
Or	43.028	47.500	40.710	40.710	5.490	7.095	9.682	43.635	43.130
Ab	56.601	52.460	58.811	58.811	66.063	64.859	66.816	56.227	56.830
An	0.372	0.040	0.480	0.480	28.447	28.046	23.502	0.138	0.040

CAT# = total cation numbers

Major oxide analyses for selected nepheline phenocrysts

Sample	NEP-01	NEP-02	NEP-03	NEP-04	NEP-05	NEP-06	Average
SiO_2	44.01	43.34	44.24	43.44	43.19	43.8	43.67
TiO_2	0.03	0.02	0.02	0.03	0.01	0.08	0.03
Al_2O_3	33.97	33.77	34.12	33.88	33.72	33.11	33.76
FeO	0.46	0.38	0.11	0.44	0.35	0.57	0.39
CaO	2.12	1.9	2.07	1.62	1.32	0.84	1.65
MgO	0.13	0.06	0	0.14	0.05	0.01	0.07
Na_2O	15.84	16.26	15.44	16.54	16.74	16.75	16.26
K_2O	3.71	3.94	3.76	4.28	4.33	4.45	4.08
Total	100.27	99.67	99.76	100.37	99.71	99.61	99.90

Nepheline cation numbers on basis of 32 oxygens

Si	8.348	8.298	8.401	8.279	8.287	8.407	8.337
Ti	0.004	0.003	0.003	0.004	0.001	0.012	0.005
Al	7.595	7.621	7.637	7.61	7.625	7.49	7.596
Fe^{2+}	0.073	0.061	0.017	0.07	0.056	0.091	0.061
Ca	0.431	0.39	0.421	0.331	0.271	0.173	0.336
Mg	0.037	0.017	0	0.04	0.014	0.003	0.019
Na	5.826	6.036	5.685	6.112	6.227	6.233	6.020
K	0.898	0.962	0.911	1.041	1.06	1.089	0.994
CAT #	23.212	23.388	23.075	23.487	23.541	23.498	23.367
R	7.586	7.778	7.438	7.815	7.829	7.668	7.686
Ne	81.507	82.364	80.000	81.841	81.926	80.333	81.329
Ks	13.959	14.614	14.267	15.506	15.507	15.624	14.913
Q	4.534	3.022	5.732	2.655	2.567	4.043	3.759

$R = (Na + K + 2Ca)$

Appendix-III

Chemical composition of silicate-melt inclusions

Major oxide composition and CIPW calculated for silicate-melt inclusion SM-01

Oxides	SM-1a	SM-1b	SM-1c	SM-1d	SM-1e	SM-1f	Average
SiO_2	61.85	60.75	62.97	64.51	63.46	63.07	62.77
TiO_2	0.16	0.11	0.29	0.40	0.28	0.33	0.26
Al_2O_3	25.53	27.44	25.25	25.76	25.77	25.62	25.90
FeO	0.52	0.34	0.62	0.16	0.39	0.17	0.37
MnO	0.24	0.02	0.05	0.19	0.27	0.21	0.16
MgO	<dl	<dl	<dl	<dl	<dl	<dl	<dl
CaO	0.29	0.30	0.35	0.33	0.34	0.38	0.33
SrO	0.16	0.31	0.41	0.29	0.43	0.83	0.41
Na_2O	5.44	4.18	5.84	4.49	2.48	3.08	4.25
K_2O	4.64	4.55	4.61	4.09	4.39	4.61	4.48
P_2O_5	0.72	0.74	0.59	0.80	0.86	1.04	0.79
Total	99.55	98.74	100.98	101.02	98.67	99.34	99.72

Oxides	SM-1a	SM-1b	SM-1c	SM-1d	SM-1e	SM-1f	Average
SiO_2	62.13	61.53	62.36	63.86	64.32	63.49	62.94
TiO_2	0.16	0.11	0.29	0.40	0.28	0.33	0.26
Al_2O_3	25.65	27.79	25.00	25.50	26.12	25.79	25.97
FeO	0.52	0.34	0.61	0.16	0.40	0.17	0.37
MnO	0.24	0.02	0.05	0.19	0.27	0.21	0.16
MgO	<dl	<dl	<dl	<dl	<dl	<dl	<dl
CaO	0.29	0.30	0.35	0.33	0.34	0.38	0.33
SrO	0.16	0.31	0.41	0.29	0.44	0.84	0.41
Na_2O	5.46	4.23	5.78	4.44	2.51	3.10	4.26
K_2O	4.66	4.61	4.57	4.05	4.45	4.64	4.49
P_2O_5	0.72	0.75	0.58	0.79	0.87	1.05	0.79
Total	100.00	100.00	100.00	100.00	100.00	100.00	100.00

CIPW norms

q	12.88	19.61	12.21	23.26	32.84	28.06	21.48
c	11.70	15.97	10.72	13.90	17.29	15.82	14.23
or	27.79	27.40	27.28	24.09	26.40	27.69	26.78
ab	46.60	36.05	49.23	37.87	21.40	26.49	36.27
wo	0.54	0.43	1.27	1.15	-	0.18	0.71
hd	1.60	0.78	1.42	-	-	0.30	1.03
opx	-	-	-	-	0.31	-	0.31
fs	-	-	-	-	0.77	-	0.77
il	0.31	0.21	0.55	0.74	0.54	0.64	0.50
ru	-	-	-	0.01	-	-	0.01
ap	1.73	1.79	1.40	1.89	2.08	2.50	1.90

Major oxide composition and CIPW calculated for silicate-melt inclusion SM-02

Oxides	SM-2a	SM-2b	SM-2c	SM-2d	SM-2e	SM-2f	Average
SiO_2	54.70	57.12	53.36	56.68	56.66	57.97	56.08
TiO_2	0.30	0.24	0.27	0.27	0.25	0.36	0.28
Al_2O_3	23.57	24.89	22.42	24.39	25.00	25.03	24.22
FeO	0.03	0.30	0.28	0.43	0.11	0.46	0.27
MnO	0.47	0.39	0.30	0.22	0.16	0.25	0.30
MgO	<dl	<dl	<dl	<dl	<dl	<dl	<dl
CaO	0.60	0.66	1.08	0.62	0.58	0.92	0.74
SrO	0.21	0.20	0.14	0.23	0.50	0.49	0.30
Na_2O	3.68	3.74	4.23	4.29	4.77	5.32	4.34
K_2O	4.27	4.93	4.54	4.73	4.22	5.03	4.62
P_2O_5	0.86	0.71	0.98	0.75	1.18	1.06	0.92
Total	88.69	93.18	87.60	92.61	93.43	96.89	92.07

Oxides	SM-2a	SM-2b	SM-2c	SM-2d	SM-2e	SM-2f	Average
SiO_2	61.68	61.30	60.91	61.20	60.64	59.83	60.93
TiO_2	0.34	0.26	0.31	0.29	0.27	0.37	0.31
Al_2O_3	26.58	26.71	25.59	26.34	26.76	25.83	26.30
FeO	0.03	0.32	0.32	0.46	0.12	0.47	0.29
MnO	0.53	0.42	0.34	0.24	0.17	0.26	0.33
MgO	<dl	<dl	<dl	<dl	<dl	<dl	<dl
CaO	0.68	0.71	1.23	0.67	0.62	0.95	0.81
SrO	0.24	0.21	0.16	0.25	0.54	0.51	0.32
Na_2O	4.15	4.01	4.83	4.63	5.11	5.49	4.70
K_2O	4.81	5.29	5.18	5.11	4.52	5.19	5.02
P_2O_5	0.97	0.76	1.12	0.81	1.26	1.09	1.00
Total	100.00	100.00	100.00	100.00	100.00	100.00	100.00

CIPW norms

q	19.36	17.82	13.60	14.89	14.22	8.68	14.76
c	14.64	14.46	12.13	13.26	13.59	11.31	13.23
or	28.59	31.43	30.85	30.35	26.92	31.02	29.86
ab	35.28	34.14	41.16	39.42	43.58	46.98	40.09
wo	0.29	0.03	0.99	0.19	0.85	1.09	0.57
cpx	-0.41	0.16	-1.67	-0.15	-1.56	-1.85	-0.91
hd	0.92	1.79	1.35	1.51	0.18	1.40	1.19
il	0.65	0.49	0.59	0.56	0.51	0.71	0.59
ap	2.31	1.81	2.67	1.93	3.02	2.62	2.39

Major oxide composition and CIPW calculated for silicate-melt inclusion SM-03

Oxides	SM-3a	SM-3b	SM-3c	SM-3d	SM-3e	SM-3f	Average
SiO_2	61.14	60.77	54.09	44.31	57.16	60.05	56.25
TiO_2	0.14	0.25	0.27	0.31	0.34	0.25	0.26
Al_2O_3	29.07	29.01	26.26	21.09	31.44	25.64	27.09
FeO	0.44	0.49	0.13	0.49	0.42	0.62	0.43
MnO	0.06	0.43	0.42	0.26	0.00	0.28	0.24
MgO	<dl	<dl	<dl	<dl	<dl	<dl	<dl
CaO	0.63	0.65	0.72	0.75	0.71	0.67	0.69
SrO	0.23	0.51	0.51	0.26	0.24	0.73	0.41
Na_2O	5.32	4.33	5.36	2.24	2.36	3.27	3.81
K_2O	3.04	3.45	3.24	2.99	2.79	3.04	3.09
P_2O_5	0.41	0.51	0.63	0.10	0.45	0.48	0.43
Total	100.48	100.40	91.63	72.80	95.91	95.03	92.71

Oxides	SM-3a	SM-3b	SM-3c	SM-3d	SM-3e	SM-3f	Average
SiO_2	60.85	60.53	59.03	60.87	59.60	63.19	60.68
TiO_2	0.14	0.25	0.29	0.43	0.35	0.26	0.29
Al_2O_3	28.93	28.89	28.66	28.97	32.78	26.98	29.20
FeO	0.44	0.49	0.14	0.67	0.44	0.65	0.47
MnO	0.06	0.43	0.46	0.36	0.00	0.29	0.27
MgO	<dl	<dl	<dl	<dl	<dl	<dl	<dl
CaO	0.63	0.65	0.79	1.03	0.74	0.71	0.76
SrO	0.23	0.51	0.56	0.36	0.25	0.77	
Na_2O	5.29	4.31	5.85	3.08	2.46	3.44	4.07
K_2O	3.03	3.44	3.54	4.11	2.91	3.20	3.37
P_2O_5	0.41	0.51	0.69	0.14	0.47	0.51	0.45
Total	100.00	100.00	100.00	100.00	100.00	100.00	100.00

CIPW norms

q		19.25	22.35	12.05	25.63	34.15	35.07	24.75
c		16.95	18.23	15.37	18.05	25.46	16.89	18.49
or		18.05	20.47	21.12	24.45	17.26	17.95	19.88
ab		45.24	36.80	50.02	26.23	20.91	27.65	34.48
an		0.45	-	-	4.25	0.61	0.19	1.38
wo		1.53	-	0.87	0.01	0.23	-	0.66
cpx		-2.69	-	-1.48	0.26	-0.37	-	-1.07
	hd	1.30	-	1.19	2.27	0.41	-	1.29
opx		-	0.52	-	-	-	0.67	0.60
	fs	-	1.29	-	-	-	1.25	1.27
il		0.27	0.48	0.57	0.81	0.68	0.47	0.55
ap		0.98	1.21	1.65	0.33	1.12	1.14	1.07

Major oxide composition and CIPW calculated for silicate-melt inclusion SM-04

Oxides	SM-4a	SM-4b	SM-4c	SM-4d	SM-4e	SM-4f	Average
SiO_2	57.67	60.21	47.91	60.85	59.81	58.38	57.47
TiO_2	0.00	0.00	0.13	0.14	0.05	0.15	0.08
Al_2O_3	26.72	25.55	21.89	25.52	27.33	28.15	25.86
FeO	0.31	0.26	0.43	0.31	0.09	0.27	0.28
MnO	<dl	<dl	<dl	<dl	0.03	0.09	0.06
MgO	<dl	<dl	<dl	<dl	<dl	<dl	<dl
CaO	0.57	0.72	1.40	0.55	0.54	0.52	0.72
SrO	0.31	0.37	0.50	0.26	0.28	0.08	0.30
Na_2O	4.63	4.65	3.89	4.44	4.64	5.16	4.57
K_2O	4.94	4.75	4.33	5.20	5.30	4.90	4.90
P_2O_5	<dl	0.03	0.34	<dl	0.03	<dl	0.13
Total	95.15	96.54	80.82	97.27	98.10	97.70	94.26

Oxides	SM-4a	SM-4b	SM-4c	SM-4d	SM-4e	SM-4f	Average
SiO_2	60.61	62.37	59.28	62.56	60.97	59.75	60.92
TiO_2	0.00	0.00	0.16	0.14	0.05	0.15	0.08
Al_2O_3	28.08	26.47	27.08	26.24	27.86	28.81	27.42
FeO	0.33	0.27	0.53	0.32	0.09	0.28	0.30
MnO	<dl	<dl	<dl	<dl	0.03	0.09	0.06
MgO	<dl	<dl	<dl	<dl	<dl	<dl	<dl
CaO	0.60	0.75	1.73	0.57	0.55	0.53	0.79
SrO	0.33	0.38	0.62	0.27	0.29	0.08	
Na_2O	4.87	4.82	4.81	4.56	4.73	5.28	4.85
K_2O	5.19	4.92	5.36	5.35	5.40	5.02	5.21
P_2O_5	<dl	0.03	0.42	<dl	0.03	<dl	0.16
Total	100.00	100.00	100.00	100.00	100.00	100.00	100.00

CIPW norms

q	11.31	14.89	8.14	15.33	12.30	9.64	11.94
c	12.92	12.07	11.31	11.95	13.39	13.78	12.57
or	31.08	29.40	31.90	31.94	32.15	29.90	31.06
ab	41.72	41.21	41.03	39.05	40.30	45.09	41.40
an	4.70	3.54	5.89	3.08	2.55	2.85	3.77
wo	1.43	1.40	-	1.81	1.03	1.82	1.50
hd	1.07	0.68	-	0.22	0.27	0.81	0.61
opx	-	-	0.44	-	-	-	0.44
fs	-	-	0.62	-	-	-	0.62
il	-	-0.04	0.31	0.28	0.10	0.29	0.19
ap	-0.68	0.07	1.00	-0.10	0.07	-0.07	0.05
fr	0.05	-	-	0.01	-	0.01	0.02

Major oxide composition and CIPW calculated for silicate-melt inclusion SM-05

Oxides	SM-5a	SM-5b	SM-5c	SM-5d	SM-5e	SM-5f	Average
SiO_2	61.93	59.05	48.21	52.37	59.19	61.00	56.96
TiO_2	0.21	0.27	0.23	0.31	0.32	0.05	0.23
Al_2O_3	30.06	27.22	24.54	24.52	28.66	27.81	27.14
FeO	0.49	0.48	0.42	0.78	0.75	0.66	0.60
MnO	0.10	0.28	0.24	0.23	0.29	0.38	0.25
MgO	<dl	<dl	<dl	<dl	<dl	<dl	<dl
CaO	0.28	0.40	0.30	0.41	0.33	0.22	0.32
SrO	0.50	0.04	0.58	0.00	0.31	0.35	0.30
Na_2O	2.61	6.98	1.82	4.39	5.31	3.66	4.13
K_2O	3.67	5.69	4.05	5.77	4.96	5.35	4.92
P_2O_5	0.30	0.15	0.44	0.13	0.16	0.33	0.25
Total	100.15	100.56	80.83	88.91	100.28	99.81	95.09

Oxides	SM-5a	SM-5b	SM-5c	SM-5d	SM-5e	SM-5f	Average
SiO_2	61.84	58.72	59.64	58.90	59.02	61.12	59.87
TiO_2	0.21	0.27	0.28	0.35	0.32	0.05	0.25
Al_2O_3	30.01	27.07	30.36	27.58	28.58	27.86	28.58
FeO	0.49	0.48	0.52	0.88	0.75	0.66	0.63
MnO	0.10	0.28	0.30	0.26	0.29	0.38	0.27
MgO	<dl	<dl	<dl	<dl	<dl	<dl	<dl
CaO	0.28	0.40	0.37	0.46	0.33	0.22	0.34
SrO	0.50	0.04	0.72	0.00	0.31	0.35	0.32
Na_2O	2.61	6.94	2.25	4.94	5.30	3.67	4.28
K_2O	3.66	5.66	5.01	6.49	4.95	5.36	5.19
P_2O_5	0.30	0.15	0.54	0.15	0.16	0.33	0.27
Total	100.00	100.00	100.00	100.00	100.00	100.00	100.00

CIPW norms

q	32.81	-	27.43	4.96	9.07	19.11	18.68
c	21.91	8.58	21.43	12.01	14.40	16.16	15.75
or	21.80	33.82	29.88	38.57	29.44	31.95	30.91
ab	22.20	51.09	19.23	42.02	45.13	31.29	35.16
an	-	2.88	-	1.34	0.60	-	1.61
ne	-	4.51	-	-	-	-	4.51
wo	-	1.50	-	0.32	-	-	0.91
hd	-	1.81	-	2.87	-	-	2.34
opx	0.29	-	0.58	-	0.39	1.04	0.58
fs	0.74	-	1.05	-	1.39	2.02	1.30
il	0.40	0.52	0.55	0.67	0.61	-0.10	0.44
ap	0.71	-0.36	1.30	0.35	0.38	0.79	0.53
fr	-	0.03	-	-	-	-	0.03